UNIVERSITEIT VAN PRETORIA
UNIVERSITY OF PRETORIA
YUNIBESITHI YA PRETORIA

The *in-silico* evaluation and synthesis of silicon-based analogues of the cholinesterase inhibitor Donepezil

by

Sergio Lovisa

Submitted in partial fulfilment of the requirements for the degree

Magister Scientiae

In the Faculty of Natural and Agricultural Science

University of Pretoria

Pretoria

May 2020

Supervisor: Dr Darren L. Riley

Co-Supervisor: Dr Jenny-Lee Panayides

© University of Pretoria

Acknowledgements

Thank you to my supervisors Darren and Jenny for being patient and always willing to explain the finer details of chemistry and sharing their experience of their time from their postgrad studies.

I would like to thank Sasol for sponsoring my bursary which made my postgraduate studies possible.

I am forever grateful to my friends and family, especially to my mother, father and brothers who was always there to listened to my ranting when things were going disastrous or swell, for their unyielding support and encouragement.

I would like to thank Wynand for always hearing me out and bouncing ideas off him and always being there to give me a hand in the lab when I really needed it. Thank you for always starting the day with me with a strong cup of java before the day's work. Love you lots my funny butt.

© University of Pretoria

Declaration

I, Sergio Lovisa, declare that the dissertation, which I hereby submit for the degree MSc. Chemistry at the University of Pretoria, is my own work and has not previously been submitted by me for a degree at this or any other institution.

Dr Frikkie Malan at the University of Pretoria recorded and solved the crystal structure presented in this dissertation.

All mass spectrums were recorded by the water lab at University of Pretoria by Madelien Wooding, however, sample preparation was completed by myself.

Signature: 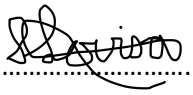

Date: 02-07-2020

© University of Pretoria

Abstract

Alzheimer's disease (AD) is a multi-factorial and irreversible progressive neurodegenerative disease of growing social and financial concern. Donepezil is one of the best therapeutic drugs for the alleviation of the symptoms associated with AD available today, due to its competitive inhibition against both acetylcholinesterase (AChE) activity and AChE induced Aβ aggregation. The use of silicon as an alternative to carbon in medicinal chemistry has become a useful tool to increase the lipophilicity and absorption of drug molecules. In many literature examples silicon has been shown to increase blood brain barrier (BBB) penetration of molecules. This study was undertaken to identify potential lead compounds based on the donepezil scaffold with incorporated silicon groups for increase lipophilicity and BBB penetration through *in-silico* methods.

The study utilized the Schrödinger suite to develop and validate a method for the screening of silylated derivatives of donepezil for inhibition of AChE. A typical workflow was first used as described in literature, whereby the prepared ligands where docked using Glide XP into the prepared protein as the first screening step and prime MM-GBSA as the second step. It was then discovered in literature that improved models could be produced by introducing ConfGen and macro model minimization into the workflow as provided in the Schrödinger suite. The new workflow model was then validated by screening a small library of known actives compounds (against AChE) in the new model and the scored ligands were analysed through the enrichment task within the Schrödinger suite. The enrichment function compares the scored ligands against a list of the known active compounds sorted from highest to lowest activity for comparison. Additional enrichment scores are then assigned to each ligand to assess which model performed well in selecting the higher activity molecules first over molecules with lower activity.

Several ligand scaffolds were identified which are predicted to have improved and comparable binding energies to donepezil (-72.990). The most promising *in silico* leads identified have the indanone ring system of donepezil replaced with a silylated acetophenone ring which is linked to the benzyl piperidine ring system by either an ether (-75.736) or β-keto (-71.922) linker. In both instances *O*-silylation of the indanone ring system showed the best binding scores. In addition, *O*-silylation of the indanone moiety and *C*-silylation of the benzyl moiety of donepezil also showed great promise with comparable scores to donepezil.

© University of Pretoria

Access to several promising silylated analogues was attempted with limited success. The isolation of the acetophenone ether linker derivative (*Z*)-2-((1-benzylpiperidin-4-yl)methoxy)-1-phenylethenol was achieved. In addition, the formation of (*Z*)-2-(2-((1-benzylpiperidin-4-yl)methoxy)-1-hydroxyvinyl)phenol occurred, but as a mixture of inseparable products. The desired analogues were shown to be synthetically accessible, however, the synthetic procedures still require reaction optimisation to produce the ligands in sufficient quantity and quality for biological testing and further derivatisation.

© University of Pretoria

Table of Contents

Acknowledgements i
Declaration ii
Abstract iii
Chapter 1 Introduction to Alzheimer's disease 1
1.1 Alzheimer's disease: 1
1.1.1 What is Alzheimer's disease? 1
1.1.2 History of the disease 1
1.1.3 Types of Alzheimer's disease 1
1.1.4 Why is Alzheimer disease a problem? 2
1.2 Hypotheses 3
1.2.1 Tau protein hypothesis 3
1.2.2 Oxidative stress hypothesis 4
1.2.3 Metal ions hypothesis 6
1.2.3.1 Essential metal ions 6
1.2.3.2 Non-essential metal ions 7
1.2.4 Inflammatory hypothesis 7
1.2.4.1 Astrocytes 8
1.2.5 Cholinergic hypothesis 10
1.2.5.1 History 10
1.2.5.2 Pathogenesis 10
1.2.5.3 Acetylcholine metabolic cycle: 11
1.2.5.4 Acetylcholinesterase catalytic site 12
1.2.6 β-Amyloid cascade hypothesis 13
1.2.6.1 Pathogenesis 14
1.2.6.2 Acetylcholine esterase PAS 16
1.3 Treatment and therapies 16
1.4 Duel AChE and PAS inhibitors 17
1.5 Multi-target AD inhibitors 20
1.6 Donepezil 21
1.6.1 Synthesis of donepezil[53] 23
Chapter 2 Silicon chemistry 24
2.1 Silicon as an element 24
2.2 Silicon in medicinal chemistry 24
2.3 Literature review 25
2.3.1 Alternative metabolic pathways with silicon analogs 25

© University of Pretoria

2.3.2 Transition state mimics 26
2.3.3 Increase in electropositivity 27
2.3.4 Increased lipophilicity 28
Chapter 3 Computational modelling 31
3.1 Computational chemistry 31
3.1.1 Structural based drug design 32
3.1.1.1 Models based on force fields 32
3.1.1.2 Quantum mechanical models 33
3.1.2 Ligand based drug design 34
3.2 Docking based virtual screening 34
3.2.1 Schrödinger Suite 35
3.2.1.1 Prime MM-GBSA 35
3.2.1.1 Force field 36
3.3 Model assessment 36
3.3.1 Enrichment factors 36
3.3.1.1 Enrichment factor (EF) 36
3.3.1.2 Rough initial enrichment (RIE) 37
3.3.1.3 Area under the accumulative curve (AUAC) 37
3.3.1.4 Receiver operating characteristic (ROC) Curves 38
3.3.1.5 Boltzmann-enhanced discrimination of ROC (BEDROC): 40
3.4 Selected case studies 41
3.5 Proposed virtual screening workflow 48
3.6 Aims and Objectives 49
3.6.1 Computational study 49
3.6.2 Synthesis of identified scaffolds 50
Chapter 4 Computational results 51
4.1 General 51
4.2 Tasks utilised in the Schrodinger suite 52
4.2.1 Protein preparation wizard[91] 52
4.2.2 Grid generation[91] 52
4.2.3 Ligand preparation (LigPrep)[91] 52
4.2.4 ConfGen[97] 53
4.2.5 Glide[93] 53
4.2.6 Minimisation[98] 53
4.2.7 Prime-MM-GBSA[96] 53
4.2.8 Enrichment[96] 54

© University of Pretoria

4.3 Initial Model development 54
4.4 Ligand selection for validation of workflow 56
4.5 Optimisation of the standard workflow 56
4.5.1 Results 57
4.6 Validation of new models 60
4.6.1 Results 61
4.7 Optimisation of combined workflow parameters 62
4.8 Enzyme selection and comparison 64
4.8.1 Structural comparison 65
4.8.1.1 Tetronarce californica[52] 65
4.8.1.2 Homo sapiens[35,36] 66
4.8.1.3 Comparison 67
4.8.2 Screening comparison 68
4.9 Computational results 70
4.9.1 Fragment **I** - Indanone derivatives 71
4.9.1.1 O-Silylations 71
4.9.1.1.1 Silyl derivatives at position 5 71
4.9.1.1.2 Silyl derivatives at position 6 73
4.9.1.1.3 Bis and tethered silyl derivatives 74
4.9.1.2 Sila derivatives containing silicon-carbon bonds 75
4.9.1.2.1 Derivative containing silicon-carbon bonds at position 4 76
4.9.1.2.2 Derivatives containing silicon-carbon bonds at position 5 77
4.9.1.2.3 Derivatives containing silicon-carbon bonds at position 6 79
4.9.1.2.4 Derivatives containing silicon-carbon bond at position 7 81
4.9.2 Fragment **II** - Indanone linker derivatives 83
4.9.3 Fragment **III** - Piperidine derivatives 86
4.9.4 Fragment **IV** – Piperidine benzyl-linker derivatives 88
4.9.5 Fragment **V** - Benzyl derivatives 89
4.9.5.1 Ortho, Meta, Para substitution at 0 Å MM-GBSA 90
4.9.5.2 Increased flexibility at 1 Å MMG-BSA 92
4.9.5.2.1 Ortho substitution 93
4.9.5.2.2 Meta substitution 96
4.9.5.2.3 Para substitution 98
4.9.6 Acetophenone derivatives 101
4.9.6.1 β-Diketo-system 101
4.9.6.2 Ether-linkage 104

© University of Pretoria

4.9.7 Conclusion 108
Chapter 5 Synthesis discussion and results 111
5.1 Introduction 111
5.1.1 The synthesis of donepezil[53] 111
5.1.2 Synthesis of silylated analogues 112
5.2 Validation of synthetic methodology through the synthesis of donepezil 113
5.2.1 Benzylation of ethyl isonipecotate (**32**) to prepare ester (**31**)[53] 113
5.2.2 Reduction of ester (**31**) to alcohol (**30**)[53] 114
5.2.3 Swern oxidation of alcohol (**30**) to aldehyde (**28**)[53] 115
5.2.4 Aldol condensation of aldehyde (**28**) and dimethoxy indanone (**29**) to prepare alkene (**27**)[53] 117
5.2.5 Reduction of alkene (**27**) to afford donepezil (**3**)[53] 118
5.2.5.1 Approach 1 118
5.2.5.2 Approach 2 118
5.3 Indanone moiety derivatisation 120
5.3.1 *O*-Silylated scaffolds 120
5.3.1.1 Mono demethylation of dimethoxy indanone[103] 121
5.3.1.2 Di-demethylation of the dimethoxyindanone[103] 124
5.3.1.3 O-Silylation of mono-hydroxy indanone (**244**) 125
5.3.1.4 O-Silylation of dihydroxy indanone (**245**) 126
5.3.1.5 Aldol condensation of aldehyde (**28**) and silyl protected indanone (**246**)[53] 127
5.3.2 *C*-Silylated scaffolds 128
5.3.2.1 Bromination of 1-indanone (**251**)[104] 129
5.3.2.2 C-silylation of bromoindanone[105] 130
5.3.3 Conclusion 131
5.4 Benzyl moiety derivatization 131
5.4.1 Donepezil synthesis route[53] 132
5.4.1.1 Benzylation of ethyl isonipecotate with halobenzyl groups[53] 132
5.4.1.2 Reduction of esters (**261** and **262**) to alcohols (**263** and **264**)[53] 133
5.4.1.3 Swern oxidation of alcohols (**263** and **264**) to aldehydes (**265** and **266**)[53] 134
5.4.1.4 Aldol condensation of aldehydes (**265** and **266**) with dimethoxy indanone (**29**) to prepare alkenes (**267** and **268**)[53] 135
5.4.1.5 C-Silylation of alkene (**268**)[105] 136
5.4.2 *C*-Silylation of halo-toluenes 137
5.4.2.1 Approach 1 138
5.4.2.2 Approach 2 138

© University of Pretoria

5.4.3 Conclusion 139
5.5 Acetophenone replacement of the indanone moiety 139
5.5.1 Acetophenone analogues of donepezil 139
5.5.1.1 Aldol condensation of acetophenone and aldehyde (**28**) to prepare alkene (**274**)[53] 140
5.5.1.2 Chloride (**243**) substitution with acetophenone (**275**) to prepare alkane (**276**) 140
5.5.2 β-Diketo linkage 141
5.5.2.1 O-Silylation of hydroxy acetophenone (**277** and **278**)[120] 141
5.5.2.2 Claisen condensation of O-silylated acetophenones (**279** and **280**) with carboxylate (**31**)[106] 142
5.5.3 Ether-linkages 143
5.5.3.1 α Bromination of acetophenone (**283**)[107] 144
5.5.3.2 Williamson ether formation with bromoacetophenone (**283**) and alcohol (**30**) to prepare ether (**284**) 145
5.5.3.3 Acetyl protection of hydroxy acetophenone[107] 146
5.5.3.4 Bromination of acetylated acetophenone[107] 147
5.5.3.5 Williamson ether formation with bromo acetyl acetophenone (**287** and **288**) and alcohol (**30**) to prepare ether (**289** and **290**) 148
5.5.3.6 Deacetylation of ether (**290**)[107] 149
5.5.3.7 O-Silylation of the mixed ether product[120] 150
5.5.4 Conclusion 151
5.6 Overall Conclusion 151
Chapter 6 Conclusion and future work 153
6.1 Conclusion: 153
6.2 Future work: 153
6.2.1 Computational work: 153
6.2.2 Synthesis work: 156
6.2.2.1 Silyl Indanone analogues alternative routes: 156
6.2.2.1.1 *O*-Silylation (section 5.3.1): 156
6.2.2.1.1 *C*-Silylation (section 5.3.2): 156
6.2.2.2 Silyl Benzyl analogues alternative routes (section 5.4): 157
6.2.2.3 Acetophenone derivatives (section 5.5): 157
Chapter 7 Methodology 158
7.1 General Methods 158
7.2 Purification of Solvents[115] 158
7.3 Experimental procedures 159
7.3.1 Validation of synthetic methodology through the synthesis of donepezil 159

© University of Pretoria

7.3.1.1 Ethyl 1-benzylpiperidine-4-carboxylate (**31**)[53] 159
7.3.1.2 (1-benzylpiperidin-4-yl)methanol (**30**)[53] 160
7.3.1.3 1-benzylpiperidine-4-carbaldehyde (**28**)[53] 160
7.3.1.4 (E)-2-((1-benzylpiperidin-4-yl)methylene)-5,6-dimethoxy-2,3-dihydro-1H-inden-1-one (**27**)[53] 161
7.3.1.5 Preparation of donepezil (**3**) 162
7.3.1.5.1 Approach 1 162
7.3.1.5.1.1 2-((1-benzylpiperidin-4-yl)methyl)-5,6-dimethoxy-2,3-dihydro-1*H*-inden-1-one (**3**) 162
7.3.1.5.2 Approach 2 163
7.3.1.5.2.1 (1-benzylpiperidin-4-yl)methyl methanesulfonate (**240**) 163
7.3.1.5.2.2 (1-benzylpiperidin-4-yl)methyl 4-methylbenzenesulfonate (**241**) 164
7.3.1.5.2.3 1-benzyl-4-(bromomethyl)piperidine (**242**) 164
7.3.1.5.2.4 1-benzyl-4-(chloromethyl)piperidine (**243**)[113] 165
7.3.2 Indanone moiety derivatisation 166
7.3.2.1 O-Silylated scaffolds 166
7.3.2.1.1 5-hydroxy-6-methoxy-2,3-dihydro-1*H*-inden-1-one (**244**)[103] 166
7.3.2.1.2 5,6-dihydroxy-2,3-dihydro-1*H*-inden-1-one (**245**)[103] 167
7.3.2.1.3 5-((*tert*-butyldimethylsilyl)oxy)-6-methoxy-2,3-dihydro-1*H*-inden-1-one (**246**) 167
7.3.2.1.4 5-((*tert*-butyldiphenylsilyl)oxy)-6-methoxy-2,3-dihydro-1*H*-inden-1-one (**247**) 168
7.3.2.1.5 5,6-bis((*tert*-butyldimethylsilyl)oxy)-2,3-dihydro-1*H*-inden-1-one (**248**) 169
7.3.2.1.6 (*E*)-2-((1-benzylpiperidin-4-yl)methylene)-5-((*tert*-butyldimethylsilyl)oxy)-6-methoxy-2,3-dihydro-1*H*-inden-1-one (**249**)[53] 169
7.3.2.1.7 (*E*)-2-((1-benzylpiperidin-4-yl)methylene)-5,6-dihydroxy-2,3-dihydro-1*H*-inden-1-one (**Z**)[126] 170
7.3.2.2 C-Silylated scaffolds 171
7.3.2.2.1 6-bromo-2,3-dihydro-1*H*-inden-1-one (**251**)[104] 171
7.3.2.2.2 6-(trimethylsilyl)-2,3-dihydro-1*H*-inden-1-one (**252**)[105] 172
7.3.3 Benzyl moiety derivatization: 172
7.3.3.1 Donepezil synthesis route: 172
7.3.3.1.1 Ethyl 1-(2-chlorobenzyl)piperidine-4-carboxylate (**261**)[53] 172
7.3.3.1.2 Ethyl 1-(4-chlorobenzyl)piperidin-4-carboxylate (**262**)[53] 173
7.3.3.1.3 (1-(2-chlorobenzyl)piperidin-4-yl)methanol (**263**)[53] 174
7.3.3.1.4 (1-(4-chlorobenzyl)piperidin-4-yl)methanol (**264**)[53] 175
7.3.3.1.5 1-(2-chlorobenzyl)piperidine-4-carbaldehyde (**265**)[53] 175
7.3.3.1.6 1-(4-chlorobenzyl)piperidine-4-carbaldehyde (**266**)[53] 176

© University of Pretoria

7.3.3.1.7 (*E*)-2-((1-(2-chlorobenzyl)piperidin-4-yl)methylene)-5,6-dimethoxy-2,3-dihydro-1*H*-inden-1-one (**267**)[53] 177

7.3.3.1.8 (*E*)-2-((1-(4-chlorobenzyl)piperidin-4-yl)methylene)-5,6-dimethoxy-2,3-dihydro-1*H*-inden-1-one (**268**)[53] 178

7.3.3.1.9 (*E*)-5,6-dimethoxy-2-((1-(4-(trimethylsilyl)benzyl)piperidin-4-yl)methylene)-2,3-dihydro-1*H*-inden-1-one (**269**)[105] 179

7.3.3.1.10 (*E*)-5,6-dimethoxy-2-((1-(4-(triethylsilyl)benzyl)piperidin-4-yl)methylene)-2,3-dihydro-1*H*-inden-1-one (**270**)[105] 179

7.3.3.2 C-silylation of halo-toluenes 180

7.3.3.2.1 T*ert*-butyldiphenyl(*p*-tolyl)silane (**272**) 180

7.3.3.2.2 Trimethyl(*p*-tosyl)silane (**273**) 181

7.3.4 Acetophenone replacement of the indanone moiety: 182

7.3.4.1 Donepezil acetophenone analogues: 182

7.3.4.1.1 (*E*)-3-(1-benzylpiperidin-4-yl)-1-(3,4-dimethoxy)prop-2-en-1-one (**274**)[53] 182

7.3.4.1.2 3-(1-benzylpiperidin-4-yl)-1-phenylpropan-1-one (**276**) 182

7.3.5.2 β-diketo linkage: 183

7.3.5.2.1 1-(4-((*tert*-butyldiphenylsilyl)oxy)phenyl)ethanone (**279**) 183

7.3.5.2.2 1-(2-((*tert*-butyldiphenylsilyl)oxy)phenyl)ethenone (**280**) 184

7.3.5.2.3 1-(1-benzylpiperidin-4-yl)-3-(4-((*tert*-butyldiphenylsilyl)oxy)phenyl)propane-1,3-dione (**281**)[106] 184

7.3.5.2.4 1-(1-benzylpiperidin-4-yl)-3-(2-((*tert*-butyldiphenylsilyl)oxy)phenyl)propane-1,3-dione (**282**)[106] 185

7.3.5.3 Ether-linkages: 186

7.3.5.3.1 2-bromo-1-phenylethanone (**283**)[107] 186

7.3.5.3.2 (*Z*)-2-((1-benzylpiperidin-4-yl)methoxy)-1-phenylethenol (**284**) 186

7.3.5.3.3 4-acetylphenylacetate (**285**)[107] 187

7.3.5.3.4 2-acetylphenylacetate (**286**)[107] 188

7.3.5.3.5 4-(2-bromoacetyl)phenylacetate (**287**)[107] 188

7.3.5.3.6 2-(2-bromoacetyl)phenylacetate (**288**)[107] 189

7.3.5.3.7 4-(2-((1-benzylpiperidin-4-yl)methoxy)acetyl)phenyl acetate (**289**) 190

7.3.5.3.8 (*Z*)-2-(2-((1-benzylpiperidin-4-yl)methoxy)-1-hydroxyvinyl)phenol (**291**) 190

7.3.5.3.9 (*Z*)-2-(2-((1-benzylpiperidin-4-yl)methoxy)-1-hydroxyvinyl)phenol (**291**)[107] 191

7.3.5.3.10 2-((1-benzylpiperidin-4-yl)methoxy)-1-(2-((tert-butyldimethylsilyl)oxy)phenyl)ethenone (**292**) 192

7.3.5.3.11 2-((1-benzylpiperidin-4-yl)methoxy)-1-(2-((tert-butyldiphenylsilyl)oxy)phenyl)ethenone (**293**) 192

7.3.5.3.12 2-((1-benzylpiperidin-4-yl)methoxy)-1-(2-((triphenylsilyl)oxy)phenyl)ethenone (**294**) 193

© University of Pretoria

7.3.5.3.13 2-((1-benzylpiperidin-4-yl)methoxy)-1-(2-(((2,3-dimethylbutane-2 yl)dimethylsilyl)oxy)phenyl)ethenone (**295**) 193
Chapter 8 References 194
Appendix A 203
Appendix B 204
B.1 Ethyl 1-benzylpiperidine-4-carboxylate (31) 204
B.1.1 ^{1}H and ^{13}C NMR spectra of compound (31) 204
B.1.2 HRMS spectrum of compound (31) 205
B.1.3 IR spectrum of compound (31) 205
B.2 (1-benzylpiperidin-4-yl)methanol (30) 206
B.2.1 ^{1}H and ^{13}C NMR spectra of compound (30) 206
B.2.2 HRMS spectrum of compound (30) 207
B.2.3 IR spectrum of compound (30) 207
B.3 1-benzylpiperidine-4-carbaldehyde (28) 208
B.3.1 ^{1}H and ^{13}C NMR spectra of compound (28) 208
B.3.2 HRMS spectrum of compound (28) 209
B.3.3 IR spectrum of compound (28) 209
B.4 (*E*)-2-((1-benzylpiperidin-4-yl)methylene)-5,6-dimethoxy-2,3-dihydro-1*H*-inden-1-one (27) 210
B.4.1 ^{1}H and ^{13}C NMR spectra of compound (27) 210
B.4.2 HRMS spectrum of compound (27) 211
B.4.3 IR spectrum of compound (27) 211
B.5 1-benzyl-4-(chloromethyl)piperidine (243) 212
B.5.1 ^{1}H and ^{13}C NMR spectra of compound (243) 212
B.6 5-hydroxy-6-methoxy-2,3-dihydro-1*H*-inden-1-one (244) 213
B.6.1 ^{1}H and ^{13}C NMR spectra of compound (244) 213
B.6.2 HRMS spectrum of compound (244) 214
B.6.3 IR spectrum of compound (244) 214
B.6.4 XRD Resolved image of compound (244) 215
B.7 5,6-dihydroxy-2,3-dihydro-1*H*-inden-1-one (245) 216
B.7.1 ^{1}H and ^{13}C NMR spectra of compound (245) 216
B.7.2 HRMS spectrum of compound (245) 217
B.7.3 IR spectrum of compound (245) 217
B.8 5-((tert-butyldimethylsilyl)oxy)-6-methoxy-2,3-dihydro-1*H*-inden-1-one (246) 218
B.8.1 ^{1}H and ^{13}C NMR spectra of compound (246) 218
B.8.2 HRMS spectrum of compound (246) 219
B.8.3 IR spectrum of compound (246) 219

© University of Pretoria

B.9 5-((tert-butyldiphenylsilyl)oxy)-6-methoxy-2,3-dihydro-1*H*-inden-1-one (247) 220
B.9.1 ^{1}H and ^{13}C NMR spectra of compound (247) 220
B.9.2 HRMS spectrum of compound (247) 221
B.10 5,6-bis((tert-butyldimethylsilyl)oxy)-2,3-dihydro-1*H*-inden-1-one (248) 222
B.10.1 ^{1}H and ^{13}C NMR spectra of compound (248) 222
B.10.2 HRMS spectrum of compound (248) 223
B.10.3 IR spectrum of compound (248) 223
B.11 6-bromo-2,3-dihydro-1*H*-inden-1-one (251) 224
B.11.1^{1}H and ^{13}C NMR spectra of compound (251) 224
B.11.2 IR spectrum of compound (251) 225
B.12 Ethyl 1-(2-chlorobenzyl)piperidine-4-carboxylate (261) 226
B.12.1 ^{1}H and ^{13}C NMR spectra of compound (261) 226
B.12.2 HRMS spectrum of compound (261) 227
B.12.3 IR spectrum of compound (261) 227
B.13 Ethyl 1-(4-chlorobenzyl)piperidin-4-carboxylate (262) 228
B.13.1 ^{1}H and ^{13}C NMR spectra of compound (262) 228
B.13.2 HRMS spectrum of compound (262) 229
B.13.3 IR spectrum of compound (262) 229
B.14 (1-(2-chlorobenzyl)piperidin-4-yl)methanol (263) 230
B.14.1 ^{1}H and ^{13}C NMR spectra of compound (263) 230
B.14.2 HRMS spectrum of compound (263) 231
B.14.3 IR spectrum of compound (263) 231
B.15 (1-(4-chlorobenzyl)piperidin-4-yl)methanol (264) 232
B.15.1 ^{1}H and ^{13}C NMR spectra of compound (264) 232
B.15.2 HRMS spectrum of compound (264) 233
B.15.3 IR spectrum of compound (264) 233
B.16 1-(2-chlorobenzyl)piperidine-4-carbaldehyde (265) 234
B.16.1 ^{1}H and ^{13}C NMR spectra of compound (265) 234
B.16.2 HRMS spectrum of compound (265) 235
B.16.3 IR spectrum of compound (265) 235
B.17 1-(4-chlorobenzyl)piperidine-4-carbaldehyde (266) 236
B.17.1 ^{1}H and ^{13}C NMR spectra of compound (266) 236
B.17.2 HRMS spectrum of compound (266) 237
B.17.3 IR spectrum of compound (266) 237
B.18 (*E*)-2-((1-(4-chlorobenzyl)piperidin-4-yl)methylene)-5,6-dimethoxy-1-indanone (267) 238
B.18.1 ^{1}H and ^{13}C NMR spectra of compound (267) 238

© University of Pretoria

B.18.2 HRMS spectrum of compound (267) 239
B.18.3 IR spectrum of compound (267) 239
B.19 1-(4-((*tert*-butyldiphenylsilyl)oxy)phenyl)ethanone (279) 240
B.19.1 ^{1}H and ^{13}C NMR spectra of compound (279) 240
B.19.2 HRMS spectrum of compound (279) 241
B.19.3 IR spectrum of compound (279) 241
B.20 1-(2-((*tert*-butyldiphenylsilyl)oxy)phenyl)ethenone (280) 242
B.20.1 ^{1}H and ^{13}C NMR spectra of compound (280) 242
B.20.2 HRMS spectrum of compound (280) 243
B.20.3 IR spectrum of compound (280) 243
B.21 2-bromo-1-phenylethanone (283) 244
B.21.1 ^{1}H and ^{13}C NMR spectra of compound (283) 244
B.21.2 IR spectrum of compound (283) 245
B.22 (*Z*)-2-((1-benzylpiperidin-4-yl)methoxy)-1-phenylethenol (284) 246
B.22.1 ^{1}H and ^{13}C NMR spectra of compound (284) 246
B.22.2 HRMS spectrum of compound (284) 247
B.22.3 IR spectrum of compound (284) 247
B.23 4-acetylphenylacetate (285) 248
B.23.1 ^{1}H and ^{13}C NMR spectra of compound (285) 248
B.23.2 IR spectrum of compound (285) 249
B.24 2-acetylphenylacetate (286) 250
B.24.1 ^{1}H and ^{13}C NMR spectra of compound (286) 250
B.24.2 IR spectrum of compound (286) 251
B.25. 4-(2-bromoacetyl)phenylacetate (287) 252
B.25.1 ^{1}H and ^{13}C NMR spectra of compound (287) 252
B.25.2 IR spectrum of compound (287) 253
B.26 2-(2-bromoacetyl)phenylacetate (288) 254
B.26.1 ^{1}H and ^{13}C NMR spectra of compound (288) 254
B.27 (*Z*)-2-(2-((1-benzylpiperidin-4-yl)methoxy)-1-hydroxyvinyl)phenol (291) 255
B.27.1 ^{1}H and ^{13}C NMR spectra of compound (291) 255
B.27.2 HRMS spectrum of compound (291) 256
B.27.3 IR spectrum of compound (291) 256

© University of Pretoria

Chapter 1 Introduction to Alzheimer's disease

1.1 Alzheimer's disease:

1.1.1 What is Alzheimer's disease?

Alzheimer's disease (AD) was first characterised by Alois Alzheimer in 1907, as an irreversible and progressive neurodegenerative disease and one of the most common forms of dementia.[1,2] AD is associated with severe behavioural abnormalities, lowered cognitive function as well as progressive and severe memory loss.[1,5] AD is a multi-factorial disease, with many different physiological changes in the brain, making the pathogenesis of the disease difficult to determine.[1] The most prominent characteristics of the AD pathology are chronic inflammation, the formation of senile plaques and neurofibrillary tangles (NFT), elevated oxidative stress, disturbance of homeostasis of essential metal ions and a diminished cholinergic system with atrophy and loss of synapses.[6]

1.1.2 History of the disease

Alois Alzheimer first described the disease in the early 1900's when a 51-year-old woman by the name of Auguste Deter showed signs that she was suffering from hallucinations, psychosocial and cognitive impairment and disorientation.[7,8] After a post-mortem of her brain it was observed that her cerebral cortex had thinned and extracellular deposits and neurofibrillary tangles were present. The latter two are characteristic hallmarks of the disease, now known as senile plaques.[8]

1.1.3 Types of Alzheimer's disease

There are currently two forms of AD disease, familial and sporadic. In the familial variant genetic studies show mutations in the amyloid precursor protein (APP), presenilin 1 and presenilin 2 genes, which is proposed to be linked to errors in the functioning of the β-amyloid cascade.[9–11] Presenilin 1 and 2 are proteins that function as aspartyl proteases, which catalyse the severance of APP close to the γ-secretase site.[10,11] Mutations in these genes increases the ratios of $A\beta_{42}$: $A\beta_{40}$ species, advancing the pathology of the disease.[10,11] Sporadic AD is age-related and multi-factorial, making the initiation of the pathology difficult to identify.[1] The familial variant has the lowest prevalence accounting for only 5 % of all cases with the remainder comprised of the sporadic form.[9] Familial AD typically has a

© University of Pretoria

much earlier onset of the pathology and commonly accounts for individuals suffering from the disease before the age of 60.

1.1.4 Why is Alzheimer disease a problem?

AD is of a growing international social and financial concern, particularly, as the average life expectancy is increasing with improved health care and medical advancements. In 2015 approximately 44 million people worldwide were estimated to have dementia and this value is expected to have increased by 71% by 2050.[12] It is estimated that 5.7 million Americans aged 65 and over suffered from AD in 2018, and by 2050 the number is estimated to increase to 13.8 million in America (Figure 1.1).[13] In 2018, an estimated expenditure of $277 billion was spent on medical services and health care for people with dementia of age 65 and older in the USA.[13] In 2015 an estimated 2.13 million people of age 60 and older in sub-Saharan Africa (SSA) suffered from AD,[14] and it is predicted that by 2050 this will increase to 7.62 million.[14] The total cost of dementia was estimated at $6.2 billion in 2015 in SSA.[14] Unfortunately, statistical information for SSA is difficult to obtain as many people afflicted by the disease remain undiagnosed due to lack of awareness and/or access to medical services.

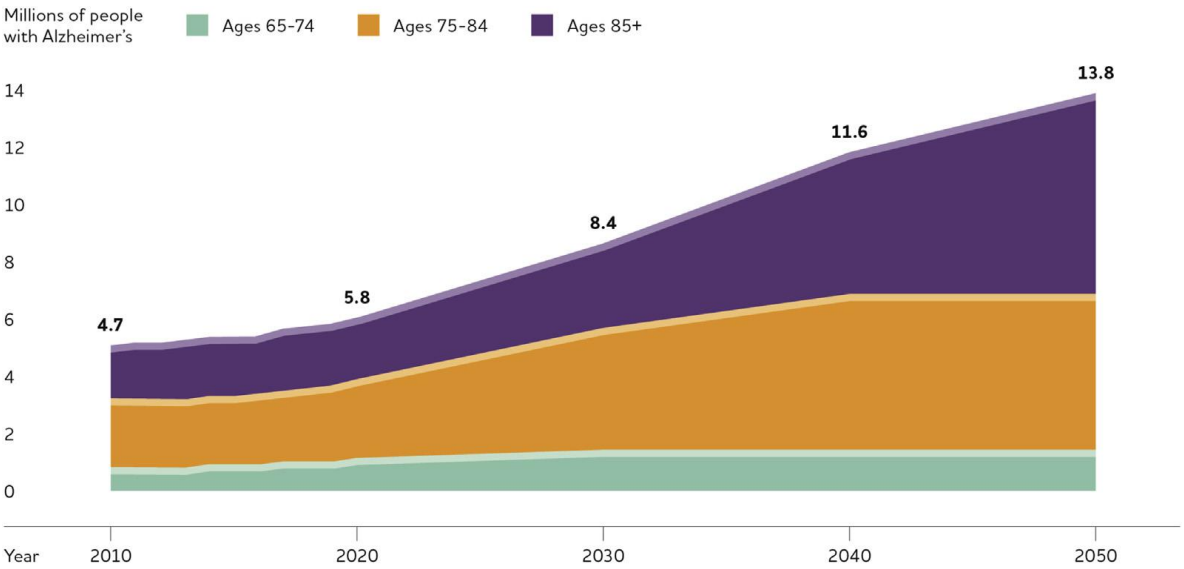

Figure 1.1: Expected prevalence increase of AD in America from 2010 to 2050. Reproduced from Alzehimer Association report 2018.[13]

© University of Pretoria

1.2 Hypotheses

Current evidence suggests multiple hypotheses for the pathogenesis of AD. Established hypotheses may be separated as: a deficit in cholinergic neurotransmitters (cholinergic hypothesis);[1,5,15–17] aggregation of amyloid beta plaques;[15,16] and hyperphosphorylation of tau proteins.[15,16,18] More recent hypotheses under investigation include: oxidative stress injury from reactive oxygen species reacting with polyunsaturated fatty acids, leading to cell apoptosis and lipid peroxidation (oxidative stress hypothesis);[16] influx of toxic metal ions due to degradation of the regulation system, effecting oxidative stress response of mitochondria and misfolding of proteins;[16] and chronic inflammatory response caused by large populations of mononuclear leucocytes, which over produce inflammatory response factors, killing neighbouring neurons (inflammatory hypothesis).[16]

1.2.1 Tau protein hypothesis

Tau are microtubule associated proteins (MAP), which regulate the spatial organisation, assembly and dynamic behaviour of microtubules within the cell.[19] Tau proteins are phosphoproteins that are highly soluble and are predominantly found in the axons of neurons.[19] Tau has six isoforms in the adult brain with the tau gene consisting of 15 exons, with various splicing patterns forming the 6 isoforms.[19,20] Tau proteins stabilise microtubules by binding with their microtubule binding domains, which requires the tau protein to have been partially phosphorylated.[21] Tau has a proline rich *N*-terminal that is phosphorylated and hyperphosphorylated, that can compete with ionic interactions that are responsible for critical structural interactions.[21] Microtubules consist of dimer units of α-tubulin and β-tubulin, which are globular proteins and are very dynamic as they are continuously assembled and disassembled.[22] They have a number of important roles from maintaining cell structure, transportation of organelles, cell locomotion and movement.[22]

One of the pathological hallmarks of AD is the presence of insoluble structures called neurofibrillary tangles (NFTs) in the brain, which are composed of agglomerated insoluble hyperphosphorylated tau proteins.[19] This observation led to the tau hypothesis, in which modification of the tau protein is seen as an important factor in the pathology of the disease.[15,18] Neurodegeneration induced by tau is likely to be a combination of the formation of toxic species (soluble oligomeric tau molecules) and loss of function (microtubules).[19] Hyperphosphorylation of tau proteins reduces the binding affinity to microtubules, causing dissociation of the tau microtubule complex and diminishing microtubule function leading to neuronal loss and synaptic dysfunction.[19] Hyperphosphorylated tau proteins can

© University of Pretoria

assemble into varying filaments that form NFTs, but can also sequester standard tau proteins allowing for aggregation within the cell. [18,19] Aggregation of the hyperphosphorylated tau proteins is detrimental to microtubule function, as the microtubules are no longer stabilised and they cannot maintain their structure leading to cell structure deterioration and neuronal loss (Figure 1.2).[18,19] Alternative modification of tau molecules can also advance the pathology and include ubiquitination, glycosylation, truncation and *O*-Glc*N*Acylation.[19] The factors responsible for the aggregation of the protein are not yet well understood, as many potential changes within the neurons can cause or enhance the amount of aggregation of the protein.[18]

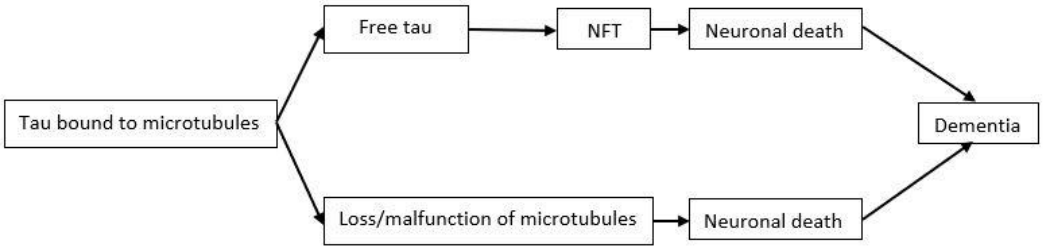

Figure 1.2: Schematic diagram of the cause and consequence of the Tau hypothesis. Recreated from Mohandas E, Rajmoham V, Raghunath B, 2009.[23]

1.2.2 Oxidative stress hypothesis

Oxidative stress is caused by reactive oxygen and nitrogen species (ROS), which have a beneficial role in signalling pathways, however, can also play a detrimental role initiating the deterioration of cell structures such as DNA, cell walls and organelles.[6] All living cells typically have a reductive environment and try to maintain this equilibrium environment through homeostasis by detoxifying, removal or repairing the damage inflicted by the ROS.[24] When the equilibrium is disturbed an overproduction or decrease in detoxification of ROS such as peroxides and free radicals occurs, leading to the damage of various cell components and structures. The corresponding affected cells are then said to be under oxidative stress.[24] The brain is particularly susceptible to oxidative stress as it consumes 20 % more oxygen in comparison to the total consumption of the body. The brain is made up of neurons, which contain a high polyunsaturated fat content, that can react with ROS causing peroxidation of lipids and leading to molecular apoptosis.[6,25] Additionally neurons contain less glutathione which is an antioxidant that reacts with ROS in its reduced form to neutralise the species and is enzymatically reduced to regenerate its antioxidant state.[6,26]

© University of Pretoria

Mounting evidence has shown that oxidative stress precedes the central neuropathological hallmarks of AD and that both NFTs and senile plaques are neuroprotective responses, preventing neuronal loss.[25] This is supported by *in situ* studies which showed that AD subjects with decreased Aβ deposition and NFT (earlier period of AD), had more pronounced oxidative stress.[25] This observation was consistent with cerebrospinal fluids having elevated levels of oxidised nucleic acids within AD subjects within the early stages of the disease.[25] These observations suggest that Aβ deposition is a neuroprotective response to oxidative stress, by the sequestration of reactive metal species and is supported by elevated levels of zinc, copper and iron found within the cores and rims of Aβ deposits.[25] The presence of NFTs in neurons has been shown to result in decreased levels of oxidised nucleic acids compared to neurons with the absence of NFTs.[25] The mechanism of NFTs against oxidative stress is unknown, but high levels of reactive iron species correlates strongly with NFTs, and tau may act as an antioxidant as it can bind both copper and iron.[25]

Aβ accumulations have an oxidant ability due to the accumulation of chelated metal/s, which leads to further oxidative stress, creating a negative feedback loop.[27] Further oxidative stress response is caused by the accumulation of both SP and NFTs leading to and sustaining inflammatory reactions.[27] Chronic inflammation causes neurodegeneration, permanent cell injury and lastly cell death, which all manifest from the early to final stages of AD (Figure 1.3).[27]

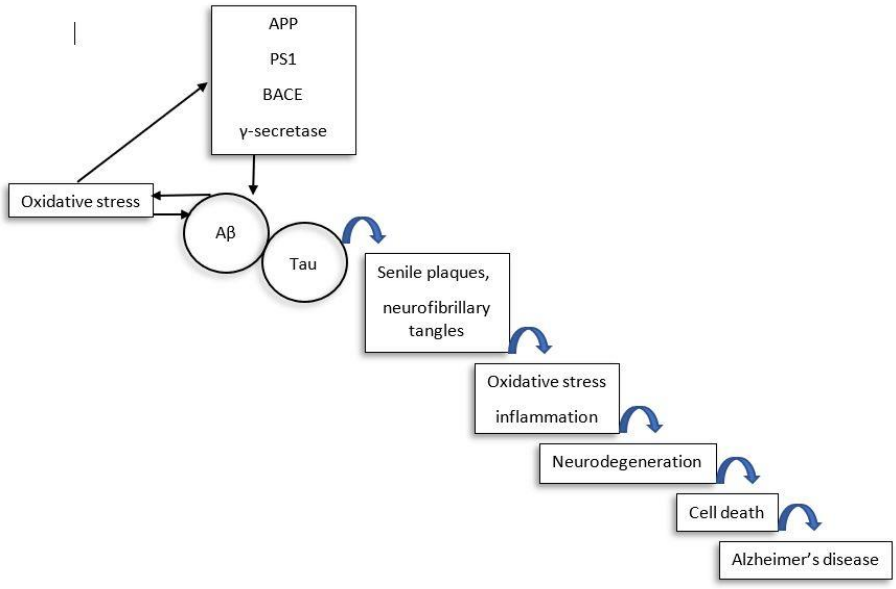

Figure 1.3: Schematic diagram of cause and effect of the oxidative stress hypothesis. Recreated from Domenico P, 2008.[27]

© University of Pretoria

1.2.3 Metal ions hypothesis

Metal ions are of interest as they play an important role in homeostasis and in biological molecules as co-factors or components that regulate or interact with a large number of other molecules.[6,28] The optimal concentration range of essential metal ions is very narrow with only subtle differences between concentrations which would be regarded as toxic vs deficient. As such, strict regulation of the concentrations of essential metal ions is required, while non-essential ions at low concentrations have detrimental effects on essential metal ions physiological functions.[28] Essential metals are iron, zinc and copper, whereas non-essential metals are aluminium, cadmium and lead.[28,29]

1.2.3.1 Essential metal ions

Iron is important as it is a redox active metal that has important roles in DNA synthesis, signalling, respiration, repair, energy metabolism and most importantly oxygen homeostasis.[28] Copper is also a redox active metal and is an essential co-factor for enzyme catalysis, which controls a vast number of regulatory and biochemical functions within a cell.[28] Some of these functions are synaptic transmission, synthesis of catecholamines, immune function, activation of neuropeptides, antioxidant defence and hormones and connective tissue formation.[28,29] Zinc is not a redox active metal, but is important in the modulation of cognitive processes, synaptic plasticity, neuronal function and neurotransmission.[28] The importance of zinc in the brain is accentuated by the fact that the brain has the highest concentrations of zinc in the body, and 70 % of proteins within the brain require zinc for their catalytic or structural functions.[28]

Aging studies have shown that individuals suffering from AD also have increased levels of copper and iron.[6,28] Interestingly, post-mortem examination of brains has shown decreased levels of copper and iron in serum, but an increase of copper, iron and zinc levels in Aβ Plaques and NFT.[28,29] It has also been shown that copper, iron and zinc can enhance Aβ and tau aggregation, which not only interrupts homeostasis of the essential metals, but also increases the toxicity of Aβ Plaques and NFTs.[28,29] The high concentrations of the two redox active metals in both the Aβ Plaques and NFTs act as catalytic sites for redox activity and greatly contribute to oxidative stress (Figure 1.4).[28,29] Zinc entrapped in the Aβ Plaques and NFTs inhibits APP ferroxidase and subsequently increases iron and ROS levels.[28] Zinc has also been shown to promote hyperphosphorylation of tau proteins, by inactivation of tau phosphatases.[28]

© University of Pretoria

1.2.3.2 Non-essential metal ions

Aluminium is a known neurotoxin with high levels of exposure causing cerebral impairment, such as the deterioration of short-term memory.[28,29] A number of studies have shown that areas with water sources high in aluminium have higher AD incidence and mortality and this is further supported by observations that aluminium can promote NFT like structure formation and neurofibrillary degeneration (Figure 1.4).[28,29] Cadmium is an environmental carcinogen and is a heavy metal with the unique property of being water-soluble, which allows it to be concentrated within the food chain.[28] Recent studies have shown a strong association of AD mortality with cadmium blood levels and there is mounting evidence of cadmium being involved in Aβ plague and tau aggregation.[28]

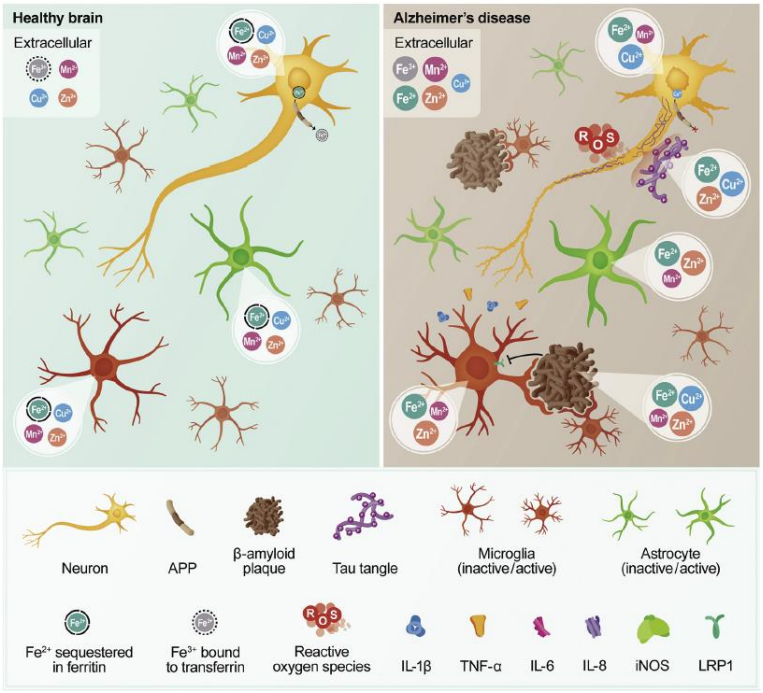

Figure 1.4: Comparison of a healthy brain and an Alzheimer's disease brain in term of the metal ion hypothesis. Recreated from Haut TJ, et al. 2019.[28]

1.2.4 Inflammatory hypothesis

Another pathological hallmark for AD is chronic inflammation of the brain, which is characteristic of elevated levels of macrophages and mononuclear leucocytes within the central nervous system (CNS).[16] Post-mortem examinations of AD patients showed an over expression of pro-inflammatory cytokines and acute phase protein in the brain tissue as compared to normal brain levels.[16] The main cause of the inflammatory response are astrocytes and microglia, which produce various pro-inflammatory mediators and when released can cause cell death of adjacent neurons.[16] In the later

© University of Pretoria

stages of AD the increased burden of oxidative stress causes upregulation of immune cell mediators, which in turn induces overproduction of pro-inflammatory promotors leading to inflammation.[30] A positive feed-back loop is induced by the inflammatory cascade being stabilised and leading to chronic inflammation and cell damage or neuronal death (Figure 1.5).[30]

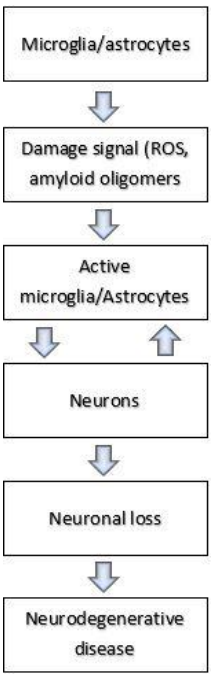

Figure 1.5 Proposed feedback loop between neurodegeneration and immune cells. Recreated from E Bagyinszky, et al. 2017.[30]

1.2.4.1 Astrocytes

Astrocytes compose 25 % of the volume of the brain and are the most abundant cell within the CNS.[10,30] Astrocytes play an important role in: blood brain barrier (BBB) maintenance and formation, homoeostasis regulation, synaptogenesis, glutamate turnover and ion balance maintenance.[10,30] Post mortem examination of AD brains has shown the presence of reactive astrocytes, which are formed by increased levels of glial fibrillary acidic protein and hypertrophy, while activated astrocytes were observed around Aβ Plaques.[10]

Astrogliosis occurs when the levels of astrocytes increase to abnormal amounts caused by neuronal death, this can be caused by several factors including neurodegenerative diseases, trauma to the CNS and infection.[10] A correlation between cognitive decline and the degree of astrogliosis has been noted in AD.[10] The role of astrogliosis in the pathogenesis of AD was supported as activated astrocytes upregulate an acute-phase protein called a1-antichymotrypsin, which enhances tau phosphorylation and Aβ deposition.[10] Additionally, astrocytes associated with Aβ Plaques can express beta-secretase 1

© University of Pretoria

(BACE-1), which is normally restricted to neurons.[10] As a result neurons become increasingly vulnerable as the neuro protective function of reactive astrocytes seems to be abandoned, making the neurons susceptible to oxidative stress and excitotoxicity.[10] Aβ deposits prompt astrocytes to release ROS and inflammatory cytokines, tumour necrosis factor alpha (TNFα) and interleukin 1 beta (IL-1β), in addition the Aβ fragments on their own stimulate an inflammatory response through nuclear factor kappa B (NF-κB) and calcineurin within the brain.[9,10,30] Furthermore, TNFα and IL-1β cause astrocyte activation as a secondary response, which compromises the longstanding survival of the neurons.[9,10]

1.2.4.2 Microglia

Microglia are the primary cells in the CNS immune system, they execute phagocytosis, release cytotoxic mediators and act as antigen-presenting cells.[9,10] The CNS is rich in microglia, but the substantia nigra and hippocampus have the highest concentrations and microglia are crucial for development of the CNS and CNS homeostasis.[10] Microglia within a resting state release growth factors, which aid in synaptic pruning, neurogenesis, neuroprotection and formation of the CNS at the embryo stage.[9,10]

Microglia are pro-inflammatory instead of phagocytic in AD brains, as phagocytosis of microglia cells is diminished in pro-inflammatory regions, reducing Aβ clearance by micoglia.[10] Studies using animal models have shown neuronal loss mediated by tau proteins due to neuroinflammation; this was supported by the removal of tau-positive neurons before NFT formation by activated microglia in transgenic mice models.[10] Transgenic model studies have shown that tau pathology is aggravated by peripheral inflammation induced by lipopolysaccharides through the cyclin-dependant kinase 5 (CDK5) mediated pathway, as well as giving support that amyloidosis is intensified by activated microglia.[10,30] Aβ peptides can bind as lipopolysaccharides giving rise to peripheral inflammation and Aβ deposition further increases inflammation through activated microglia leading to chronic inflammation.[30]

© University of Pretoria

1.2.5 Cholinergic hypothesis

1.2.5.1 History

In 1936 the Nobel prize was shared by Henry Dale and Otto Loewi for the characterisation and identification of acetylcholine, from their pioneering work on chemical neurotransmission.[5] The discovery of cholinergic neurotransmission was critical, as a cholinergic hypothesis was described for several brain functions and dysfunctions such as, traumatic brain injury, schizophrenia, depression, delirium to sleep regulation and affective disorders.[5] The most renowned dysfunction associated with the cholinergic hypothesis was its connection to dementia and cognitive function.[5] This connection was established by early pharmacologic studies on the interference of acetylcholine using anticholinergic drugs, which caused memory deficits and amnestic effects similar to those in non-demented elderly subjects.[5]

The decades between the mid-sixties and eighties is considered the golden age of neurotransmitters, as the studies of immunohistochemistry, electrophysiology, morphology, biochemistry and pharmacology jointly discovered and characterised the most important neurotransmitters and their respective receptors, as well as "delineating the chemical neuroanatomy of the brain".[5] World research efforts led to the idea that neural disturbances and neuropathologies are connected to altered neurotransmitter systems.[5] Alterations within neurochemical pathways from examined post-mortem brains of patients afflicted with various neuropathologies were studied with increasing interest in the hopes that the knowledge gained could be used to find treatments for the diseases.[5] Treatments were designed based on the idea of correcting the neurochemical alteration found in the post-mortem examinations of the afflicted patients. In the seventies and eighties this approach was applied to AD patients, which led to the emergence and momentum of the cholinergic hypothesis.[5]

1.2.5.2 Pathogenesis

Post mortem examination of the brains of AD patients showed low/lowered levels of the neurotransmitter acetylcholine in the basal forebrain, the nucleus basalis magnocellularis of Meynert, cortex and the hippocampus.[1,15] This phenomenon was discovered to be caused by a decrease in the activity of choline acetyltransferase and a reduction in the depolarization-induced acetylcholine release out of, and uptake into, the neuronal cells.[5] The number of cholinergic projection neurons were also observed to be significantly reduced in the nucleus basalis of Meynert, suggesting that the

© University of Pretoria

deterioration the cholinergic connection between the nucleus of Meynert and the cortex and hippocampus, was a major pathogenesis event of AD.[5] The pyruvate dehydrogenase complex, an enzyme essential in the synthesis of acetylcholine was observed to have reduced activity in AD patients, but is usually very active in cholinergic neurons.[5]

Data on rats and humans suggested that the decrease in the number of muscarinic binding sites in varying regions of the brain, were not affected by AD, but were instead age-related.[5] However, the α-4 subtype of the nicotinic receptor was consistently observed to have reduced activity in AD patients, while other muscarinic receptor subtypes were not significantly affected.[5,15] Muscarinic and nicotinic receptors are two families of membrane-bound proteins, which mediate the cellular actions of acetylcholine.[31] These two families of proteins are structurally diverse and are comprised of many subtypes, expressed post- and pre-synaptically in specific regions of the peripheral and central nervous systems.[31]

AD patients experience a deficit in nerve growth factor (NGF) in their basal forebrain neurons. NGF is produced in the hippocampus and cortex and retrogradely transported to the cell bodies.[5] NGF is a survival factor for cholinergic neurons of the nucleus basalis of Meynert expressing both low and high affinity receptors for neurotrophin.[5,32] Tyrosine kinase receptor A (trkA), a high affinity receptor was observed to be less prevalent in these neurons from AD patients.[2,5,15] Neurotrophin are a family of proteins, responsible for the function, maintenance and development of the nervous system.[32] Evidence indicates that the deficit of NGF is due to dysfunction of its retrograde transport system and not due to insufficient production of the peptide.[5,15]

Evidence suggests that acetylcholine has a critical role in memory and learning processes, as well as many other functions within the cerebral cortex and hippocampus.[1] It was previously believed that loss of memory in aging individuals was caused by neuronal cell loss. Due to improved stereological techniques, however, Mark and co-workers reported that neuronal cell loss was found predominately in pathological aging such as AD patients, while loss of memory in non-pathological aging is due to dendritic, synaptic and axonal degradation with insignificant to no cell loss.[15]

1.2.5.3 Acetylcholine metabolic cycle:

Acetyltransferase is responsible for the production of the acetyl choline are from acetyl coenzyme A (Acetyl CoA) and choline (Figure 1.6).[17] Acetyl CoA is produced from pyruvate from glycolysis which is

© University of Pretoria

the acetyl source and coenzyme-A.[33] Acetyl CoA and choline is then enzymatically bound to from acetyl choline by acetyltransferase within the neuron. Acetyl choline is then transported out of the neuron through vesicle transportation and into the synaptic cleft releasing the neurontransmitter.[33] Excess acetyl choline is hydrolzed into choline and acetate by acetylcholine esterase in the synaptic cleft and choline is recovered by a high affinity choline transporter, by co-transport with sodium ions into the nerve through membrane-bound proteins and the cycle begins anew.[33]

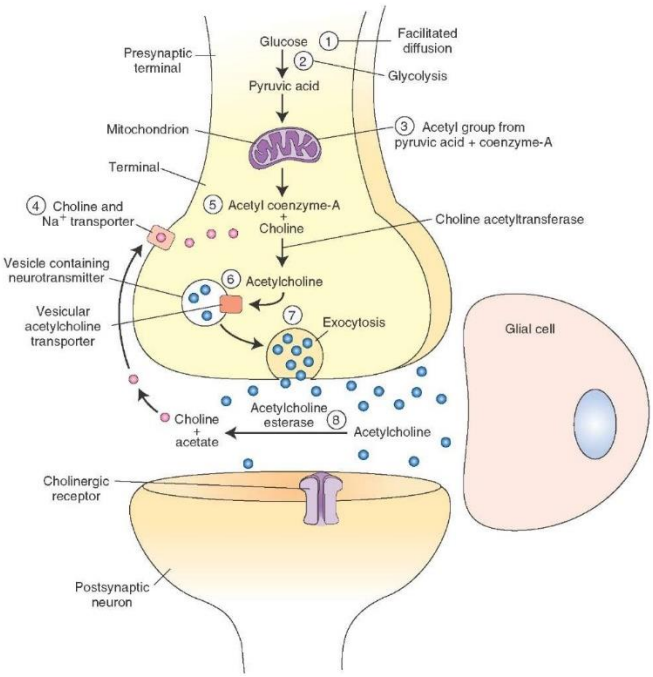

Figure 1.6: The catalytic cycle of acetylcholine in a cholinergic nerve. Reproduced from Crankshaft publishing. 2018.[34]

1.2.5.4 Acetylcholinesterase catalytic site

Homo sapiens AChE is a protein dimer comprised of identical A and B subunits, that each consist of 1084 amino acids and form a combination of 26 α helices and 24 β sheets.[35,36] The catalytic site (CAS) consists of 3 amino acids, Ser-203, His-447 and Glu-334 and is located inside a gorge, which is lined with aromatic residues. Trp-286 is located at the entrance of the gorge at the peripheral anionic site (PAS), which ensures that molecules interacting with the site will be guided to the catalytic site deeper inside the gorge.[35,36]

The catalytic cycle (Figure 1.7) of acetylcholinesterase starts with an acetylation step, which is initiated by the proton transfer from the Ser-203 alcohol to His-447.[37] The Ser-203 oxygen then initiates a nucleophilic attack on the carbonyl carbon of the acetylcholine forming an intermediate.[37] A proton

© University of Pretoria

transfer to the ester oxygen of acetylcholine causes bond breakage and choline is ejected as the leaving group and Ser-203 is left acetylated. The second catalytic step is deacetylation and is initiated by the protonation of His-447 by a water molecule followed by nucleophilic attack by the oxygen atom on the carbonyl of the acetyl group.[37] The sp^3 tetrahedral intermediate collapses back to the sp^2 carbonyl which acts as a leaving group and picks up a proton from His-447 to facilitate reforming the Ser-203 alcohol and releasing acetic acid.[37] The role of Glu-334 has not been determine as yet, but two hypotheses try to explain its role in the catalytic cycle.[37] The first hypothesis suggests that a hydrogen bond between His-447 and Glu-334 is formed, which stabilises the transition state or intermediate during the catalytic reaction.[37] The second hypothesis suggests that Glu-334 carboxylate group stabilises the transition state and intermediate, by electrostatic interactions between the imidazolium group and acetylcholine.[37]

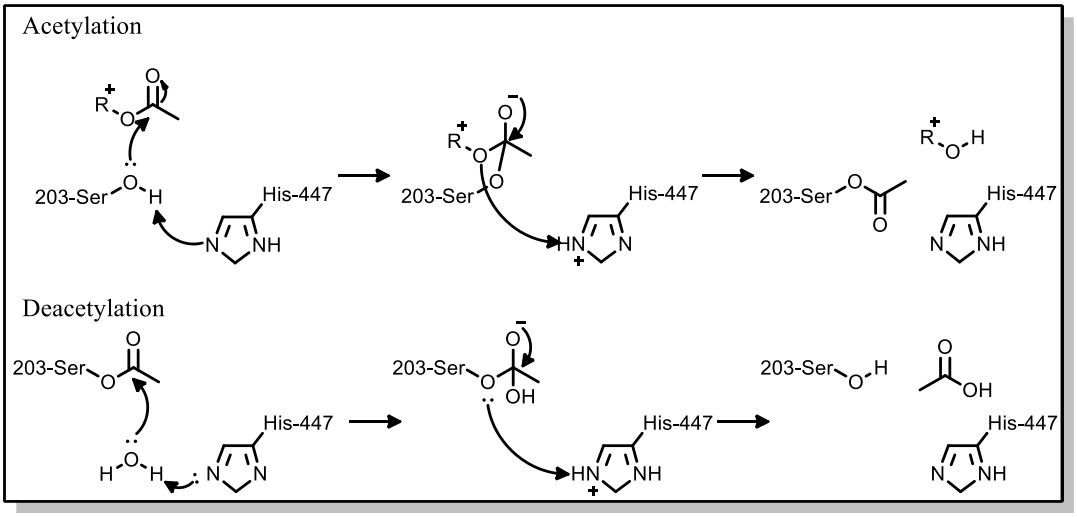

Figure 1.7: Catalytic cycle of acetylcholinesterase recreated from Zhou Y & Wang S & Zhang Y, 2010.[37]

1.2.6 β-Amyloid cascade hypothesis

The β-amyloid cascade hypothesis was proposed when two other histopathological hallmarks were found to occur along with the deficit of acetylcholine in the cholinergic system.[15] It is proposed that β-amyloid peptides induce neurodegenerative changes in the cholinergic terminals, through the deposition of extracellular β-amyloid plaques in the hippocampus and cerebral cortex, as well as the formation of neurofibrillary tangles within select cortical pyramidal neurons.[1,15,38] Early onset of the disease has linked genetic factors responsible for the recycling, trafficking and processing of the amyloid protein to the familial form of the disease.[1] Degradation or loss of the cholinergic terminals is still debated, whether it is the primary or secondary event to the β-amyloid pathology.[15]

© University of Pretoria

1.2.6.1 Pathogenesis

β-amyloid(1-40) and β-amyloid(1-42) monomers were detected to be the main peptides responsible for the formation of Alzheimer's plaques, and β-amyloid(1-42) was observed to be more neurotoxic and more fibrillogenic.[15] These high-molecular weight and insoluble fibres are the main component of the senile plaques (Figure 1.8), and were previously thought to be have been the most toxic bodies responsible for the cholinergic neurodegeneration.[15] More recently, soluble oligomers and monomers of Aβ peptides with low-molecular weight and protofibrils, have been shown to be the most toxic bodies causing memory loss and neuronal dysfunction in AD.[8,15] Prefibrillar assemblies of β-amyloid in varying animal and cell models, were shown to cause electrophysiological changes, neurotoxicity and interference of cognitive function.[8,15]

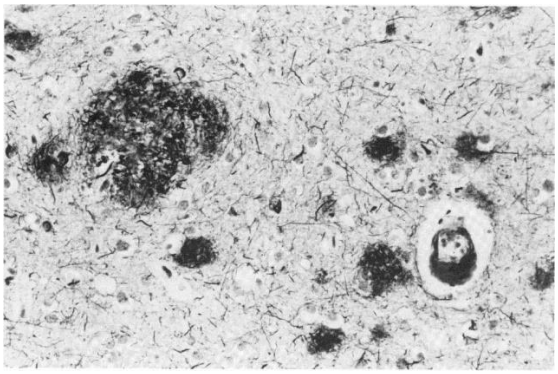

Figure 1.8: Bielschowsky stain of senile plaque in an AD patients' brain. Recreated from Rogers J, Morrison JH, 1985.[39]

It has been reported that the senile plaques have been observed in healthy human brains, that don't show signs of AD, which suggests that the formation of the tangles and plaques is a process arising from reaction to injuries and aids in the maintenance of cell functions.[8,25,40] Aβ proteins are found within neurons in non-AD brains through their development from infancy to adulthood, are produced during neuronal activity and are important for memory and synaptic plasticity.[3,8] Aged individuals, however, have a marked reduction of up to 20 % of intercellular Aβ proteins and a further decrease is noted in individuals with sporadic AD, with this decrease being most noticeable at the hippocampal level.[8] Current evidence of the importance of the type of Aβ peptides to the pathology of AD, was reported when soluble Aβ proteins were found in extracts of the senile plaques of AD brains and Aβ oligomers (derived either synthetically or naturally secreted) were administered to animal models, which then illustrated degeneration of memory and hippocampal synaptic plasticity.[8] In addition, it was observed that even before amyloid deposition, APP transgenic mice illustrated cognitive strain, which suggests that in early stages of AD soluble Aβ proteins may mediate neuronal dysfunction.[8]

© University of Pretoria

A study using transgenic mice (Tg2576) that "express the Swedish double mutation of human amyloid precursor protein (APP)", showed little correlation between the aggregation of insoluble Aβ-peptides, memory impairment and neuronal loss. "Immunohistochemical and audioradiographic radioligand binding studies" of brain sections of these mice showed lowered cholinergic density in cholinergic nicotinic acetylcholine receptors (nAChR) and cholinergic muscarinic acetylcholine receptors (mAChR) binding levels within the cerebral cortex before the start of plaque deposition.[15] This may demonstrate why before there is considerable plaque formation there is already an early onset of cholinergic dysfunction in progress in AD.[15]

Tg2576 mice were further used to determine whether β-amyloid peptides mediate cholinergic dysfunction by targeting key enzymes in brain glycolysis, as acetylcholine synthesis requires acetyl-CoA, which is produced through glucose degradation in glycolysis.[15] Phosphofructokinase (PFK) activity and expression was studied in aging Tg2576 mices' cerebral cortexes.[15] PFK enzyme activity, protein level and PFK-C mRNA was notably reduced contrasted to non-transgenic littermates, while no difference in mRNA levels of the other isoforms of PFK was observed.[15] This study illustrated that elevated and lasting β-amyloid burden decreases PFK activity in neurons associated with β-amyloid plaques, impairing glucose metabolism in the cerebral cortex.[15]

Clinical trials of drugs targeting Aβ-proteins to decrease their levels have been unsuccessful and suggest that the amyloid cascade hypothesis is insufficient to explain AD pathogenesis.[8] Evidence of healthy brains containing Aβ-proteins for normal functioning of the brain adds to the insufficiency of the hypothesis.[3,8] A recent work by Puzzo and colleagues hypothesised that the monomers of Aβ-proteins oligomerise to a degree and if a critical point is not passed, plays a physiological role in neuron transmission, but will cause interference if the oligomerisation critical point is exceeded.[8] The degree of the oligomerisation may also affect the binding selectivity of the Aβ-protein, resulting in interference with various receptors causing a synergistic or additive effect.[8] Evidence supporting the hypothesis is that the monomers compete in binding to the insulin receptor and are concentration dependent, as well, various Aβ-species bind at different concentrations to hippocampal neurons affecting neurotransmissions.[8] More so, Aβ-40 interacts with both alpha7 and alpha4β2 nAChRs, but will selectively interact with α7-nAChR at low concentration at the picomolar level and with both receptors at the nanomolar level.[8] Aβ peptides/proteins at low concentrations play a positive role in memory and synaptic plasticity, but at high concentrations have a negative impact and cause synaptic failure (See Puzzo and Arancio, 2013 for a review).[41] In light of this it was proposed that if Aβ proteins

© University of Pretoria

could not play its physiological role, a negative feedback mechanism would cause an increase in Aβ proteins levels leading to the accumulation of the protein at abnormal levels, causing memory loss and synaptic dysfunction.[8] More work is needed to identify the true pathology of Aβ-proteins.

1.2.6.2 Acetylcholine esterase PAS

Acetylcholine esterase (AChE) is a facilitator of Aβ-monomer aggregation at its peripheral anionic site (PAS) which is located at the entrance to the enzyme binding site, the PAS acts as a seeding site for the low weight oligomers.[3,4] The self-induced aggregation of the Aβ monomers forms toxic Aβ complexes, but these are less toxic than the AChE- Aβ complexes formed by seeding at the PAS.[3,4] The PAS consists of 5 amino acids, Tyr-70, Asp-72, Tyr-121, Trp-279 and Tyr-334 (*Torpedo*), which are located at the entrance to the gorge forming a rich hydrophobic region.[4,42]

1.3 Treatment and therapies

There is no current cure for AD, only therapies that alleviate symptoms and delay the progression of the disease.[1,5] Three drugs are approved by the Food and Drug Admiration (FDA), rivastigmine (**1**), galantamine (**2**) and donepezil (**3**), for the treatment of mild to moderate AD (Figure 1.9).[1,5,16] All three drugs are AChE inhibitors, and the most widely prescribed drug is donepezil.[1] Small improvements in global and cognitive functioning have been shown in clinical trials with donepezil, but patients still decline over time.[1,5] Two additional FDA approved drugs include memantine (**4**) and *N*-methyl D-aspartate (NMDA) receptor antagonist (**5**), used for moderate to severe AD.[16]

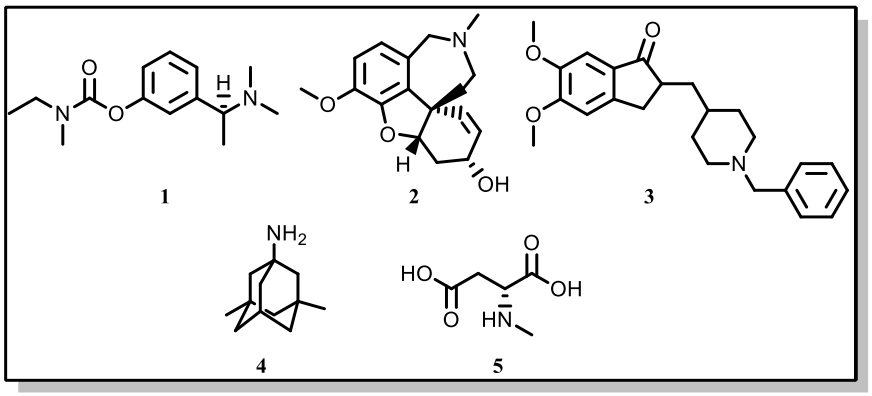

Figure 1.9: FDA approved drugs for the treatment of AD.

© University of Pretoria

1.4 Dual AChE and PAS inhibitors

As discussed in the β-amyloid hypothesis acetylcholinesterase acts as a seed site which enhances Aβ aggregation at the PAS.[43] Research into dual AChE and PAS inhibitors gained focus when a ligand could be designed to bind to both the CAS as well as the PAS.[43] The dual binding would then act by both increasing acetylcholine levels as well as delaying plaque deposition.[43] The paradigm shift of "one molecule one target" approached to a ligand with multiple bindings and inhibitions was seen as a significant breakthrough.[43] However, limited success has been seen with these designed inhibitors, as only slight improvements have been seen in AD patients.[43]

Xie and colleagues synthesised a library of bis(-)-nor-meptazinol (**6**) ligands with various alkane linkers, which allowed simultaneous binding of both the CAS and PAS (Figure 1.10).[44] These compounds showed a correlation between the length of the linker and inhibition activity of AChE, with a nine-carbon linker illustrating the best activity at an IC_{50} of 3.9 nM (**7**).[44] The same compounds showed an IC_{50} of 16.6 µM against Aβ amyloid aggregation induced by AChE.[44]

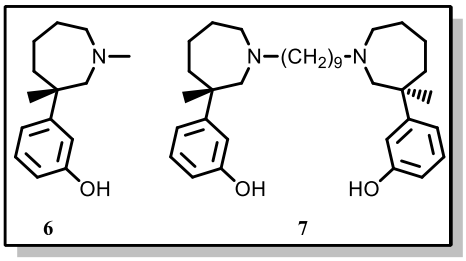

*Figure 1.10: Structures of nor-meptazinol monomer (**6**) and of the best scoring ligand (**7**). Recreated from Xie, et al. 2007.*[44]

Muñoz-Ruiz and colleges worked on dual inhibitors using tacrine as the scaffold for the CAS binding unit and an indole ring for the PAS binding unit, connected with various linkers (Figure 1.11).[45] The tacrine unit had a chlorine on the 6th position as it was previously illustrated to enhance the activity against AChE.[45] The library focused on different linkers in between the tacrine and indole moieties to explore the effect they had on the pharmacological properties of the ligands.[45] The library produced showed a higher affinity to AChE rather than butyrylcholinesterace (BChE) with the best IC_{50} of 2µM against AChE and with 5 compounds showing lower IC_{50} values than propidium against Aβ amyloid aggregation.[45] These 5 compounds had various linker lengths in between the tacrine and indole moiety, but with an amide functional group at various points in the linker.[45] In particular two compounds (**8** and **9**) showed potent activity against AChE with an IC_{50} of 20 and 60 pM respectively.

© University of Pretoria

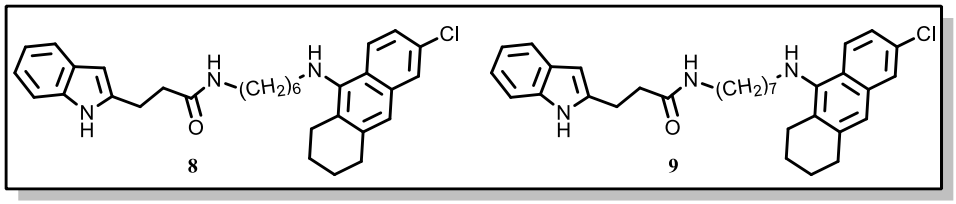

Figure 1.11: Structure of the two best inhibitors developed by Muñoz-Ruiz and co-workers. Recreated from Muñoz-Ruiz, et al. 2005.[45]

Gemma and colleagues designed dual inhibitors using tacrine and huperzine A as the two binding units with various substitutions of the huperzine A moiety, with methylene linkers of various lengths (Figure 1.12).[46] The aim of the study was to design inhibitors that would not only bind to both the CAS and PAS in human acetylcholinesterase (hAChE), but also with human butyrylcholinesterace (hBChE).[46] The linker played an important role in binding as Gemma and colleagues describe a midgorge binding site in both hAChE and hBChE in which a number of the linkers had interaction, increasing stabilisation and potency.[46] The midgorge site was found to be a conserved aspartic acid (Asp, D) residue in both enzymes and was D74 and D70 in hAChE and BChE respectively.[46] A handful of compounds (**10-12**) synthesised by the group showed high affinity to both AChE and BChE, which had various binding modes with the tacrine and huperzine A binding units binding to either the CAS or PAS sites.[46]

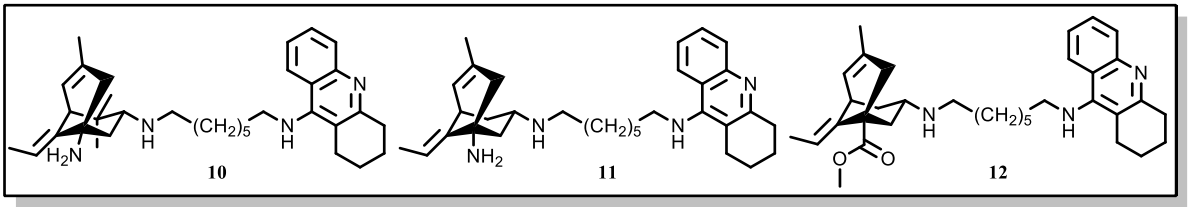

Figure 1.12: Structures of the 3 best compounds synthesised by Gemma and co-workers. Recreated from Gemma, et. al. 2006.[46]

Kwon and colleagues drug design focused on piperidine containing compounds with various groups bound on opposite ends of the ring as binding units to the PAS or CAS sites (Figure 1.13).[47] A carbon linker bound to the piperidine nitrogen with either an ester or amide functional group was bound to various functionalised aromatic groups and investigated for CAS binding.[47] A short ether linker opposite the nitrogen of the piperidine ring was bound to either a benzyl or benzhydryl group for PAS binding.[47] A compound (**13**) with a benzhydryl group as the PAS binding unit and a 4-chlorobenzene group as the CAS binding unit showed selective inhibition of AChE compared to BChE with an IC_{50} of 0.32 µM, as well as good inhibition against Aβ amyloid aggregation.[47] The study also identified two compounds (**14** and **15**) that had great activity and selectivity to BChE, which shared halobenzene groups for CAS binding and a benzyl moiety for PAS binding, as well as a carbamate linker.[47]

© University of Pretoria

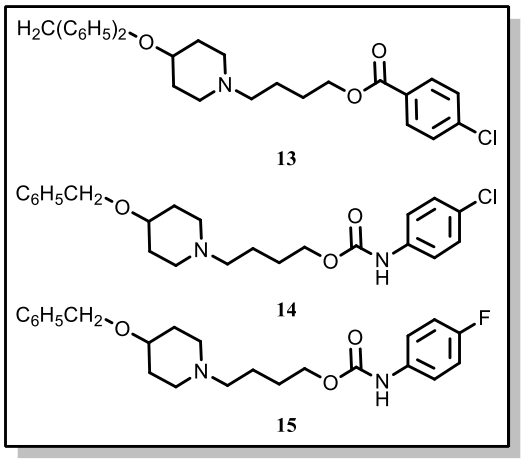

*Figure 1.13: Structures of best AChE inhibitor (**13**) and of two potential BChE inhibitors (**14** and **15**) developed by Kwon and co-workers. Kwon, et. al. 2007.*[47]

Lemes and colleagues worked on derivatising the cardanol scaffold to design AChE dual inhibitors of both the PAS and CAS sites, as cardanol had been previously shown to have activity against AChE (Figure 1.14).[48] Cardanol is a phenolic lipid and a by-product of cashew processing and was considered a waste product, but now has gained interested as a starting material to high value chemicals.[48] Cardanol was used as the PAS binding unit with fifteen carbon chain linkers with different degrees of saturation.[48] The CAS binding unit had the greatest variability in the library and various substituted pyrrolidine, piperidine and morpholine moieties were used, with substitutions ranging from *O*-acetyl, *N*-substitution, hydroxylation, *O*-dimethylcarbamates and *N*-ethyl-N(2-methoxybenzyl)amino groups.[48] The library of compounds was tested for a number of biological parameters, such as activity against both AChE and BChE, as well as blood brain barrier penetration, cytotoxicity and inhibition of Aβ aggregation.[48] A compound (**16**) with good activity against both AChE (IC_{50} = 6.6 µM) and BChE (IC_{50} = 5.0 µM), as well as comparable BBB penetration as donepezil was identified.[48]

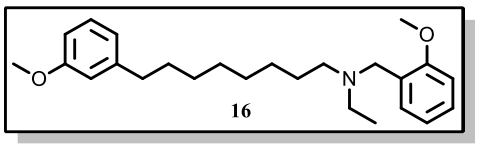

Figure 1.14: Structure of best dual inhibitor of AChE and BChE developed by Lemes and co-workers. Lemes, et.al. 2016.[48]

© University of Pretoria

1.5 Multi-target AD inhibitors

A library of compounds using rivastigmine coupled to either ferulic or caffeic acid moieties were developed by Chen and colleagues, as potential multifunctional inhibitors against AChE, BChE, Aβ aggregation and ROS scavengers (Figure 1.15).[49] The whole library of compounds showed an increased activity against AChE as compared to rivastigmine, as well as decent affinity to both AChE and BChE.[49] The radical scavenging activity of the library was tested using a 1,1-diphenyl-2-picryl-hydrazyl (DPPH) assay, with two compounds illustrating high activities near 70 %.[49] Two compounds also showed high activity against Aβ aggregation comparable to Congo red, with an additional two compounds showing marked activities.[49] The neuroprotective study indicated that the rivastigmine-caffeic acid analogous had stronger neuroprotective activity against peroxide induced oxidative stress.[49] The group successfully synthesised a multifactorial inhibitor (**17**) with inhibition activity against both AChE and BChE, Aβ aggregation and with good radical scavenger activity, which can be used a potential lead compound for further development.[49]

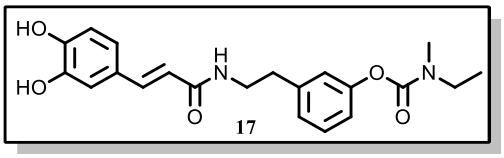

Figure 1.15: Structure of multifactorial inhibitor developed by Chen and co-workers. Chen, et. al. 2017.[49]

A ligand library of coupled coumarin and *N*-benzylpiperidine moieties was developed by Xie and colleagues as multifunctional inhibitors of AD.[50] The design of the ligands was for inhibition activity against AChE and BChE by binding to both the CAS and PAS sites, as well as activity against monoamine oxidase B (MAO-B).[50] Screening of the library indicated a ligand (**18**) with good activity against all targets and was seen in molecular modelling to interact with the CAS and PAS, as well as the midgorge site in both hAChE and hBChE via competitive inhibition.[50] The ligand (**18**) also showed good BBB penetration and no cytotoxicity, making the ligand a potential lead compound for further development.[50] The ligand (**18**) consisted of the coumarin moiety for PAS binding, with the linker an ether of two methylenes in length to an amine directly bonded to the *N*-benzylpiperidine group, which was for CAS binding.[50]

© University of Pretoria

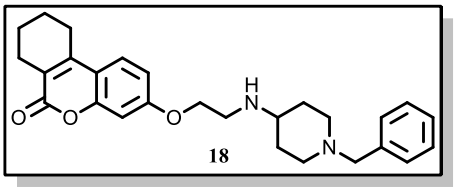

Figure 1.16: Structure of multifactorial inhibitor developed by Xie and co-workers. Xie, et al. 2016.[50]

Gabr and Abdel-Raziq used the donepezil scaffold to develop a ligand library with amide linkers between the piperidine and methoxylated aromatic groups, to try and incorporate BACE-1 and metal chelating activity to the ligands, while maintaining activity against AChE (Figure 1.17).[51] The amide linker was introduced to allow hydrogen bonding between the amine and an aspartate amino acid that was previously identified as the catalytic site of BACE-1.[51] The methoxylated aromatic groups were used for PAS binding and the benzylated piperidine moiety for CAS binding, but had either a methyl or carbonyl linker bonded to the nitrogen of the piperidine ring.[51] The authors were successful in synthesising a ligand (**19**) with better inhibition activity to hAChE (IC_{50} = 4.11 nM) and potent activity against BACE-1 (IC_{50} = 18.3 nM) and an additional two ligands with comparable activity to donepezil.[51]

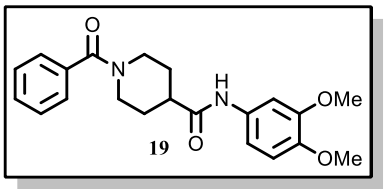

Figure 1.17: Structure of multifactorial inhibitor developed by Gabr and Abdel-Raziq. Gabr MT, Abdel-Raziq MS. 2018.[51]

1.6 Donepezil

Donepezil was developed by Sugimoto and co-workers starting in 1983 (Figure 1.18).[52] The group failed to develop non-toxic tacrine analogues and through random screening identified an *N*-benzylpiperazine ligand (**20**), which was originally developed for the treatment of anti-arterial sclerosis.[52] Compound **20** had an IC_{50} of 12.6 µM in the random screening, which is a moderate inhibition activity and the group saw potential in the ligand.[52] The group then developed an extensive library of about 700 compounds based on compound **20**.[52] The inhibition activity of the ligand drastically increased with the replacement of the *N*-benzylpiperazine with an *N*-benzylpiperidine group (**21**).[52] The ether linker was then replaced with an amide group (**22**), which subsequently increased activity against AChE.[52] Substitution of the benzamide with other groups at the fourth position decreased activity, except for the substitution of a benzyl sulphonyl that increased potency (**23**).[52] Unfortunately, the ligand was found to have a short half-life and bioavailability making it

© University of Pretoria

unsuitable.[52] A ketone moiety (**24**) was then used to replace the amide linker which maintained activity, but a cyclic-lactam (**25**) substitution further enhanced the activity.[52] These findings were then used to develop an indanone derivative (**26**), which was further developed through a structure activity relationship study and led to the discovery of donepezil (**3**). [52]

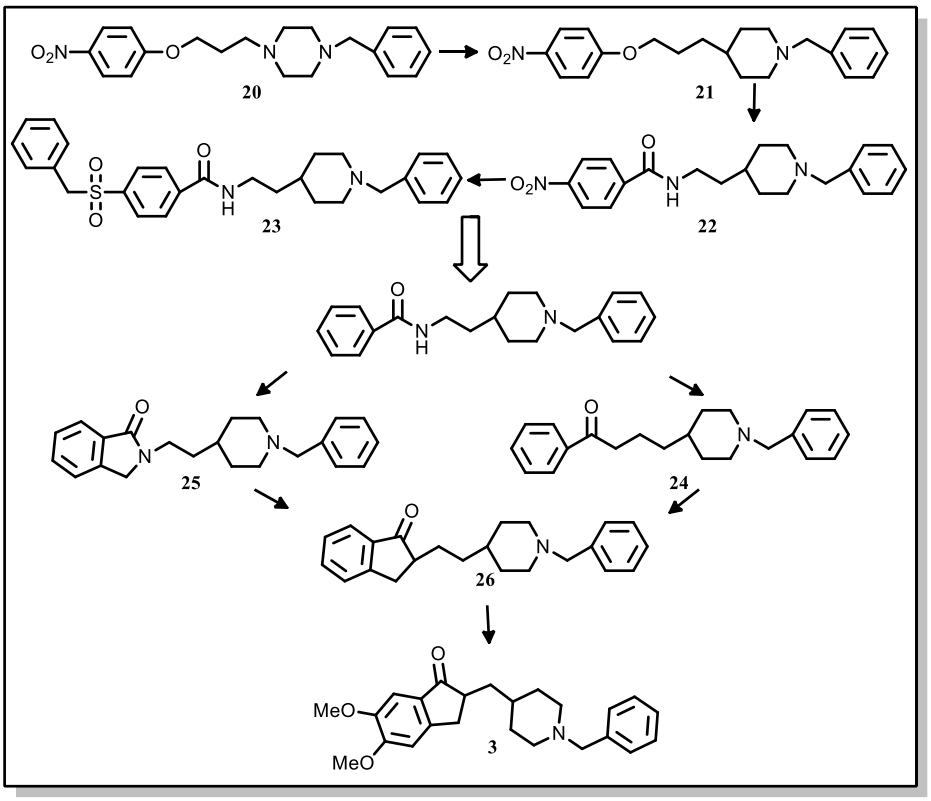

Figure 1.18: Structures of the synthetic route performed by Sugimoto and co-worker to discover donepezil. Recreated from Sugimoto, et al. 2000.[52]

Donepezil's activity is due to a number of interactions within the binding site of the hAChE binding pocket which include: pi-pi stacking interactions of the indole ring of Trp-286 with the indanone moiety; water molecule mediated hydrogen bonding interactions between the protonated nitrogen of the piperidine ring with Tyr-337 and Tyr-341; and lastly pi-pi interactions of His-447 with the benzyl group bound to the piperidine ring.[35,36] A donepezil molecule spans the length of the active site gorge and interacts with both the catalytic and the peripheral anionic sites.[35,36] The catalytic site consists of 3 amino acids, Ser-203, His-447 and Glu-334 and is located inside a gorge.[35,36] Donepezil interacts with the CAS through pi-pi bonding with the benzyl moiety and His-447 and through this interaction causes competitive inhibition of AChE. Trp-286 is at the PAS near the entrance of the binding pocket and undergoes pi-pi stacking with donepezils' indanone moiety, which plays a role in the inhibition of hAChE Aβ-monomer aggregation.

© University of Pretoria

1.6.1 Synthesis of donepezil[53]

2-((1-Benzylpiperidin-4-yl)methyl)-5,6-dimethoxy-2,3-dihydro-1*H*-inden-1-one (**3**) (Donepezil) was formed by hydrogenation of (*E*)-2-((1-benzylpiperidin-4-yl)methylene)-5,6-dimethoxy-2,3-dihydro-1*H*-inden-1-one (**27**), which was subsequently formed by an aldol condensation between 1-benzylpiperidine-4-carbaldehyde (**28**) and 5,6-dimethoxy-2,3-dihydro-1*H*-inden-1-one (**29**). 1-Benzylpiperidine-4-carbaldehyde (**28**) was formed from the Swern oxidation of (1-benzylpiperidin-4-yl)methanol (**30**), which was formed by the reduction of ethyl 1-benzylpiperidine-4-carboxylate (**31**). Ethyl 1-benzylpiperidine-4-carboxylate (**31**) was formed by the benzylation of ethyl piperidine-4-carboxylate (**32**) with benzyl chloride (**33**).

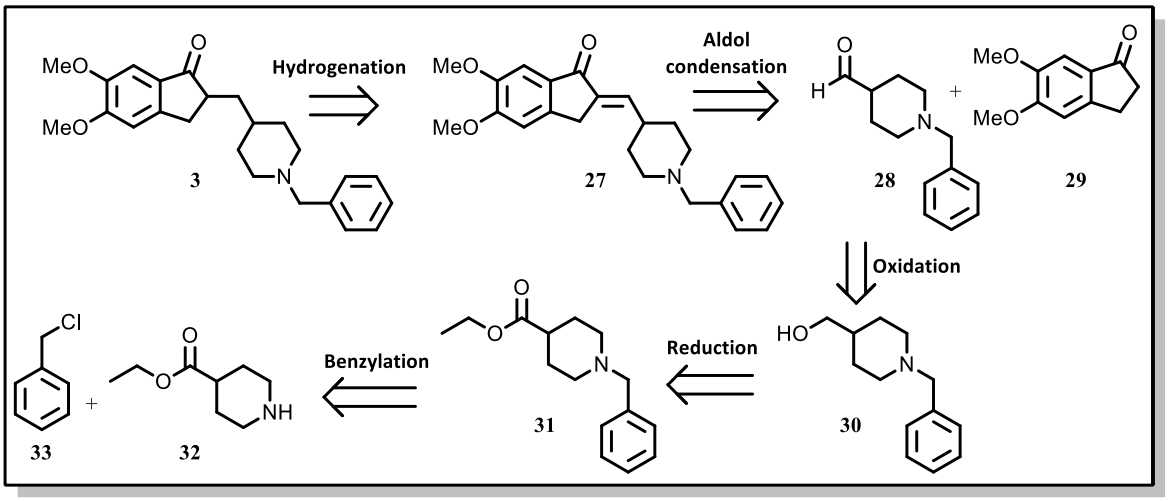

Scheme 1.1 The retrosynthetic route for the synthesis of donepezil.

Donepezil (**3**) is still one of the best therapeutic drugs for the treatment of AD available today, due to its competitive inhibition against both AChE activity and AChE induced Aβ aggregation.[1,3,4] Donepezil (**3**) ignited substantial research interest over the last few decades on dual or multifactorial inhibitors for AD based on its core scaffold.[51] It is used as a standard or control in many drug discovery programs due to its high activity, and FDA approved drug status. The synthesis is fairly short (with a few reaction steps) and simple to perform and was therefore chosen as the parent scaffold for further drug development research that will be reported in this dissertation.

© University of Pretoria

Chapter 2 Silicon chemistry

2.1 Silicon as an element

Silicon is one of the many elements of the periodic table, belonging to the third period and in the fourth group.[54] It is the second most abundant element on earth and is mostly found bound to oxygen as silica and silicates.[54] Silicon is isoelectronic to carbon as it has the same number of valence electrons, but has unique properties compared to carbon.[54] Carbon is the basic building block of life as it can form stable bonds with other carbons, whereas silicon forms weak bonds to other silicon atoms and is more likely to bond to oxygen due to higher bond stability.[54]

2.2 Silicon in medicinal chemistry

The use of silicon as an alternative to carbon in medicinal chemistry is of interest in light of its unique properties in comparison to carbon: 1) silicon-carbon (1.87 Å) bonds are longer compared to carbon-carbon (1.54 Å) bonds and allows for alternative conformations or profiles of the molecule, affecting receptor interactions due to increased flexibility;[54,55] 2) silicon forms different stabilized compounds to carbon, such as diols which are unstable with carbon and undergo dehydration, whereas silicon diols are stable; 3) silicon has an expanded coordination number of six;[54,55] 4) silicon has a higher electropositivity compared to carbon, which makes silicon bonds more polarized, making silanols more acidic and better hydrogen bond donors;[54,55] 5) incorporation of silicon into ligand scaffolds potentially increases lipophilicity, which allows for better cell and blood brain barrier (BBB) penetration.[54,55]

Silicon switching has become a useful tool in medicinal chemistry to increase the lipophilicity of a drug molecule. There are a number of literature examples of successful silicon switching in which one or two carbon atoms within a drug molecule are replaced with silicon atoms to increase the lipophilicity and absorption of the drug molecule.[56] Silicon switching can have great benefits for treatment of neurological diseases/disorders, which require pharmaceuticals to cross the BBB to reach the target sites.[57] This technique can be used to alter the absorption, distribution, metabolism, excretion and toxicity (ADMET) properties and increase the bioavailability of the molecules at the target sites.[58]

© University of Pretoria

2.3 Successful case studies

2.3.1 Alternative metabolic pathways with silicon analogs

Silicon may change the bonding properties when incorporated into a ligand as a carbon substitute, but it can also alter how the body processes the molecule. Haloperidol (**34**) is an excellent example as it is used as an antipsychotic and when metabolized it forms a metabolite similar in structure to 1-methyl-4-phenylpyridinium (MMP^+, **35**), which is a neurotoxic compound that targets neurons that produce dopamine (Figure 2.1).[59,60] Take and colleagues synthesized the corresponding silicon analogue (**36**) with the silicon incorporated into the piperidine ring opposite the ring nitrogen.[59] The silicon analog did not undergo dehydration because of the silanol stability and instability of a Si=C bond, which prevented the transformation of the piperidine ring into the aromatic group with a charged nitrogen (MMP^+).[55,60]

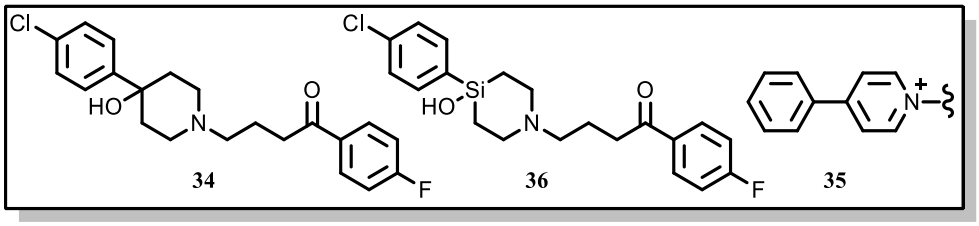

*Figure 2.1: Structures of haloperidol (**34**), its silane analogue (**36**) and the structure of MMP^+ moiety (**35**). Recreated from Tacke, et al. 2004.*[59]

Loperamide (**37**) is a commonly used antidiarrheal medication, which has the same functional groups as haloperidol and follows the same metabolic pathway forming MMP^+ like metabolites that are neurotoxic (Figure 2.2).[61] Geyer and colleagues incorporated the same silicon substitution in the piperidine ring and observed that the silicon analogue (**38**) only had two metabolites similar to three of the stable metabolites formed from the carbon analogue of loperamide.[61] A third metabolite was observed, but it was unique to the silane analogue and was seen to have a high clearance and was removed swiftly from the body due to its highly polar nature.[61] The silane analogue overall had a swift removal of its metabolite, decreased the burden of the metabolite on the body and prevented formation of the neurotoxic metabolite.[61]

© University of Pretoria

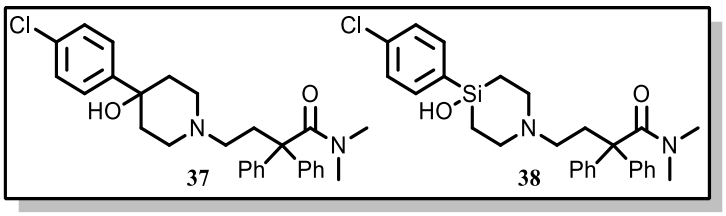

*Figure 2.2: Structure of loperamide (**37**) and its silane analogue (**38**). Recreated from Geyer, et al. 2015.*[61]

2.3.2 Transition state mimics

Protease enzymes hydrolyze the amide bond between peptides by adding water across the amide to form a diol, which is stabilised by the enzyme and the diol then collapses to release the individual peptides.[62] Molecules that are able to mimic the diol transition state and are not hydrolysed can be utilised as potential inhibitors.[54,62] These mimics are of interest as a number of proteases play a role in several diseases making them potential targets for disease control.[54,62]

Silicon is more likely to have sp^3 over sp^2 hybridization allowing silanediols to be favoured over silanes, due to the increased stability.[62] This property was utilized by Sieburth and co-workers to design various protease inhibitors which incorporated silanediols (Figure 2.3).[62] The group successfully utilised silanediols through incorporation in aspartic protease inhibitors to target HIV protease with similar, but lower potency relative to current therapeutics available today.[62] In doing so, the team successfully illustrated the use of silanols as transition state mimic inhibitors for angiotensin-converting enzyme, achieving an IC_{50} of 14 nM with a silanediol tripeptide.[63] Further examples of inhibition of thermolysin and serine protease using silanediol inhibitors were investigated by the same group.[64–66]

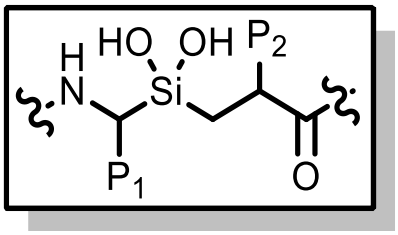

Figure 2.3: General formula for silanediol inhibitors of protease enzymes. Recreated from Chen, et al. 2001.[62]

Blunder and colleagues investigated the use of silanetriols as mimics of ester hydrolysis, which form a carbon diol and an ether during the transition state (Figure 2.4).[67] Three ligands with increasing steric bulk were tested against AChE at a concentrations of 100 µM and all three ligands were found to have reversible inhibition and negligible cytotoxicity.[67] The least bulky ligand was seen to have the best

© University of Pretoria

inhibition with a moderate IC_{50} value of 121 µM as a cyclohexylsilanetriol ligand, which had approximately half the inhibition of galantamine hydrobromide.[67]

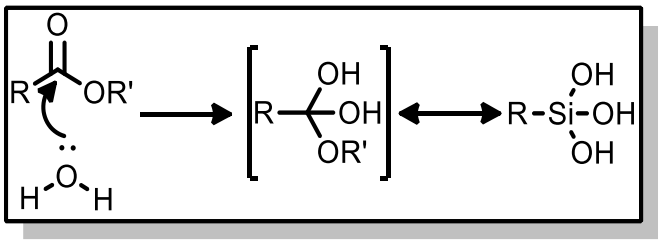

Figure 2.4: Comparison of ester hydrolysis transition state with silanetriol. Recreated from Blunder, et al. 2011 [67]

2.3.3 Increase in electropositivity

Zifrosilone (**39**) is a trifluoromethyl ketone with an incorporated silicon, which underwent clinical trials as an AChE inhibitor (Figure 2.5).[54] It was developed from an ammonium/silicon switch of a trifluoromethyl ketone (**40**), which was previously reported to have activity against AChE.[54] The silicon switch allowed for a partial charge to form within the molecule due to the increased electropositivity of silicon, which created beneficial interactions with the catalytic site (CAS) of the enzyme.[54] The partial charge is more beneficial, as fully charged species have poor BBB penetration.[68]

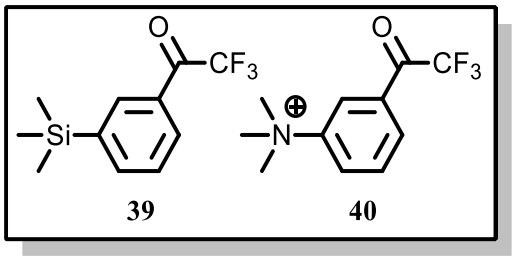

*Figure 2.5: Structure of Zifrosilone (**39**) and the original trifluoromethyl ketone structure (**40**). Recreated from Ramesh, et al. 2018.*[54]

This tactic was then utilised by Daiss and colleagues during the development of the muscarinic M2 receptor allosteric agent W84 (**41**) (Figure 2.6).[68] W84 (**41**) inhibits the release of [^{3}H] *N*-methylscoplamine ([^{3}H]-NMS) from the M2 receptor, by binding to an allosteric site on the receptor.[68] A charged nitrogen to silicon shift (**42**) of one of the two charged nitrogens (Figure 2.6), showed an increased affinity for the [^{3}H]-NMS bound receptor and no affinity for the free receptor.[68] This is advantageous as uncharged molecules have better BBB penetration and can be utilised for muscarinic allosteric modulators within the brain to prevent dissociation of acetylcholine from the receptors.[68]

© University of Pretoria

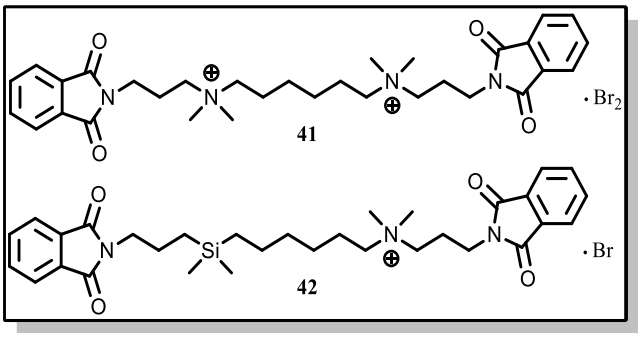

*Figure 2.6: Structure of W84 (**41**) and silicon incorporated analogue (**42**). Recreated from Daiss, et al. 2002.*[68]

Muscarinic antagonists for the treatment of Parkinson's disease were studied by Tacke and co-workers and the structural pharmacology relationship for affinity and selectivity to muscarinic subtypes on previously developed ligands (Figure 2.7).[69] The silanol and carbinol analogs and their effects on affinity and selectivity were studied and it was found that the silanols in general had greater affinities to all the muscarinic subtypes compared to the carbinols.[69] A silanol analog (**43**) had increased affinities of factors up to 81 times for all the muscarinic subtypes, as compared to the carbinol analog.[69] This illustrated the usefulness of silicon substitution in drug design as a potential means of increasing the biological activity of pharmaceuticals.[69]

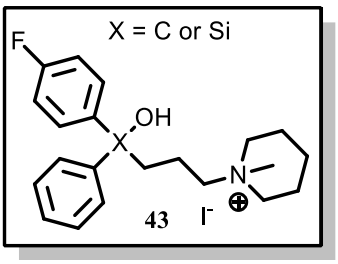

*Figure 2.7: Structure of muscarinic antagonist (**43**) with significant difference in affinity between the silicon and carbon analogs. Recreated form Tacke, et al. 1995.*[69]

2.3.4 Increased lipophilicity

Two camptothecins, topotecan (**44**) and Camptothecin -11 (CPT-11, **45**) are FDA approved therapeutics in the treatment of cancerous tumors, through the inhibition of DNA topoisomerase 1.[70,71] In human plasma the camptothecin family have two forms at equilibrium, which are the lactone and active form and the water hydrolysed carboxylate and inactive form.[70,71] Human serum albumin (HSA) protein shifts the equilibrium toward the carboxylate form as it preferentially binds to the inactive form.[70] Bom and colleagues worked on derivatizing a ligand library based on the camptothecin scaffold (**46**), by incorporation of silicon within the scaffold to increase lipophilicity and stability within

© University of Pretoria

human plasma (Figure 2.8).[70] Various silicon groups were incorporated at P_7, with either a hydrogen or alcohol placed at P_{10} and a hydrogen at P_9.[70] A particular ligand (**47**) had a 25-fold increase in lipophilicity, as well as improved blood stability due to reduced affinity for HSA, allowing for the active lactone to be present within both liposomal and cellular bilayers.[70] The silyl incorporated ligand had comparable activity to the FDA approved topotecan and CPT-11, with superior stability in human plasma and it was shown to have activity against a broad spectrum of human tumors, making it a potential lead compound for further development.[70,71]

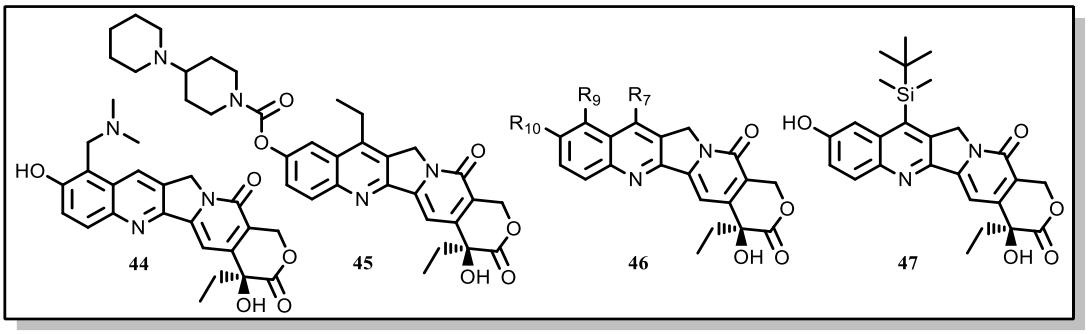

*Figure 2.8: Structure of topotecan (**44**), CPT-11 (**45**), general structure of derivatized scaffold (**46**) and lead compound with silyl group incorporated (**47**). Recreated from Bom, et al. 2000.*[70]

Gately and West worked on derivatizing the indomethacin (**48**) scaffold with silicon to reduce the toxicity of the pharmaceutical, which caused hepatic and renal insufficiency and gastrointestinal erosions (Figure 2.9).[56] Indomethacin is used in the treatment of cancer by targeting cyclooxygenase-II (COX-II), as it is over expressed in cancerous tumors.[56] The toxicity of indomethacin was due to little selectivity between COX-I and COX-II, with inhibition of COX-I causing the side effects.[56] Silicon substituted analogues (**49**) were focused on the addition of an amide with various length alkyl chains and silyl groups at the bottom section of the molecule.[56] The silicon substituted ligands have the same mode of action, but had improved selectivity and activity to COX-II, as the enhanced lipophilicity increased tumor absorption and improved inhibition.[56]

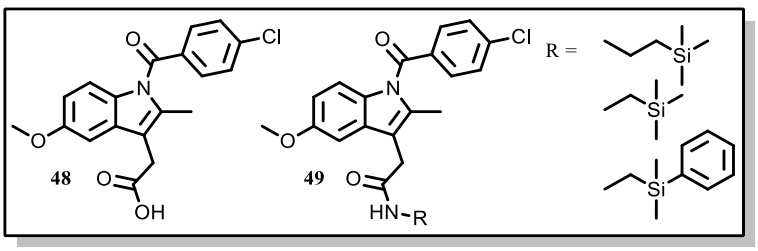

*Figure 2.9: Structure of indomethacin (**48**) and the general derivatized scaffold (**49**). Recreated from Gately & West, 2007.*[56]

© University of Pretoria

Seetharamsingh and co-workers worked on oxazolidinone antibiotics, but specifically on linezolid (**50**) to increase the bioavailability of the antibiotics within the brain (Figure 2.10).[57] Linezolid (**50**) was first marketed for use against ribosomal protein synthesis to repress bacterial growth and has broad spectrum activity against gram-positive bacteria.[57] The objective of the study was to incorporate silicon within the antibiotic to increase the BBB penetration, to allow it to be used against CNS infections.[57] The silicon was incorporated in the piperidine ring moiety opposite the nitrogen with various carbon groups bonded to the silicon or to the aromatic group preceding the piperidine ring.[57] The amide group on the opposite end of the molecule was also altered within the library of compounds.[57] Three ligands (**51**) (**a**-**c**) from the library showed great potential as lead compounds with a 30-fold increase in brain: plasma ratio.[57]

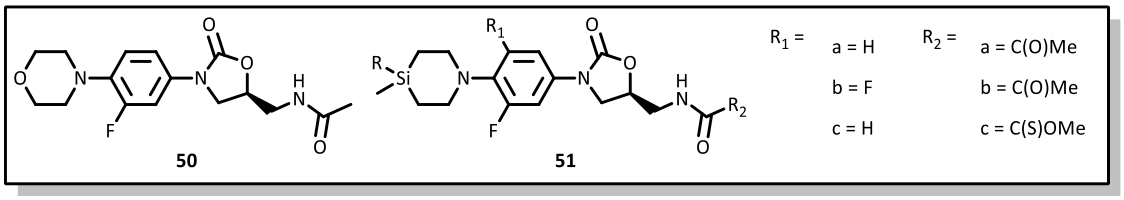

*Figure 2.10: Structure of linezolid (**50**) and the general structure of the derivatized scaffold (**51**). Recreated from Seetharamsingh, et al. 2015.*[57]

The use of silicon as an alternative to carbon in medicinal chemistry has become a useful tool to increase the lipophilicity and absorption of drug molecules. In many literature examples silicon has been shown to increase BBB penetration of drug molecules. Thus, silicon was incorporated into the molecular scaffolds of the theoretical ligand library which will be investigated during this study, with the aim of enhancing the absorption and bioavailability of AD drugs within the brain.

© University of Pretoria

Chapter 3 Computational modelling

3.1 Computational chemistry

Computational chemistry is a theoretical approach based on physics algorithms, used to imitate chemical reactions or properties of molecules or atoms.[72] Drug discovery and design programs have various computational methods to calculate or predict chemical properties, such as drug-target binding or assessing chemical properties of newly designed ligands.[72]

Computational chemistry is routinely used in drug discovery programs to decrease cost and time for identifying drug candidates.[72] This process is typically divided into three stages i) hit identification, ii) lead generation and iii) lead optimisation (Figure 3.1).[72] Hit identification involves finding compounds with promising activity or properties against a chosen target.[72] Lead generation involves modification of the scaffold and functional groups to generate many analogues to improve potency. Lastly, optimisation of potent compound's chemical properties or target interactions are made for beneficial activity in lead optimisation.[72] Computational chemistry can aid in all activities along the drug discovery flow, however, with the use of several resources with specific functions and applications.[72] Typical design methods are structure-based drug design (SBDD) that utilises a target's structural data or ligand-based drug design (LBDD) which uses a known pharmaceutical scaffold, with no structural data available on the target.[72] Drug candidates are synthesised and tested for *in vivo* inhibitory activity and efficacy and are referred back to the computational modelling for model assessment and further model improvement.[72]

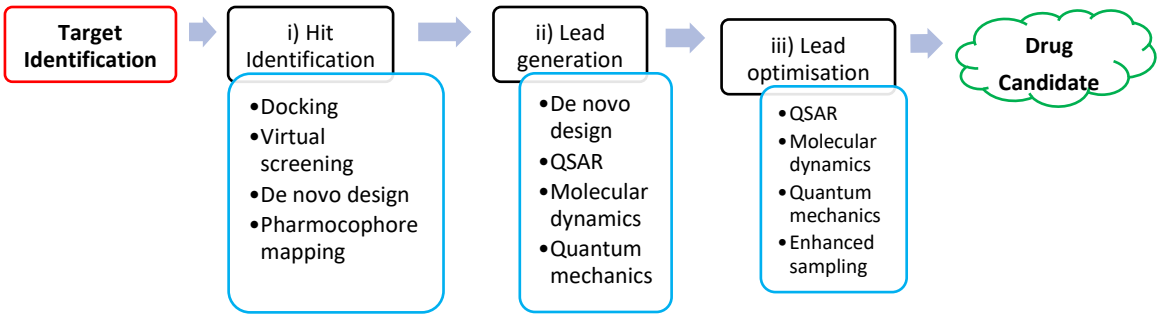

Figure 3.1: Drug discovery flow. Recreated from Palermo and De Vivo. 2015.[72]

© University of Pretoria

Numerous methods are used today including free energy perturbation (FEP), molecular dynamics (MD) and more recently quantum mechanics (QM) and hybrid models.[72] FEP is used for accurate approximations of the free energy of binding between chemically similar compounds for lead generation and optimisation.[72] MD is used as a practical method to estimate ligand kinetics and energies in target binding for lead optimisation.[72] QM has more recently been used in lead generation and optimisation in SBDD and in hybrid QM/MM models for covalent inhibitor interaction studies.[72] Many challenges are faced in ligand design and high potency is not the only factor to be considered or desired.[72] Efficacy and toxicity are also major factors to be considered before commercialisation of a pharmaceutical and are both heavily influenced by the absorption, distribution, metabolism, excretion and toxicity (ADMET) properties of a compound.[72] The ADMET properties must be considered early within the drug discovery flow to limit failures later down the line, where heavy financial investment is required.[72] Computational methods such as quantitative structure-activity relationship (QSAR) and chemometrics are used to predicts these properties.[72]

3.1.1 Structure based drug design

SBDD relies on foreknowledge of the target protein structure and is typically obtained from high resolution X-ray crystallography (XRD) or nuclear magnetic resonance (NMR) data.[72] Thorough analysis of the ligand target interactions allows for rational design of compounds with potentially increased selectivity, potency or affinity.[72] SBDD methods mostly play a role in the 1st and 2nd stages of the drug discovery flow where MD and Monte Carlo (MC) simulations or force field and QM models are used.[72]

3.1.1.1 Models based on force fields

Models based on force fields use molecular mechanics (MM) to calculate the potential energy of a system by the summation of all the parameterised contributions, which are used to simulate experimental data.[72] Four mathematical expressions are typically used to calculate the different contributions of the bonding, non-bonding, van der Waals and electrostatic interactions within a system.[72] Models based on force fields are extensively used as they require considerably less computational resources as compared to QM models and methods such as virtual screening (VS), classical MD, *de novo* design and molecular docking are used.[72]

Molecular docking and VS are used to assess how well a ligand docks within the target site and is based on the premise that if a compound fits well within the target site it will likely interfere with its

© University of Pretoria

function.[72] VS typically starts with expansive libraries of compounds which are systematically reduced to potential hit compounds, which are screened for *in vivo* activity and if proven to be active are then used to design new therapeutics.[72] Hit compounds typically have a 50 % inhibition concentration (IC_{50}) between ten to a hundred micromolar and lead compounds typically exhibit IC_{50} values in the lower nanomolar range.[72] *De novo* design involves the building of a compound from scratch within the target site.[72] Chemical groups are incorporated in positions within the target site to allow for beneficial interactions with protein residues or chemical groups in the target structure.[72]

MD models can simulate the interactions between a ligand and target over a period of time and assess the energy of the whole system using Newtonian mechanics.[72] Classical MD models can accurately estimate the free energy of binding between the ligand and target, taking into consideration the entropic, temperature effects and flexibility of the target.[72] However, it is much more computationally expensive, time consuming and is typically used in lead optimisation where very few compounds are assessed and includes FEP and MC simulations.[72]

3.1.1.2 Quantum mechanical models

QM models are used to determine the reactivity, structure, dynamics and energies of molecules and are the most computationally demanding and advanced models available.[72] QM models are either based on density functional theory (DFT) or *ab initio* methods.[72] *Ab initio* methods aim to resolve the Schrödinger equation and the systems wave function.[72] DFT is based on the idea that the "ground state energy of a system of interacting electrons is a unique function of its electron density" and was theorised in 1964 by Kohn and Hohenberg, and has a balance between computational expense and accuracy.[72] Drug design in QM models depends on electrostatic potential diagrams to determine the target binding site and its characteristics, such as likely protonation states of chemical groups.[72] QM also plays a vital role in improving force fields to better describe unique molecules including pharmaceuticals.[72] Reaction mechanisms can be studied to better understand inhibitory or catalytic reactions for better design of ligands against respective enzymes.[72] The limitation of QM is that the calculations are theoretically done in the gaseous state and within small systems, which is not the case for biological reactions which occur in large systems in liquid mediums.[72] These limits are usually overcome by hybrid models of QM/MM, where the ligand target interaction is examined with more detail (QM) and the rest of the system is simplified using MM.[72]

© University of Pretoria

3.1.2 Ligand based drug design

LBDD relies on existing knowledge of active compounds against a particular target where the structural data of the target is unknown.[72] The known actives compounds are used to create a pharmacophore model, which has descriptors describing chemical information shared amongst the active compounds in spatial orientation to each other.[72] These descriptors include physicochemical information such as polarizability, molecular weight, electronegativity, geometry, aromaticity, solvation properties and surface accessible area.[72] The descriptors are used to design or identify potential active compounds, which can be tested with a similarity coefficient that aids in predicting whether a molecule will be active against a set target.[72] QSAR models are built using electronic and geometric descriptors that can predict biological activity of unique compounds not used in the model development set.[72] 3D QSAR models take into account tautomers, conformations, stereoisomers, orientations and protonation states within the initial ligand library.[72] Furthermore, more complex 4D and 5D models can also account for energy contributions, such as conformation entropy and solvation energy.[72]

3.2 Docking based virtual screening

Docking based virtual screening is amongst the most widely used structure based virtual screening (SBVS) and is applied by using a target's structural data and screening a compound library against the structure.[73,74] The compound library usually needs to be prepared before the VS, as the compounds are typically in a 2D format that need to be transformed into a 3D format reflecting important structural data, such as protonation states, stereoisomers and tautomers.[73] The target structure also needs some preparation to ensure that no errors from the structure elucidation affect the VS results, such as missing residue side chains or incorrect dihedral angles and steric clashes.[73] The compound library is docked into the target site and scored using a docking program, which models ligand target interactions, including bonding and steric interactions using the physicochemical properties of the ligand.[73,74] Scoring functions are typically mathematical algorithms which estimate the energy contributions for each ligand target interaction and the summation of the contributions are used to assign a final score to each ligand.[73] The scores and other criteria in a post-processing step are used to assess which ligands can be potential hit/lead compounds for further study or development for a set target.[73] This method has good efficiency, but has fair accuracy that can discriminate against binding and non-binding compounds, however, it can't rank active compounds.[74]

© University of Pretoria

3.2.1 Schrödinger Suite

The SBVS performed in this study was performed using the Schrödinger suite and final scoring of ligands was conducted using the Prime MM-GBSA calculation.[75] A typical workflow using the Schrödinger suite is to prepare the ligands using *LigPrep*, initial ligand docking with *Glide* and redocking using Prime MM-GBSA to estimate ligand binding affinities.[75] Additional steps preceeding the docking include protein preparation and grid generation which are discussed in chapter 4, as well as *LigPrep* and *Glide*.[75]

3.2.1.1 Prime MM-GBSA

MM-GBSA stands for MM with the generalised Born Surface Area solvation model.[75] MM-GBSA estimates ligand activity as binding strength which is determined from calculating the free energy of binding (ΔG_{bind}) in equation 1.[75] ΔG_{bind} is calculated by estimating the free energy difference between the complex and the free ligand and target for the free energies of minimisation (ΔE_{MM}), solvation (ΔG_{Solv}) and surface area energies (ΔG_{SA}).[75] MM-GBSA requires a ligand-complex input from molecular docking before it can perform its calculations.[75] In the Schrödinger suite the MM-GBSA calculates the ΔG_{bind} in a cycle approach with 4 different snap shots of the bound and unbound ligand and target, instead of a continuous MD simulation to decrease the computational resources required, allowing for faster modelling times.[76] The 4 snap shots include the ligand and target bound and unbound in both a solvated environment and a vacuum environment to calculate ΔG_{bind} (Figure 3.2) using equation 2.[76]

Equation 1: $$\Delta G_{bind} = \Delta E_{MM} + \Delta G_{Solv} + \Delta G_{SA}$$

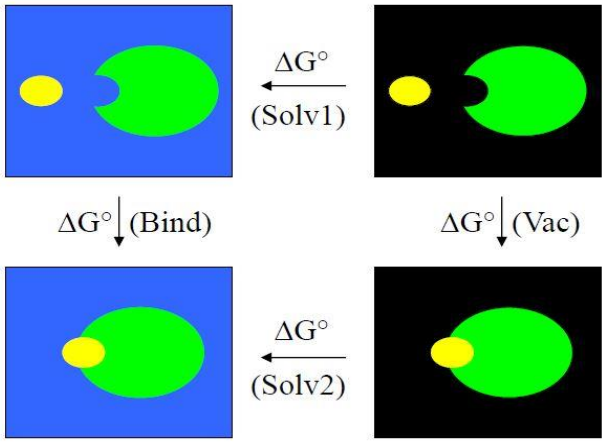

Figure 3.2: The thermodynamic cycle of the MM-GBSA calculation. Recreated from Steinbrecher T. 2016 Schrödinger presentation.[5]

© University of Pretoria

Equation 2:[76] $$\Delta G_{bind} = \langle \Delta G_{vacuum} - \Delta G_{Solv1} + \Delta G_{Solv2} \rangle$$

3.2.1.1 Force field

The OPLS_2005 force field was used in the entirety of the *in-silico* study, which is a Schrödinger developed force field based and improved from the OPLS-AA and OPLS_2001 force fields.[77] The OPLS_2005 was developed for improved coverage of organic functionality and a number of parameters have been revised for higher level of QM theories and was validated over a large test.[77] The improved parameters include additional bending, torsional and stretching parameters and charges of organic functionalities, has improved support for fixed charges and polarizable groups for better handling of non-bonded interactions.[77]

3.3 Model assessment

Assessment or validation of models is required to evaluate whether their predications can be relied upon for the given study as different models are suited for different tasks.[78] Virtual screening methods require assessments that typically use metrics or enrichment factors which assess whether the model can distinguish between active and inactive compounds, to evaluate the reliability of the lead or hit compounds predicted by the model before further development.[78] A number of the enrichment factors can be used with the focus being on robust initial enhancement (RIE), enrichment factor (EF), area under the accumulative curve (AUAC), receiver operating characteristic (ROC) curve and lastly the Boltzmann-enhanced discrimination of ROC (BEDROCK).[78]

3.3.1 Enrichment factors

3.3.1.1 Enrichment factor (EF)

EF is a simple measure of the number of active compounds selected within a defined fraction of an ordered list in relation to a random distribution.[78] The metric is used as a simple early recognition measure as the defined fraction is typically used within the cut off value and used to define the hit/lead compounds from the inactive compounds in terms of the scores given within the model.[78] This is used to assess if the model can select or predict actives compounds before inactive compounds, which is important in drug discovery programs, as the top-ranking compounds are typically selected for further development or evaluation.[78] The metric has the advantage that compounds are not weighed equally

© University of Pretoria

assisting in distinguishing excellent ligands from lower preforming compounds.[78] However, the metric is dependent on the size of the library and performs better if the library is considerably larger than the cut off number of ligands that will be selected for further development or evaluation.[78] A second disadvantage of the metric, is that its value varies with the size of the library making comparison between studies difficult for early recognition assessment.[78] Additionally, the metric can't distinguish a better model which has selected more active compounds earlier (ranked higher) within the same cut off region compared to a model that selected the same number of active compounds but later in the cut off region, when the library is of equal size.[78]

3.3.1.2 Rough initial enrichment (RIE)

The RIE metric was developed by Sheridan and colleagues to continuously decrease the weight exponentially of a compound as a function of rank.[78,79] This was developed to circumvent the disadvantage of the EF metric having large variations when the number of active compounds within the library is small.[78] RIE has been successfully applied to distinguish models that have selected the same number of active compounds within the cut off region, but has assigned a better score to the model which selected active compounds earlier within the list.[78] Additionally, the RIE metric includes all the active compounds contribution within the metrics final score.[78] A disadvantage of the metric is that the maximum and minimum values are affected by the number of active compounds within the library and the total size of the library.[78]

3.3.1.3 Area under the accumulative curve (AUAC)

AUAC is a widely applied metric for assessing the performance of models and is based on the relevant rank of an entry on the abscissa against the accumulative number of active compounds retrieved on the ordinate at x, when the entries are ranked from highest to lowest scored on the ranking method.[78] It illustrates the probability of an active compounds to be selected before the applicable rank at x.[78] The best score achievable with AUAC is 1 when all active compounds are selected first and the worst is 0 when all the active compounds are selected last and a uniform distribution of active compounds will give a score of 0.5.[78] AUAC is related to ROC curves, but has the disadvantage in that the maximum and minimum scores are dependent on the ratio of actives to inactive compounds within the compound set.[78]

© University of Pretoria

3.3.1.4 Receiver operating characteristic (ROC) Curves

ROC curves are a 2D representations of models, showing their performance and performance trade-offs. Two important performance metrics used are *true positive rate* (*tpr*) (Equation 3) and *false positive rate* (*fpr*) (Equation 4), defined as TP as true positives and FP as false positive:[80]

Equation 3: $Tpr = \frac{TP}{TP+FN}$ = recall,

Equation 4: $Fpr = \frac{FP}{TN+FP}$

Plotting of the positive rate (y) against the false positive rate (x) is how a ROC curve is illustrated (Figure 3.3).[80] The are many regions within a ROC curve as illustrated in Figure 3.3, where the diagonal line from 0 to 1 is a line depicting a model that is completely random, which cannot distinguish true positives from false positives.[80] Graphs in the conservative region pick up very few false positive errors, whereas in the bottom left corner no false positives will be chosen, as well as no true positives.[80] Graphs in the liberal region has a great number a false positives, but with a good positive rate.[80] The top right corner designates everything as positive, so won't miss true positives, but will not differentiate between false and true positives.[80] The top left corner indicates a model that picks up all true positives and no false positives, ie 100% *tpr* and 0% *fpr*.[80] The ROC graphs are typically utilised as illustrative curves as this is more indicative/informative than point graphs (Figure 3.4).[80] Models that produce ROC curves closer to the perfect curve perform more efficiently than those closer to the random line (Figure 3.4).[80] In Figure 3.4 the green graph indicates an almost perfect model, while the light purple graph indicates a good model and the red and orange graphs subsequently poorer models. Visual representation of models using ROC are easier to use to distinguish optimal from sub-optimal models.

© University of Pretoria

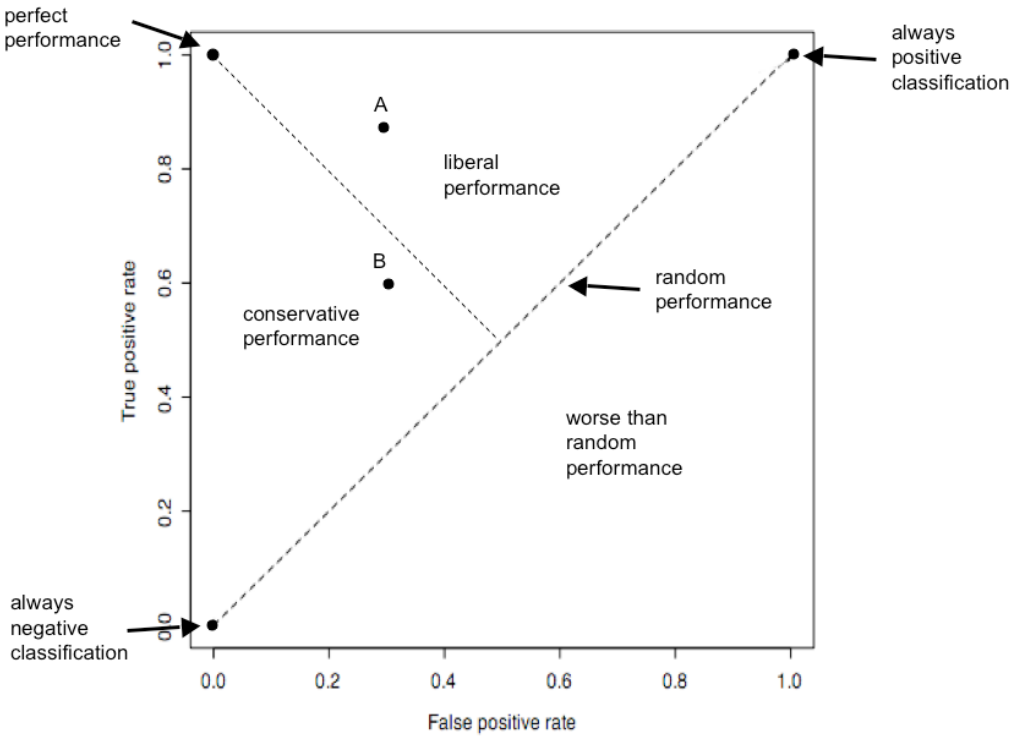

Figure 3.3: Regions of a ROC curve. Recreated from Hamel L.[80]

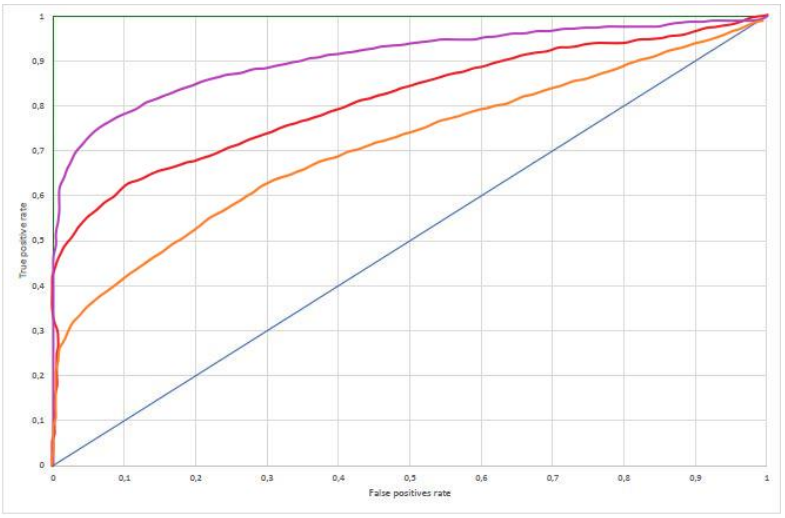

Figure 3.4: ROC curve examples of various performance.

ROC graphs can be used as a singular value, which is similar to the AUAC metric, with 1 being a perfect model taking up all the area under the curve. This is a nice way to summarise and compare many ROC curves, however, using the value itself without inspection of the illustrated curve can be misleading. A ROC curve with a score of 0.5 can be obtained in three different way as depicted in Figure 3.5. All three graphs have a value of 0.5, but graph B is the best curve as it picks half the true positives before it deviates, while graph C is the worst, as it picks all the true negatives before picking true and false

© University of Pretoria

positives. Graph A is again a model that picks randomly and can't distinguish between true and false negatives.

Figure 3.5: Various ROC curves all with an AUAC = 0.5.

3.3.1.5 Boltzmann-enhanced discrimination of ROC (BEDROC):

There are numerous evaluation methods used for VS, but no consensus has been reached on which should be used.[78] Most of these evaluation methods have the "early recognition" problem, in which the methods don't give improved scores or preference for models that identify true positives (actives), before false positive compounds.[78] Early recognition is important as only a very small portion of the compound library will be tested for *in vitro* activity and it is typically the top set of compounds within the VS workflow that are selected.[78] Most evaluation methods fail to distinguish between the three cases indicated in Figure 3.5, even though the performances are significantly different.[78] *EF* is a metric used to help identify early recognition, but *EF* has been shown to have great variability and its values are affected by the ratio of active compounds within the list.[78] *RIE* does not suffer from the early recognition problem, but suffers from variability between cross comparisons, as it is highly dependent on the ratio of active co0mpounds within the VS list. [78]

A new metric called Boltzmann-enhanced discrimination of receiver operating characteristic (*BEDROC*) was adapted from generalising the ROC metric to alleviate the early recognition problem.[78] The metric is similarly bound to [0:1] like the ROC metric, but an exponential parameter α is included to identify early recognition.[78] Truchon and Bayly designed the metric to have the probability of selecting a ranked active compound before a random compound following the exponential of the α parameter.[78] This is true when αR_a <<1 and the metric must be released from the saturation effect, which would

© University of Pretoria

hamper comparison between models for cross-evaluation.[78] The saturation effect is when the ratio of active compounds differs between different models, but uses the same ranking method causing variation within the metric.[78] This may arise when there are too many active compounds, which then saturate the front of the list, making it difficult to identify between excellent and moderate ligands or between models that have performances that differ significantly.[78] Parameter α was proposed to be set to 20, making 80% of the maximum contribution to be from 8% of the list, illustrating a BEDROC score of 0.5.[78] This makes BEDROC suited for the early recognition metric instead of ROC's departure from random metric.[78] Where the early recognition is important, there are practical guidelines provided and for more information on the derivatisation of the BEDROC metric please see Truchon JF, Bayly CI, 2007, J. Chem. Inf. Model.[78]

3.4 Selected case studies

Gao and colleagues studied a number of flavonoids previously reported to have inhibitory activity against influenza H1N1 neuraminidase (NA), to identify key interactions for rational drug design of NA inhibitors.[81] A 3D QSAR model was selected from three developed hypothesized models, which were generated with the Prime module in the Schrödinger suite and used a total of thirty-five previously screened flavonoid based inhibitors.[81] The chosen QSAR model had one aromatic ring, three hydrogen bond donors, one positively charged group and one hydrogen bond acceptor and was validated by the test set.[81] The protein preparation wizard was used to prepare the protein (PDB: 1A4G) structure and the active site was designated with the receptor grid generation module for molecular docking of the thirty-five flavonoids.[81] The molecular docking was conducted to identify key interactions and functional groups within the compound set and was accomplished with *Glide* extra precision (XP).[81] The study identified key interactions such as hydroxyl groups at positions 3 and 4 that were predicted to increase activity, while a hydroxyl group at position 6 could decrease activity (Figure 3.6). Additionally, hydroxyl groups at position 5 and 7 were found to be critical for NA binding.[81] This study illustrated the application of 3D QSAR studies in the identification of key functional groups and interactions within a scaffold that could be utilised for rational drug design.[81]

© University of Pretoria

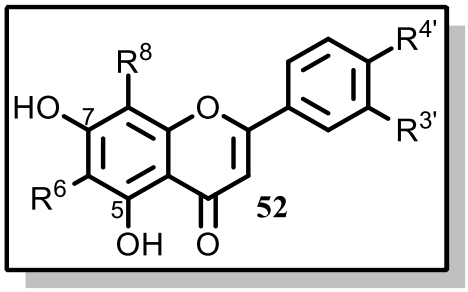

*Figure 3.6: General flavonoid structure (**52**) with numbered substitution positions. Recreated from Goa, et al. 2011.*[81]

Shelke and co-workers developed a pharmacophore and 3D QSAR model from monoamine oxidase-A (MAO-A) inhibitors to identify new compounds for the potential treatment of psychiatric disorders including depression.[82] The Schrödinger suite was utilised for this study and the *Phase* module was used to create the pharmacophore and 3D QSAR model, with the use of 82 compounds of previously reported pyrrole or indole based inhibitors.[82] These compounds were prepared using *LigPrep* and numerous conformers were generated using *ConfGen* to create the pharmacophore consisting of four main bonding groups, including two hydrophobic groups, a hydrogen bonding group and lastly an aromatic ring.[82] The model was then used for the virtual screening of compounds from the ZINC database, with a number of filters used to identify potential hit compounds.[82] The crystal structure (PDB: 1O5W) of MOA-A was prepared in the protein preparation wizard module and the active site was assigned with the receptor grid generation module.[82] A total of 140'000 compounds from the ZINC database were prepared in *LigPrep* and pre-screened through the pharmacophore model to yield 30'052 compounds with desired properties.[82] Conformers of these compounds were produced using *ConfGen* and were comprehensively re-screened through the pharmacophore leading to 28'288 hits.[82] A fitness score filter of more than 60 % was applied, further reducing the hits to 1'572 compounds.[82] The hits were then filtered by selecting compounds with predicted pK_i of less than 1 to give 960 hits.[82] These compounds were docked in *Glide* standard precision (SP) and compounds with scores of less than -8.0 were retained to give 247 hits, these were redocked with *Glide* XP and with the same restriction applied to yield the final 11 compounds.[82] These 11 compounds (**53**-**63**) were identified as prospective hit compounds for further development and inhibition studies against MAO-A.[82]

© University of Pretoria

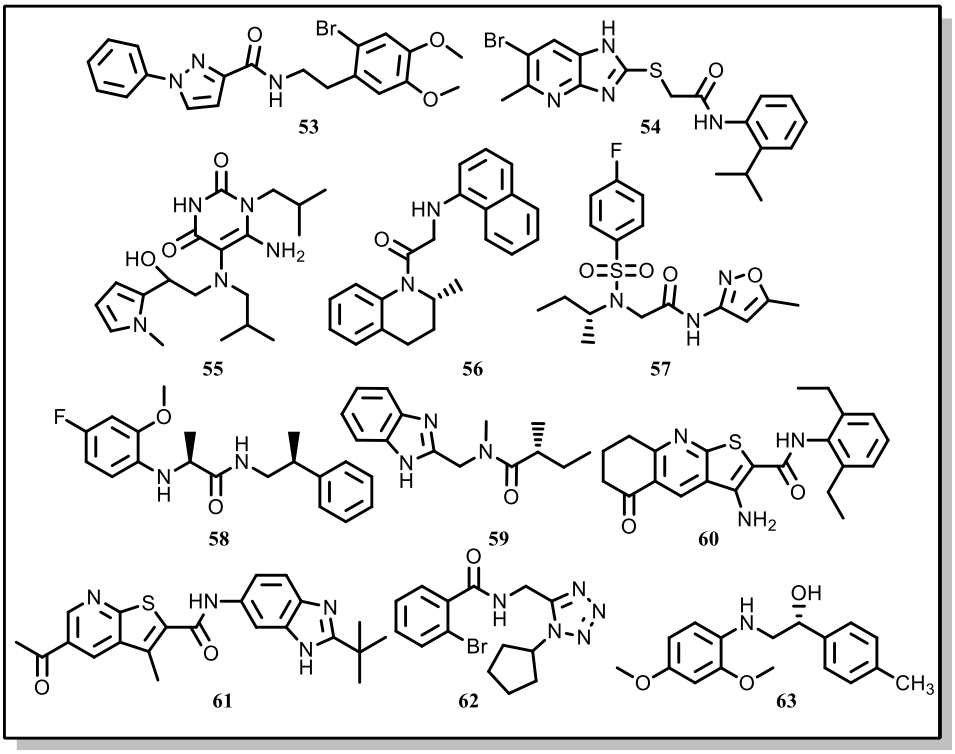

Figure 3.7: Structure of the 11 lead compounds identified by Shelke and co-worker. Recreated from Shelk, et al. 2011.[82]

Veeramachaneni and colleagues used the Schrödinger suite to identifying potential therapeutics targeting pancreatic lipase in an effort to treat obesity.[83] Pancreatic lipase is a key enzyme within the triglyceride metabolism and hydrolyses glycerides into fatty acids and glycerol.[83] The active site of the enzyme was previously identified as three critical residues, Asp-176, His-263 and Ser-152, with the serine being the key residue in the hydrolysis reaction.[83] Veeramachaneni and co-workers took advantage of the previously described active site (crystal structure) and used an FDA approved drug orlistat (**64**) to run a shape-based virtual screening method on the 169'109 natural compounds within the ZINC database.[83] Shape-based virtual screening searched for molecules within the database that have similar electrostatic properties and shapes to orlistat (**64**) and predicted 117 hits to have similar activity and binding.[83] The selected 117 compounds were then subjected to *QikProp* which assesses the ADME properties of the ligands, the predicted CNS activity score was taken as the primary factor and the Lipinski's rule of 5 was taken as the second factor further reducing the set to 9 hit compounds.[83] The top 9 selected ligands were then prepared using *LigPrep*, docked using *Glide* and rescored with Prime MM-GBSA.[83] Three compounds (**65**-**67**) were identified as potential leads by the predicted ligand affinities for further development, as these compounds were predicted to have essential hydrogen bonding interactions with Ser-152, as well as other beneficial interactions and energetic stability (Figure 3.8).[83]

© University of Pretoria

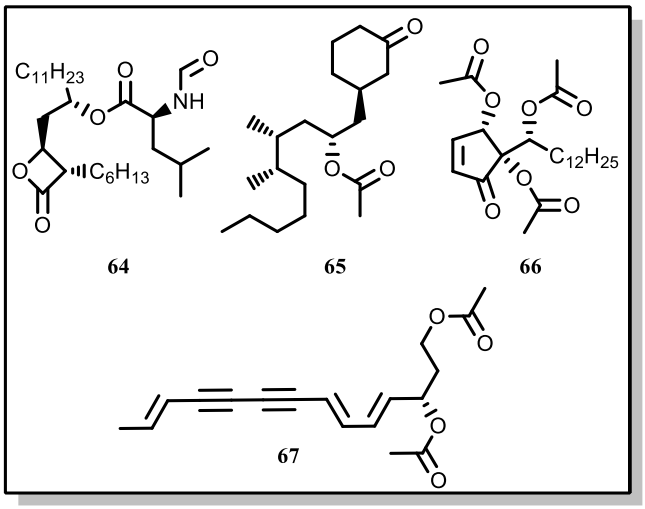

*Figure 3.8: Structure of orlistat (**64**) and top three compounds (**65-67**) identified by Veeramachaneni and co-workers. Recreated from Veeramachaneni, et al. 2015.*[83]

Subhani and colleagues utilised molecular docking and homology modelling to identify potential therapeutics against multi drug resistant protein 1 (MDR1) for the treatment of non-small cell lung cancer (NSCLC).[84] MDR1 is an efflux pump which is an efficient transporter of a large variety of therapeutics, decreasing the efficacy of the treatment of cancer and has therefore become a desired drug target.[84] Five drugs including gemcitabine, paclitaxel, cisplatin, docetaxel and carboplatin were investigated in the binding of MDR1 to identify beneficial binding interactions and as potential lead compounds.[84] A homology model was developed for MDR1 using NCBI protein Blast which identified *Mus musculus* (house mouse) MDR1 protein structure to best resemble the human protein, through protein sequence comparison.[84] The Schrödinger suite (2014-3) was utilised in this *in silico* study, which started with a four protein model generated using the knowledge-based method in Prime.[84] The lowest energy model was selected and further refined using the protein preparation wizard and was validated in PROCHECK using a Ramachandran plot.[84] The five ligands were prepared using *LigPrep* and were then pre-docked using *Glide* XP before docking with induced fit docking (IFD) module.[84] IDF takes the flexibility of the protein into account and creates a number of entries with various protein conformations.[84] The ligand binding affinity was then predicted by running the IFD entries through Prime MM-GBSA, which identified paclitaxel (**68**) and gemcitabine (**69**) as potential lead compounds against MDR1 (Figure 3.9).[84] Paclitaxel (**68**) and gemcitabine (**69**) underwent an experimental *in vitro* study which showed good correlation to the computational study and identified the combination of the two compounds as a potential treatment for NSCLC.[84]

© University of Pretoria

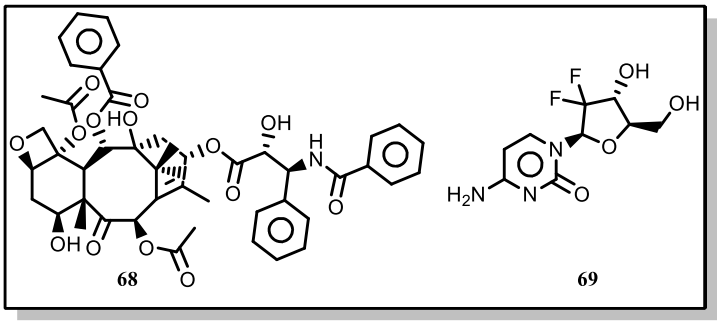

*Figure 3.9: Structure of paclitaxel (**68**) and gemcitabine (**69**) identified by Subhani and colleagues. Recreated from Subhani, et al. 2015.*[84]

A more recent study on identifying potential MDR1 inhibitors was undertaken by Gade *et. al*. using pharmacophore and 3D QSAR modelling with molecular docking.[85] The Schrödinger suite was utilised for this study with the Phase module used to develop the pharmacophore and QSAR model, that used thirty-seven acridone based compounds (**70**) previously studied within the group to create the models.[85,86] These compounds were prepared using *LigPrep* before model development and produced a pharmacophore consisting of three aromatic rings and two hydrogen bond acceptor groups.[85] The NCI 2012 chemical database was used for screening, each compound was prepared in *LigPrep* and ten conformers of each molecule were generated before screening, to improve sampling.[85] A number of filters were applied within the Phase module during screening which reduced a total of 265'242 compounds to 25 hit compounds, which were further assessed using *QikProp* to evaluate their ADME properties.[85] These compounds were docked in a prepared MDR1 protein (PDB: 4Q9H, house mouse) using *Glide* XP and Prime MM-GBSA to assess the binding affinities which identified a lead compound (**71**).[85,86] A human homologous protein structure model was developed using the Prime module and the crystal structure of *Mus musculus* (PDB: 3G60, house mouse) and was validated using a Ramachandran plot.[85] The protein model was used for the MD simulation of the lead compound (**71**) to identify conformation changes between the ligand and protein over a period of time to better understand the binding mechanics of acridone based compounds (Figure 3.10).[85] This study illustrated the role of combined computational methods in the identification and design of potentially potent MDR1 inhibitors.[85]

© University of Pretoria

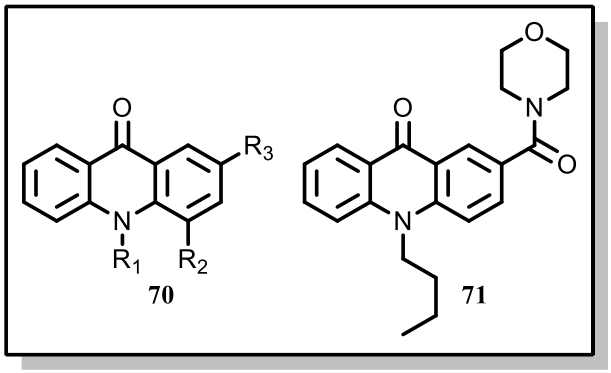

*Figure 3.10: Structure of the general acridone structure (**70**) and the top scoring compound (**71**) identified by Gade and co-workers. Recreated by Gade, et al. 2015.*[85]

Goyal and co-workers developed potential dual inhibitors for Alzheimer's disease (AD) targeting both acetylcholinesterase (AChE) and β-amyloid cleavage enzyme (BACE-1).[87] The ligand library was based on 1,4-dihydropyridine (DHP) analogues (**72**) as DHP has shown good inhibition against BACE-1.[87] The library started with twenty compounds which shared the DHP backbone and had various substituents at four substitution sites (Figure 3.10) and were prepared using Vlife molecular design suite (Vlife MDS) to convert the 2D structures to 3D and further optimise the entries.[87] The compounds were broken up into four fragments and a group-based QSAR (GQSAR) analysis was performed to produce 705 physicochemical descriptors using Vlife MDS, which was further refined to 311 independent descriptors.[87] The compound set was divided randomly into a test set and training set to generate the GQSAR model, which was further validated using two methods. The two methods used included the leave one out method and prediction of the pIC_{50} of the test set and statistical correlation between the predicted and experimental values.[87] A combinatorial ligand was created using a module within Vlife MDS called Leadgrow and was prepared and docked into a prepared BACE-1 structure (PDB 2B8L) using *LigPrep* and *Glide* respectively from the Schrödinger suite (2009).[87] The *Glide* docking was completed using the XP setting for higher accuracy.[87] Lastly the library was also docked against AChE (4M0E) using *Glide* XP and high scoring ligands were further assessed using Lipinski rule of 5, which resulted in identification of two lead compounds (**73** and **73**) for further development as dual inhibitors of both AChE and BACE-1 (Figure 3.11).[87]

© University of Pretoria

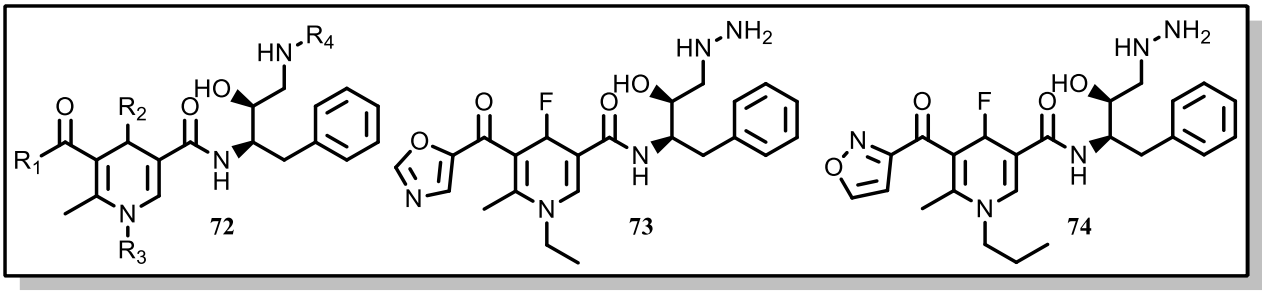

*Figure 3.11: Structure of general DHP analogues (**72**) and top two identified ligands (**73** and **74**). Recreated from Goyal, et. al. 2014.*[87]

Vijayakumar and colleagues identified potential natural products for the treatment of AD through the use of molecular docking and MD simulations against AChE.[88] Natural products were targeted as many patients believe such derived pharmaceuticals have fewer adverse side effects.[88] All the *in-silico* work was performed within the Schrödinger suite and started with twenty compounds from the Chemspider database and used the human AChE (PDB: 1B41) protein structure.[88] The protein was prepared using the protein preparation wizard module and the compounds' preparation with the *LigPrep* module.[88] After this, molecular docking was performed with *Glide* XP and the ligand binding affinities were assessed using Prime MM-GBSA.[88] Rutin (**75**), a natural flavonoid, was identified due to its overall superior score and its ligand-protein interactions were further assessed using MD simulations with the *Desmond* software.[88] The MD simulation illustrated stable ligand-protein binding for a period of thirty nanoseconds (ns) after a seventeen ns equilibrium period.[88] Additionally, ADME analysis of all the compounds with the QikProp module was performed, to predict potential efficacy and toxicity of the library.[88] The study illustrated the identification of potential natural products for the treatment of AD and identified rutin (**75**) as a top candidate for further development and study, as well as additional promising compounds including (+)-procyanidin B2 (**76**), glycyrrhizin (**77**), hesperidin (**78**) and narirutin (**79**) (Figure 3.12).[88]

© University of Pretoria

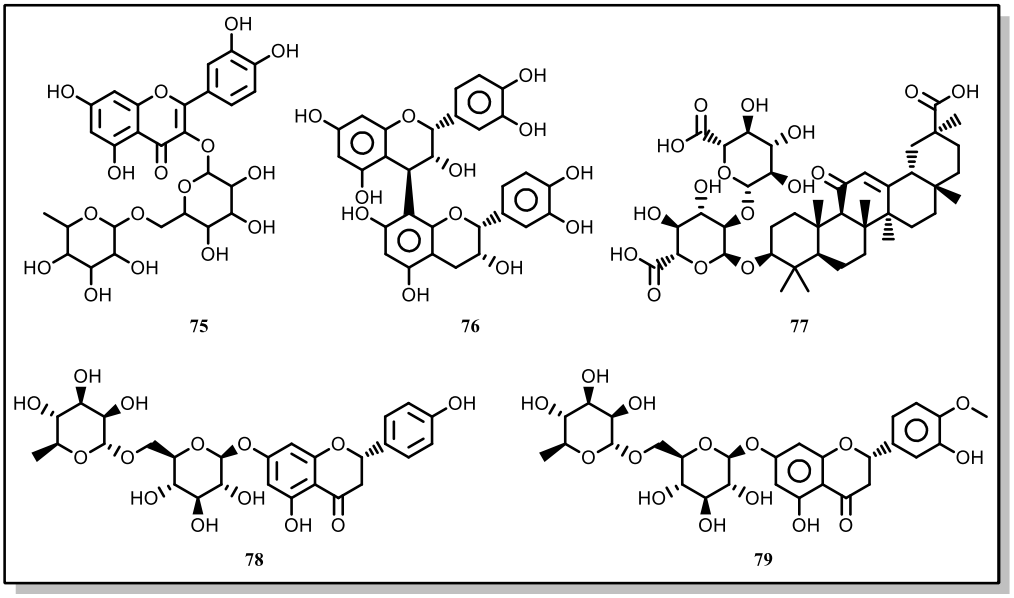

*Figure 3.12: Structures of rutin (**75**, (+)-procyanidin B2 (**76**), and glycyrrhizin (**77**), hesperidin (**78**) and narirutin (**79**). Recreated from Vijayakumar, et al. 2018.*[88]

3.5 Proposed virtual screening workflow

A standard workflow as described in literature[83,89,90] will be used to screen the virtual ligand library proposed in this dissertation against acetylcholinesterase of *Tetronarce californica* (1EVE) using the Schrödinger suite (Figure 3.13). The PDB will be prepared using the protein preparation wizard module and thereafter the active site will be designated with the Receptor Grid generation module. The proposed ligand library will be prepared using the *LigPrep* modules, before docking with *Glide* and rescoring with Prime MM-GBSA set at 0 Å initially. The initial model will be assessed with known active compounds from the ChEMBL database.

© University of Pretoria

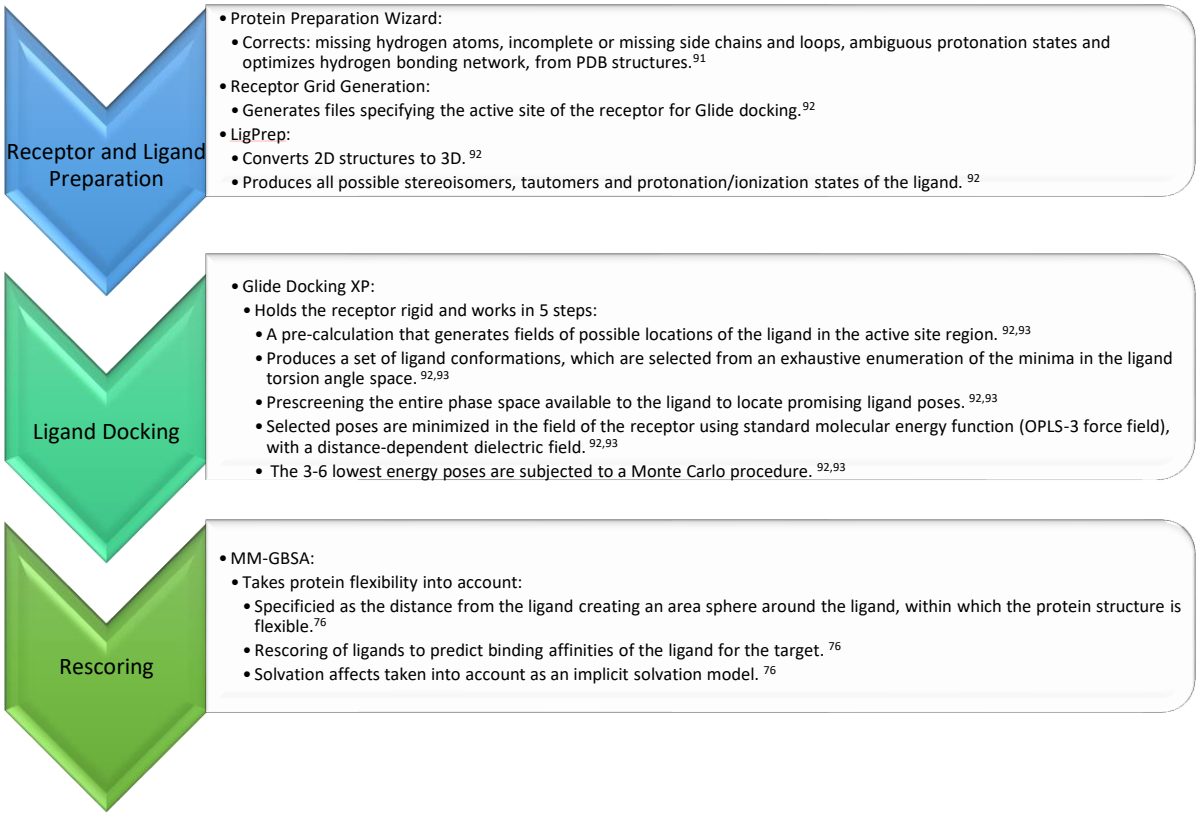

Figure 3.13: Standard molecular docking workflow with additional information pertaining to each step.[76,91–93]

3.6 Aims and Objectives

3.6.1 Computational study

1. Model development.
    1. Identify suitable protein structure of AChE.
    2. Develop and prepare theoretical silicon derivatised donepezil-based library.
    3. Run standard workflow model on theoretical silicon derivatised library.
2. Evaluation of developed model.
    1. Identify known active compounds with donepezil like structures to build a test set.
    2. Evaluate developed model and assess model using known metrics (enrichment).
3. Model refinement.
    1. Refine the developed model, possibly incorporating the use *ConfGen* and Macro model minimization separately and in combination with the test set (known active compounds).
    2. Evaluate refined model's results using enrichment metrics.
    3. Analyse and determine the best performing model.
4. Evaluation of theoretical silicon derivatised donepezil-based library with chosen model.
    1. Identify promising scaffolds through assessment of docking scores and predicted protein ligand interactions.

© University of Pretoria

3.6.2 Synthesis of identified scaffolds

1. Preparation of donepezil (model study).
    1. Validate current synthetic route for the preparation of donepezil to gain insight into the chemistry and conditions required for accessing the core scaffold on which the *in silico* modelling was based.
2. Synthesis of silylated analogues of donepezil identified in the *in silico* study.
    1. Identify at least two silylated scaffolds that are predicted to have comparable activities and binding models to donepezil and which are predicted to be synthetically accessible.
    2. Synthesis of identified silylated scaffolds through modification of chemistry from the model study.
    3. Derivatisation of silylated scaffolds where possible to afford a library of molecules for biological screening.

© University of Pretoria

Chapter 4 Computational results

4.1 General

In this study a theoretical library of silicon containing compounds based upon the scaffold of the commercially available and FDA approved cholinesterase inhibitor donepezil were assessed under *in silico* conditions (Figure 4.1). Silicon was chosen as literature has shown that incorporation of silicon within a ligand scaffold can increase the lipophilicity of a drug, which is a property of paramount importance for pharmaceuticals targeting neurodegenerative disease.[56,57,70] The optimal lipophilicity of a molecule is critical for drug absorption through the blood brain barrier and careful control of the range of this property together with the total polar surface area of the molecule can allow one to increase the bioavailability of the drug within the brain, assisting in efficacy and activity of the pharmaceutical.[94] A virtual screening workflow was used to predict the binding energies and properties of the virtual library when bound to acetylcholinesterase (AChE). Five main silyl analogue classes based upon both the donepezil and its related unreduced scaffold which contains an alkene linker between the indanone and piperidine motifs were envisaged, looking at i) the silylation of the indanone ring through O-Si or C-Si bonds, ii) the direct silylation of the benzyl ring, iii) the replacement of the methyl linker between the indanone and piperidine rings with a silicon group, iv) the replacement of the benzylic methyl with a silico group and v) the replacement of the piperidine nitrogen with silicon.

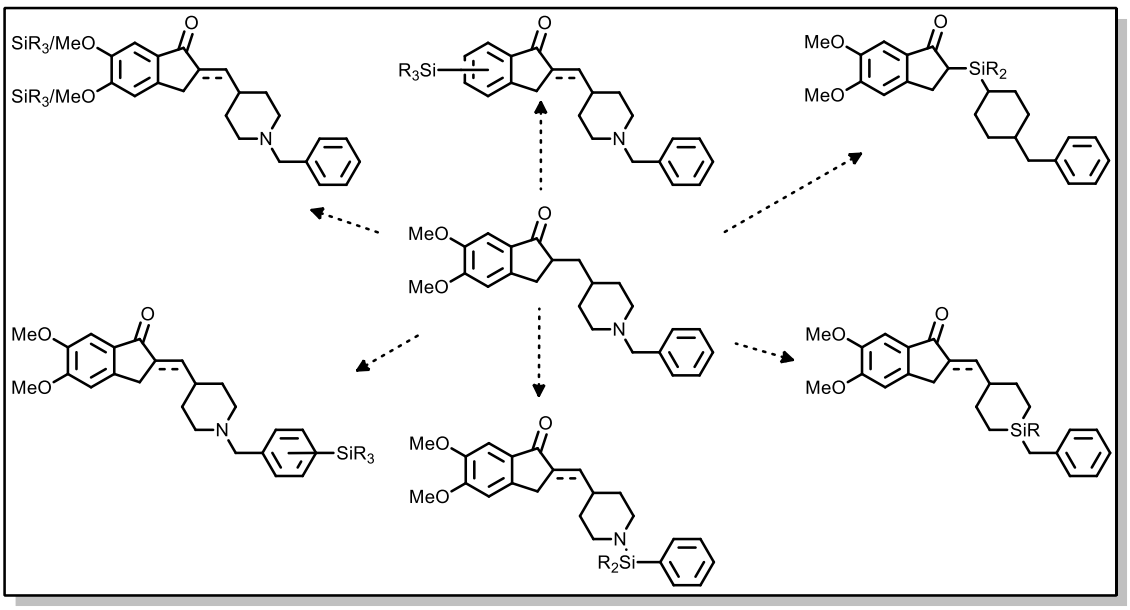

Figure 4.1: Generic structures of targeted silicon containing derivatives of donepezil.

© University of Pretoria

The Schrodinger software suite was utilised with its *canvas* (2018-1)[95] and *maestro* (2018-1)[96] programs for the entire virtual section of this study. Several tasks within this suite were utilised for the model development of this study and are discussed below.

4.2 Tasks utilised in the Schrodinger suite

4.2.1 Protein preparation wizard[91]

This task is essential for preparing protein structures for docking and other calculations, as PDB structure files don't contain all the information from the actual protein captured using x-ray crystallography (XRD). PDB structure files mainly consist of the heavy atoms of the protein, co-factors and metal ions, in addition, the files typically do not contain ionisation and tautomeric states, bond orders and formal atomic charges of the protein. Light atoms such as hydrogen and carbon are not always detected by XRD and may lead to missing hydrogens and protein side chains in the PDB structure file. The task detects these errors, corrects them in the appropriate positions and relieves any steric clashes formed from the placement. Standard settings with additional, 'fill in missing side chains using prime' and 'fill in missing loops using Prime' in the first tab and in the last tab removed water with less than 1 H-bonds to non-waters options were used.

4.2.2 Grid generation[91]

This task creates a virtual box around the binding site of a protein to restrict calculations to dock ligands only within the box. This ensures that the area in which the ligands can interact with the protein is limited, substantially decreasing the computational resources required for the calculation. Not all PDB structure files contain a ligand bound in the binding site of the protein and such proteins require the binding site/pocket to be identified beforehand. Standard settings were used.

4.2.3 Ligand preparation (LigPrep)[91]

This task is responsible for converting the two-dimensional structures of ligands to their respective three-dimensional conformations, including all stereogenic and structural isomers. The task also optimises geometries and generates low-energy ring conformations of the enumerated isomers. Standard settings were used with additional 'generate all combinations' setting for chiral centres.

© University of Pretoria

4.2.4 ConfGen[97]

The task generates rigid conformers of the ligand with different geometries of different potential energies. The function used in ConfGen is similar to an inbuilt function within the glide task, but it produces many more iterations for a single ligand. The task was utilised with standard setting with the target number of conformers' set to 64.

4.2.5 Glide[93]

This task docks the ligand in possible locations at which the ligand may bind to the active site of the enzyme. The search area for this calculation has to be predefined using the grid generation task within the desired protein structure. Glide holds the protein structure rigid, while changing the conformation of the ligand within the binding pocket. Favourable positions are scored (docking score) based on favourable hydrogen-bonding, hydrophobic, metal-ligand interaction and are also penalized for steric clashes. This calculation also includes a cut off function that removes ligands which do not meet the threshold value. Standard settings were used at extra precision (XP), except for calculations that had confgen preceding glide, then the ligands were held as rigid instead of flexible.

4.2.6 Minimisation[98]

The task optimises ligand geometries by calculating the potential energy of each conformer with solvation effects and bonding interactions accounted for. Standard settings were used, with the *PRCG* method used, the maximum number of iterations was set to 1000.

4.2.7 Prime-MM-GBSA[96]

MM-GBSA takes protein flexibility into account, as opposed to the rigid protein approach used during glide docking. The flexibility of the protein is specified as a distance from the ligand creating an area sphere around the ligand, within which the protein structure can move in order to accommodate the binding ligand. Any part of the protein which falls outside of this area sphere is held rigid as before, to reduce the computational time required for the calculation. Solvation effects such as hydrogen bonding networks are considered, and the technique uses an implicit solvent model. Standard settings

© University of Pretoria

were used, except for flexibility as described by distance from the ligand in angstroms, which was varied as indicated for specific calculations.

4.2.8 Enrichment[96]

A task that is utilised to calculate multiple parameters as a means to assess a model's predictive function against a known library of active compounds. The library or selection of compounds that is to be assessed should be ranked in ascending order with no duplicate compounds. A premade list of active compounds is needed with the number of decoys within the selection of compounds. The selection of compounds is then compared against the premade list of active compounds, to assess how many of the highest-ranking compounds are active and/or decoys. The parameters that can be calculated are; BEDROC, ROC, AUAC, RIE, EF, EF*, EF', DEF, DEF*, DEF', Eff and FOD.

4.3 Initial Model development

The protein data bank structure file (PDB) of 1EVE was used in this study, as the same enzyme is typically used for *in vitro* biological evaluation of inhibitory activity against AChE.[53] The PDB 1EVE consists of the AChE enzyme of the species *Tetronarce californica* (Pacific electric ray, *t*AChE), as well as donepezil which is bound in the active site. The bound ligand simplified the docking procedure as the protein is already in a state/conformation suited for donepezil and donepezil-like compounds.

The binding properties of the ligands were predicted using the suite's Prime MM-GBSA calculation, using the MM-GBSA bind energy. MM-GBSA bind energy is used as an estimate of the binding affinity of the ligand to the enzyme and therefore represents an estimated value of the IC_{50}. This is a theoretical approach to identifying potential lead compounds that may bind efficiently to the target. It is pertinent to note that the MM-GBSA score can be used to distinguish between good ligands and bad ligands, but is not accurate enough to rank the ligands in terms of IC_{50} values.

The initial model started with the 1EVE crystal structure and the proposed silicone derivatised ligand library. The protein needed to be prepared for the docking study, but the "remove waters" (RMW) setting needed to first be determined, before the docking study could commence. The setting is a numerical value that determines which waters are removed based on the number of hydrogen bonds a particular water has to non-water molecules. Donepezil was prepared using *LigPrep*, which resulted in 4 entries. These entries where then glide docked with 4 prepared PDB structures with the RMW

© University of Pretoria

setting varying from 1 to 4, where 1 will have the most waters and 4 the least number of waters. The results were then ranked in ascending order based on their docking scores. The prepared protein entry with the highest score was then superimposed over the 1EVE PDB crystal structure containing bound donepezil and the entry with the lowest RMSD score was selected as the best prepared protein for model use. The results are shown in table 4.1, with RMW 1 affording the best docking and RMSD scores, furthermore a near identical binding pose to the PDB's docked donepezil was obtained (Figure 4.2).

Table 4.1: Docking and RMSD scores of the best docked donepezil entry in the 4 prepared proteins with varying removed water options.

Entry	Docking score	RMSD
RMW 1	-14.539	0.6391
RMW 2	-13.713	0.8306
RMW 3	-13,370	0.6998
RMW 4	-12.380	1.3140

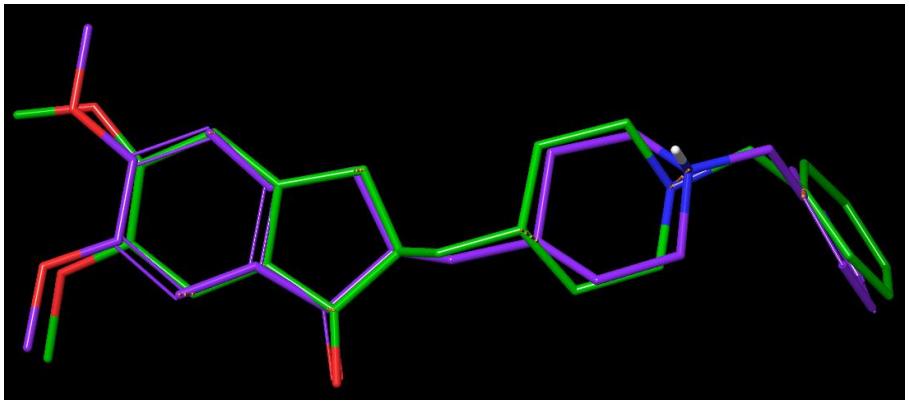

Figure 4.2: Docked RMW1 donepezil (purple) superimposed with 1EVE PDB donepezil (green).

A standard workflow as described in literature[89,90] was used to screen the virtual ligand library with 1EVE prepared with RMW1 and Prime MM-GBSA set at 0 Å. This workflow used *LigPrep* to prepare the ligands and thereafter, docked the ligands using Glide and subsequently Prime MM-GBSA at 0 Å. The final results were obtained, but the model needed to be assessed for its accuracy and reliability. To assess the standard workflow methodology, a small library of known active compounds were used to test if there was any correlation between the binding energy and inhibition activity (IC_{50} value) of

© University of Pretoria

the compounds. The active AChE compounds were obtained from the ChEMBL data-base, ChEMBL is an online database of bioactive drug-like small molecules and their biological properties.[99] Unfortunately, the known active library showed no correlation between the binding energy and the inhibition activity (IC_{50} value) of the compounds indicating that the current model was predicting active and inactive compounds randomly. As a result, it was then attempted to develop an improved model, which would allow the distinction between active and inactive compounds.

4.4 Ligand selection for validation of workflow

At the time of the study, several libraries of known AChE inhibitors were available and were separated depending on which species of AChE enzyme was used to assess the biological activity of the compound. The libraries chosen for this study were those assessed for activity against *Tetronarce californica* and *Electricus electrophorus*, containing 371 and 4081 compounds respectively. The *Electricus electrophorus* library was included to ensure a large enough data set to reliably assess the workflow. This addition was motivated, as Kruger and colleagues noted that "donepezil has a high affinity for AChE, binding to both *Electricus electrophorus* and Mouse AChE in the nano-molar range", and being comparable to the donepezil binding with *Tetronarce californica* (IC_{50} = 5.7nm).[52,100] *Electricus electrophorus* has no available protein structure to date, with only a reconstructed protein structure based on the mouse protein. As a result, it was decided to include these compounds based upon the hypothesis that the known active drugs of *Electricus Electrophorus*, which are structurally similar to donepezil will have similar binding affinities to *Tetronarce californica*.

The combined libraries were then imported into Canvas and a structure decomposition task was performed. This task breaks the compounds into fragments and assesses how frequently they appear among all the entries. Fragments of the donepezil scaffold were chosen and compounds with structural similarity to donepezil were visually inspected and chosen.[95] Only donepezil-like compounds were selected leading to an active compound library of 56 compounds (Figure A1, appendix A) used to assess the workflows.

4.5 Optimisation of the standard workflow

An attempt was undertaken to improve the accuracy and precision of the standard workflow model through the optimisation of the protein preparation and taking into account the flexibility of the

© University of Pretoria

protein within the Prime MM-GBSA calculation. Four prepared proteins were used, RMW1, RMW2, RMW3 and RMW4 and the MM-GBSA calculation was performed at 0, 3 and 5 Å.

The models were assessed using a combination of ROC curves, ROC, BEDROC, RIE, AUAC and EF (at 1% and 10%) scores. ROC curve scores should not be used without the visual representation of the data in a ROC curve, as there are a number of ways a ROC score can be obtained, and both are needed for proper assessment of a model.[78,80] The BEDROC score is a score that was described to assess the "early recognition" of a model, more specifically, it assesses if the model will identify active before inactive compounds, which is an important property for lead drug identification in modelling.[78] All the enrichment scores are discussed in detail in chapter 3. These were calculated using the enrichment calculation and through manual processing of the data in excel using pivot tables.[96]

As there is no database with known inactive compounds targeting AChE, it makes calculating the enrichment of the workflows challenging, where the enrichment refers to how likely the model is to select an active over an inactive ligand. To circumvent this issue, some of the known active compounds used, were designated as inactive/decoys if they displayed an IC_{50} value below a designated threshold. A 500 nmol IC_{50} threshold was decided upon, leading to a library of 21 active compounds and 35 "decoys". In literature it is common to have exceedingly more decoys than active compounds and hence a lower threshold was used.[78] Decoys from the DUD-E data base were not used for the rationale that these compounds have not been tested against AChE and as such cannot be designated as a decoy.

4.5.1 Results

The 1EVE RMW1 0 Å model was arguably the best scoring model when compared to the analogous 3 and 5 Å models, however, the difference in the performance was minimal as is evident when looking at the ROC curves (Graph 4.1). As a result, large differences in the predictive function of the remaining three models was not expected, which only differed in terms of the number of waters present.
As predicted the 1EVE prepared protein RMW2, RMW3 and RMW4 all performed similarly with only minor differences (Graph 4.1). In the case of the 1EVE RMW2 the 0 and 3 Å models had improved "early recognition" compared to the 5 Å model, however, other enrichment factors suggested only minor differences between the three models with only the 5 Å having worse EF scores at 1 % and 10 % (Table 4.2). In the 1EVE RMW3 3 Å model the BEDROC score was poorer than in the analogues 0 and 5 Å models (Table 4.2). Finally, the 1EVE RMW4 showed no marked differences between the three

© University of Pretoria

models with comparable enrichment factors, the EF at 1 % and 10 % did show some minor variations (Table 4.2).

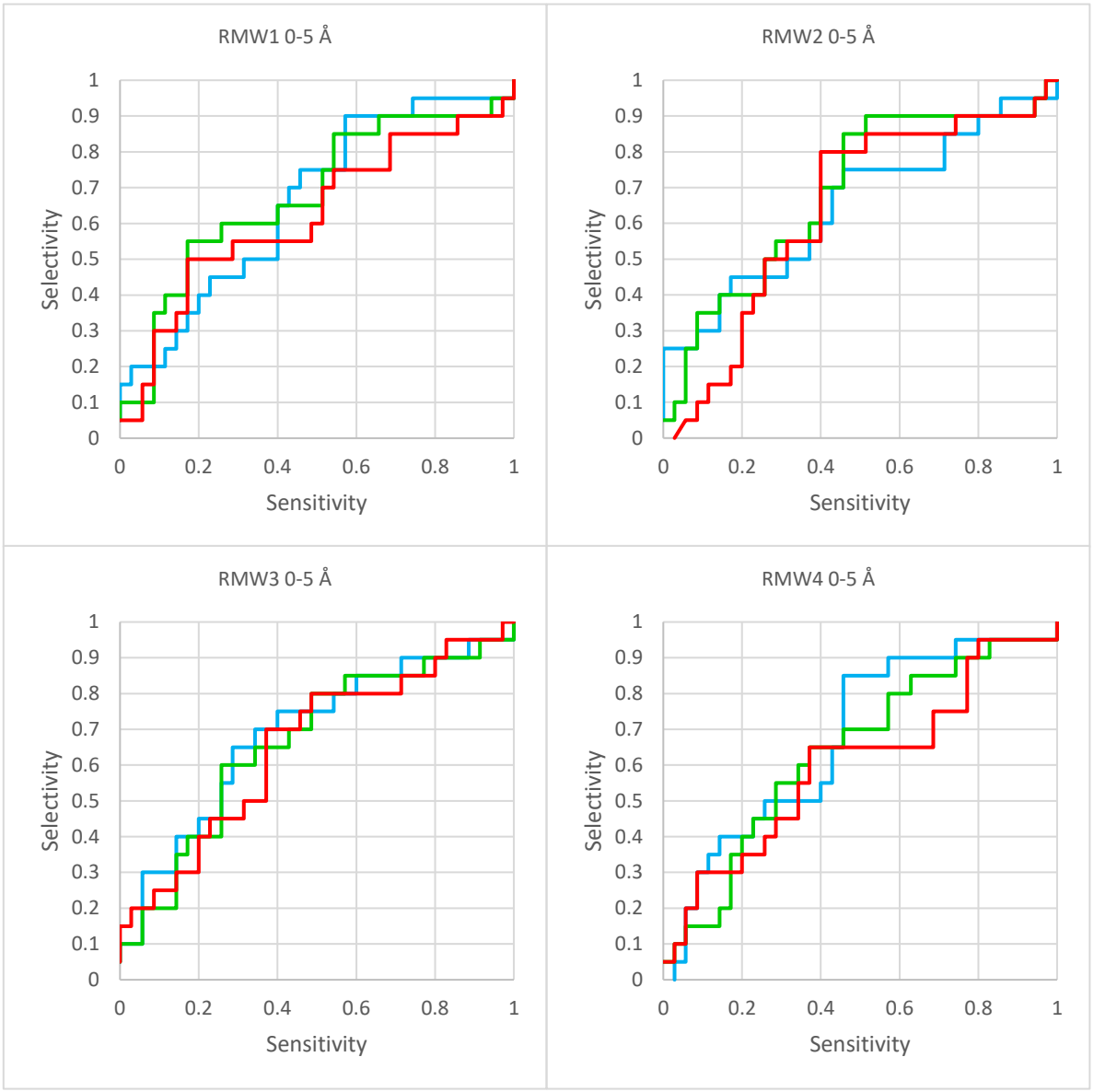

Graph 4.1: ROC curves of the 4 prepared proteins at different RMW settings for the standard workflow, at varying distance of flexibility within the MM-GBSA calculation; 0 Å —, 3 Å —, 5 Å —.

© University of Pretoria

Table 4.2: Total comparison of all four prepared proteins, using ROC, BEDROC and AUAC scores.

Parameter	RMW1			RMW2			RMW3			RMW4		
	0 Å	3 Å	5 Å	0 Å	3 Å	5 Å	0 Å	3 Å	5 Å	0 Å	3 Å	5 Å
ROC	0.71	0.68	0.62	0.65	0.69	0.64	0.69	0.66	0.65	0.67	0.64	0.60
BEDROC	0.698	0.623	0.571	0.687	0.612	0.419	0.636	0.587	0.619	0.560	0.523	0.562
AUAC	0.63	0.61	0.58	0.59	0.62	0.59	0.62	0.60	0.60	0.61	0.59	0.56
RIE	2.31	1.82	1.55	2.38	1.76	0.77	1.95	1.83	2.13	1.34	1.54	1.70
EF 1 %	2.8	2.8	2.8	2.8	2.8	0	2.8	2.8	2.8	0	2.8	2.8
EF 10 %	1.8	1.4	1.4	2.3	1.8	0.92	1.8	1.8	1.8	1.8	1.4	1.8

In Table 4.2 the highest (best) scores are highlighted in blue and the second highest in green, to assist in the comparison between all the parameters. RMW1 at 0 Å has the total best score for ROC, BEDROC and AUAC and is second to RMW2 at 0 Å in regard to the best RIE score. The BEDROC score is arguably the most important factor and is essential for identifying models with "early recognition", as such, BEDROC is afforded higher priority over the other scores. That being said, the ROC curves of the four best models, 1EVE RMW1 0 Å, RMW2 0 Å, RMW2 3 Å and RMW3 0 Å suggest that the models don't differ much, (Graph 4.2) and it was expected that there would be no marked difference in the models' predictive function using the "optimised" parameters.

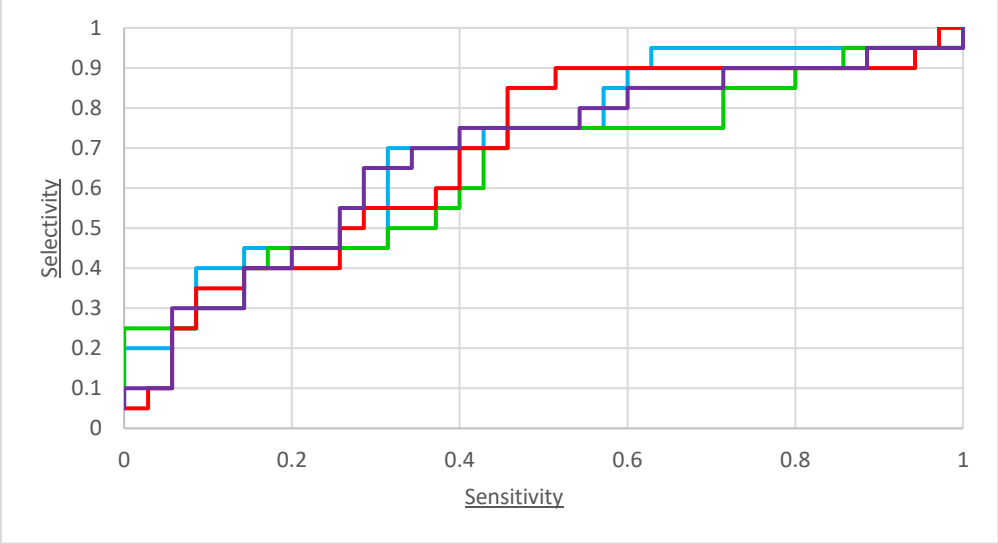

Graph 4.2: ROC curves of the 4 best scored standard workflow, with different RMW prepared proteins and at varying distance of flexibility within the MM-GBSA calculation; RMW1 0 Å —, RMW2 0 Å —, RMW2 3 Å —, RMW3 0 Å —.

© University of Pretoria

4.6 Validation of new models

A presentation by *Schrodinger* showed that incorporation of *Confgen*[101] and M*arcoModel* [98] minimization calculations in the workflow, improved the model's predictive function considerably.[102] Based upon work published by Schrodinger, the new approaches (Figure 4.3) were tested to assess how well the new models were able to select the known active compounds from 'inactive' compounds.

The standard workflow has a total of three calculations in series, namely *Ligprep*, *Glide* and Prime MM-GBSA (Figure 4.3). The first experimental workflow had one additional calculation called *ConfGen* after *Ligprep*, which is used to produce exhaustive iterations of 3D conformers of the ligands with varying energies to improve the sampling of the Glide calculation. The second experimental workflow had one additional calculation called *Minimisation* from the Marco model suite, which calculates the potential energies of the geometries of the ligand entries and optimises them before Prime MM-GBSA. The combined workflow includes both *ConfGen* before *Glide* and *Minimisation* before Prime MM-GBSA.

The models were tested with the same parameters used in the original model to limit the number of variables in the initial stage of model development. The parameters used were the prepared 1EVE protein with RMW1 and the flexibility of the Prime MM-GBSA calculation was held at 0 Å. Further parameter optimisation was performed after the calculation workflow was optimised.

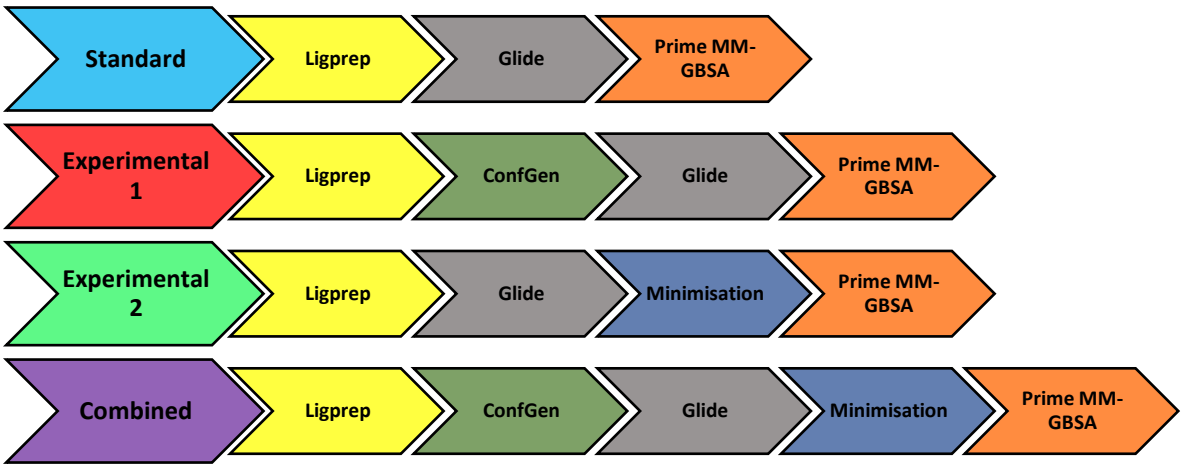

Figure 4.3: Schematic diagram of the modelling workflows, with the standard and 3 new experimental workflows.

© University of Pretoria

4.6.1 Results

An interesting observation was that ligand 1560 (all entries) (Figure 4.4) was consistently removed from the workflow when *ConfGen* was not utilised before *Glide*. This occurred, because the generated conformers of the ligand scored poorly in the *Glide* calculation, to the extent that it did not meet the threshold and was removed. This ligand was also allocated as an active ligand out of the 56, as it has an IC_{50} of 21.4 nM. This illustrates that *ConfGen* is much more enumerative than the in-built glide version. This led to the active lists for the standard and experimental 2 workflows having 20 active compounds and 35 “decoys”, as ligand 1560 had to be removed from the active list.

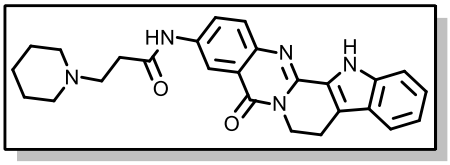

Figure 4.4: Structure of ligand 1560.

The combined experimental workflow showed an improvement in its BEDROC score and subsequently has better early recognition compared to the other models, as shown in the ROC curve (Graph 4.3), with the sharp increase in the graph at x = 0. The combined workflow also has a more arched ROC curve, which indicates it has a higher true positive rate compared to the other models. The combined workflow also scored the best average of the EF score (Table 4.3). The experimental 1 workflow did the worst in all the parameters, but not markedly when compared with the standard and experimental 2 workflows. The combination of all the calculations into a linear workflow was shown to greatly increase performance.

© University of Pretoria

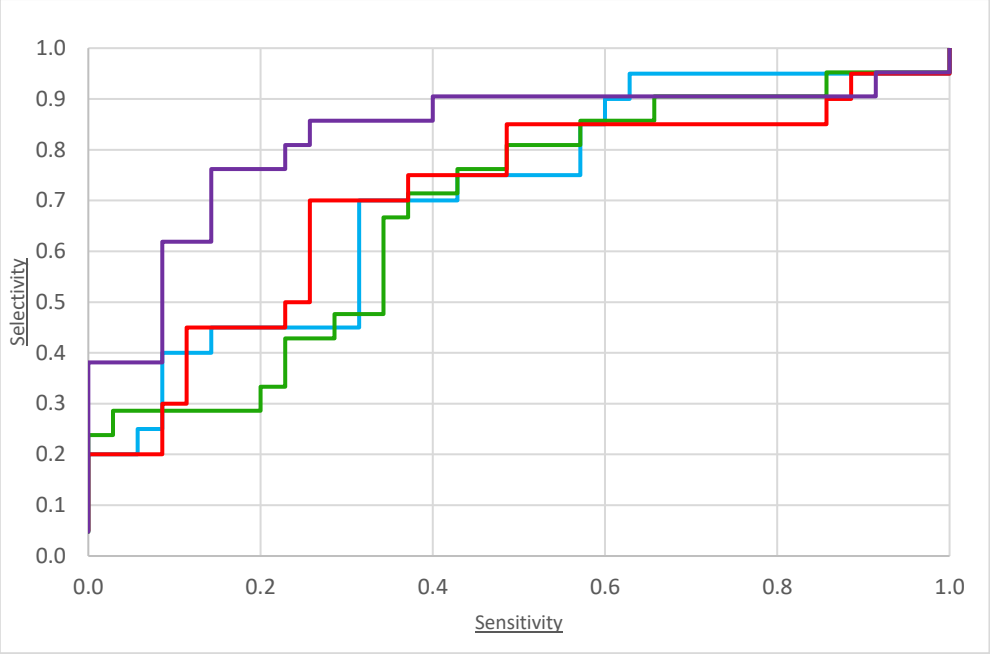

Graph 4.3: ROC curves of the standard and the 3 experimental workflows. Standard workflow —, Experimental workflow 1 —, Experimental workflow 2 —, Combined workflow —.

Table 4.3: Workflow comparisons of the enrichment scores.

Parameter	Standard	Experimental 1	Experimental 2	Combined
ROC	0.71	0.68	0.71	0.83
BEDROC	0.698	0.690	0.696	0.865
AUAC	0.63	0.61	0.63	0.70
RIE	2.31	2.34	2.27	2.56
EF 1 %	2.8	2.7	2.8	2.7
EF 10 %	1.8	2.2	1.8	2.7

4.7 Optimisation of combined workflow parameters

The accuracy and precision of the combined workflow model was investigated by the optimisation of the protein preparation and taking into account, the flexibility of the protein within the Prime MM-GBSA calculation. Four prepared proteins were used, RMW1, RMW2, RMW3 and RMW4 and the MM-GBSA calculation was performed at 0, 3 and 5 Å.

© University of Pretoria

Overall, the 1EVE prepared protein RMW1 at 0 Å had better parameters with superior “early recognition”, however, it was not markedly different from the 5 Å model (Table 4.4). 1EVE prepared protein RMW2 showed no large differences between the models (Graph 4.4) and 1EVE prepared protein RMW3 model, at 0 Å had a better “early recognition”, but did not differ markedly with the other parameters compared to the other two models (Graph 4.4 and Table 4.4). The 1EVE prepared protein RMW4 model, at 0 Å had a better BEDROC score and true positive rate, as seen by the sharper back curve of the ROC curve, as it was closer to x = 0 and y = 1 (Graph 4.4). The 3 Å calculation did substantially worse for the EF score at both 1 % and 10 %.

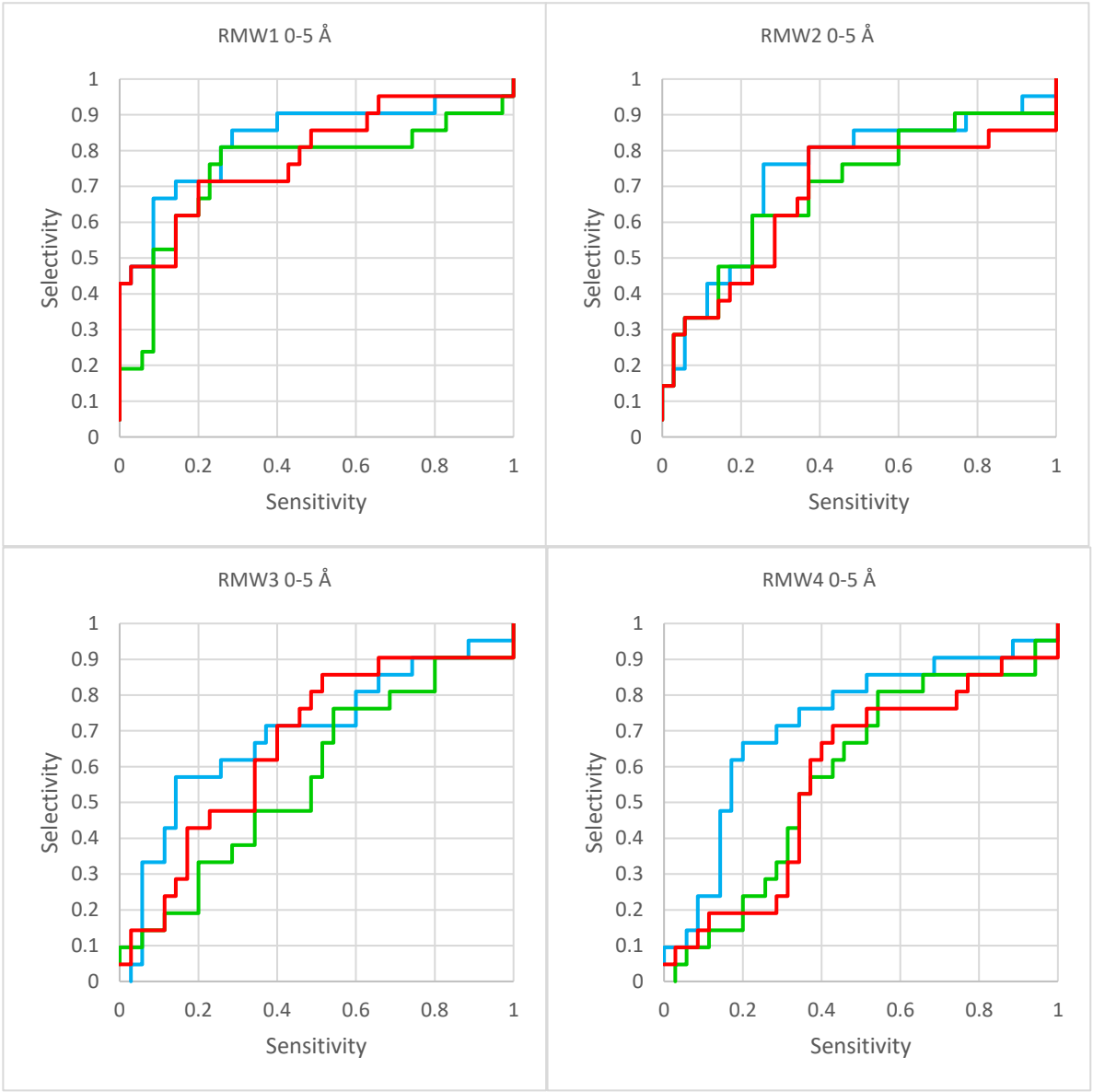

Graph 4.4: ROC curves of the 4 prepared proteins at different RMW settings for the combined workflow, at varying distance of flexibility within the MM-GBSA calculation; 0 Å —, 3 Å —, 5 Å —.

© University of Pretoria

Table 4.4: Comparison of the combined workflow with all four prepared proteins and all the enrichment scores.

Parameter	RMW1			RMW2			RMW3			RMW4		
	0 Å	3 Å	5 Å	0 Å	3 Å	5 Å	0 Å	3 Å	5 Å	0 Å	3 Å	5 Å
BEDROC	0,888	0,76	0,857	0,718	0,721	0,706	0,634	0,505	0,568	0,634	0,411	0,454
ROC	0,83	0,75	0,79	0,73	0,7	0,67	0,69	0,57	0,66	0,72	0,58	0,57
RIE	2,6	2,26	2,59	2,18	2,25	2,24	1,41	1,66	1,63	1,78	0,98	1,41
AUAC	0,71	0,65	0,68	0,65	0,62	0,61	0,62	0,54	0,6	0,64	0,55	0,55
EF 1 %	2.7	2.7	2.7	2.7	2.7	2.7	0	2.7	2.7	2.7	0	2.7
EF 10 %	2.7	1.8	2.7	1.8	2.2	2.2	1.8	1.3	1.3	1.3	0.89	1.3

In conclusion, the RMW1 prepared proteins were shown to be the best models with the greatest optimisation observed at 0 Å followed by the analogous 5 Å model. As such the 1EVE RMW1 at 0 Å is justifiably the optimised parameters that should give the most reliable results with the proposed screening of the virtual library of silylated donepezil derivatives.

4.8 Enzyme selection and comparison

The two enzymes that were under consideration were *t*AChE (1EVE) and 4EY7, *Homo sapiens* (*h*AChE) AChE. 1EVE was chosen initially as it would be the enzyme utilised for biological screening of any compounds synthesised as part of this project.[53] This ensured that any biological results obtained would be comparable to the modelling work, and allow one to assess if any correlation could be seen between the theoretical and experimental work. Thereafter, 4EY7 was a natural second candidate as the human enzyme is the ultimate target of the drug discovery program. The use of 4EY7 may also give more accurate results compared to 1EVE in terms of predicting the activity of the lead compounds for human use, as there may be significant structural differences that could affect the results if one was used over the other. A structural and screening comparison between the two-potential protein structures was performed.

© University of Pretoria

4.8.1 Structural comparison

4.8.1.1 Tetronarce californica AChE[52]

1EVE is a single AChE protein belonging to the α/β proteins, consisting of 537 amino acids in a combination of 12 β-sheets surrounded by 14 α helices. The active site consists of three significant amino acids, His-440, Ser-200 and Glu-327, which are situated within a long and restricted chasm. The chasm's walls consist of fourteen aromatic amino acid residues, with the side chains lining the walls of the chasm. At the entrance of the gorge Trp-279 is located at the peripheral anionic site of the gorge, and guides interacting molecules to the catalytic site deeper in the gorge.

Donepezil binding to *t*AChE has five distinct interactions (Figure 4.5) consisting of: pi-pi stacking of the indole ring of Trp-279 with the indanone moiety; an interaction between the Arg-289 main carbonyl and the methoxy group on the indanone moiety; a hydrogen bonding interaction with Tyr-70 interacting with the carbonyl of the indanone moiety; multiple interactions of the protonated nitrogen of the piperidine ring with Phe-330, Tyr-121 and Asp-72; and lastly pi-pi interactions of Trp-84 with the benzyl group bonded to the piperidine ring. A donepezil molecule spans the length of the active site gorge and interacts with both the catalytic and anionic peripheral sites.

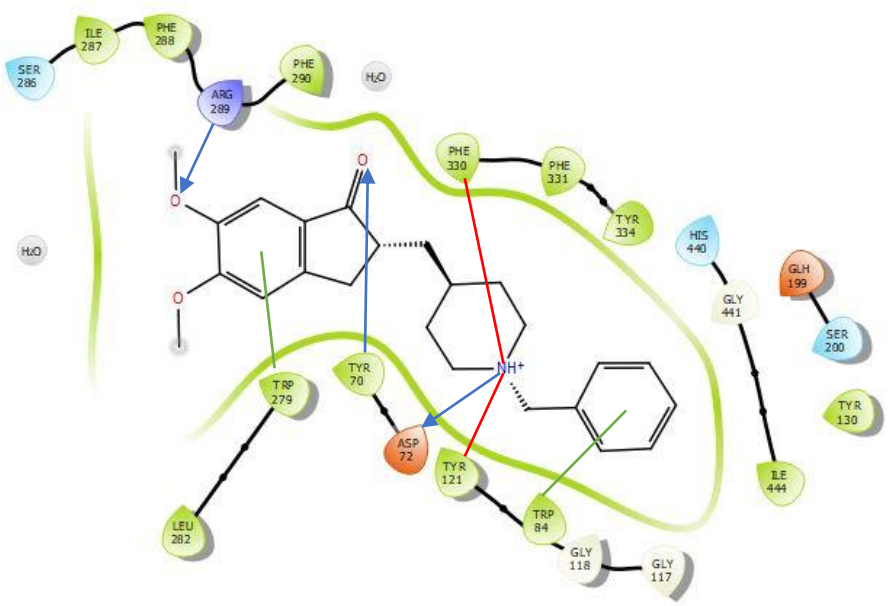

Figure 4.5: Interaction diagram of donepezil and tAChE. Hydrogen bonding —, pi-pi interactions —, pi-cation —.

© University of Pretoria

4.8.1.2 Homo sapiens AChE[35,36]

4EY7 is a protein dimer consisting of identical A and B subunits that consist of 1084 amino acids each and forms a combination of 26 α helices and 24 β sheets. The catalytic site consists of 3 amino acids, Ser-203, His-447 and Glu-334 and is located inside a gorge, which is lined with aromatic residues. Trp-286 is located at the entrance of the gorge at the peripheral anionic site, which ensures that molecules interacting with the site will be guided to the catalytic site deeper inside the gorge.

Donepezil binding to the *h*AChE has a number of distinct interactions (Figure 4.6) consisting of: pi-pi stacking interactions of the indole ring of Trp-286 with the indanone moiety; a water molecule mediated hydrogen bonding interactions between the protonated nitrogen of the piperidine ring with Tyr-337 and Tyr-341; and lastly pi-pi interactions of Trp-86 with the benzyl group bonded to the piperidine ring. A donepezil molecule spans the length of the active site gorge and interacts with both the catalytic and anionic peripheral sites.

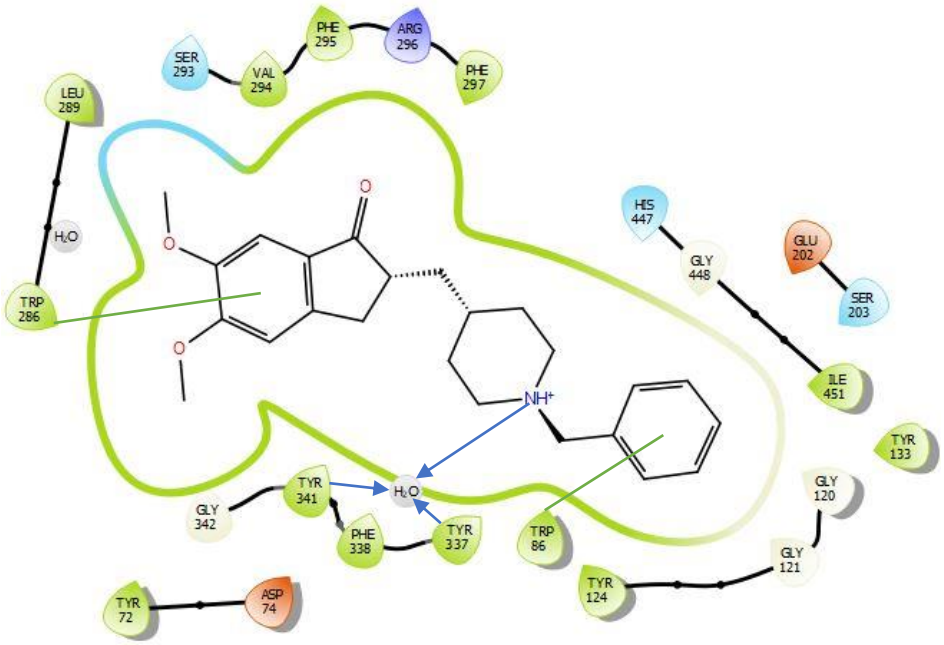

Figure 4.6: Interaction diagram of donepezil and hAChE. Hydrogen bonding —, pi-pi interactions —.

© University of Pretoria

4.8.1.3 Comparison

The bonding pattern of donepezil between *t*AChE and *h*AChE is comparable. Superimposing the ligands within each of the different enzymes binding sites for comparison of the different binding modes, gave a RMSD score of 0.2537. The RMSD score shows a close similarity between the two binding states and indicates that they are conserved between the two species (Figures 4.7 and 4.8). Upon comparison of the amino acid residues within the binding pockets of each enzyme, it was observed that the residues are nearly identical, except for a Phe-330 in *t*AChE, which is a Tyr-337 in *h*AChE (Figure 4.9).[36] That being said, a noticeable difference between the two enzymes is the channel volumes of the binding pocket, with *t*AChE having a larger channel volume (727 Å) compared to the *h*AChE (683 Å), as calculated by Cheung and colleagues.[36]

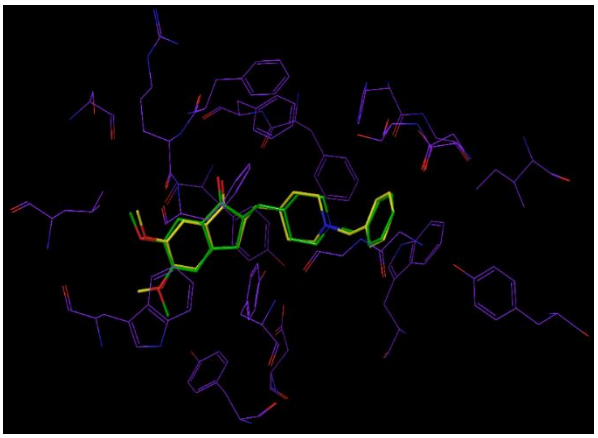

Figure 4.7: Binding comparison of donepezil from 1EVE (yellow) and 4EY7 (green) bound in 1EVE.

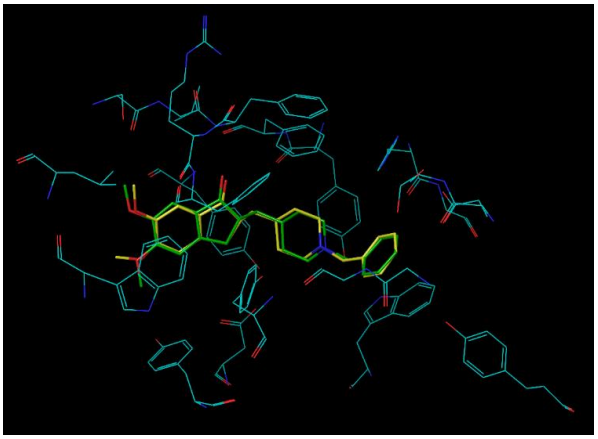

Figure 4.8: Binding comparison of donepezil from 1EVE (yellow) and 4EY7 (green) bound in 4EY7.

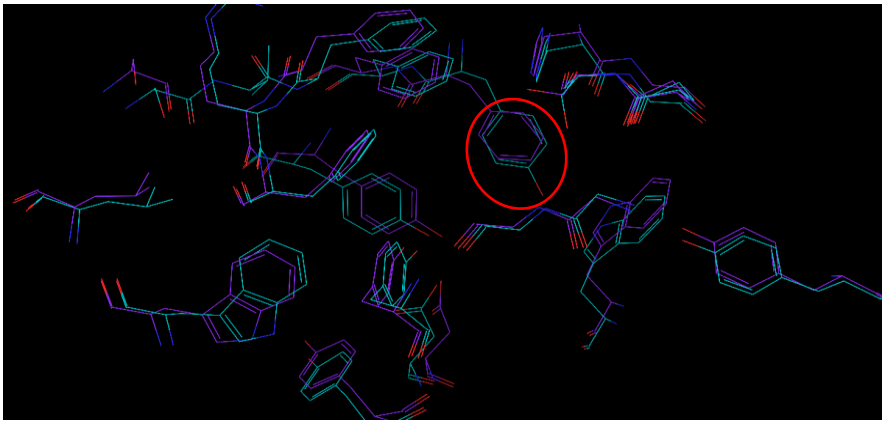

Figure 4.9: Binding site comparison of 1EVE (purple) and 4EY7 (blue), with Phe-330 (purple) and Tyr-337 (blue) indicated by a red circle.

© University of Pretoria

4.8.2 Screening comparison

The small library of known donepezil like active compounds were screened against 4EY7 to assess if there was any significant difference between the two protein models. 4EY7 was prepared at RMW1 which was the best prepared protein for 1EVE and was run at 0, 1, 3 and 5 Å within the Prime MM-GBSA calculation (Graph 4.5).

E4Y7 at 0 Å was the best model as it had the best scores in all the enrichment factors, except for the EF scores where it performed comparably to the other models.

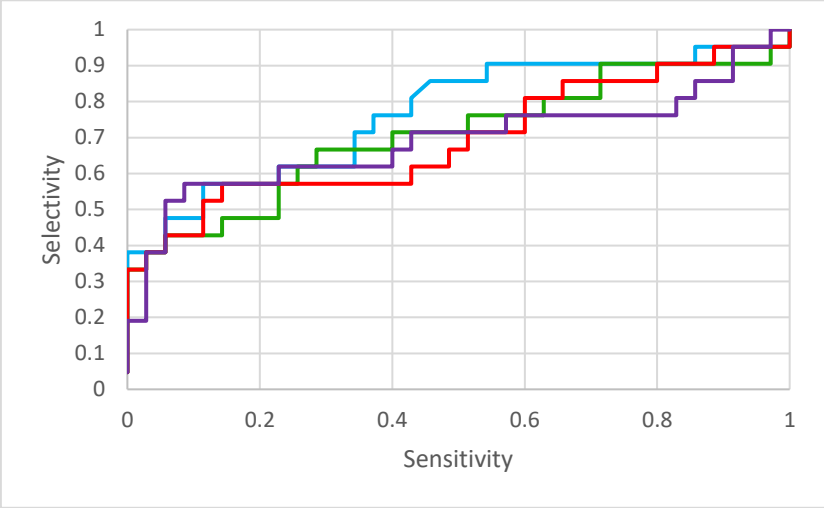

Graph 4.5: ROC curves of 4 combined models with the 4EY7 protein prepared with RMW1 at 0, 1, 3 and 5 Å flexibility in the Prime MM-GBSA calculation. 0 Å —, 1 Å —, 3 Å —, 5 Å —.

Table 4.5: Comparison of the varying flexibilities used in the Prime MM-GBSA calculation of 4EY7 and all the enrichment scores.

Parameter	0 Å	1 Å	3 Å	5 Å
ROC	0.77	0.71	0.69	0.69
BEDROC	0.836	0.799	0.806	0.803
AUAC	0.67	0.63	0.62	0.62
RIE	2.56	2.52	2.53	2.42
EF 1 %	2.7	2.7	2.7	2.7
EF 10 %	2.7	2.7	2.7	2.2

© University of Pretoria

The protein models are generally comparable, however, when looking at the true positive rate, 1EVE was markedly different as seen by the higher curvature of the ROC curve (Graph 4.6). 1EVE was selected for the screening of the proposed ligand library as its predictive function was better than that 4EY7. It was fortunate that the optimised parameters were at 0 Å flexibility, as it required the least amount of computational power. As the flexibility of the protein is increased, the computational resources required increase. As a means of comparison for a compound set of 5010 ligands, 0 Å took 11 hrs 22 min, 3 Å took 40 hrs 30 min and 5 Å took 42 hrs 25 min when using 20 CPU's to complete the calculation.

Table 4.6: Parameter comparison of the best 4EY7 and 1EVE protein models and all the enrichment scores.

Parameter	1EVE Combined	Human 0 Å
ROC	0.83	0.77
BEDROC	0.865	0.836
AUAC	0.70	0.67
RIE	2.56	2.56
EF 1 %	2.7	2.7
EF 10 %	2.7	2.7

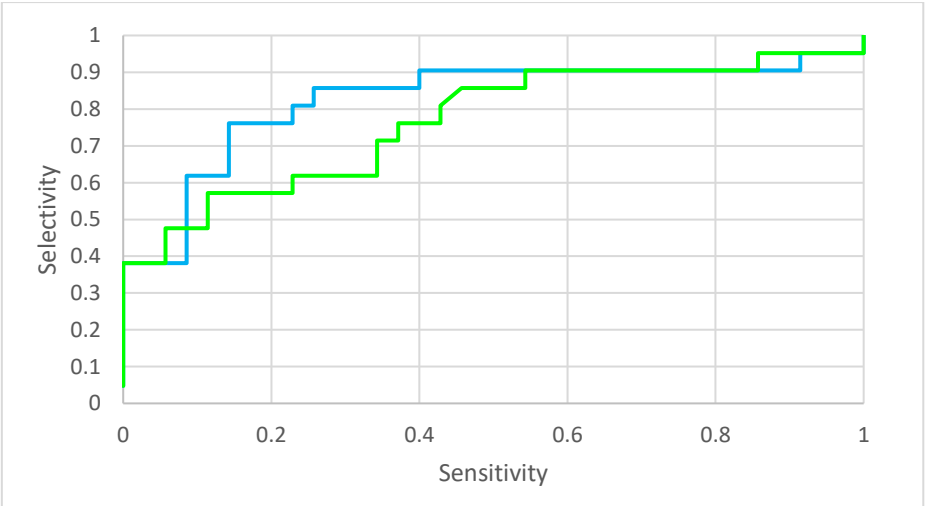

Graph 4.6: Comparison of the best models ROC curves of 1EVE & 4EY7. 1EVE Combined workflow RMW1 0 Å —, 4EY7 Combined workflow RMW1 0 Å —.

© University of Pretoria

4.9 Computational results

Donepezil has an MM-GBSA bind energy of -72.990 as calculated at 0 Å. The model predicted the binding pose of donepezil accurately, comparing well with that in PDB 1EVE (Figure 4.10). In subsequent images, comparing donepezil with proposed silicon derivatives, donepezil will be represented in green and the silicon derivatives in purple to aid in comparison, it was elected to use the numbering convention as shown in Figure 4.11 as a matter of convenience.

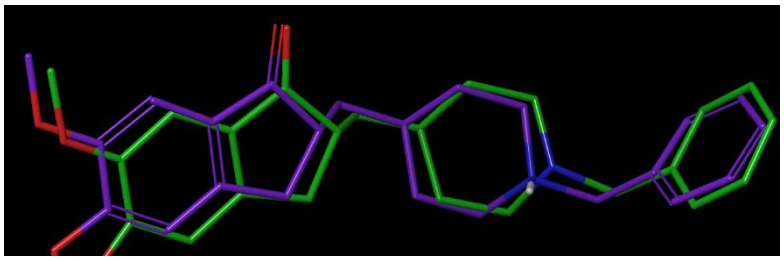

Figure 4.10: Binding pose of docked donepezil (purple) compare to the PDB 1EVE donepezil (green).

The silicon functionalisation of the donepezil scaffold was broken down into five main sections consisting of either a moiety or a linker between moieties (Figure 4.11). Fragment **I** focused on the indanone moiety and has two subsections that separate the derivatives based on the type of bond formed, with either oxygen-silicon or carbon-silicon bonds (see Section 4.9.1). Fragment **II** is centred on the modification of the methyl linker between the indanone and the piperidine moieties (see Section 4.9.2). Fragment **III** is focused on the replacement of the piperidine ring nitrogen with a silicon group (see Section 4.9.3). Fragment **IV** will discuss the replacement of the methyl linker between the piperidine and benzyl moieties with a silyl group (see Section 4.9.4). Finally, fragment **V** focuses on the derivatisation of the benzyl moiety with carbon-silicon bonds (see Section 4.9.5).

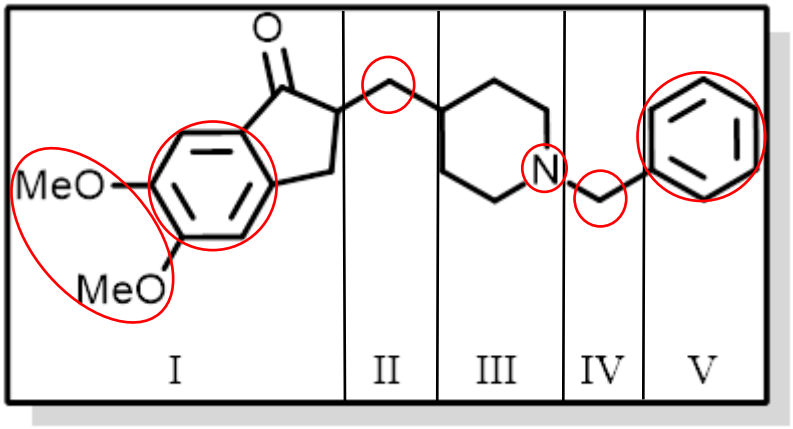

Figure 4.11: Breakdown of donepezil into fragments.

© University of Pretoria

4.9.1 Fragment **I** - Indanone derivatives

4.9.1.1 O-Silylations

The functionalisation of the indanone ring using oxygen-silicon bond formation (*O*-silylation) was considered (Figure 4.12). The oxygen atoms of the methoxy groups are important for hydrogen bonding with polar amino acid side chains within the binding pocket and it is preferable that these interactions be retained (see Section 4.8.1). The modified proposed silyl groups may allow for new Van der Waals (hydrophobic) and pi-pi stacking interactions, the latter being dependant on the nature of the silane groups.

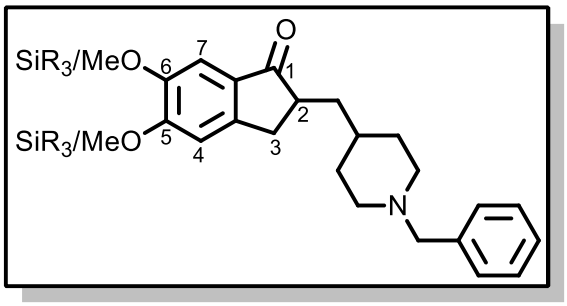

Figure 4.12: Line structure of donepezil, with numbering of the indanone moiety.

4.9.1.1.1 Silyl derivatives at position 5

A series of fifty-six virtual compounds which contain a silyl group at the 5th position were analysed. The top ten scoring structures were visually inspected, and all the ligands aligned very well with the docked pose for donepezil from the PDB 1EVE (Figure 4.13).

© University of Pretoria

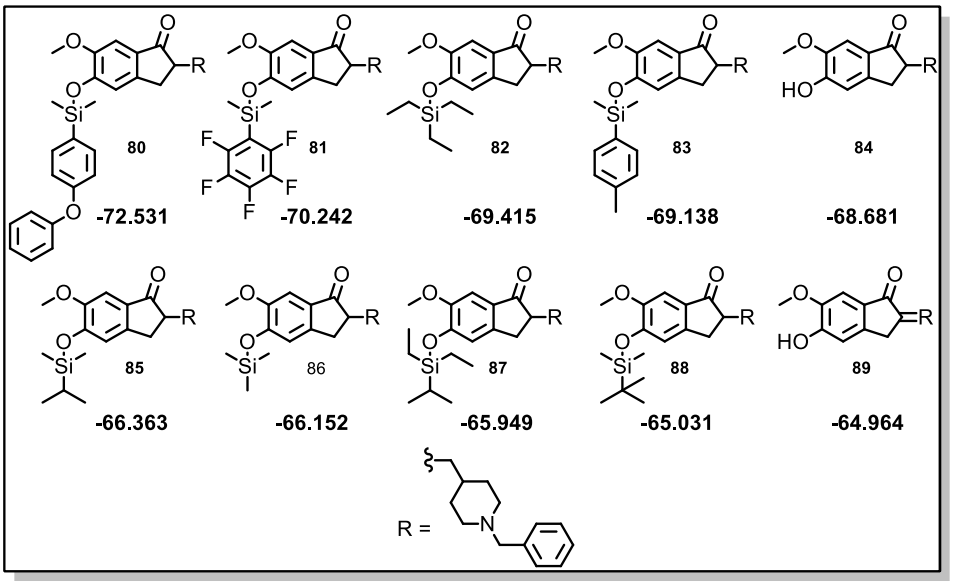

Figure 4.13: Structures and docking scores of silicon derivatives (O-silylation) on oxygen at position 5 and synthetic intermediates of the indanone moiety.

The bonding interactions found in donepezil were conserved across most of compounds within the series. An interesting result was observed with compound **80** wherein the model predicts pi-pi stacking interactions of the extended phenol group with Tyr-270 outside the binding site (Figure 4.14). Compound **83** had a similar pi-pi stacking interaction with Trp-279 (Figure 4.15), however, the pi-pi stacking interaction was preferred in the case of compound **80** due to the molecule's increased flexibility which arises from the rotatable ether linker between the two aromatic rings as seen in the lower MM-GBSA score. Interestingly compound **81** which is structurally similar to **83** had no additional pi-pi interactions and was not placed near any aromatic amino acid side chains.

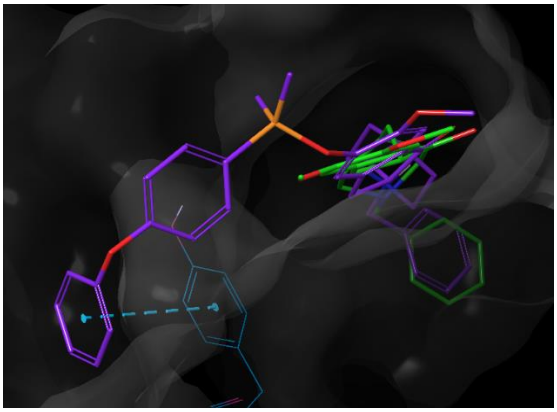

*Figure 4.14: Pi-pi stacking interactions between structure **80** (purple) and Tyr-270 outside of the binding pocket*

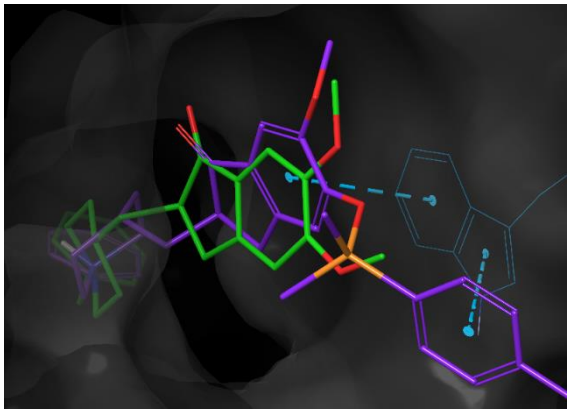

*Figure 4.15: Pi-pi stacking interactions between structure **83** (purple) and Trp-279 outside the binding pockets entrance (blue).*

© University of Pretoria

4.9.1.1.2 Silyl derivatives at position 6

In the case of similar silylations at the 6th position, all the ligands with the exception of **95** (Figure 4.16) showed comparable binding poses to that of donepezil with identical bonding interactions. An interesting bonding pattern was observed with **98**, wherein the indanone moiety was rotated by 180° to accommodate pi-pi stacking interactions between both the indanone moiety's and bonded silyl group's aromatic rings with Trp-279 (Figure 4.17). To accommodate the rotation the hydrogen bonding interaction between the indanone carbonyl and Arg-289 is lost.

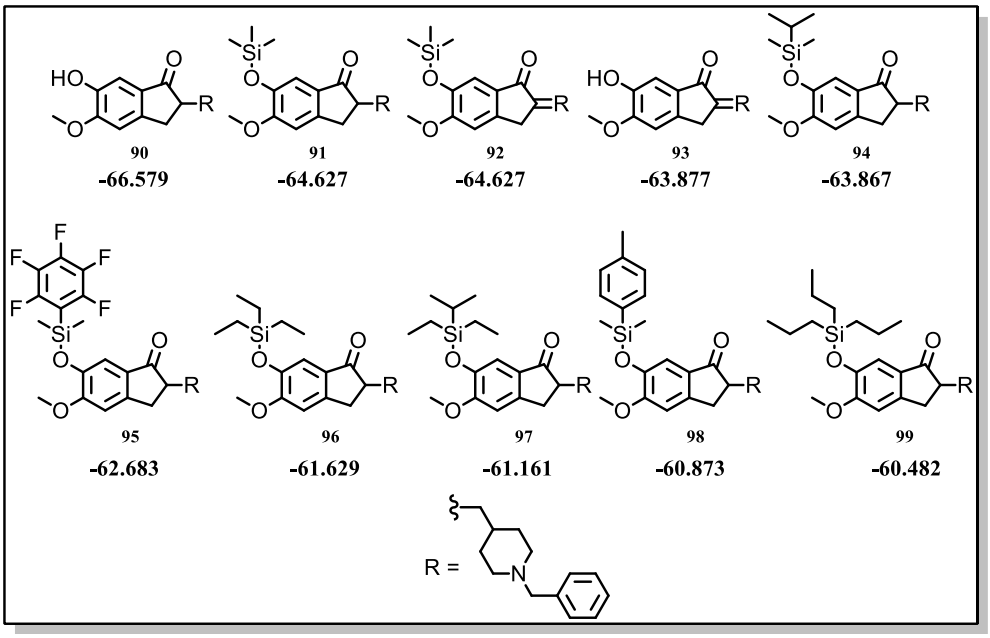

Figure 4.16: Structures and docking scores of silicon derivatives (O-silylation) on oxygen at position 6 and synthetic intermediates of the indanone moiety.

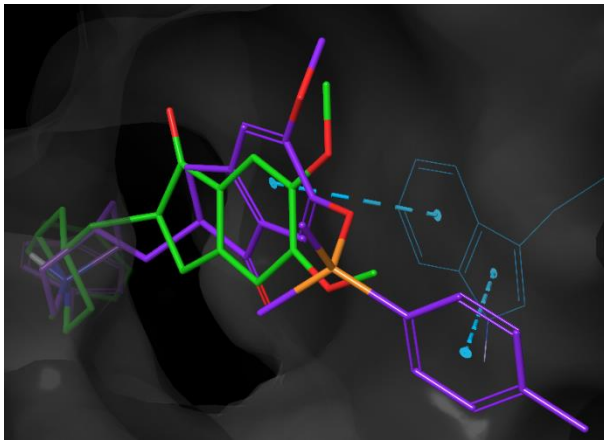

*Figure 4.17: 180° rotation of the indanone moiety (structure **98**; purple) to accommodate pi-pi stacking interaction with Trp-279 outside the binding pocket entrance (blue).*

© University of Pretoria

The alignment of all the docked ligands was comparable to donepezil in 1EVE. Substitution on the 6th position seems to be less favoured than substitution of the 5th position, this is likely due to the fact that there appears to be more space available at the bottom of the binding pocket's entrance than at the top. The restricted space in the upper portion of the binding pocket causes substitution at the 6th position to be strained and the indanone group has to twist or rotate its position to accommodate the substitutions. Several of the analogues had similar or slightly weaker docking scores to donepezil and represented promising analogues for prioritisation in drug development.

4.9.1.1.3 Bis and tethered silyl derivatives

A series of seventy-four ligands were investigated with silyl substituents on both oxygen atoms at the 5th and 6th position, which consisted of either two individual substitutions or tethered groups (Figure 4.18, only the top ten compounds are illustrated). Surprisingly, bulky derivatives (compounds **100**, **101** and **102**) where the 5th and 6th position were tethered together were predicted to have good MM-GBSA bind energies and had comparable scores to some of the better scoring systems where there was only substitution at either the 5th or 6th position.

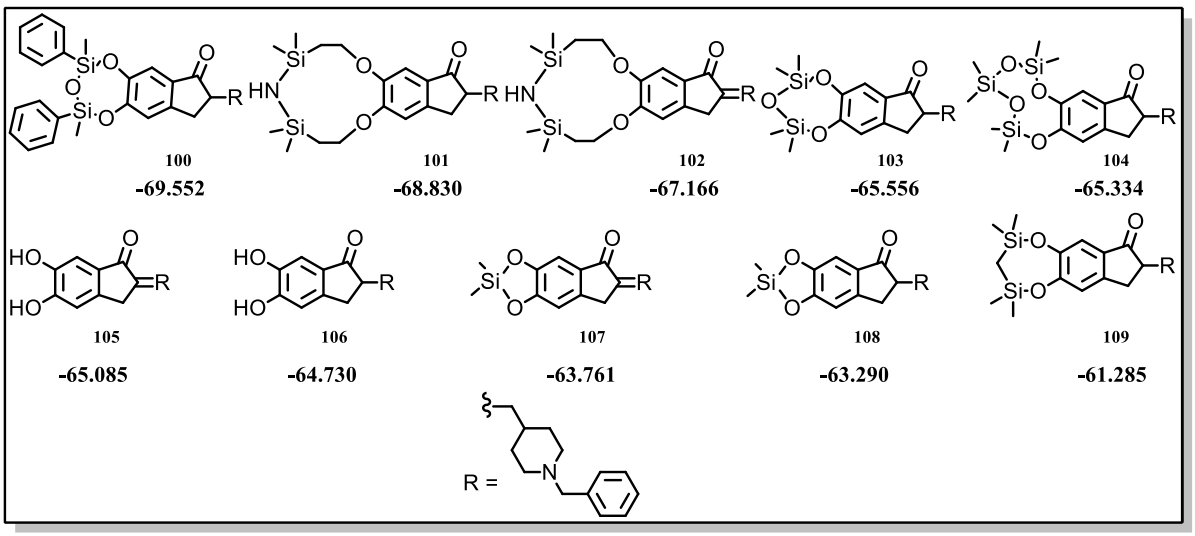

Figure 4.18: Structures and docking scores of Bis and tethered O-silylation analogues with substituents on oxygens at positions 5 and 6 and synthetic intermediates of the indanone moiety.

Docking shows that the tethers protruded out of the binding pocket (Figure 4.19), but the oxygen-silicon ether linkages impart flexibility and length to accommodate the bulky substitutions, making binding possible. The small and medium tethered analogues (compounds **103**-**109**) had comparable binding interactions to donepezil (Figure 4.20), with additional pi-pi interactions with the tethers that

© University of Pretoria

contain additional aromatic groups. Unsurprisingly, the large and bulky bis-substitutions, as well as the large bulky tethered substitutions were not favoured, due to steric hindrance of all the R groups placed within the restricted binding pocket entrance. To accommodate the R groups, they had to spread out outside the binding pocket, preventing the rest of the ligand from entering the binding pocket efficiently (Figure 4.21). The medium bis-substitutions prevented the benzyl moiety from interacting with the cationic active site (CAS) at the bottom of the gorge and with the more hindered substitutions, the piperidine nitrogen and indanone bonding interactions were also lost. In general, the tethered or small di-substitutions had comparable scores to donepezil and could be considered for lead compound development.

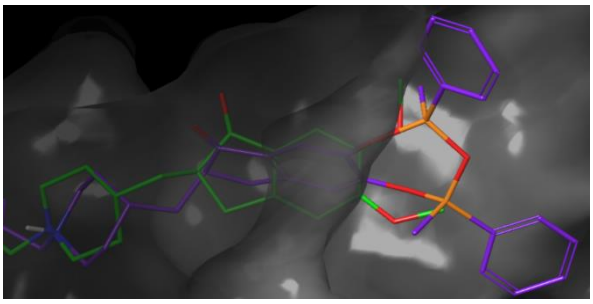

*Figure 4.19: Tethered substitutions of structure **101** (purple) sticking outside of the binding pocket.*

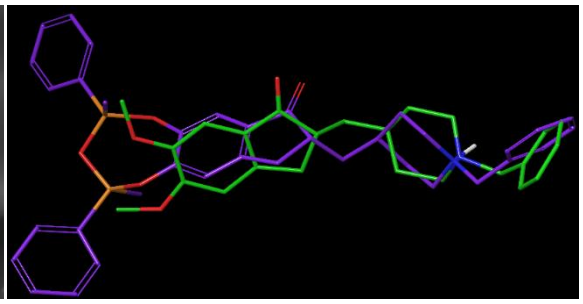

*Figure 4.20: Comparable binding of structure **101** (purple) compared to docked donepezil in PDB 1EVE (green).*

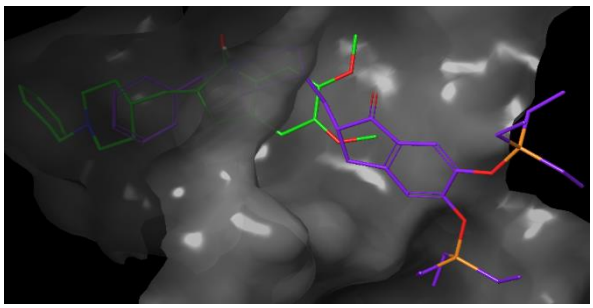

Figure 4.21: Bis-substituted ligands couldn't sully enter the binding pocket as the substitutions caused to much steric hindrance.

4.9.1.2 Silane derivatives containing silicon-carbon bonds

The functionalisation of the indanone group with direct carbon-silicon bonds was considered (Figure 4.22) as an alternative to *O*-silylation, as the latter is limited experimentally to large bulky silanes, with small non-bulky silanes generally being labile in aqueous solution. The carbon-silicon bond is more stable, allowing for smaller unhindered silanes to be considered. The loss of the oxygen does however mean that the hydrogen bonding interactions from the oxygens on the indanone ring in donepezil will

© University of Pretoria

be lost, however, the modified silane groups may allow for additional Van der Waals (hydrophobic), as well as pi-pi stacking interactions depending on the nature of the silane groups.

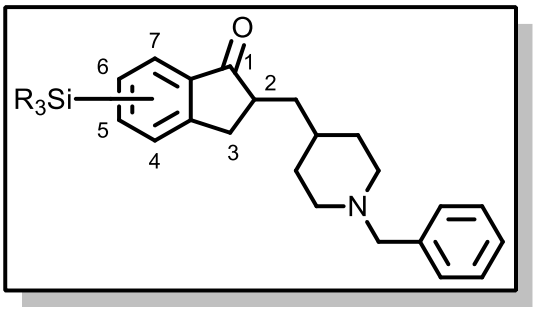

Figure 4.22: Line structure of donepezil with substitution on the indanone moiety and with indanone moiety numbered.

4.9.1.2.1 Derivative containing silicon-carbon bonds at position 4

A series of fifty ligands with a carbon-silicon bond at position 4 in the indanone group were analysed. Interestingly, and surprisingly, quite large substitutions at the 4th position of the indanone ring position were found to be favourable (Figure 4.23).

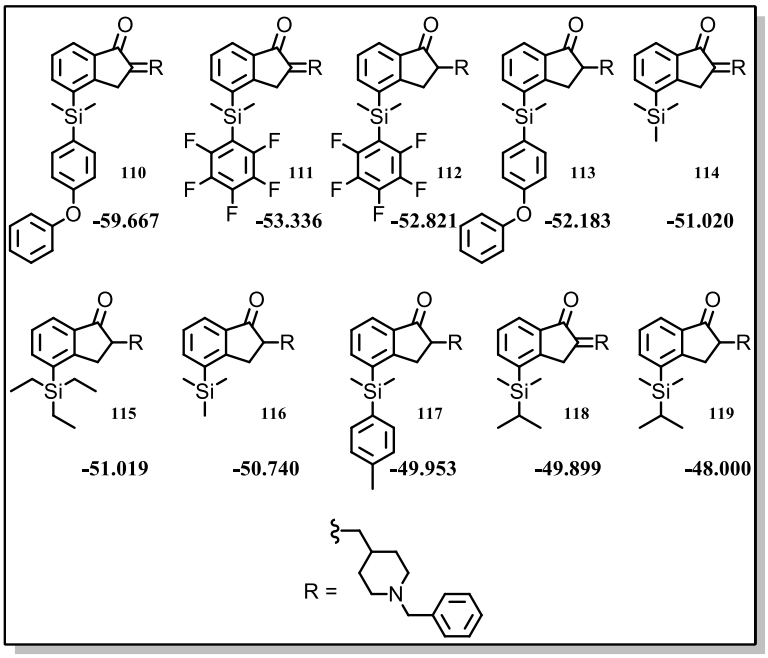

Figure 4.23: Structures and docking scores of silicon-carbon bond derivatives at position 4 in the indanone moiety.

Substitutions at this position forces the indanone moiety higher in the entrance of the binding pocket in order to accommodate the bulky groups, however, the piperidine and benzyl moieties are still observed to have similar binding poses to that of donepezil (Figure 4.24). Strangely, the triethyl silane

© University of Pretoria

substitution was observed to be too bulky, hindering the entry of the indanone moiety into the binding pocket, preventing the benzyl moiety from reaching the CAS (Figure 4.25).

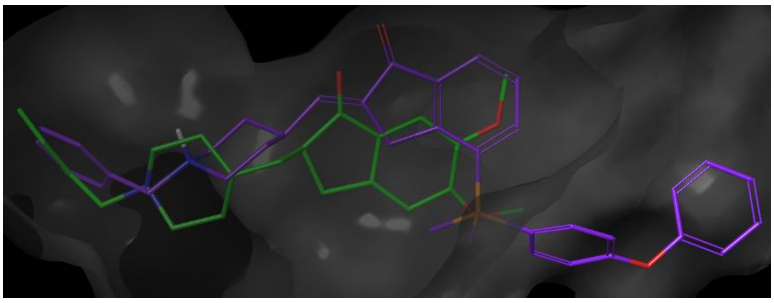

*Figure 4.24: The indanone moiety of structure **110** (purple) was forced higher in the binding pocket to accommodate the large silyl substitution, but the piperidine and benzyl moieties still have comparable binding to donepezil (green).*

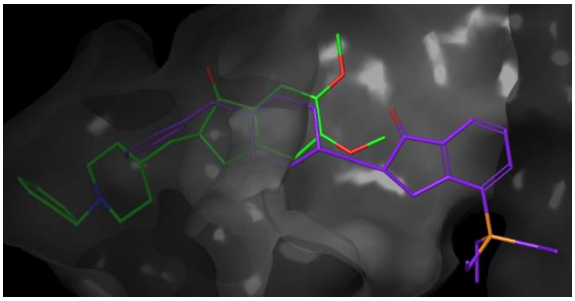

*Figure 4.25: The functionalisation with triethyl silane (structure **115**) prevented the entry of the indanone moiety into the binding pocket, due to the steric hindrance of the substituent.*

4.9.1.2.2 Derivatives containing silicon-carbon bonds at position 5

Substitution at the 5th position (Figure 4.26), seemed more favourable in terms of space, as the indanone moiety was not forced into the higher position observed with derivatives substituted at the 4th position. All the substitutions at the 5th position were placed outside the binding pocket with the donepezil scaffold either completely or almost completely entering the binding pocket depending on the substituent.

© University of Pretoria

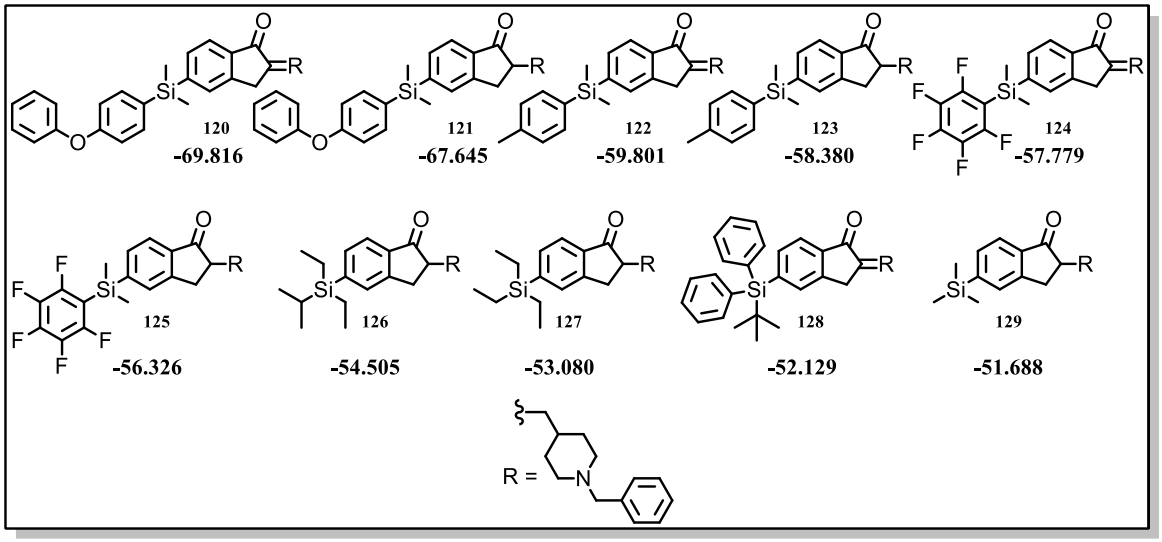

Figure 4.26: Structures and docking scores of silicon-carbon bond derivatives at position 5 in the indanone moiety.

Compound **120** overlaps with donepezil quite well and had additional pi-pi stacking interactions between its benzyl silyl substitution and Tyr-70 outside of the binding pocket (Figure 4.27). Compounds **121** and **128** also had an alternative pi-pi stacking interaction with Tyr-70, however, they were orientated further out of the binding pocket to accommodate the interaction, preventing the benzyl moiety from reaching the CAS (Figure 4.28). In the case of **121** a lower MM-GBSA bind energy was observed in comparison to structurally similar **120**, as it was pulled further out of the binding pocket due to an additional pi-pi stacking interaction between the aromatic ring in the indanone moiety and Trp-279 (Figure 4.29). The additional pi-pi stacking interaction was facilitated by the alkane linker and the increased flexibility, allowed the indanone group more room to move and adopt pi-pi stacking interactions, in addition the extended aromatic group of the silyl substituent also displayed pi-pi stacking with Tyr-70. The pi-pi stacking interactions of compound **121** orientated the ligand further out the pocket, preventing the benzyl moiety from reaching and interacting with the CAS site, however, the benzyl group had further pi-pi stacking interactions with Tyr-334 contributing to the high docking score.

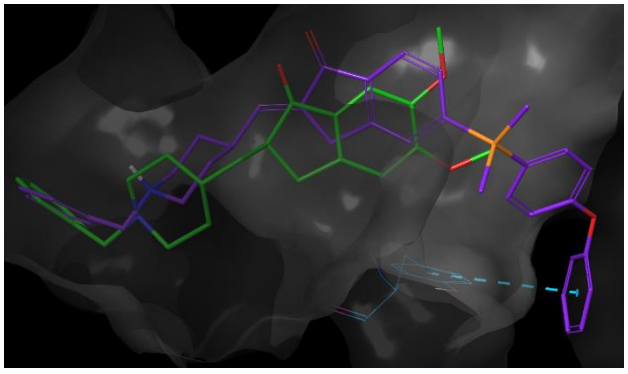

*Figure 4.27: Substitutions at the 5th position (structure **120**; purple) of the indanone ring sticking out of the bonding pocket and interacting with Tyr-70 (blue) via pi-pi stacking interactions.*

© University of Pretoria

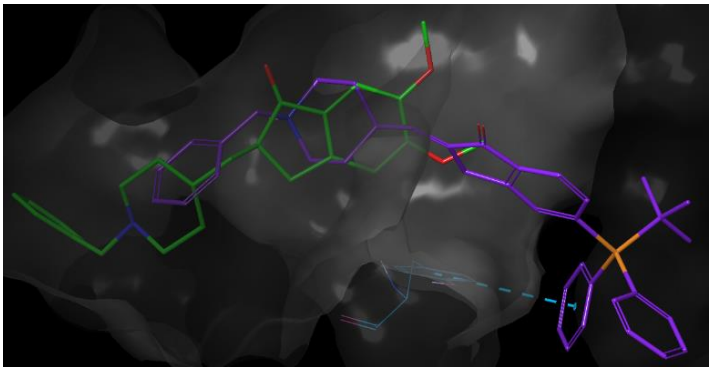

*Figure 4.28: Structure **128** (purple) pulled out of the binding pocket, because of the bulky substitution stabilized by pi-pi stacking interactions with Tyr-70 (blue).*

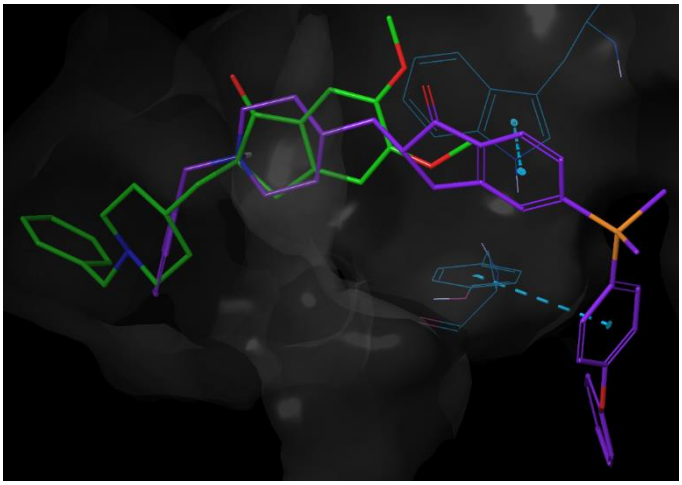

*Figure 4.29: Structure **121** (purple) has an additional pi-pi stacking interaction with Trp-279 and Tyr-70 stabilising the ligand, preventing the benzyl moiety from interacting with the CAS site.*

4.9.1.2.3 Derivatives containing silicon-carbon bonds at position 6

Derivatives with a substituent at the 6th position in the indanone moiety stuck out of the binding pocket in a similar fashion to that seen with the substitutions at the 5th position (Figure 4.30). The binding scores, however, suggested that the 6th position was less favoured with many ligand's indanone moieties being raised and twisted in the pocket to accommodate the substituents (Figure 4.31).

© University of Pretoria

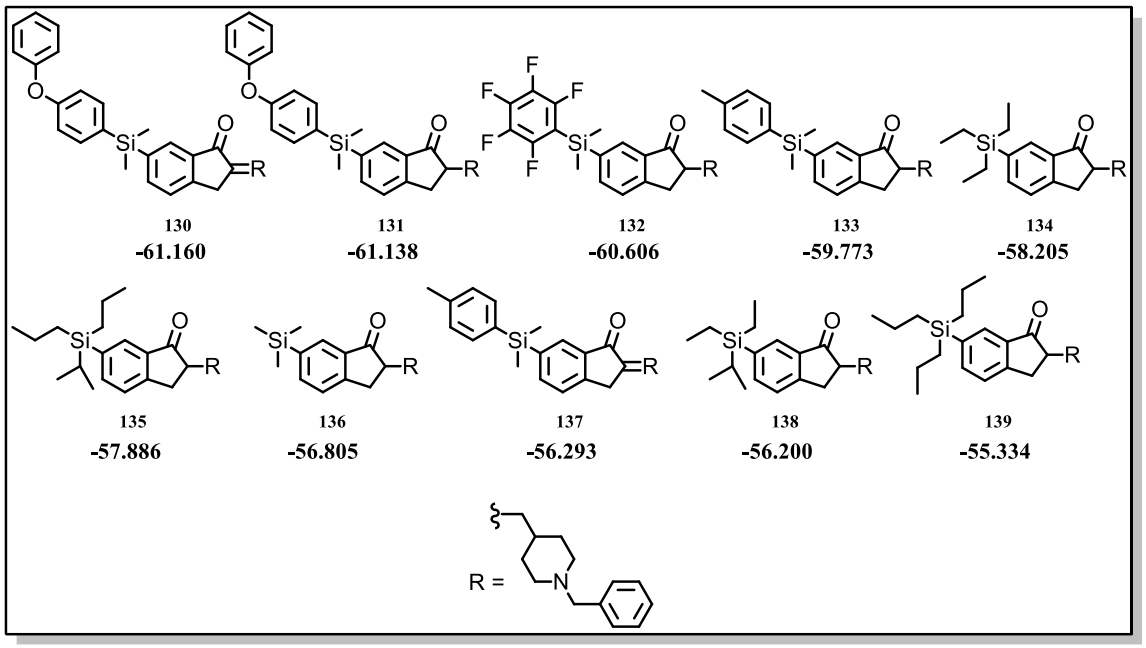

Figure 4.30: Structures and docking scores of silicon-carbon bond derivatives at position 6 in the indanone moiety.

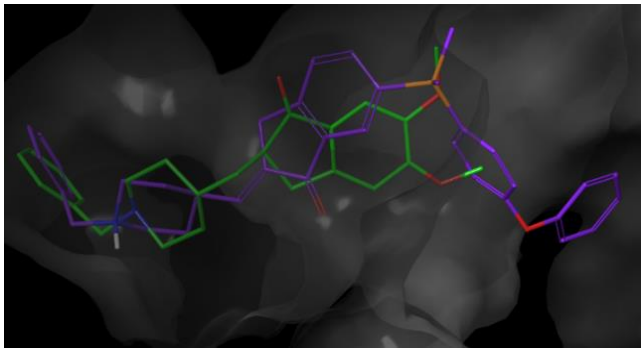

*Figure 4.31: Rotation of the indanone moiety in structure **130** (purple) to accommodate large substitutions.*

The larger bulkier alkyl and aromatic substituents tended to have more distortions, while the smaller substituents conformed to the same or similar binding pose as donepezil (Figure 4.32). The binding poses and interactions of the rest of the molecules (piperidine and benzyl moieties) were similar to that of donepezil. Compound **131** was predicted to have additional pi-pi stacking interactions with Tyr-70, but the indanone moiety was twisted roughly 180° to facilitate this interaction (Figure 4.33). Compound **131** was capable of the pi-pi stacking interactions, as it had an alkane linker, which had more freedom of rotation than structure **130**, which has an alkene linker. The distortion of the larger substituents that forced the twisting of the indanone moiety to accommodate the substituents, results in loss of the hydrogen bonding interaction between the carbonyl oxygen of the indanone with Arg-289. Compound **137** was the one ligand to have additional pi-pi interactions with Trp-279, without distorting the rest of the molecule and having the same interactions as donepezil (Figure 4.34).

© University of Pretoria

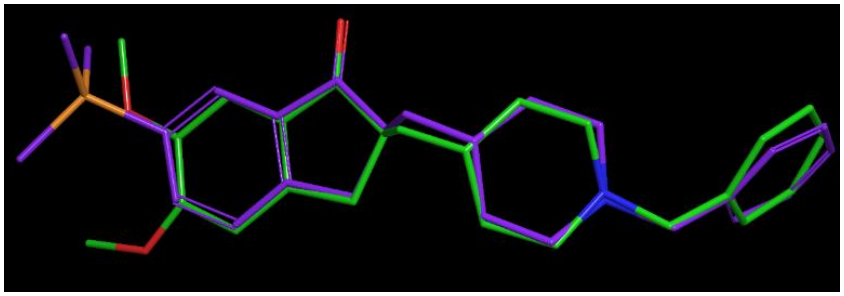

*Figure 4.32: Smaller substitutions (structure **136**; purple) had almost identical binding poses as donepezil (green).*

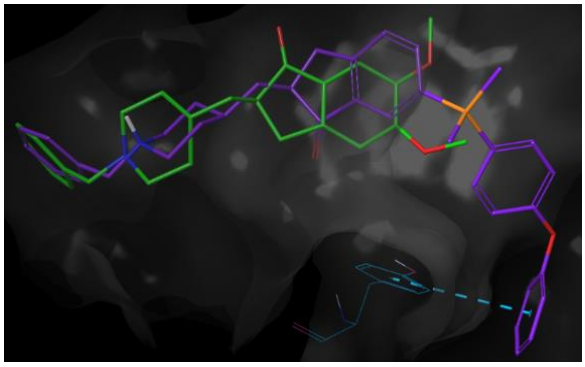

*Figure 4.33: Structure **131** (purple) had pi-pi stacking interactions between its extended aromatic group and Tyr-70 (blue).*

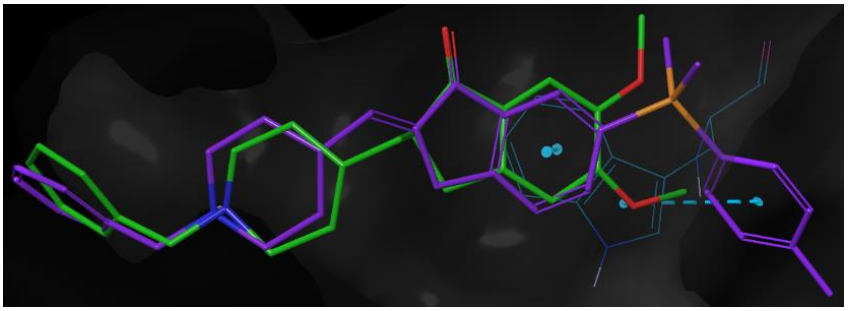

*Figure 4.34: Structure **137** (purple) with addition pi-pi interactions with Trp-279, but not distortion of the molecule.*

4.9.1.2.4 Derivatives containing silicon-carbon bond at position 7

Substitution of the 7th position on the indanone moiety (Figure 4.35) was the least favourable with most of the substituents causing the indanone moiety to rotate by approximately 180^{o}. The rotation allowed the substituents to point down into the binding pocket with the exception of the smallest substituent in the form of trimethyl silane (Figure 4.36). The important hydrogen bonding interaction between the carbonyl oxygen of the indanone with Arg-289 was lost for all the derivatives with the exceptions of **142** and 1**43** due to the twisting of the indanone moiety to accommodate the substituents. The rest of the molecule had comparable binding interactions to those seen with

© University of Pretoria

donepezil. In the case of compound **141** additional pi-pi stacking interactions with the extended benzene ring and Tyr-70 were observed (Figure 4.37).

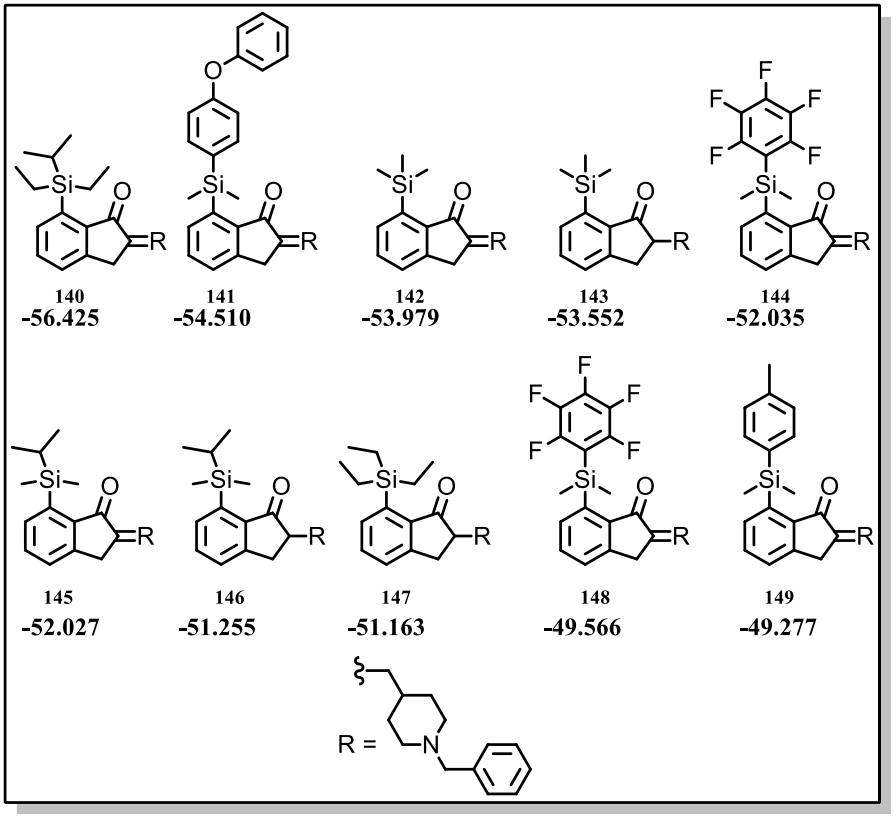

Figure 4.35: Structures and docking scores of silicon-carbon bond derivatives at the 7th position in the indanone moiety.

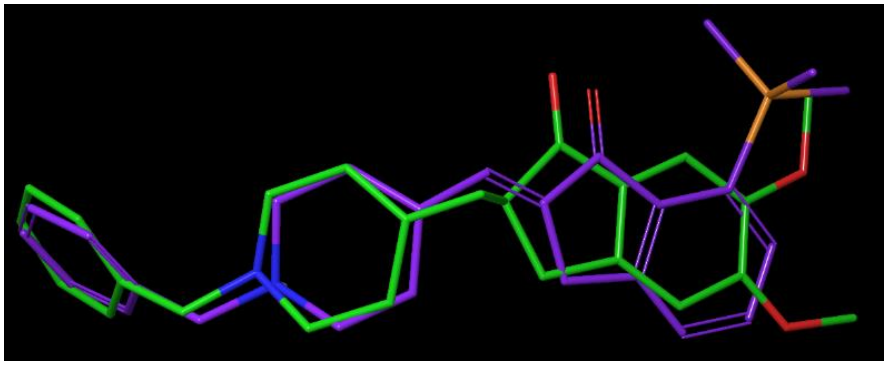

*Figure 4.36: The smallest substitution of trimethyl silane (structure **140**, purple) was the only substitution to allow for a similar binding pose to donepezil (green).*

© University of Pretoria

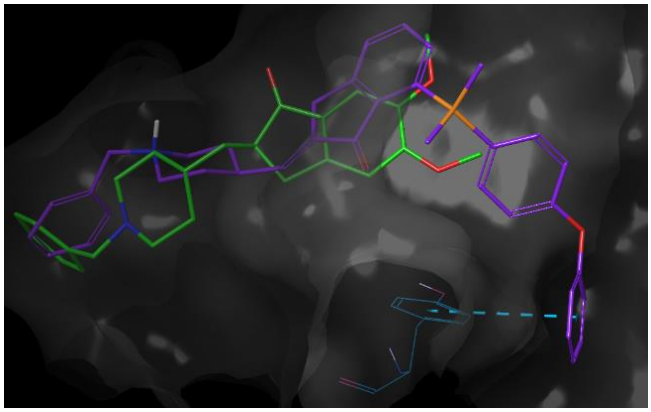

*Figure 4.37: Large substitutions cause the indanone moiety (purple) to rotate 180º to allow the substitutions to point down into the pocket, where there is more space. Structure **141** (purple) was stabilised by pi-pi stacking interactions with Tyr-70 and is extended aromatic group on the silyl substitution.*

In summation, most of the compounds with the different substitutions had comparable binding poses to donepezil with the exception of i) compounds with aromatic substituents on the silyl groups which allow the formation of additional pi-pi interactions or ii) bulky substituents. In both instances entry of the molecule into the binding pocket is limited, preventing the benzyl moiety reaching the CAS. In general substitution at the 5th position was shown to be the most favoured, followed by the 6th position. Substitution at the 5th position had more space to accommodate large and bulky substitutions and still allow for comparable binding to donepezil. In Comparison, the 6th position has less space and the indanone has to be raised or twisted in the binding pocket to accommodate large substitutions. Substitution at the 4th position forces the indanone group higher in the binding pocket to allow for the substituents, but arguably, has more space than derivatives with substitutions at the 7th position which required the indanone to rotate by 180^{o}. Overall substituents at the 7th position were the least favoured. None of the ligands scored as high as donepezil at -72.990, with the highest scoring analogue **120** having a docking score of -69.816. Overall, the derivatives screened are promising, however, are expected to have lower activities than donepezil.

4.9.2 Fragment **II** - Indanone linker derivatives

Functionalisation of the methyl linker between the indanone and piperidine moieties was investigated (Figure 4.38). It was anticipated that the silylation of the linker wouldn't remove the flexibility of the linker, but may add bonding interactions such as van der Waals interactions with hydrophobic amino acid side chains within the binding pocket. Only short alkyl chain substituents on the silyl group were considered as bulky groups were expected to be detrimental to the flexibility of the linker.

© University of Pretoria

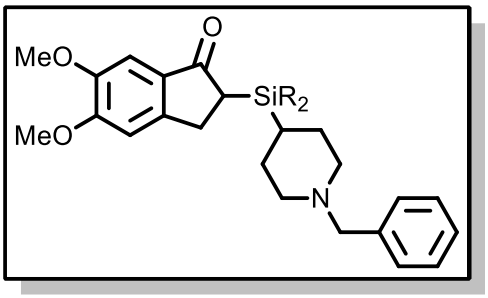

Figure 4.38: Line structure of donepezil with silyl substitutions on indanone linker.

As expected, even moderately bulky substitutions at the indanone linker weren't favoured with binding scores improving as the size of the substituents decreased (Figure 4.39). When compared to the MM-GBSA binding energy of donepezil, only the dimethyl substituted silicon allowed for comparable binding to donepezil. In this case the piperidine ring has to twist to accommodate the substituent (Figure 4.40), however, none of the nitrogen interactions are lost. The single substitution of an isopropyl or diethyl and bulkier substitutions restricted entry into the binding pocket preventing the benzyl group from being able to reach the CAS (Figure 4.41). *tert*-Butyl and *n*-butyl substitutions were too bulky to allow entry of the ligand and the indanone group instead was observed to enter and bind in the entrance of the pocket (Figure 4.42).

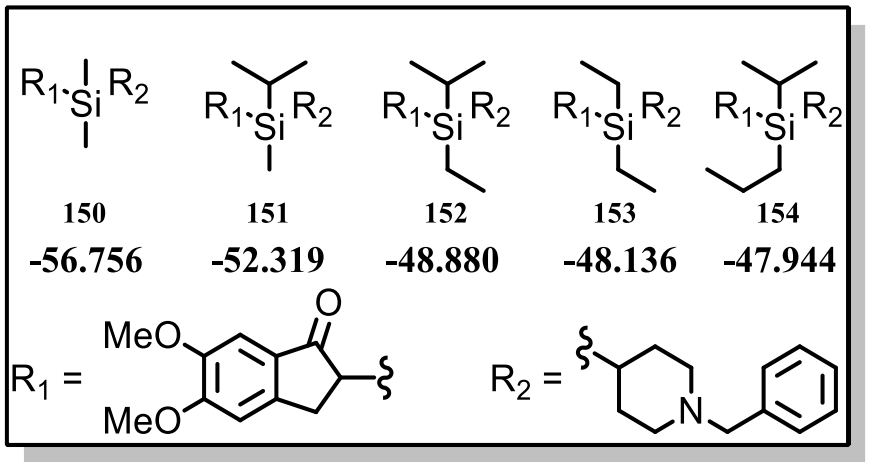

Figure 4.39: Structures and docking scores of silicon derivatives at the indanone linker moiety.

© University of Pretoria

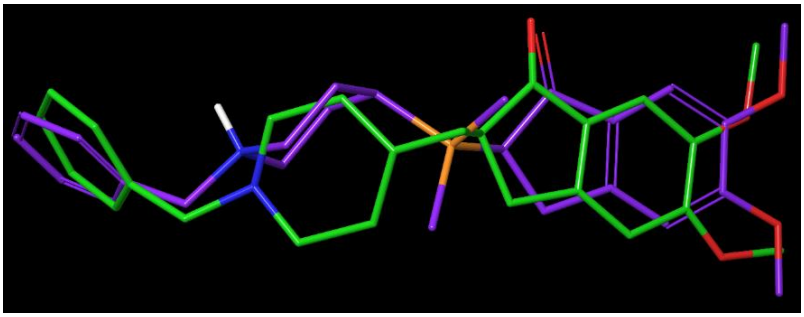

*Figure 4.40: Dimethyl substitution (**150**) of the indanone linker moiety (purple) allowed for a similar binding pose as donepezil (green) with rotation of the piperidine ring to accommodate the substitution.*

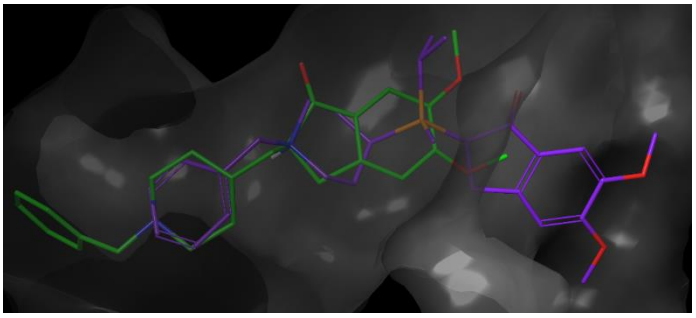

*Figure 4.41: Bulkier substitutions of isopropyl or ethyl prevented the ligand from entering the binding pocket completely (structure **151** purple).*

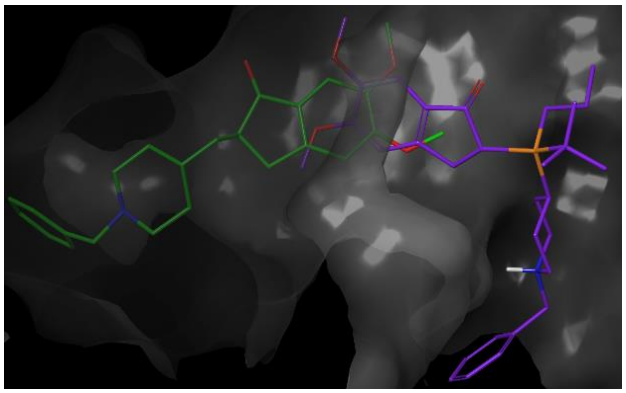

Figure 4.42: Tert-butyl and n-butyl substitutions (purple) completely blocked the ligands entry into the binding pocket, with only the indanone moiety entering the binding pocket in a reverse fashion.

Overall, the silicon linker derivatives scored poorly, with the binding modes of the ligands illustrating that they are disfavoured for all the substitutions, with only the small dimethyl derivative displaying arguably modest binding. They are primarily disfavoured as they prevent efficient entry of the ligand into the pocket and as a result the piperidine and benzyl moiety's interaction with the CAS is lost. As such, the indanone linker analogues should be considered low priority for synthetic development.

© University of Pretoria

4.9.3 Fragment **III** - Piperidine derivatives

The replacement of the piperidine nitrogen with silyl derivatives was investigated (Figure 4.43). The nitrogen is typically placed within the binding pocket in a region where some flexibility is allowed, as the ring can twist and distort. Silicon is a very electropositive element that is able to form polarised bonds, without a formal charge and has be shown in literature to successfully replace charged amines and still retain essential ionic interactions.[54,55,68] The piperidine nitrogen is typically protonated at physiological pH and this charge can hinder BBB penetration and replacement of the nitrogen with silicon may increase BBB penetration through increased lipophilicity and could retain essential bonding interaction of the piperidine nitrogen within AChE.[68] Only single substitutions were investigated with small to medium alkyl groups to limit steric bulk. It was hypothesised that the silicon group would allow for potential van der Waals interactions with the aromatic amino acid side chains found deep in the pocket, as well as mimicking the protonated nitrogen's binding interactions.

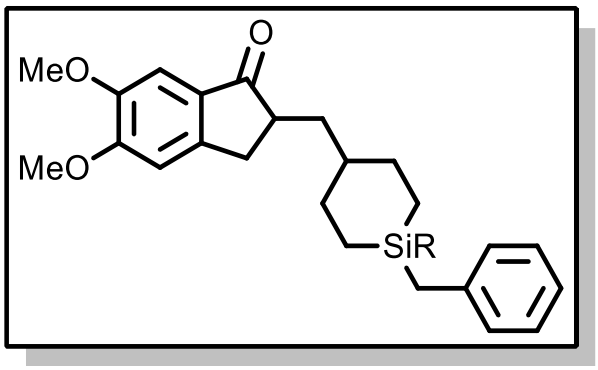

Figure 4.43: Line structure of donepezil with silyl substitutions in the nitrogen position in the piperidine ring.

As with the previously discussed linker between the indanone and piperidine rings, only small silyl groups allowed for proper binding of the ligand (Figure 4.44). In the case of the methyl substituted silicon the piperidine ring has to rotate by approximately 90° in order to accommodate the substitution (Figure 4.45). Substitution of an ethyl silane blocked the ligand from entering the binding pocket and bulkier substitutions behaved similarly (Figure 4.46).

© University of Pretoria

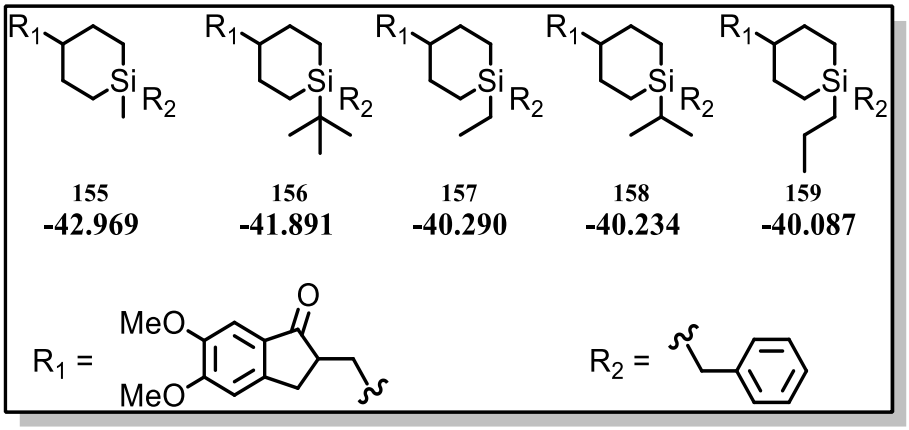

Figure 4.44: Structures and docking scores of silicon substitutions at the nitrogen's position in the piperidine moiety.

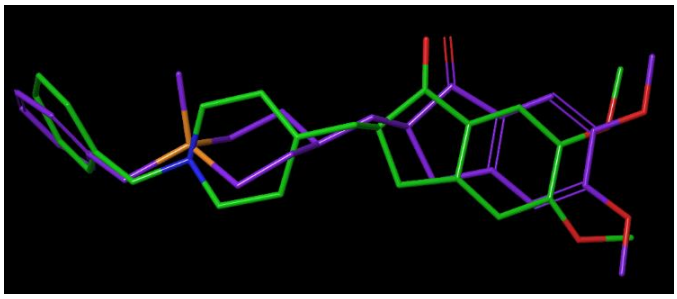

*Figure 4.45: Methyl silane substitution at the nitrogen of the piperidine ring moiety (structure **155**; purple) allowed for comparable binding to donepezil (green).*

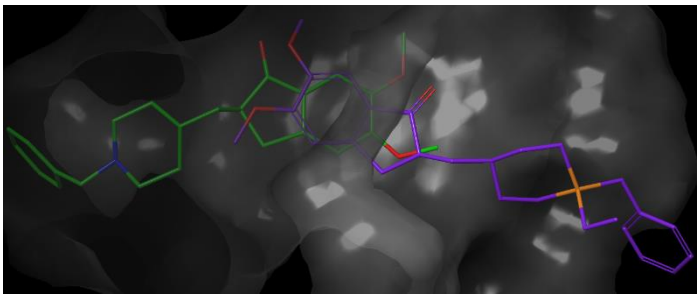

*Figure 4.46: Ethyl silane substitution (structure **157**; purple) blocked entry of the ligand into the binding pocket.*

The loss of the piperidine ring nitrogen was detrimental to the binding of the molecule as it lost essential bonding interactions, as evidenced by the low MM-GBSA bind energies. Only the smallest substitution of a methyl silane showed comparable binding interactions to donepezil, but was unfavoured with an overall low binding score of -42.969. All the other analogues either partially or completely prevented entry into the binding pocket thereby restricting access to the CAS in addition to having lost the interactions associated with the piperidine nitrogen in donepezil.

© University of Pretoria

4.9.4 Fragment **IV** – Piperidine benzyl-linker derivatives

Functionalisation of the methyl linker between the piperidine and the benzyl aromatic ring was investigated (Figure 4.47), as the silylation won't remove the flexibility of the linker, but may add bond interactions such as van der Waals interactions with hydrophobic amino acid side chains within the gorge of the binding pocket. Again, only short alkyl chain substitutions on the silyl group were considered as bulky groups were anticipated to be detrimental to the flexibility of the linker.

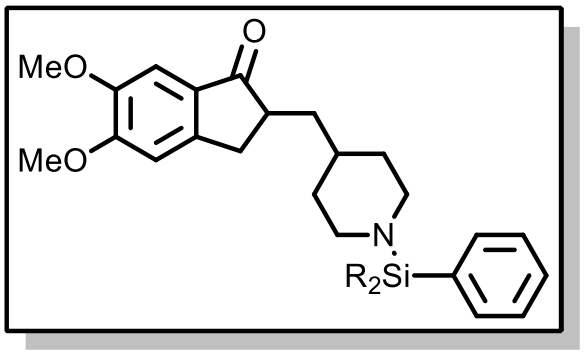

Figure 4 47: Line structure of donepezil with silyl substitutions of the benzyl linker.

The benzyl linker analogues had low MM-GBSA energies (Figure 4.48), but the dimethyl silane (**160**) substitution pattern in the linker moiety was the only example to allow for proper binding of the ligand, with the piperidine ring twisting to accommodate the substitution, but still having comparable binding to donepezil (Figure 4.49). Substitution with a diethyl silane or larger substituents blocked the entry of the ligand into the binding pocket (Figure 4.50) and prevented essential bonding interactions.

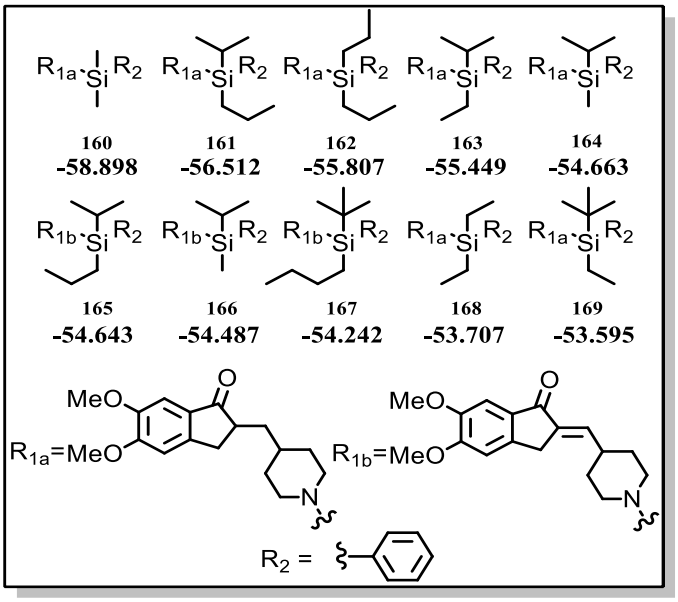

Figure 4.48: Structures and docking scores of silicon derivatives at the benzyl linker moiety.

© University of Pretoria

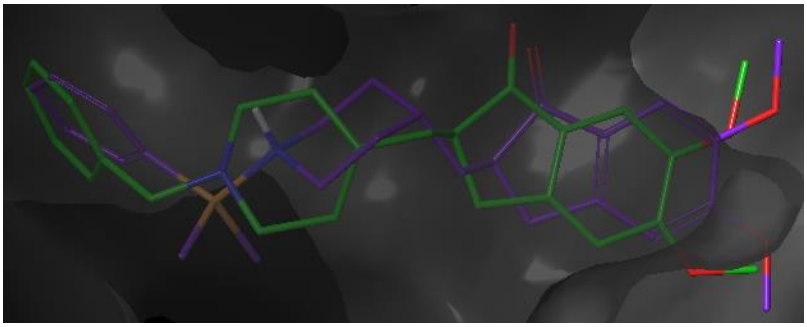

*Figure 4.49: Dimethyl silane substitution at the benzyl linker (structure **160**, purple) has a similar binding pose to donepezil (green), with the piperidine ring twisting to accommodate the alkyl substitution.*

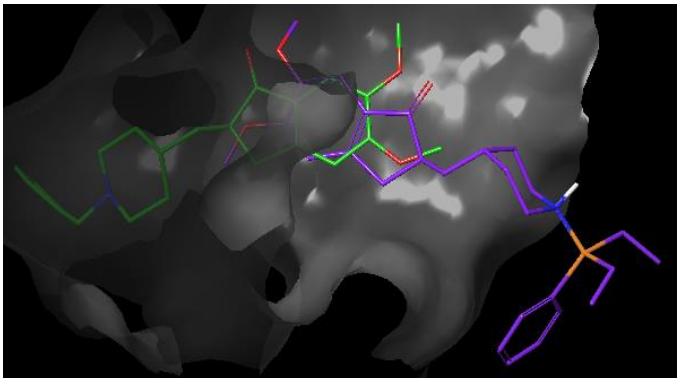

*Figure 4.50: Diethyl silane or larger substitutions (structure **168**; purple) prevented the ligand from entering the binding pocket.*

4.9.5 Fragment **V** - Benzyl derivatives

Functionalisation of the benzyl moiety was investigated (Figure 4.51), as the CAS consists of mainly aromatic and hydrophobic amino acid side chains. Silylation of the benzyl moiety could enhance van de Waals or pi-pi stacking interactions or provide additional interactions in this hydrophobic region. Only derivatives with direct carbon-silicon bonds were considered as the pocket has restricted space and although synthetically easier to access, the silylation of benzyl alcohols would be too sterically hindered to allow access to the CAS.

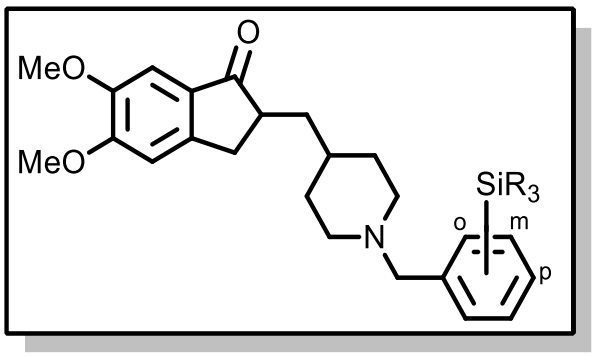

Figure 4.51: Line structure of donepezil with silyl substitutions on the benzyl moiety.

© University of Pretoria

4.9.5.1 Ortho, Meta, Para substitution at 0 Å MM-GBSA

A series of ortho, meta and para silyl benzyl derivatives were investigated, and in all cases (Figures 4.52, 4.53 and 4.54) were found to have been docked outside the binding pocket with the indanone binding in a reverse fashion at the entrance of the binding pocket (Figures 4.55, 4.56, 4.57 and 4.58). The docking scores are arguably fair and are attributed to pi-pi stacking interactions with Tyr-70 and the benzyl moiety or an aromatic group in the silane substitution and Trp-279 with the indanone moiety.

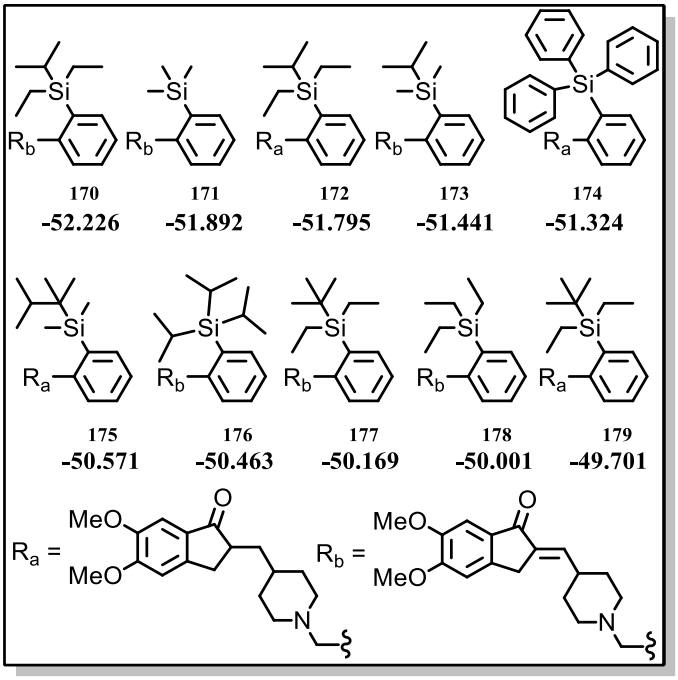

Figure 4.52: Structures and docking scores of silicon derivatives at ortho position in the benzyl moiety.

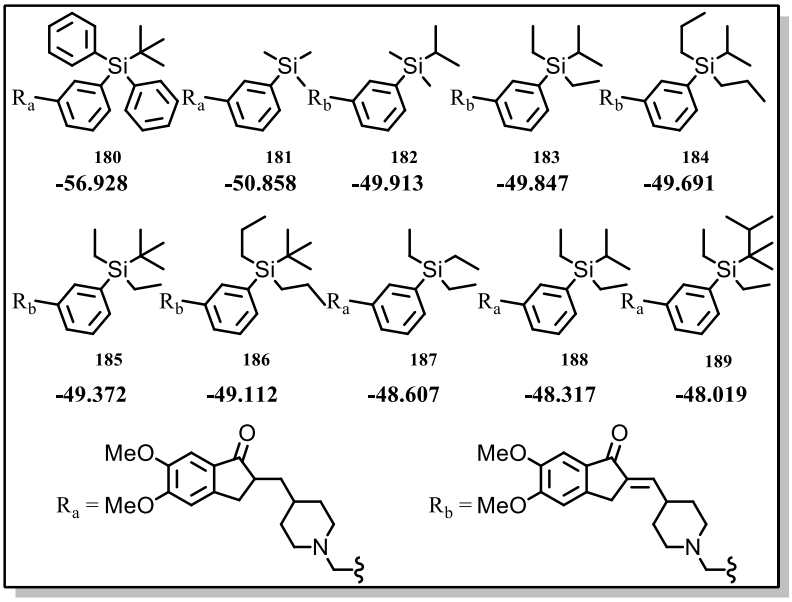

Figure 4.53: Structures and docking scores of silicon derivatives at meta position in the benzyl moiety.

© University of Pretoria

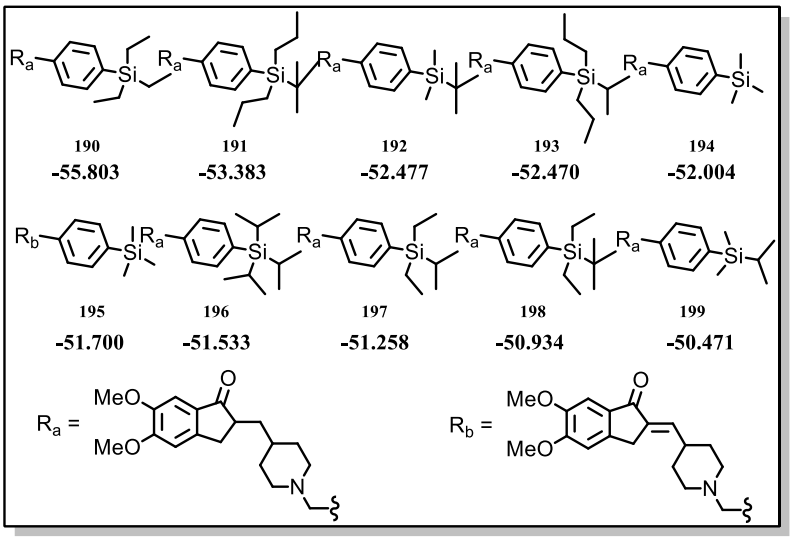

Figure 4.54: Structures and docking scores of silicon derivatives at para position in the benzyl moiety.

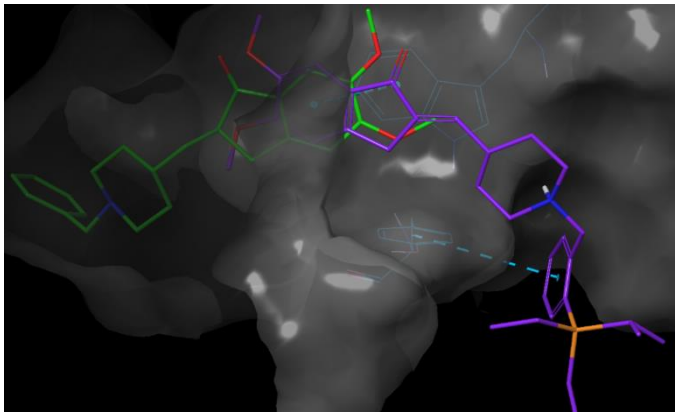

*Figure 4.55: Substitution at ortho position (structure **170**; purple), binding outside of the binding pocket; pi-pi stacking interaction with Tyr-70 (blue) and Trp-279 (blue) stabilising the ligand.*

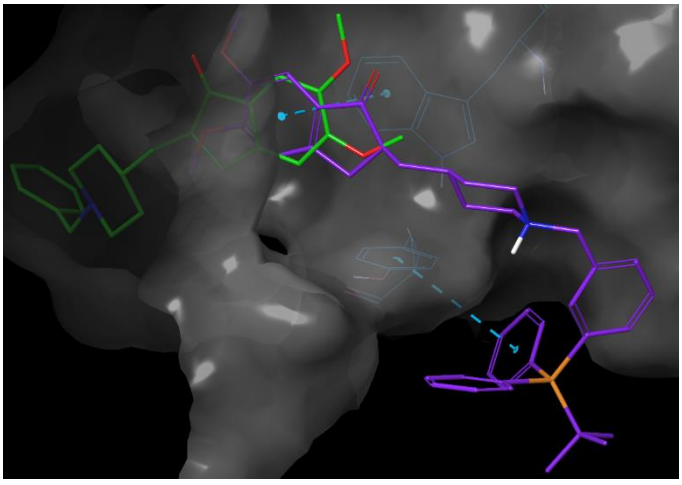

*Figure 4.56: Pi-pi stacking interactions between structure **180** (purple) and Tyr-70 (grey) and Trp-279 stabilising the ligand.*

© University of Pretoria

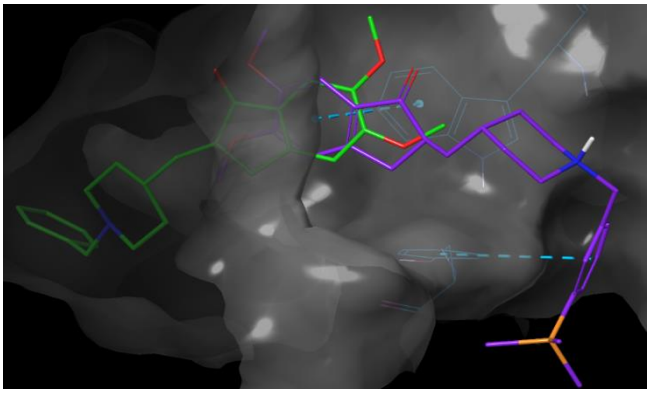

*Figure 4.57: Trimethyl substitution at meta-position (structure **181**; purple), binding outside of the binding pocket.*

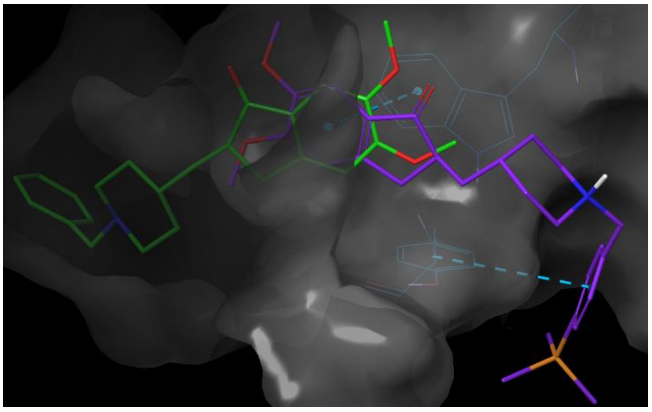

*Figure 4.58: Trimethyl substitution at the para-position (structure **195**; purple), caused binding outside of the binding pocket, with pi-pi stacking interactions with the ligand indanone moiety and Trp-279 (blue) and with the benzyl group and Try-70 (blue).*

It was suspected that the model was biased against the proposed benzyl derivatives, as none of the ligands were observed to dock within the binding pocket. As such it was elected to re-evaluate the proposed benzyl derivatives using a higher flexibility within the MM-GBSA calculation.

4.9.5.2 Increased flexibility at 1 Å MMG-BSA

A comparison between donepezil from the PDB and donepezil docked into 1EVE at 1 Å, was performed to ascertain if the 1 Å model has reliable docking modes for the benzyl substitutions (Figure 4.59).

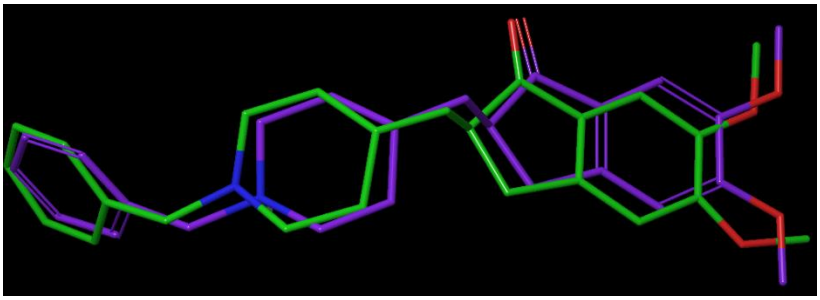

Figure 4.59: Docked donepezil (purple) from the 1 Å calculation, has a comparable binding mode to donepezil (green) from 1EVE.

© University of Pretoria

The bonding mode of the 1 Å MM-GBSA calculation was found to be comparable to the PDB 1EVE binding mode with the exception that the ligand is slightly pulled out of the binding pocket. Donepezil at 1 Å had a score of -74.382. All the same interactions seen for donepezil at 0 Å were conserved at 1 Å flexibility in the Prime MM-GBSA calculation.

4.9.5.2.1 Ortho substitution

The docking was repeated using the 1 Å MM-GBSA calculation and in this instance the increased flexibility of the calculation now allowed the ligands to bind within the pocket. Once again, in all instances with the exception of compound **200** (Figure 4.60 & 4.61), a reversed binding mode was observed, however, now instead of being docked completely out of the binding pocket, as seen in the 0 Å calculation there was clear entry into the pocket (Figure 4.62). Even though the majority of the ligands are bound in the reverse mode, the MM-GBSA energies (Figure 4.60) are observed to be comparable to donepezil and this may be indicative of a different binding mode.

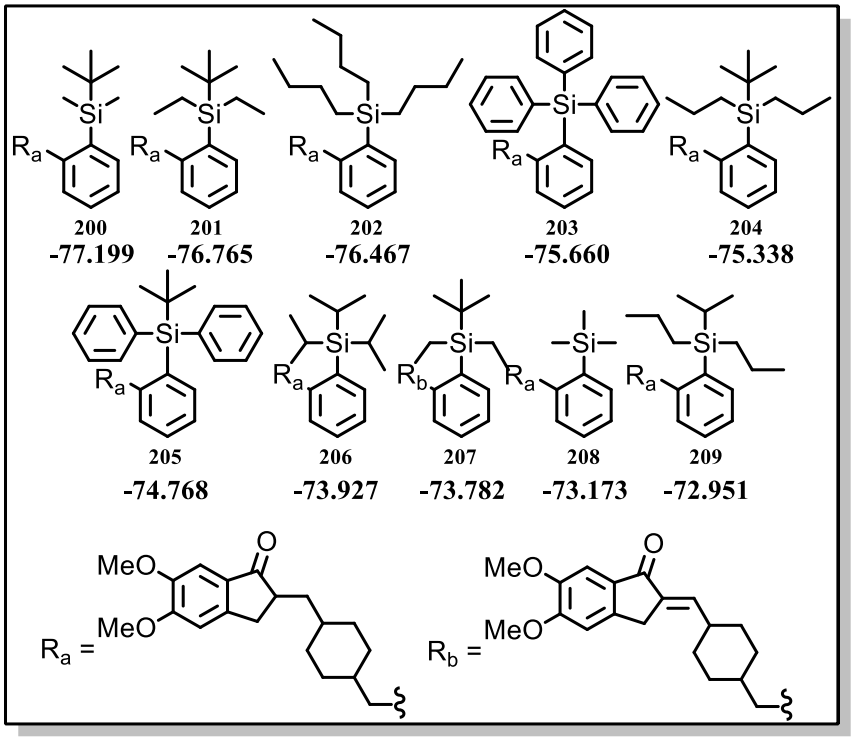

Figure 4.60: Structures and docking score of silicon derivatives at ortho position in the benzyl moiety.

© University of Pretoria

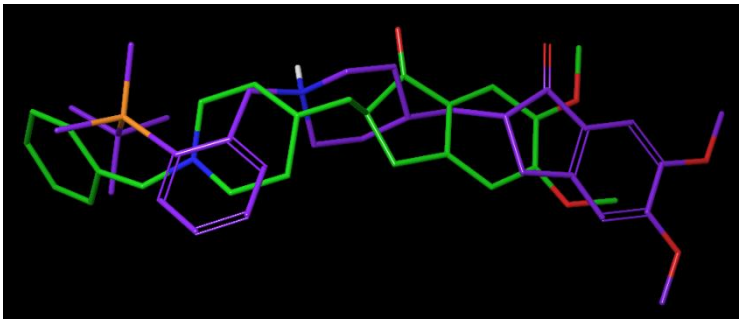

*Figure 4.61: Ligand **200** has the correct binding mode, as compared to donepezil (green), but pulled out the binding pocket slightly to allow for the bulky benzyl substitution on the ortho position.*

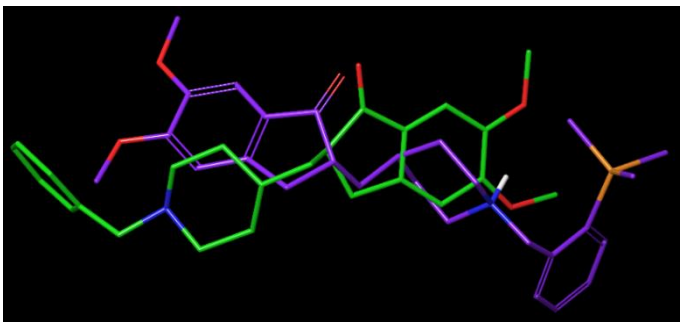

*Figure 4.62: Ligand **208** with trimethylsilyl substitution binding in the reverse position, even though it is the least sterically hindered substitution.*

In considering a potentially different binding mode compounds **201** and **203** were investigated showing typical interactions with alkyl or aromatic substitutions on the silyl group (Figure 4.63 and 4.64). Compound **201** has alternative hydrogen bonding interactions for both the methoxy group at the 6th position and the carbonyl oxygen through water molecules forming hydrogen bonding networks. The methoxy group at the 6th position had bonding interactions with Ser-200, Gly-118 and Gly-119, whereas the carbonyl has bonding interactions with just Phe-288. The protonated nitrogen of the piperidine ring didn't have any hydrogen bonding interactions, but two pi-cation interactions with Trp-279 are noted, however, no pi-pi stacking interactions were seen. Compound **203** has alternative hydrogen bonding interactions with a water molecule at the back of the gorge, facilitating a hydrogen bonding network with Ser-200 and Gly-118 and the methoxy group at the 5th position. The protonated nitrogen of the piperidine has lost all its typical interactions observed in donepezil, but has an alternative pi-cation interaction with Trp-279, which also has pi-pi stacking interactions with a benzene group in the silyl substituents.

© University of Pretoria

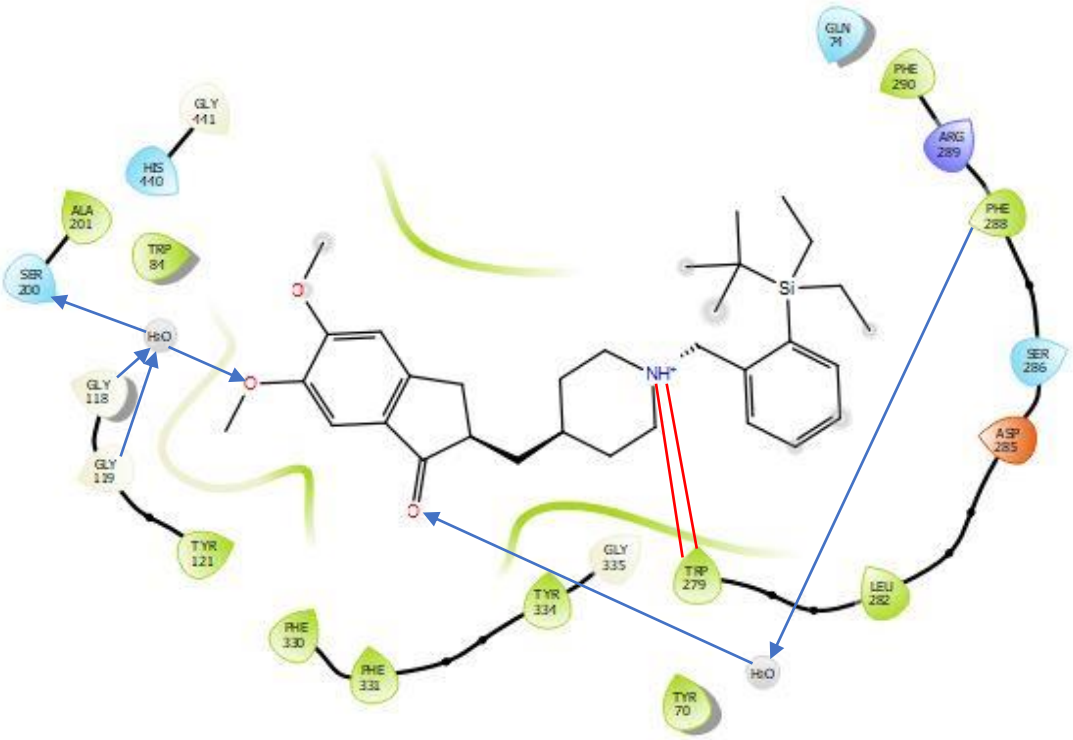

*Figure 4.63: Ligand binding diagram for structure **201**. Hydrogen bonding —, pi-pi interactions —, pi-cation —.*

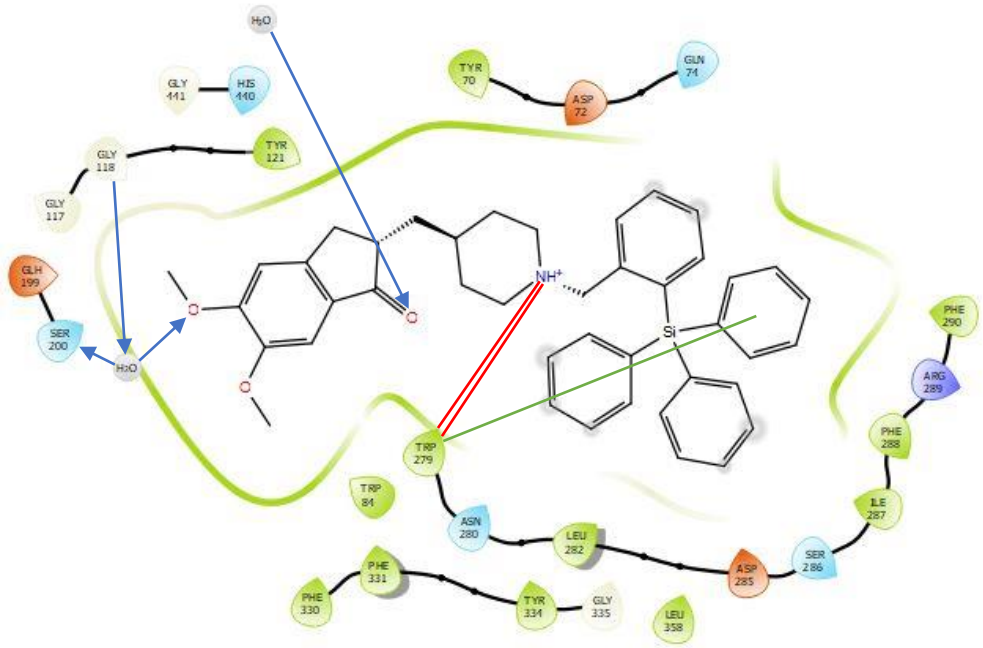

*Figure 4.64: Ligand binding diagram of structure **203**. Hydrogen bonding —, pi-pi interactions —, pi-cation —.*

© University of Pretoria

4.9.5.2.2 Meta substitution

A series of silylated benzyl derivatives in a meta orientation to the piperidine were assessed for the binding efficiency. The less hindered substituents as seen in ligands **210**, **211** and **214** (Figure 4.65) were observed to bind in a similar manner as donepezil, however, they were forced further out the binding pocket to allow for the substituents on the benzyl moiety (Figure 4.66). The rest of the ligands were bound in the reverse pose, with the benzyl moiety protruding outside the binding pocket.

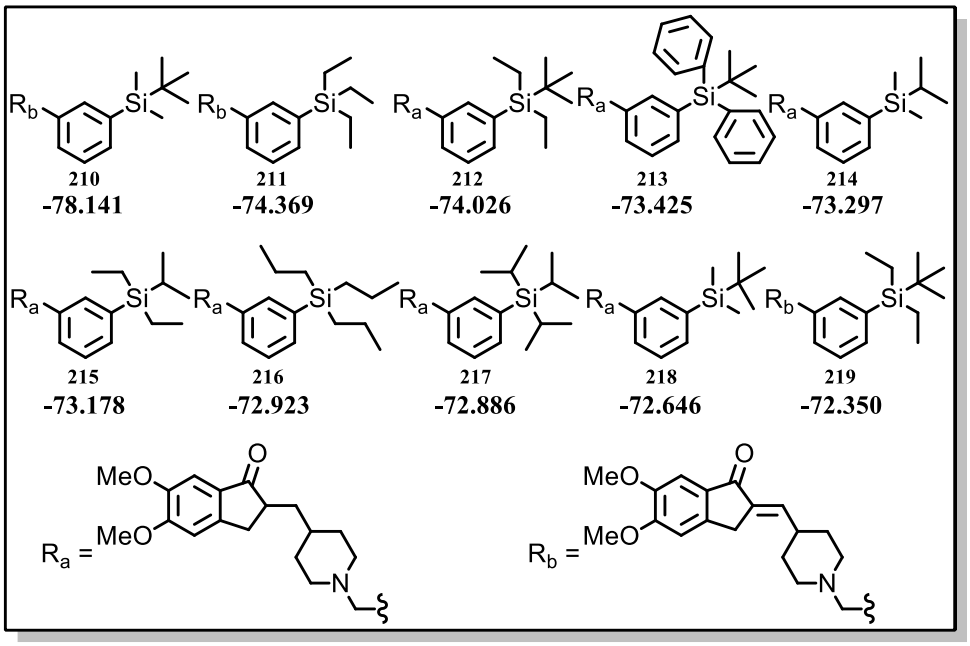

Figure 4.65: Structures and docking scores of silicon derivatives at meta position in the benzyl moiety.

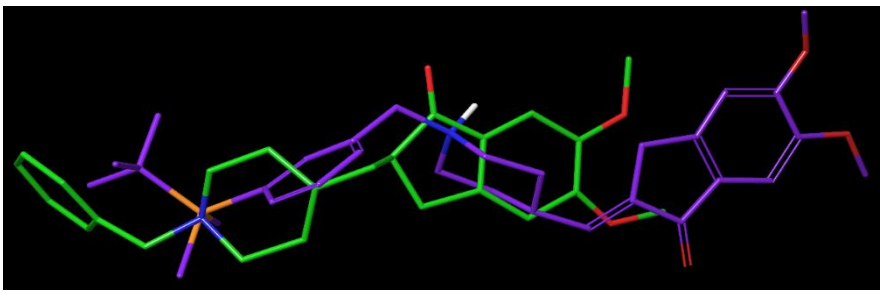

*Figure 4.66: Ligand **210** has the correct binding mode, as compared to donepezil (green), but pulled out the binding pocket slightly to allow for the bulky benzyl substitution on the meta position.*

Compound **212** and **213**'s bonding interactions were assessed to see what typical interactions occur with alkyl and aromatic substitutions of analogues that are bound in the reverse mode (Figure 4.67 and 4.68). Compound **212** didn't have any pi-pi stacking interactions, but had alternative hydrogen

© University of Pretoria

bonding interactions with the methoxy group in the 6th position with a water molecule facilitating a hydrogen bonding network with Ser-200, Gly 118 and Gly-119 at the back of the binding pocket. The carbonyl oxygen also has a hydrogen bonding network with a water molecule facilitating bonding to Phe-288. The protonated piperidine nitrogen has hydrogen bonding to Tyr-334 and pi-cation interactions with Trp-279. Compound **213** had no hydrogen bonding with its methoxy group oxygen atoms, however, it has a more extensive hydrogen bonding network with its carbonyl through a water molecule to Phe-331 and Phe-288. The protonated piperidine nitrogen had no stabilising interactions, but the aromatic group of the indanone moiety had pi-pi stacking interactions with Phe-330 and the aromatic group of the silyl substitution had similar interactions with Trp-279.

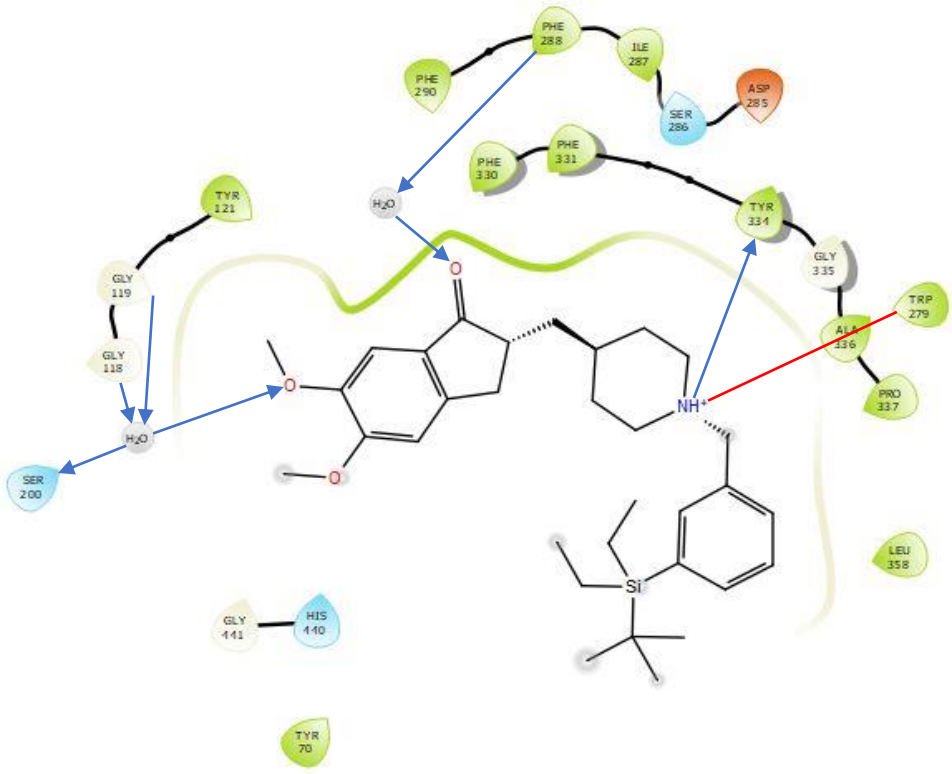

*Figure 4.67: Ligand interaction diagram of structure **212**. Hydrogen bonding —, pi-cation —.*

© University of Pretoria

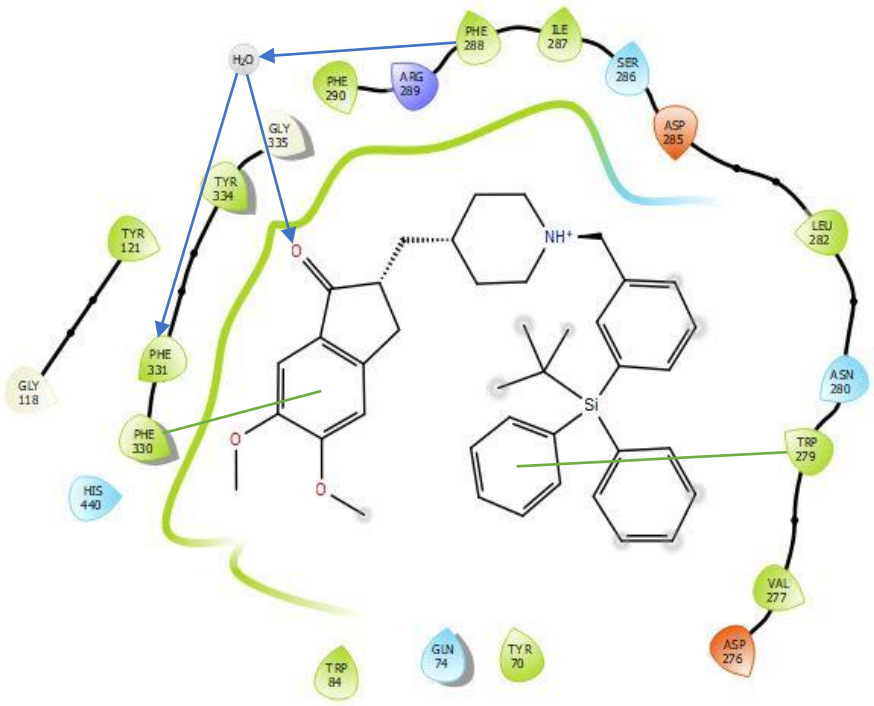

*Figure 4.68: Ligand boning diagram of structure **213**: Hydrogen bonding —, pi-pi interactions —.*

4.9.5.2.3 Para substitution

A series of derivatives with the silyl benzyl substituents in the para position were assessed, and again all the ligands with the exception of the smallest silyl groups docked in the reverse binding mode within the binding pocket. The *tert*-butyldimethyl (Compound **222**) (Figure 4.69), trimethyl and triethyl (not listed in Figure 4.69) substituted system docked in the correct binding mode, but again were forced further out the binding pocket to allow space to accommodate the increased steric bulk (Figure 4.70).

© University of Pretoria

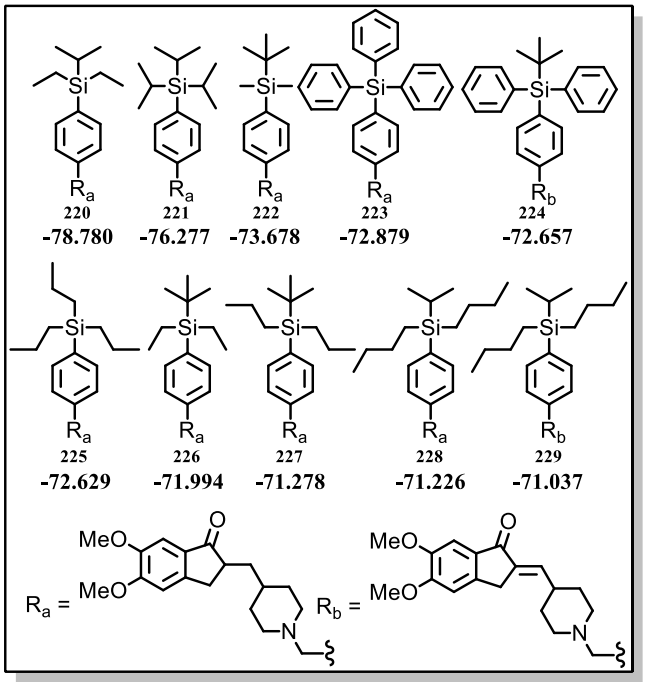

Figure 4.69: Structures and docking score of silicon derivatives at para position in the benzyl moiety.

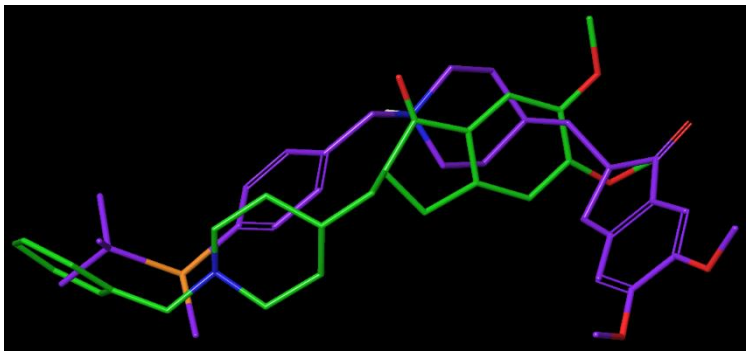

*Figure 4.70: Ligand **222** had the correct binding mode, as compared to donepezil (green), but was pulled slightly out the binding pocket to allow for the bulky benzyl substitution on the para position.*

Compound **220** and **223**'s interactions were evaluated for typical bonding interactions for aromatic and alkyl substituents at the para position of reverse bound derivatives (Structure 4.71 and 4.72). Compound **220** had the most extensive hydrogen bonding networks facilitated by water molecules between the methoxy group at position 6 and Ser-200 and Gly-118 and the carbonyl oxygen with Tyr-334 and Phe-288. Pi-pi stacking interactions occurred between the indanone moiety and Phe-331 and the benzyl moiety with Tyr-70 and a pi-cation interaction between the protonated nitrogen of the piperidine moiety and Trp-279 was present. In the case of compound **223** the methoxy group at position 6 had hydrogen bonding interactions with Ser-200 and Gly-119 through a water molecule and the aromatic group of the indanone moiety had double pi-pi interactions with His-440 and Phe-330. The protonated nitrogen of the piperidine ring had only one pi-cation interaction with Trp-279 and

© University of Pretoria

the aromatic groups on the silyl substitution had no pi-pi interactions at the entrance of the binding pocket.

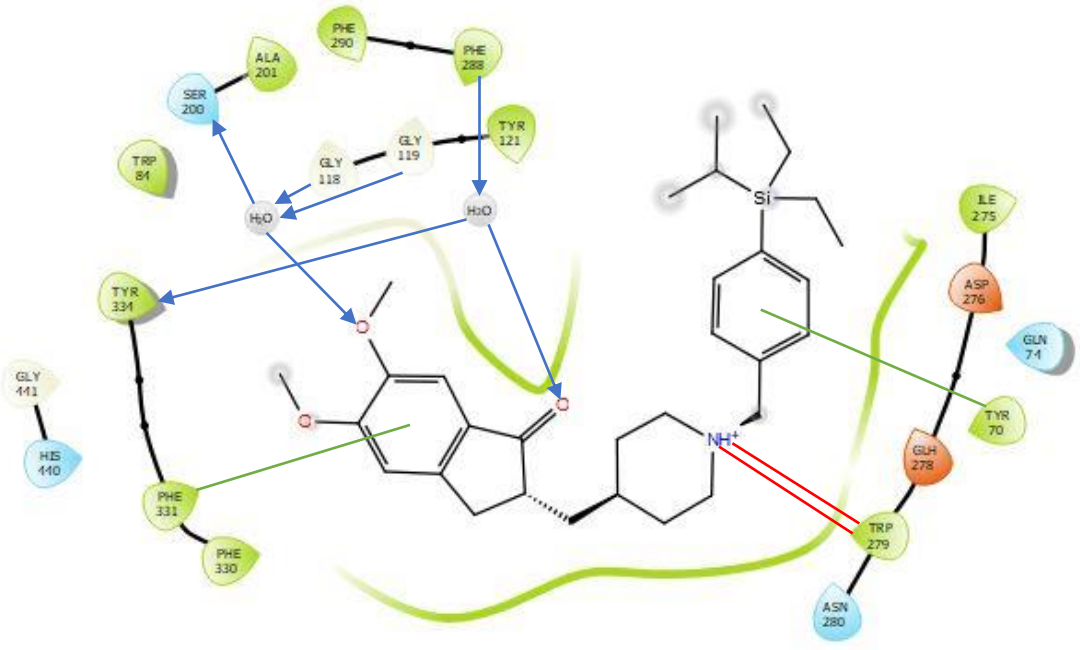

*Figure 4.71: Ligand binding diagram of structure **220**. Hydrogen bonding —, pi-pi interactions —, pi-cation —.*

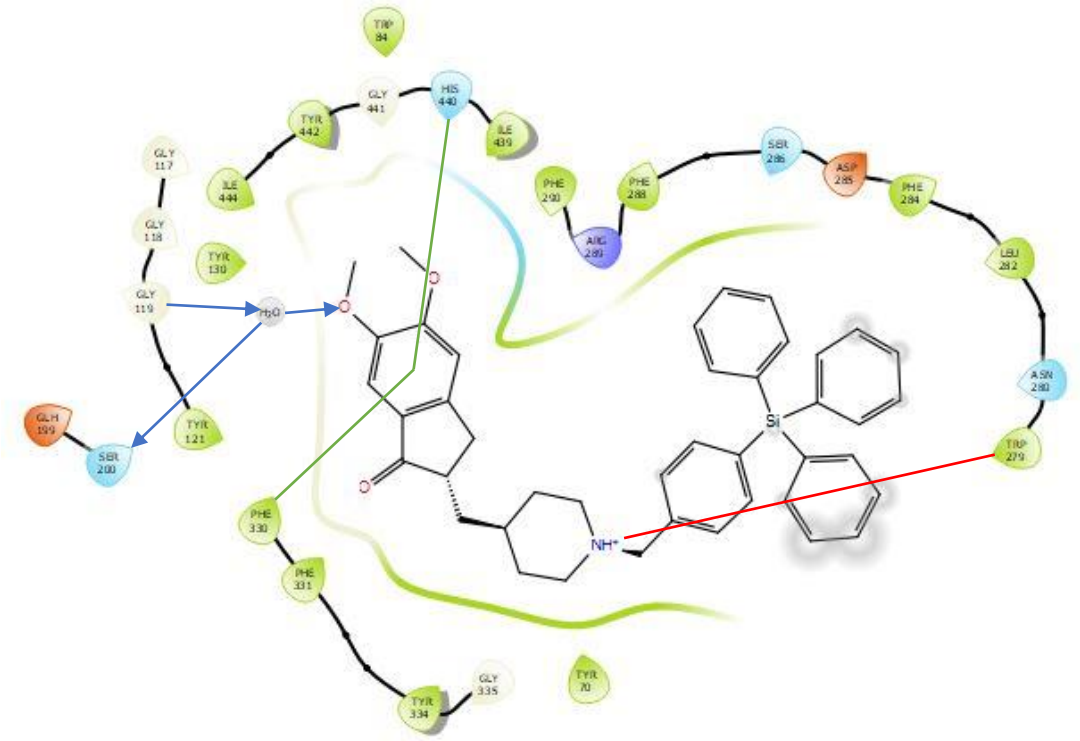

*Figure 4.72: Ligand binding diagram of structure **223**. Hydrogen bonding —, pi-pi interactions —, pi-cation —.*

© University of Pretoria

4.9.6 Acetophenone derivatives

Although not originally planned the replacement of the indanone moiety with acetophenone was also considered, this decision was driven by the fact that in previous in-house projects the indanone moiety had proven to be synthetically challenging to functionalise. Acetophenone was hypothesised to behave similarly to indanone albeit with increased flexibility as the five membered ring from the moiety is removed. Synthetically, this was proposed to make the ketone more accessible, as it is no longer locked in a planar position and more readily allows functionalisation of the alpha position through halogenation followed by S_N2 substitution.

4.9.6.1 β-Diketo-system

A β-diketo-system was considered as the α-carbon between the two ketones will provide additional length and flexibility to accommodate large substituents (Figure 4.73) and the second carbonyl may also provide additional hydrogen bonding capacity, potentially increasing the stability and reactivity of the ligands.

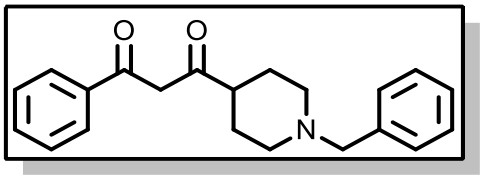

Figure 4.73: Line structure of the unsubstituted acetophenone derivative with the β-diketo linker.

Initially it was envisaged to investigate β-diketo-systems wherein the aromatic ring from the "acetophenone" moiety contained a silyl group bound through an oxygen atom at either the ortho, meta or para position. In the case of meta substitutions a series of systems with large to medium silanes (Figure 4.74) had similar binding modes to donepezil and docked well in the binding pocket (Figure 4.75). Medium sized substitutions on the para position also docked in the binding pocket (Figure 4.76), but were placed slightly out of the binding pocket, while large substitutions with aromatic rings or long alkyl substitutions were too bulky to allow the ligand to successfully enter the pocket fully (Figure 4.77).

© University of Pretoria

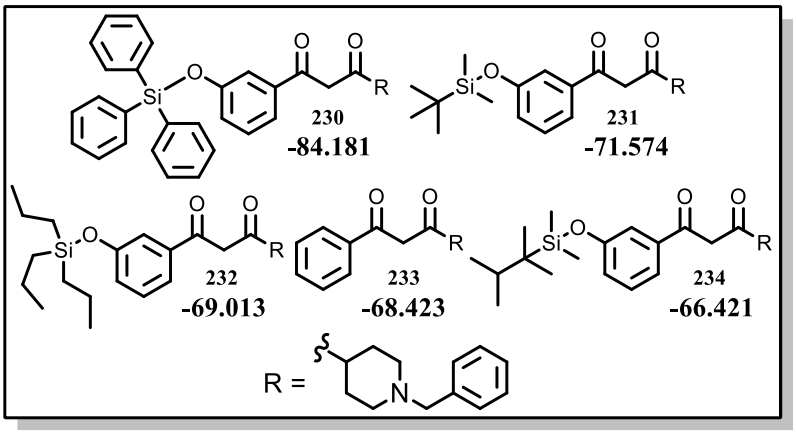

Figure 4.74: Structures and docking scores of O-silylated diketo acetophenone derivatives.

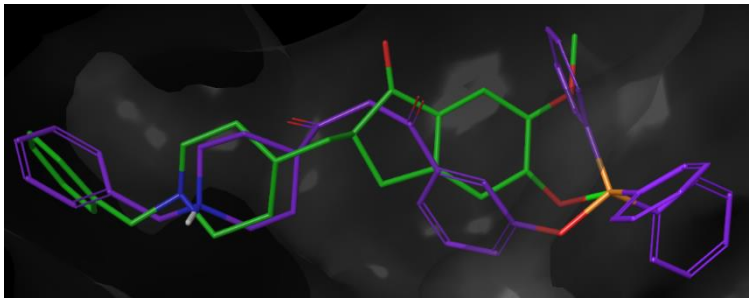

Figure 4.75: Substitution on the meta position with a large silane (purple), forced the acetophenone moiety to dip lower into the pocket. Large substitution of triphenylsilane still docked within the binding pocket and was comparable with donepezil (green).

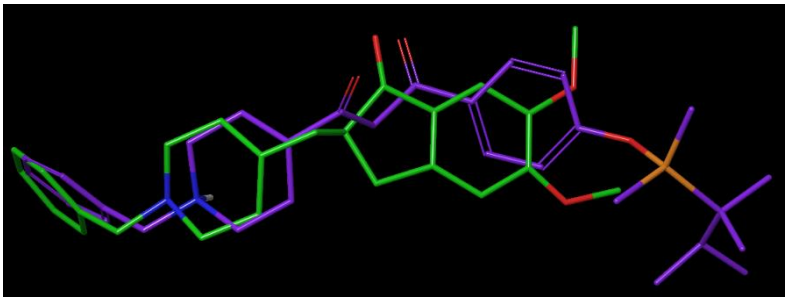

Figure 4.76: A medium sized para substitution of dimethylthexylsilane diketo acetophenone (purple) has a comparable binding mode as donepezil (green).

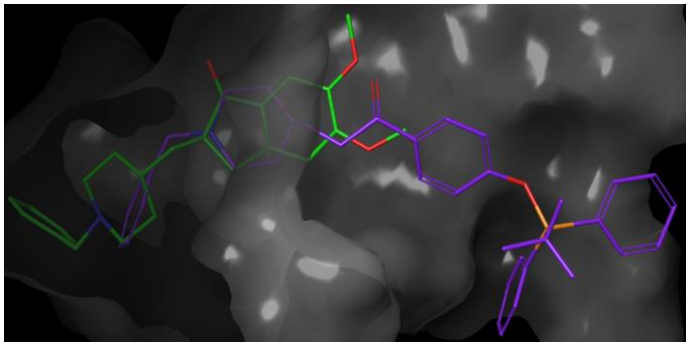

Figure 4.77: Substitution of large bulky groups, such as tert-butyldiphenylsilane on the diketo acetophenone (purple), pulls the ligand further out of the binding pocket.

© University of Pretoria

Attempts to dock analogous ortho substituted rings were unfavourable with the steric bulk of the ligands preventing full insertion of the ligand into the binding pocket, with the exception of the *tert*-butyldimethylsilane group. The ortho substitution of *tert*-butyldimethylsilane was accommodated by an 180° rotation of the acetophenone moiety (Figure 4.78), placing the bulky substituent at the bottom of the pocket. The meta substitution was favoured over the para and ortho substitutions, as the alpha carbon of the β-diketo linker provided flexibility to accommodate the substitutions. The para substitutions are less favoured, as the silyl substitutions orientate the ligands further out the binding pocket reducing or preventing CAS binding.

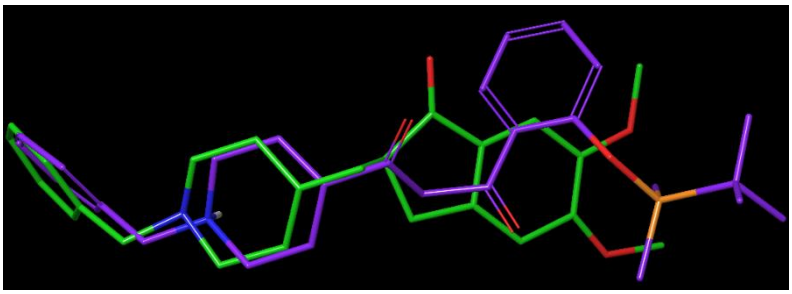

Figure 4.78: Substitution of tert-butyldimethylsilane (purple) on the ortho position has comparable binding mode to donepezil (green). The substitution was accommodated by a 180° rotation of the acetophenone moiety.

The binding interactions of the unsubstituted acetophenone (**233**) derivative were inspected to determine if similar or different binding interactions occur for the β-diketo linker as compared to donepezil (Figure 4.79). The typical hydrogen bonding interactions of the piperidine nitrogen (discussed in Section 4.8.1.1) of donepezil were replaced with pi-cation interactions with Tyr-334, Trp-84 and Phe-330 for the β-diketo linker derivative. The two carbonyls of the β-diketo linker also had alternative hydrogen bonding interactions facilitated by a water molecule to a hydrogen bonding network with Phe-331 and Phe-288. The aromatic ring of the acetophenone moiety did have an analogous pi-pi stacking interaction as the indanone moiety in donepezil, but instead with Trp-279 near the entrance of the binding pocket. The substituted β-diketo linkers had a variation of these interactions depending on how the piperidine and benzyl moieties shifted in the binding pocket to accommodate the substitutions and their interactions.

© University of Pretoria

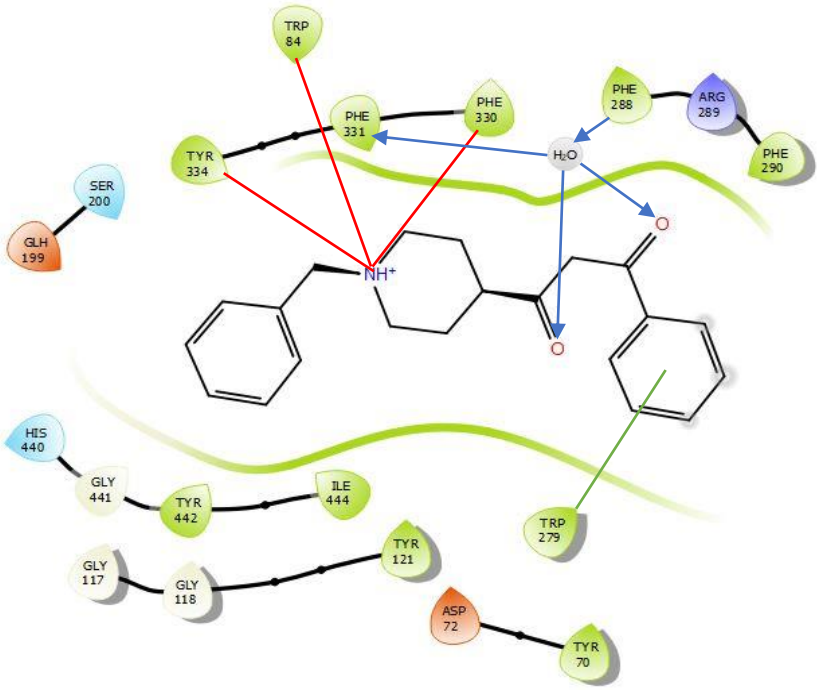

*Figure 4.79: Ligand interaction diagram of unsubstituted acetophenone (**233**) with a β-diketo linker. Hydrogen bonding —, pi-pi interactions —, pi-cation —.*

The β-diketo linker analogues had docking scores that were higher than or comparable to donepezil (Figure 4.74) and are promising scaffolds for further development.

4.9.6.2 Ether-linkage

As an alternative to the β-diketo system an analogous system wherein one of the carbonyl groups was replaced with an ether linker was investigated. The linker gives comparable length to the β-diketo system and slightly improved flexibility (Figure 4.80). The ether oxygen is a H-bond acceptor and may also provide for additional binding interactions.

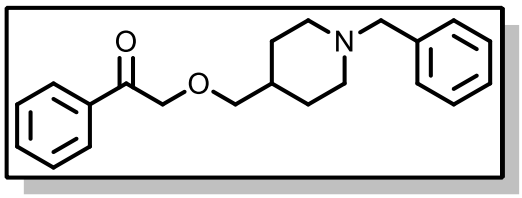

Figure 4.80: Line structure of the ether-linkage acetophenone derivative with no substitution.

All the substitutions on the meta position (Figure 4.81) docked well in the binding pocket, but to accommodate the substitutions the acetophenone moiety was dipped down in the pocket (Figure

© University of Pretoria

4.82), shifting the carbonyl away and disrupting the hydrogen bonding interaction with Tyr-70, but forming a new interaction with Phe-331 mediated through a water molecule.

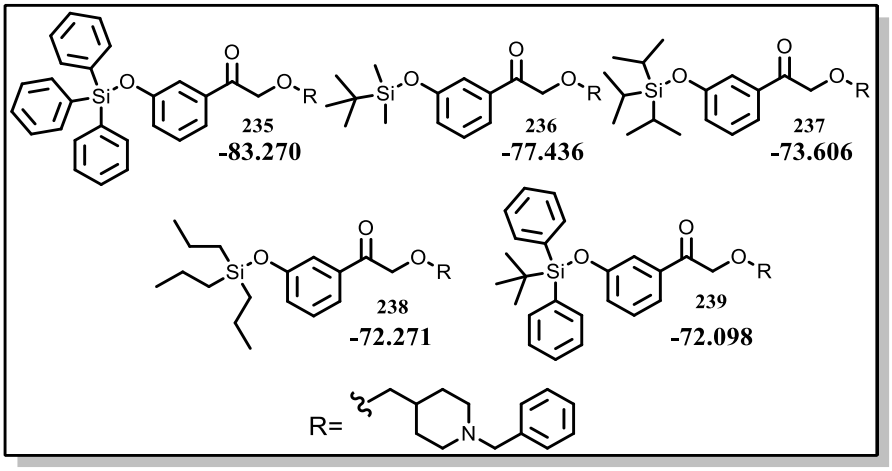

Figure 4.81: Structures and docking scores of O-silylated ether-linkage acetophenone derivatives.

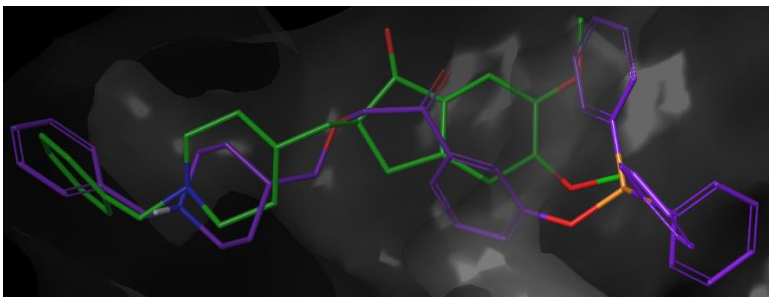

*Figure 4.82: Substitution of the ether-linkage acetophenone with triphenylsilane (**235** purple) at the meta position, doesn't pull the ligand out of the binding pocket, even though it is a bulky substituent.*

Substitution at the para position with small to large substituents gave compounds with similar binding modes as donepezil, with no major shifts in the acetophenone positioning. Surprisingly, sterically bulky *tert*-butyldiphenylsilane had a comparable binding mode to donepezil (Figure 4.83), but substitution with triisopropylsilane was too sterically bulky and forced the acetophenone moiety out of the pocket. In the latter case, the benzyl moiety was still close enough to interact with the CAS site (Figure 4.84).

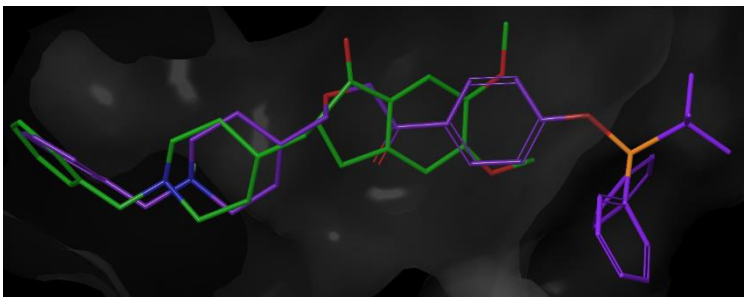

Figure 4.83: Substitution of tert-butyldiphenylsilane (purple) on the para position docked comparably to donepezil (green).

© University of Pretoria

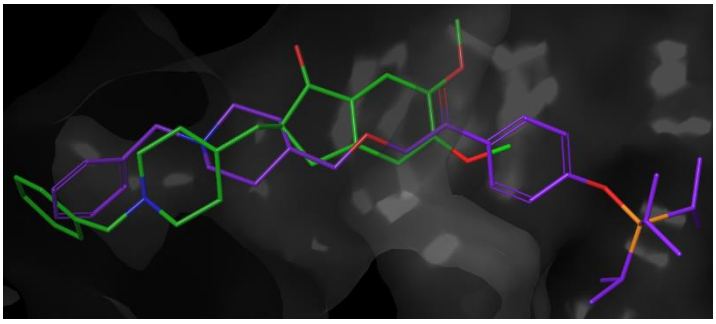

Figure 4.84: Substitution of triisopropylsilane (purple) on the para position, does pull the ligand out of the binding pocket due to steric hindrance.

Ortho substitution forced an 180° rotation of the acetophenone moiety to accommodate large or branched substituents (Figure 4.85), with very large substitutions forcing most of the ligand out of the pocket (Figure 4.86). The meta substitutions were favoured over the para and the ortho analogues as the ether-linkage allowed for added flexibility and length to accommodate the substituents favourably and may allow bulkier substituents to show activity as the benzyl moiety can still reach the CAS site.

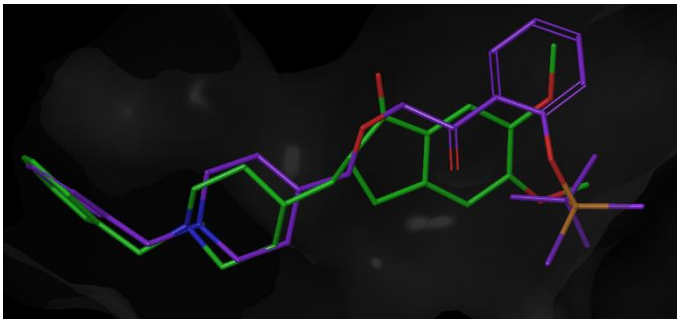

Figure 4.85: Substitution of tert-butyldimethylsilane (purple) on the ortho position has comparable docking mode to donepezil (green). The substitution was accommodated by a 180° rotation of the acetophenone moiety.

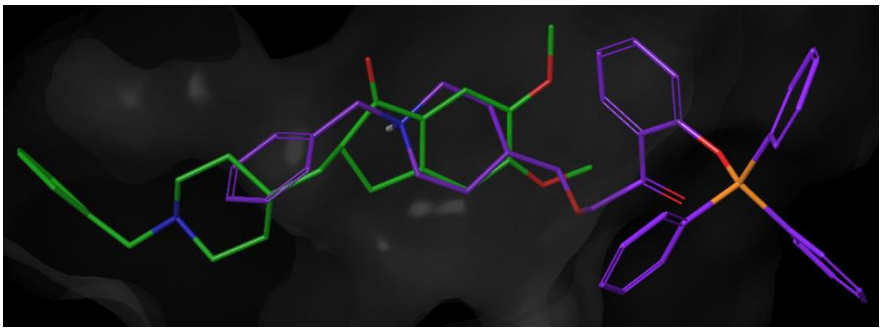

Figure 4.86: Substitution of large bulky groups such as triphenylsilane on the ortho position (purple), pulled the ligand out of the binding pocket.

© University of Pretoria

The binding interactions of the unsubstituted acetophenone ether derivative was inspected to compare the bonding interactions between the ether linker analogue and donepezil, to assess if they are similar or differ considerably (Figure 4.87). As seen for the β-diketo linker analogue, the typical hydrogen bonding interactions of the piperidine nitrogen (discussed in Section 4.8.1.1) were replaced with pi-cation interactions with Trp-84, Tyr334 and Phe-330 for the ether linker derivative. The ether oxygen of the linker also had alternative hydrogen bonding interactions facilitated by a water molecule to a hydrogen bonding network with Phe-331 and Phe-288. The aromatic ring of the acetophenone moiety had the same pi-pi stacking interactions as the indanone moiety in donepezil, with Trp-279 near the entrance of the binding pocket, as well as the pi-pi stacking interactions between the benzyl moiety and Trp-84. The substituted ether linker analogues had an assortment of these interactions depending on the substitutions and how they distorted the benzyl and piperidine moieties in the binding pocket to accommodate the substitutions and their interactions.

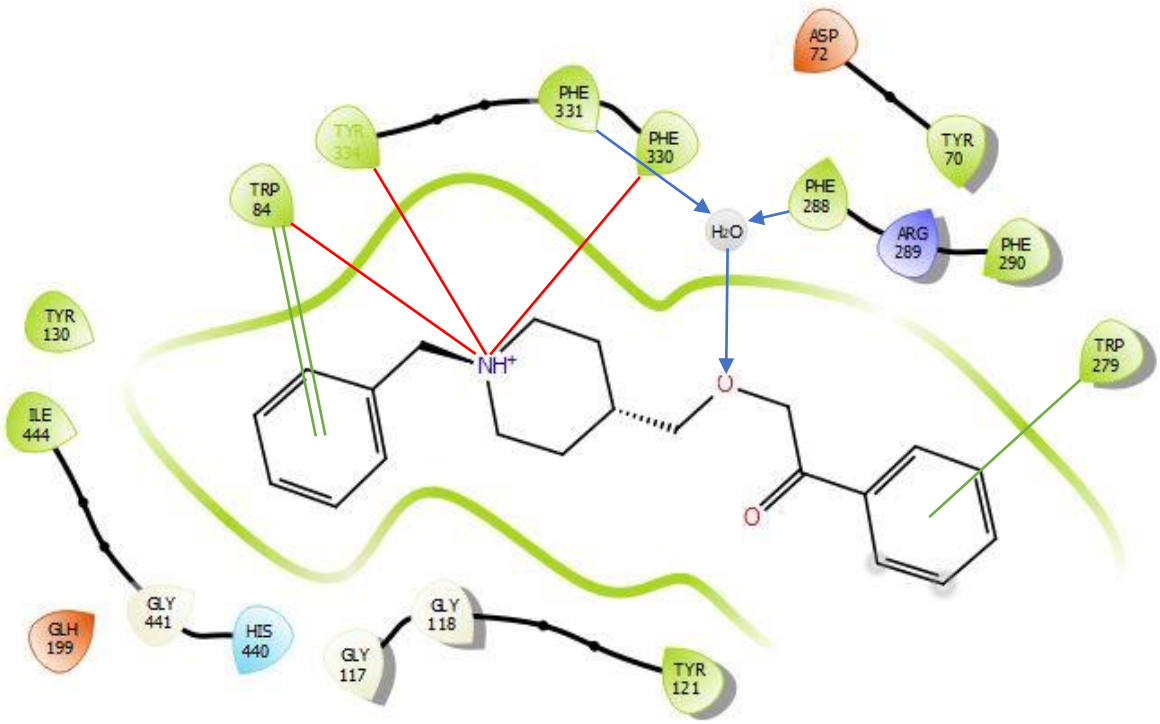

Figure 4.87: Ligand binding diagram of unsubstituted acetophenone with an ether linker. Hydrogen bonding —, pi-pi interactions —, pi-cation —.

The ether linker analogues had high to similar MM-GBSA energies as donepezil (Figure 4.81) and should be considered for further development.

© University of Pretoria

4.9.7 Conclusion

The *in-silico* study facilitated the development of a validated method for the screening of derivatised ligands based on the donepezil scaffold. The model was used to identify silylated derivatives of donepezil with promising binding interactions and docking score for further development.

Substitution on both the 5th and the 6th position of the indanone ring was favoured, whether it be a direct *C*-silicon bond, an *O*-silylation or tethered silyl substituents. In comparison, substitution at the 4th and especially at the 7th position on the indanone moiety appear to be highly disfavoured. All substitutions had comparable binding of the benzyl and piperidine moiety, however, some of the bonding interactions of the indanone moiety were lost.

Silyl substitution of the indanone-piperidine ring linker, the piperidine ring and the benzylic CH_2 group were limited to methyl silane substitutions, as longer chains and bulkier substituents prevented the entry of the ligand into the binding pocket. In general the ligands could not enter the binding site and none of the bonding interactions typical of donepezil could occur, except for a single pi-pi stacking interaction between the indanone moiety and an aromatic amino acid side chain near the entrance of the binding pocket.

Substitution on the benzyl ring is completely unfavourable, as even the smallest silyl groups (trimethyl silanes) prevented the entry of the ligand into the binding pocket at 0 Å. At 1 Å the ligands could enter into the binding pocket and interact with the residues, however, all the ligands had a reverse binding orientation with the exception of the smallest substituents.

The 1 Å Prime MM-GBSA calculation showed an alternative binding mode for the benzyl derivatives where the indanone moiety is at the bottom of the binding pocket and the benzyl group bonded at the entrance of the binding pocket. The binding interactions for the ortho, meta and para derivatives vary according to the substitution on the benzyl moiety. Consistent bonding interactions between the different analogues were observed, such as hydrogen bonding interactions of the methoxy with Ser-200 and Gly-118 or Gly-119 facilitated by a water molecule. The carbonyl oxygen of the indanone typically has a hydrogen bonding interaction through a water molecule with Phe-228, but may include Tyr-334 and Phe-331 for a number of substituents. The protonated nitrogen of the piperidine ring varies quite significantly from no interactions to several, which typically include pi-cation interactions with Trp-279. Pi-stacking interactions are the least consistent with only the para substitutions typically

© University of Pretoria

having them for both alkyl and aromatic substitutions and for the meta substitutions with aromatic silyl groups.

The exchange of the indanone moiety for the more flexible acetophenone moiety seems to be favourable, but only for the meta substituents, while the para and especially the ortho substituents were less favoured. Meta substitution of the β-diketo system favoured large to small substituents, with large aromatic systems being the most favoured due to additional pi-pi stacking interactions, stabilising the ligand near the entrance of the binding pocket. Para substitutions with medium to small substituents were somewhat favoured, while large substitutions were completely disfavoured. All ortho substitutions are unfavoured due to the steric hindrance of the substituents being at a right angle to the linker, making the ligand unable to rotate or bend in such a way to allow access to the binding pocket. The β-diketo linker has several bonding interactions in common with donepezil, namely the pi-pi stacking interactions of the indanone/acetophenone aromatic group with Trp-279 and a pi-cation interaction between the protonated nitrogen of the piperidine ring and Phe-330. In addition, bonding interactions that are unique to the acetophenone β-diketo linker were observed wherein there is a hydrogen bonding network of the second carbonyl of the linker with Phe-331 and Phe-288 and additional pi-cation interactions of the protonated nitrogen of the piperidine ring with Tyr-334 and Trp-84.

The ether-linkage added length and freedom of rotation allowing more flexibility to accommodate very large *O*-silylated groups, except for sterically hindered branched alkyl substitutions. The ether-linkage was favoured especially for meta substituents including very large aromatic substituents, as pi-pi stacking interactions stabilised the ligand near the entrance of the binding pocket. The para substituted analogues were slightly less favoured and the ortho substituents were the least favoured. The ether linker added considerable length to the molecule and even though some bulky substituents were disfavoured and forced the acetophenone moiety further out the binding pocket, the benzyl moiety could usually still reach the CAS site due to the added length. The ether linker has comparable interactions to donepezil, including pi-pi interactions of the benzyl moiety with Trp-84 and between Trp-279 and the indanone/acetophenone moiety, as well as the pi-cation interaction between Phe-330 and the protonated nitrogen of the piperidine ring. Interactions unique to the ether acetophenone system included the hydrogen bonding network of the ether oxygen and Phe-331 and Phe-288 through a water molecule and additional pi-cation interactions with Tyr-334 and Trp-84 with the piperidine nitrogen.

© University of Pretoria

The combined workflow model gave reliable results and should be considered for use in drug discovery programs. This workflow, however, is not viable for HTPS (high through put screening), as confgen will exponentially increase the amount time and computational resources required to run downfield calculations and increase efforts in data management and analysis time. It should, however, be considered for final screening of lead compounds obtained through HTPS.

© University of Pretoria

Chapter 5 Synthesis discussion and results

In the previous chapter several silylated analogues of the donepezil scaffold were identified through *in silico* modelling for further development and in this chapter synthetic access to these scaffolds will be discussed. *O* and *C*-silylated derivatives of the indanone moiety were identified (Section 4.9.1) as potential hit scaffolds and these will be discussed in Section 5.3. Derivatives with *C*-silylation of the benzyl moiety (Section 4.9.5) were also evaluated as one of the top scaffolds in the *in-silico* study and preparation of these compounds is described in Section 5.5. The replacement of the indanone moiety with an acetophenone group was also investigated (Section 4.9.6) and these replacements when containing a β-keto (Section 4.9.6.1) or ether (Chapter 4.9.6.2) linker scored as the top two scaffolds, access to these is discussed in Section 5.6. The synthetic work started with the synthesis of donepezil as many analogues were planned to follow a similar synthetic plan and this was performed as a model study and to familiarise ourselves with the chemistry involved.

5.1 Introduction

5.1.1 The synthesis of donepezil[53]

The synthesis of donepezil (**3**) was envisaged by the hydrogenation of alkene **27**, which in turn is prepared by an aldol condensation between aldehyde **28** and dimethoxy indanone (**29**). Aldehyde **28** can be prepared by the Swern oxidation of alcohol **30**, which is derived by the reduction of ester **31**. Finally, ester **31** could be prepared by the benzylation of ethyl isonipecotate (**32**) with benzyl chloride (**33**) (Scheme 5.1). This synthetic plan was previously validated in house by Divan van Greunen (PhD student) and was followed with little to no deviations.[53]

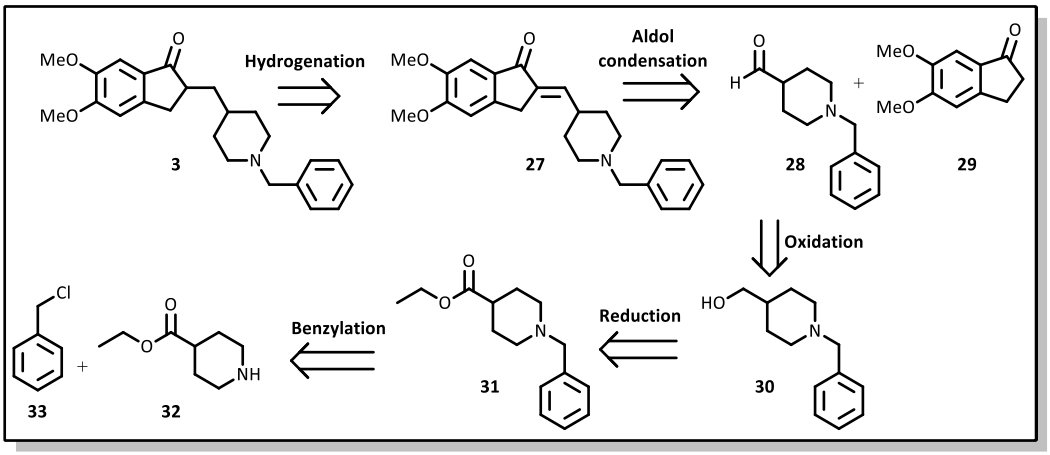

Scheme 5.1: The retrosynthetic route from donepezil.

© University of Pretoria

5.1.2 Synthesis of silylated analogues

In this chapter, synthetic attempts to access six silylated scaffolds as shown in Figure 5.1 will be discussed. The first silylated scaffold to be prepared is the replacement of the methoxy groups of the indanone moiety (**A**) with *O*-silylated groups and this was planned to be achieved by the demethylation of the methoxy groups with the use of aluminium trichloride, as demonstrated by Pietrasik, Szydłowska and Krówczyński.[103] After demethylation, *O*-silylation would follow with the desired bulky silane, after which time the *O*-silylated indanone would then undergo aldol coupling with aldehyde **28** to form the coupled product.[53] Lastly hydrogenation of the alkene catalysed by palladium on carbon and hydrogen gas would produce the final ligands.[53]

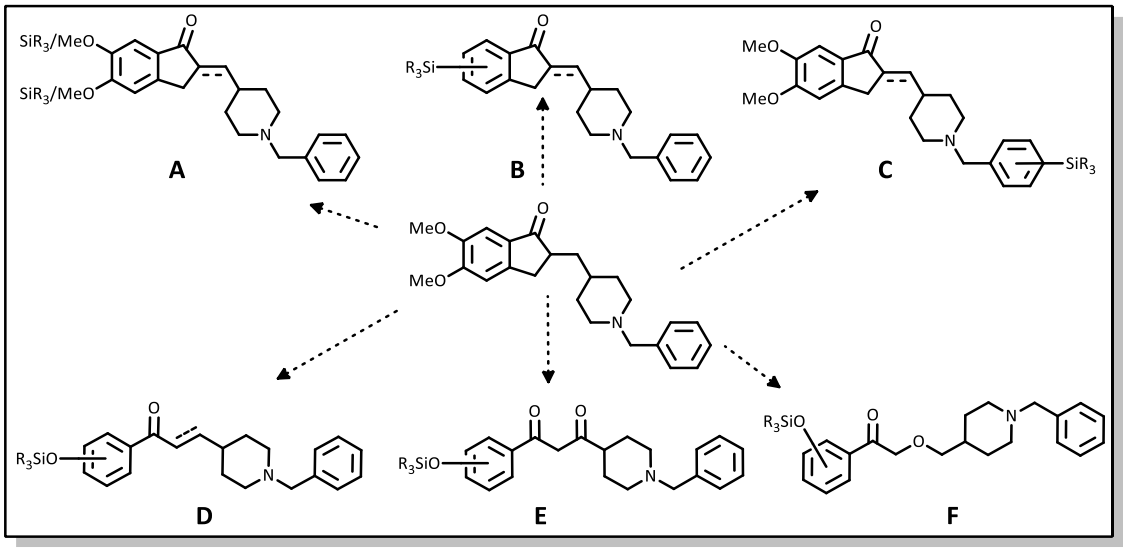

Figure 5.1: Generic structures of targeted silicon containing derivatives of donepezil that are planned to be accessed synthetically.

The second scaffold targeted is the *C*-silylation of the indanone moiety (**B**) which would be achieved by halogenation of the aromatic ring as reported by Gómez and co-worker with the use of aluminum trichloride and liquid bromine.[104] After bromination of the ring, lithium halogen exchange of the bromine with the respective silane was planned following the protocol outlined by Masson and colleagues.[105] The prepared *C*-silylated indanone would then undergo aldol coupling with aldehyde **28** followed by hydrogenation of the alkene to prepare the final compounds.[53]

The third scaffold to be prepared is the *C*-silylation of the benzyl group (**C**) and was planned to be incorporated through a halobenzyl group during the benzylation of carboxylate **32** into the scaffold and following the same synthetic plan as donpezil up to and including the hydrogenation step. After

© University of Pretoria

preparation of the hydrogenated halobenzyl compound, *C*-silylation of the aromatic ring through lithium halogen exchange as described by Masson and colleagues with the respective silane will be prepared to obtain the desired ligands.[105]

Replacement of the indonone ring-system was also envisaged as previous work undertaken within the research group had shown challenges when working with this moiety.[53] The acetophenone group was chosen as it's similar to the indaone ring, except the alpha carbon is no longer trapped in a planar orientation. The fourth scaffold (**D**) was envisaged to have the acetophenone replace the indanone moiety and follow the same synthetic route as donepezil with *O*-silylation of the acetophenone from the respective hydroxy acetophenone derivatives.[53]

The fifth scaffold was planned to have the acetopheone moiety and a β-keto linker (**E**) as the *in-silico* study showed favourable hydrogen bonding interactions with the two carbonyl groups. *O*-Silylation of hydroxyacetophenone was planned to be accomplished by bulky silane protection of the alcohol, to prevent side reactions during the Claisen condensation with carboxylate **31** based on an appraoch previously reported by Inagaki and co-workers.[106] A deprotection of the silyl group would then be performed followed by *O*-siylation with the desired silanes to form the final compounds.

The sixth and final scaffold is the *O*-silylation of the acetophenone moiety with an ether linker (**F**) to the piperidine benzyl system, the ether linker was envisaged to be introduced through a Williamson type etherfication between acetyl protected acetopheneone and alcohol **30**. The acetophenone will need to be protected before bromination to allow for bromination of the α carbon and not the aromatic ring, both procedures of the acetyl protection and bromination follow Riley's procedures with little deviation.[107] After bromination the protected bromoacetophenone is then reacted with alcohol **30** under basic conditions to prepare the ether linked compound, which would then be deprotected and *O*-silylated with the desired silanes.

5.2 Validation of synthetic methodology through the synthesis of donepezil

5.2.1 Benzylation of ethyl isonipecotate (32) to prepare ester 31[53]

The first step involved the benzylation of ethyl isonipecotate (**32**) to afford ethyl 1-benzylpiperidine-4-carboxylate (**31**) (Scheme 5.2). The benzylation proceeds via an S_N2 displacement reaction between the piperidine nitrogen and benzyl chloride (**33**) in the presence of triethylamine. The purification of

© University of Pretoria

ester **31** was achieved by addition of 3 M sodium hydroxide solution to the reaction mixture, which converted unreacted benzyl chloride to benzyl alcohol, thereafter, basification and aqueous extraction facilitated the removal of the benzyl alcohol and unreacted ethyl isonipecotate (**32**). Ester **31** was obtained in 99 % yield as a clear yellow oil.

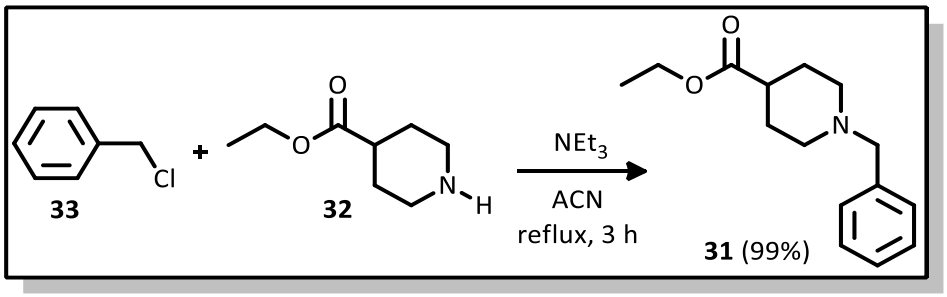

*Scheme 5.2: Benzylation of ethyl isonipecotate (**32**) to form ester **31**.*

The ^{1}H NMR spectrum displayed characteristic aromatic peaks as a multiplet at 7.34 – 7.17 ppm integrating for 5 protons corresponding to the benzyl group. These were further confirmed by the presence of the respective carbon peaks at 138.28, 129.21, 128.30 and 127.13 ppm in the ^{13}C NMR spectrum. Further evidence was given by the FTIR spectrum which clearly illustrated a carbon-nitrogen stretching frequency at 1259 cm^{-1} and the mass spectrum showed a mass ion at *m/z* 248.1640 (100 %), with the molecular ion mass requiring 248.1645.

5.2.2 Reduction of ester **31** to alcohol **30**[53]

Ethyl 1-benzylpiperidine-4-carboxylate (**31**) was subsequently reduced to (1-benzylpiperidn-4-yl)methanol (**30**) in the presence of sodium bis(2-methoxyethoxy)aluminium hydride (Red-Al) (Scheme 5.3). Red-Al is a hydride source with two hydrides available per Red-Al complex, an excess of the hydride source was needed for the reduction of the ester, with the first nucleophilic attack converting the ester to an aldehyde and the second the aldehyde to an alkoxide, which is later protonated to form the alcohol. As Red-Al is mildly moisture sensitive and the reduction reaction is exothermic in nature, the reaction was performed under inert conditions at 0 °C. Upon completion of the reaction, any remaining Red-Al was quenched with basic sodium hydroxide solution. Thereafter, an extractive work-up allowed isolation of the pure alcohol **30** as a clear oil in 95 % yield, with no further purification required.

© University of Pretoria

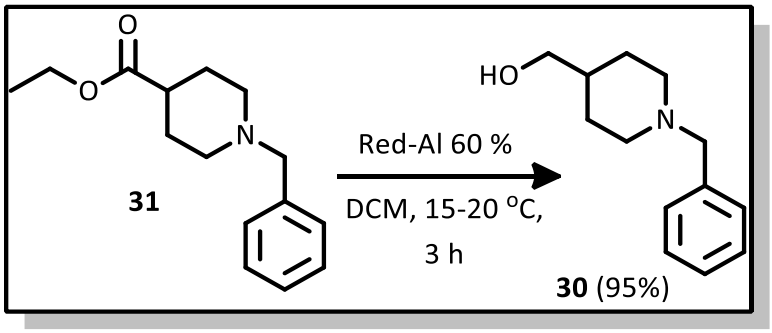

*Scheme 5.3: Reduction of ester **31** to alcohol **30**.*

Alcohol **30** was characterized in the ^{1}H NMR spectrum by the disappearance of the quartet integrating for two protons at 4.10 ppm and a triplet integrating for three protons at 1.22 ppm corresponding to the ethyl group of carboxylate **31**, the appearance of the CH_2 peak adjacent to the alcohol as a doublet integrating for two protons at 3.42 ppm was noted and a broad singlet integrating for one proton at 2.67 ppm corresponded to the alcohol. In the ^{13}C NMR spectrum the disappearance of the carbonyl peak at 175.29 ppm and the ethyl peaks of carboxylate **31** at 60.35 and 14.31 ppm was noted. Additional evidence from the FTIR spectrum clearly showed an alcohol signal at 3326 cm^{-1} and the mass spectrum showed an ion at *m/z* 206.1559 (100 %), with the molecular ion mass requiring 206.1539.

5.2.3 Swern oxidation of alcohol 30 to aldehyde 28[53]

The preparation of 1-benzylpiperidine-4-carbaldehyde (**28**) was the third step and involved a classical Swern oxidation, allowing the selective oxidation of the alcohol to the aldehyde oxidation level (Scheme 5.4).

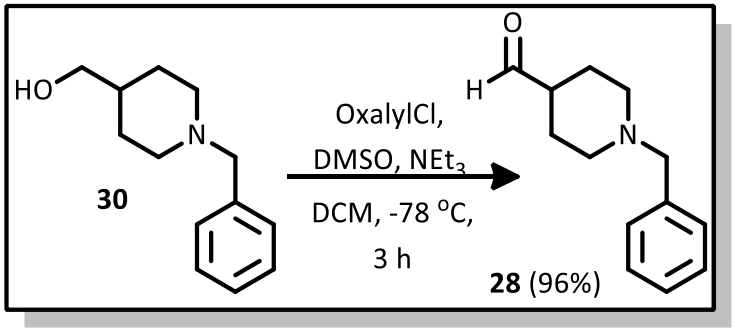

*Scheme 5.4: Swern oxidation of alcohol **30** to prepare aldehyde **28**.*

© University of Pretoria

Mechanistically the reaction proceeds through four *in-situ* intermediates (Scheme 5.5). The first intermediate (A) is formed by the condensation of dimethyl sulfoxide with oxalyl chloride releasing a chloride ion, which subsequently attacks the sulphur group to afford chlorodimethylsulfonium (B) wherein the sulfur atom retains a positive charge. Thereafter, the alcohol group attacks the sulphur displacing the chloride anion to afford intermediate C. Finally, deprotonation of the methyl group followed by a hydrogen shift releases the desired aldehyde **28** and dimethyl sulphide.

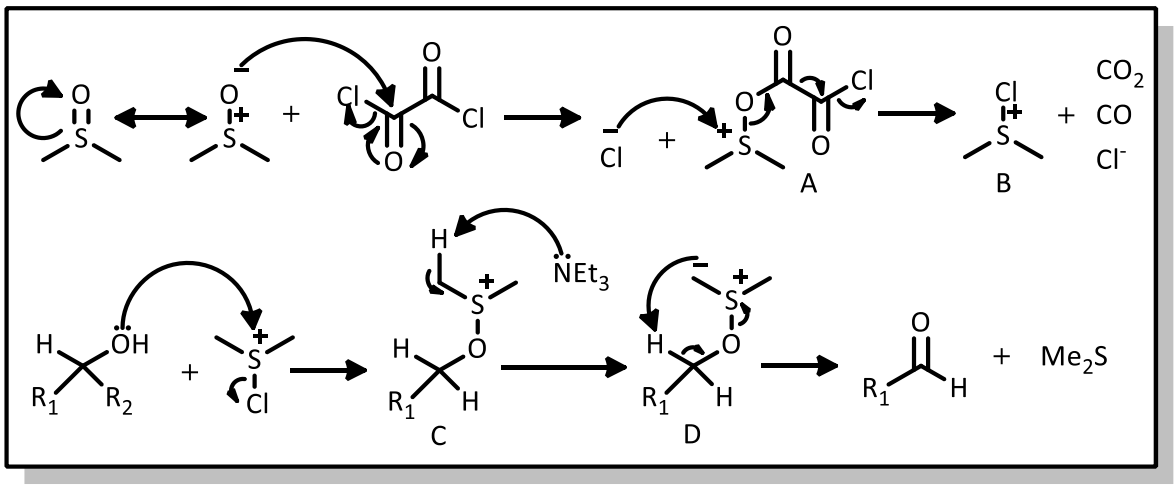

Scheme 5.5: Reaction mechanism of the Swern oxidation, adapted from K.Savin.[108]

The Swern oxidation was performed by pre-cooling oxalyl chloride to -78 °C, followed by slow addition of triethylamine and alcohol **30**. The maintenance of low temperatures and slow addition is critical to limit the formation of localised hotspots in the reaction mixture, which can cause intermediate degradation. An aqueous extractive work up removed unreacted starting material and by-products affording aldehyde **28** in 96 % yield as a clear orange oil, which required no further purification. Aldehyde **28** was characterized in the ^{1}H NMR spectrum by the appearance of the aldehyde proton peak as a singlet at 9.61 ppm integrating for one proton and the disappearance of the CH_2 peak adjacent to the alcohol doublet integrating for two protons at 3.42 ppm and the broad singlet integrating for one proton at 2.67 ppm from the alcohol signal. In the ^{13}C NMR spectrum the appearance of the aldehyde carbonyl peak at 204.10 ppm was noted and additional evidence was seen in the FTIR spectrum with a clear carbonyl (C=O) stretching signal at 1722 cm^{-1} and the aldehyde carbon-hydrogen stretching signal at 2802 cm^{-1}. Finally, the mass spectrum showed an ion at *m/z* 204.1408 (5 %) and at *m/z* 236.1643 (48 %), with the molecular ion requiring 204.1383 and the methanol adduct requiring 236.1645.

© University of Pretoria

5.2.4 Aldol condensation of aldehyde **28** and dimethoxy indanone (**29**) to prepare alkene **27**[53]

(*E*)-2-((1-Benzylpiperidin-4-yl)methylene)-5,6-dimethoxy-2,3-dihydro-1*H*-inden-1-one (**27**) was prepared by the aldol condensation of 5,6-dimethoxy-1-indanone (**29**) with 1-benzylpiperidine-4-carbaldehyde (**28**) (Scheme 5.6). Initially, dimethoxy indanone (**29**) was dissolved in methanol and a saturated sodium hydroxide solution (prepared in a 4:1 methanol/distilled water mix) was added dropwise at 40-45 °C followed by dropwise addition of aldehyde **28** in methanol. A slow addition was important to minimise any self-condensation of the aldehyde. The alkene **27** was precipitated out of the cooled reaction mixture in a 74 % yield as a beige solid, by addition of cold distilled water and no additional purification was required.

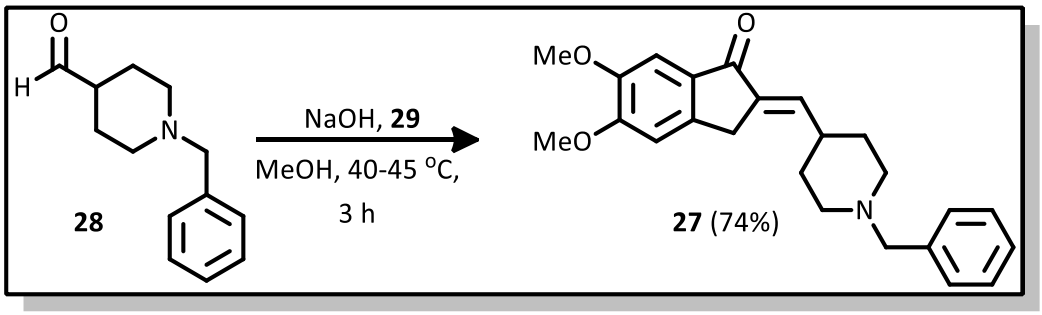

*Scheme 5.6: Aldol condensation of aldehyde **28** and dimethoxy indanone (**29**) to prepare alkene **27**.*

The ^{1}H NMR spectrum showed the presence of an alkene peak as a doublet integrating for two protons at 6.66 ppm and the CH_2 of the dimethoxy indanone (**29**) moved from a doublet at 2.57 ppm to a singlet at 3.58 ppm integrating for two protons. Additionally, the disappearance of the multiplet signal of the α-carbon CH_2 peak of **29** at 2.95 ppm was noted. The *J*-coupling of the alkene peak was 9.7 Hz, indicating an *E* conformation of the double bond. The ^{13}C NMR spectrum showed the alkene carbon peak at 139.90 ppm and in the FTIR spectrum a conjugated carbon double bond (C=C) stretching peak was observed at 1646 cm^{-1} and a *trans* carbon double bond (C=C) bending signal at 980 cm^{-1}. The mass spectrum showed an ion at *m/z* 378.2097 (100 %), with the molecular ion requiring 378.2064. The experimental melting point of 176-177 °C was close to literature values of 171-174 °C.[53]

© University of Pretoria

5.2.5 Reduction of alkene 27 to afford donepezil (3)[53]

5.2.5.1 Approach 1

The first attempt to prepare donepezil (**3**) was through the hydrogenation of alkene **27** (Scheme 5.7). The reaction mixture was prepared by dissolving the alkene (**27)** in tetrahydrofuran under a hydrogen atmosphere and treating with 10 % palladium on carbon for 30 min. Several reductions were performed, unfortunately in all cases ^{1}H NMR analysis showed either no conversion or cleavage of the alkene bond, the latter was evidenced by the observed presence of uncoupled dimethoxy indanone (**29**).

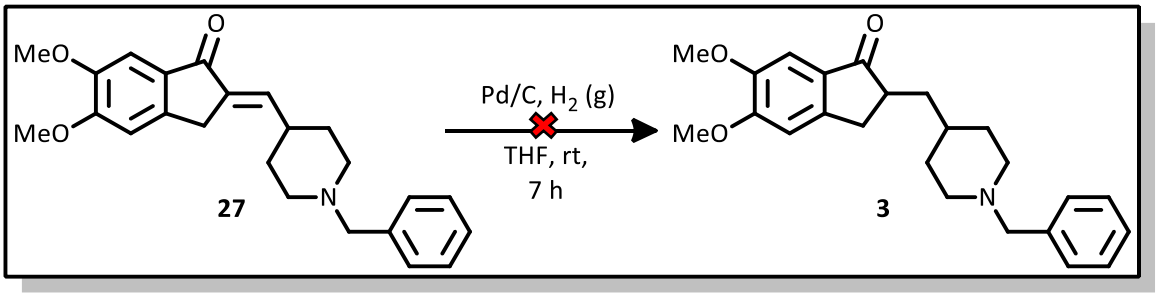

*Scheme 5.7: Hydrogenation of alkene **27** to produce donepezil (**3**).*

Although the envisaged hydrogenation of **27** has been successfully performed in-house, the conversion is plagued with reproducibility issues.[53] It is hypothesised that the issues are arising as the alkene is part of a conjugated system with an aromatic ring which greatly reduces its reactivity.[109] In addition, in past efforts we have noted that one also has to contend with unwanted debenzylation of the benzylated piperidine ring. These difficulties prompted us to explore alternative synthetic routes to afford donepezil (**3**).

5.2.5.2 Approach 2

An alternative synthetic route was envisaged wherein the alcohol group of **30** is converted into a better leaving group (mesyl, tosyl, bromo, chloro) and displaced in a direct substitution with the enolate form of dimethoxy indanone (**29**) (Scheme 5.8). The approach would then allow direct access to donepezil, bypassing both the Swern oxidation and the problematic hydrogenation step, and would further reduce the number of synthetic steps from five to three (not including the activation of the alcohol group).

© University of Pretoria

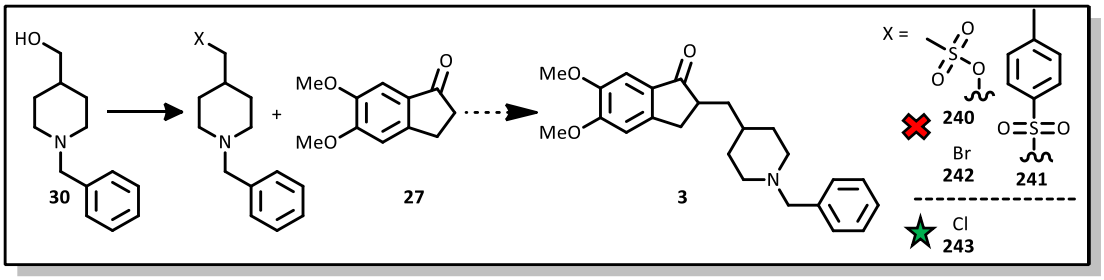

*Scheme 5.8: Alcohol **30** substitution to a better leaving group and the subsequent S_N2 reaction with dimethoxy indanone (**29**) to prepare donepezil (**3**).*

Initially, access to **3** was attempted in a one pot procedure wherein alcohol **30** was mesylated to afford **240** under inert conditions, followed by the addition of **29** in the presence of a bulky non-nucleophilic base potassium *tert*-butoxide. It was elected to use a one-pot approach as mesylates are often unstable and moisture sensitive. Unfortunately, in this instance, no product formation was observed.

The substitution with tosyl chloride to afford **241** involved performing the process under inert conditions in the presence of triethylamine at 0 °C.[110] In this instance the reaction mixture was stirred for 78 hours at room temperature, before being worked up and purified by column chromatography. Unfortunately, NMR analysis of the column fractions did not show the formation of the desired products.

The displacement of the alcohol with a bromide group to prepare **242** was attempted on several occasions with a number of different brominating reagents, including hydrobromic acid and tri-phenyldibromophosphorane. Substitution of alcohol **30** with hydrobromic acid was attempted twice, once with and once without concentrated sulphuric acid. The approach involved dissolving alcohol **30** in 65 % hydrobromic acid, followed by refluxing for several hours. Thereafter, an aqueous work up was performed, however, NMR analysis of the crude material again showed no product formation.
In the tri-phenyldibromophosphorane approach for bromide substitution of alcohol **30**, triphenyl phosphine was used with liquid bromine which was added dropwise to the triphenyl phosphine under inert conditions, followed by stirring for 30 minutes at 0-10 °C.[111] Thereafter, alcohol **30** was added and the reaction mixture was stirred for 12 hours at room temperature, at which time an aqueous work up was performed. Once again NMR analysis of the crude reaction material did not indicate the formation of the desired product.

The substitution of alcohol **30** to form the analogous chloride **243** was successfully achieved with the use of phosphoryl chloride. Phosphoryl chloride is typically used in the presence of a base for the

© University of Pretoria

dehydration of primary alcohols to afford an alkene, however, in the absence of a strong base it allows the formation of alkyl chlorides instead.[112] A solution of alcohol **30** in phosphoryl chloride was stirred for 12 hours at room temperature, after which time the excess phosphoryl chloride was evaporated *in vacuo*.[113] A basic work up was performed with solid sodium bicarbonate. The use of solid sodium bicarbonate was based on the premise that it would not dissolve into the organic solution and as such would limit the formation of the unwanted elimination product. The chloride **243** was obtained in a poor yield of 19 % as a clear oil, however, no further purification was required. The formation of compound **243** was evidence by the disappearance of the CH_2OH carbon peak at 67.64 ppm in the ^{13}C spectrum and the appearance of the CH_2Cl carbon peak at 50.18 ppm.

As the process proved to be low yielding, it was elected to forgo the investigations looking at the displacement of the chlorine of **243** with **29** to prepare **3**. At this point in time, it was felt that further investigation into the preparation of donepezil utilising this approach would not be the most efficient use of time as it was not one of the primary aims of the research. As such, it was elected to use the remaining time to focus on the preparation of silylated analogues of donepezil (**3**) instead.

5.3 Indanone moiety derivatisation

5.3.1 *O*-Silylated scaffolds

The *in-silico* study indicated that the single silylation of the methoxy oxygen at either position 5 and 6 or a double substitution with tethered silanes showed promise and ranked in positions 3-5 out the proposed derivatives. For the synthesis of silicon indanone derivatives, it was elected to demethylate dimethoxy indanone (**29**) and focus on the introduction of bulky silanes on one or both alcohols (Figure 5.2).

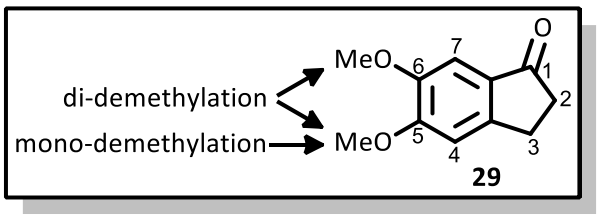

*Figure 5.2: Structure of dimethoxy indanone (**29**) and targeted section for O-silylation.*

As proposed in the *in-silico* studies the *O*-silylation of the alcohols would hopefully retain the important oxygen interactions seen with the methoxy groups in donepezil (**3**) but would potentially introduce additional binding interactions depending on the nature of the silyl groups. The *O*-silylations

© University of Pretoria

were limited to bulky substituents as small groups such as trimethyl silane when bound to oxygen are labile under aqueous conditions and as such were not seen as being suitable as targets.

The *in-silico* investigations identified several *O*-silylated derivatives of the indanone moiety which could be potential hit compounds. These compounds showed comparable or slightly lower scores compared to donepezil (**3**), with additional binding interactions depending on the incorporated silyl groups. As a result, we selected a range of *O*-silylated indanone analogues for synthesis. The *O*-silylated systems were envisaged to be produced following a similar synthetic route to that of donepezil (Scheme 5.9).[53]

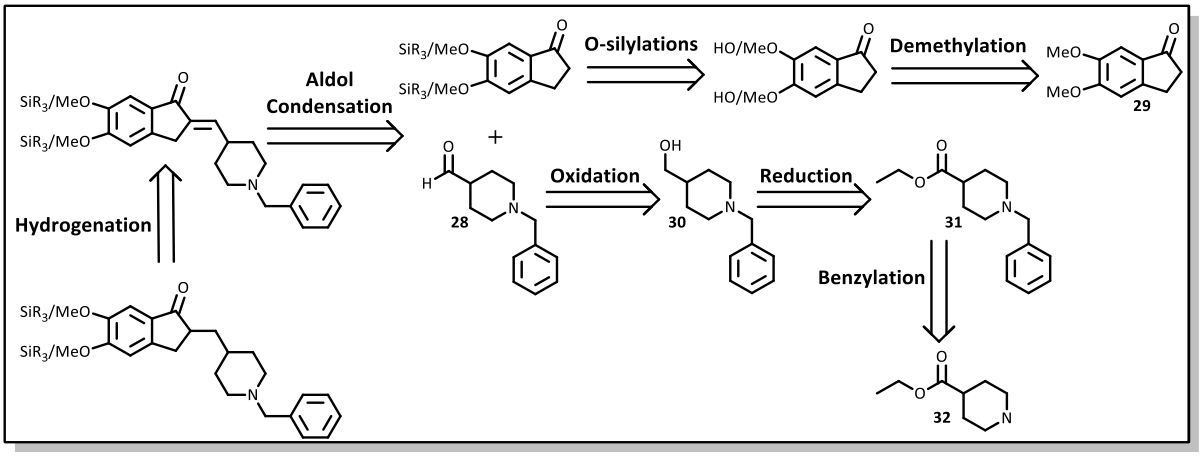

Scheme 5.9: The retrosynthetic route for the silyl protected products.

The approach required additional steps for the preparation of silylated indanone derivatives prior to the aldol coupling with aldehyde **28**. Starting from dimethoxy indanone (**29**), a mono or di-demethylation was envisaged followed by *O*-silylation of the resulting free alcohol(s). Thereafter, the synthetic scheme follows the approach previously described for the synthesis of donepezil (Scheme 5.9).

5.3.1.1 Mono demethylation of dimethoxy indanone[103]

5-Hydroxy-6-methoxy-1-indanone (**244**) was prepared by the demethylation of dimethoxy indanone (**29**) using aluminium trichloride in toluene. The reaction is a Lewis acid process wherein of a lone pair of electrons on the methoxy oxygen are donated to the empty p-orbital of the aluminium in the aluminium trichloride, resulting in a displacement of a chloride ion (Scheme 5.10).

© University of Pretoria

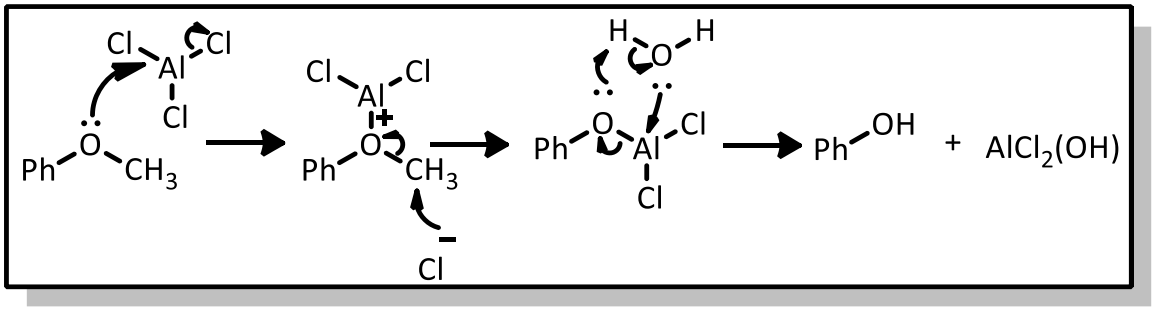

Scheme 5.10: Demethylation mechanism using aluminium trichloride, adapted from B. Arifin, et.al.2015.[114]

The resulting intermediate has a positively charged oxygen atom which pulls more electron density from the carbon weakening the bond, allowing the free chloride ion to attack the carbon ad release a methyl chloride. The oxygen-aluminium chloride intermediate reacts on addition of water to the system, wherein the oxygen from a water molecule attacks the aluminium atom resulting in an phenoxide anion to leave which is subsequently protonated to afford the desired alcohol and aluminium dichloride hydroxide. The aluminium dichloro hydroxide then reacts with two more water molecules to form aluminium (III) hydroxide.[114]

Pietrasik, Szydłowska and Krówczyński demethylated 5,6,7-trimethoxy-1-indanone with aluminium trichloride in toluene by refluxing for 30 minutes, after which time the reaction mixture was then poured into an ice/hydrochloric acid solution and the crude residue was filtered off and crystallised from water.[103] The demethylation of **29** (Scheme 5.11) followed a similar procedure except extended reaction times were used, as well as an aqueous extraction of the toluene fraction. Thereafter, the crude material was purified by column chromatography with pre-basified silica. The mono-demethylated alcohol **244** was obtained in a yield of 35 % as a light brown solid. The dihydroxy derivative **245** was also produced in the reaction, however, with careful control of the reaction time its formation could be minimised.

© University of Pretoria

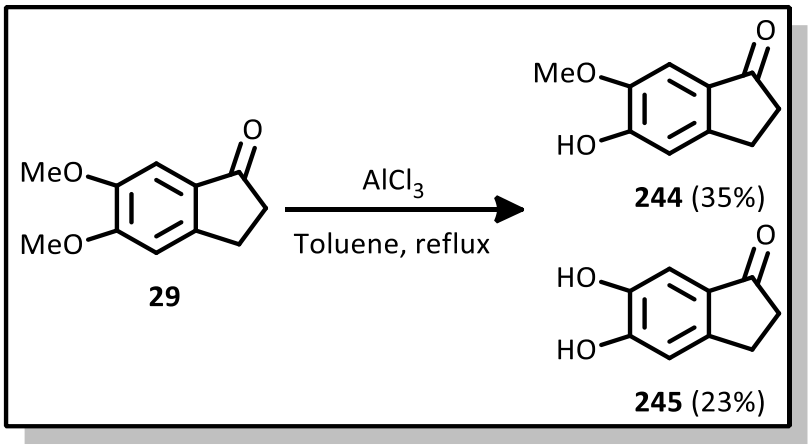

*Scheme 5.11: Mono and di-demethylation of dimethoxy indanone (**29**).*

The ^{1}H NMR spectrum of **244** showed the disappearance of the methoxy group singlet which integrated for three protons at 3.97 ppm, this was also confirmed in the ^{13}C NMR spectrum with the disappearance of the respective carbon peak at 56.37 ppm. Further evidence was provided by the presence of an alcohol stretching and bending frequency at 3043 and 1410 cm^{-1} respectively in the FTIR spectrum, as well as a mass ion in the mass spectrum at *m/z* 179.0733 (100 %), with the molecular ion requiring 179.0703.

Despite several attempts, the yields obtained for this reaction remained consistently low and attempts to increase the yield by employing longer reaction times simply led to an increase in the yield of the dihydroxy derivative **245**. In addition, reaction times of more than 3 hours caused degradation products to become the main constituent of the reaction mixture and after 6 hours no product or starting material was observed. Various reaction times and the associated yields of the mono and di-demethylated products are recorded in Table 5.1.

Table 5.1: Yield of mono and di-demethylated products with the corresponding reaction times.

Yield (%)		Reaction time (hrs)
(**244**)	(**245**)	
25	2	0.5-1
7	7	1.5
35	23	3

© University of Pretoria

The yield of the mono demethylated product also increased, with the exception of 1.5-hours reaction time, which had losses due to challenges faced during the purification of the crude material. These losses where due to the product being retained and decomposing on the silica, which was resolved in subsequent reactions with the use of basified silica.

Interestingly XRD suggests that the mono demethylation was regioselective with demethylation being observed at the 5th position. One should, however, be cognisant of the fact that this is not conclusive evidence as a single crystal was selected for XRD analysis and it is conceivable that there was a mixture of crystals present and the derivative obtained was only the 5-hydroxy-6-methoxy- derivative as seen by XRD (Figure 5.3).

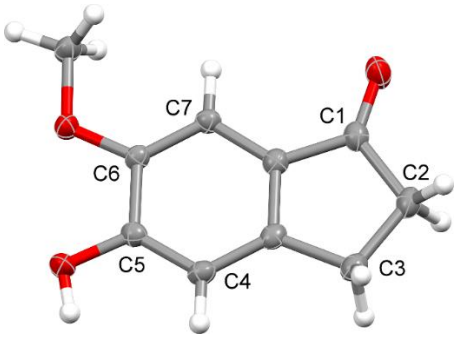

*Figure 5.3: Resolved XRD structure of mono demethylated dimethoxy indanone (**244**).*

That being said, it is not unreasonable to expect this regioselectivity as the methoxy group at the 6th position is arguably more electron deficient and therefore less nucleophilic, than the group at the 5th position due to more extensive resonance delocalisation through both the aromatic ring and the carbonyl group of the indanone ring system**.** Additionally, the acyl group can also decrease the electron density of the methoxy group through electron withdrawing effects.

5.3.1.2 Di-demethylation of the dimethoxyindanone[103]

Dihydroxy compound **245** was prepared by di-demethylation of **29** (Scheme 5.11) like the mono-demethylated product, however, with extended reaction times of two to three hours. An aqueous work up was followed by washing with brine which facilitated the precipitation of the product (**245**) in a yield of 23 % as a brown solid. The dihydroxy compound (**245**) was characterised by ^{1}H NMR spectroscopy, the spectrum of which showed the disappearance of the two methoxy singlet peaks at 3.97 and 3.92 ppm. The corresponding disappearance of the carbon peaks at 56.37 and 56.28 ppm in the ^{13}C NMR spectrum was also noted. Further evidence was the presence of three alcohol peaks at

© University of Pretoria

3413, 3069 and 1461 cm^{-1} in the FTIR spectrum, as well as the mass ion in the mass spectrum at *m/z* 165.0575, with the molecular ion requiring 165.0546.

*5.3.1.3 O-Silylation of mono-hydroxy indanone (**244**)*

The silylation of mono-hydroxy indanone (**244**) was performed under inert conditions at reflux temperatures with *tert*-butyldimethyl(chloro)silane and *tert*-butyldiphenyl(chloro)silane (Scheme 5.12).

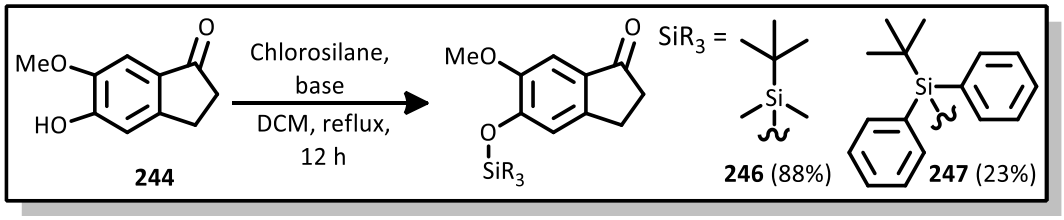

*Scheme 5.12: O-silylation of hydroxyindanone **244**.*

Inert conditions were necessary as halosilanes can readily convert to the respective silanols in the presence of moisture. An aqueous work up was performed, followed by purification using column chromatography with basified silica to afford the desired products.[115]

5-((*tert*-Butyldimethylsilyl)oxy)-6-methoxy-2,3-dihydro-1*H*-inden-1-one (**246**) was obtained in a yield of 88 % as a white solid. Analysis of the ^{1}H NMR spectrum showed the appearance of the dimethyl hydrogens as a singlet peak integrating for six protons at 0.17 ppm and the trimethyl protons also appeared as a singlet peak integrating for nine protons at 0.99 ppm, with the respective carbon peaks at 25.72 and 18.64 ppm being noted in the ^{13}C NMR spectrum. Additionally, the quaternary carbon of the *tert*-butyl group was noted at -4.46 ppm. Further evidence was the silicon methyl signals at 1248, 832 and 779 cm^{-1} in the FTIR Spectrum.[116] Lastly, a mass ion was found at *m/z* at 293.1587 (100 %) with the molecular ion requiring 293.1567.

Structural analogue 5-((*tert*-butyldiphenylsilyl)oxy)-6-methoxy-2,3-dihydro-1*H*-inden-1-one (**247**) was obtained in a yield of 23 % as a white solid when using the same synthetic approach. Analysis of the ^{1}H NMR spectrum showed the appearance of two trimethyl singlet peaks at 1.12 and 1.07 ppm, both integrating for nine protons. Additionally, the silyl aromatic peaks appeared as two multiplets at 7.74 – 7.66 and 7.45 – 7.33 ppm integrating for eight and twelve protons respectively (it is suspected that there was free silane contaminating the sample, causing the increased number of protons integrated

© University of Pretoria

to what was expected). The respective trimethyl carbon peaks were found at 26.69 and 26.65 ppm and the aromatic silyl peaks appeared at 135.34, 134.94, 130.01, 129.79, 127.86 and 127.81 ppm in the ^{13}C NMR spectrum. The increased number of protons of the *O*-silylated group in the ^{1}H NMR spectrum was noted. Additional evidence was provided by the mass ion in the mass spectrum at *m/z* at 417.188 (100 %), with the molecular ion requiring 417.1880.

*5.3.1.4 O-Silylation of dihydroxy indanone (**245**)*

O-silylation of (**245**) followed the same procedure as utilised for the mono-silylation reactions, but in this instance, double the number of equivalents of the silane was used and the reaction mixture was stirred for an extended period of time for 24 hours at high temperatures as it was expected that the reaction would be hindered by the substitution of two sterically bulky silanes (Scheme 5.13).

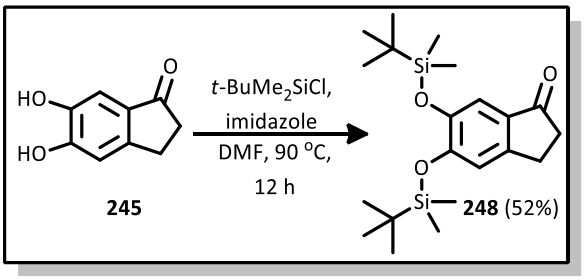

*Scheme 5.13: Di-O-silylation of dihydroxyindanone (**245**).*

Disilylated compound (**248**) was obtained in a yield of 52 %, as an off-white solid. The appearance of two singlet peaks both integrating for nine protons each at 0.99 and 0.98 ppm corresponded to the two *tert*-butyl groups and an additional two singlet peaks both integrating for six protons each at 0.25 and 0.21 ppm corresponded to the two dimethyl groups in the ^{1}H NMR spectrum (Figure 5.4). The corresponding trimethyl carbon peaks appeared at 26.03 and 25.99 ppm and the respective carbon peaks for the dimethyl carbons appeared at 18.70 and 18.59 ppm within the ^{13}C NMR spectrum. In addition, the quaternary silyl carbon peaks were noted at -3.88 and -4.00 ppm. Further evidence was given in the FTIR spectrum with three silicon methyl signals at 1252, 834 and 779 cm^{-1}.[116] Finally, a mass ion peak was found in the mass spectrum at *m/z* 393.228 (100 %), with the molecular ion requiring 393.2276.

© University of Pretoria

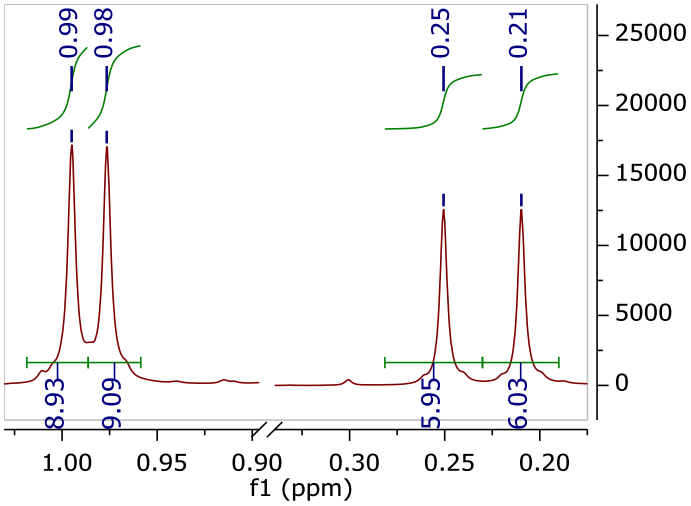

*Figure 5.4: ^{1}H NMR spectrum of the dimethyl and trimethyl groups of the two O-silyl groups of **248**.*

*5.3.1.5 Aldol condensation of aldehyde **28** and silyl protected indanone **246***[53]

The preparation of the *O*-silylated alkene **249** was attempted by the aldol condensation of **246** and **28** and followed a similar approach to that described in Section 5.2.4 (Scheme 5.14). Once the reaction was deemed complete, the reaction mixture was cooled to room temperature to facilitate the precipitation of the product, however, in this instance no precipitate was observed. The crude material was instead purified using column chromatography, with basified silica to prevent removal of the silyl group.[115] Unfortunately, NMR analysis of the column fractions showed no product formation and instead only desilylated indanone was observed.

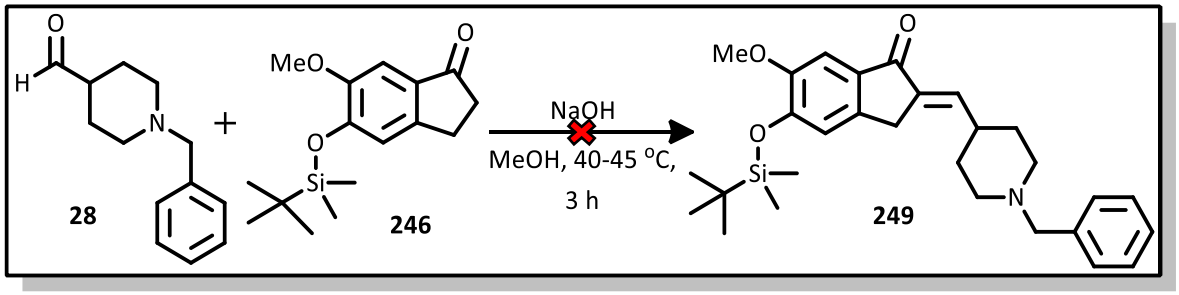

*Scheme 5.14: Aldol coupling of O-silylated indanone **246** and aldehyde **28**.*

The methoxide or hydroxide ions formed *in situ* in the deprotonation reaction may have caused the de-silylation of the indanone, forming **244** and *tert*-butyldiphenylsilanol. This was unexpected as bulky *O*-silyl groups are typically base stable. The methoxide or hydroxide may have been small enough to allow nucleophilic attack on the hindered electrophilic silicon, causing the de-silylation of the indanone. Unfortunately, in subsequent investigations, the de-silylation appeared to be preferred and

© University of Pretoria

attempts to circumvent this by demethylating the alkene **27** and silylating after the aldol condensation did not meet with success (Section 6.3.2.1.7).

5.3.2 *C*-Silylated scaffolds

Donepezil analogues with *C*-silylations at positions 5 and 6 on the indanone moiety had similar binding poses and interactions to donepezil (**3**), but with poorer docking scores, as shown in the *in-silico* study. *C*-silylation at position 5 and 6 on the indanone was found to have additional interactions with the binding site depending on the incorporated silyl group. The *in-silico* study showed that aromatic silyl groups with aromatic systems on a flexible linker had additional pi-pi stacking interactions with amino acid residues outside the binding pocket (Section 4.9.1.2.2 and 4.9.1.2.3). These interactions are unique and as such it was elected to prepare *C*-silylated indanone donepezil analogues for further evaluation (Figure 5.5). Additionally, carbon silicon bonds are more stable than the silicon oxygen bond allowing the use of small non-bulky silicon groups in addition to large bulky silicon groups.

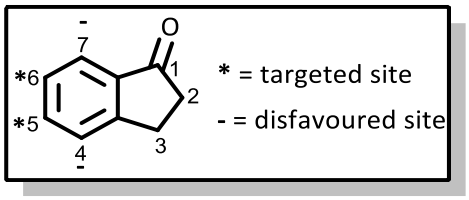

Figure 5.5: Structure of the 1-indanone and the targeted and unfavoured sites for C-silylation.

Synthesis of the *C*-silylated analogues was anticipated to follow a similar synthetic scheme as that employed in the preparation of donepezil (**3**), with additional steps required for the preparation of the *C*-silylated indanone moieties (Scheme 5.15). The *C*-silylated indanone moieties were planned to be accessed through the lithium halogen exchange reaction from the respective halogenated indanone.

© University of Pretoria

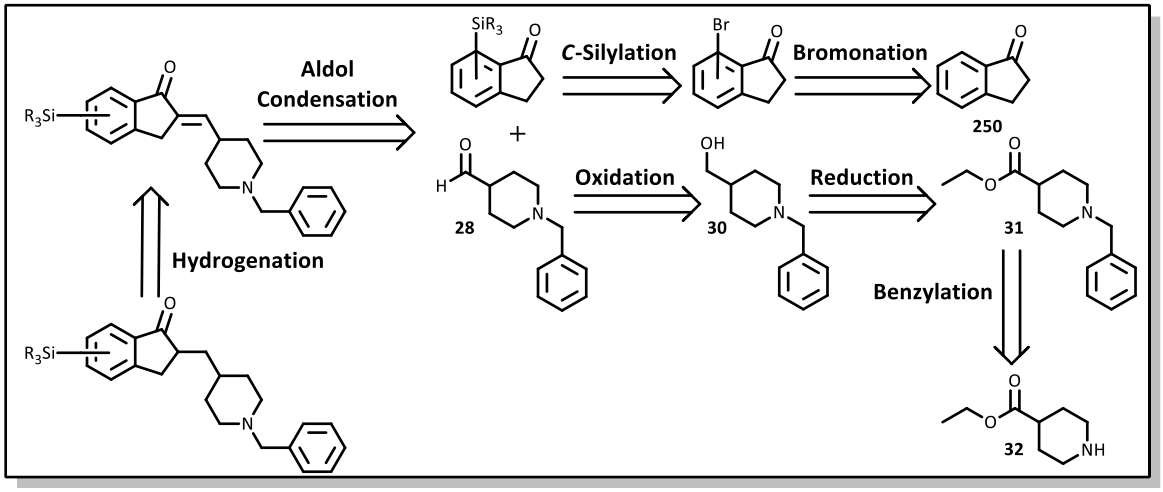

Scheme 5.15: The retrosynthetic route for the carbon-silicon bonded products.

*5.3.2.1 Bromination of 1-indanone (**251**)*[104]

Bromoindanone (**251**) was prepared from 1-indanone (**250**) using liquid bromine and aluminium trichloride as described by Gómez and co-workers (Scheme 5.16). Liquid bromine was added to **250** at 110 °C and was stirred for 30 minutes, after which time an aqueous work up was performed and the crude material was purified using column chromatography. A mixture of brominated products formed and separation was challenging as co-elution was observed in several of the column fractions. 6-Bromoindanone (**251**) was isolated from the mix as a red brown solid in a yield of 20 %.

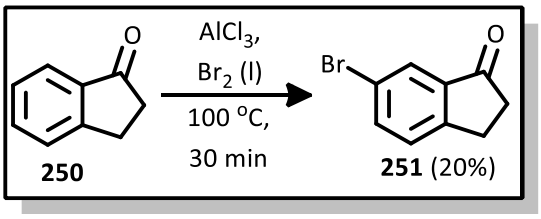

*Scheme 5.16: Bromination of 1-indanone (**250**).*

The characteristic aromatic C-H splitting pattern of doublet (7.75 ppm), triplet (7.58 ppm), doublet (7.48 ppm) and triplet (7.36 ppm) in the ^{1}H NMR spectrum was replaced with the appearance of a singlet (7.87 ppm), doublet (7.68 ppm) and doublet (7.36 ppm) splitting pattern confirming the replacement of the hydrogen at position 6. In addition, the migration of two protons signals downfield due to de-shielding of electrons of the protons adjacent to the bromine was observed, as well as the disappearance of the triplet proton signal at 7.58 ppm gave further evidence of the bromination at position 6. In the ^{13}C NMR spectrum the disappearance of the corresponding aromatic C-H carbon at

© University of Pretoria

123.83 ppm and the appearance of a 3rd aromatic quaternary carbon at 121.70 ppm was noted. Furthermore, a C-Br stretching signal was observed at 661 cm^{-1} in the FTIR spectrum.

5.3.2.2 C-silylation of bromoindanone[105]

C-Silylation of the bromo indanone was planned to utilise an organometallic exchange. Lithium halogen exchange was elected as opposed to a Grignard reaction as in the latter case, the main product would be the self-condensation product arising from condensation at the indanone carbonyl. Lithium halogen exchange was thought to allow for the lithiated product to be able to react with the desired silane and limit self-condensation of the indanone by nucleophilic attack of the carbonyl.

The preparation of 6-(trimethylsilyl)-2,3-dihydro-1*H*-inden-1-one (**252**) was attempted from **251** using lithium halogen exchange adapting a protocol reported by Mason and colleagues, who performed the lithiation reaction at sub-zero temperatures (Scheme 5.17).[105] A solution of 1.6 M *n*-butyl lithium solution was added to a solution of **251**, inert conditions were employed as *n*-butyl lithium is moisture sensitive. After full addition of *n*-butyl lithium the reaction mixture was stirred for 1 hour at -78 °C to facilitate the quantitative formation of the lithiated intermediate, after which time chlorotrimethylsilane was added at -78 °C. An aqueous work up was performed, and the crude residue was purified using column chromatography, however, NMR analysis of the column fractions did not indicate the formation of the desired product.

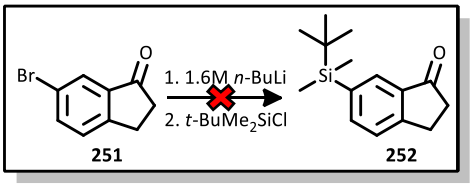

*Scheme 5.17: C-silylation of 6-bromoindanone (**252**).*

A second approach was followed wherein the reaction solution was left to warm up to room temperature after the addition of the halosilane as reported by Ngo and Lin.[117] The heating was to provide additional energy for the lithiated intermediate to attack the halosilane. Unfortunately, NMR analysis of the crude material again showed no product formation.

Despite several attempts we were unable to directly silylate the indanone ring. We hypothesised that the lithium halogen exchange may not be suitable for the indanone system, as potential interference interactions with the carbonyl may be preventing the lithiated intermediate from forming.

© University of Pretoria

5.3.3 Conclusion

The preparation of the *O*-silylated indanone analogues was partially successful in reference to the original synthetic plan, as the demethylation of the indanone methoxy groups and subsequent *O*-silylation was achieved. Challenges with the aldol coupling reaction between aldehyde **28** and the *O*-silylated indanone were experienced and access to the final compounds was therefore not achieved. Access to the *C*-silylated analogues had challenges early in the synthetic plan as the carbonyl is suspected to cause interference during the lithium halogen exchange reaction which prevented preparation of the *C*-silylated indanone derivatives. The aldol coupling of the *C*-silylated indanone analogues could therefore not be attempted.

5.4 Benzyl moiety derivatization

Investigation of the *C*-silylation of the benzyl ring in the *in-silico* study indicated that the *C*-silylated benzyl derivatives had a reversed binding mode to donepezil (**3**) (Section 4.9.5). This implied that the indanone moiety would bind to the catalytic site (CAS) and the benzyl group to the peripheral anionic site (PAS), with the substituted silyl groups within or projecting out of the binding pocket entrance. These structures were investigated at a 1 Å level of flexibility within the MM-GBSA calculation and were assigned similar scores as donepezil (1 Å) by the model. These analogues (*ortho*, *meta* and *para* substitutions) were elected for preparation due to comparable binding scores to donepezil (**3**) and further investigation of the reverse binding mode and its potential effect in enzyme binding to AChE. The ortho and para analogues were investigated first as the starting materials were readily available and development of the meta analogues were to follow if synthesis of the ortho and para analogues proved successful (Figure 5.6).

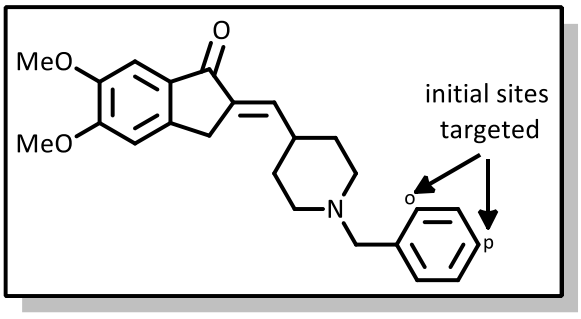

*Figure 5.6: Structure of alkene **27** with illustration of intended targeted sites for C-silylation of the benzyl group.*

© University of Pretoria

5.4.1 Donepezil synthesis route[53]

The benzyl moiety derivatives were planned to synthetically follow the same synthetic approach as donepezil (**3**), except halo benzyl derivatives would be used with an additional step for *C*-silylation of the benzyl group (Scheme 5.18).

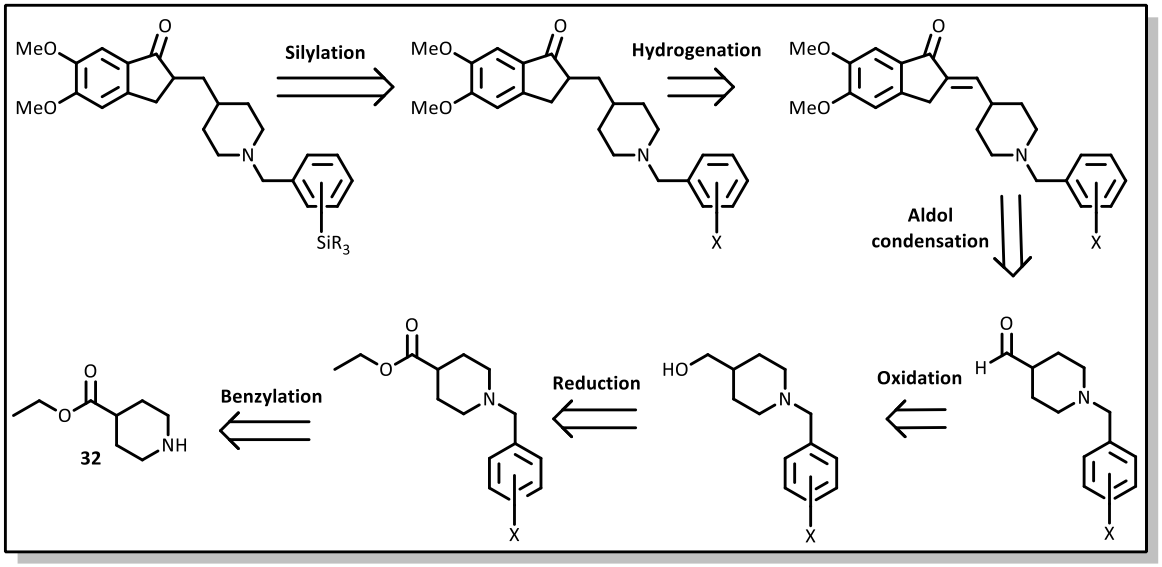

Scheme 5.18: The retrosynthetic route for the silyl derivative in the benzyl moiety.

Incorporation of the *C*-Silyl group at the alkene level was planned, as challenges with the hydrogenation step were encountered during the model study and the alkene derivatives were also of interest. For *C*-silylation of the of benzyl moiety we planned to use lithium halogen exchange to form the final products, as the Grignard reaction intermediate was as noted before expected to attack the carbonyl of the indanone.

5.4.1.1 Benzylation of ethyl isonipecotate with halobenzyl groups[53]

Ethyl 1-(2-chlorobenzyl)piperidine-4-carboxylate (**261**) was prepared by the benzylation of **32** with 2-chlorobenzyl chloride (**259**) and followed the same procedure used for 5.2.1 (Scheme 5.19) affording **261** as a light yellow oil. A near quantitative yield was obtained, however, trapped residual solvents were noted within the product oil.

© University of Pretoria

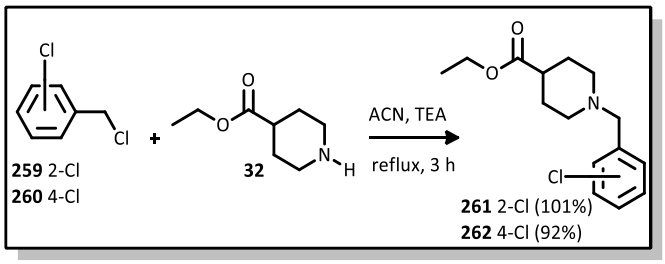

*Scheme 5.19: Benzylation of ethyl isonipecotate (**32**) with chlorobenzyl chlorides.*

Compound **261** was characterized by the appearance of the benzyl aromatic peaks as two set of doublets at 7.48 and 7.32 ppm and two sets of triplets at 7.21 and 7.16 ppm all integrating for one proton each in the ^{1}H NMR spectrum. The respective aromatic carbon signals were noted at 134.24, 130.59, 129.44, 128.07 and 126.69 ppm in the ^{13}C NMR spectrum. Further evidence was given by a carbon-nitrogen stretching frequency at 1259 cm^{-1} in the FTIR spectrum, as well as a mass ion at *m/z* 282.127 (100 %) in the mass spectrum, with the molecular ion requiring 282.1255.

Structural analogue ethyl 1-(4-chlorobenzyl)piperidine-4-carboxylate (**262**) was prepared using the same procedure described in Section 5.2.1, but using 4-chlorobenzyl chloride (**260**) instead of the analogues *ortho*-system (Scheme 5.19). The highest yield obtained for this step was 92 % affording **262** as a light-yellow oil. The appearance of a multiplet at 7.33 – 7.19 ppm that integrated for four protons correlated to the chlorobenzyl group of **262** in the ^{1}H NMR spectrum. In the ^{13}C NMR spectrum two carbon signals at 132.74, 130.38 and 128.44 ppm were noted and corresponded to the four sp^{2} carbons of the benzyl ring, as the carbons opposite each other within the ring would be equivalent due to symmetry. Further evidence was given by a carbon-nitrogen stretching frequency at 1259 cm^{-1} in the FTIR spectrum, as well as a mass ion at *m/z* 282.127 (100 %) in the mass spectrum showed, with the molecular ion requiring 282.1255.

*5.4.1.2 Reduction of esters **261** and **262** to alcohols **263** and **264***[53]

Preparation of both ethyl (1-(2-chlorobenzyl)piperidin-4-yl)methanol (**263**) and (1-(4-chlorobenzyl)piperidin-4-yl)methanol (**264**) followed a similar procedure as the reduction of **261** and **262** using sodium bis(2-methoxyethoxy)aluminium hydride (Red-Al) (Scheme 5.20).

© University of Pretoria

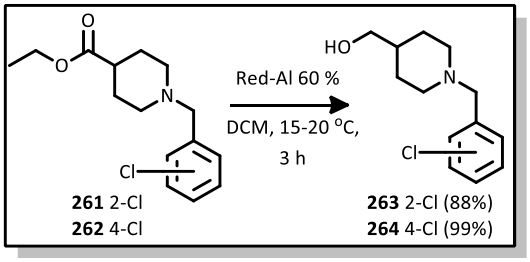

*Scheme 5.20: Reduction of esters **261** and **262** to alcohols **263** and **264** using Red-Al.*

The highest yield obtained for **263** was 88 %, it was recovered as a clear oil and was characterized by the disappearance of the quartet integrating for two protons at 4.12 ppm and the triplet integrating for three protons at 1.24 ppm which corresponded to the ethyl group in **261**. Additionally, the appearance of the doublet peak integrating for two protons at 3.48 ppm corresponded to the CH_2 protons adjacent to the alcohol and the appearance of the alcohol peak at 1.85 ppm as a broad singlet integrating for one proton in ^{1}H NMR spectrum was noted. The disappearance of the carbonyl peak at 175.34 ppm and the respective ethyl carbon peaks at 60.37 and 14.34 ppm in the ^{13}C NMR spectrum was further evidence. Lastly, an alcohol O-H stretching signal at 3330 cm^{-1} in the FTIR spectrum was noted, as well as a mass ion at *m/z* 240.117 (100 %) in the mass spectrum, with the molecular ion requiring 240.1150.

Alcohol **264** was obtained as a clear oil in a yield of 99 %. In a similar fashion to that described above **264** was also characterised by the disappearance of the ethyl peaks of **262** at 4.13 ppm (quartet integrating for two protons) and at 1.25 ppm (triplet integrating for three protons) in the ^{1}H NMR spectrum. The appearance of the CH_2 peak adjacent to the alcohol at 3.45 ppm integrating for two protons and an alcohol signal at 2.77 ppm as a broad singlet integrating for one proton in the ^{1}H NMR spectrum was noted. The disappearance of the ethyl carbon peaks of **262** at 60.39 and 14.33 ppm, as well as the carbonyl peak at 175.28 ppm was seen in the ^{13}C NMR spectrum. Additional evidence in the FTIR spectrum was an alcohol O-H stretching signal at 3333 cm^{-1} and in the mass spectrum a mass ion at *m/z* 240.116 (100 %) was noted, with the molecular ion requiring 240.1150.

*5.4.1.3 Swern oxidation of alcohols **263** and **264** to aldehydes **265** and **266***[53]

Preparation of the chlorobenzyl aldehydes **265** and **266** was also performed utilising the same Swern oxidation procedure noted in Section 5.2.3 (Scheme 5.21).

© University of Pretoria

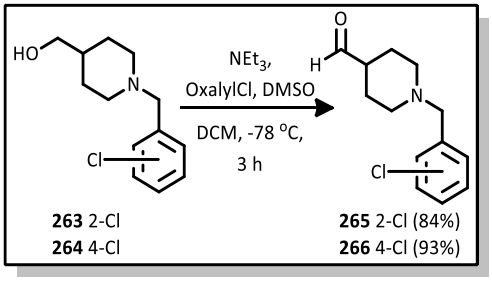

*Scheme 5.21: Reaction scheme of Swern oxidation of alcohols **263** and **264** to aldehydes **265** and **266**.*

The highest yield obtained for **265** was 84 % as an orange oil and was characterized by the appearance of the aldehyde proton peak at 9.65 ppm as a singlet integrating for one proton, as well as the disappearance of a doublet integrating for two protons at 3.48 ppm which was from the CH_2 proton peak adjacent to the alcohol. In addition, the broad singlet integrating for one proton corresponding to the alcohol at 2.08 ppm of **263** in the ^{1}H NMR spectrum disappeared as well. The corresponding carbonyl carbon peak at 204.08 ppm in the ^{13}C NMR spectrum was noted. Additional evidence in the FTIR spectrum was the aldehydes carbon hydrogen (HC=OCR) and carbonyl (C=O) signals at 2804 and 1722 cm^{-1} respectively. Lastly, the mass spectrum showed mass ions at *m/z* 238.100 (3 %), and at *m/z* 270.127 (100 %), with the molecular ion requiring 238.0993 and the methanol adduct requiring 270.1255.

Aldehyde **266** was prepared in a yield of 93 % as an orange oil. The appearance of a singlet proton peak integrating for one proton at 9.66 ppm corresponded to the formation of the aldehyde and the disappearance of the CH_2 peak and peaks seen at 3.45 and 2.77 ppm for alcohol **264** in the ^{1}H NMR spectrum was noted. The aldehyde's carbonyl carbon peak was observed at 203.91 ppm in the ^{13}C NMR spectrum. Additionally, an aldehyde hydrogen (HC=O) and carbonyl (C=O) signals at 2805 and 1722 cm^{-1} respectively were noted in the FTIR spectrum. Lastly, two mass ions in the mass spectrum were observed at *m/z* 238.101 (2 %) and at *m/z* 270.126 (98 %), with the molecular ion requiring 238.0993 and the methanol adduct requiring 270.1255.

*5.4.1.4 Aldol condensation of aldehydes **265** and **266** with dimethoxy indanone (**29**) to prepare alkenes **267** and **268***[53]

(*E*)-2-((1-(2-Chlorobenzyl)piperidin-4-yl)methylene)-5,6-dimethoxy-2,3-dihydro-1*H*-inden-1-one (**267**) and (*E*)-2-((1-(4-chlorobenzyl)piperidin-4-yl)methylene)-5,6-dimethoxy-2,3-dihydro-1*H*-inden-1-one (**268**) were prepared by the aldol condensation of **29** with **265** and **266** respectively and followed the same procedure used to prepare **27**, see Section 5.1.4 (Scheme 5.22). Unfortunately, in the case of

© University of Pretoria

267 no product precipitated out of solution and further purification of the crude material did not yield any product.

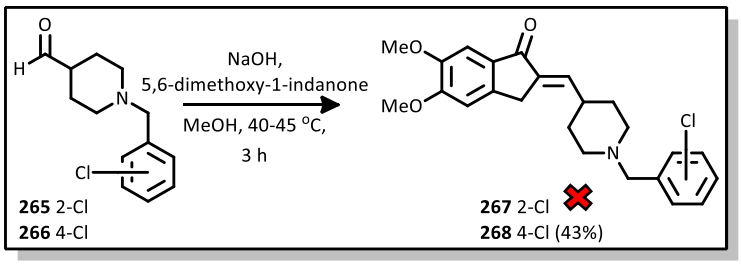

*Scheme 5.22: Aldol condensation of aldehydes **265** and **266** and dimethoxy indanone (**29**) to prepare alkenes **267** and **268**.*

Preparation of **268** was achieved in a yield of 43 % with the product afforded as an off white solid. The material was characterised by the presence of an alkene peak at 6.66 ppm as a doublet integrating for one proton in the ^{1}H NMR spectrum. Additionally, the appearance of a singlet proton signal at 3.59 ppm was noted which integrated for two protons and corresponded to the CH_2 group adjacent to the alkene, previously a multiplet at 2.57 ppm integrating for two protons was noted for the starting material **29**. The *J*-coupling for the alkene is 9.6 Hz which is typical of an *E* conformation. The appearance of the alkene peak at 139.84 ppm in the ^{13}C NMR spectrum, as well as a conjugated C=C and *trans* C=C signals at 1643 and 979 cm^{-1} in the FTIR spectrum was further evidence of **268**. Lastly, a mass ion at *m/z* 412.172 (100 %) in the mass spectrum was noted, with the molecular ion requiring 412.1674.

*5.4.1.5 C-Silylation of alkene **268***[105]

Derivatisaton of *C*-silylated **268** to prepare **269** and **270** followed a similar lithium halogen exchange procedure as that described in Section 5.3.2.2, where the reaction mixture was slowly heated to room temperature after addition of the chlorosilane (Scheme 5.23). It was anticipated that the benzyl aromatic ring would be more conductive to lithium than the indanone ring system which previously had proven challenging. In this instance the *C*-silylation of **268** was attempted twice with two different chlorosilanes and unfortunately, NMR analysis of the crude material from both reactions did not show the formation of the desired product.

© University of Pretoria

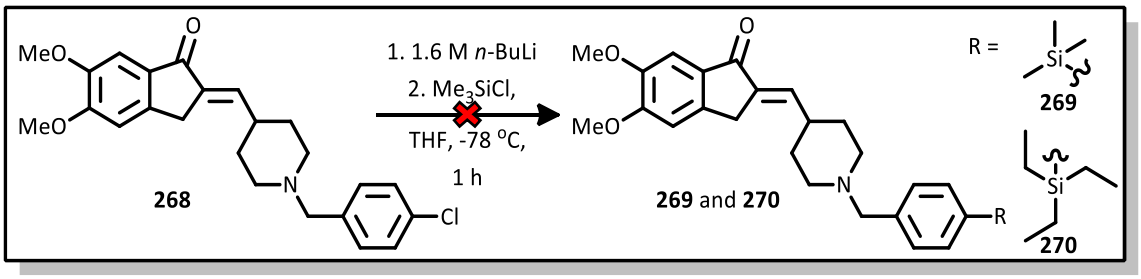

*Scheme 5.23: C-silylation of alkene **268**.*

Interestingly the alkene peak was observed more upfield at 4.41 ppm, rather than at 6.66 ppm for **268** in the ^{1}H NMR spectrum. The electron density of the alkene was increased and its peaks pushed upfield in the ^{1}H NMR spectrum, which suggests that the lithium ion may have formed a complex with the carbonyl and alkene, preventing the lithium halogen exchange reaction.

5.4.2 *C*-Silylation of halo-toluenes

The alkene and carbonyl of the indanone moiety was suspected to have formed a stable complex with the lithium ion of the *n*-butyl lithium reagent, preventing the lithium halogen exchange reaction. Introduction of the silyl groups before the benzylation step was then attempted as interference of the other functional groups would not be present. The approach would allow the use of either a lithium halogen exchange or a Grignard synthetic route. In the latter case it would have to start from the toluene and not the benzyl chloride to prevent self-condensation. Thereafter, the *C*-silylated chlorobenzyl analogues could be accessed by the halogenation of the methyl group, followed by the benzylation of **32** and thereafter the general approach used in the preparation of donepezil (**3**) (Scheme 5.24).

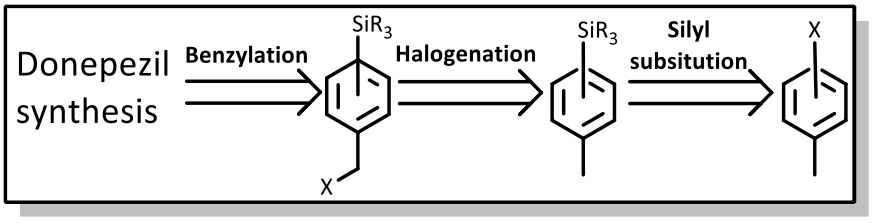

Scheme 5.24: Retrosynthesis of the silicon derivatise benzyl intermediates.

© University of Pretoria

5.4.2.1 Approach 1

The first approach to the *C*-silylation of the halotoluene derivatives was attempted using the lithium halogen exchange following the modified procedure used by Masson and colleagues.[105] The *C*-silyl substitution of chlorosilane **272** was attempted with 4-chlorotoluene (**271**) and *n*-butyl lithium under inert conditions (Scheme 5.25).[105] The reaction procedure used required no heating of the reaction solution after the addition of the halo silane.

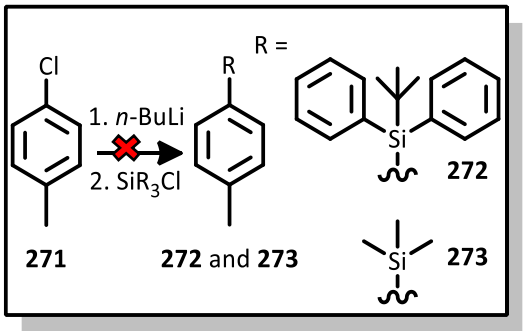

*Scheme 5.25: C-silylation of **271**.*

Post reaction, NMR analysis of the crude material in the ^{13}C NMR spectrum showed that the silanol had formed instead of the desired product. The second attempt was similar to the first attempt except that the reaction solution was heated to room temperature and left to stir for six hours, before the reaction solution was worked up, as described by Ngo and Lin.[117] The reaction solution was worked up with a saturated ammonium chloride solution to prevent hydroxide formation.[118] Again, the NMR analysis of the crude material indicated no product or silanol formation. The third attempt followed the same procedure as the second attempt, except the reaction was done in freshly distilled diethyl ether, once again, NMR analysis of the crude material did not indicate the desired product.[118]

5.4.2.2 Approach 2

The second approach utilised the Grignard reaction as it was considered robust chemistry to access the *C*-silylated toluene analogue **273** (Scheme 5.25). The first attempt used 4-chlorotoluene and magnesium metal under inert conditions and was stirred for 6 hours at room temperature to allow quantitative formation of the Grignard intermediate. The chlorosilane was then added to the solution and the reaction mixture was stirred for 12 hours at room temperature, followed by an aqueous work up. Unfortunately, NMR analysis of the crude material did not show the desired product. The second attempt followed a similar procedure to the first, except all the reagents were added at the same time

© University of Pretoria

and the reaction mixture was refluxed for 12 hours under inert conditions as previously reported by Sleevi and co-workers.[119] The reaction mixture was worked up, but NMR analysis of the crude material indicated no product formation.

5.4.3 Conclusion

Access to the *C*-silylated benzyl analogues was partially successful as access to the originally planned haloalkene derivative **268** was achieved. However, *C*-silylation of **268** was problematic as the alkene and carbonyl of the indanone moiety were suspected to interfere in the lithium halogen exchange reaction as seen by the alkene doublet proton signal shift upfield in the ^{1}H NMR spectrum. The alternative route to access the *C*-silylated benzyl analogues was unsuccessful as the desired products could not be obtained from either the lithium halogen exchange or the Grignard reaction.

5.5 Acetophenone replacement of the indanone moiety

Acetophenone was investigated as a potential alternative to the indanone moiety, as the electronic system of the indanone moiety has in the past proven difficult to work with.[53] The acetophenone was considered as it has one carbon less than the indanone moiety, which releases the α carbon from a planar orientation making it more accessible. Investigation of the acetophenone replacement in the *in-silico* study identified the β-keto and ether linker analogues as the top two scoring systems, which had better or equivalent binding scores to donepezil (**3**) (section 4.9.6).

5.5.1 Acetophenone analogues of donepezil

The first acetophenone analogues targeted involved the replacement of the indanone moiety with the alkene and alkane linker, following the same synthetic route as donepezil (**3**) in Scheme 5.1. If successful available hydroxy acetophenone derivatives would be utilised to provide the aromatic alcohol for varying *O*-silylations.

© University of Pretoria

*5.5.1.1 Aldol condensation of acetophenone and aldehyde **28** to prepare alkene **274***[53]

Preparation of alkene **274** was attempted following the same protocol in Section 5.2.4 (Scheme 5.26), however, no precipitate was observed. An aqueous workup was then performed on the crude material, unfortunately, NMR analysis of the crude material did not indicate the formation of the desired product. The acetophenone had no electron donating groups on the aromatic ring as is the case with the indanone moiety, which may be required for enough election density to be moved to the carbonyl for effective enolate formation.

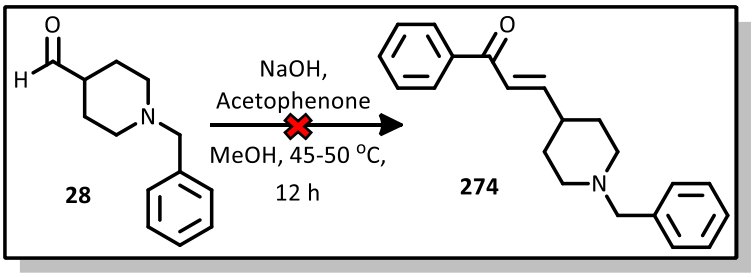

*Scheme 5.26: Aldol condensation of acetophenone and aldehyde **28** to prepare alkene **274**.*

*5.5.1.2 Chloride **243** substitution with acetophenone **275** to prepare alkane **276***

The preparation of coupled scaffold **276** was attempted by enolising **275** and then effecting an S_N2 displacement of the chloro group in **243** (Scheme 5.27). The reaction was performed under inert conditions to prevent moisture forming hydroxide ions, which would react with **243** forming alcohol **30** as an unwanted side product. Potassium carbonate was used as it is a weak base and should not attack the alkyl chloride. Post reaction an aqueous extraction was performed, unfortunately, NMR analysis of the crude material indicated no product formation.

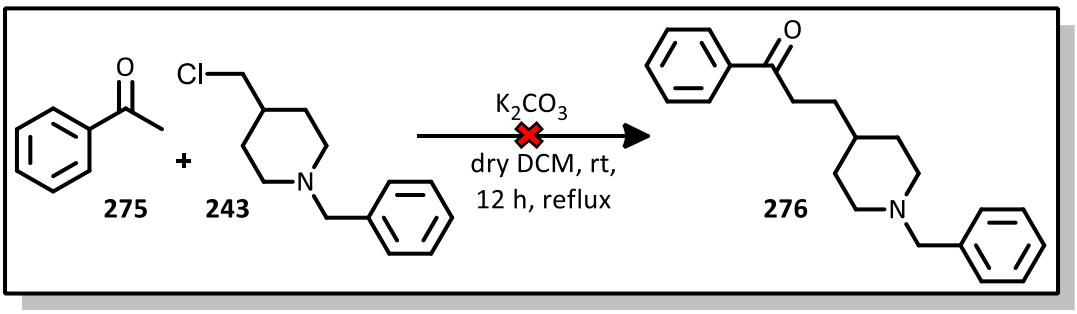

*Scheme 5.27: Alcohol **30** substitution with acetophenone **275**.*

© University of Pretoria

5.5.2 β-Diketo linkage

The β-diketo linker system had the second highest binding energy of all the theoretical scaffolds (Section 4.9.6.1). The high binding energy was attributed to additional hydrogen bonding interactions with the di- carbonyls, as well as additional pi-pi interactions with the piperidine nitrogen with several amino acid residues within the binding pocket. Preparation of the β-diketo linker analogues was elected for further study to evaluate the potential benefits of the predicted binding interactions of the ligand with AChE.

The β-diketo linker system was to be formed from a Claisen condensation of the silyl protected hydroxy acetophenone and **31** (Scheme 5.28).

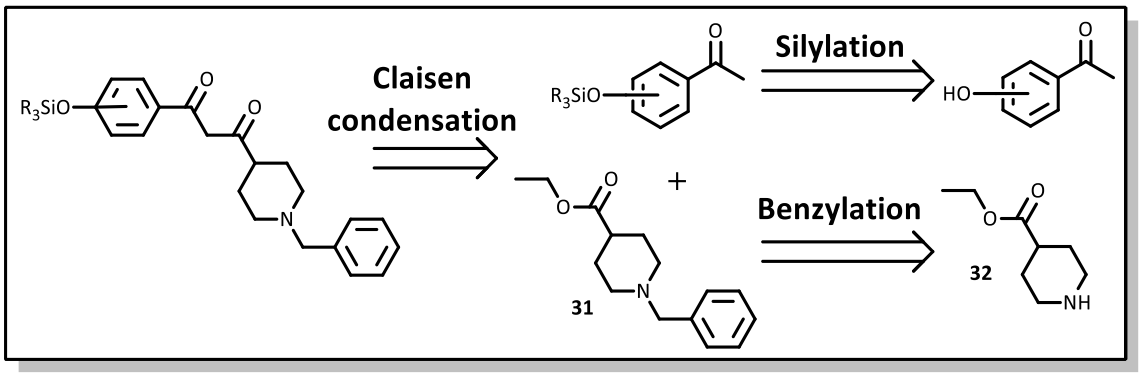

Scheme 5.28: The retrosynthetic route of the β-diketo-linkage system.

The hydroxyacetophenone was protected with a bulky silane and **31** was formed by benzylation of **32** with **33**. The acetophenone could be protected in bulk with a selected silane and after the Claisen condensation could be deprotected with *tert*-butyl ammonium fluoride and then *O*-silylation of the free alcohol with the desired silyl groups could be performed. Bulky silyl groups were used as they are base stable and the Claisen condensation requires basic conditions in order to form the β-diketo linker.

*5.5.2.1 O-Silylation of hydroxy acetophenone **277** and **278***[120]

O-Silylation of the hydroxy acetophenones **277** and **278** followed the same procedure as that used for the *O*-silylation of **244** in section 5.3.1.3 (Scheme 5.29). Both **277** and **278** were protected with chloro(*tert*)butyldiphenylsilane under inert conditions in the presence of triethylamine.

© University of Pretoria

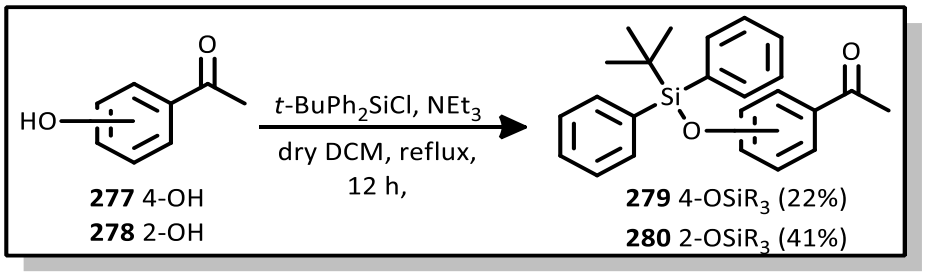

Scheme 5.29: O-silylation of hydroxy acetophenone.

Compound **279** was prepared as a white solid in a yield of 22 % and was characterised by the appearance of the silyl aromatic multiplets at 7.77 – 7.68 and 7.42 – 7.35 ppm integrating for six and four protons respectively, as well as the appearance of a second singlet peak at 1.11 ppm integrating for nine protons, which corresponded to the three silyl methyl groups in the ^{1}H NMR spectrum. In the ^{13}C NMR spectrum the corresponding aromatic carbon peaks were observed at 135.53, 130.79, 130.30 and 128.07 ppm, as well as the silyl methyl peaks at 26.52 ppm. Additionally, a silicon phenyl signal was observed at 1110 cm^{-1} in the FTIR spectrum and a mass ion at *m/z* at 375.178 (100 %) was noted in the mass spectrum, with the molecular ion requiring 375.1775.[116]

The highest yield obtained for **280** was 41 % and it was isolated as a white solid. Characteristically there was the appearance of three multiplets at 7.78 – 7.68, 7.48 – 7.42 and 7.42 – 7.34 ppm integrating for four, two and four protons respectively corresponding to the aromatic silyl groups, as well as the appearance of a singlet at 1.08 ppm integrating for nine protons corresponding to the *tert*-butyl group of **280** in the ^{1}H NMR spectrum. The carbon signals at 135.45, 131.99, 129.83 and 128.12 ppm were from the aromatic silyl carbons and the carbon signal at 26.49 ppm corresponded to the three methyl carbons of the silyl *tert*-butyl group in the ^{13}C NMR spectrum. Additionally, a silicon phenyl signal was observed at 1110 cm^{-1} in the FTIR spectrum and a mass ion in the mass spectrum at *m/z* at 397.170 (10 %) was noted, with the sodium adduct requiring 397.159.[116]

*5.5.2.2 Claisen condensation of O-silylated acetophenones **279** and **280** with carboxylate **31**[106]*

The preparation of β-diketo linkers **281** and **282** was attempted from *O*-silylated acetophenones **279** and **280** and carboxylate **31** using a Claisen condensation reaction previously reported by Inagaki and co-workers.[106] The Claisen condensation involves the formation of the enolate of an α-carbonyl system, which then under goes nucleophilic attack of an ester at the carbonyl carbon (Scheme 5.30). The carbonyl of the ester is temporally converted into an alkoxide with a negative charge placed on

© University of Pretoria

the oxygen, which then moves back down to the carbonyl carbon the alkoxide acts as the leaving group forming the β-diketo system.

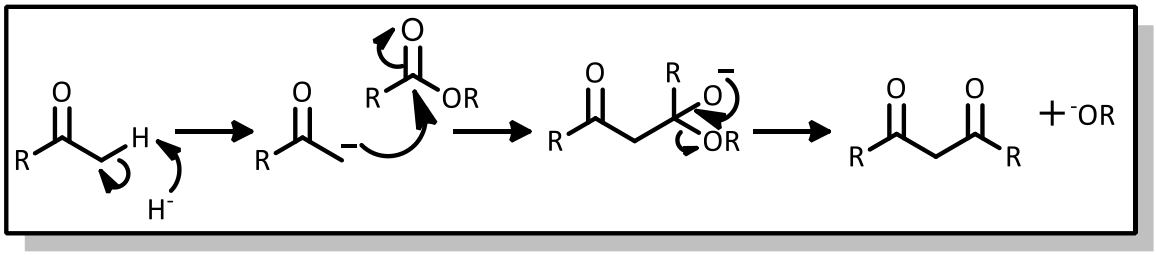

Scheme 5.30: Claisen condensation reaction mechanism recreated from J.G Smith.[112]

Attempted preparation of **281** and **282** was performed under inert conditions wherein sodium hydride was added to a solution of **279** or **280** and **31**, which was then stirred for 12 hours at room temperature (Scheme 5.31). After reaction monitoring using thin layer chromatography potassium-*tert*-butoxide was added in excess and the reaction mixture was stirred for an additional 12 hours at room temperature. An aqueous workup was performed and unfortunately NMR analysis of the crude material did not indicate the formation of the desired product.

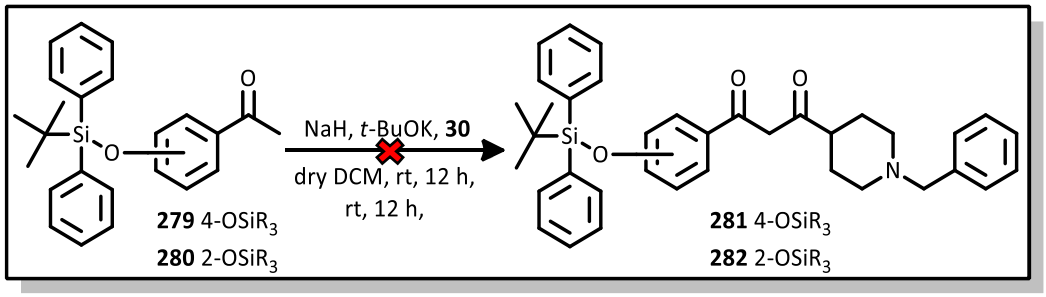

*Scheme 5.31: Claisen condensation of O-silylated acetophenones **279** and **280** and carboxylate **31** to prepare **281** and **282**.*

5.5.3 Ether-linkages

The acetophenone ether linker scaffold was predicted to have the highest binding energy amongst all the scaffolds evaluated within the *in-silico* study (Section 4.9.6.2). The ether analogues were predicted to have conserved donepezil interactions, such as pi-pi interactions of the indanone moiety within the acetophenone replacement, as well as the benzyl group interactions. The carbonyl and ether oxygen had alternative hydrogen bonding interactions creating a hydrogen bonding network with several amino acid residues. The piperidine nitrogen lost the hydrogen bonding interactions typical of

© University of Pretoria

donepezil, however, it has pi-cation interactions with several protein residues. The ether scaffold was elected for preparation as it was predicted to have the best binding to AChE.

The silylated ether linker products (**G**) were to be formed from the free alcohol ether linker (**H**), which was subsequently formed from the acetyl protected product (**I**) (Scheme 5.32).

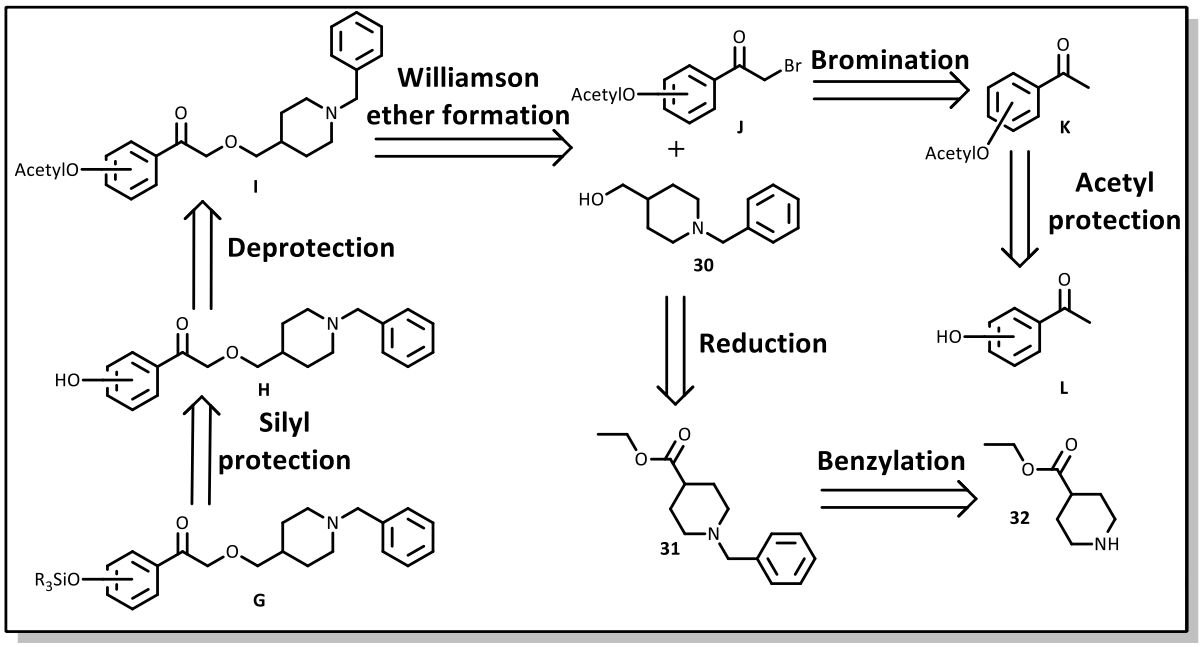

Scheme 5.32: The retrosynthetic route of the silyl protected ether derivatives.

The acetyl protected product **I** would be prepared using Williamson ether synthesis with the brominated acetyl protected acetophenone **J** and **30**. The brominated protected acetophenones would be brominated using liquid bromine from the protected acetophenone **K**, which would have previously been protected **L** using acetic anhydride. Acetyl protection must precede bromination or bromination of the phenol activated aromatic ring will be the preferential product over bromination at the α-carbon. Acetyl protection groups were used as they are acid stable to protect against cleavage arising from residual hydrobromic acid which is present in the liquid bromine during the bromination step.

*5.5.3.1 α Bromination of acetophenone **283***[107]

The preparation of the ether linker analogues was first performed on the unsubstituted acetophenone **275** as its binding score was comparable to that of donepezil (**3**) (Section 4.9.6.2). Bromination of the

© University of Pretoria

α-carbon was the first step, as previously performed by Riley and followed with exception to an extended reaction time.[107]

Compound **283** was prepared by the slow addition of liquid bromine to a solution of **275** after which time the solution was stirred for 12 hours at room temperature (Scheme 5.33). An aqueous workup was performed, and the product was used as is with no further purification required. The halogenated species **283** was obtained in a highest yield of 91 % as a green solid.

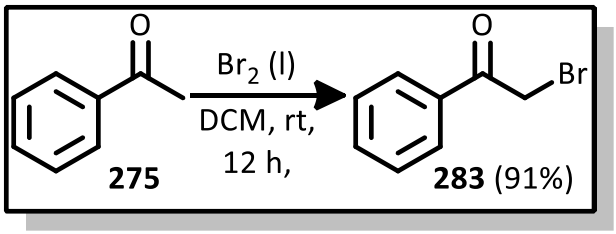

*Scheme 5.33: Bromination of acetophenone **275** to prepare **283**.*

The disappearance of the α-carbon methyl singlet integrated for three protons at 2.59 ppm and the appearance of the bromomethyl singlet integrating for two protons at 4.46 ppm in the ^{1}H NMR spectrum was evidence of the formation of **283**. Additionally, in the ^{13}C NMR spectrum the disappearance and appearance of the α carbon methyl at 26.67 ppm and the bromomethyl carbon peak at 31.03 ppm respectively were noted. Lastly, a C-Br signal was observed within the FTIR spectrum at 680 cm^{-1}.

*5.5.3.2 Williamson ether formation with bromoacetophenone **283** and alcohol **30** to prepare ether **284***

The next step was the formation of the ether bond using a Williamson ether approach between **283** and **30**, which is a S_N2 reaction of an alkyl halide using a strong nucleophile (Scheme 5.34).[112]

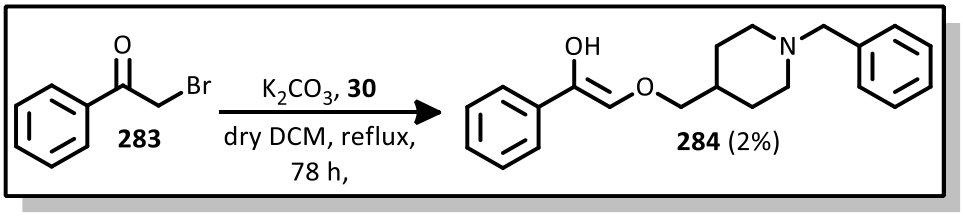

*Scheme 5.34: Substitution of bromoacetophenone **283** and alcohol **30** to prepare ether **284**.*

© University of Pretoria

The preparation of **284** was performed under inert conditions with **283** and **30**, which were refluxed for 78 hours in the presence of excess potassium carbonate after which time an aqueous workup was performed. The crude material was purified using column chromatography and the highest yield obtained for **284** was 2 % as an orange oil. The formation of **284** was characterised by the presence of the CH_2 peak adjacent to the ether oxygen at 3.44 ppm as a doublet integrating for two protons and the alkene doublet peak at 4.37 ppm integrating for one proton in the ^{1}H NMR spectrum. The respective carbons in the ^{13}C NMR spectrum were noted at 67.94 and 70.34 ppm. The *J* coupling of the alkene is 9.6 Hz and indicates a *cis* or *Z* conformation. The benzyl piperidine linker CH_2 was expected at 3.48 ppm in the ^{1}H NMR spectrum and at 63.52 ppm in the ^{13}C NMR spectrum, however, two sets of doublets integrating for one proton each at 3.27 and 2.97 ppm were observed, with the corresponding carbon at 31.57 ppm being assigned to the benzyl linker. Additionally, an alcohol, conjugated carbonyl (C=O) and carbon-nitrogen signals were observed at 3346, 1678 and 1225 cm^{-1} in the FTIR spectrum. Lastly, a mass ion at *m/z* 324.197 (100 %), with the molecular ion requiring 324.1958 was also noted. The intended product was not obtained as expected and was found instead to be in the enolate form. The enolate may be converting between the carbonyl and enolate for continuously as indicated by the conjugated C=O IR signal.

5.5.3.3 Acetyl protection of hydroxy acetophenone[107]

Preparation of the *O*-silylated analogues of the ether linker system required the hydroxy acetophenones (**277** and **278**) to be acetyl protected before the bromination of the α-carbon, as bromination of the aromatic ring would be the major product without acetyl protection. The acetyl protection followed the same method as previously performed by Riley (Scheme 5.35). Acetic anhydride was added to a solution of hydroxy acetophenone in the presence of potassium carbonate and was stirred at room temperature for 12 hours. An aqueous workup was performed, and the product was used without further purification.

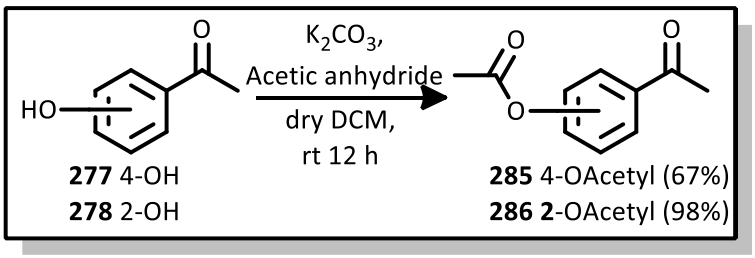

Scheme 5.35: Acetyl protection of hydroxy acetophenone.

© University of Pretoria

Compound **285** was derived as a white solid in a yield of 67 % and was characterised by the appearance of a second alkyl peak for the acetyl group as a singlet integrating for three protons at 2.23 ppm in the ^{1}H NMR spectrum and the appearance of a second carbonyl peak at 169.01 ppm and the corresponding acetyl carbon signal at 21.28 ppm in the ^{13}C NMR spectrum. Additionally, an ester carbonyl (C=O) signal was observed at 1748 cm^{-1} in the FTIR spectrum.

Preparation of **286** followed the same procedure as that described for the preparation of **285**, except triethylamine was utilised instead of potassium carbonate. The desired **286** was obtained with a highest yield of 98 % as a white solid. In the ^{1}H NMR spectrum a singlet peak 2.35 ppm integrating for three protons corresponded to the acetyl methyl protons and its respective carbon was observed at 21.26 ppm, in the ^{13}C NMR spectrum, with the acetyl's carbonyl carbon noted at 169.63 ppm. Lastly, an ester carbonyl (C=O) signal was noted at 1751 cm^{-1} in the FTIR spectrum.

5.5.3.4 Bromination of acetylated acetophenone[107]

The following step was the bromination of the α-carbon, to allow for S_N2 substitution. Bromination of the acetyl protected acetophenones **285** and **286** was performed by the slow addition of liquid bromine to a solution of **287** or **288** and was stirred at room temperature, until the solution turned clear (Scheme 5.36) as utilised for **283** and performed previously by Riley.[107] An aqueous workup was then performed and the products **287** and **288** were used without further purification.

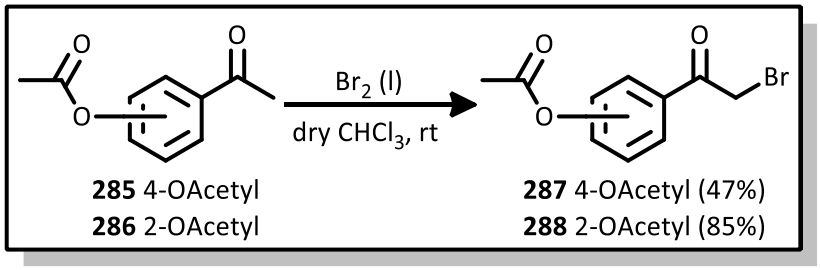

Scheme 5.36: Bromination of the acetyl protected acetophenones.

Compound **287** was obtained in a highest yield of 84 % as a white solid and was characterised by the disappearance of the α-methyl peak singlet at 2.59 ppm which integrated for three protons and the appearance of the bromo methyl singlet at 4.43 ppm integrating for two protons in the ^{1}H NMR spectrum. The disappearance of the α-methyl carbon signal at 26.73 ppm and the appearance of the bromomethyl carbon signal at 30.74 ppm in the ^{13}C NMR spectrum was noted. Additionally, a carbon-bromide signal at 646 cm^{-1} in the FTIR spectrum was observed.

© University of Pretoria

In the case of **288** the desired product was obtained as a white solid in a highest yield of 85 %. The disappearance of a singlet signal integrating for three protons at 2.56 ppm corresponding to the α-methyl and the appearance of a singlet signal at 4.40 ppm integrating for two protons corresponding to the bromomethyl peak in the ^{1}H NMR spectrum showed that the desired product had formed. The bromomethyl carbon peak appearing at 33.87 ppm, and the α-methyl carbon disappearing at 29.45 ppm in the ^{13}C NMR spectrum were noted.

*5.5.3.5 Williamson ether formation with bromo acetyl acetophenone **287** and **288** and alcohol **30** to prepare ether **289** and **290***

The following step after bromination of **277** and **278** was the preparation of **289** and **290**, which was attempted following the same procedure as 5.6.3.2, except dry acetonitrile was used in order to access higher reflux temperatures (Scheme 5.37). The crude material was purified by column chromatography, but NMR analysis of the column fractions for **290** did not indicate the formation of the desired product.

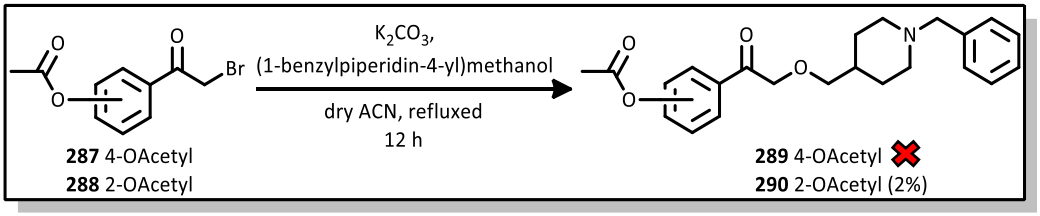

*Scheme 5.37: Williamson ether formation with bromo acetyl acetophenone **287** and **288** and alcohol **30** to prepare ether **289** and **290**.*

In the case of **290** the desired product was isolated in a yield of 2 % as a dark red oil and the low yield obtained was due to the extensive purification required to isolate the product. NMR analysis of the purified fraction suggests a mixture of products with and without the acetyl protection, and like 5.5.3.2 the carbonyl was found to be in an enolate form **291** (Figure 5.7).

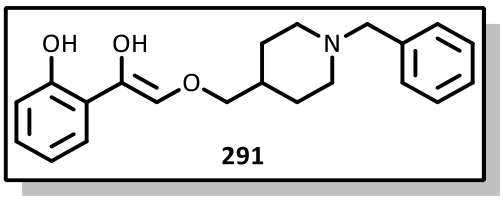

*Figure 5.7: Structure of major product as enolate form **291** of **290**.*

© University of Pretoria

Product **291** was characterised by the appearance of the alkene doublet of doublets at 4.05 ppm integrating for one proton and the shifted doublet for the CH_2 adjacent to the ether appeared peak at 3.49 ppm and integrating for two protons in the ^{1}H NMR spectrum, with the respective carbons in the ^{13}C NMR spectrum appearing at 72.68 and 67.40 ppm. The carbons of the aromatic region showed both the acetophenone and the benzyl peaks, however the acetophenone carbon peaks resembled that of the unprotected starting material (2-hydroxy acetophenone) which has a splitting pattern of a doublet, triplet, doublet and triplet starting from the most downfield peak, whereas the protected acetophenone splitting pattern is a doublet, triplet, triplet and a doublet. There is a peak typical of the acetyl methyl at 3.56 ppm with its peak area reduced and doesn't integrate for the full three protons. The protons for the benzyl groups usual splitting pattern were not present as a multiplet, but instead as a doublet, triplet, triplet in region 7.32-7.13 ppm with the carbon peaks appearing at 129.41, 128.55 and 126.43 ppm in the ^{13}C NMR spectrum. It was also noted that the CH_2 benzyl linker proton peak area was reduced markedly in both the proton and carbon at 2.04 ppm and 21.04 ppm respectively (the starting material proton and carbon spectra were used to identify the peaks, assuming the peaks would be at similar ppm values as that part of the molecule wasn't modified). There was an extra CH_2 carbon peak at 29.97 ppm that could be the product benzyl peak, but it has two separate proton peaks at 3.31 ppm and 3.01 ppm coupling to the carbon peak and was much further up field than the starting material benzyl carbon peak. The doublet of doublets at 4.05 ppm integrates for one proton in the ^{1}H NMR spectrum and a carbon signal at 72.68 ppm in the ^{13}C NMR spectrum. This suggests that the ketone next to the ether may be in an enolate state. Additionally, a mass ion in the mass spectrum at *m/z* 340.190 (100 %)was noted, with the molecular ion requiring 340.1907 (deprotected product) and an alcohol, conjugated carbonyl (C=O) and cis alkene (C=C) signals were observed at 3399, 1667 and 698 $cm^{-1}$the FTIR spectrum.

If the enolate form is the preferred form then during purification basified silica should be used to prevent the hydroxyl group from interacting with the silica and preventing it from sticking to the column, which would reduce decomposition and residence time within the column. This may have been the major reason for the low yield obtained. Additionally, product may be lost in the water fraction during the aqueous workup, as the two alcohols may increase water solubility of the product.

*5.5.3.6 Deacetylation of ether **290***[107]

© University of Pretoria

The deprotection of the residual acetyl protected product was attempted following the protocol previously performed by Riley, which involved stirring a solution of the mixed products with potassium carbonate in methanol at room temperature for 1-3 hours (Scheme 5.38). An extended reaction time of 12 hours was utilised, after which time an aqueous workup was performed and the crude material was purified using column chromatography. NMR analysis of the purified fractions did not indicate full deprotection and the spectra was difficult to interpret as more unidentified peaks were present and it was therefore inconclusive whether the deacetylation was successful.

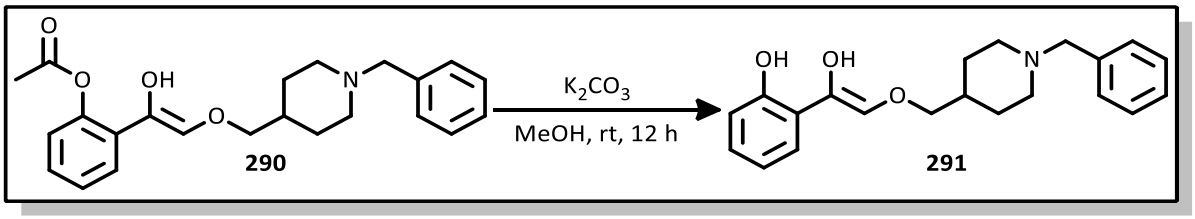

*Scheme 5.38: Deacetylation of ether **290**.*

NMR analysis was not clear in whether the deprotection worked, the aromatic region of the fraction was expanded with the characteristic peaks of the starting material, but the integration was double the number of protons that was expected. Two alcohol signals at 3514 and 3394 cm^{-1} were observed in the FTIR spectrum and the mass spectrum was inconclusive as no molecular ion or adducts were observed. As so little material was obtained, further purification was avoided and the material was used as is in an attempted *O*-silylation with the hope that purification would be simplified post-silylation.

5.5.3.7 O-Silylation of the mixed ether product[120]

O-Silylation of the mixed product fraction was attempted in parallel using four halo silanes (Figure 5.8), using the same protocol as reported in Section 5.3.1.3. A solution of the mixed products and the respective halosilane were refluxed for 12 hours in the presence of triethylamine under inert conditions (Scheme 5.39). An aqueous workup was performed, and the crude material was purified using column chromatography using basified silica. Unfortunately, NMR analysis of the column fractions did not show the desired products.

© University of Pretoria

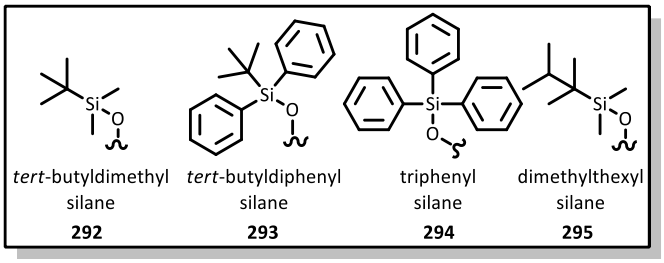

*Figure 5.8: Silanes used in attempted protection of **291**.*

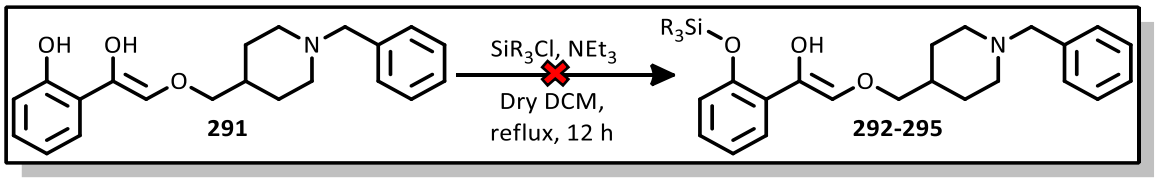

Scheme 5.39: O-silylation of the mixed ether product.

Deprotonation of the alcohol and the resulting alkoxide may have formed a hydrogen bonding interaction with the adjacent enolate alcohol preventing reactivity. The bulky halo silanes may be prevented from reacting due to the steric hindrance of the alcohol's position adjacent to the ketone/enolate, as well as the bulky alkyl substituents of the silyl substitutions.

5.5.4 Conclusion

Access to the β-keto linker analogues was unsuccessful as challenges were experienced in the Claisen condensation reaction and no product was isolated. However, preparation of the ether linker was successful, as **284** was successfully isolated and **291** was shown to be formed, but in a mixture of products. This illustrates that access to the desired ether ligands for further development is achievable, but reaction optimisation is required to access these compounds.

5.6 Overall Conclusion

The synthesis had limited success, the preparation of the indanone analogues (*O* and *C*-silylated), *C*-silylated benzyl and β-keto acetophenone analogues were unsuccessful. However, access to the ether acetophenone analogues was shown to be successful as **284** was isolated and **291** was shown to be formed, but in a mixture of products.

© University of Pretoria

Access to the *O*-silylated indanone analogues was not achieved as the aldol condensation of the aldehyde **28** and *O*-silylated indanone moieties did not yield the desired coupling product, as the *O*-silylated indanone was desilylated back to **244**. *C*-Silylation of the indanone was also unsuccessful and it is suspected that the carbonyl is causing interference during the lithium halogen exchange reaction and forming undesired side products.

Preparation of the *C*-silylated benzyl derivatives was also not achieved as the carbonyl and alkene in the coupled intermediate **268** are suspected to form a complex with the lithium ion as seen by the upfield shift of the alkene signal in the ^{1}H NMR spectrum. The alternative synthetic route investigated to access the *C*-silylated toluene intermediates was also unsuccessful as no product was isolated from either the lithium halogen exchange or Grignard reaction.

Derivatisation of the β-keto acetophenone was unsuccessful as the formation of the β-keto linker using the Claisen condensation was not achieved. Access to the acetophenone ether was partially successful as no hit compounds were isolated, but access to the analogues was proven to be achievable as **284** was isolated and **291** was shown to have formed, however both compounds were isolated in very low yields.

Although the derivatisation of the donepezil scaffold has presented unforeseen challenges it is worth noting that Inagaki and co-workers were successful in the preparation of various β-diketo systems, which utilised the same “chemistry” in order to produce their desired compounds.[106] Additionally, a number of groups have successfully utilised either the Grignard or lithium halogen exchange reaction to successfully incorporate a silicon carbon bond.[105,117,119] Therefore, it may be worthwhile in optimising reaction conditions for isolation of the desired products discussed in this study. Envisaged future work is discussed in Chapter 6.

© University of Pretoria

Chapter 6 Conclusion and future work

6.1 Conclusion:

This study utilised *in-silico* approaches to investigate the potential inhibitory activity of silylated analogues of the FDA approved cholinesterase inhibitor donepezil. Using the Schrödinger suite, a validated method was developed using known therapeutics from the ChEMBL database. Several ligand scaffolds were predicted with improved and comparable binding energies to donepezil (-72.990) for further development. Acetophenone replacement of the indanone moiety with either an ether (-75.736) or β-keto (-71.922) linker showed the most promise, in both instances *O*-silylation of the indanone ring system were shown to be most favourable. Likewise, *C*-silylation of the benzyl moiety also showed great promise with comparable scores to donepezil. Access to these analogues was attempted with limited success with isolation of an acetophenone ether linker derivative **284** and **291** being shown to be prepared, but in a mixture of products. These desired analogues have been shown to be synthetically accessible, however, the synthetic procedures still require reaction optimisation to produce the ligands for biological testing and further derivatisation.

6.2 Future work:

6.2.1 Computational work:

The hypothesis of whether the RMW 1 model was the optimised prepared protein for 4EY7 needs to be confirm or invalidate. This will require that the ligand library of 4EY7 be run at RMW 2, 3 and 4 and the enrichment scores and ROC curves checked to ascertain which parameters represent the optimised model.

A summary table of the various analogues and the average MM-GBSA bind energies is illustrated to identify the best analogues for further development (Table 6.1 and Figure 6.1). The indanone moiety with the *O*-silylations at both the 5th and 6th position and tethered derivatives, as well as the *C*-silylations at both the 5th and 6th position should be considered, because of the comparable MM-GBSA energies (*O*-silylations) to donepezil. The *C*-silylation derivatives scored fairly (6th and 5th) compared to donepezil, but the bond stability allowing for smaller substitutions should be considered for the greater variation within the derivatives. The indanone and benzyl linkers should not be considered for further development as only a single substitution had comparable binding to donepezil and the same

© University of Pretoria

was seen for the piperidine derivatives and should also not be considered. The benzyl substitutions had a reverse binding mode to donepezil, but had comparable MM-GBSA bind energies to donepezil and should be developed further to test the reverse binding mode hypothesis. The acetophenone derivatives with both the β-diketo and ether linkers should also be developed further as they had additional binding interactions when compared to donepezil and had better to comparable MM-GBSA bind energies to donepezil.

The model should be tested with various molecular scaffolds to test the versatility of the model, but if the versatility proves to be poor, then the model should be utilised for drug development of ligands using the core donepezil scaffold.

Table 6.1: Summary of potential analogue with the average MM-GBSA bind energy score of top derivatives.

MM-GBSA flexibility (Å)	Derivative	Average MM-GBSA bind energy
0	Acetophenone ether	-75.736
0	Donepezil	-72.990
0	Acetophenone β-keto	-71.922
0	Indanone (Si-O) 5th	-67.847
0	Indanone (Si-O) Bis	-65.459
0	Indanone (Si-O) 6th	-63.041
0	Indanone (Si-C) 6th	-58.340
0	Indanone (Si-C) 5th	-58.115
0	Benzyl linker	-55.200
0	Indanone (Si-C) 7th	-52.379
0	Indanone (Si-C) 4th	-51.864
0	Indanone linker	-50.807
0	Piperidine nitrogen	-41.094
1	Benzyl ortho	-75.003
1	Donepezil	-74.382
1	Benzyl meta	-73.724
1	Benzyl para	-73.244

© University of Pretoria

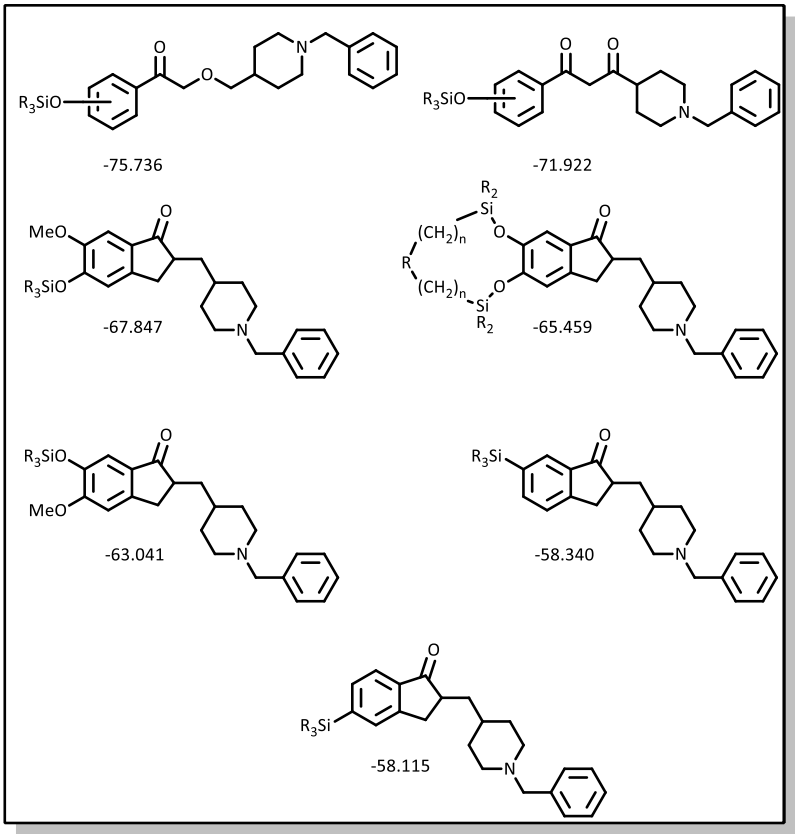

Figure 6.1: Structures and average docking scores of the top 7 silyl derivatised donepezil scaffolds.

Additionally, Du and colleagues tested various docking workflows to test the accuracy of the models and found that an induced fit docking (IFD) and quantum mechanics-polarised ligand docking (QLPD) based MM-GBSA workflow had a better accuracy compared to the *Glide* workflow. The QLPD also showed better correlation between predicated binding energies and experimental IC_{50} values, which can be tested for the further development of the model discussed in this work, to investigate if the models' predictions can be further improved.[75]

Further assessment of the proposed ligand library to evaluate the adsorption, distribution, metabolism and excretion (ADME) properties to evaluate the predicted physicochemical properties using the *QikProp* module within the Schrödinger suite to be performed.

© University of Pretoria

6.2.2 Synthesis work:

6.2.2.1 Silyl Indanone analogues alternative routes:

6.2.2.1.1 *O*-Silylation (Section 5.3.1):

De-methylation of the alkene **27** (Figure 6.2) is to be investigated to prepare the free alcohol for *O*-silylation with the desired silanes to produce the silylated coupled products for further development. The substitution reaction of alcohol **30** with a better leaving groups need to be optimised for improved yields to investigate alternative route to preparing donepezil (**3**). Testing of the demethylation of donepezil (Figure 6.2) is also to be investigated to produce the free alcohol for *O*-silylation and preparation of the alkane coupled silylated products for further development. The *O*-silylation procedure of the free alcohol derivatives can also be optimised for improved yields.

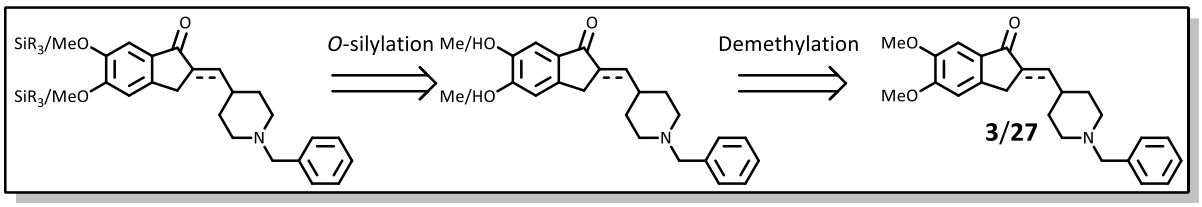

Figure 6.2: Retrosynthesis of alternative synthetic route for silicon incorporated coupled analogues with either an alkane or alkene indanone piperidine linker.

6.2.2.1.2 *C*-Silylation (Section 5.3.2):

Synthesis of the indanone with the already bound silyl group would be the optimal route to obtain the desired products as lithiation with the carbonyl present causes undesired side reactions. Access to the silylated indanone through an alternative retrosynthetic route (Figure 6.3) from the Friedel Crafts acylation of carboxylic acid **296** is proposed.[121] Carboxylic acid **296** can be prepared from the oxidation of aldehyde **297**, which can be produced by the ozonolysis of alkene **298**. Alkene **298** is proposed to be formed by the lithium halogen exchange of halo benzyl **299**. Lastly, halo benzyl **299** can be accessed through Friedel crafts alkylation of the corresponding halobenzene analogue.

© University of Pretoria

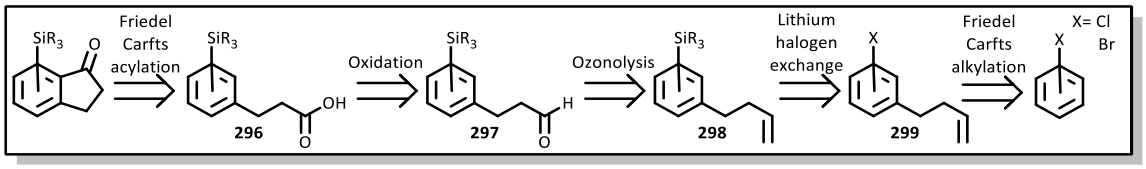

Figure 6.3: Retrosynthesis of alternative synthetic route for silicon incorporated indanone derivatives. Recreated from Oliverio M, et al. 2014.[121]

6.2.2.2 Silyl Benzyl analogues alternative routes (Section 5.4):

The incorporation of silicon into an aromatic ring using lithium halogen exchange has been reported, therefore, optimisation of the lithium halogen exchange and the subsequent S_N2 reaction needs to be investigated. The desired benzyl derivatives should be silylated before benzylation of the piperidine ring as the carbonyl may react with the lithiated reagent and form unwanted by products.

6.2.2.3 Acetophenone derivatives (Section 5.5):

An investigation in the use of various non-nucleophilic bases for the formation of the β-diketo analogues (Section 5.5.2) can be undertaken.

Finally, optimisation of the formation of the ether linker (Section 5.5.3) analogues needs to be performed, in particular, to improve isolated yields. In addition, the optimisation of the *O*-silylation step is also required.

© University of Pretoria

Chapter 7 Methodology

7.1 General Methods

All solvents, chemicals, and reagents were obtained commercially and used without further purification. ^{1}H NMR (300 MHz), (400 MHz) and ^{13}C NMR (75 MHz), (101MHz) spectra were recorded on a Bruker ULTRASHIELD 300 or a Bruker ULTRASHIELD 400 instrument, using $CDCl_3$ and MeOD-d_4. $CDCl_3$ contained tetramethylsilane as an internal standard. Chemical shifts, δ, are reported in parts per million (ppm), and splitting patterns are given as singlet (s), doublet (d), triplet (t), quartet (q), or multiplet (m). Coupling constants, *J,* are expressed in Hertz (Hz). Mass spectra were recorded in electron spray ionisation (ESI) mode on a Waters Synapt G2 Mass Spectrometer at 70 eV and 200 mA. Samples were dissolved in methanol to an approximate concentration of 10 µg/mL. Infrared spectra were run on a Bruker ALPHA Platinum ATR spectrometer. The absorptions are reported on the wavenumber (cm^{-1}) scale, in the range 400 - 4000 cm^{-1}. Melting points were measured on a Stuart Melting Point SMP10 microscope and are uncorrected. The retention factor (R_f) values denoted are for thin layer chromatography (TLC) on aluminium-backed Macherey-Nagel ALUGRAM Sil G/UV_{254} plates pre-coated with 0.25 mm silica gel 60, spots were visualised with UV light and basic potassium permanganate spray reagent. Chromatographic separations were performed on Macherey-Nagel Silica gel 60 (particle size 0.063 – 0.200 mm). Pre-prepared silica (basified silica) used for column chromatography, where specified in the text, was prepared as follows:

The silica required for the column was pre-prepared by shaking with a 10 % triethylamine: dichloromethane (*v/v*) solution, used in the ratio of 1 cm^3 solution per gram of silica, for 15 min at rt. Thereafter, the silica was dried by removing the solvent *in vacuo.*[115] Yields refer to isolated pure products unless stated otherwise. Each compound is named either according to PerkinElmer's *ChemDraw Version 15.0.0.106* or according to common names. The numbering of compounds was not done according to priority, but rather to the author's convenience for characterization.

7.2 Purification of Solvents[115]

Solvents used in reactions under dry, argon atmospheres were distilled over the appropriate drying mediums under a nitrogen atmosphere:

- Tetrahydrofuran and diethyl ether were pre-dried in solvent bottles and then distilled from sodium metal wire and benzophenone.

© University of Pretoria

- Toluene was distilled from sodium metal.
- Dichloromethane and acetonitrile were distilled from calcium hydride powder.

7.3 Experimental procedures

7.3.1 Validation of synthetic methodology through the synthesis of donepezil

*7.3.1.1 Ethyl 1-benzylpiperidine-4-carboxylate (**31**)*[53]

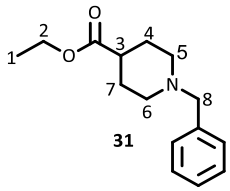

31

A solution of ethyl isonipecotate (**32**) (5.00 mL, 32.44 mmol, 1.0 eq.), triethylamine (13.50 mL, 96.86 mmol, 3.0 eq.) and benzyl chloride (**33**) (4.40 mL, 38.24 mmol, 1.2 eq.) in dry acetonitrile (100 mL) was refluxed for 3 h under an argon atmosphere. Thereafter, the solvent was evaporated *in vacuo* and the reaction mixture was dissolved in ethyl acetate (50 mL), washed with a 3 M sodium hydroxide solution (4x40 mL) and distilled water (3x20 mL). The organic fraction was separated, dried (sodium sulphate), filtered and evaporated *in vacuo*, to afford ethyl 1-benzylpiperidine-4-carboxylate (**31**) (7.926 g, 99 %) as a transparent orange oil, which was used as is without further purification. $\mathbf{R_f}$ = 0.21 (1:3 EtOAc : hexane); **^{1}H NMR (300 MHz, Chloroform-*d*)**; δ 7.34 – 7.17 (m, 5H, Ph), 4.10 (q, *J* = 7.1 Hz, 2H, H-2), 3.48 (s, 2H, H-8), 2.90 – 2.78 (m, 2H, H-5)*, 2.32 – 2.20 (m, 1H, H-3), 2.02 (t, *J* = 11.3, 2.9 Hz, 2H, H-6)*, 1.92 – 1.68 (m, 4H, H-4 & H-7)*, 1.22 (t, *J* = 7.1 Hz, 3H, H-1); **^{13}C NMR (75 MHz, $CDCl_3$)**; δ 175.29 (C=O), 138.28 (quaternary Ar-C), 129.21 (Ph), 128.30 (Ph), 127.13 (Ph), 63.30 (C-8), 60.35 (C-2), 52.96 (C-5 & C-6)^, 41.23 (C-3), 28.31 (C-7 & C-4)^, 14.31 (C-1); **υ_{max} (neat)/cm^{-1}** 2944, 2801, 2760, 1728 (C=O stretching), 1448, 1371, 1259 (C-N stretching), 1168 (ester C-O stretching), 1046, 736, 698; **MS HRMS m/z (ESI)** calculated for ($C_{15}H_{21}NO_2$): 248.1645, found: [M + H] 248.1640. * These assignments may be interchangeable. ^ These assignments may be interchangeable.

© University of Pretoria

*7.3.1.2 (1-Benzylpiperidin-4-yl)methanol (**30**)*[53]

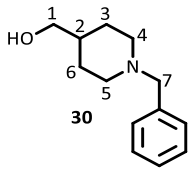

30

Red-Al 60 % (27.00 mL, 83.02 mmol, 2.6 eq.) was added dropwise to a solution of ethyl 1-benzyl-piperidine-4-carboxylate (**31**) (7.884 g, 31.88 mmol, 1.0 eq.) in dry dichloromethane (100 mL) at 15-20 °C under an argon atmosphere. The reaction mixture was stirred for 3 h at rt after which time was quenched with a 10 % sodium hydroxide solution and diluted with distilled water (40 mL) and a saturated sodium sulphate solution (15 mL). The reaction mixture was stirred for 45 min and the organic fraction was separated, washed with distilled water (3x20 mL) and a saturated sodium sulphate solution (3x20 mL). The organic fraction was dried (sodium sulphate), filtered and evaporated *in vacuo,* to afford (1-benzylpiperidin-4-yl)methanol (**30**) (5.406 g, 83 %) as a transparent orange oil, which was used as is without further purification. **R_f** = 0.25 (1:9 MeOH : DCM); **^{1}H NMR (300 MHz, Chloroform-*d*)**; 7.35 – 7.12 (m, 5H, Ph), 3.48 (s, 2H, H-7), 3.42 (d, *J* = 6.3 Hz, 2H, H-1), 2.88 (d, 2H, H-4)*, 2.67 (s, 1H, O-H), 1.94 (t, *J* = 11.7, 2.5 Hz, 2H, H-5)*, 1.68 (d, *J* = 13.1, 2.4 Hz, 2H, H-3)*, 1.45 (m, 1H, H-2), 1.56 – 1.35 (m, 2H, H-6)*; **^{13}C NMR (75 MHz, $CDCl_3$)**; δ 138.12 (quaternary Ar-C), 129.42 (Ph), 128.23 (Ph), 127.08 (Ph), 67.64 (C-1), 63.52 (C-7), 53.47 (C-4 & C-5)^, 38.54 (C-2), 28.79 (C-3 & C-6)^; **υ_{max} (neat)/cm^{-1}** 3326 (O-H stretching), 2916, 1452, 1366, 1259, 1113, 1040 , 697; **MS HRMS m/z (ESI)** calculated for ($C_{13}H_{19}NO$): 206.1539, found: [M + H] 206.1559. * These assignments may be interchangeable. ^ These assignments may be interchangeable.

*7.3.1.3 1-Benzylpiperidine-4-carbaldehyde (**28**)*[53]

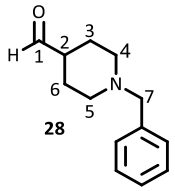

28

A solution of dimethyl sulfoxide (6.00 mL, 84.47 mmol, 3.2 eq.) in dry dichloromethane (15 mL) was added dropwise to an oxalyl chloride (3.00 mL, 35.45 mmol, 1.3 eq.) solution in dry dichloromethane (15 mL) at -78 °C under an argon atmosphere. The reaction mixture was stirred for 30 min before a solution of (1-benzyl-piperidin-4-yl)methanol (**30**) (5.406 g, 26.33 mmol, 1.0 eq.) in dry

© University of Pretoria

dichloromethane (10 mL) was added dropwise at -78 °C and stirred for 30 min. Triethylamine (18.80 mL, 134.88 mmol, 5.1 eq.) was added dropwise at -78 °C and stirred for 30 min. The reaction mixture was warmed up to rt after which time it was diluted with distilled water (150 mL). The organic fraction was separated, washed with a saturated sodium chloride solution (3x50 mL), dried (Na_2SO_4), filtered and evaporated *in vacuo,* to afford 1-benzylpiperidine-4-carbaldehyde (**28**) (4.293 g, 80 %) as an orange oil, which was used as is without further purification. **R_f** = 0.38 (1:9 MeOH : DCM); **^{1}H NMR (300 MHz, Chloroform-*d*)**; δ 9.61 (s, 1H, H-1), 7.36 – 7.13 (m, 6H, Ph), 3.47 (s, 2H, H-7), 2.27 – 2.15 (m, 2H, H-4)*, 2.20 (m, 1H, H-2), 2.08 (td, *J* = 11.1, 2.9 Hz, 2H, H-5)*, 1. 85 (m, 2H, H-3)*, 1.91 – 1.80 (m, 2H, H-6)*; **^{13}C NMR (75 MHz, $CDCl_3$)**; δ 204.10 (C-1), 138.27 (quaternary Ar-C), 129.15 (Ph), 128.29 (Ph), 127.12 (Ph), 63.30 (C-7), 52.55 (C-4 & C-5)^, 48.04 (C-2), 25.51 (C-3 & C-6)^; **υ_{max} (neat)/cm^{-1}** 2939, 2802 (aldehyde C-H stretching), 1722(C=O stretching), 1449, 1366, 1263, 1114, 1071, 966, 736, 698; **MS HRMS m/z (ESI)** calculated for ($C_{13}H_{17}NO$): 204.1383, [M + CH_3OH + H] 236.1645, found: [M + H] 204.1408, [M + CH_3OH + H] 236.1643. * These assignments may be interchangeable. ^ These assignments may be interchangeable.

*7.3.1.4 (E)-2-((1-benzylpiperidin-4-yl)methylene)-5,6-dimethoxy-2,3-dihydro-1H-inden-1-one (**27**)*[53]

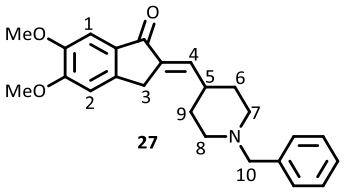

27

A sodium hydroxide solution (0.885 g, 22.12 mmol, 8.9 eq.) in methanol and water (50 mL, 4:1) was added dropwise to a solution of 5,6-dimethoxy-1-indanone (**29**) (0.507 g, 2.49 mmol, 1.0 eq.) in methanol (30 mL) over 45 min at 40-45 °C. The mixture was stirred for 30 min before a solution of 1-benzylpiperidine-4-carbaldehyde (**28**) (1.061 g, 5.22 mmol, 2.1 eq.) in methanol (10 mL) was added dropwise and stirred for 2 h at 40-45 °C. The solution was cooled to rt after which time distilled water (30 mL) was added and the reaction mixture was triturated for 30 min. The solids were filtered off, washed with additional distilled water (30 mL) and dried *in vacuo*, to afford (*E*)-2-((1-benzylpiperidin-4-yl)methylene)-5,6-dimethoxy-2,3-dihydro-1*H*-inden-1-one (**27**) (0.378 g, 40 %) as a white powder, which was used as is without further purification. **R_f** = 0.83 (1:9 MeOH : DCM); **mp** 176-177 °C; **^{1}H NMR (400 MHz, Chloroform-*d*)**; δ 7.37 – 7.29 (m, 5H, Ph), 7.28 (s, 1H, H-2)<, 6.89 (s, 1H, H-1)<, 6.66 (d, *J* = 9.7 Hz, 1H, H-4), 3.97 (s, 3H, O-CH_3), 3.92 (s, 3H, O-CH_3), 3.58 (s, 2H, H-3), 3.55 (s, 2H, H-10), 2.94 (d, *J* = 11.5 Hz, 2H, H-7)*, 2.41 – 2.27 (m, 1H, H-5), 2.09 (t, *J* = 10.2 Hz, 2H, H-8)*, 1.75 – 1.58 (m, 4H, H-6 & H-9)*; **^{13}C NMR (101 MHz, $CDCl_3$)**; δ 192.69 (C=O), 155.44 (quaternary Ar-C), 149.65 (quaternary Ar-C),

© University of Pretoria

144.62 (quaternary Ar-C), 139.90 (C-4), 138.27 (quaternary C=CH), 135.78 (quaternary Ar-C), 132.00 (quaternary Ar-C), 129.35 (Ph), 128.34 (Ph), 127.18 (Ph), 107.37 (C-1)', 105.18 (C-2)', 63.60 (C-10), 56.37 (O-CH_3), 56.28 (O-CH_3), 53.17 (C-7 & C-8)^, 37.36 (C-5), 31.31 (C-5 & C-9)^, 29.63 (C-3); **υ_{max} (neat)/cm^{-1}** 2927, 2756, 1687 (conjugated C=O stretching), 1646 (conjugated C=C stretching), 1602, 1498, 1452, 1307, 1214, 1070, 980 (*trans* C=C bending), 733, 696; **MS HRMS m/z (ESI)** calculated for ($C_{24}H_{27}NO_3$): 378.2064, found: [M + H] 378.2097. < These assignments may be interchangeable. * These assignments may be interchangeable. ' These assignments may be interchangeable. ^ These assignments may be interchangeable.

*7.3.1.5 Preparation of donepezil (**3**)*

7.3.1.5.1 Approach 1

7.3.1.5.1.1 2-((1-Benzylpiperidin-4-yl)methyl)-5,6-dimethoxy-2,3-dihydro-1*H*-inden-1-one (**3**)

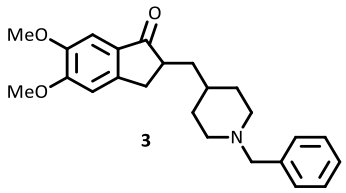

3

Attempt 1:[53]

(*E*)-2-[(1-benzylpiperidin-4-yl)methylene]-5,6-dimethoxy-2,3-dihydro-1*H*-inden-1-one (**27**) (1.456 g, 3.02 mmol, 1.0 eq.) was dissolved in tetrahydrofuran (30 mL) and stirred for 30 min at rt. 10 % palladium on carbon (0.076 g, 25 mg/mmol) was added to the solution and was stirred for 10 h under a hydrogen atmosphere. The catalyst was removed by filtering the reaction mixture through celite and the solvent was evaporated *in vacuo*. NMR spectroscopy of the crude mixture did not show the desired product. Other attempts with varying reaction times and solvents (tetrahydrofuran, methanol) did not yield the desired product.

© University of Pretoria

7.3.1.5.2 Approach 2

7.3.1.5.2.1 (1-Benzylpiperidin-4-yl)methyl methanesulfonate (**240**)

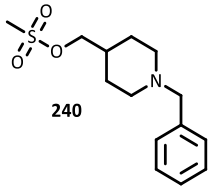

240

Attempt 1:[122]
Mesyl chloride (0.40 mL, 5.15 mmol, 1.3 eq.) was added to a solution of (1-benzylpiperidin-4-yl)methanol (**30**) (0.791 g, 3.85 mmol, 1.0 eq.) and triethylamine (1.60 mL, 11.48 mmol, 3.0 eq.) in dry dichloromethane (30 mL) and was refluxed for 12 h under an argon atmosphere. Potassium-*tert*-butyl (0.950 g, 8.46 mmol, 2.2 eq.) was added to a solution 5,6-dimethoxy-1-indanone (0.768 g, 4.00 mmol, 1.0 eq.) in dry dichloromethane (60 mL) and was stirred for 1 h under an argon atmosphere. The indanone reaction solution was added to the alcohol solution in portions and after full addition, the reaction mixture was refluxed for 12 h. The reaction mixture was washed with distilled water (4x40 mL) and the organic fraction was separated, dried (sodium sulphate), filtered and evaporated *in vacuo*. The crude material was purified using column chromatography (3:1 EtOAc : hexane). NMR analysis indicated no product formation.

Attempt 2:[122]
Mesyl chloride (0.20 mL, 2.58 mmol, 1.5 eq.) was added to a solution of (1-benzylpiperidin-4-yl)methanol (**30**) (0.352 g, 1.72 mmol, 1.0 eq.) and imidazole (0.612 g, 9.00 mmol, 5.2 eq.) in dry dichloromethane (30 mL) under a argon atmosphere and was stirred for 30 min at rt. A solution of 5,6-dimethoxy-1-indanone (**27**) (0.380 g, 1.98 mmol, 1.2 eq.) in dry dichloromethane (10 mL) was added dropwise and stirred for 12 h at rt. The reaction solution was refluxed for 5 h after reaction monitoring via TLC. Distilled water (50 mL) was added and the organic fraction was separated, washed with distilled water (2x30 mL), dried (sodium sulphate), filtered and evaporated *in vacuo*. NMR analysis of the crude material indicated no product formation.

© University of Pretoria

7.3.1.5.2.2 (1-Benzylpiperidin-4-yl)methyl 4-methylbenzenesulfonate (**241**)

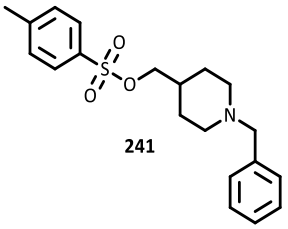

241

Attempt 1:[123]

A solution of (1-benzylpiperidin-4-yl)methanol (**30**) (0.305 g, 1.49 mmol, 1.0 eq.), 4-toluenesulfonyl chloride (0.351 g, 1.84 mmol, 1.2 eq.) and triethylamine (0.65 mL, 4.66 mmol, 3.1 eq.) in dry dichloromethane (30 mL) under an argon atmosphere was stirred for 12 h at rt. The reaction mixture was washed with distilled water (3x30 mL), dried (sodium sulphate), filtered and evaporated *in vacuo*. The crude material was purified using column chromatography (3:1 EtOAc : hexane). NMR analysis indicated no product formation in the column fractions.

Attempt 2:[110]

A solution of (1-benzylpiperidin-4-yl)methanol (**30**) (0.878 g, 4.28 mmol, 1.0 eq.) and triethylamine (1.50 mL, 10.76 mmol, 2.5 eq.) in dry dichloromethane (10 mL) was added dropwise to a stirring solution of 4-toluenesulfonyl chloride (0.836 g, 4.39 mmol, 1.0 eq) in dry dichloromethane (20 mL) under an argon atmosphere at 0 °C. The reaction mixture was stirred at rt for 78 h. The reaction mixture was washed with distilled water (3x30 mL), dried (sodium sulphate), filtered and evaporated *in vacuo*. The crude material was purified using column chromatography (3:1 EtOAc : hexane). NMR analysis indicated no product formation in the column fractions.

7.3.1.5.2.3 1-Benzyl-4-(bromomethyl)piperidine (**242**)

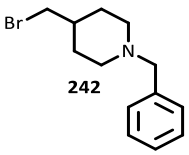

242

Attempt 1:[124]

(1-Benzylpiperidin-4-yl)methanol (**30**) (0.864 g, 4.21 mmol, 1.0 eq.) was dissolved in 65 % hydrobromic acid (20 mL) and refluxed for 3 hours. The reaction mixture was extracted with dichloromethane (6x10

© University of Pretoria

mL) and the organic fraction was washed with a saturated potassium bicarbonate solution (3x30 mL) and a saturated sodium sulphate solution (3x30 mL). The organic fraction was separated, dried (sodium sulphate), filtered and evaporated *in vacuo*. NMR analysis of the crude material indicated no product formation.

Attempt 2:[125]

(1-Benzylpiperidin-4-yl)methanol (**30**) (0.864 g, 4.21 mmol, 1.0 eq.) was dissolved in 65 % hydrobromic acid (20 mL) solution and concentrated sulphuric acid (10 mL) was added dropwise. The reaction mixture was refluxed for 5 h and then an ice-water mixture (50 mL) was added to the reaction mixture and was extracted with dichloromethane (6x10 mL). The organic fraction was washed with a saturated potassium bicarbonate solution (3x30 mL), a saturated sodium sulphate solution (3x30 mL), dried (sodium sulphate), filtered and evaporated *in vacuo*. NMR analysis of the crude material indicated no product formation.

Attempt 3:[111]

Liquid bromine (0.15 mL, 2.91 mmol, 2.0 eq.) was added dropwise to a solution of triphenyl phosphine (0.462 g, 1.76 mmol, 1.2 eq.) in dry acetonitrile (20 mL) under an argon atmosphere at 0-10 °C and stirred for 30 min. A solution of (1-benzylpiperidin-4-yl)methanol (**30**) (0.305 g, 1.49 mmol, 1.0 eq.) in dry acetonitrile (5 mL) was added and stirred at rt for 12 h. The solvent was evaporated *in vacuo* and the reaction mixture was dissolved in dichloromethane (30 mL) and washed with distilled water (4x30 mL). The organic fraction was separated, dried (sodium sulphate), filtered and evaporated *in vacuo*. NMR analysis of the crude material indicated no product formation.

7.3.1.5.2.4 1-Benzyl-4-(chloromethyl)piperidine (**243**)[113]

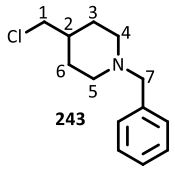

243

A solution of (1-benzylpiperidin-4-yl)methanol (**30**) (1.006 g, 4.90 mmol, 1.0 eq.) and phosphoryl chloride (17.00 mL, 182.38 mmol, 37.2 eq.) was stirred at rt for 12 h. The excess phosphoryl chloride was evaporated *in vacuo* and the reaction mixture was diluted with dichloromethane (30 mL), quenched with sodium bicarbonate solids (5.00 g) and poured into an ice/water mixture (100 mL). The organic fraction was separated, washed with distilled water (3x30 mL), dried (sodium sulphate) and

© University of Pretoria

evaporated *in vacuo,* to afford 1-benzyl-4-(chloromethyl)piperidine (**243**) (0.213 g, 19 %) as an orange oil, which was used as is without further purification. **R_f** = 0.65 (3:1 EtOAc : hexane); **^{1}H NMR (400 MHz, Chloroform-*d*)**; δ 7.36 – 7.19 (m, 4H, Ph), 3.49 (s, 2H, H-7), 3.40 (d, *J* = 6.6 Hz, 2H, H-1), 2.90 (d, 2H, H-4)*, 1.95 (td, *J* = 11.8, 2.6 Hz, 2H, H-5)*, 1.71 – 1.56 (d, 2H, H-3)*, 1.41 – 1.23 (m, 1H, H-2), 1.33 (m, 2H, H-6)*; **^{13}C NMR (101 MHz, $CDCl_3$)**; δ 138.48 (Ph, quaternary C), 129.25 (Ph), 128.27 (Ph), 127.07 (Ph), 63.36 (C-7), 53.32 (C-4 & C-5)^, 50.18 (C-1), 38.68 (C-2), 30.14 (C-4 & C-5)^. * these assignments may be interchangeable. ^ these assignments may be interchangeable.

7.3.2 Indanone moiety derivatisation

7.3.2.1 O-Silylated scaffolds

7.3.2.1.1 5-Hydroxy-6-methoxy-2,3-dihydro-1*H*-inden-1-one (**244**)[103]

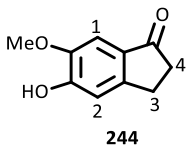

244

Aluminium trichloride (20.752 g, 155.63 mmol, 3.0 eq.) was added to a solution of 5,6-dimethoxy-1-indanone (**29**) (10.010 g, 52.08 mmol, 1.0 eq.) in toluene (100 mL) and was refluxed for 1 h. The reaction mixture was poured into an ice hydrochloric acid mixture (150 mL) and stirred for 30 min – 1 h. The aqueous layer was separated and extracted with dichloromethane (3x50 mL) and the organic fraction was dried (sodium sulphate), filtered and evaporated *in vacuo*. The crude material was purified using column chromatography (pre-prepared/basified silica and 3:1 EtOAc : hexane), to afford 5-hydroxy-6-methoxy-2,3-dihydro-1*H*-inden-1-one (**244**) (2.274 g, 25 %) as a light brown powder. **R_f** = 0.29 (3:1 EtOAc : hexane); **mp** 138-140 °C; **^{1}H NMR (300 MHz, Methanol-d_4)**; δ 7.09 (s, 1H, H-2)*, 6.83 (d, *J* = 1.0 Hz, 1H, H-1)*, 3.85 (s, 3H, O-CH_3), 3.05 – 2.88 (m, 2H, H-4), 2.57 (m, 2H, H-3); **^{13}C NMR (75 MHz, MeOD)**; δ 208.70 (C=O), 155.83 (quaternary Ar-C), 153.33 (quaternary Ar-C), 149.67 (quaternary Ar-C), 129.63 (quaternary Ar-C), 112.73 (C-1)^, 105.25 (C-2)^, 56.42 (O-CH_3), 56.36 (O-CH_3), 37.42 (C-3), 26.17 (C-4); **υ_{max} (neat)/cm^{-1}** 3043 (O-H stretching), 2933, 2843, 2779, 1653, 1568, 1410 (O-H bending), 1299,1268, 1206, 1125, 1035, 850, 808, 639; **MS HRMS m/z (ESI)** calculated for ($C_{10}H_{10}O_3$): 179.0703, found: [M + H] 179.0733. * These assignments may be interchangeable. ^These assignments may be interchangeable.

© University of Pretoria

7.3.2.1.2 5,6-Dihydroxy-2,3-dihydro-1*H*-inden-1-one (**245**)[103]

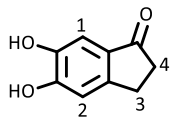

245

Aluminium trichloride (20.752 g, 155.63 mmol, 3.0 eq.) was added to a solution of 5,6-dimethoxy-1-indanone (**29**) (10.010 g, 52.08 mmol, 1.0 eq.) in toluene (100 mL) and was refluxed for 1 h. The reaction mixture was poured into an ice hydrochloric acid mixture (150 mL) and stirred for 30 min - 1 h. The aqueous layer was separated and a saturated sodium chloride solution (100 mL) was added and stirred for 12 h. The solids were filtered and dried *in vacuo*, to afford 5,6-dihydroxy-2,3-dihydro-1*H*-inden-1-one (**245**) (0.627 g, 7 %) as a dark brown powder, which was used as in without further purification. **R_f** = 0.00 (3:1 EtOAc : hexane); **mp** 107-109 °C; **^{1}H NMR (300 MHz, Methanol-d_4)**; δ 7.04 (s, 1H, H-2)*, 6.84 (s, 1H, H-1)*, 3.03 – 2.89 (m, 2H, H-4), 2.65 – 2.53 (m, 2H, H-3); **^{13}C NMR (101 MHz, MeOD)**; δ 208.85 (C=O), 152.03 (quaternary Ar-C), 147.10 (quaternary Ar-C), 129.88 (quaternary Ar-C), 112.53 (C-1)^, 108.90 (C-2)^, 37.49 (C-3), 26.11 (C-4); **υ_{max} (neat)/cm^{-1}** 3413 (O-H stretching), 3069 (O-H stretching), 2537, 2304, 1630, 1578, 1461 (O-H bending), 1323, 1281, 1206, 1121, 1011, 876, 855, 711, 610; **MS HRMS m/z (ESI)** calculated for ($C_9H_8O_3$): 165.0546, found: [M + H] 165.0575. * These assignments may be interchangeable. ^ These assignments may be interchangeable.

7.3.2.1.3 5-((*Tert*-butyldimethylsilyl)oxy)-6-methoxy-2,3-dihydro-1*H*-inden-1-one (**246**)

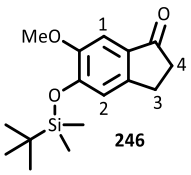

246

Tert-butyl(chloro)dimethylsilane (1.794 g, 11.90 mmol, 1.3 eq.) was added to a solution of 5-hydroxy-6-methoxy-2,3-dihydro-1*H*-inden-1-one (**244**) (1.602 g, 8.99 mmol, 1.0 eq.) and imidazole (1.192 g, 17.51 mmol, 1.9 eq.) in dry dichloromethane (50 mL) under a argon atmosphere and refluxed for 12 h. The reaction mixture was diluted with distilled water (30 mL) and the organic fraction was separated, washed with distilled water (3x30 mL), dried (sodium sulphate), filtered and evaporated *in vacuo*. The crude material was purified using column chromatography (pre-prepared/basified silica and 1:9 EtOAc : hexane), to afford 5-((*tert*-butyldimethylsilyl)oxy)-6-methoxy-2,3-dihydro-1*H*-inden-1-one (**246**) (2.302 g, 88 %) as a white crystalline solid. **R_f** = 0.77 (1:1 EtOAc : hexane); **mp** 172-174 °C;

© University of Pretoria

^{1}H NMR (300 MHz, Chloroform-*d*); δ 7.15 (s, 1H, H-2)*, 6.87 (s, 1H, H-1)*, 3.81 (s, 3H, O-C$\underline{H}_3$), 3.07 – 2.93 (m, 2H, H-4), 2.68 – 2.56 (m, 2H, H-3), 0.99 (s, 9H, Si-C-(C$\underline{H}_3$)$_3$), 0.17 (s, 6H, Si-(C$\underline{H}_3$)$_2$); **^{13}C NMR (75 MHz, CDCl$_3$)**; δ 206.13 (C=O), 152.22 (quaternary Ar-C), 151.43 (quaternary Ar-C), 149.97 (quaternary Ar-C), 130.97 (quaternary Ar-C), 117.63 (C-1)^, 104.92 (C-2)^, 55.59 (O-$\underline{C}$H$_3$), 55.53 (O-$\underline{C}$H$_3$), 36.70 (C-3)^, 25.72 (Si-C-($\underline{C}$H$_3$)$_3$), 25.30 (C-4)^, 18.64 (Si-($\underline{C}$H$_3$)$_2$), -4.46 (Si-$\underline{C}$-(CH$_3$)$_3$), -4.50 (Si-$\underline{C}$-(CH$_3$)$_3$); **υ_{max} (neat)/cm^{-1}** 2926, 2855, 1706 (C=O stretching), 1580, 1488, 1312, 1312, 1248 (Si-CH$_3$), 1122, 1034, 867, 832 (Si-CH$_3$), 779 (Si-CH$_3$)[116], 689; **MS HRMS m/z (ESI)** calculated for ($C_{16}H_{24}O_3Si$): 293.1567, found: [M + H] 293.1587. * These assignments may be interchangeable. ^ These assignments may be interchangeable.

7.3.2.1.4 5-((*Tert*-butyldiphenylsilyl)oxy)-6-methoxy-2,3-dihydro-1*H*-inden-1-one (**247**)

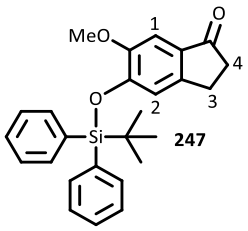

Tert-butyl(chloro)diphenylsilane (0.40 mL, 1.54 mmol, 1.3 eq.) was added to a solution of 5-hydroxy-6-methoxy-2,3-dihydro-1*H*-inden-1-one (**244**) (0.210 g, 1.18 mmol, 1.0 eq.) and imidazole (0.250 g, 3.67 mmol, 3.1 eq.) in dry dichloromethane (50 mL) under an argon atmosphere and was stirred for 12 h at 40-50 °C. Distilled water (50 mL) was added and the organic fraction was separated, washed with distilled water (3x30 mL), dried (sodium sulphate), filtered and evaporated *in vacuo*. The crude material was purification using column chromatography (pre-prepared/basified silica and 1:9 EtOAc : hexane), to afford 5-((*tert*-butyldiphenylsilyl)oxy)-6-methoxy-2,3-dihydro-1*H*-inden-1-one (**247**) (0.114 g, 23 %) as an off white solid. **R$_f$** = 0.19 (1:9 EtOAc : hexane); **^{1}H NMR (400 MHz, Chloroform-*d*)**; δ 7.74 – 7.66 (m, 8H, Si-(C$_6\underline{H}_5$)$_2$), 7.45 – 7.33 (m, 12H, Si-(C$_6\underline{H}_5$)$_2$), 7.08 (s, 1H, H-2)*, 6.72 (s, 1H, H-1)*, 3.57 (s, 3H, O-C$\underline{H}_3$), 2.86 – 2.80 (m, 2H, H-4), 2.61 – 2.54 (m, 2H, H-3), 1.12 (s, 10H, Si-(C$\underline{H}_3$)$_3$), 1.07 (s, 9H, Si-(C$\underline{H}_3$)$_3$); **^{13}C NMR (101 MHz, CDCl$_3$)**; δ 206.26 (C=O), 152.01 (quaternary Ar-C), 151.12 (quaternary Ar-C), 149.72 (quaternary Ar-C), 135.34 (Si-($\underline{C}_6$H$_5$)$_2$), 135.31 (quaternary Ar-C), 134.94 (Si-($\underline{C}_6$H$_5$)$_2$), 132.93 (quaternary Ar-C), 130.80 (quaternary Ar-C), 130.01 (Si-($\underline{C}_6$H$_5$)$_2$), 129.79 (Si-($\underline{C}_6$H$_5$)$_2$), 127.86 (Si-($\underline{C}_6$H$_5$)$_2$), 127.81 (Si-($\underline{C}_6$H$_5$)$_2$), 116.98 (C-1)^, 105.03 (C-2)^, 55.41 (O-$\underline{C}$H$_3$), 36.66 (C-3), 26.69 (Si-C-($\underline{C}$H$_3$)$_3$), 26.65 (Si-C($\underline{C}$H$_3$)$_3$), 25.27 (C-4), 19.99 (Si-$\underline{C}$-(CH$_3$)$_3$), 19.16 (Si-$\underline{C}$-(CH$_3$)$_3$); **MS HRMS m/z (ESI)** calculated for ($C_{26}H_{28}O_3Si$): 417.1880, found: [M + H] 417.188. * These assignments may be interchangeable. ^ These assignments may be interchangeable.

© University of Pretoria

7.3.2.1.5 5,6-Bis((*tert*-butyldimethylsilyl)oxy)-2,3-dihydro-1*H*-inden-1-one (**248**)

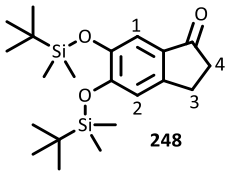

248

Tert-butyl(chloro)dimethylsilane (0.346 g, 2.29 mmol, 4.1 eq.) was added to a solution of 5,6-dihydroxy-2,3-dihydro-1*H*-inden-1-one (**245**) (0.092 g, 0.56 mmol 1.0 eq.) and imidazole (0.155 g, 2.27 mmol, 4.1 eq.) in dry dimethylformamide (16 mL) under a argon atmosphere and stirred for 24 h at 90 °C. The reaction mixture was diluted with distilled water (30 mL) and extracted with diethyl ether (3X30 mL). The organic fraction was washed with a saturated sodium chloride solution (20 mL), dried (sodium sulphate), filtered and evaporated *in vacuo*. The crude material was purified using column chromatography (pre-prepared/basified silica and 1:9 EtOAc : hexane), to afford 5,6-bis((*tert*-butyldimethylsilyl)oxy)-2,3-dihydro-1*H*-inden-1-one (**248**) (0.114 g, 52 %) as a white solid. **R_f** = 0.89 (3:1 EtOAc : hexane); **mp** 64-68 °C; **^{1}H NMR (300 MHz, Chloroform-*d*)**; δ 7.16 (s, 1H, H-2)*, 6.85 (s, 1H, H-1)*, 3.04 – 2.93 (m, 2H, H-4), 2.68 – 2.59 (m, 2H, H-3), 0.99 (s, 9H, Si-C-(C$\underline{H}_3$)$_3$), 0.98 (s, 9H, Si-C-(C$\underline{H}_3$)$_3$), 0.25 (s, 6H, Si-(C$\underline{H}_3$)$_2$), 0.21 (s, 6H, Si-(C$\underline{H}_3$)$_2$); **^{13}C NMR (75 MHz, $CDCl_3$)**; δ 205.87 (C=O), 154.18 (quaternary Ar-C), 149.94 (quaternary Ar-C), 147.43 (quaternary Ar-C), 130.85 (quaternary Ar-C), 117.37 (C-1)^, 114.25 (C-2)^, 36.83 (C-3), 26.03 (Si-C-(C$\underline{H}_3$)$_3$), 25.99 (Si-C-(C$\underline{H}_3$)$_3$), 25.35 (C-4), 18.70 (Si-(C$\underline{H}_3$)$_2$), 18.59 (Si-(C$\underline{H}_3$)$_2$), -3.88 (Si-C-(CH$_3$)$_3$), -4.00 (Si-C-(CH$_3$)$_3$); **υ_{max} (neat)/cm^{-1}** 2930 , 2858, 1708 (C=O stretching), 1604, 1487, 1322 , 1252 (Si-CH$_3$), 1200, 1123, 1011, 909, 834 (Si-CH$_3$), 779 (Si-CH$_3$)[116], 686; **MS HRMS m/z (ESI)** calculated for ($C_{21}H_{36}O_3Si_2$): 393.2276, found: [M + H] 393.228. * These assignments may be interchangeable. ^ These assignments may be interchangeable.

7.3.2.1.6 (*E*)-2-((1-benzylpiperidin-4-yl)methylene)-5-((*tert*-butyldimethylsilyl)oxy)-6-methoxy-2,3-dihydro-1*H*-inden-1-one (**249**)[53]

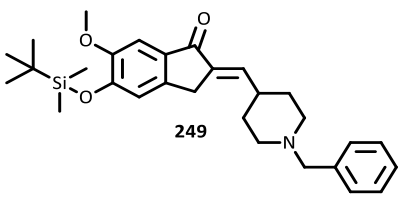

249

© University of Pretoria

Attempt 1:

A sodium hydroxide solution (0.633 g, 15.83 mmol, 9.2 eq.) in methanol and water (50 mL, 4:1) was added dropwise to a solution of 5-((*tert*-butyldimethylsilyl)oxy)-6-methoxy-1-indanone (**246**) (0.507 g, 1.73 mmol, 1.0 eq.) in methanol (50 mL) over 45 min at 40-45 °C. The mixture was stirred for 30 min before a solution of 1-benzylpiperidine-4-carbaldhyde (**28**) (0.424 g, 2.08 mmol, 1.2 eq.) in methanol (10 mL) was added dropwise and was stirred for 2 h. The solution was cooled to rt after which time the solvent was evaporated *in vacuo* and distilled water (50 mL) was added. The water solution was extracted with dichloromethane (3x30 mL), the organic fraction was separated, washed with distilled water (2x30 mL), dried (sodium sulphate), filtered and evaporated *in vacuo*. The crude material was purified using column chromatography (pre-prepared/basified silica and 10 % MeOH : DCM). NMR indicated deprotection of the protected indanone and not product formation.

Attempt 2:

A solution of Imidazole (0.708 g, 10.41 mmol, 6.8 eq.) in dry acetonitrile (10 mL) was added dropwise to a solution of 5-((*tert*-butyldimethylsilyl)oxy)-6-methoxy-1-indanone (**246**) (0.502 g, 1.72 mmol, 1.2 eq.) in dry acetonitrile (50 mL) under a argon atmosphere at 40-50 °C and stirred for 30 min. A solution of 1-benzylpiperidin-4-carbaldehyde (**28**) (0.313 g, 1.54 mmol, 1.0 eq.) in dry acetonitrile (10 mL) was added dropwise and was stirred for 12 h at 40-50 °C. A solution of potassium-*tert*-butoxide in *tert*-butanol (5 mL) was added dropwise and stirred for 12 h. The solvent was evaporated *in vacuo* and distilled water (50 mL) and dichloromethane (50 mL) was added and the organic fraction was separated, washed with distilled water (2x30 mL), dried (sodium sulphate), filtered and evaporated *in vacuo*. NMR analysis of the crude material indicated no product formation.

7.3.2.1.7 (*E*)-2-((1-benzylpiperidin-4-yl)methylene)-5,6-dihydroxy-2,3-dihydro-1*H*-inden-1-one (**Z**)[126]

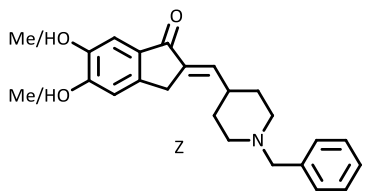

A solution of boron tribromide (2.50 mL, 25.95 mmol, 3.3 eq.) in dry dichloromethane (10 mL) was added dropwise to a solution of (*E*)-2-((1-benzylpiperidin-4-yl)methylene)-5,6-dimethoxy-2,3-dihydro-1*H*-inden-1-one (**27**) (2.939 g, 7.79 mmol, 1.0 eq) in dry dichloromethane (25 mL) under an argon atmosphere at - 40 °C. The reaction mixture was stirred for 12 h at rt after which time an ice/water

© University of Pretoria

mixture (50 mL) was added and the aqueous layer were separated and the water was blown off over 48 h. The crude material was purified using column chromatography (pre-prepared/basified silica MeOH), unfortunately no product formation was observed.

7.3.2.2 C-Silylated scaffolds

7.3.2.2.1 6-Bromo-2,3-dihydro-1*H*-inden-1-one (**251**)[104]

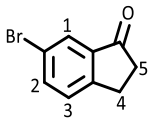

251

1-Indanone (**250**) (5.049 g, 38.20 mmol, 1.0 eq.) and aluminium trichloride (16.788 g, 125.90 mmol, 3.3 eq.) was mixed to form a homogenous mixture and was heated to 110 °C for 30 min. Liquid bromine (3.00 mL, 58.24 mmol, 1.5 eq.) was added dropwise and the reaction mixture was stirred for 1 h. The reaction mixture was cooled to rt after which time an ice-water mixture (100 mL) was added and extracted with diethyl ether (5x30 mL). The organic fraction was washed with distilled water (3x30 mL), a saturated sodium bicarbonate solution (3x30 mL) and a saturated sodium sulphate solution (3x30 mL). The organic fraction was separated, dried (sodium sulphate), filtered and evaporated *in vacuo*. The crude material was purified using column chromatography (1:9 EtOAc : hexane), to afford 6-bromo-2,3-dihydro-1*H*-inden-1-one (**251**) (0.953 g, 12 %) as a red brick solid. $\mathbf{R_f}$ = 0.75 (1:1 EtOAc : hexane); **mp** 105-106 °C; **^{1}H NMR (400 MHz, Chloroform-*d*)**; δ 7.87 (d, *J* = 1.9 Hz, 1H, H-1), 7.68 (dd, *J* = 8.2, 1.9 Hz, 1H, H-2), 7.36 (d, *J* = 8.1 Hz, 1H, H-3), 3.15 – 3.05 (m, 2H, H-5), 2.77 – 2.67 (m, 2H, H-4); **^{13}C NMR (101 MHz, $CDCl_3$)**; δ 205.50 (C=O), 153.71 (quaternary Ar-C), 139.07 (quaternary Ar-C), 137.47 (C-2), 128.39 (C-3), 126.89 (C-1), 121.70 (quaternary Ar-C), 36.63 (C-4), 25.64 (C-5); **υ_{max} (neat)/cm^{-1}** 2920, 2852, 1699 (conjugated C=O stretching), 1433, 1245, 1183, 1108, 827, 661 (C-Br stretching); **MS HRMS m/z (ESI)** data was inconsistent.

© University of Pretoria

7.3.2.2.2 6-(Trimethylsilyl)-2,3-dihydro-1*H*-inden-1-one (**252**)[105]

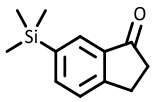

252

A 1.6 M n-butyl lithium solution (1.70 mL, 2.72 mmol, 1.4 eq.) in hexane was added to a crude solution of 6-bromo-1-indanone (**251**) (0.417 g, 1.97 mmol, 1.0 eq.) in dry tetrahydrofuran (30 mL) under an argon atmosphere at -78 °C. The solution was stirred for 30 min before chlorotrimethylsilane (0.40 mL, 3.15 mmol, 1.6 eq.) was added and stirred for 1 h at -78 °C. The reaction mixture was heated up to rt thereafter, the solvent was evaporated *in vacuo*. The reaction mixture was dissolved in dichloromethane (30 mL), washed with distilled water (3x10 mL), dried (sodium sulphate), filtered and evaporated *in vacuo*. NMR analysis of the crude material did not indicate that the desired product was formed.

7.3.3 Benzyl moiety derivatization:

7.3.3.1 Donepezil synthesis route:

7.3.3.1.1 Ethyl 1-(2-chlorobenzyl)piperidine-4-carboxylate (**261**)[53]

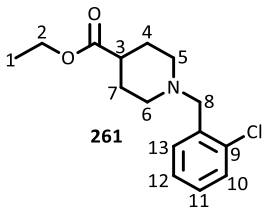

261

A solution of ethyl isonipecotate (**32**) (5.00 mL, 32.44 mmol, 1.0 eq.), triethylamine (13.00 mL, 93.27 mmol, 2.9 eq.) and 2-chlorobenzyl chloride (**259**) (4.80 mL, 37.98 mmol, 1.2 eq.) in dry acetonitrile (40 mL) under an argon atmosphere was refluxed for 3 h. The reaction mixture was evaporated *in vacuo* and dissolved in ethyl acetate (50 mL) and washed with a 3 M sodium hydroxide solution (4x40 mL) and distilled water (3x20 mL). The organic fraction was separated, dried (sodium sulphate), filtered and evaporated *in vacuo*, to afford ethyl 1-(2-chlorobenzyl)piperidine-4-carboxylate (**261**) (9.257 g, 101 %) as a transparent orange oil, which was uses as is without further purification. $\mathbf{R_f}$ = 0.54 (1:3 EtOAc : hexane); **^{1}H NMR (400 MHz, Chloroform-*d*)**; δ 7.48 (dd, *J* = 7.5, 1.8 Hz, 1H, H-10), 7.32 (d, *J* =

© University of Pretoria

7.8, 1.5 Hz, 1H, H-13), 7.21 (t, *J* = 7.5, 1.5 Hz, 1H, H-12)^, 7.16 (t, *J* = 7.6, 1.9 Hz, 1H, H-11)^, 4.12 (q, *J* = 7.1 Hz, 2H, H-2), 3.59 (s, 2H, H-8), 2.88 (dt, *J* = 11.3, 3.9 Hz, 2H, H-5)*, 2.35 – 2.23 (m, 1H, H-3), 2.13 (t, *J* = 11.4, 2.7 Hz, 2H, H-6)*, 1.94 – 1.84 (m, 2H, H-4)*, 1.84 – 1.71 (m, 2H, H-7)*, 1.24 (t, *J* = 7.1 Hz, 3H, H-1); **^{13}C NMR (101 MHz, $CDCl_3$)**; δ 175.34 (C=O), 136.29 (quaternary Ar-C), 134.24 (quaternary Ar-C), 130.59 (C-10), 129.44 (C-13), 128.07 (C-11)>, 126.69 (C-12)>, 60.37 (C-2), 59.46 (C-8), 53.14 (C-5 & C-6)<, 41.25 (C-3), 28.47 (C-4 & C-7)<, 14.34 (C-1); **υ_{max} (neat)/cm^{-1}** 2945, 2803, 2761, 1728 (C=O stretching), 1443, 1259 (C-N stretching), 1170 (ester C-O stretching), 1045, 751; **MS HRMS m/z (ESI)** calculated for ($C_{15}H_{20}NO_2Cl$): 282.1255, found: [M + H] 282.127. ^ These assignments may be interchangeable. * These assignments may be interchangeable. > These assignments may be interchangeable. < These assignments may be interchangeable.

7.3.3.1.2 Ethyl 1-(4-chlorobenzyl)piperidin-4-carboxylate (**262**)[53]

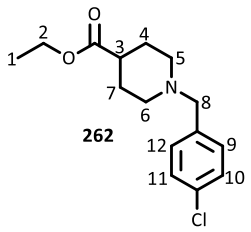

262

A solution of ethyl isonipecotate (**32**) (5.00 mL, 32.44 mmol, 1.0 eq.), triethylamine (13.00 mL, 93.27 mmol, 3.0 eq.) and 4-chlorobenzyl chloride (**260**) (6.192 g, 38.45 mmol, 1.2 eq.) in dry acetonitrile (40 mL) under an argon atmosphere was reflux for 3 h. The solvent was evaporated *in vacuo* and the reaction mixture was dissolved in ethyl acetate (50 mL) and washed with a 3 M sodium hydroxide solution (4x40 mL) and distilled water (3x20 mL). The organic fraction was separated, dried (sodium sulphate), filtered and evaporated *in vacuo*, to afford ethyl 1-(4-chlorobenzyl)piperidin-4-carboxylate (**262**) (8.448 g, 92 %) as a transparent orange oil, which was used as is without further purification. **R_f** = 0.33 (1:3 EtOAc : hexane); **^{1}H NMR (400 MHz, Chloroform-*d*)**; δ 7.33 – 7.19 (m, 4H, Ph), 4.13 (q, *J* = 7.1 Hz, 2H, H-2), 3.45 (s, 2H, H-8), 2.82 (d, *J* = 11.5, 3.8 Hz, 2H, H-5)*, 2.35 – 2.20 (m, 1H, H-3), 2.02 (t, *J* = 11.6, 2.4 Hz, 2H, H-6)*, 1.94 – 1.82 (m, 2H, H-4)*, 1.82 – 1.67 (m, 2H, H-7)*, 1.25 (t, *J* = 7.1 Hz, 3H, H-1); **^{13}C NMR (101 MHz, $CDCl_3$)**; δ 175.28 (C=O), 137.13 (quaternary Ar-C), 132.74 (quaternary Ar-C), 130.38 (C-10 & C-11), 128.44 (C-9 & C-12), 62.53 (C-8), 60.39 (C-2), 52.98 (C-5 & C-6)^, 41.24 (C-3), 28.37 (C-4 & C-7)^, 14.33 (C-1); **υ_{max} (neat)/cm^{-1}** 2945, 2799, 2760, 1728 (C=O stretching), 1488, 1371, 1259 (C-N stretching), 1169 (ester C-O stretching), 1090, 1047, 810; **MS HRMS m/z (ESI)** calculated for ($C_{15}H_{20}NO_2Cl$): 282.1255, found: [M + H] 282.127. * These assignments may be interchangeable. ^ These assignments may be interchangeable.

© University of Pretoria

7.3.3.1.3 (1-(2-Chlorobenzyl)piperidin-4-yl)methanol (**263**)[53]

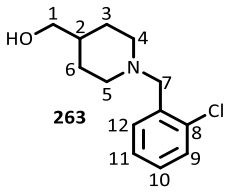

263

Red-Al 60 % (21.10 mL, 64.88 mmol, 2.0 eq.) was added dropwise to a solution of ethyl 1-(2-chlorobenzyl)piperidine-4-carboxylate (**261**) (9.141 g, 32.44 mmol, 1.0 eq.) in dry dichloromethane (50 mL) under an argon atmosphere at 15-20 °C and stirred for 3 hours at rt. The reaction mixture was quenched with a 10 % sodium hydroxide solution and diluted with distilled water (40 mL) and a saturated sodium sulphate solution (15 mL). The reaction mixture was stirred for 45 min after which time the organic fraction was separated, washed with distilled water (3x20 mL) and a saturated sodium sulphate solution (3x20 mL). The organic fraction was separated, dried (sodium sulphate), filtered and evaporated *in vacuo,* to afford (1-(2-chlorobenzyl)piperidin-4-yl)methanol (**263**) (6.8513 g, 88 %) as a transparent orange oil, which was used as is without further purification. **R_f** = 0.25 (3:1 EtOAc : hexane); **^{1}H NMR (400 MHz, Chloroform-*d*)**; δ 7.48 (dd, *J* = 7.6, 1.8 Hz, 1H , H-9), 7.33 (dd, *J* = 7.8, 1.5 Hz, 1H, H-12), 7.23 (td, *J* = 7.5, 1.5 Hz, 1H, H-11)^, 7.17 (td, *J* = 7.6, 1.9 Hz, 1H, H-10)^, 3.61 (s, 2H, H-7), 3.48 (d, *J* = 6.5 Hz, 2H, H-1), 2.93 (d, *J* = 12.3, 3.8 Hz, 2H, H-4)*, 2.08 (td, *J* = 11.7, 2.5 Hz, 2H, H-5)*, 1.85 (s, 1H, O-H), 1.71 (d, 2H, H-3)*, 1.58 – 1.44 (m, 1H, H-2), 1.37 – 1.22 (m, 2H, H-6)*; **^{13}C NMR (101 MHz, $CDCl_3$)**; δ 136.19 (quaternary Ar-C), 134.33 (quaternary Ar-C), 130.82 (C-9), 129.41 (C-12), 128.07 (C-11)>, 126.64 (C-10)>, 67.77 (C-1), 59.58 (C-7), 53.62 (C-4 & C-5)<, 38.52 (C-2), 28.89 (C-3 & C-6)<; **υ_{max} (neat)/cm^{-1}** 3330 (O-H stretching), 2915, 2803, 1740, 1441, 1367, 1138, 1041, 999, 749; **MS HRMS m/z (ESI)** calculated for ($C_{13}H_{18}NOCl$): 240.1150, found: [M + H] 240.117. ^ These assignments may be interchangeable. * These assignments may be interchangeable. > These assignments may be interchangeable. < These assignments may be interchangeable.

© University of Pretoria

7.3.3.1.4 (1-(4-chlorobenzyl)piperidin-4-yl)methanol (**264**)[53]

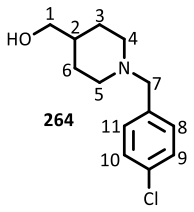

264

Red-Al 60 % (19.50 mL, 59.96 mmol, 2.0 eq.) was added dropwise to a solution of ethyl 1-(4-chlorobenzyl)piperidine-4-carboxylate (**262**) (8.448 g, 29.98 mmol, 1.0 eq.) in dry dichloromethane (50 mL) under an argon atmosphere at 15-20 °C and stirred for 3 h. The reaction mixture was heated up to rt and then quenched with a 10 % sodium hydroxide solution and diluted with distilled water (40 mL) and a saturated sodium sulphate solution (15 mL). The reaction mixture was stirred for 45 min and the organic fraction was separated, washed with distilled water (3x20 mL) and a saturated sodium sulphate solution (3x20 mL). The organic fraction was dried (sodium sulphate), filtered and evaporated *in vacuo,* to afford (1-(4-chlorobenzyl)piperidin-4-yl)methanol (**264**) (6.509 g, 91 %) as a transparent orange oil, which was used as is without further purification. $\mathbf{R_f}$ = 0.12 (3:1 EtOAc : hexane); **^{1}H NMR (400 MHz, Chloroform-*d*)**; δ 7.32 – 7.14 (m, 4H, Ph), 3.53 – 3.39 (m, 4H, H-1 & H-7), 2.88 (d, *J* = 11.8, 3.4 Hz, 2H, H-4)*, 2.77 (s, 1H, O-H), 1.95 (t, *J* = 11.7, 2.6 Hz, 2H, H-5)*, 1.71 (d, *J* = 13.2, 4.6, 2.5 Hz, 2H, H-3)*, 1.55 – 1.41 (m, 1H, H-2), 1.27 (qd, *J* = 12.1, 3.9 Hz, 2H, H-6)*; **^{13}C NMR (101 MHz, $CDCl_3$)**; δ 136.81 (quaternary Ar-C), 132.73 (quaternary Ar-C), 130.63 (C-9 & C-10), 128.35 (C-8 & C-11), 67.59 (C-1), 62.70 (C-7), 53.43 (C-4 & C-5)^, 38.48 (C-2), 28.77 (C-3 & C-6)^; **υ_{max} (neat)/cm^{-1}** 3333 (O-H stretching), 2916, 2805, 1741, 1489, 1368, 1088, 1041, 911, 806, 729; **MS HRMS m/z (ESI)** calculated for ($C_{13}H_{18}NOCl$): 240.1150, found: [M + H] 240.116. * These assignments may be interchangeable. ^ These assignments may be interchangeable.

7.3.3.1.5 1-(2-Chlorobenzyl)piperidine-4-carbaldehyde (**265**)[53]

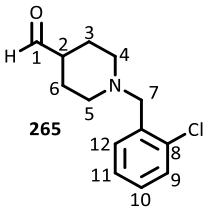

265

A solution of dimethyl sulfoxide (1.00 mL, 14.16 mmol, 3.0 eq.) in dry dichloromethane (20 mL) was added dropwise to a solution of oxalyl chloride (0.60 mL, 7.08 mmol, 1.5 eq.) in dry dichloromethane

© University of Pretoria

(20 mL) under an argon atmosphere at -78 °C and was stirred for 30 min. A solution of (1-(2-chlorobenzyl-piperidin-4-yl) methanol (**263**) (1.131 g, 4.72 mmol, 1.0 eq.) in dry dichloromethane (10 mL) was added dropwise and stirred for 30 min at -78 °C. Triethylamine (3.30 mL, 23.60 mmol, 5.0 eq.) was added dropwise and stirred for 30 min at -78 °C. The reaction mixture was warmed up to rt after which time distilled water (150 mL) was added. The organic fraction was separated, washed with a saturated sodium sulphate solution (3x50 mL), dried (sodium sulphate), filtered and evaporated *in vacuo,* to afford 1-(2-chlorobenzyl)piperidine-4-carbaldehyde (**265**) (0.926 g, 83 %) as an orange oil, which was used as is without further purification **R_f =** 0.57 (3:1 EtOAc : hexane); **^{1}H NMR (400 MHz, Chloroform-*d*)**; δ 9.65 (s, 1H, H-1), 7.45 (dd, *J* = 7.5, 1.9 Hz, 1H, H-9), 7.33 (dd, *J* = 7.8, 1.5 Hz, 1H, H-12), 7.22 (td, 1H, H-11)^, 7.17 (td, 1H, H-10)^, 3.60 (s, 2H, H-7), 2.90 – 2.80 (m, 2H, H-4)*, 2.30 – 2.16 (m, 3H, H-5 & H-2)*, 1.93 – 1.83 (m, 2H, H-3)*, 1.76 – 1.62 (m, 2H, H-6)*; **^{13}C NMR (101 MHz, $CDCl_3$)**; δ 204.08 (C-1), 136.11 (quaternary Ar-C), 134.29 (quaternary Ar-C), 130.64 (C-9), 129.48 (C12), 128.17 (C-11)>, 126.70 (C-10)>, 59.46 (C-7), 52.69 (C-4 & C-5)<, 48.01 (C-2), 25.59 (C-3 & C-6)<; **υ_{max} (neat)/cm^{-1}** 2941, 2804 (aldehyde C-H stretching), 1722 (C=O stretching), 1443, 1365, 1341, 1260, 1141, 1037, 966, 751, 684; **MS HRMS m/z (ESI)** calculated for ($C_{13}H_{16}NOCl$): [M + H] 238.0993, [M + CH_3OH + H] 270.1255, found: [M + H] 238.100, [M + CH_3OH + H] 270.127. ^ These assignments may be interchangeable. * These assignments may be interchangeable. > These assignments may be interchangeable. < These assignments may be interchangeable.

7.3.3.1.6 1-(4-Chlorobenzyl)piperidine-4-carbaldehyde (**266**)[53]

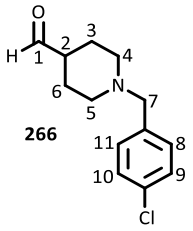

266

A solution of dimethyl sulfoxide (1.00 mL, 14.08 mmol, 2.9 eq.) in dry dichloromethane (20 mL) was added dropwise to a solution of oxalyl chloride (0.60 mL, 7.09 mmol, 1.5 eq.) in dry dichloromethane (20 mL) under an argon atmosphere at -78 °C and was stirred for 30 min. A solution of (1-(4-chlorobenzyl-piperidin-4-yl) methanol (**264**) (1.154 g, 4.81 mmol, 1.0 eq.) in dry dichloromethane (10 mL) was added dropwise at -78 °C and stirred for 30 min. Triethylamine (3.40 mL, 24.39 mmol, 5.1 eq.) was added dropwise at -78 °C and stirred for 30 min. The reaction mixture was heated up to rt and then diluted with distilled water (150 mL) and the organic fraction was separated and washed with a saturated sodium sulphate solution (3x50 mL). The organic fraction was dried (sodium sulphate),

© University of Pretoria

filtered and evaporated *in vacuo,* to afford 1-(4-chlorobenzyl)piperidine-4-carbaldehyde (**266**) (0.726 g, 63 %) as an orange oil, which was used as is without further purification. $\mathbf{R_f}$ = 0.33 (3:1 EtOAc : hexane); **^{1}H NMR (300 MHz, Chloroform-*d*)**; δ 9.66 (s, 1H, H-1), 7.32 – 7.23 (m, 4H, Ph), 3.47 (s, 2H, H-7), 2.80 (m, 2H, H-4)*, 2.34 – 2.18 (m, 1H, H-2), 2.11 (t, *J* = 11.0, 2.9 Hz, 2H, H-5)*, 1.95 – 1.84 (m, 2H, H-3)*, 1.76 – 1.61 (m, 2H, H-6)*; **^{13}C NMR (101 MHz, $CDCl_3$)**; δ 203.91 (C-1), 137.10 (quaternary Ar-C), 132.88 (quaternary Ar-C), 130.38 (C-9 & C-10), 128.51 (C-8 & C-11), 62.55 (C-7), 52.60 (C-4 & C-5)^, 48.05 (C-2), 25.61 (C-3 & C-6)^; **υ_{max} (neat)/cm^{-1}** 2940, 2805 (aldehyde C-H stretching), 1722 (C=O stretching), 1489, 1445, 1365, 1339, 1260, 1086, 1014, 966, 800, 666, 496; **MS HRMS m/z (ESI)** calculated for ($C_{13}H_{16}NOCl$): [M + H] 238.0993, [M + CH_3OH + H] 270.1255, found: [M + H] 238.101, [M + CH_3OH + H] 270.126. * These assignments may be interchangeable. ^ These assignments may be interchangeable.

7.3.3.1.7 (*E*)-2-((1-(2-chlorobenzyl)piperidin-4-yl)methylene)-5,6-dimethoxy-2,3-dihydro-1*H*-inden-1-one (**267**)[53]

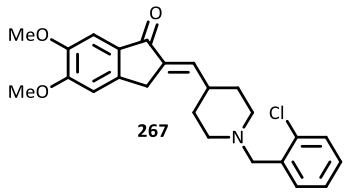

267

A solution of sodium hydroxide (0.874 g, 21.86 mmol, 5.1 eq.) in methanol and water (25 mL, 4:1) was added dropwise to a solution of 5,6-dimethoxy-1-indanone (**29**) (0.995 g, 5.18 mmol, 1.2 eq.) in methanol (10 mL) over 45 min at 40-45 °C. The reaction mixture was stirred for 30 min and before a solution of 1-(2-chlorobenzyl)piperidine-4-carbaldhyde (**265**) (0.780 g, 3.84 mmol, 1.0 eq.) in methanol (10 mL) was added dropwise and stirred for 2 h 40-45 °C. The solvent was evaporated *in vacuo* and distilled water (50 mL) was added and stirred for 30 min. Dichloromethane (50 mL) was added to the reaction mixture and the organic fraction was separated, washed with distilled water (2x30 mL) and a saturated sodium sulphate solution (3x30 mL). The organic fraction was separated, dried (sodium sulphate), filtered and evaporated *in vacuo*. The crude mixture was purified using column chromatography (1:9 MeOH : DCM). NMR analysis of the column fraction did not indicate the desired product.

© University of Pretoria

7.3.3.1.8 (*E*)-2-((1-(4-chlorobenzyl)piperidin-4-yl)methylene)-5,6-dimethoxy-2,3-dihydro-1*H*-inden-1-one (**268**)[53]

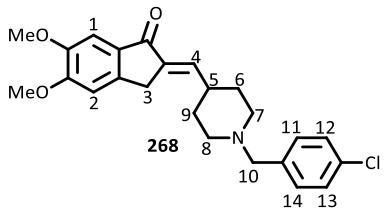

A sodium hydroxide solution (0.892 g, 22.31 mmol, 7.3 eq.) in methanol and water (25 mL, 4:1) was added dropwise to a solution of 5,6-dimethoxy-1-indanone (**29**) (0.726 g, 3.05 mmol, 1.0 eq.) in methanol (10 mL) over 45 min at 40-45 °C. The reaction mixture was stirred for 30 min before a solution of 1-(4-chlorobenzyl)piperidine-4-carbaldhyde (**266**) (0.712 g, 3.70 mmol, 1.2 eq.) in methanol (10 mL) was added dropwise and stirred for 2 h at 40-45 °C. The solution was cooled to rt after which time the precipitate was filtered off and washed with cold methanol (2x10 mL) and put aside. The solvent was evaporated in *vacuo* and distilled water (50 mL) was added. The reaction mixture was stirred for 30 min and dichloromethane (50 mL) was added to the solution and the organic fraction was separated, washed with distilled water (2x30 mL), a saturated sodium sulphate solution (3x30 mL), dried (sodium sulphate), filtered and evaporated *in vacuo*. The crude material was purified using column chromatography (5% MeOH : DCM), to afford (*E*)-2-((1-(4-chlorobenzyl)piperidin-4-yl)methylene)-5,6-dimethoxy-2,3-dihydro-1*H*-inden-1-one (**268**) (0.535 g, 43 %) as beige solid. **R_f** = 0.44 (5% MeOH : DCM); **mp** 162-164 °C; **^{1}H NMR (400 MHz, Chloroform-*d*)**; δ 7.31 – 7.25 (m, 6H, Ph & H-2)$^<$, 6.90 (s, 1H, H-1)$^<$, 6.66 (d, *J* = 9.6, 2.0 Hz, 1H, H-4), 3.98 (s, 3H, O-CH_3), 3.93 (s, 3H, O-CH_3), 3.59 (s, 2H, H-3), 3.48 (s, 2H, H-10), 2.89 (d, *J* = 11.7, 3.6 Hz, 2H, H-7)*, 2.41 – 2.26 (m, 1H, H-5), 2.05 (td, *J* = 11.4, 2.7 Hz, 2H, H-8)*, 1.76 – 1.60 (m, 4H, H-6 & H-9)*; **^{13}C NMR (101 MHz, $CDCl_3$)**; δ 192.73 (C=O), 155.44 (quaternary Ar-C), 149.64 (quaternary Ar-C), 144.63 (quaternary Ar-C), 139.84 (C-4), 137.01 (quaternary Ar-C), 135.81 (quaternary Ar-C), 132.81 (quaternary Ar-C), 131.99 (quaternary Ar-C), 130.53 (C-12 & C-13), 128.48 (C-11 & C-14), 107.35 (C-1)$^'$, 105.16 (C-2)$^'$, 62.83 (C-10), 56.39 (O-CH_3), 56.29 (O-CH_3), 53.17 (C-7 & C-8)$^$, 37.34 (C-5), 31.35 (C-6 & C-9)$^$, 29.63 (C-3); **υ_{max} (neat)/cm^{-1}** 2921, 2787, 2762, 1689 conjugated (C=O stretching), 1643 (conjugated C=C stretching), 1603, 1584, 1500, 1313, 1218, 1078, 979 (*trans* C=C bending), 805, 764, 602, 459; **MS HRMS m/z (ESI)** calculated for ($C_{24}H_{26}NO_3Cl$): 412.1674, found: [M + H] 412.172. $^<$ These assignments may be interchangeable. * These assignments may be interchangeable. $^'$ These assignments may be interchangeable. $^$ These assignments may be interchangeable.

© University of Pretoria

7.3.3.1.9 (*E*)-5,6-dimethoxy-2-((1-(4-(trimethylsilyl)benzyl)piperidin-4-yl)methylene)-2,3-dihydro-1*H*-inden-1-one (**269**)[105]

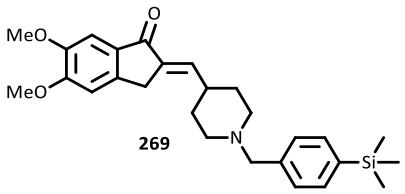

269

A 1.6 M n-butyl lithium solution (0.60 mL, 0.96 mmol, 2.0 eq.) in hexane was added to a solution of (*E*)-2-((1-(4-chlorobenzyl)piperidin-4-yl)methylene)-5,6-dimethoxy-2,3-dihydro-1*H*-inden-1-one (**268**) (0.201 g, 0.49 mmol, 1.0 eq.) in dry tetrahydrofuran (30 mL) under an argon atmosphere at -78 °C. The solution was stirred for 30 min before chlorotrimethylsilane (0.10 mL, 0.79 mmol, 1.6 eq.) was added and stirred for 1 h at -78 °C. The reaction mixture was heated to rt and the solvent was evaporated *in vacuo* and the mixture was dissolved in dichloromethane (30 mL) and washed with distilled water (3x10 mL). The organic fraction was dried (sodium sulphate), filtered and evaporated *in vacuo*. NMR analysis of the crude material did not indicate product formation.

7.3.3.1.10 (*E*)-5,6-dimethoxy-2-((1-(4-(triethylsilyl)benzyl)piperidin-4-yl)methylene)-2,3-dihydro-1*H*-inden-1-one (**270**)[105]

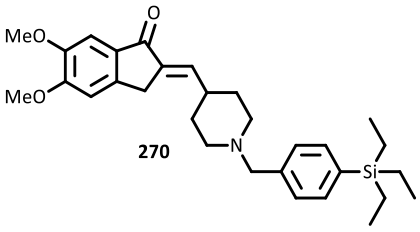

270

A 1.6 M n-butyl lithium solution (0.25 mL, 0.40 mmol, 1.3 eq.) in hexane was added to a solution of (*E*)-2-((1-(4-chlorobenzyl)piperidin-4-yl)methylene)-5,6-dimethoxy-2,3-dihydro-1*H*-inden-1-one (**268**) (0.133 g, 0.32 mmol, 1.0 eq.) in dry tetrahydrofuran (30 mL) under an argon atmosphere at -78 °C. The reaction mixture was stirred for 30 min before chlorotriethylsilane (0.60 mL, 3.57 mmol, 11.00 eq.) was added and stirred for 1 h at -78 °C. The reaction mixture was heated to rt and the solvent was evaporated *in vacuo* and the mixture was dissolved in dichloromethane (15 mL) and washed with distilled water (3x10 mL). The organic fraction was dried (sodium sulphate), filtered and evaporated *in vacuo*. NMR analysis of the crude material did not indicate product formation.

© University of Pretoria

7.3.3.2 C-silylation of halo-toluenes

7.3.3.2.1 T*ert*-butyldiphenyl(*p*-tolyl)silane (**272**)

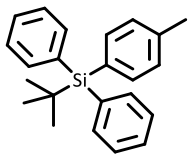

272

Attempt 1:[117]

A 3.8 M n-butyl lithium solution (1.20 mL, 4.61 mmol, 1.1 eq.) in hexane was added dropwise to a solution of 4-chlorotoluene (0.50 mL, 4.26 mmol, 1.0 eq.) in dry tetrahydrofuran (30 mL) under an argon atmosphere and was stirred for 30 min at -72 °C. *Tert*-butyl(chloro)diphenylsilane (8.00 mL, 8.00 mmol, 1.9 eq.) was added and was stirred for 30 min. Distilled water (50 mL) was added to the solution and stirred for 12 h. The organic layer was separated, and the aqueous layer was extract with dichloromethane (40 mL) and the combined organic layers was washed with distilled water (3x30 mL). The organic fraction was dried (sodium sulphate), filtered and evaporated *in vacuo*. No product formation was observed, formation of the silanol was observed via ^{13}C NMR.

Attempt 2:[118]

A 1.5 M n-butyl lithium solution (2.00 mL, 3.00 mmol, 1.4 eq.) in hexane was added dropwise to a solution of 4-chlorotoluene (0.25 mL, 2.11 mmol, 1.0 eq.) in dry tetrahydrofuran (30 mL) under an argon atmosphere and was stirred for 30 min at -72 °C. *Tert*-butyl(chloro)diphenylsilane (0.66 mL, 2.54 mmol, 1.2 eq.) was added and the solution was left to stir for 20 min. The reaction mixture was heated to rt and stirred for 6 h. A saturated ammonium chloride solution (30 mL) was added and stirred for 12 h. The organic layer was separated and the aqueous layer was extract with dichloromethane (40 mL) and the combined organic layers was washed with distilled water (3x30 mL), dried (sodium sulphate), filtered and evaporated *in vacuo*. NMR analysis of the crude material indicated no product formation.

Attempt 3:[118]

A 1.5 M n-butyl lithium solution (2.00 mL, 3.00 mmol, 1.4 eq.) in hexane was added dropwise to a solution of 4-chlorotoluene (0.25 mL, 2.11 mmol, 1.0 eq.) in dry diethyl ether (30 mL) under an argon atmosphere and was stirred for 30 min at -72 °C. *Tert*-butyl(chloro)diphenylsilane (0.66 mL, 2.54 mmol, 1.2 eq.) was added and the solution was stirred for 20 min. The reaction mixture was heated

© University of Pretoria

to rt and stirred for 6 h. A saturated ammonium chloride solution (30 mL) was added and stirred for 12 h. The organic layer was separated and the aqueous layer was extract with dichloromethane (40 mL) and the combined organic layers was washed with distilled water (3x30 mL). The organic fraction was dried (sodium sulphate), filtered and evaporated *in vacuo*. NMR analysis of the crude material indicated no product formation.

7.3.3.2.2 Trimethyl(*p*-tosyl)silane (**273**)

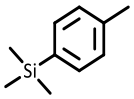

273

Attempt 1:[117]

A solution of 4-chlorotoluene (0.20 mL, 1.69 mmol, 1.0 eq.) and magnesium metal (0.140 g, 5.71 mmol, 3.4 eq.) in dry diethyl ether (20 mL) under an argon atmosphere was stirred at rt for 2 h. Chlorotrimethylsilane (0.26 mL, 2.03 mmol, 1.2 eq.) was added and the reaction mixture was stirred for 12 h at rt. Distilled water (50 mL) was added to the reaction mixture and the organic fraction was separated. The aqueous fraction was extracted with ethyl acetate (30 mL) and the combine organic fractions were washed with distilled water (2x30 mL), dried (sodium sulphate), filtered and evaporated *in vacuo*. NMR analysis of the crude material indicated no product formation.

Attempt 2:[119]

A solution of 4-chlorotoluene (0.20 mL, 1.69 mmol, 1.0 eq.), magnesium metal (0.149 g, 6.15 mmol, 3.6 eq.) and chlorotrimethylsilane (0.26 mL, 2.05 mmol, 1.2 eq.) in dry tetrahydrofuran (30 mL) under an argon atmosphere was refluxed for 12 h. Distilled water (50 mL) was added and the organic fraction was separated. The aqueous fraction was extracted with ethyl acetate (30 mL) and the combine organic fractions were washed with distilled water (2x30 mL), dried (sodium sulphate), filtered and evaporated *in vacuo*. NMR analysis of the crude material indicated no product formation.

Attempt 3:[118]

A 1.5 M n-butyl lithium solution (2.00 mL, 3.00 mmol, 1.4 eq.) in hexane was added dropwise to a solution of 4-chlorotoluene (0.25 mL, 2.11 mmol, 1.0 eq.) in dry tetrahydrofuran (30 mL) under an argon atmosphere and was stirred for 30 min at -72 °C. Chlorotrimethylsilane (0.40 mL, 3.15 mmol, 1.5 eq.) was added and the solution was stirred for 20 min. The reaction mixture was heated to rt and stirred for 12 h. A saturated ammonium chloride (35 mL) solution was added and stirred for 12 h. The

© University of Pretoria

organic layer was separated and the aqueous layer was extract with dichloromethane (40 mL) and the combined organic layers was washed with distilled water (3x30 mL), dried (sodium sulphate), filtered and evaporated *in vacuo*. NMR analysis of the crude material indicated no product formation.

7.3.4 Acetophenone replacement of the indanone moiety:

7.3.4.1 Donepezil acetophenone analogues:

7.3.4.1.1 (*E*)-3-(1-benzylpiperidin-4-yl)-1-(3,4-dimethoxy)prop-2-en-1-one (**274**)[53]

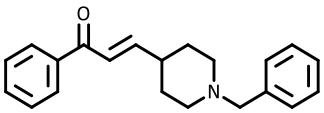

274

A sodium hydroxide solution (0.656 g, 16.39 mmol, 8.3 eq.) in methanol (15 mL) was added dropwise to a solution of acetophenone (**275**) (0.28 ml, 2.40 mmol, 1.2 eq.) in methanol (15 mL) and was stirred for 45 min at 50 °C. A solution of 1-benzylpiperidine-4-carbaldehyde (**28**) (0.401 g, 1.97 mmol, 1 eq.) in methanol (10 ml) was added dropwise and stirred for 12 h at 50 °C. The solvent was evaporated *in vacuo* and the reaction mixture was dissolved in dichloromethane (40 mL), washed with distilled water (3x30 mL), dried (sodium sulphate), filtered ad evaporated *in vacuo*. NMR analysis of the crude material did not indicate the desired product.

7.3.4.1.2 3-(1-Benzylpiperidin-4-yl)-1-phenylpropan-1-one (**276**)

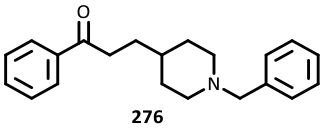

276

Attempt 1:[122]

A solution of (1-benzylpiperidin-4-yl)methanol (**30**) (0.352 g, 1.72 mmol, 1.0 eq.), methanesulfonyl chloride (0.20 mL, 2.58 mmol, 1.5 eq.) and imidazole (0.603 g, 8.86 mmol, 5.2 eq.) in dry dichloromethane (30 mL) under an argon atmosphere was stirred for 30 min at rt. A solution of acetophenone (0.22 mL, 1.89 mmol, 1.1 eq.) in dry dichloromethane (10 mL) was added dropwise and stirred for 12 h at rt. The solution was refluxed for 5 h and distilled water (50 mL) was added and the

© University of Pretoria

organic fraction was separated, washed with distilled water (2x30 mL), dried (sodium sulphate), filtered and evaporated *in vacuo*. NMR analysis of the crude material indicated no product formation.

Attempt 2:

A solution of 1-benzyl-4(chloromethyl)piperidine (**243**) (0.184 g, 0.82 mmol, 1.0 eq.), acetophenone (**275**) (0.12 mL, 1.03 mmol, 1.3 eq.) and potassium carbonate (1.588 g, 11.49 mmol, 11.0 eq.) in dry dichloromethane (30 mL) under an argon atmosphere, was refluxed for 12 h. Distilled water (50 mL) was added and the organic fraction was separated, washed with distilled water (2x30 mL), dried (sodium sulphate), filtered and evaporated *in vacuo*. NMR analysis of the crude material indicated no product formation.

7.3.5.2 β-Diketo linkage:

7.3.5.2.1 1-(4-((*Tert*-butyldiphenylsilyl)oxy)phenyl)ethanone (**279**)

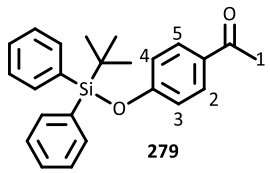

279

A solution of 4'-hydroxyacetophenone (**277**) (4.937 g, 36.28 mmol, 1.0 eq.), triethylamine (15.50 mL, 111.21 mmol, 3.1 eq.) and *tert*-butyl(chloro)diphenylsilane (11.50 mL, 44.22 mmol, 1.2 eq.) in dry dichloromethane (20 mL) under an argon atmosphere was refluxed for 12 h. Distilled water (50 mL) was added to the reaction mixture and the organic fraction was separated and washed with distilled water (3x30 mL). The organic fraction was dried (sodium sulphate), filtered and evaporated *in vacuo*. The crude material was purified using column chromatography (pre-prepared/basified silica and 1:9 EtOAc : hexane), to afford 1-(4-((*tert*-butyldiphenylsilyl)oxy)phenyl)ethenone (**279**) (3.0 g, 22 %) as a white crystalline solid. **R_f** = 0.46, (1:9 EtOAc : hexane); **mp** 110-114 °C; **^{1}H NMR (400 MHz, Chloroform-*d*)**; δ 7.77 – 7.68 (m, 6H, Si-($C_6\underline{H}_5$)$_2$), 7.48 – 7.42 (m, 2H, H-2 & H-5), 7.42 – 7.35 (m, 5H, Si-($C_6\underline{H}_5$)$_2$), 6.83 – 6.77 (m, 2H, H-3 & H-4), 2.48 (s, 3H, H-1), 1.11 (s, 9H, Si-C-($C\underline{H}_3$)$_3$); **^{13}C NMR (101 MHz, $CDCl_3$)**; δ 197.05 (C=O), 160.16 (quaternary Ar-C), 135.53 (Si-($\underline{C}_6H_5$)$_2$), 132.26 (quaternary Ar-C), 130.79 (quaternary Ar-C), 130.45 (C-2 & C-5) 130.30 (Si-($\underline{C}_6H_5$)$_2$), 128.07 Si-($\underline{C}_6H_5$)$_2$), 119.76 (C-3 & C-4), 26.52 (Si-C-($\underline{C}H_3$)$_3$), 26.45 (Si-$\underline{C}$-(CH_3)$_3$), 19.59 (C-1); **υ_{max} (neat)/cm^{-1}** 3068, 2928, 1667 (C=O stretching), 1592, 1503, 1424, 1359, 1250, 1174, 1109 (Si-Ph)[116], 902, 815, 740, 697, 618; **MS HRMS m/z (ESI)** calculated for ($C_{24}H_{26}O_2Si$): 375.1775, found: [M + H] 375.178.

© University of Pretoria

7.3.5.2.2 1-(2-((*Tert*-butyldiphenylsilyl)oxy)phenyl)ethenone (**280**)

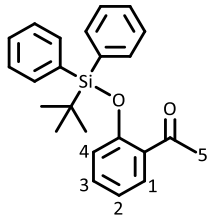

280

A solution of 2'-hydroxyacetophenone (**278**) (4.42 mL, 36.72 mmol, 1.0 eq.), triethylamine (15.50 mL, 111.21 mmol, 3.0 eq.) and *tert*-butyl(chloro)diphenylsilane (11.50 mL, 44.22 mmol, 1.2 eq.) in dry dichloromethane (20 mL) under an argon atmosphere was refluxed for 12 h. Distilled water (50 mL) was added to the reaction mixture and the organic fraction was separated, washed with distilled water (3x30 mL), dried (sodium sulphate) and evaporated *in vacuo*. The crude material was purified using column chromatography (pre-prepared/basified silica and 1:9 EtOAc : hexane), to afford 1-(2-((*tert*-butyldiphenylsilyl)oxy)phenyl)ethenone (**280**) (5.579 g, 41 %) as a white crystalline powder. **R_f** = 0.55 (1:9 EtOAc : hexane); **mp** 82-83 °C; **^{1}H NMR (400 MHz, Chloroform-*d*)**; δ 7.78 – 7.68 (m, 4H, Si-($C_6\underline{H}_5$)$_2$), 7.58 (d, *J* = 7.7, 1.9 Hz, 1H, H-1), 7.48 – 7.42 (m, 2H, Si-($C_6\underline{H}_5$)$_2$), 7.42 – 7.34 (t, 4H, Si-($C_6\underline{H}_5$)$_2$), 6.97 (t, *J* = 7.6, 2.0 Hz, 1H, H-2), 6.88 (t, *J* = 7.4 Hz, 1H, H-3), 6.47 (d, *J* = 8.2 Hz, 1H, H-4), 2.78 (s, 3H, H-5), 1.08 (s, 9H, Si-C-($C\underline{H}_3$)$_3$); **^{13}C NMR (75 MHz, $CDCl_3$)**; δ 201.28 (C=O), 154.36 (quaternary Ar-C), 135.45 (Si-($\underline{C}_6H_5$)$_2$), 132.46 (C-1), 131.99 ((Si-($\underline{C}_6H_5$)$_2$)), 131.10 (C-2), 130.28 (C-3), 129.83 (quaternary Ar-C), 128.12 (Si-($\underline{C}_6H_5$)$_2$), 121.14 (C-4), 120.70 (quaternary Ar-C), 31.90 (Si-$\underline{C}$-(CH_3)$_3$), 26.49 (Si-C-($\underline{C}H_3$)$_3$), 19.43 (C-5); **υ_{max} (neat)/cm^{-1}** 3067, 2931, 2857, 1671 (C=O stretching), 1594, 1477, 1357, 1289, 1234, 1110 (Si-Ph)[116], 902, 750, 700, 615; **MS HRMS m/z (ESI)** calculated for ($C_{24}H_{26}O_2Si$): [M + Na] 397.1594, found: [M + Na] 397.159.

7.3.5.2.3 1-(1-Benzylpiperidin-4-yl)-3-(4-((*tert*-butyldiphenylsilyl)oxy)phenyl)propane-1,3-dione (**281**)[106]

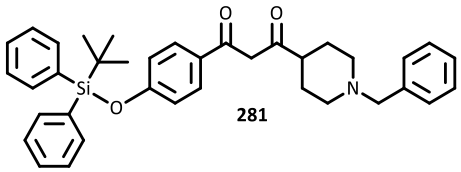

281

A solution of ethyl-1-benzylpiperidine-4-carboxylate (**31**) (1.638 g, 6.62 mmol, 1.2 eq.) in dry dichloromethane (10 mL) was added dropwise to a solution of 1-(4-((*tert*-

© University of Pretoria

butyldiphenylsilyl)oxy)phenyl)ethenone (**279**) (1.983 g, 5.53 mmol, 1.0 eq.) and sodium hydride 60 % (0.230 g, 5.76 mmol, 1.0 eq.) in dry dichloromethane (50 mL) under an argon atmosphere was stirred at rt for 12 h. The reaction was monitored via TLC and no conversion was observed, after which time potassium-*tert*-butoxide (1.37 g, 12.21 mmol, 2.2 eq.) was added to the reaction solution and stirred for 12 h at rt. Distilled water (100 mL) was added and the organic fraction was separated, washed with distilled water (2x30 mL), dried (sodium sulphate), filtered and evaporated *in vacuo*. NMR analysis of the crude material indicated only starting material.

7.3.5.2.4 1-(1-Benzylpiperidin-4-yl)-3-(2-((*tert*-butyldiphenylsilyl)oxy)phenyl)propane-1,3-dione (**282**)[106]

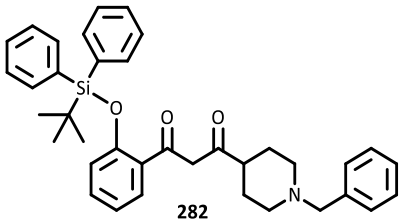

282

A solution of ethyl-1-benzylpiperidine-4-carboxylate (**31**) (4.560 g, 18.44 mmol, 1.2 eq.) in dry dichloromethane (10 mL) was added dropwise to a solution of 1-(2-((*tert*-butyldiphenylsilyl)oxy)phenyl)ethenone (**280**) (5.538 g, 15.45 mmol, 1.0 eq.) and sodium hydride 60 % (0.632 g, 15.81 mmol, 1.0 eq.) in dry dichloromethane (50 mL) under an argon atmosphere and was stirred at rt for 12 h. The reaction was monitored via TLC and no conversion was observed, after which time potassium-*tert*-butoxide (3.67 g, 32.71 mmol, 2.1 eq.) was added to the reaction solution and stirred for 12 h at rt. Distilled water (100 mL) was added and the organic fraction was separated, washed with distilled water (2x30 mL), dried (sodium sulphate) and evaporated *in vacuo*. NMR analysis of the crude material indicated only starting material.

© University of Pretoria

7.3.5.3 Ether-linkages:

7.3.5.3.1 2-Bromo-1-phenylethanone (**283**)[107]

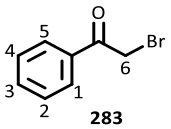

283

Liquid bromine (0.90 mL, 17.57 mmol, 1.0 eq.) was added dropwise to a solution of acetophenone (**275**) (2.00 mL, 17.15 mmol, 1.0 eq.) in dichloromethane (30 mL) and stirred for 12 h at rt. Distilled water (20 mL) was added to the reaction mixture and the organic fraction was separated, washed with distilled water(2x30 mL). Distilled water (100 mL) was added to the organic fraction and was stirred vigorously for an 1 h and then separated, dried (sodium sulphate), filtered and evaporated *in vacuo,* to afford 2-bromo-1-phenylethanone (**283**) (3.098 g, 91 %) as a light green solid, which was used as is without further purification. **R_f** = 0.70 (1:9 EtOAc : hexane); **mp** 49-50 °C; **^{1}H NMR (400 MHz, Chloroform-*d*)**; δ 7.98 (d, 2H, H-1 & H-5), 7.61 (t, 1H, H-3), 7.49 (t, 2H, H-2 & H-4), 4.46 (s, 2H, H-6); **^{13}C NMR (101 MHz, $CDCl_3$)**; δ 191.41 (C=O), 134.11 (quaternary Ar-H), 134.07 (C-3), 129.05 (C-1 & C-5), 128.99 (C-2 & C-4), 31.03 (C-6); **υ_{max} (neat)/cm^{-1}** 3058, 3001, 2950, 1688 (C=O stretching), 1587, 1444, 1389, 1276, 1191, 987, 746, 680 (C-Br stretching), 617; **MS HRMS m/z (ESI)** data was inconsistent.

7.3.5.3.2 (*Z*)-2-((1-benzylpiperidin-4-yl)methoxy)-1-phenylethenol (**284**)

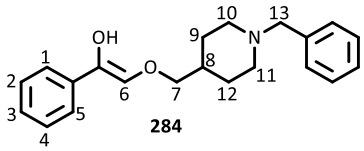

284

A solution of (1-benzylpiperidin-4-yl)methanol (**30**) (0.544 g, 2.65 mmol, 1.1 eq.), potassium carbonate (2.301 g, 16.45 mmol, 6.6 eq.) and 2-bromo-1-phenylethanone (**283**) (0.483 g, 2.43 mmol, 1.0 eq.) in dry dichloromethane (10 mL) under an argon atmosphere was refluxed for 78 h. Distilled water (30 mL) was added and the organic fraction was separated, washed with distilled water (2x30 mL), dried (sodium sulphate) and evaporated *in vacuo*. The crude material was purified using column chromatography (3:1 EtOAc : hexane), to afford (*Z*)-2-((1-benzylpiperidin-4-yl)methoxy)-1-phenylethenol (**284**) (0.019 g, 2 %) as an orange oil. **R_f** = 0.55 (3:1 EtOAc : hexane); **^{1}H NMR (400 MHz, Chloroform-*d*)**; δ 7.88 (d, 2H, H-1 & H-5), 7.47 (t, 1H, H-3), 7.37 (t, *J* = 8.4, 7.0 Hz, 2H, H-2 & H-4), 7.24

© University of Pretoria

– 7.07 (m, 5H, Ph), 4.37 (dd, *J* = 9.6, 4.0 Hz, 1H, H-6), 3.44 (d, *J* = 6.3 Hz, 2H, H-7), 3.27 (dd, *J* = 13.2, 9.7 Hz, 1H, H-13), 3.10 (d, *J* = 13.0, 3.7, 2.9 Hz, 1H, H-10)*, 2.97 (dd, *J* = 13.2, 4.0 Hz, 1H, H-13), 2.84 (d, 1H, H-11)*, 2.57 (td, *J* = 11.5, 2.7 Hz, 1H, H-10)*, 2.27 (td, *J* = 11.5, 2.7 Hz, 1H, H-11)*, 1.89 (s, 1H, O-H), 1.77 (p, *J* = 12.2, 2.9 Hz, 1H, H-9)*, 1.62 (d, *J* = 12.1, 2.8 Hz, 1H, H-12)*, 1.52 – 1.38 (m, 1H, H-8), 1.33 – 1.27 (m, 1H, H-9)*, 1.17 – 1.01 (m, 1H, H-12)*; **^{13}C NMR (101 MHz, $CDCl_3$)**; δ 198.90 (C=O), 139.54 (quaternary Ar-C), 137.66 (quaternary Ar-C), 132.84 (C-3), 129.53 (Ph), 128.64 (Ph), 128.46 (C-1 & C-5), 128.42 (C-2 & C-4), 126.12 (Ph), 70.34 (C-6), 67.94 (C-7), 50.76 (C-10)^, 48.82 (C-11)^, 38.73 (C-8), 31.57 (C-13), 29.61 (C-9)^, 29.26 (C-12)^; **υ_{max} (neat)/cm^{-1}** 3346 (O-H stretching), 2922, 1678 (conjugated C=O stretching), 1598, 1447, 1379, 1225 (C-N stretching), 1036, 941, 745, 694 (cis C=C bending); **MS HRMS m/z (ESI)** calculated for ($C_{21}H_{25}NO_2$): 324.1958, found: [M + H] 324.197. * These assignments may be interchangeable. ^ These may be interchangeable.

7.3.5.3.3 4-Acetylphenylacetate (285)[107]

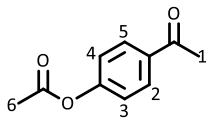

285

Acetic anhydride (5.20 mL, 55.08 mmol, 1.5 eq.) was added to a solution of 4'-hydroxyacetophenone (**277**) (4.995 g, 36.69 mmol, 1.0 eq.) and potassium carbonate (19.787 g, 143.17 mmol, 3.9 eq.) in dry dichloromethane (100 mL) under an argon atmosphere at 0 °C and was stirred at rt for 12 h. Distilled water (100ml) was added to the reaction mixture and stirred for 1 h. The organic fraction was separated, washed with distilled (2x50ml), dried (sodium sulphate), filtered and evaporated *in vacuo,* to afford 4-acetylphenylacetate (**285**) (4.359 g, 67 %) as a white crystalline solid, which was used as is without further purification. **R_f** = 0.56 (1:3 EtOAc : hexane); **mp** 54-55 °C; **^{1}H NMR (400 MHz, Chloroform-*d*)**; δ 7.99 (d, 2H, H-2 & H-5), 7.19 (d, 2H, H-3 & H-4), 2.59 (s, 3H, H-1), 2.32 (s, 3H, H-6); **^{13}C NMR (101 MHz, $CDCl_3$)**; δ 196.99 (C=O), 169.01 (C=O), 154.48 (quaternary Ar-C), 134.86 (quaternary Ar-C), 130.08 (C-2 & C-5), 121.90 (C-3 & C-4), 26.73 (C-1), 21.28 (C-6); **υ_{max} (neat)/cm^{-1}** 3071, 2988, 1748 (ester C=O stretching), 1671 (conjugated C=O stretching), 1591, 1417, 1357, 1265, 1190, 1007, 956, 911, 852, 623, 589; **MS HRMS m/z (ESI)** data was inconsistent.

© University of Pretoria

7.3.5.3.4 2-Acetylphenylacetate (**286**)[107]

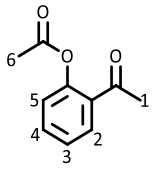

286

A solution of 2'-hydroxyacetophenone (**278**) (4.40 mL, 36.55 mmol, 1.0 eq.), triethylamine (13.20 mL, 94.71 mmol, 2.6 eq.) and acetic anhydride (6.00 mL, 63.47 mmol, 1.7 eq.) in dichloromethane (100 mL) was refluxed for 12 h. The solvent was evaporated *in vacuo* and the solids were washed with cold distilled water, dried *in vacuo* to afford 2-acetylphenylacetate (**286**) (6.398 g, 98 %) as a white crystalline solid, which was used as is without further purification. **R_f** = 0.62 (1:3 EtOAc : hexane); **mp** 89-92 °C; **^{1}H NMR (400 MHz, Chloroform-*d*)**; δ 7.81 (d, *J* = 7.8, 1.8 Hz, 1H, H-2)^, 7.54 (t, *J* = 7.7, 1.7 Hz, 1H, H-3)', 7.32 (t, *J* = 7.6, 1.4 Hz, 1H, H-4)', 7.12 (d, *J* = 8.1, 1.4 Hz, 1H, H-5)^, 2.56 (d, *J* = 1.7 Hz, 3H, H-1, H-1), 2.35 (d, *J* = 1.7 Hz, 3H, H-6); **^{13}C NMR (101 MHz, $CDCl_3$)**; δ 197.69 (C=O), 169.63 (C=O), 149.15 (quaternary Ar-C), 133.57 (C-2)$^+$, 130.77 (quaternary Ar-C), 130.42 (C-3)$^>$, 126.16 (C-4)$^>$, 123.95 (C-5)$^+$, 29.45 (C-1), 21.26 (C-6); **υ_{max} (neat)/cm^{-1}** 1751 (ester C=O stretching), 1678 (Conjugated C=O stretching), 1599, 1426, 1363, 1191, 1070, 956, 912, 825, 768, 580; **MS HRMS m/z (ESI) MS HRMS m/z (ESI)** data was inconsistent. ^ These assignments may be interchangeable. ' These assignments may be interchangeable. $^>$ These assignments may be interchangeable. $^+$ These assignments may be interchangeable.

7.3.5.3.5 4-(2-Bromoacetyl)phenylacetate (**287**)[107]

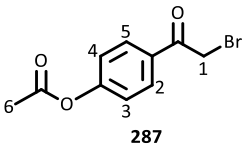

287

Liquid bromine (1.20 mL, 23.42 mmol, 1.0 eq.) was added dropwise to a solution of 4-acetylphenylacetate (**285**) (4.197 g, 23.55 mmol, 1.0 eq.) in dry chloroform (30 mL) under an argon atmosphere. The reaction solution was stirred until it turned clear after which time distilled water (50 mL) was added. The organic fraction was separated, washed with distilled water (2x30 mL), dried (sodium sulphate), filtered and evaporated *in vacuo,* to afford 4-(2-bromoacetyl)phenylacetate (**287**)

© University of Pretoria

(4.166 g, 73 %) as an off white solid, which was used as is without further purification. **R_f** = 0.64 (1:3 EtOAc : hexane); **mp** 60-62 °C; **^{1}H NMR (400 MHz, Chloroform-*d*)**; δ 8.02 (d, *J* = 8.7 Hz, 2H, H-2 & H-5), 7.23 (d, *J* = 8.8 Hz, H-3 & H-4), 4.43 (s, 2H, H-1), 2.33 (s, 3H, H-6); **^{13}C NMR (101 MHz, $CDCl_3$)**; δ 190.38 (C=O), 168.94 (C=O), 155.08 (quaternary Ar-C), 131.58 (quaternary Ar-C), 130.80 (C-2 & C-5), 122.24 (C-3 & C-4), 30.74 (C-1), 21.29 (C-6); **υ_{max} (neat)/cm^{-1}** 3013, 2958, 1758 (ester C=O stretching), 1684 (conjugated C=O stretching), 1594, 1504, 1365, 1272, 1182, 1011, 911, 847, 646 (C-Br stretching); **MS HRMS m/z (ESI)** data was inconsistent.

7.3.5.3.6 2-(2-Bromoacetyl)phenylacetate (**288**)[107]

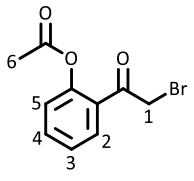

288

Liquid bromine (0.85 mL, 16.59 mmol, 1.0 eq.) was added dropwise to a solution of 2-acetylphenylacetate (**286**) (3.001 g, 16.59 mmol, 1.0 eq.) in dry chloroform (30 mL) under an argon atmosphere at rt. The reaction solution was stirred until it turned clear after which time distilled water (50 mL) was added to the reaction mixture. The organic fraction was separated, washed with distilled water (2x30 mL), dried (sodium sulphate), filtered and evaporated *in vacuo,* to afford 2-(2-bromoacetyl)phenylacetate (**288**) (3.348 g, 77 %) as an off white solid, which was used as is without further purification. **R_f** = 0.73 (1:3 EtOAc : hexane); **mp** 67-70 °C; **^{1}H NMR (400 MHz, Chloroform-*d*)**; 7.80 (dd, *J* = 7.9, 1.7 Hz, 1H, H-2)^, 7.56 (td, *J* = 8.2, 7.5, 1.7 Hz, 1H, H-3)', 7.32 (td, *J* = 7.6, 1.2 Hz, 1H, H-4)', 7.16 (dd, *J* = 8.2, 1.2 Hz, 1H, H-5)^, 4.40 (s, 2H, H-1), 2.34 (s, 3H, H-6); **^{13}C NMR (101 MHz, $CDCl_3$)**; δ 190.63 (C=O), 169.17 (C=O), 149.50 (quaternary Ar-C), 134.30 (C-2)>, 130.49 (C-3)+, 127.80 (quaternary Ar-C), 126.20 (C-4)+, 124.16 (C-5)>, 33.87 (C-1), 21.24 (C-6); **MS HRMS m/z (ESI)** data was inconsistent. ^ These assignments may be interchangeable. ' These assignments may be interchangeable. > These assignments may be interchangeable. + These assignments may be interchangeable.

© University of Pretoria

7.3.5.3.7 4-(2-((1-Benzylpiperidin-4-yl)methoxy)acetyl)phenyl acetate (289)

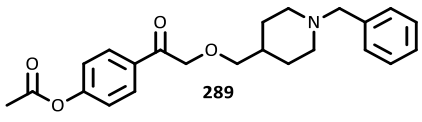

289

A solution of 4-(2-bromoacetyl)phenylacetate (**287**) (4.166 g, 16.20 mmol, 1.0 eq.), (1-benzylpiperidin-4-yl)methanol (**30**) (4.106 g, 20.00 mmol, 1.2 eq.) and potassium carbonate (7.028 g, 50.86 mmol, 3.1 eq.) in dry acetonitrile (50 mL) under an argon atmosphere was refluxed for 48 h. Distilled water (50 mL) was added to the reaction mixture and stirred for 30 min after which time dichloromethane (100 mL) was added and the organic fraction was separated, washed with distilled water (2x30 mL), dried (sodium sulphate), filtered and evaporated *in vacuo*. The crude material was purified using column chromatography (3:1 EtOAc : hexane). NMR analysis of the column fractions did not indicate the desired product.

7.3.5.3.8 (*Z*)-2-(2-((1-benzylpiperidin-4-yl)methoxy)-1-hydroxyvinyl)phenol (291)

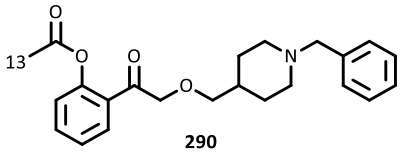

290

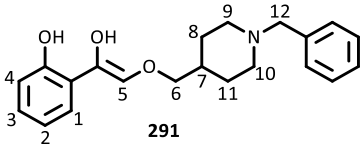

291

A solution of 2-(2-bromoacetyl)phenylacetate (**288**) (4.655 g, 18.12 mmol, 1.0 eq.), (1-benzylpiperidin-4-yl)methanol (**30**) (3.755 g, 18.29 mmol, 1.0 eq.) and potassium carbonate (7.783 g, 56.32 mmol, 3.1 eq.) in dry acetonitrile (50 mL) under an argon atmosphere was refluxed for 24 h. Distilled water (50 mL) was added to the reaction mixture and stirred for 30 min after which time dichloromethane (100 mL) was added. The organic fraction was separated, washed with distilled water (2x30 mL), dried (sodium sulphate), filtered and evaporated *in vacuo*. The crude material was purified using column chromatography (3:1 EtOAc : hexane), to afford (*Z*)-2-(2-((1-benzylpiperidin-4-yl)methoxy)-1-hydroxyvinyl)phenol (0.157 g, 2 %) as an orange oil. $\mathbf{R_f}$ = 0.53 (3:1 EtOAc : hexane); **^{1}H NMR (400 MHz, Chloroform-*d*)**; δ 7.68 (dd, *J* = 8.1, 1.7 Hz, 1H, H-1)^, 7.38 (td, *J* = 8.6, 7.2, 1.8 Hz, 1H, H-2)', 7.32 (d, *J* = 4.4 Hz, 1H, Ph), 7.23 – 7.18 (m, 2H, Ph), 7.13 (t, *J* = 6.7 Hz, 3H, Ph), 6.92 (d, *J* = 8.3, 1.0 Hz, 1H, H-4)^,

© University of Pretoria

6.79 (t, 1H, H-3)', 4.05 (dd, *J* = 10.1, 3.7 Hz, 1H, H-5), 3.49 (d, *J* = 6.4 Hz, 2H, H-6), 3.31 (dd, *J* = 13.4, 10.1 Hz, 1H, H-12), 3.07 (d, *J* = 11.6 Hz, 1H, H-9)*, 3.01 (dd, *J* = 13.4, 3.5 Hz, 1H, H-12), 2.96 (s, 1H, H-10)*, 2.67 (td, *J* = 11.7, 2.7 Hz, 1H, H-9)*, 2.38 (td, *J* = 11.8, 2.6 Hz, 1H, H-10)*, 1.85 (d, *J* = 12.8 Hz, 1H, H-8)*, 1.77 (d, *J* = 13.2 Hz, 1H, H-11)*, 1.58 – 1.51 (m, 1H, H-7), 1.47 – 1.36 (m, 2H, H-11)*, 1.31 – 1.19 (m, 2H, H-8)*; **^{13}C NMR (101 MHz, $CDCl_3$)**; δ 199.09 (C=O), 160.92 (quaternary Ar-C), 138.40 (quaternary Ar-C), 135.56 (C-2)+, 131.22 (C-1)>, 129.41 (Ph), 128.55 (Ph), 128.38 (quaternary Ar-C), 126.43 (Ph), 123.04 (quaternary Ar-C), 119.05 (C-4)>, 118.79 (C-3)+, 72.68 (C-5), 67.40 (C-6), 51.32 (C-9)<, 47.65 (C-10)<, 38.25 (C-7), 29.97 (C-12), 28.68 (C-8)<, 28.55 (C-11)<; **υ_{max} (neat)/cm^{-1}** 3399 (O-H stretching), 2927, 2858, 1730 (ester C=O), 1667 (conjugated C=O stretching), 1607, 1451, 1237, 1149, 1109, 1036, 749, 698 (cis C=C bending); **MS HRMS m/z (ESI)** calculated for ($C_{23}H_{27}NO_4$): 382.2013, found: [M + H] 382.165. Deacetylated ($C_{21}H_{25}NO_3$): 340.1907, found: [M + H] 340.190. ^ These assignments may be interchangeable. ' These assignments may be interchangeable. * These assignments may be interchangeable. + These assignments may be interchangeable. > These assignments may be interchangeable. < These assignments may be interchangeable.

7.3.5.3.9 (*Z*)-2-(2-((1-benzylpiperidin-4-yl)methoxy)-1-hydroxyvinyl)phenol (**291**)[107]

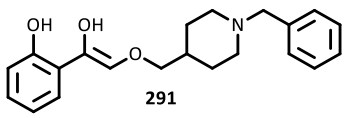

291

A solution of 2-(2-((1-benzylpiperidin-4-yl)methoxy)acetyl)phenylacetate (mixed products) (0.157 g, 0.41 mmol, 1.0 eq.) and potassium carbonate (0.195 g, 1.41 mmol, 3.4 eq.) in methanol (10 mL) was stirred for 12 h. The solvent was evaporated *in vacuo* and the solids were dissolved in dichloromethane (10 mL), washed with distilled water (3x10 mL) and the organic fraction was separated, dried (magnesium sulphate), filtered and evaporated *in vacuo*. The crude material was purified using column chromatography (3:1 EtOAc : hexane). The NMR analysis and characterisation techniques were not consistent. A crude yield of suspected 2-((1-benzylpiperidin-4-yl)methoxy)-1-(2-hydroxyphenyl)ethanone (0.087 g, 63 %) as a red solid was obtained. The data was conflicting as IR indicated an O-H stretching peak at 3399 Hz and the mass spectrum was inconclusive.

© University of Pretoria

7.3.5.3.10 2-((1-Benzylpiperidin-4-yl)methoxy)-1-(2-((tert-butyldimethylsilyl)oxy)phenyl)ethenone (**292**)

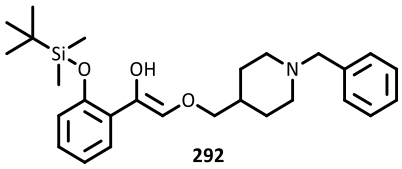

292

A solution of 2-((1-benzylpiperidin-4-yl)methoxy)-1-(2-hydroxyphenyl)ethenone (0.022 g, 0.06 mmol, 1.0 eq.), *t*-butyldimethylsilane chloride (0.020 g, 0.13 mmol, 2.0 eq.) and triethylamine (0.04 mL, 0.29 mmol, 4.5 eq.) in dry dichloromethane (10 mL) under an argon atmosphere and was refluxed for 12 h. The reaction mixture was washed with distilled water (3x10 mL) and the organic fraction was, separated, dried (magnesium sulphate), filtered and evaporated *in vacuo*. The crude material was purified using column chromatography (pre-prepared/basified silica 1:9 ethyl acetate: hexane) and the corresponding methanol fraction was columned pre-prepared/basified silica, ethyl acetate). NMR analysis of the column fractions did not indicate the desired product.

7.3.5.3.11 2-((1-Benzylpiperidin-4-yl)methoxy)-1-(2-((tert-butyldiphenylsilyl)oxy)phenyl)ethenone (**293**)

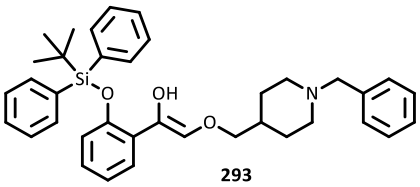

293

A solution of 2-((1-benzylpiperidin-4-yl)methoxy)-1-(2-hydroxyphenyl)ethenone (0.022 g, 0.06 mmol, 1.0 eq.), *t*-butyldiphenylsilane chloride (0.02 mL, 0.077 mmol, 1.2 eq.) and triethylamine (0.04 mL, 0.29 mmol, 4.5 eq.) in dry dichloromethane (10 mL) and was refluxed for 12 h. The reaction mixture was washed with distilled water (3x10 mL) and the organic fraction was, separated, dried (magnesium sulphate), filtered and evaporated *in vacuo*. The crude material was purified using column chromatography (pre-prepared/basified silica 1:9 ethyl acetate: hexane) and the corresponding methanol fraction was columned pre-prepared/basified silica, ethyl acetate). NMR analysis of the column fractions did not indicate the desired product.

© University of Pretoria

7.3.5.3.12 2-((1-Benzylpiperidin-4-yl)methoxy)-1-(2-((triphenylsilyl)oxy)phenyl)ethenone (**294**)

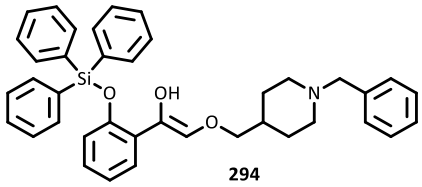

294

A solution of 2-((1-benzylpiperidin-4-yl)methoxy)-1-(2-hydroxyphenyl)ethenone (0.022 g, 0.06 mmol, 1.0 eq.), chlorotriphenylsilane (0.027 g, 0.09 mmol, 1.4 eq.) and triethylamine (0.04 mL, 0.29 mmol, 4.5 eq.) in dry dichloromethane (10 mL) and was refluxed for 12 h. The reaction mixture was washed with distilled water (3x10 mL) and the organic fraction was, separated, dried (magnesium sulphate), filtered and evaporated *in vacuo*. The crude material was purified using column chromatography (pre-prepared/basified silica 1:9 ethyl acetate: hexane) and the corresponding methanol fraction was columned pre-prepared/basified silica, ethyl acetate). NMR analysis of the column fractions did not indicate the desired product.

7.3.5.3.13 2-((1-Benzylpiperidin-4-yl)methoxy)-1-(2-(((2,3-dimethylbutane-2 yl)dimethylsilyl)oxy)phenyl)ethenone (**295**)

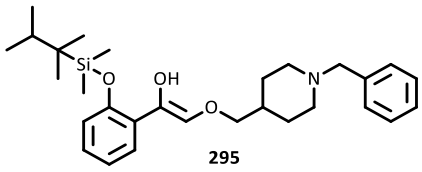

295

A solution of 2-((1-benzylpiperidin-4-yl)methoxy)-1-(2-hydroxyphenyl)ethenone (0.022 g, 0.06 mmol, 1.0 eq.), chloro(dimethyl)thexyl silane (0.02 mL, 0.10 mmol, 1.6 eq.) and triethylamine (0.06 mL, 0.43 mmol, 6.7 eq.) in dry dichloromethane (10 mL) and was refluxed for 12 h. The reaction mixture was washed with distilled water (3x10 mL) and the organic fraction was, separated, dried (magnesium sulphate), filtered and evaporated *in vacuo*. The crude material was purified using column chromatography (pre-prepared/basified silica 1:9 ethyl acetate: hexane) and the corresponding methanol fraction was columned pre-prepared/basified silica, ethyl acetate). NMR analysis of the column fractions did not indicate the desired product.

© University of Pretoria

Chapter 8 References

(1) Craig, L. A.; Hong, N. S.; Mcdonald, R. J. Neuroscience and Biobehavioral Reviews Revisiting the Cholinergic Hypothesis in the Development of Alzheimer ' s Disease. *Neurosci. Biobehav. Rev.* **2011**, *35* (6), 1397–1409. https://doi.org/10.1016/j.neubiorev.2011.03.001.

(2) Salehi, A.; Verhaagen, J.; Dijkhuizen, P. .; Swaab, D. . Co-Localization of High-Affinity Neurotrophin Receptors in Nucleus Basalis of Meynert Neurons and Their Differential Reduction in Alzheimer's Disease. *Neuroscience* **1996**, *75* (2), 373–387. https://doi.org/10.1016/0306-4522(96)00273-4.

(3) Mohamed, T.; Shakeri, A.; Rao, P. P. N. Amyloid Cascade in Alzheimer's Disease: Recent Advances in Medicinal Chemistry. *Eur. J. Med. Chem.* **2016**, *113*, 258–272. https://doi.org/10.1016/j.ejmech.2016.02.049.

(4) Carvajal, F. J.; Inestrosa, N. C. Interactions of AChE with Aβ Aggregates in Alzheimer's Brain: Therapeutic Relevance of IDN 5706. *Front. Mol. Neurosci.* **2011**, *4*. https://doi.org/10.3389/fnmol.2011.00019.

(5) Contestabile, A. The History of the Cholinergic Hypothesis. *Behavioural Brain Research*. 2011. https://doi.org/10.1016/j.bbr.2009.12.044.

(6) Liu, Z.; Zhang, A.; Sun, H.; Han, Y.; Kong, L.; Wang, X. Two Decades of New Drug Discovery and Development for Alzheimer's Disease. *RSC Adv.* **2017**, *7* (10), 6046–6058. https://doi.org/10.1039/C6RA26737H.

(7) Gurwitz, D. Auguste D and Alzheimer's Disease. *Lancet* **1997**, *350* (9073), 298. https://doi.org/10.1016/S0140-6736(05)62274-X.

(8) Puzzo, D.; Gulisano, W.; Arancio, O.; Palmeri, A. The Keystone of Alzheimer Pathogenesis Might Be Sought in Aβ Physiology. *Neuroscience* **2015**, *307*, 26–36. https://doi.org/10.1016/j.neuroscience.2015.08.039.

(9) Bolós, M.; Perea, J. R.; Avila, J. Alzheimer's Disease as an Inflammatory Disease. *Biomol. Concepts* **2017**, *8* (1), 37–43. https://doi.org/10.1515/bmc-2016-0029.

(10) Shadfar, S.; Hwang, C. J.; Lim, M.-S.; Choi, D.-Y.; Hong, J. T. Involvement of Inflammation in Alzheimer's Disease Pathogenesis and Therapeutic Potential of Anti-Inflammatory Agents. *Arch. Pharm. Res.* **2015**, *38* (12), 2106–2119. https://doi.org/10.1007/s12272-015-0648-x.

(11) Tanzi, R. E. The Genetics of Alzheimer Disease. *Cold Spring Harb. Perspect. Med.* **2012**, *2* (10), a006296–a006296. https://doi.org/10.1101/cshperspect.a006296.

(12) De Jager, C. A.; Joska, J. A.; Hoffman, M.; Borochowitz, K. E.; Combrinck, M. I. Dementia in Rural South Africa: A Pressing Need for Epidemiological Studies. *South African Med. J.* **2015**, *105* (3), 189-190. https://doi.org/10.7196/SAMJ.8904.

(13) Association, A. 2018 Alzheimer ' s Disease Facts and Figures. *Alzheimer's Dement.* **2018**, *14* (3), 367–429. https://doi.org/10.1016/j.jalz.2018.02.001.

(14) Guerchet, M.; Mayston, R.; Lloyd-Sherlock, P.; Prince, M.; Aboderin, I.; Akinyemi, R.; Paddick, S.-M.; Wimo, A.; Amoakoh-Coleman, M.; Uwakwe, R.; et al. *Dementia in Sub-Saharan Africa: Challenges and Opportunities;* London, 2017.

(15) Schliebs, R.; Arendt, T. The Cholinergic System in Aging and Neuronal Degeneration. *Behavioural Brain Research*. 2011, 221(2), 555-563.

© University of Pretoria

https://doi.org/10.1016/j.bbr.2010.11.058.

(16) Liu, Z.; Zhang, A.; Sun, H.; Han, Y.; Wang, X. Two Decades of New Drug Discovery and Development for Alzheimer ' s Disease †. *RSC Adv.* **2017**, *7* (10), 6046–6058. https://doi.org/10.1039/C6RA26737H.

(17) Hampel, H. J.; Cuello, A. C.; Grossberg, G. T. The Cholinergic System in the Pathophysiology and Treatment of Alzheimer's Disease Management of Research Integrity View Project History of Neuroscience View Project. https://doi.org/10.1093/brain/awy132.

(18) Brunden, K. R.; Trojanowski, J. Q.; Lee, V. M. Advances in Tau-Focused Drug Discovery for Alzheimer's Disease and Related Tauopathies. *Nat. Rev. Drug Discov.* **2010**, *8* (10), 783–793. https://doi.org/10.1038/nrd2959.

(19) Medina, M.; Avila, J. New Perspectives on the Role of Tau in Alzheimer's Disease. Implications for Therapy. *Biochem. Pharmacol.* **2014**, *88* (4), 540–547. https://doi.org/10.1016/j.bcp.2014.01.013.

(20) Liu, Z.; Li, P.; Wu, J.; Wang, Y.; Li, P.; Hou, X.; Zhang, Q.; Wei, N.; Zhao, Z.; Liang, H.; et al. The Cascade of Oxidative Stress and Tau Protein Autophagic Dysfunction in Alzheimer's Disease. In *Alzheimer's Disease - Challenges for the Future*; InTech, 2015. https://doi.org/10.5772/59980.

(21) Buée, L.; Delacourte, A. Tau Phosphorylation. In *Functional Neurobiology of Aging*; Elsevier, 2001; pp 315–332. https://doi.org/10.1016/b978-012351830-9/50023-8.

(22) Cooper, G. M. *The Cell: A Molecular Approch*, 2nd editio.; Sinauer Associates: Sunderland (MA), 2000.

(23) Mohandas, E.; Rajmohan, V.; Raghunath, B. Neurobiology of Alzheimer's Disease. *Indian J. Psychiatry* **2009**, *51* (1), 55–61. https://doi.org/10.4103/0019-5545.44908.

(24) Sies, H. Oxidative Stress: Oxidants and Antioxidants. *Exp. Physiol.* **1997**, *82* (2), 291–295. https://doi.org/10.1113/expphysiol.1997.sp004024.

(25) Nunomura, A.; Castellani, R. J.; Zhu, X.; Moreira, P. I.; Perry, G.; Smith, M. A. Involvement of Oxidative Stress in Alzheimer Disease. *J. Neuropathol. Exp. Neurol.* **2006**, *65* (7), 631–641. https://doi.org/10.1097/01.jnen.0000228136.58062.bf.

(26) Pocernich, C. B.; Butterfield, D. A. Elevation of Glutathione as a Therapeutic Strategy in Alzheimer Disease. *Biochim. Biophys. Acta - Mol. Basis Dis.* **2012**, *1822* (5), 625–630. https://doi.org/10.1016/j.bbadis.2011.10.003.

(27) Praticò, D. Oxidative Stress Hypothesis in Alzheimer's Disease: A Reappraisal. *Trends Pharmacol. Sci.* **2008**, *29* (12), 609–615. https://doi.org/10.1016/j.tips.2008.09.001.

(28) Huat, T. J.; Camats-Perna, J.; Newcombe, E. A.; Valmas, N.; Kitazawa, M.; Medeiros, R. Metal Toxicity Links to Alzheimer's Disease and Neuroinflammation. *J. Mol. Biol.* **2019**, *431* (9), 1843–1868. https://doi.org/10.1016/j.jmb.2019.01.018.

(29) Bolognin, S.; Messori, L.; Zatta, P. Metal Ion Physiopathology in Neurodegenerative Disorders. *NeuroMolecular Med.* **2009**, *11* (4), 223–238. https://doi.org/10.1007/s12017-009-8102-1.

(30) Bagyinszky, E.; Giau, V. Van; Shim, K.; Suk, K.; An, S. S. A.; Kim, S. Role of Inflammatory Molecules in the Alzheimer's Disease Progression and Diagnosis. *J. Neurol. Sci.* **2017**, *376*, 242–254. https://doi.org/10.1016/j.jns.2017.03.031.

(31) Eglen, R. M. Muscarinic Receptor Subtypes in Neuronal and Non-Neuronal Cholinergic

© University of Pretoria

Function. *Auton. Autacoid Pharmacol.* **2006**, *26* (3), 219–233. https://doi.org/10.1111/j.1474-8673.2006.00368.x.

(32) Huang, E. J.; Reichardt, L. F. Neurotrophins: Roles in Neuronal Development and Function. *Annu. Rev. Neurosci.* **2001**, *24* (1), 677–736. https://doi.org/10.1146/annurev.neuro.24.1.677.

(33) Amenta, F.; Tayebati, S. Pathways of Acetylcholine Synthesis, Transport and Release as Targets for Treatment of Adult-Onset Cognitive Dysfunction. *Curr. Med. Chem.* **2008**, *15* (5), 488–498. https://doi.org/10.2174/092986708783503203.

(34) Neurotransmitters (The Neuron) Part 2 http://what-when-how.com/neuroscience/neurotransmitters-the-neuron-part-2/ (accessed Aug 6, 2018).

(35) Cheung, J.; Gary, E. N.; Shiomi, K.; Rosenberry, T. L. Structures of Human Acetylcholinesterase Bound to Dihydrotanshinone I and Territrem B Show Peripheral Site Flexibility. *ACS Med. Chem. Lett.* **2013**, *4* (11), 1091–1096. https://doi.org/10.1021/ml400304w.

(36) Cheung, J.; Rudolph, M. J.; Burshteyn, F.; Cassidy, M. S.; Gary, E. N.; Love, J.; Franklin, M. C.; Height, J. J. Structures of Human Acetylcholinesterase in Complex with Pharmacologically Important Ligands. *J. Med. Chem.* **2012**, *55* (22), 10282–10286. https://doi.org/10.1021/jm300871x.

(37) Zhou, Y.; Wang, S.; Zhang, Y. Catalytic Reaction Mechanism of Acetylcholinesterase Determined by Born-Oppenheimer Ab Initio QM/MM Molecular Dynamics Simulations. *J. Phys. Chem. B* **2010**, *114* (26), 8817–8825. https://doi.org/10.1021/jp104258d.

(38) Arendt, T.; Taubert, G.; Bigl, V.; Arendt, A. Amyloid Deposition in the Nucleus Basalis of Meynert Complex : A Topographic Marker for Degenerating Cell Clusters in Alzheimer ' s Disease. *Acta Neuropathol.* **1988**, *75* (3), 226–232. https://doi.org/https://doi-org.uplib.idm.oclc.org/10.1007/BF00690530.

(39) Rogers, J.; Morrison, J. Quantitative Morphology and Regional and Laminar Distributions of Senile Plaques in Alzheimer's Disease. *J. Neurosci.* **1985**, *5* (10), 2801–2808. https://doi.org/10.1523/JNEUROSCI.05-10-02801.1985.

(40) Katzman, R.; Terry, R.; DeTeresa, R.; Brown, T.; Davies, P.; Fuld, P.; Renbing, X.; Peck, A. Clinical, Pathological, and Neurochemical Changes in Dementia: A Subgroup with Preserved Mental Status and Numerous Neocortical Plaques. *Ann. Neurol.* **1988**, *23* (2), 138–144. https://doi.org/10.1002/ana.410230206.

(41) Puzzo, D.; Arancio, O. Amyloid-β Peptide: Dr. Jekyll or Mr. Hyde? *J. Alzheimer's Dis.* **2012**, *33* (s1), S111–S120. https://doi.org/10.3233/JAD-2012-129033.

(42) Saxena, A.; Fedorko, J. M.; Vinayaka, C. R.; Medhekar, R.; Radic, Z.; Taylor, P.; Lockridge, O.; Doctor, B. P. Aromatic Amino-Acid Residues at the Active and Peripheral Anionic Sites Control the Binding of E2020 (AriceptR) to Cholinesterases. *Eur. J. Biochem.* **2003**, *270* (22), 4447–4458. https://doi.org/10.1046/j.1432-1033.2003.03837.x.

(43) Wang, Y.; Wang, H.; Chen, H. AChE Inhibition-Based Multi-Target-Directed Ligands, a Novel Pharmacological Approach for the Symptomatic and Disease-Modifying Therapy of Alzheimer's Disease. *Curr. Neuropharmacol.* **2016**, *14* (4), 364–375. https://doi.org/10.2174/1570159X14666160119094820.

(44) Xie, Q.; Wang, H.; Xia, Z.; Lu, M.; Zhang, W.; Wang, X.; Fu, W.; Tang, Y.; Sheng, W.; Li, W.; et al. Bis-(−)-nor-Meptazinols as Novel Nanomolar Cholinesterase Inhibitors with High Inhibitory Potency on Amyloid-β Aggregation. *J. Med. Chem.* **2008**, *51* (7), 2027–2036. https://doi.org/10.1021/jm070154q.

© University of Pretoria

(45) Muñoz-Ruiz, P.; Rubio, L.; García-Palomero, E.; Dorronsoro, I.; del Monte-Millán, M.; Valenzuela, R.; Usán, P.; de Austria, C.; Bartolini, M.; Andrisano, V.; et al. Design, Synthesis, and Biological Evaluation of Dual Binding Site Acetylcholinesterase Inhibitors: New Disease-Modifying Agents for Alzheimer's Disease. *J. Med. Chem.* **2005**, *48* (23), 7223–7233. https://doi.org/10.1021/jm0503289.

(46) Gemma, S.; Gabellieri, E.; Huleatt, P.; Fattorusso, C.; Borriello, M.; Catalanotti, B.; Butini, S.; De Angelis, M.; Novellino, E.; Nacci, V.; et al. Discovery of Huperzine A–Tacrine Hybrids as Potent Inhibitors of Human Cholinesterases Targeting Their Midgorge Recognition Sites. *J. Med. Chem.* **2006**, *49* (11), 3421–3425. https://doi.org/10.1021/jm060257t.

(47) Kwon, Y. E.; Park, J. Y.; No, K. T.; Shin, J. H.; Lee, S. K.; Eun, J. S.; Yang, J. H.; Shin, T. Y.; Kim, D. K.; Chae, B. S.; et al. Synthesis, in Vitro Assay, and Molecular Modeling of New Piperidine Derivatives Having Dual Inhibitory Potency against Acetylcholinesterase and Aβ1–42 Aggregation for Alzheimer's Disease Therapeutics. *Bioorg. Med. Chem.* **2007**, *15* (20), 6596–6607. https://doi.org/10.1016/j.bmc.2007.07.003.

(48) Lemes, L. F. N.; de Andrade Ramos, G.; de Oliveira, A. S.; da Silva, F. M. R.; de Castro Couto, G.; da Silva Boni, M.; Guimarães, M. J. R.; Souza, I. N. O.; Bartolini, M.; Andrisano, V.; et al. Cardanol-Derived AChE Inhibitors: Towards the Development of Dual Binding Derivatives for Alzheimer's Disease. *Eur. J. Med. Chem.* **2016**, *108*, 687–700. https://doi.org/10.1016/j.ejmech.2015.12.024.

(49) Chen, Z.; Digiacomo, M.; Tu, Y.; Gu, Q.; Wang, S.; Yang, X.; Chu, J.; Chen, Q.; Han, Y.; Chen, J.; et al. Discovery of Novel Rivastigmine-Hydroxycinnamic Acid Hybrids as Multi-Targeted Agents for Alzheimer's Disease. *Eur. J. Med. Chem.* **2017**, *125*, 784–792. https://doi.org/10.1016/j.ejmech.2016.09.052.

(50) Xie, S.-S.; Lan, J.-S.; Wang, X.; Wang, Z.-M.; Jiang, N.; Li, F.; Wu, J.-J.; Wang, J.; Kong, L.-Y. Design, Synthesis and Biological Evaluation of Novel Donepezil–Coumarin Hybrids as Multi-Target Agents for the Treatment of Alzheimer's Disease. *Bioorg. Med. Chem.* **2016**, *24* (7), 1528–1539. https://doi.org/10.1016/j.bmc.2016.02.023.

(51) Gabr, M. T.; Abdel-Raziq, M. S. Design and Synthesis of Donepezil Analogues as Dual AChE and BACE-1 Inhibitors. *Bioorg. Chem.* **2018**, *80* (June), 245–252. https://doi.org/10.1016/j.bioorg.2018.06.031.

(52) Sugimoto, H.; Yamanish, Y.; Iimura, Y.; Kawakami, Y. Donepezil Hydrochloride (E2020) and Other Acetylcholinesterase Inhibitors. *Curr. Med. Chem.* **2000**, *7* (3), 303–339. https://doi.org/10.2174/0929867003375191.

(53) van Greunen, D. G.; Cordier, W.; Nell, M.; van der Westhuyzen, C.; Steenkamp, V.; Panayides, J.-L.; Riley, D. L. Targeting Alzheimer's Disease by Investigating Previously Unexplored Chemical Space Surrounding the Cholinesterase Inhibitor Donepezil. *Eur. J. Med. Chem.* **2017**, *127*, 671–690. https://doi.org/10.1016/j.ejmech.2016.10.036.

(54) Ramesh, R.; Reddy, D. S. Quest for Novel Chemical Entities through Incorporation of Silicon in Drug Scaffolds. *J. Med. Chem.* **2018**, *61* (9), 3779–3798. https://doi.org/10.1021/acs.jmedchem.7b00718.

(55) Johansson, T.; Weidolf, L.; Popp, F.; Tacke, R.; Jurva, U. In Vitro Metabolism of Haloperidol and Sila-Haloperidol: New Metabolic Pathways Resulting from Carbon/Silicon Exchange. *Drug Metab. Dispos.* **2010**, *38* (1), 73–83. https://doi.org/10.1124/dmd.109.028449.

(56) Gately, S.; West, R. Novel Therapeutics with Enhanced Biological Activity Generated by the Strategic Introduction of Silicon Isosteres into Known Drug Scaffolds. *Drug Dev. Res.* **2007**, *68*

© University of Pretoria

(4), 156–163. https://doi.org/10.1002/ddr.20177.

(57) Seetharamsingh, B.; Ramesh, R.; Dange, S. S.; Khairnar, P. V.; Singhal, S.; Upadhyay, D.; Veeraraghavan, S.; Viswanadha, S.; Vakkalanka, S.; Reddy, D. S. Design, Synthesis, and Identification of Silicon Incorporated Oxazolidinone Antibiotics with Improved Brain Exposure. *ACS Med. Chem. Lett.* **2015**, *6* (11), 1105–1110. https://doi.org/10.1021/acsmedchemlett.5b00213.

(58) Barraza, S. J.; Denmark, S. E. Synthesis, Reactivity, Functionalization, and ADMET Properties of Silicon-Containing Nitrogen Heterocycles. *J. Am. Chem. Soc.* **2018**, *140* (21), 6668–6684. https://doi.org/10.1021/jacs.8b03187.

(59) Tacke, R.; Heinrich, T.; Bertermann, R.; Burschka, C.; Hamacher, A.; Kassack, M. U. Sila-Haloperidol: A Silicon Analogue of the Dopamine (D 2) Receptor Antagonist Haloperidol §. *Organometallics* **2004**, *23* (19), 4468–4477. https://doi.org/10.1021/om040067l.

(60) Tacke, R.; Popp, F.; Müller, B.; Theis, B.; Burschka, C.; Hamacher, A.; Kassack, M. U.; Schepmann, D.; Wünsch, B.; Jurva, U.; et al. Sila-Haloperidol, a Silicon Analogue of the Dopamine (D2) Receptor Antagonist Haloperidol: Synthesis, Pharmacological Properties, and Metabolic Fate. *ChemMedChem* **2008**, *3* (1), 152–164. https://doi.org/10.1002/cmdc.200700205.

(61) Geyer, M.; Wellner, E.; Jurva, U.; Saloman, S.; Armstrong, D.; Tacke, R. Can Silicon Make an Excellent Drug Even Better? An in Vitro and in Vivo Head-to-Head Comparison between Loperamide and Its Silicon Analogue Sila-Loperamide. *ChemMedChem* **2015**, *10* (5), 911–924. https://doi.org/10.1002/cmdc.201500040.

(62) Chen, C.-A.; Sieburth, S. M.; Glekas, A.; Hewitt, G. W.; Trainor, G. L.; Erickson-Viitanen, S.; Garber, S. S.; Cordova, B.; Jeffry, S.; Klabe, R. M. Drug Design with a New Transition State Analog of the Hydrated Carbonyl: Silicon-Based Inhibitors of the HIV Protease. *Chem. Biol.* **2001**, *8* (12), 1161–1166. https://doi.org/10.1016/S1074-5521(01)00079-5.

(63) Mutahi, M. wa; Nittoli, T.; Guo, L.; Sieburth, S. M. Silicon-Based Metalloprotease Inhibitors: Synthesis and Evaluation of Silanol and Silanediol Peptide Analogues as Inhibitors of Angiotensin-Converting Enzyme [1]. *J. Am. Chem. Soc.* **2002**, *124* (25), 7363–7375. https://doi.org/10.1021/ja026158w.

(64) Kim, J.; Glekas, A.; Sieburth, S. M. N. Silanediol-Based Inhibitor of Thermolysin. *Bioorganic Med. Chem. Lett.* **2002**, *12* (24), 3625–3627. https://doi.org/10.1016/S0960-894X(02)00804-1.

(65) Juers, D. H.; Kim, J.; Matthews, B. W.; Sieburth, S. M. Structural Analysis of Silanediols as Transition-State-Analogue Inhibitors of the Benchmark Metalloprotease Thermolysin [†,‡]. *Biochemistry* **2005**, *44* (50), 16524–16528. https://doi.org/10.1021/bi051346v.

(66) Singh, S.; Sieburth, S. M. Serine Protease Inhibition by a Silanediol Peptidomimetic. *Org. Lett.* **2012**, *14* (17), 4422–4425. https://doi.org/10.1021/ol301933n.

(67) Blunder, M.; Hurkes, N.; Spirk, S.; List, M.; Pietschnig, R. Silanetriols as in Vitro Inhibitors for AChE. *Bioorg. Med. Chem. Lett.* **2011**, *21* (1), 363–365. https://doi.org/10.1016/j.bmcl.2010.10.139.

(68) Daiss, J. O.; Duda-Johner, S.; Burschka, C.; Holzgrabe, U.; Mohr, K.; Tacke, R. N + /Si Replacement as a Tool for Probing the Pharmacophore of Allosteric Modulators of Muscarinic M 2 Receptors: Synthesis, Allosteric Potency, and Positive Cooperativity of Silicon-Based W84 Derivatives. *Organometallics* **2002**, *21* (5), 803–811. https://doi.org/10.1021/om010847j.

© University of Pretoria

(69) Tacke, R.; Terunuma, D.; Tafel, A.; Mühleisen, M.; Forth, B.; Waelbroeck, M.; Gross, J.; Mutschler, E.; Friebe, T.; Lambrecht, G. Fluorine-Containing Derivatives of the Muscarinic Antagonists Sila-Pridinol and Sila-Difenidol: Syntheses and Antimuscarinic Properties. *J. Organomet. Chem.* **1995**, *501* (1–2), 145–154. https://doi.org/10.1016/0022-328X(95)05622-V.

(70) Bom, D.; Curran, D. P.; Kruszewski, S.; Zimmer, S. G.; Thompson Strode, J.; Kohlhagen, G.; Du, W.; Chavan, A. J.; Fraley, K. A.; Bingcang, A. L.; et al. The Novel Silatecan 7- Tert - Butyldimethylsilyl-10-Hydroxycamptothecin Displays High Lipophilicity, Improved Human Blood Stability, and Potent Anticancer Activity. *J. Med. Chem.* **2000**, *43* (21), 3970–3980. https://doi.org/10.1021/jm000144o.

(71) Van Hattum, A. H.; Pinedo, H. M.; Schlüper, H. M. M.; Hausheer, F. H.; Boven, E. New Highly Lipophilic Camptothecin BNP1350 Is an Effective Drug in Experimental Human Cancer. *Int. J. Cancer* **2000**, *88* (2), 260–266. https://doi.org/10.1002/1097-0215(20001015)88:2<260::AID-IJC18>3.0.CO;2-Q.

(72) Palermo, G.; Diego, S. *Encyclopedia of Nanotechnology*; Bhushan, B., Ed.; Springer Netherlands: Dordrecht, 2014. https://doi.org/10.1007/978-94-007-6178-0.

(73) Cheng, T.; Li, Q.; Zhou, Z.; Wang, Y.; Bryant, S. H. Structure-Based Virtual Screening for Drug Discovery: A Problem-Centric Review. *AAPS J.* **2012**, *14* (1), 133–141. https://doi.org/10.1208/s12248-012-9322-0.

(74) Genheden, S.; Ryde, U. The MM/PBSA and MM/GBSA Methods to Estimate Ligand-Binding Affinities. *Expert Opin. Drug Discov.* **2015**, *10* (5), 449–461. https://doi.org/10.1517/17460441.2015.1032936.

(75) Du, J.; Sun, H.; Xi, L.; Li, J.; Yang, Y.; Liu, H.; Yao, X. Molecular Modeling Study of Checkpoint Kinase 1 Inhibitors by Multiple Docking Strategies and Prime/MM–GBSA Calculation. *J. Comput. Chem.* **2011**, *32* (13), 2800–2809. https://doi.org/10.1002/jcc.21859.

(76) Steinbrecher, T. MM-GBSA for Calculating Binding Affinity A Rank-Ordering Study for the Lead Optimization of Fxa Typical Docking Workflow. **2016**.

(77) Banks, J. L.; Beard, H. S.; Cao, Y.; Cho, A. E.; Damm, W.; Farid, R.; Felts, A. K.; Halgren, T. A.; Mainz, D. T.; Maple, J. R.; et al. Integrated Modeling Program, Applied Chemical Theory (IMPACT). *Journal of Computational Chemistry*. December 2005, pp 1752–1780. https://doi.org/10.1002/jcc.20292.

(78) Truchon, J.-F.; Bayly, C. I. Evaluating Virtual Screening Methods: Good and Bad Metrics for the "Early Recognition" Problem. *J. Chem. Inf. Model.* **2007**, *47* (2), 488–508. https://doi.org/10.1021/ci600426e.

(79) Sheridan, R. P.; Singh, S. B.; Fluder, E. M.; Kearsley, S. K. Protocols for Bridging the Peptide to Nonpeptide Gap in Topological Similarity Searches. *J. Chem. Inf. Comput. Sci.* **2001**, *41* (3–6), 1395–1406. https://doi.org/10.1021/ci0100144.

(80) Hamel, L. Model Assessment with ROC Curves. In *Encyclopedia of Data Warehousing and Mining, Second Edition*; IGI Global; pp 1316–1323. https://doi.org/10.4018/978-1-60566-010-3.ch204.

(81) Gao, L.; Zu, M.; Wu, S.; Liu, A.-L.; Du, G.-H. 3D QSAR and Docking Study of Flavone Derivatives as Potent Inhibitors of Influenza H1N1 Virus Neuraminidase. *Bioorg. Med. Chem. Lett.* **2011**, *21* (19), 5964–5970. https://doi.org/10.1016/j.bmcl.2011.07.071.

(82) Shelke, S. M.; Bhosale, S. H.; Dash, R. C.; Suryawanshi, M. R.; Mahadik, K. R. Exploration of

© University of Pretoria

New Scaffolds as Potential MAO-A Inhibitors Using Pharmacophore and 3D-QSAR Based in Silico Screening. *Bioorg. Med. Chem. Lett.* **2011**, *21* (8), 2419–2424. https://doi.org/10.1016/j.bmcl.2011.02.072.

(83) Veeramachaneni, G. K.; Raj, K. K.; Chalasani, L. M.; Annamraju, S. K.; JS, B.; Talluri, V. Shape Based Virtual Screening and Molecular Docking towards Designing Novel Pancreatic Lipase Inhibitors. *Bioinformation* **2015**, *11* (12), 535–542. https://doi.org/10.6026/97320630011535.

(84) Subhani, S.; Jayaraman, A.; Jamil, K. Homology Modelling and Molecular Docking of MDR1 with Chemotherapeutic Agents in Non-Small Cell Lung Cancer. *Biomed. Pharmacother.* **2015**, *71*, 37–45. https://doi.org/10.1016/j.biopha.2015.02.009.

(85) Gade, D. R.; Makkapati, A.; Yarlagadda, R. B.; Peters, G. J.; Sastry, B. S.; Rajendra Prasad, V. V. S. Elucidation of Chemosensitization Effect of Acridones in Cancer Cell Lines: Combined Pharmacophore Modeling, 3D QSAR, and Molecular Dynamics Studies. *Comput. Biol. Chem.* **2018**, *74*, 63–75. https://doi.org/10.1016/j.compbiolchem.2018.02.014.

(86) Rajendra Prasad, V. V. S.; Deepak Reddy, G.; Kathmann, I.; Amareswararao, M.; Peters, G. J. Nitric Oxide Releasing Acridone Carboxamide Derivatives as Reverters of Doxorubicin Resistance in MCF7/Dx Cancer Cells. *Bioorg. Chem.* **2016**, *64*, 51–58. https://doi.org/10.1016/j.bioorg.2015.11.007.

(87) Goyal, M.; Dhanjal, J. K.; Goyal, S.; Tyagi, C.; Hamid, R.; Grover, A. Development of Dual Inhibitors against Alzheimer's Disease Using Fragment-Based QSAR and Molecular Docking. *Biomed Res. Int.* **2014**, *2014*, 1–12. https://doi.org/10.1155/2014/979606.

(88) Vijayakumar, S.; Manogar, P.; Prabhu, S.; Sanjeevkumar Singh, R. A. Novel Ligand-Based Docking; Molecular Dynamic Simulations; and Absorption, Distribution, Metabolism, and Excretion Approach to Analyzing Potential Acetylcholinesterase Inhibitors for Alzheimer's Disease. *J. Pharm. Anal.* **2018**, *8* (6), 413–420. https://doi.org/10.1016/j.jpha.2017.07.006.

(89) Hayes, J. M.; Skamnaki, V. T.; Archontis, G.; Lamprakis, C.; Sarrou, J.; Bischler, N.; Skaltsounis, A.-L.; Zographos, S. E.; Oikonomakos, N. G. Kinetics, in Silico Docking, Molecular Dynamics, and MM-GBSA Binding Studies on Prototype Indirubins, KT5720, and Staurosporine as Phosphorylase Kinase ATP-Binding Site Inhibitors: The Role of Water Molecules Examined. *Proteins Struct. Funct. Bioinforma.* **2011**, *79* (3), 703–719. https://doi.org/10.1002/prot.22890.

(90) Cheng, T.; Li, Q.; Zhou, Z.; Wang, Y.; Bryant, S. H. Structure-Based Virtual Screening for Drug Discovery: A Problem-Centric Review. *AAPS J.* **2012**, *14* (1), 133–141. https://doi.org/10.1208/s12248-012-9322-0.

(91) Madhavi Sastry, G.; Adzhigirey, M.; Day, T.; Annabhimoju, R.; Sherman, W. Protein and Ligand Preparation: Parameters, Protocols, and Influence on Virtual Screening Enrichments. *J. Comput. Aided. Mol. Des.* **2013**, *27* (3), 221–234. https://doi.org/10.1007/s10822-013-9644-8.

(92) Wesley H. Brooks, †, ⊥; Kenyon G. Daniel, ‡, ⊥; Shen-Shu Sung, † and; Wayne C. Guida*, ‡,§, ∥. Computational Validation of the Importance of Absolute Stereochemistry in Virtual Screening. *J. Chem. Inf. Model.* **2008**, *48* (3), 639–645. https://doi.org/10.1021/CI700358R.

(93) Richard A. Friesner, *, †; Jay L. Banks, ‡; Robert B. Murphy, ‡; Thomas A. Halgren, ‡; Jasna J. Klicic, ‡, ∥; Daniel T. Mainz, ‡; Matthew P. Repasky, ‡; Eric H. Knoll, †; Mee Shelley, §; Jason K. Perry, §; et al. Glide: A New Approach for Rapid, Accurate Docking and Scoring. 1. Method and Assessment of Docking Accuracy. *J. Med. Chem.* **2004**, *47* (7), 1739–1749. https://doi.org/10.1021/JM0306430.

© University of Pretoria

(94) Rutkowska, E.; Pajak, K.; Jóźwiak, K. Lipophilicity--Methods of Determination and Its Role in Medicinal Chemistry. *Acta Pol. Pharm.* **2013**, *70* (1), 3–18.

(95) Schrodinger Release 2018-1. Canvas. Schrodinger: LLC, New York, NY 2018.

(96) Schrodinger Release 2018-1. Maestro. Schrodinger: LLC, New York, NY 2018.

(97) Watts, K. S.; Dalal, P.; Murphy, R. B.; Sherman, W.; Friesner, R. A.; Shelley, J. C. ConfGen: A Conformational Search Method for Efficient Generation of Bioactive Conformers. *J. Chem. Inf. Model.* **2010**, *50* (4), 534–546. https://doi.org/10.1021/ci100015j.

(98) Schrodinger Release 2018-1. MacroModel. Schrodinger: New York 2018.

(99) Gaulton, A.; Hersey, A.; Nowotka, M.; Bento, A. P.; Chambers, J.; Mendez, D.; Mutowo, P.; Atkinson, F.; Bellis, L. J.; Cibrián-Uhalte, E.; et al. The ChEMBL Database in 2017. *Nucleic Acids Res.* **2017**, *45* (D1), D945–D954. https://doi.org/10.1093/nar/gkw1074.

(100) Kryger, G.; Silman, I.; Sussman, J. L. Structure of Acetylcholinesterase Complexed with E2020 (Aricept®): Implications for the Design of New Anti-Alzheimer Drugs. *Structure* **1999**, *7* (3), 297–307. https://doi.org/10.1016/S0969-2126(99)80040-9.

(101) Schrodinger Release 2018-1. ConfGen. Schrodinger: LLC, New York, NY 2018.

(102) Steinbrecher, T. *MM-GBSA for Calculating Binding Affinity A Rank-Ordering Study for the Lead Optimization of Fxa and COX-2 Inhibitors*.

(103) Pietrasik, U.; Szydłowska, J.; Krówczyński, A. Metallomesogens Modified by Hydrogen Bonds or by Bridging GroupsNew Re-Entrant Isotropic Phase. *Chem. Mater.* **2004**, *16* (8), 1485–1492. https://doi.org/10.1021/cm034842j.

(104) Gómez-Lor, B.; Frutos, Ó. de; Ceballos, P. A.; Granier, T.; Echavarren, A. M. Synthesis of NewC3h AndC3v Truxene Derivatives. *European J. Org. Chem.* **2001**, *2001* (11), 2107–2114. https://doi.org/10.1002/1099-0690(200106)2001:11<2107::AID-EJOC2107>3.0.CO;2-F.

(105) Masson, E.; Marzi, E.; Cottet, F.; Bobbio, C.; Schlosser, M. Metalation and Derivatization of All Six Dichlorobenzotrifluorides:Site Selectivities. *European J. Org. Chem.* **2005**, *2005* (20), 4393–4400. https://doi.org/10.1002/ejoc.200500240.

(106) Inagaki, S.; Saito, K.; Suto, S.; Aihara, H.; Sugawara, A.; Tamura, S.; Kawano, T. Synthesis of 5-Aryl-3(2 H)-Furanones Using Intramolecular Cyclization of Sulfonium Salts. *J. Org. Chem.* **2018**, *83* (22), 13834–13846. https://doi.org/10.1021/acs.joc.8b02153.

(107) Riley, D. L.; Michael, S. J. P. Synthesis of Amphibian Indolizidine Alkaloids and Related Compounds from Enaminone Precursors, University of Witwatersrand, 2007.

(108) Savin, K. A. Oxidations and Reductions. In *Writing Reaction Mechanisms in Organic Chemistry*; Elsevier, 2014; pp 355–431. https://doi.org/10.1016/B978-0-12-411475-3.00007-5.

(109) van Greunen, D. G.; Johan van der Westhuizen, C.; Cordier, W.; Nell, M.; Stander, A.; Steenkamp, V.; Panayides, J.-L.; Riley, D. L. Novel N-Benzylpiperidine Carboxamide Derivatives as Potential Cholinesterase Inhibitors for the Treatment of Alzheimer's Disease. *Eur. J. Med. Chem.* **2019**, *179*, 680–693. https://doi.org/10.1016/j.ejmech.2019.06.088.

(110) Gichinga, M. G.; Striegler, S. Regioselective Alkylation of Hydroxysalicylaldehydes. *Tetrahedron* **2009**, *65* (25), 4917–4922. https://doi.org/10.1016/j.tet.2009.03.104.

(111) de la Fuente, V.; Waugh, M.; Eastham, G. R.; Iggo, J. A.; Castillón, S.; Claver, C. Phosphine Ligands in the Palladium-Catalysed Methoxycarbonylation of Ethene: Insights into the

© University of Pretoria

Catalytic Cycle through an HP NMR Spectroscopic Study. *Chem. - A Eur. J.* **2010**, *16* (23), 6919–6932. https://doi.org/10.1002/chem.200903158.

(112) Smith, J. G. *Organic Chemistry, Third Edition*, Third Edit.; McGraw-Hill, 2011.

(113) Banerjee, A.; Yadav, P. S.; Bajpai, M.; Sangana, R. R.; Gullapalli, S.; Gudi, G. S.; Gharat, L. A. Isothiazole and Isoxazole Fused Pyrimidones as PDE7 Inhibitors: SAR and Pharmacokinetic Evaluation. *Bioorg. Med. Chem. Lett.* **2012**, *22* (9), 3223–3228. https://doi.org/10.1016/j.bmcl.2012.03.025.

(114) Arifin, B.; Tang, D. F.; Achmadi, S. S. Transformation of Eugenol and Safrole into Hydroxychavicol. *Indones. J. Chem.* **2015**, *15* (1), 77–85. https://doi.org/10.22146/ijc.21227.

(115) Panayides, J.-L. The Synthesis and Biological Testing of Nucleoside Derivatives, University of the Witwatersrand.

(116) PJ. Launer, B. A. *INFRARED ANALYSIS OF ORGANOSILICON COMPOUNDS: SPECTRA-STRUCTURE CORRELATIONS*; Morrisville.

(117) Ngo, H. L.; Lin, W. Development of 4,4‘-Substituted-XylBINAP Ligands for Highly Enantioselective Hydrogenation of Ketones. *J. Org. Chem.* **2005**, *70* (4), 1177–1187. https://doi.org/10.1021/jo048333s.

(118) Kondo, S.; Watanabe, N.; Takahashi, F.; Takeda, N.; Unno, M. Synthesis and Photophysical Properties of 2,2’-Binaphthalene-Based Receptor Bearing Trimethylsilyl Groups to Improve the Solubility. *J. Incl. Phenom. Macrocycl. Chem.* **2013**, *75* (1–2), 31–38. https://doi.org/10.1007/s10847-012-0142-8.

(119) Sleevi, M. C.; Wolfe, J. F. Metalation-Carboxylation of p- and m-(Trimethylsilyl)Toluenes as a Convenient Route to [p- and m-(Trimethylsilyl)Phenyl]Acetic Acids. *J. Org. Chem.* **1980**, *45* (25), 5204–5206. https://doi.org/10.1021/jo01313a036.

(120) Weickgenannt, A.; Oestreich, M. Potassium *Tert* -Butoxide-Catalyzed Dehydrogenative Si□O Coupling: Reactivity Pattern and Mechanism of an Underappreciated Alcohol Protection. *Chem. - An Asian J.* **2009**, *4* (3), 406–410. https://doi.org/10.1002/asia.200800426.

(121) Oliverio, M.; Nardi, M.; Costanzo, P.; Cariati, L.; Cravotto, G.; Giofrè, S.; Procopio, A. Non-Conventional Methodologies in the Synthesis of 1-Indanones. *Molecules* **2014**, *19* (5), 5599–5610. https://doi.org/10.3390/molecules19055599.

(122) Park, J. S.; Im, W.; Choi, S.; Park, S. J.; Jung, J. M.; Baek, K. S.; Son, H. P.; Sharma, S.; Kim, I. S.; Jung, Y. H. Discovery and SAR of N-(1-((Substituted Piperidin-4-Yl)Methyl)-3-Methoxypiperidin-4-Yl)-2-Methoxybenzamide Derivatives: 5-Hydroxytryptamine Receptor 4 Agonist as a Potent Prokinetic Agent. *Eur. J. Med. Chem.* **2016**, *109*, 75–88. https://doi.org/10.1016/j.ejmech.2015.12.006.

(123) Fan, Y.-J.; Zhou, L.; Li, S. Catalytic Asymmetric 1,6-Conjugate Addition of in Situ Generated Para -Quinone Methides with Tritylthiol. *Org. Chem. Front.* **2018**, *5* (11), 1820–1824. https://doi.org/10.1039/C8QO00211H.

(124) Hofmann, A.; Ren, R.; Lough, A.; Fekl, U. Highly Substituted Cyclohexanes: Strong Proximity Effects Influence Synthetic Access to 1,3,5-Tris(Bromomethyl)-1,3,5-Trialkylcyclohexanes (Alkyl=methyl, n-Propyl). *Tetrahedron Lett.* **2006**, *47* (15), 2607–2610. https://doi.org/10.1016/j.tetlet.2006.02.033.

(125) Yeates, C. L.; Batchelor, J. F.; Capon, E. C.; Cheesman, N. J.; Fry, M.; Hudson, A. T.; Pudney, M.; Trimming, H.; Woolven, J.; Bueno, J. M.; et al. Synthesis and Structure–Activity Relationships

© University of Pretoria

of 4-Pyridones as Potential Antimalarials. *J. Med. Chem.* **2008**, *51* (9), 2845–2852. https://doi.org/10.1021/jm0705760.

(126) Nguyen, N. H.; Cougnon, C.; Gohier, F. Deprotection of Arenediazonium Tetrafluoroborate Ethers with BBr 3. *J. Org. Chem.* **2009**, *74* (10), 3955–3957. https://doi.org/10.1021/jo8027906.

Appendix A

Please see the accompanying DVD containing the computational data pertaining to this study

© University of Pretoria

Appendix B

B.1 Ethyl 1-benzylpiperidine-4-carboxylate (31)

B.1.1 ^{1}H and ^{13}C NMR spectra of compound (31)

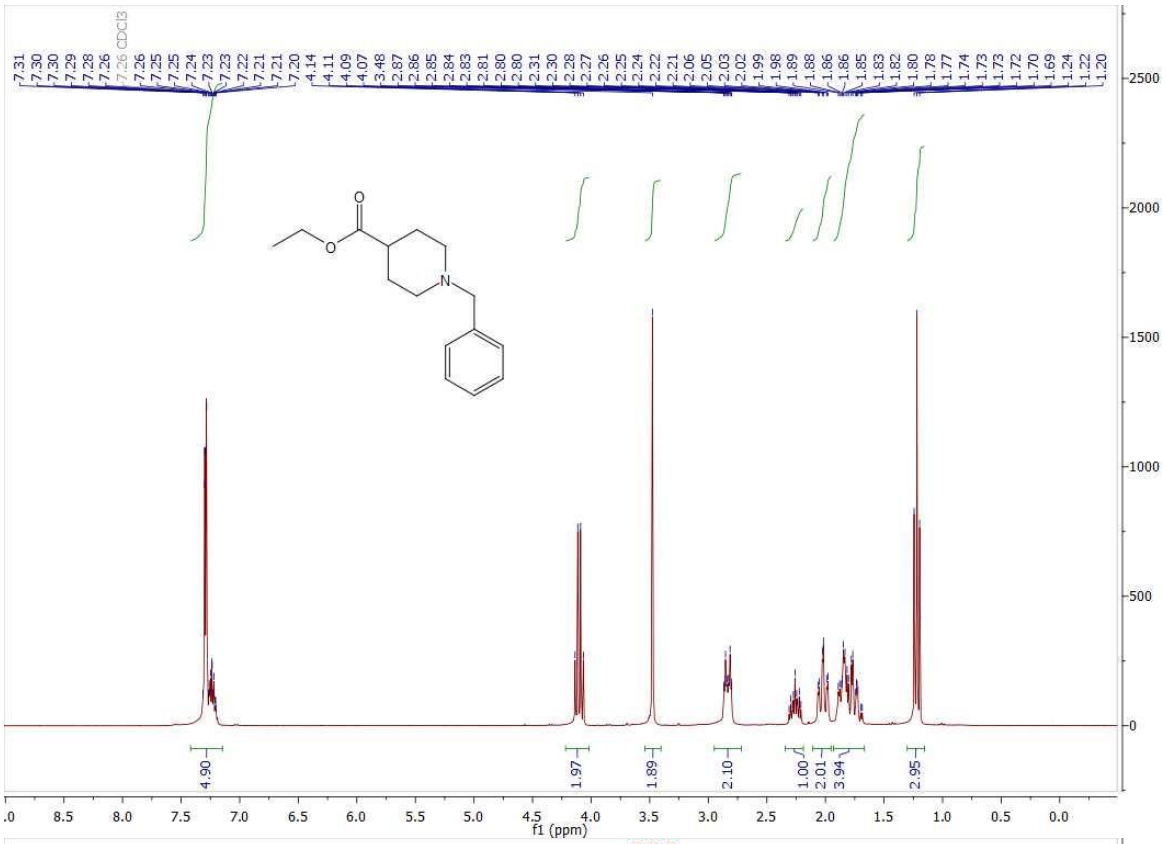

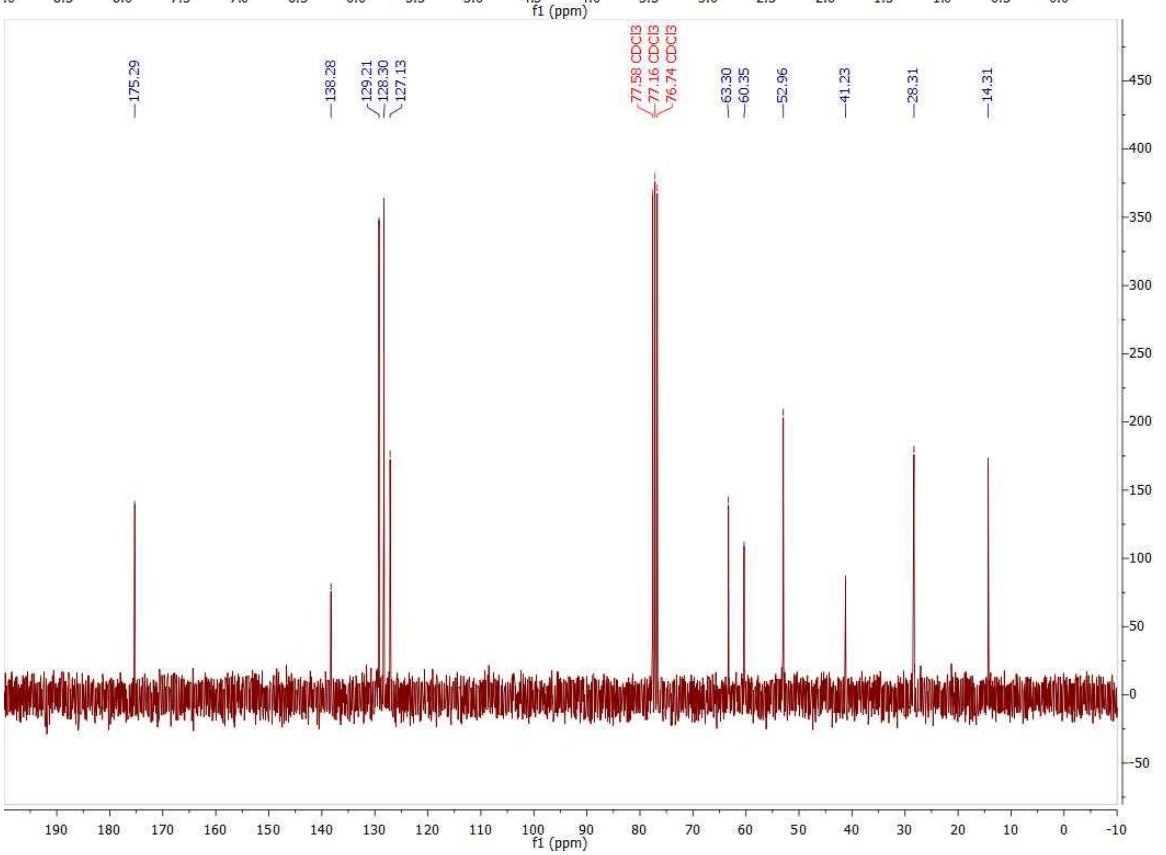

© University of Pretoria

B.1.2 HRMS spectrum of compound (31)

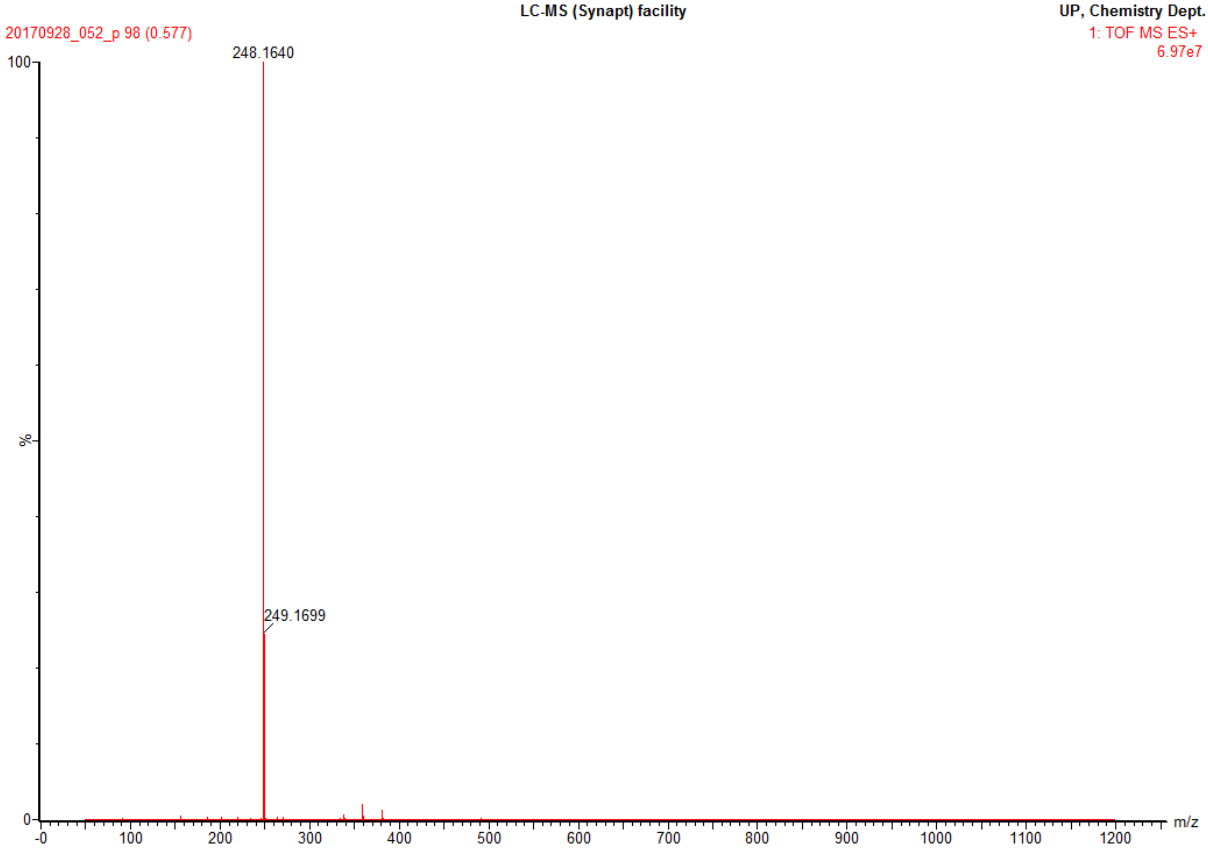

B.1.3 IR spectrum of compound (31)

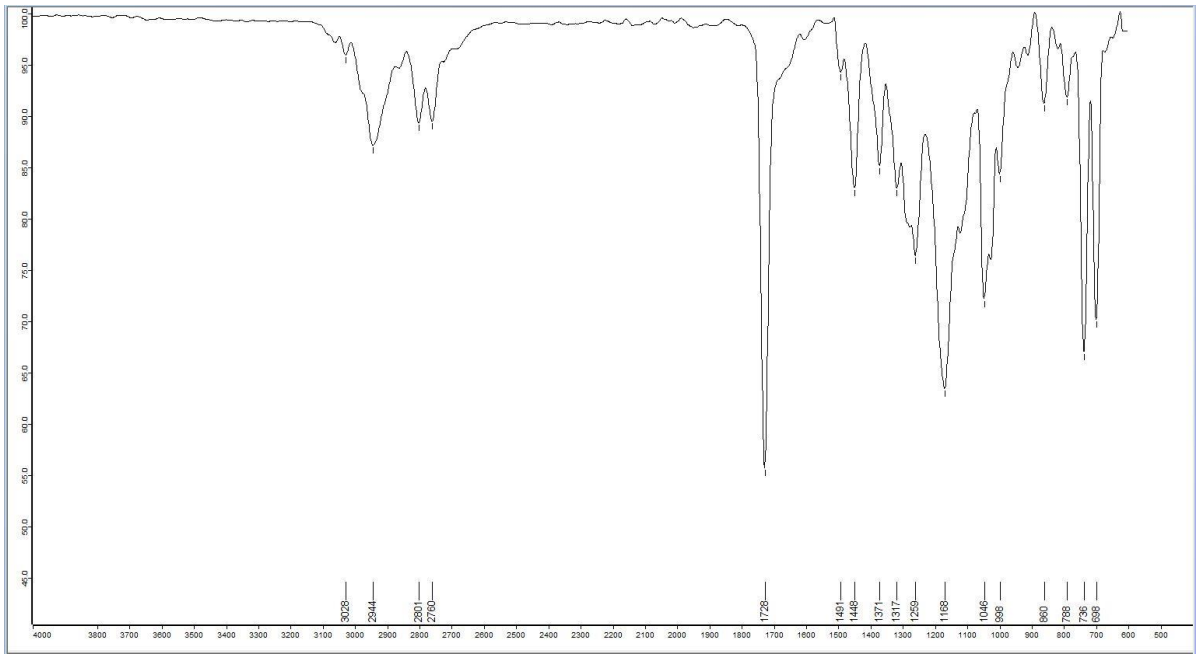

© University of Pretoria

B.2 (1-benzylpiperidin-4-yl)methanol (30)

B.2.1 ^{1}H and ^{13}C NMR spectra of compound (30)

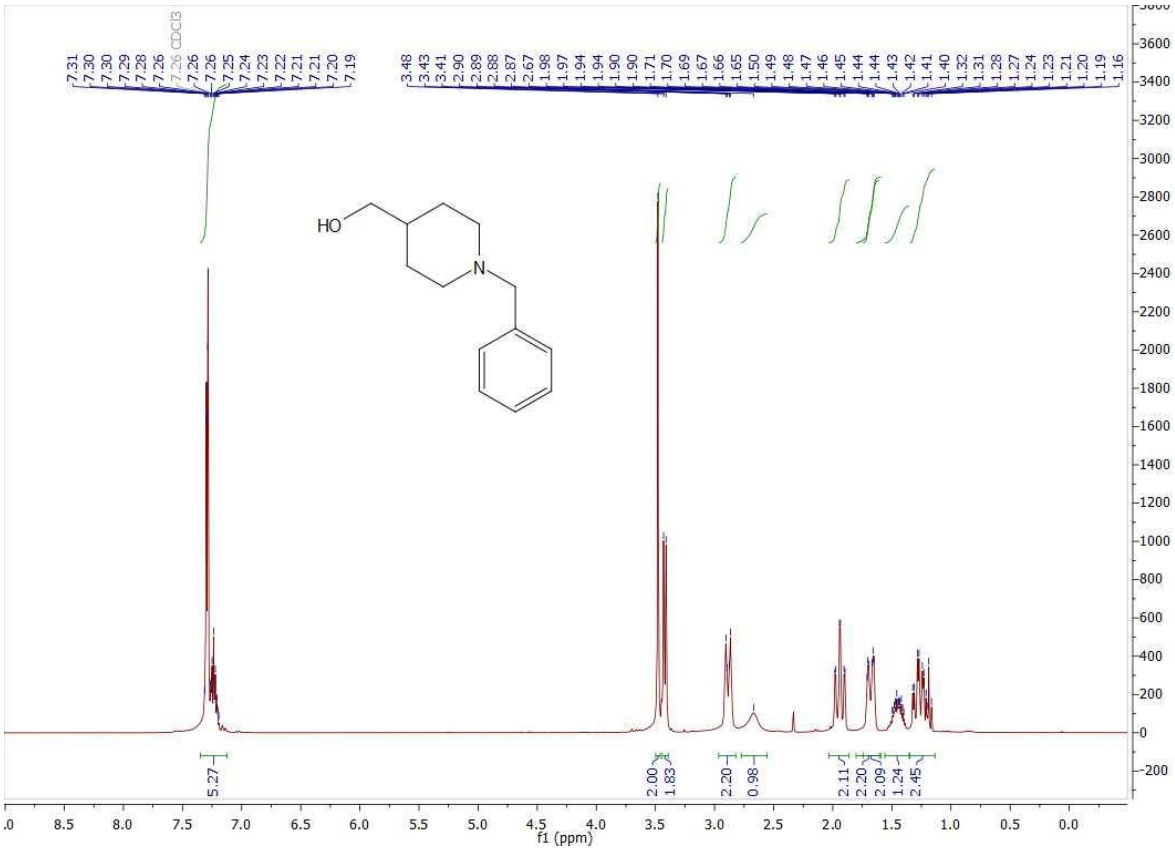

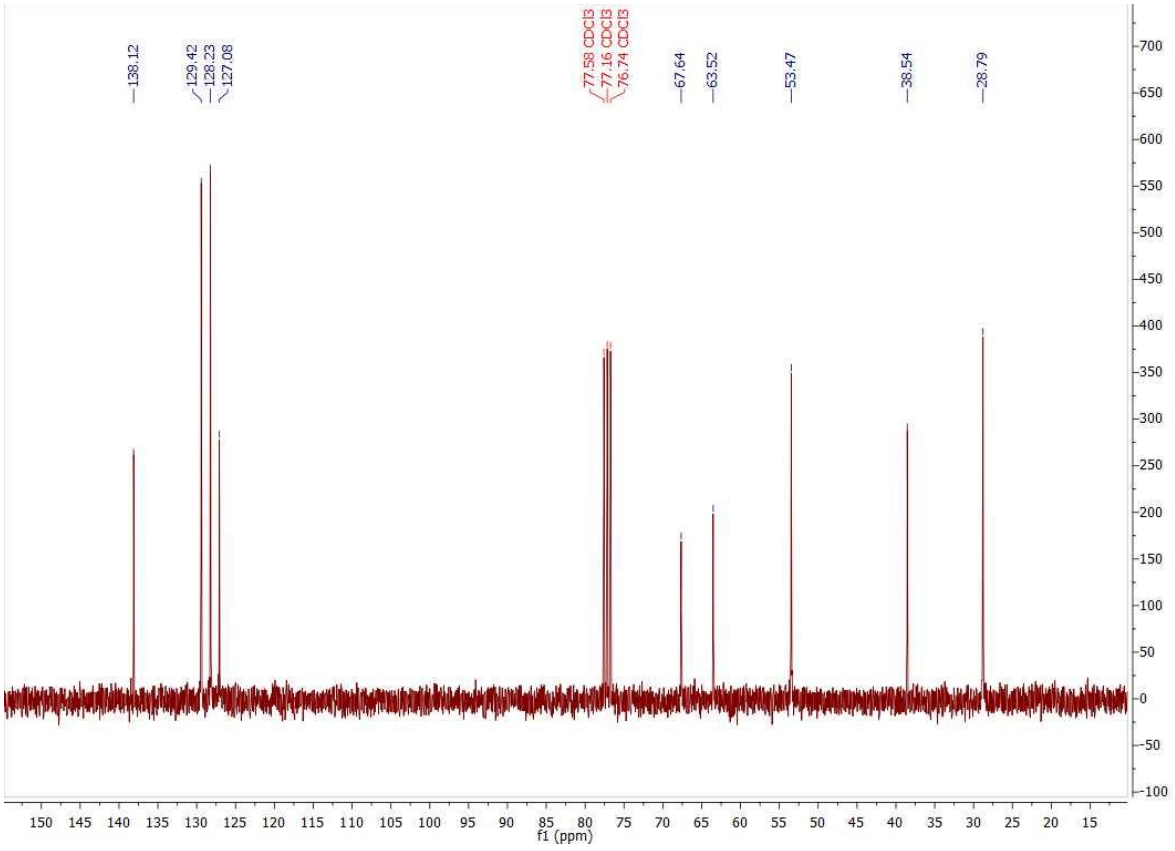

© University of Pretoria

B.2.2 HRMS spectrum of compound (30)

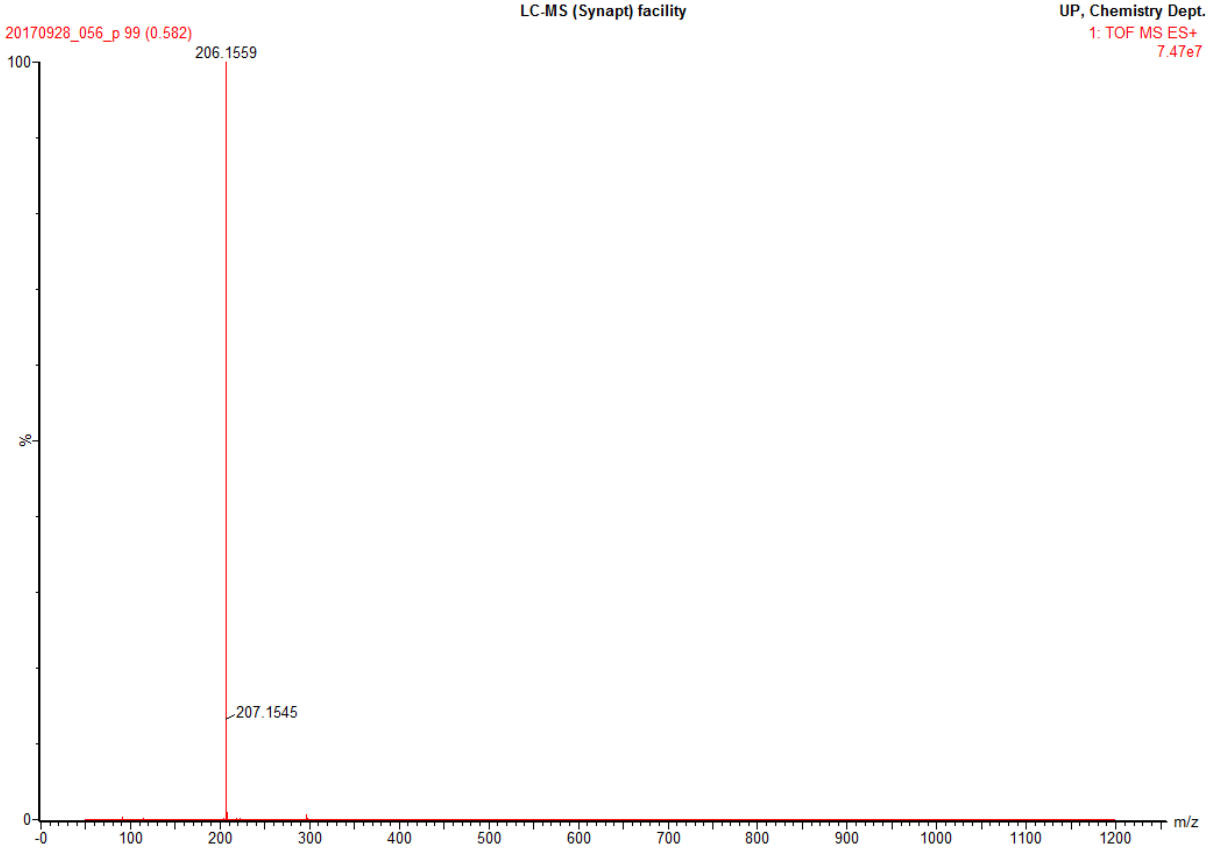

B.2.3 IR spectrum of compound (30)

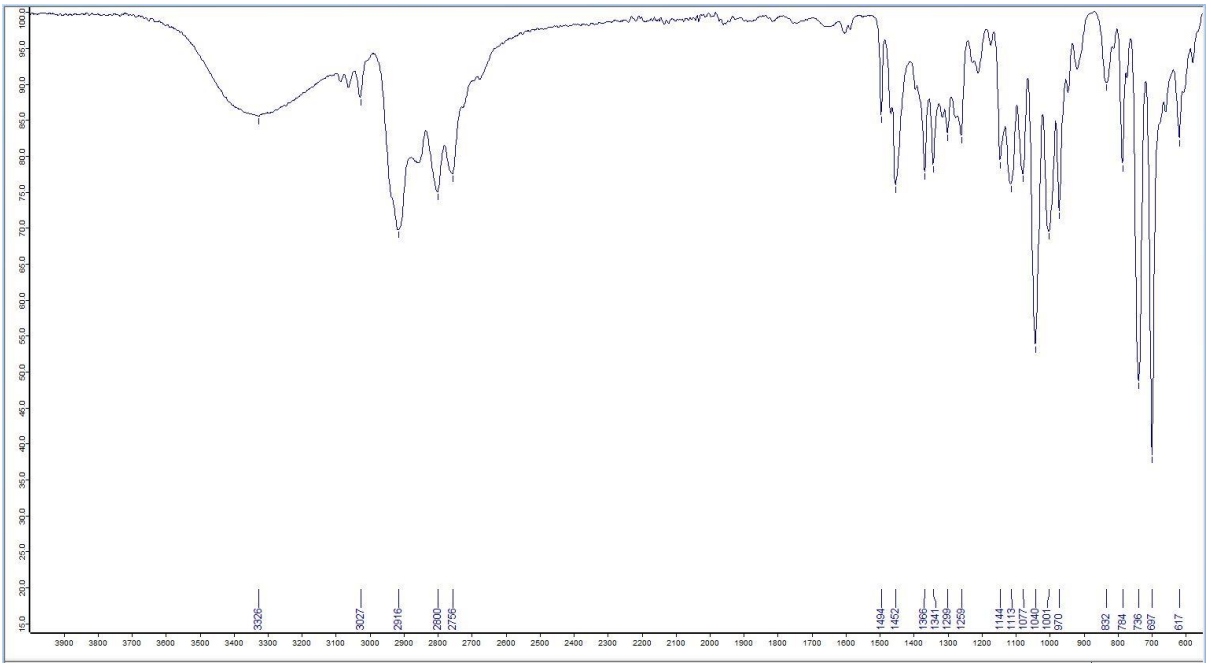

© University of Pretoria

B.3 1-benzylpiperidine-4-carbaldehyde (28)

B.3.1 ^{1}H and ^{13}C NMR spectra of compound (28)

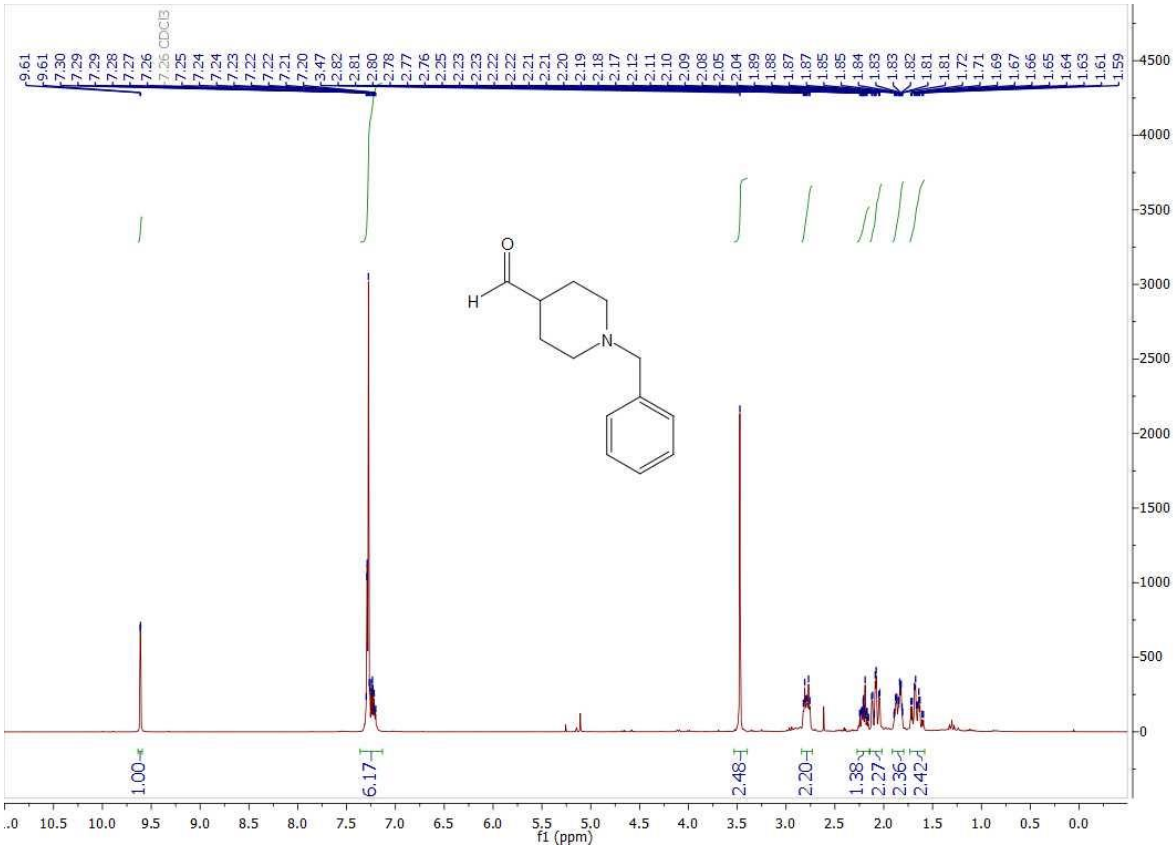

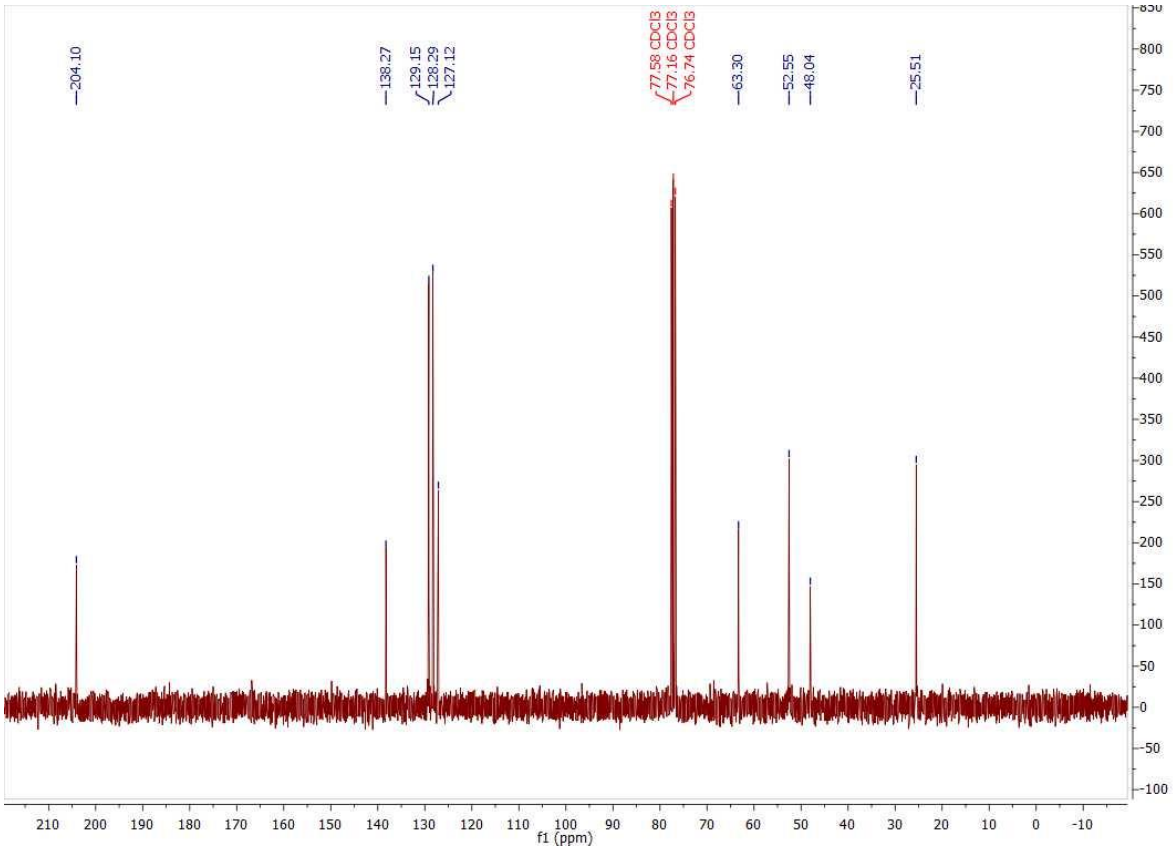

© University of Pretoria

B.3.2 HRMS spectrum of compound (28)

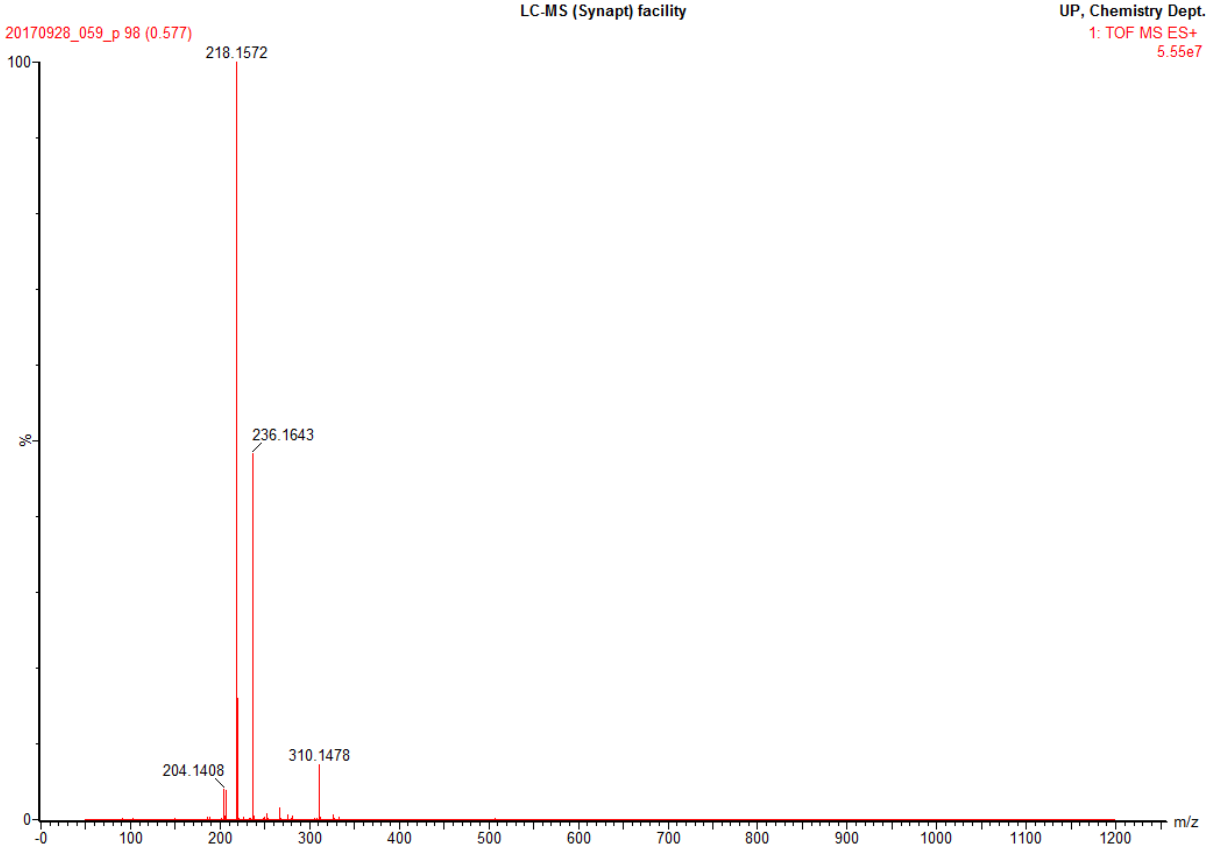

B.3.3 IR spectrum of compound (28)

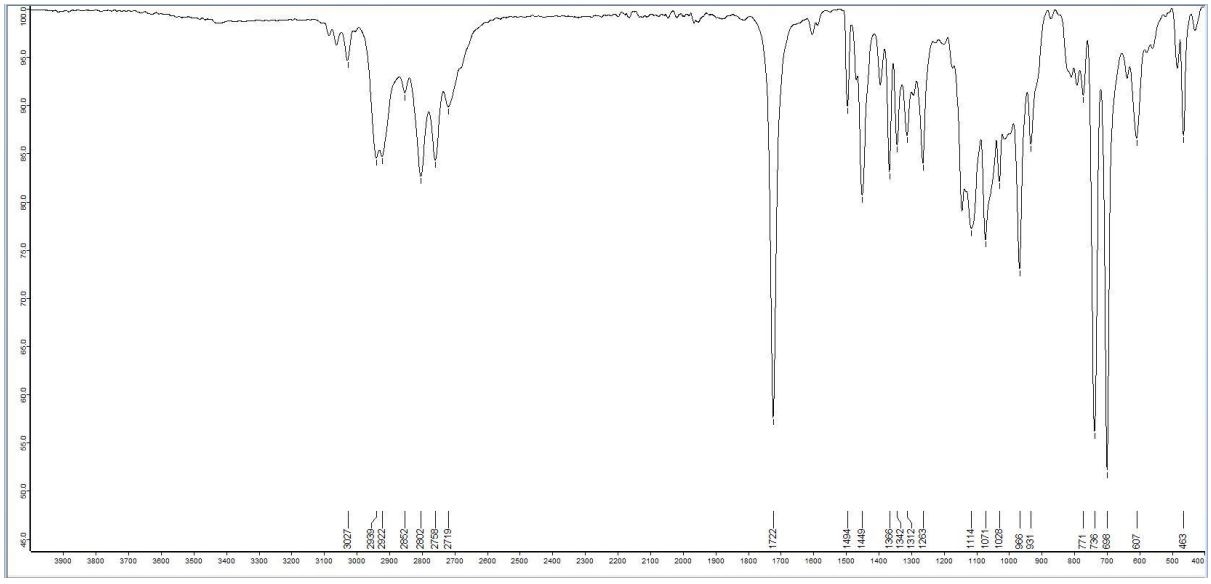

© University of Pretoria

B.4 (*E*)-2-((1-benzylpiperidin-4-yl)methylene)-5,6-dimethoxy-2,3-dihydro-1*H*-inden-1-one (27)

B.4.1 ^{1}H and ^{13}C NMR spectra of compound (27)

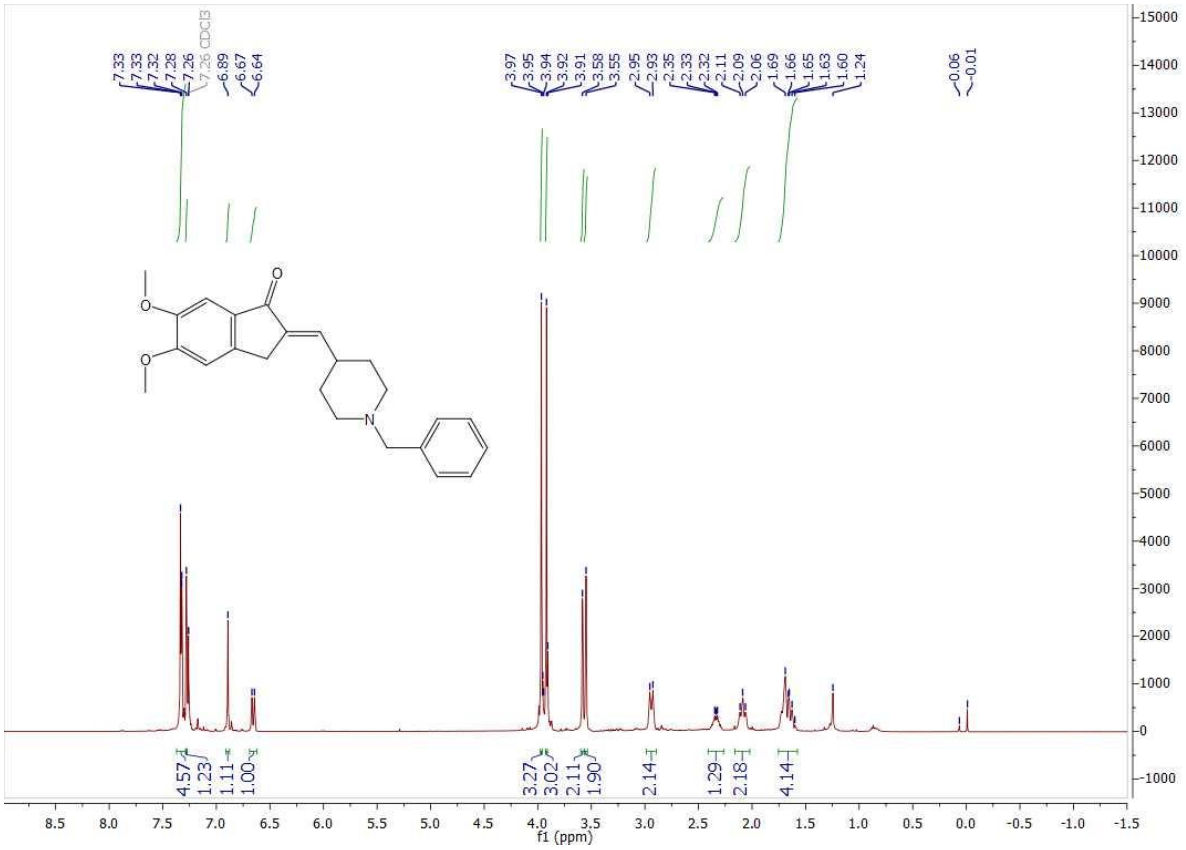

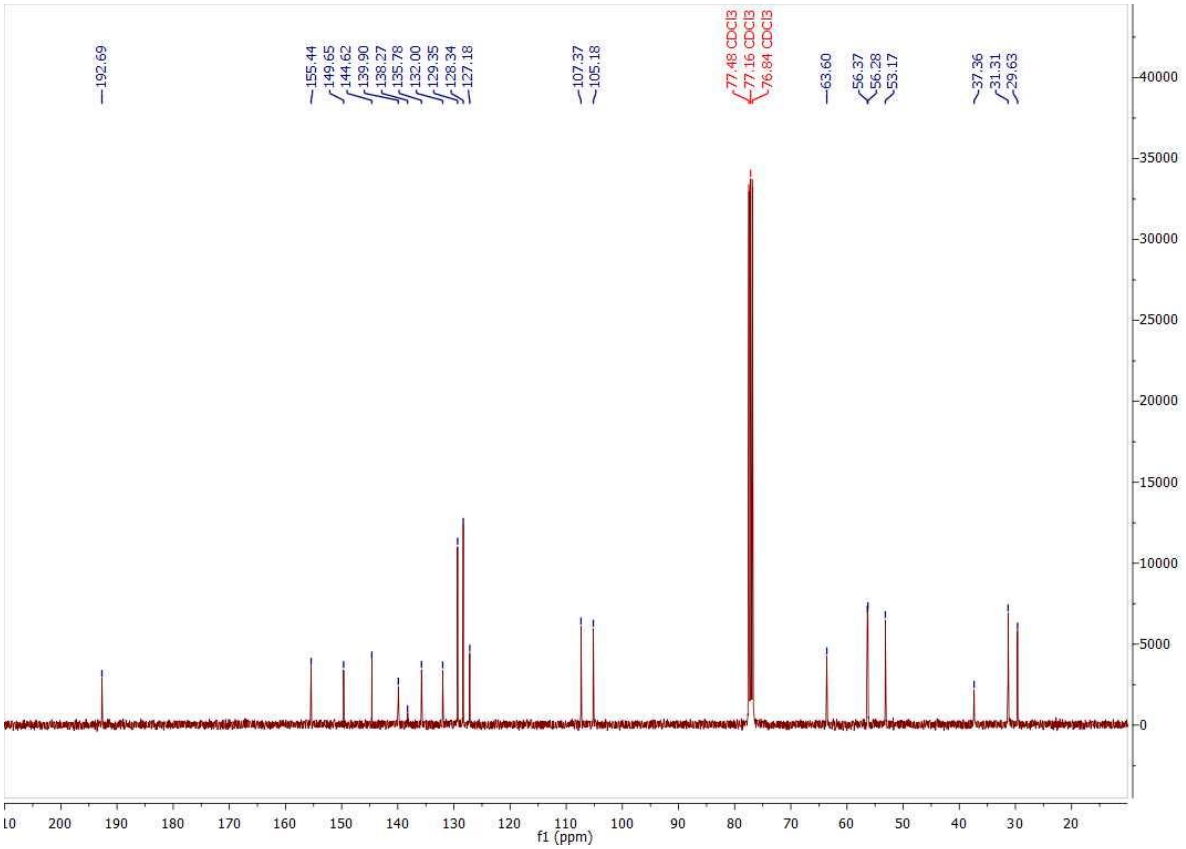

© University of Pretoria

B.4.2 HRMS spectrum of compound (27)

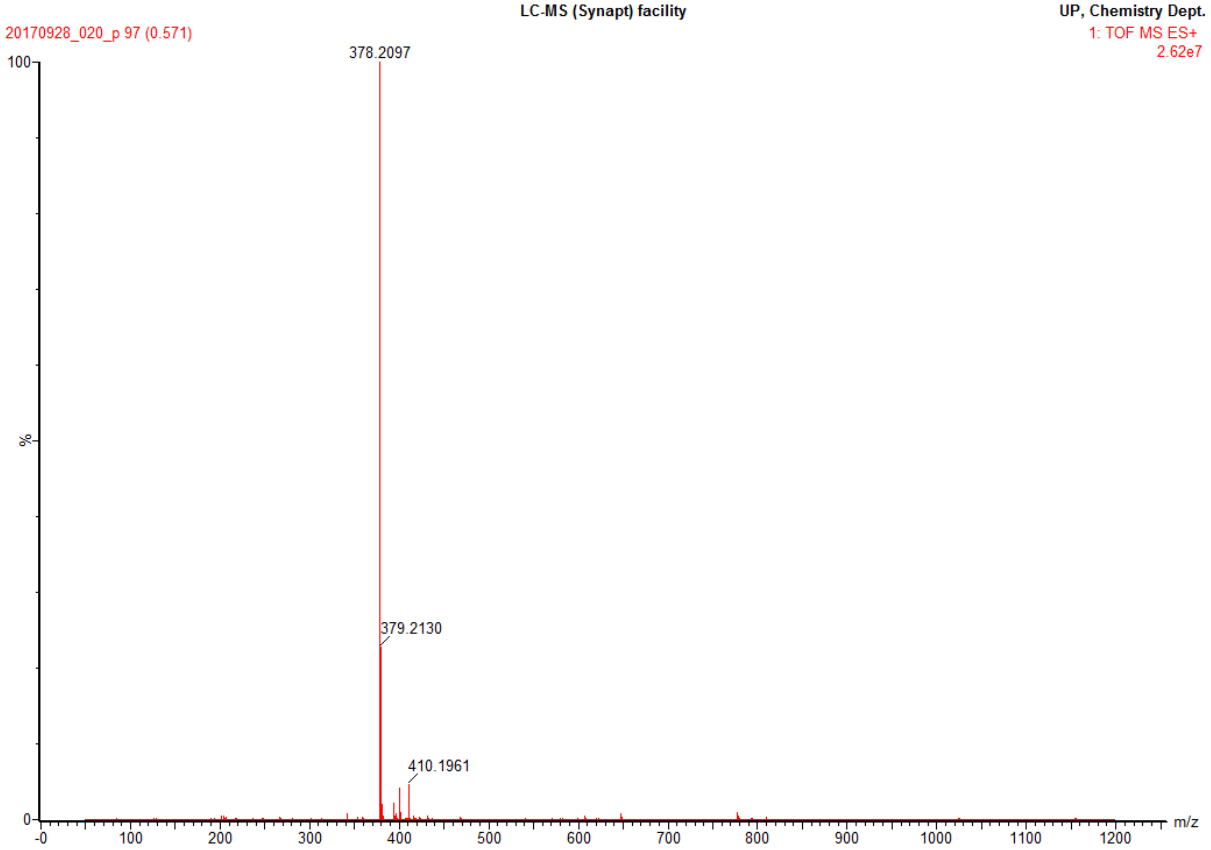

B.4.3 IR spectrum of compound (27)

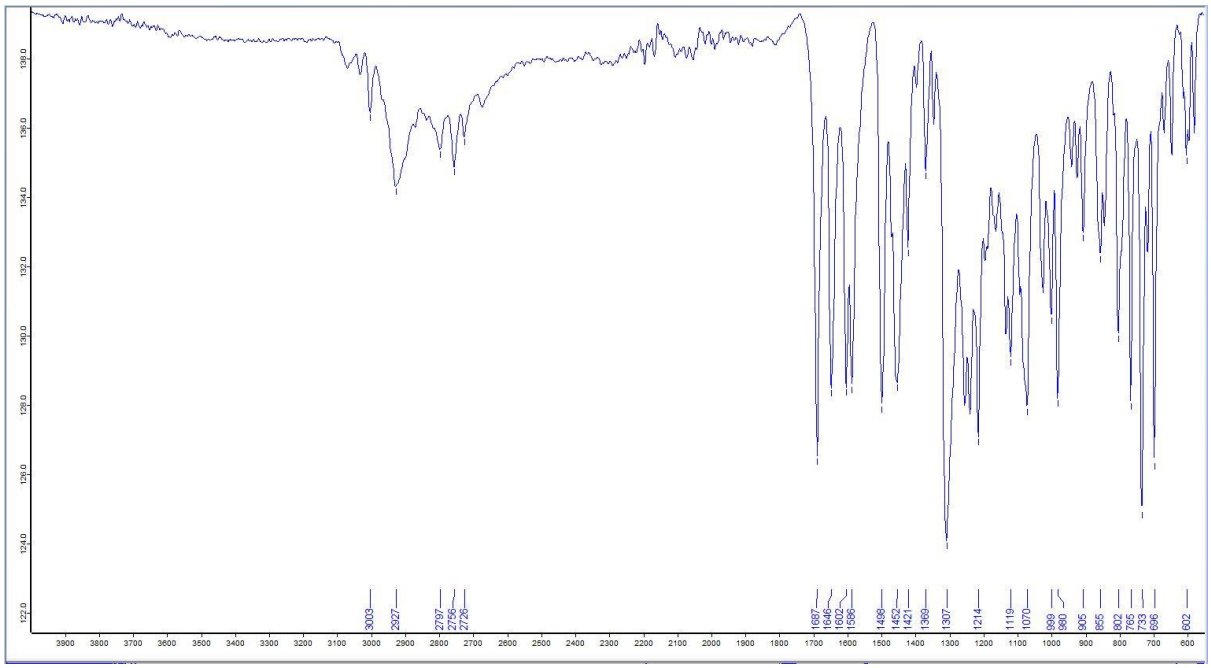

© University of Pretoria

B.5 1-benzyl-4-(chloromethyl)piperidine (243)

B.5.1 ^{1}H and ^{13}C NMR spectra of compound (243)

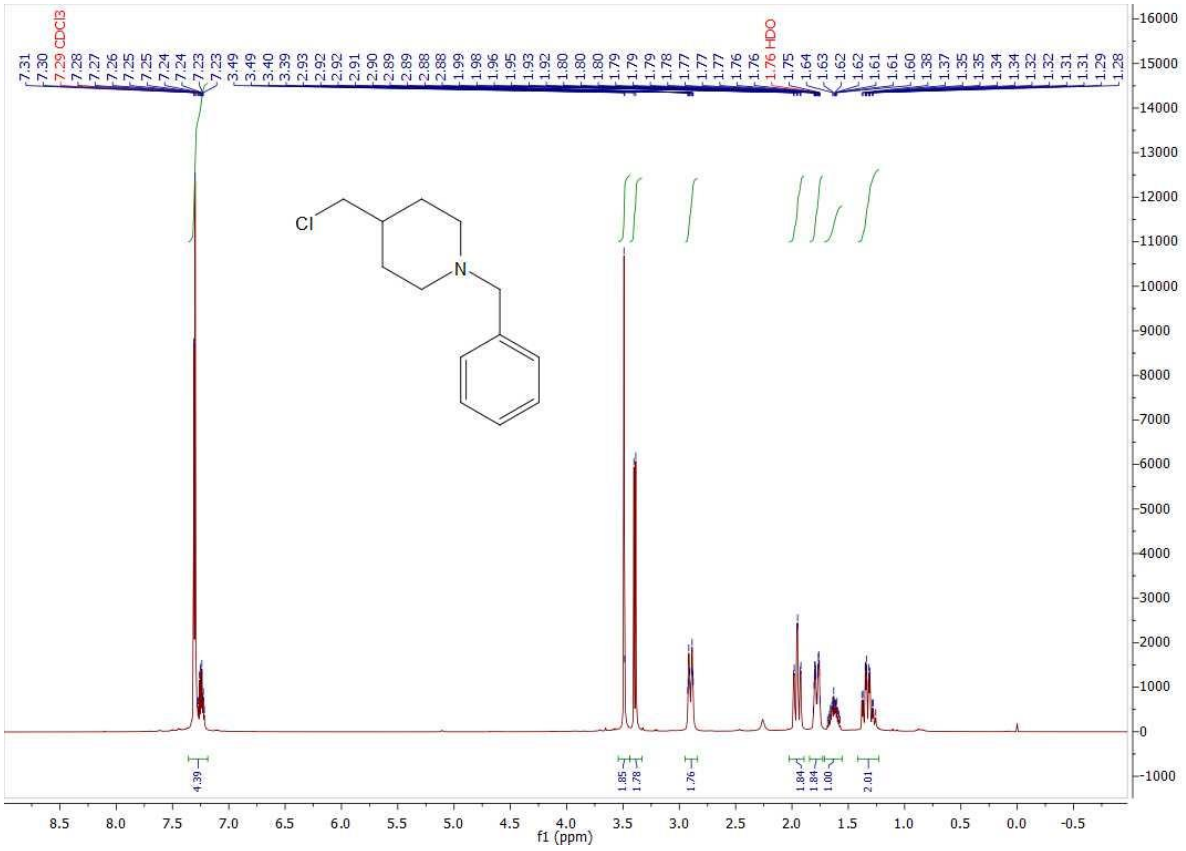

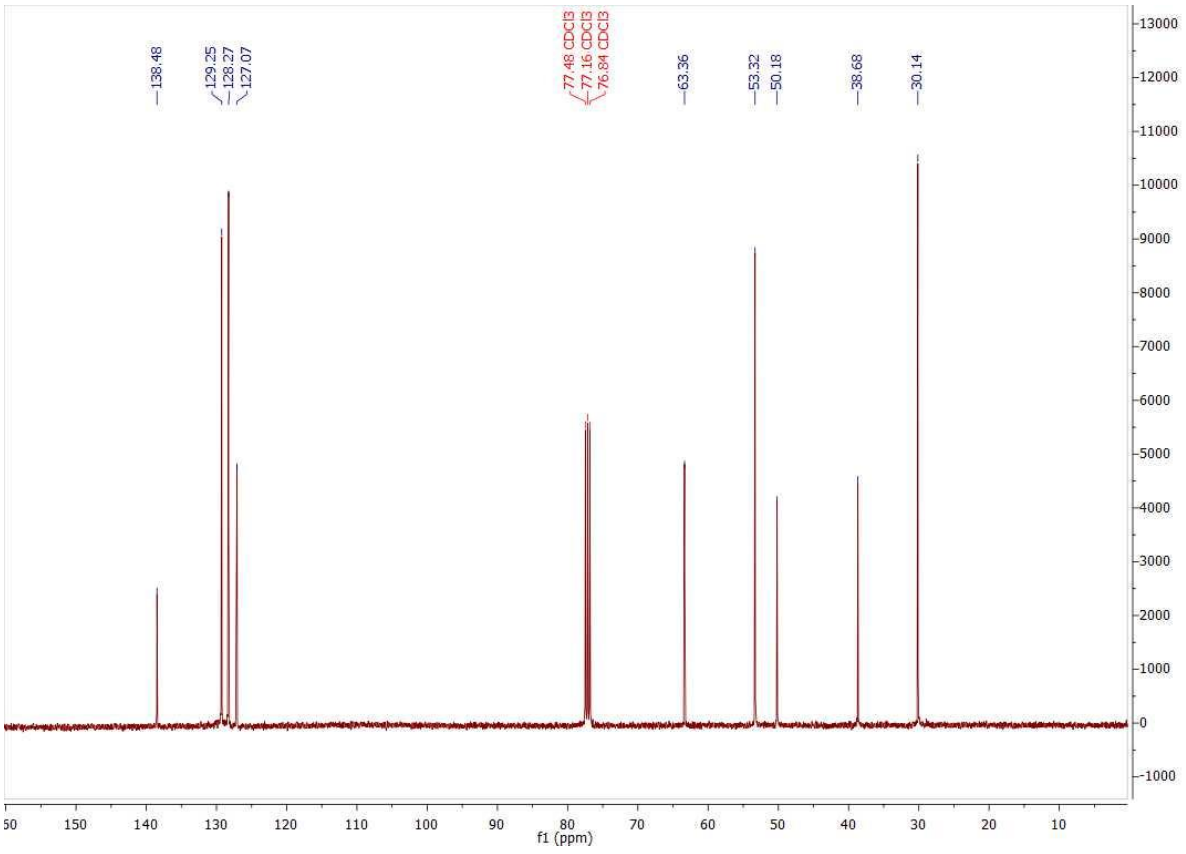

© University of Pretoria

B.6 5-hydroxy-6-methoxy-2,3-dihydro-1*H*-inden-1-one (244)

B.6.1 ^{1}H and ^{13}C NMR spectra of compound (244)

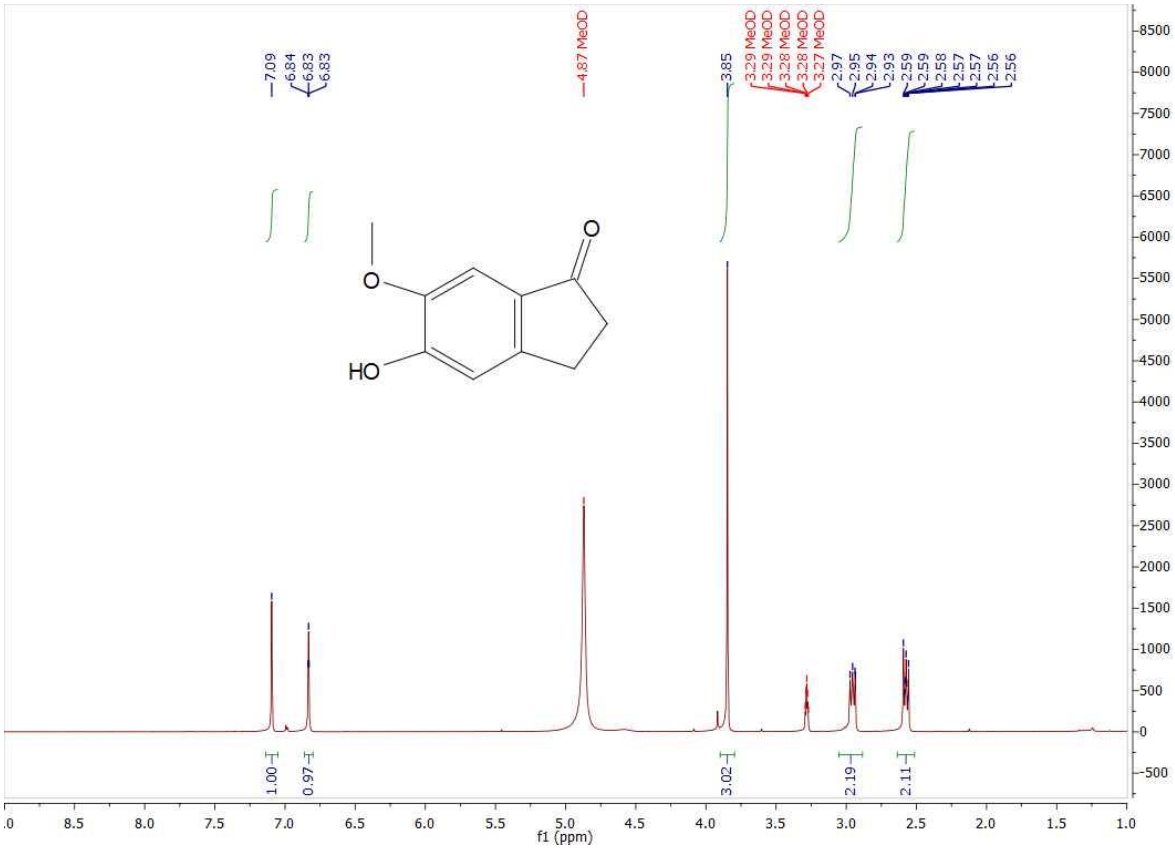

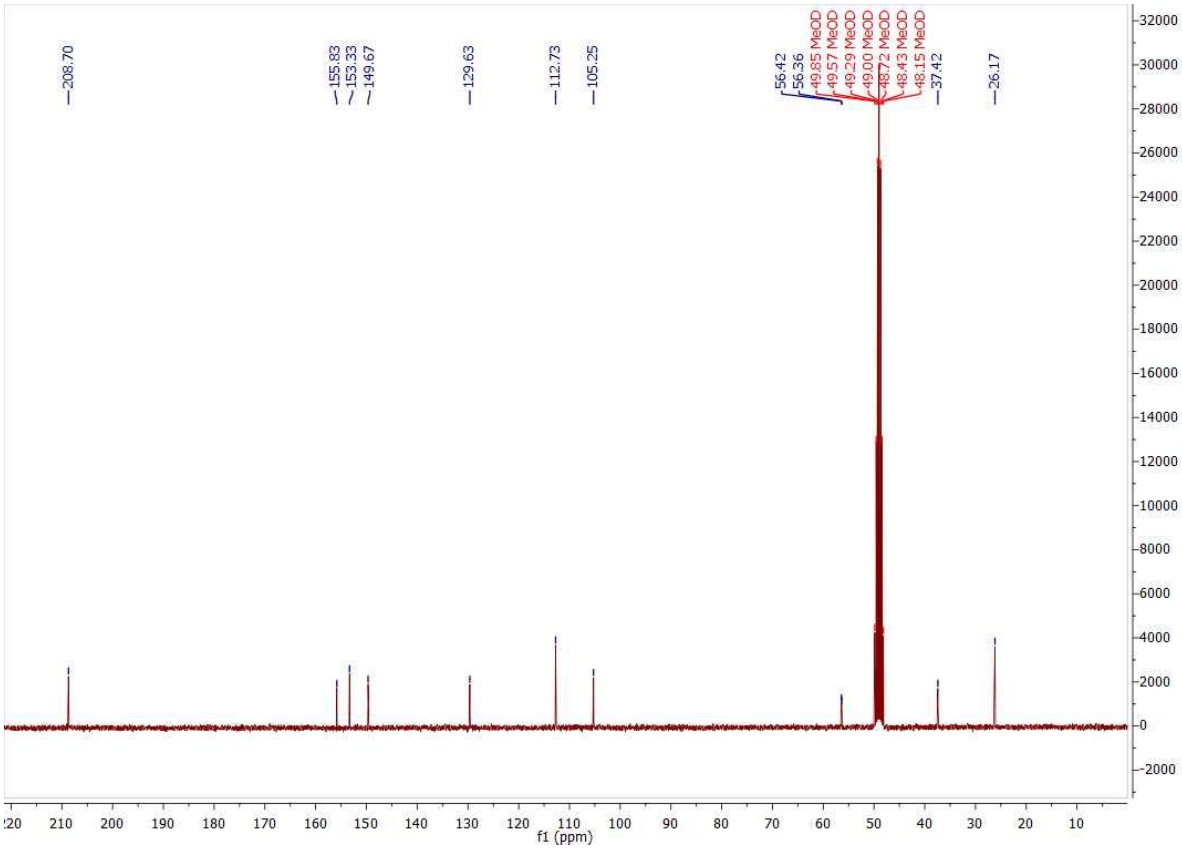

© University of Pretoria

B.6.2 HRMS spectrum of compound (244)

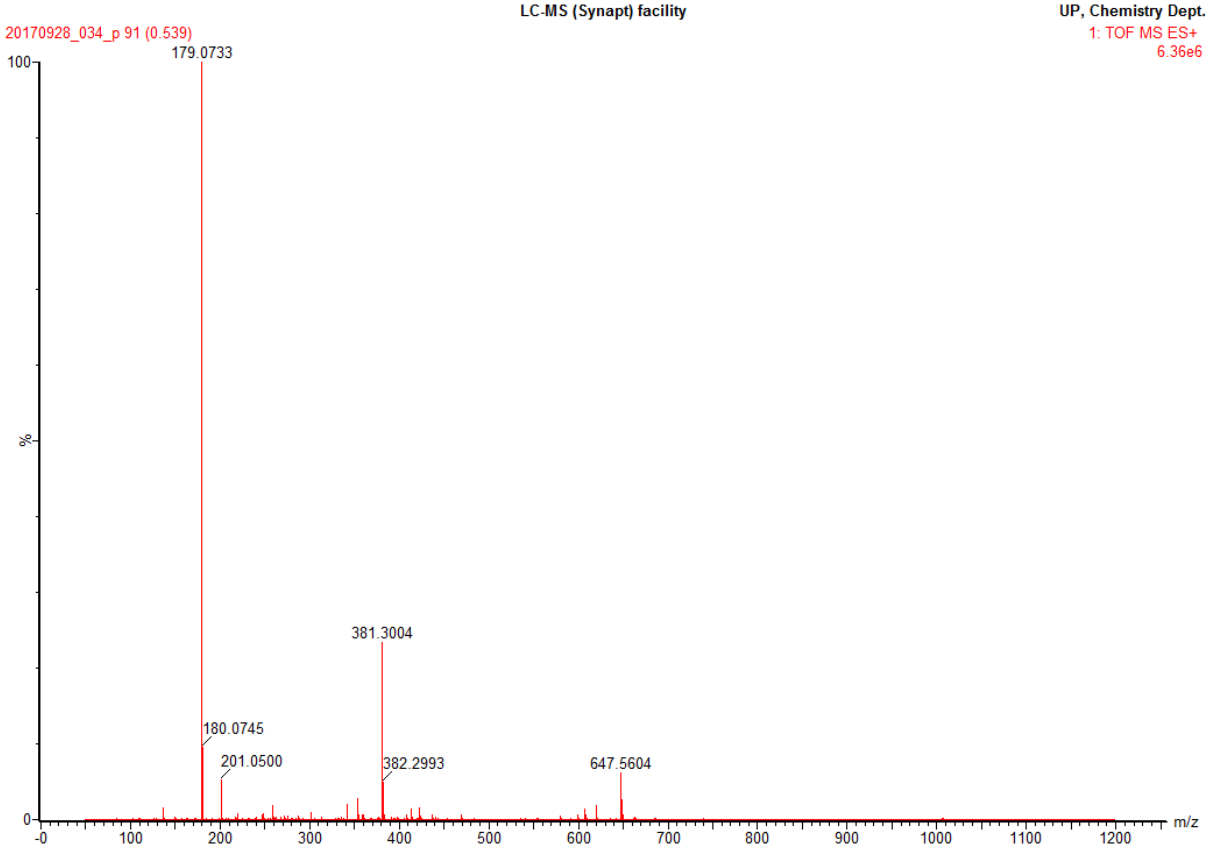

B.6.3 IR spectrum of compound (244)

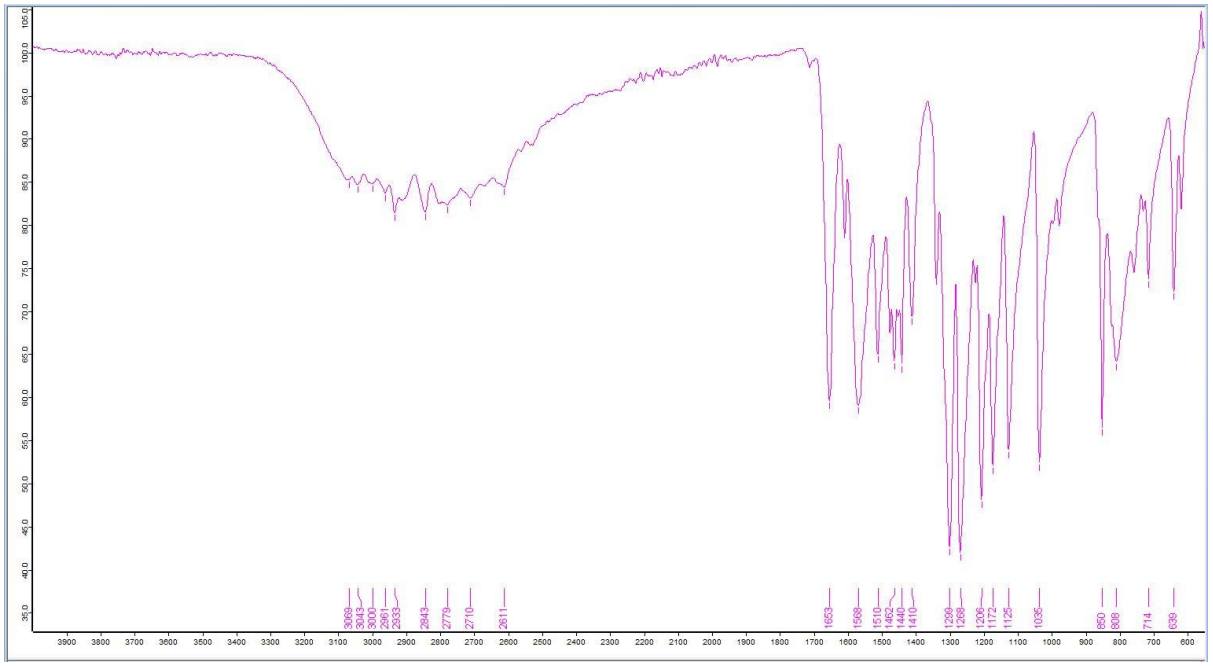

© University of Pretoria

B.6.4 XRD Resolved image of compound (244)

SLV001
R1 = 2.66%
2017/09/06

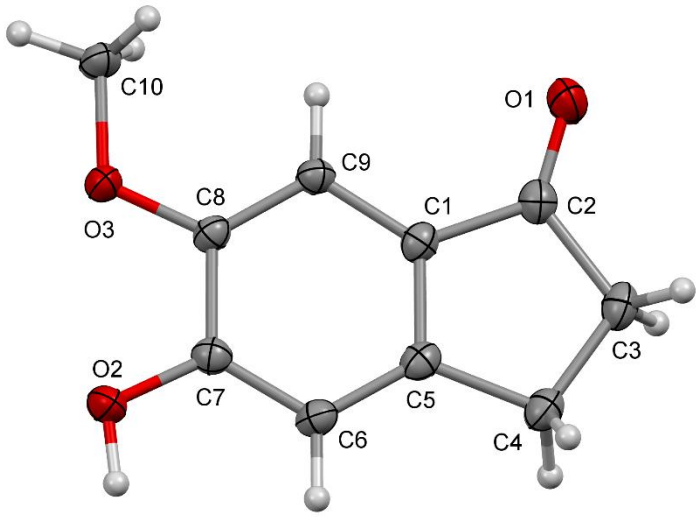

© University of Pretoria

B.7 5,6-dihydroxy-2,3-dihydro-1*H*-inden-1-one (245)

B.7.1 ^{1}H and ^{13}C NMR spectra of compound (245)

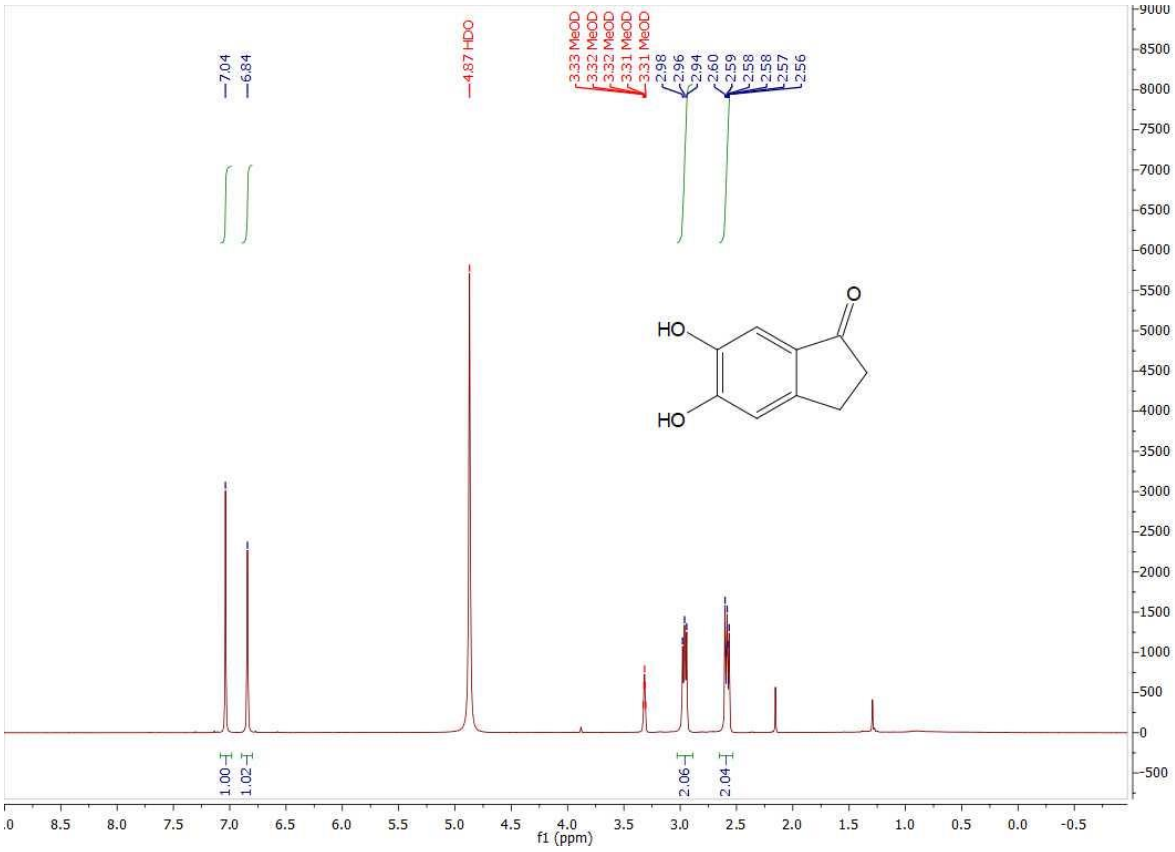

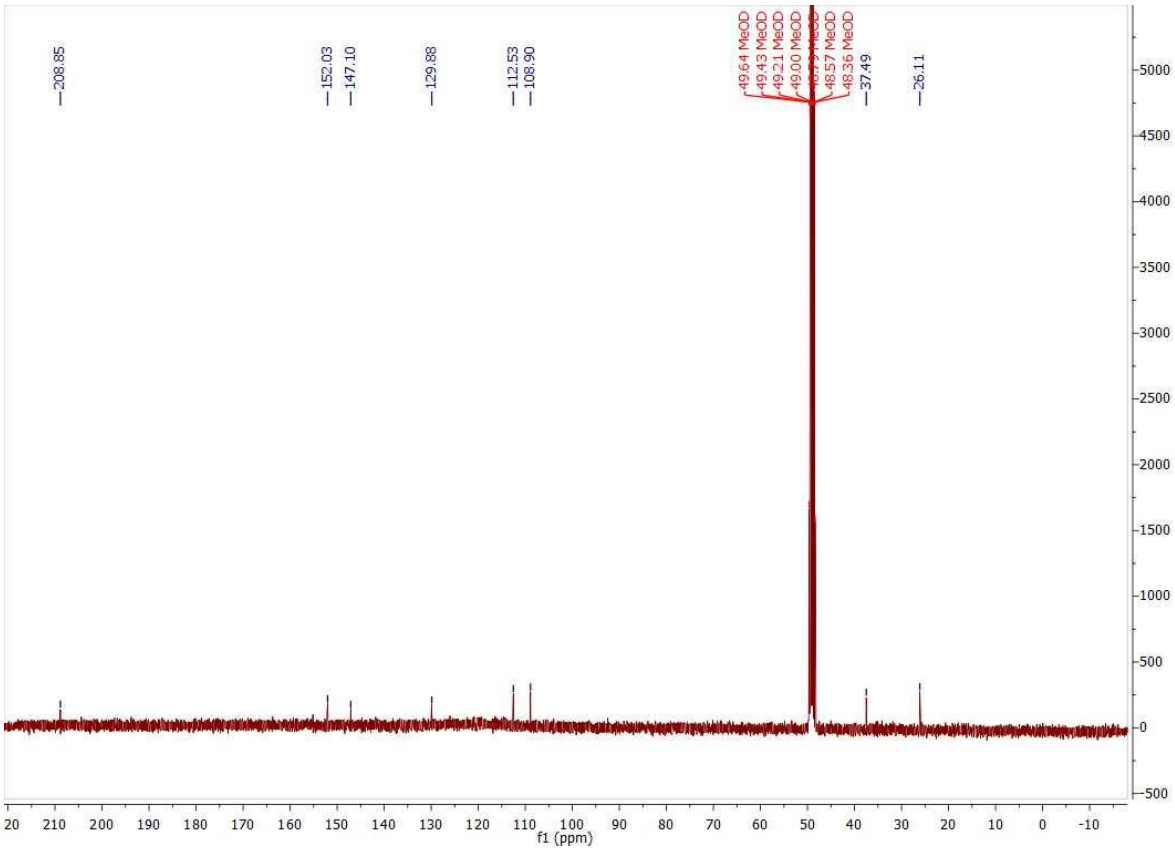

© University of Pretoria

B.7.2 HRMS spectrum of compound (245)

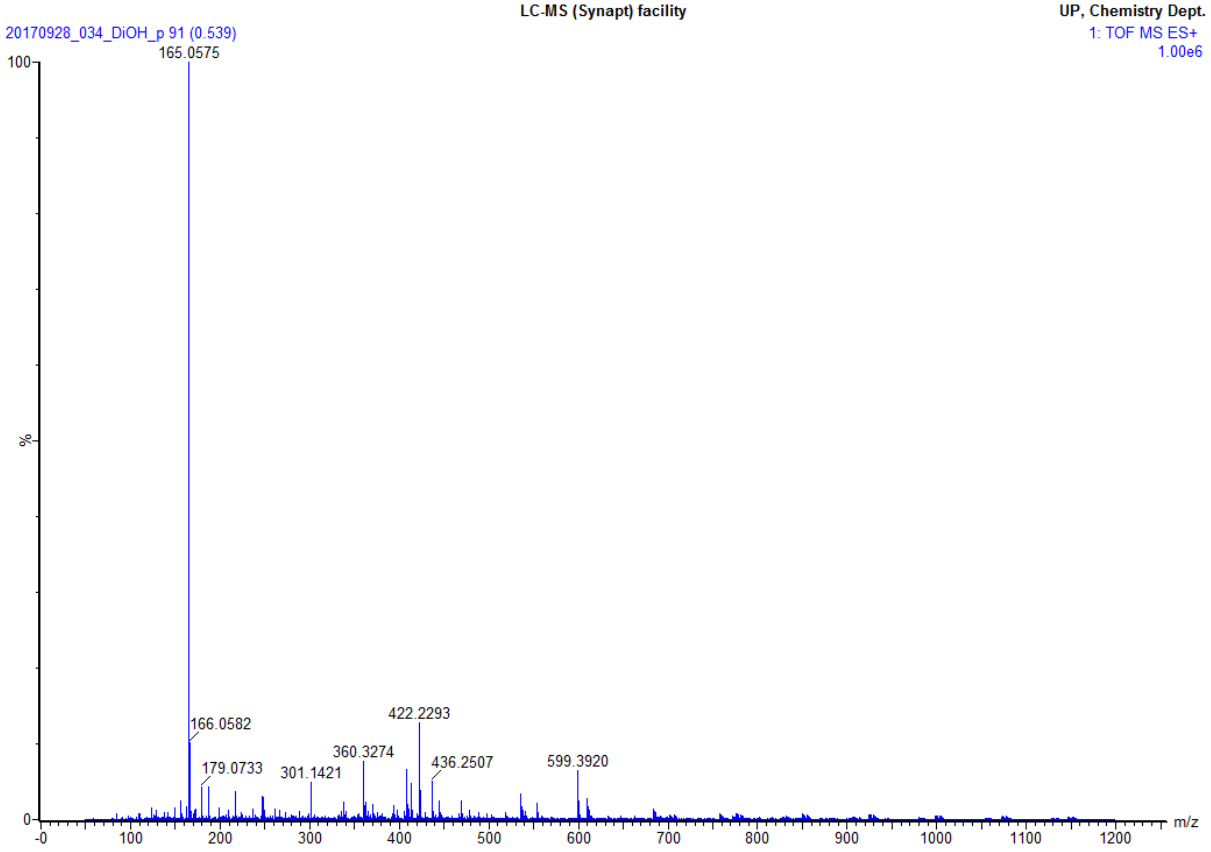

B.7.3 IR spectrum of compound (245)

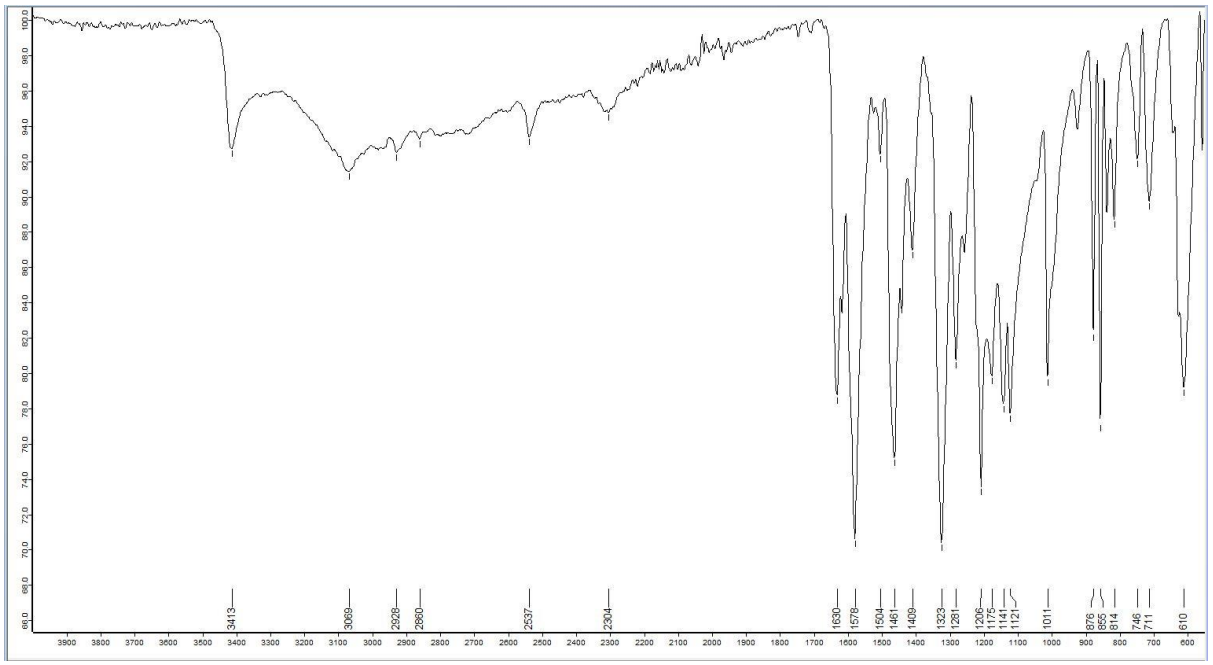

© University of Pretoria

B.8 5-((tert-butyldimethylsilyl)oxy)-6-methoxy-2,3-dihydro-1*H*-inden-1-one (246)

B.8.1 ^{1}H and ^{13}C NMR spectra of compound (246)

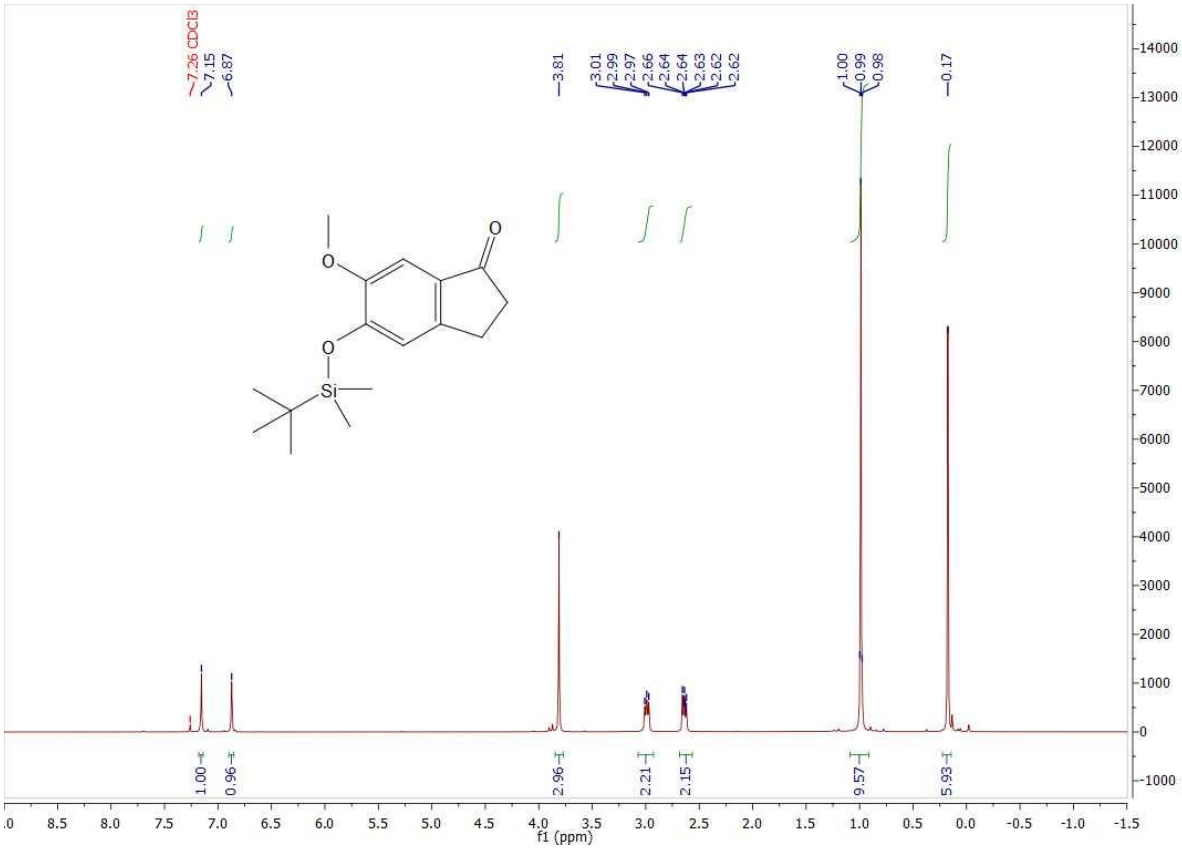

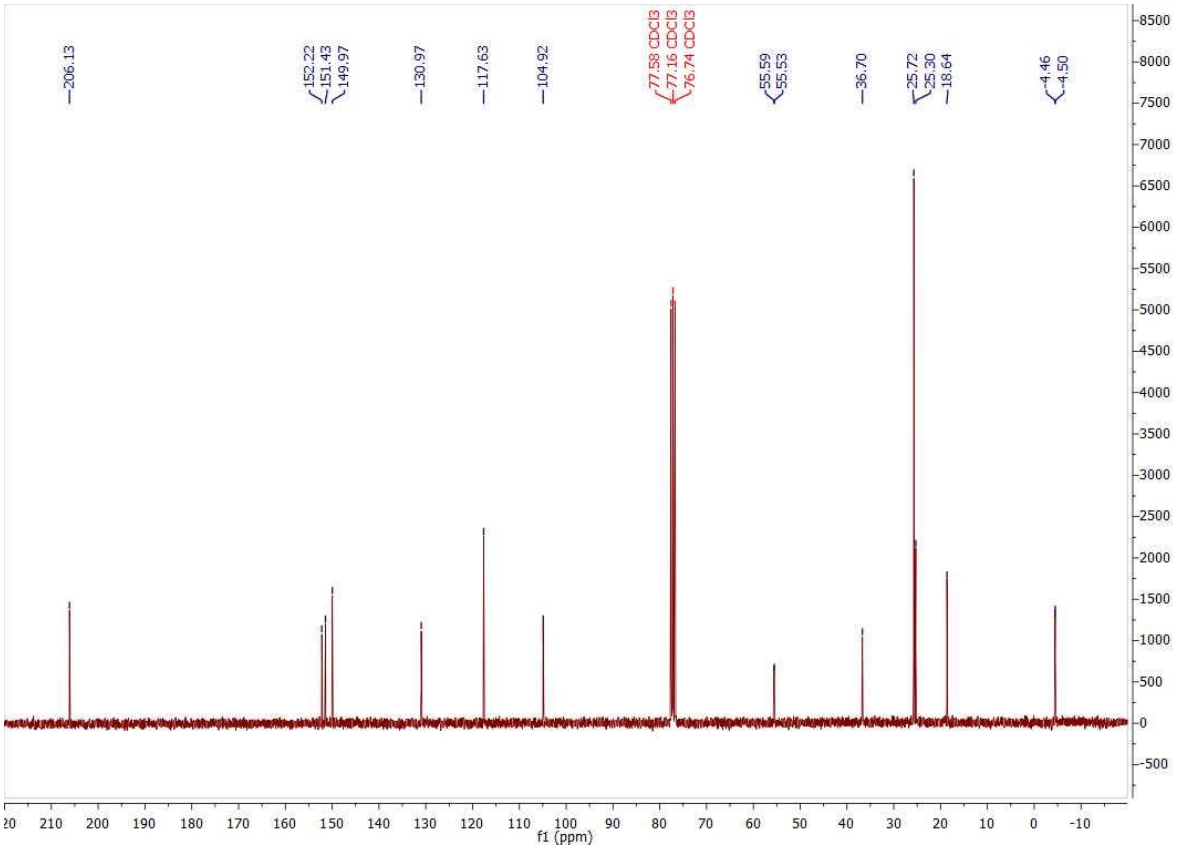

© University of Pretoria

B.8.2 HRMS spectrum of compound (246)

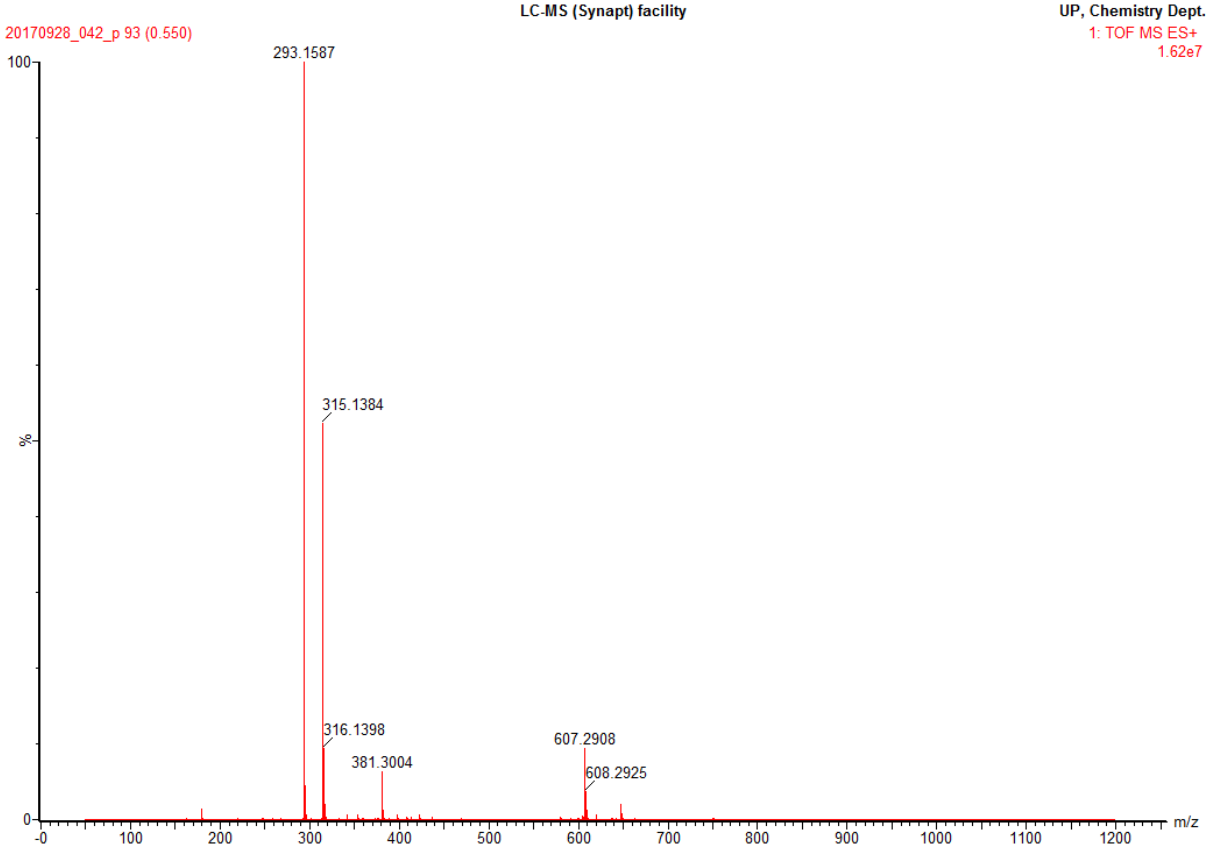

B.8.3 IR spectrum of compound (246)

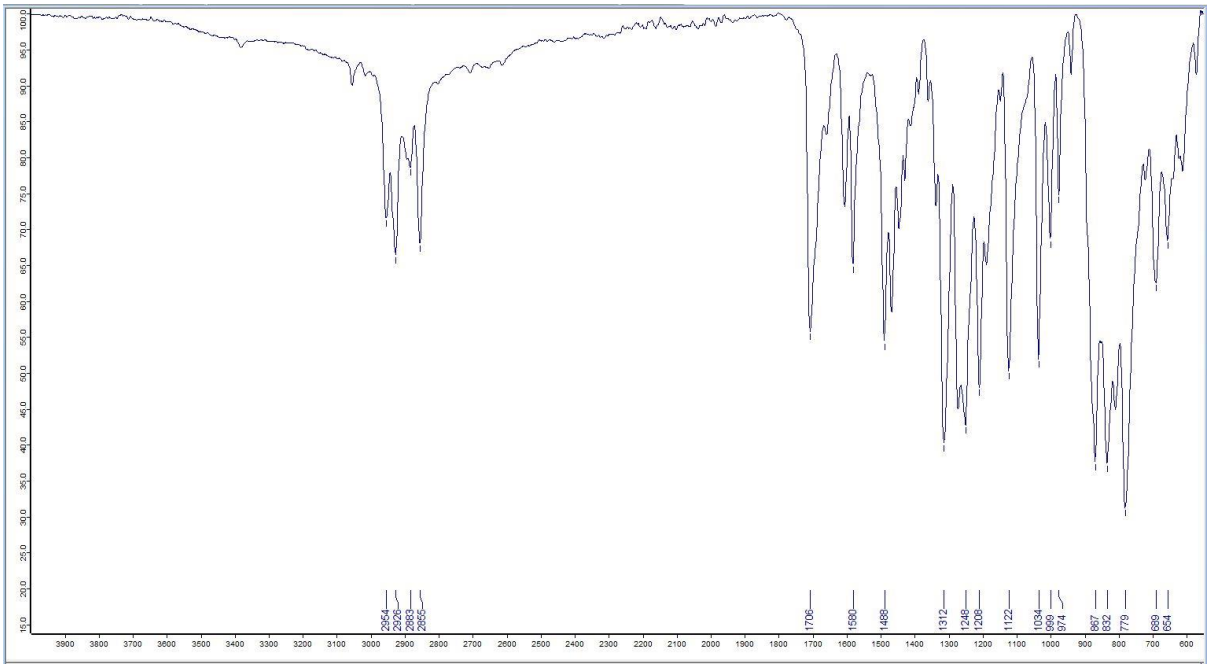

© University of Pretoria

B.9 5-((tert-butyldiphenylsilyl)oxy)-6-methoxy-2,3-dihydro-1*H*-inden-1-one (247)

B.9.1 ^{1}H and ^{13}C NMR spectra of compound (247)

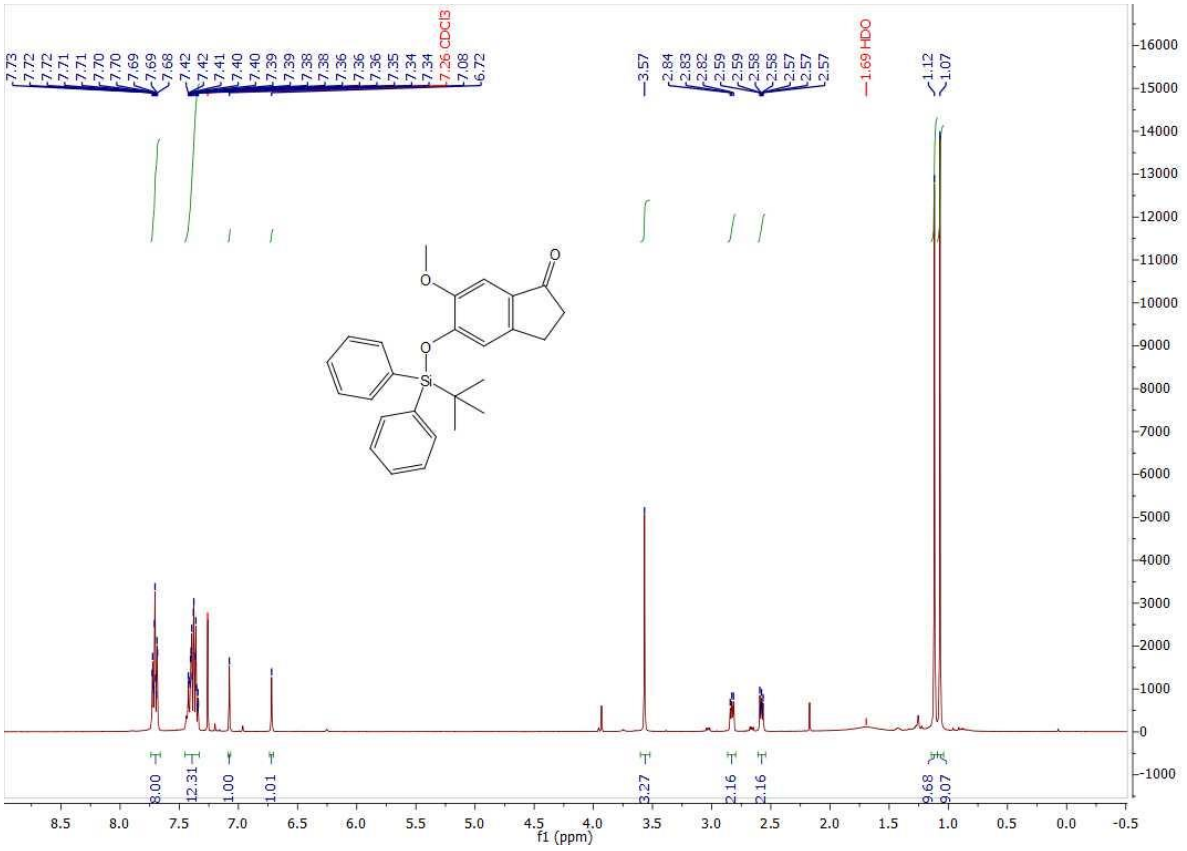

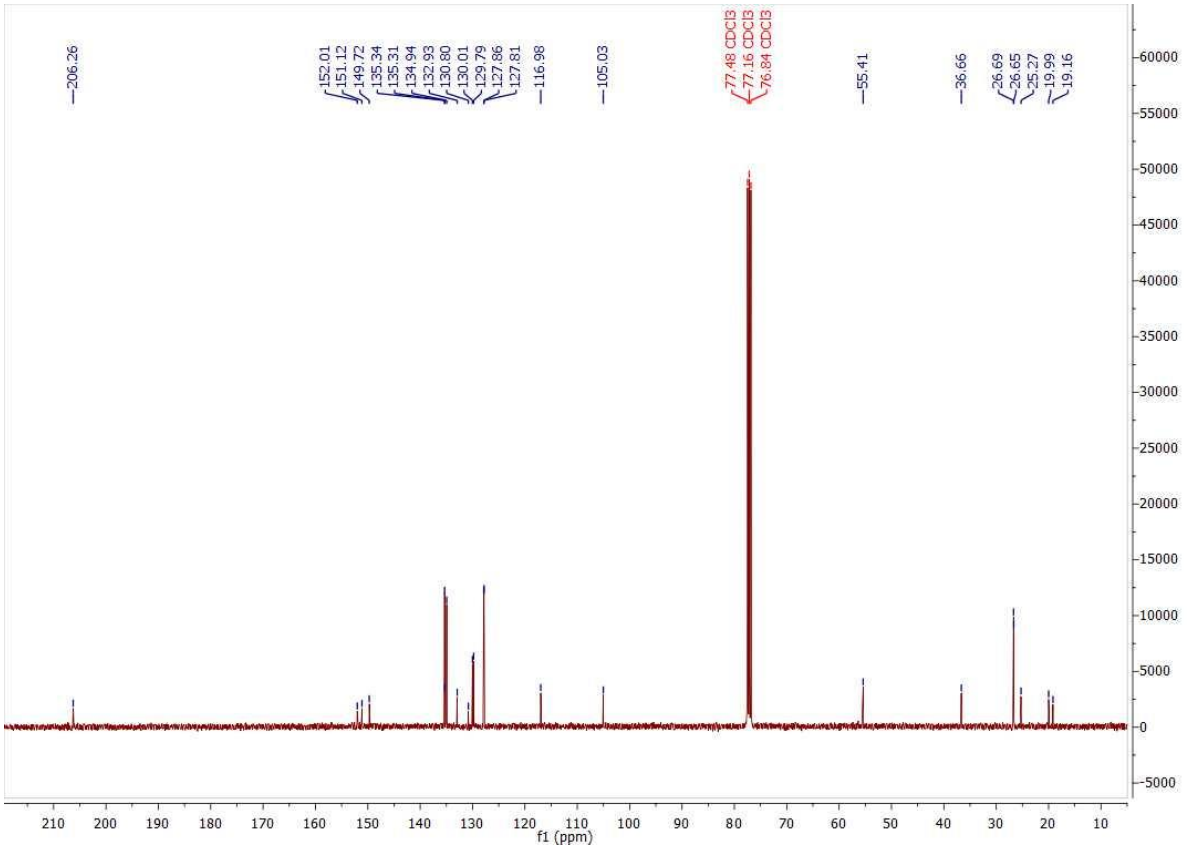

© University of Pretoria

B.9.2 HRMS spectrum of compound (247)

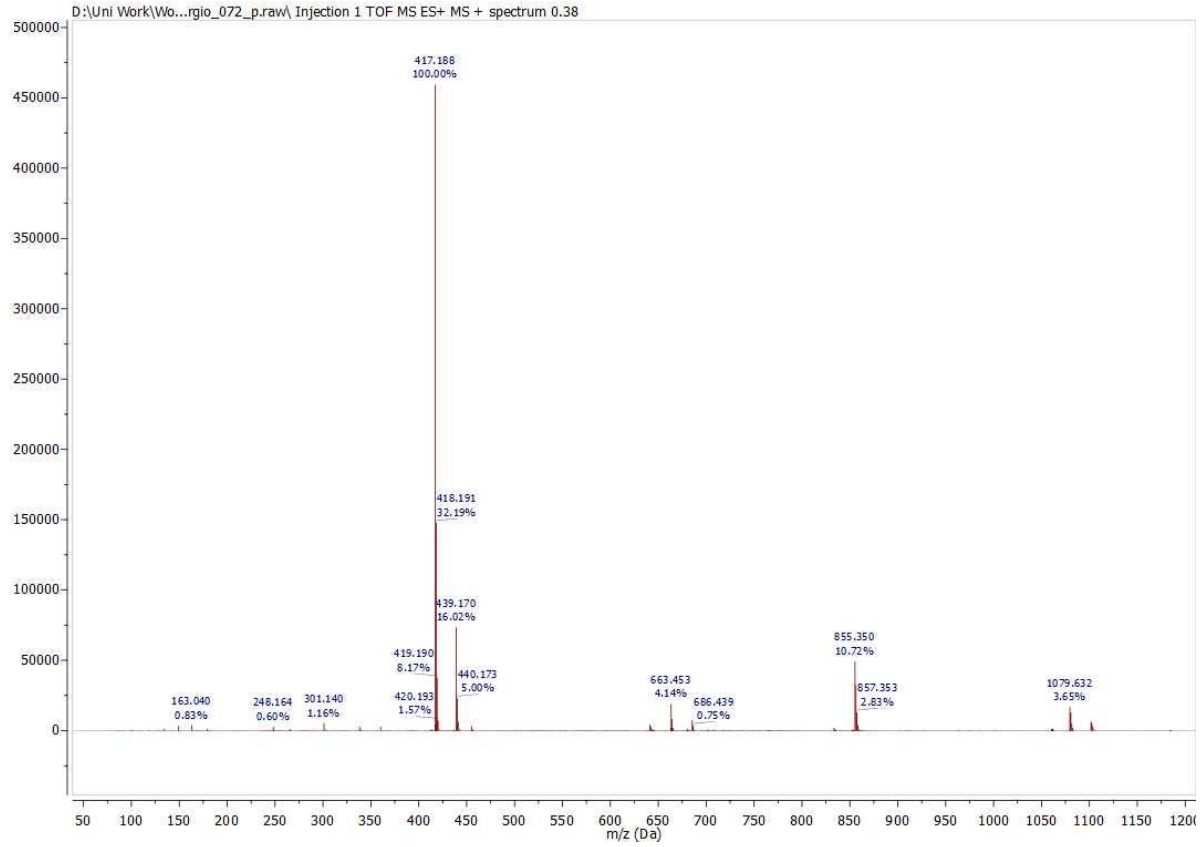

© University of Pretoria

B.10 5,6-bis((tert-butyldimethylsilyl)oxy)-2,3-dihydro-1*H*-inden-1-one (248)

B.10.1 ^{1}H and ^{13}C NMR spectra of compound (248)

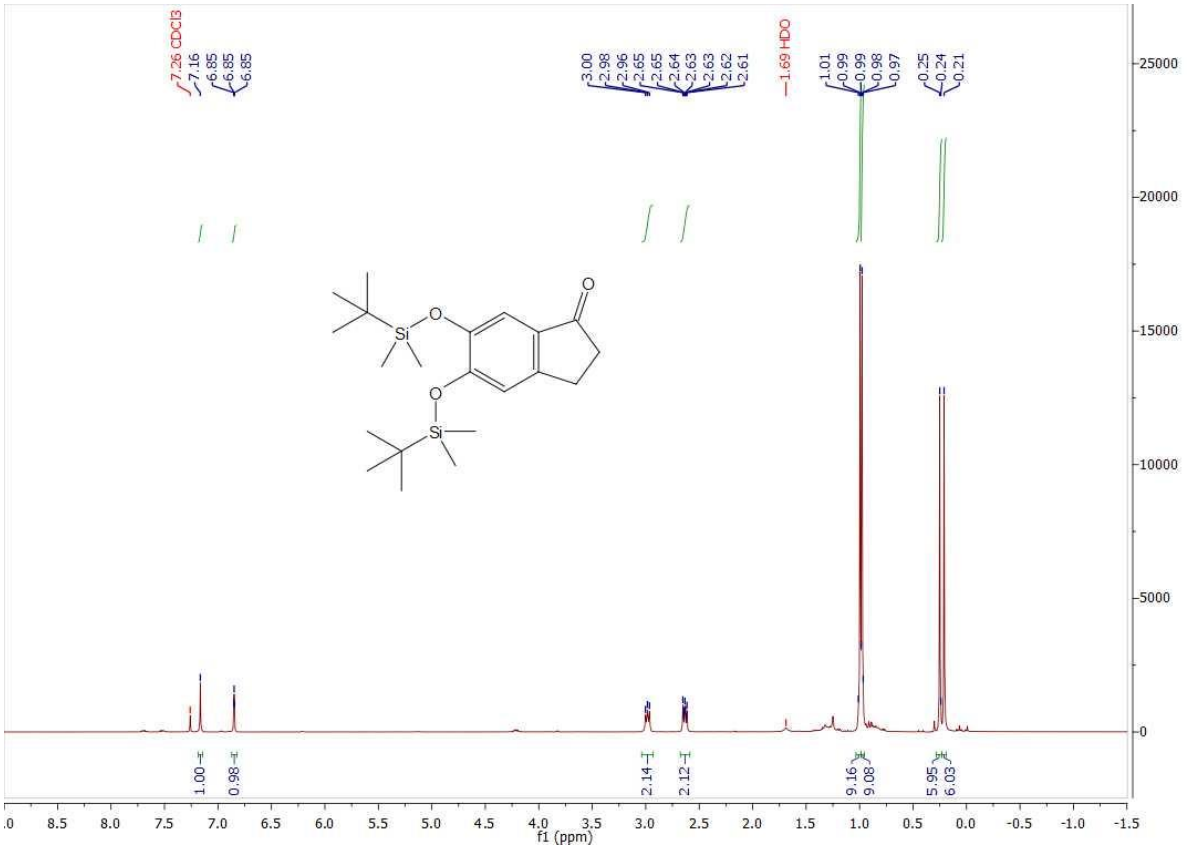

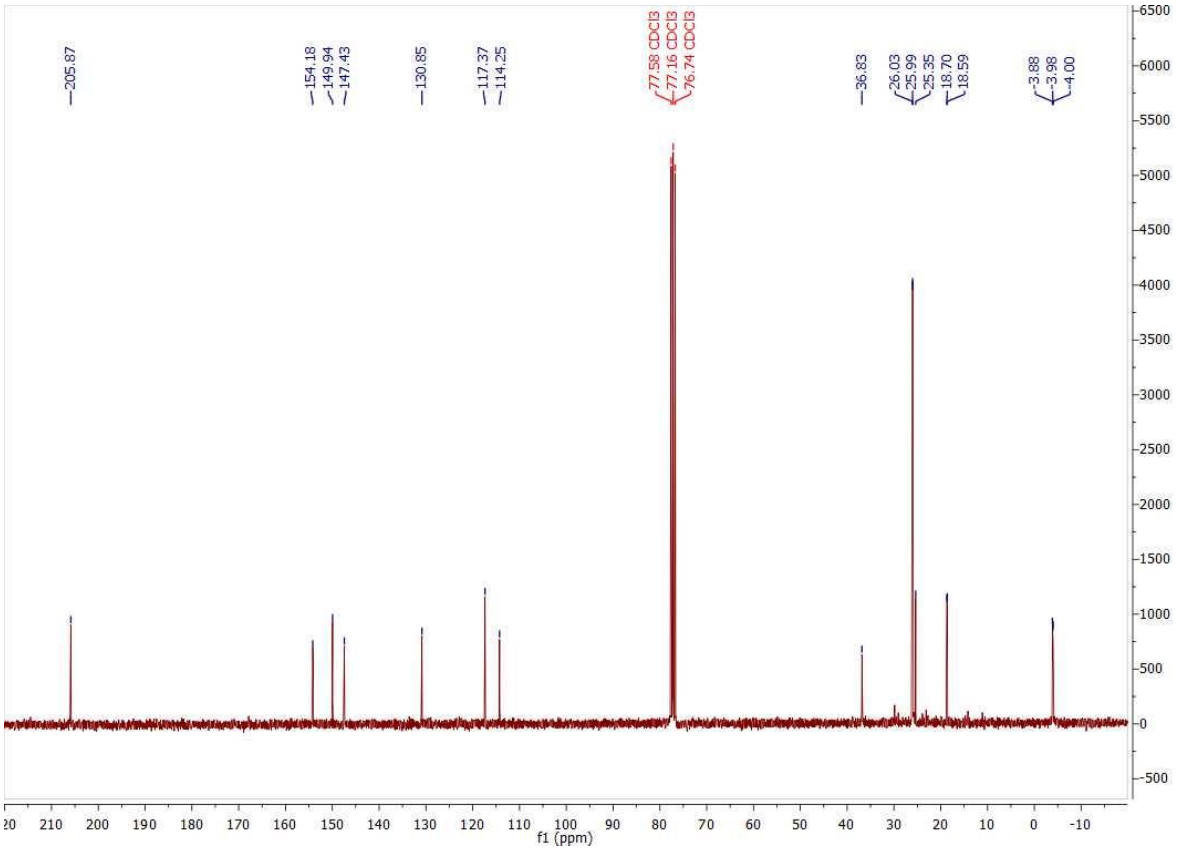

© University of Pretoria

B.10.2 HRMS spectrum of compound (248)

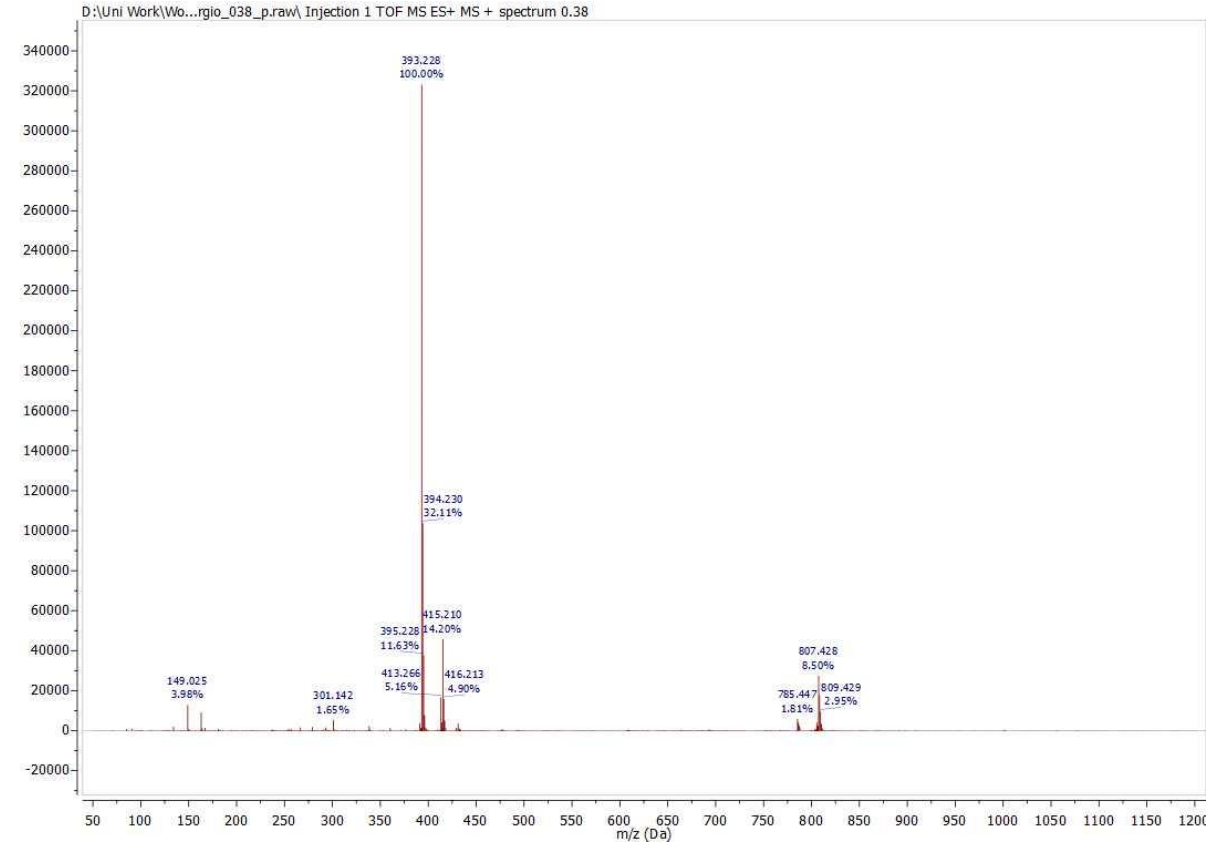

B.10.3 IR spectrum of compound (248)

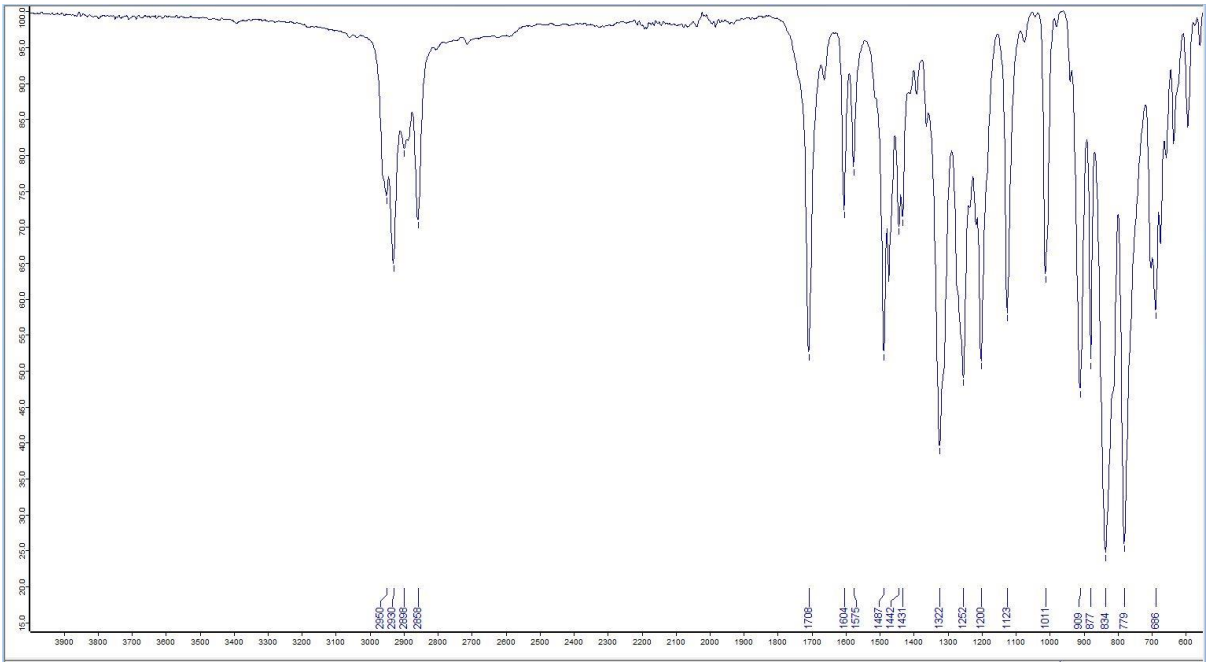

© University of Pretoria

B.11 6-bromo-2,3-dihydro-1*H*-inden-1-one (251)

B.11.1 ^{1}H and ^{13}C NMR spectra of compound (251)

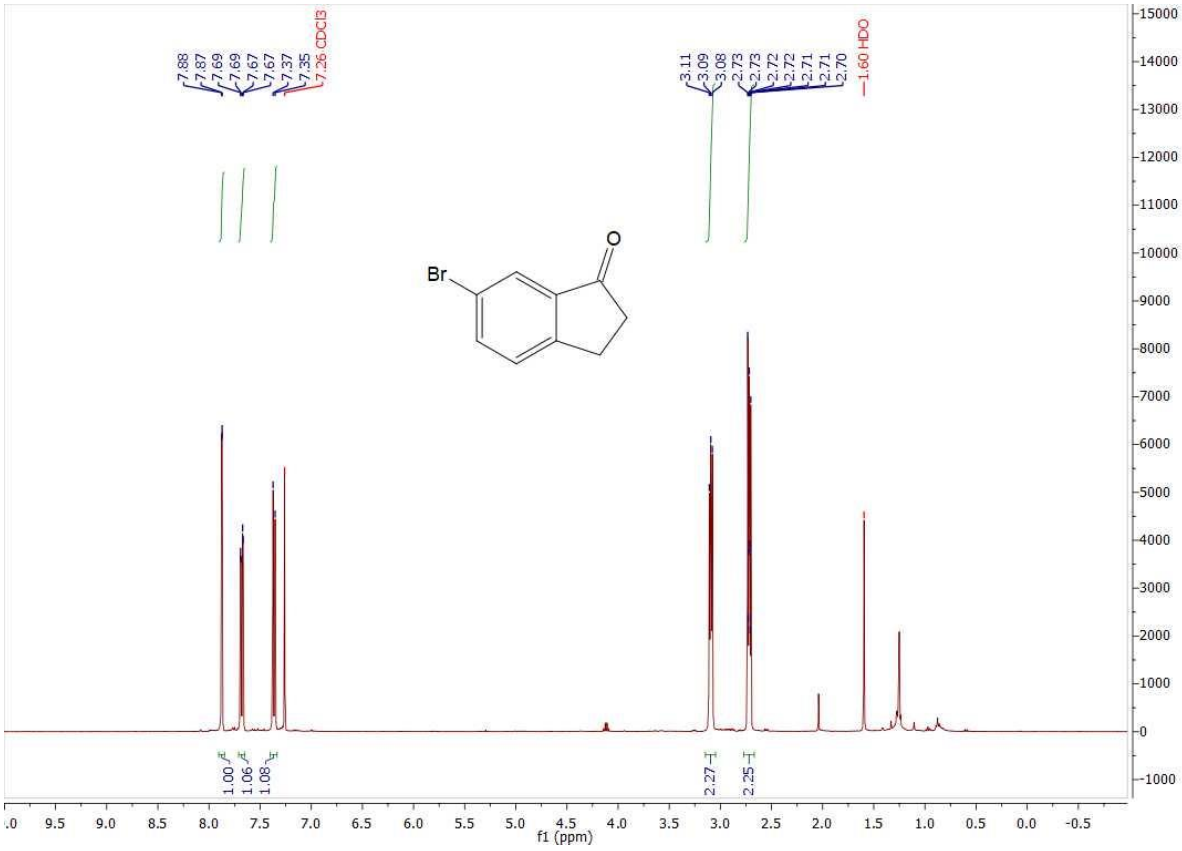

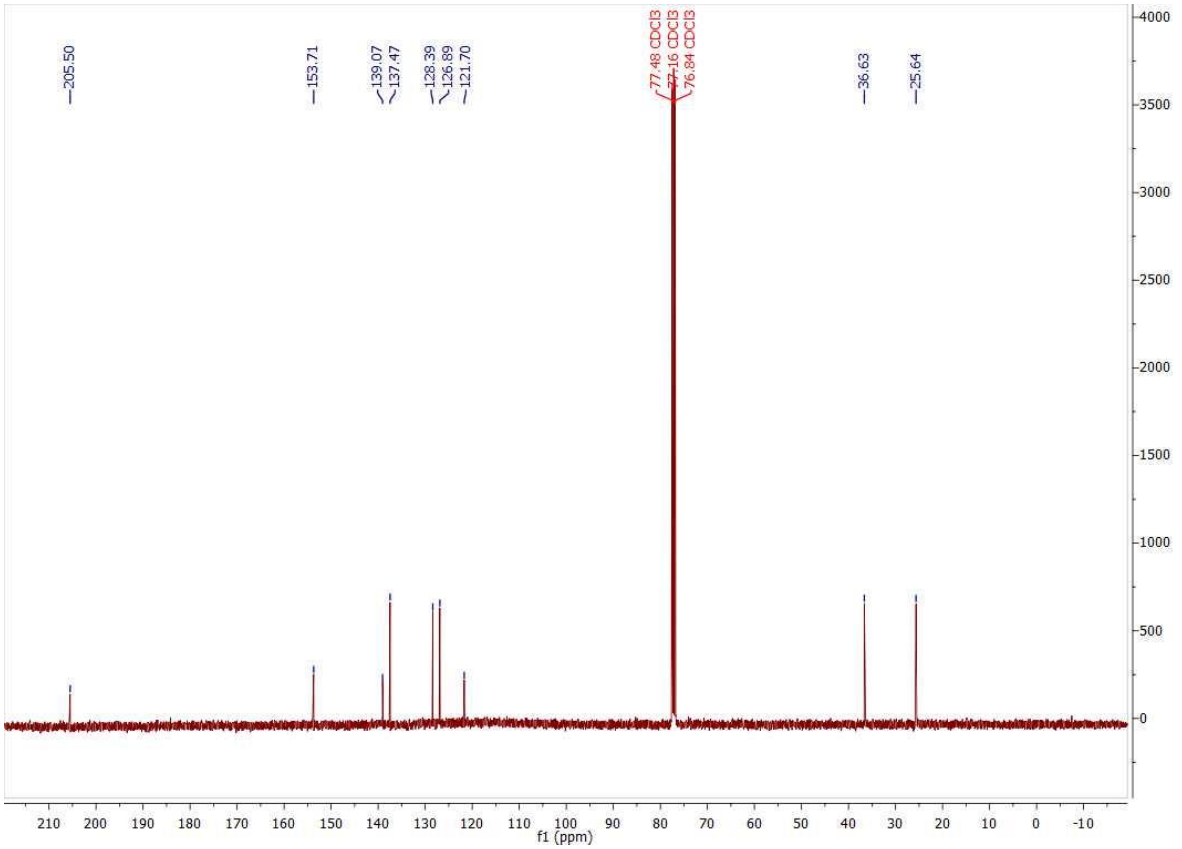

© University of Pretoria

B.11.2 IR spectrum of compound (251)

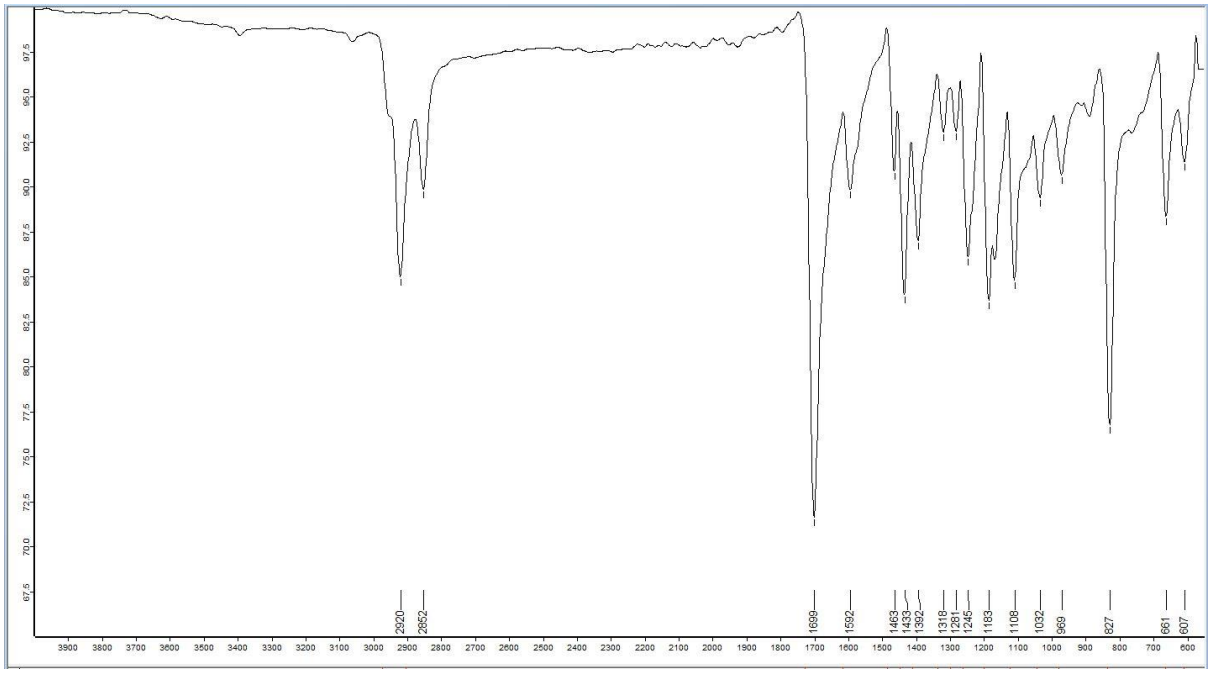

© University of Pretoria

B.12 Ethyl 1-(2-chlorobenzyl)piperidine-4-carboxylate (261)

B.12.1 ^{1}H and ^{13}C NMR spectra of compound (261)

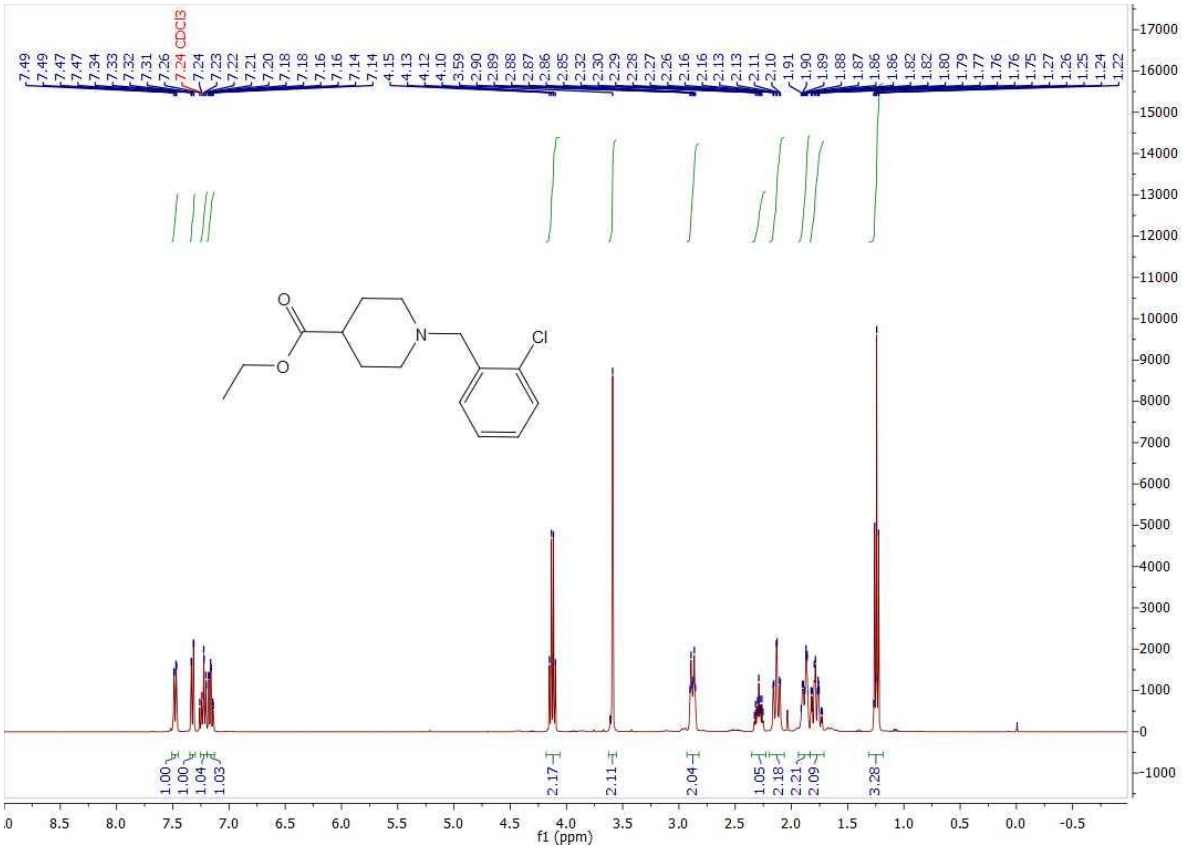

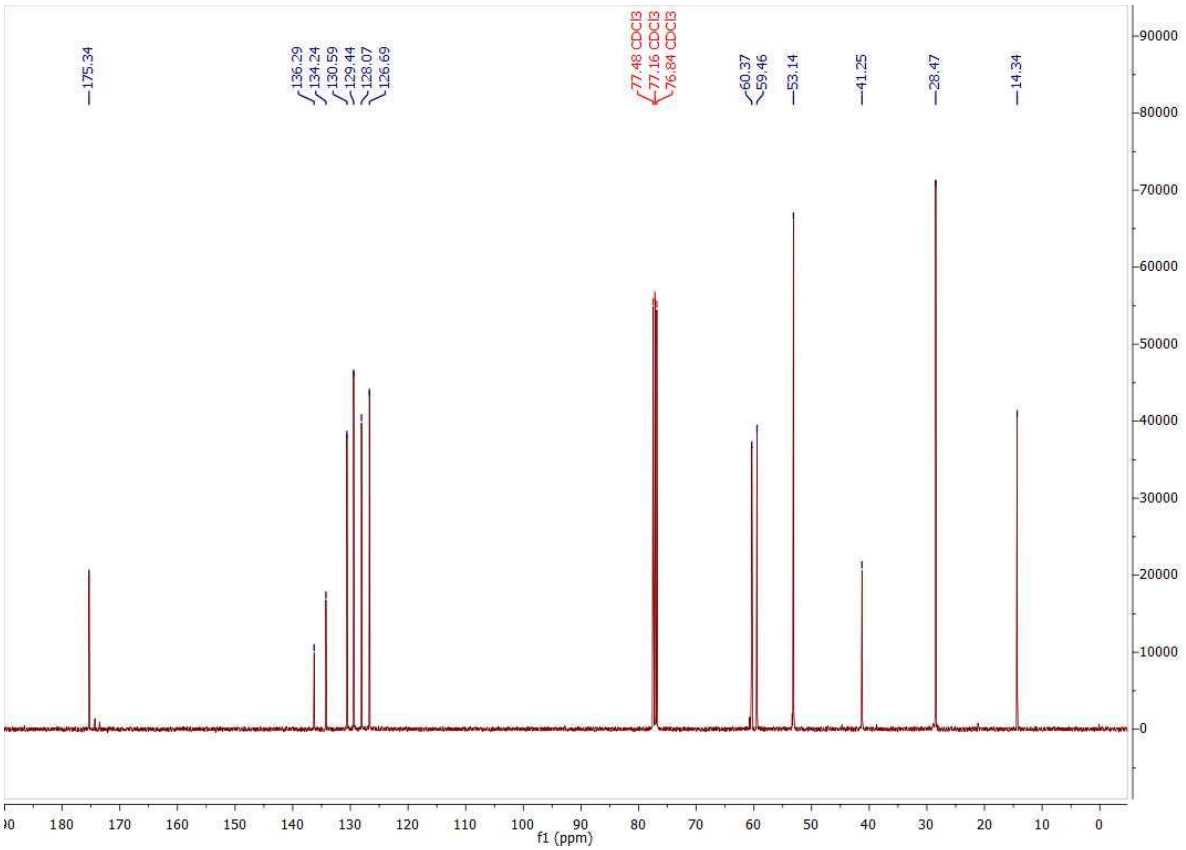

© University of Pretoria

B.12.2 HRMS spectrum of compound (261)

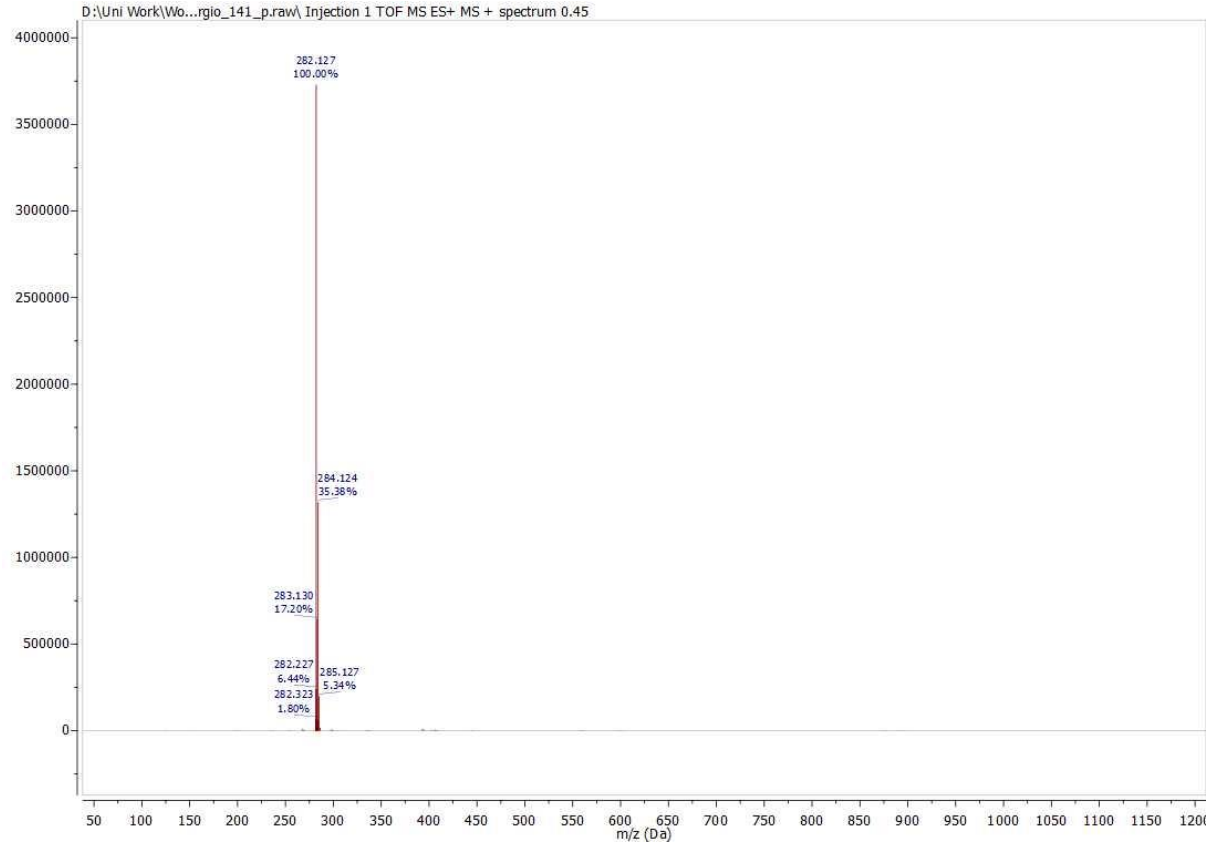

B.12.3 IR spectrum of compound (261)

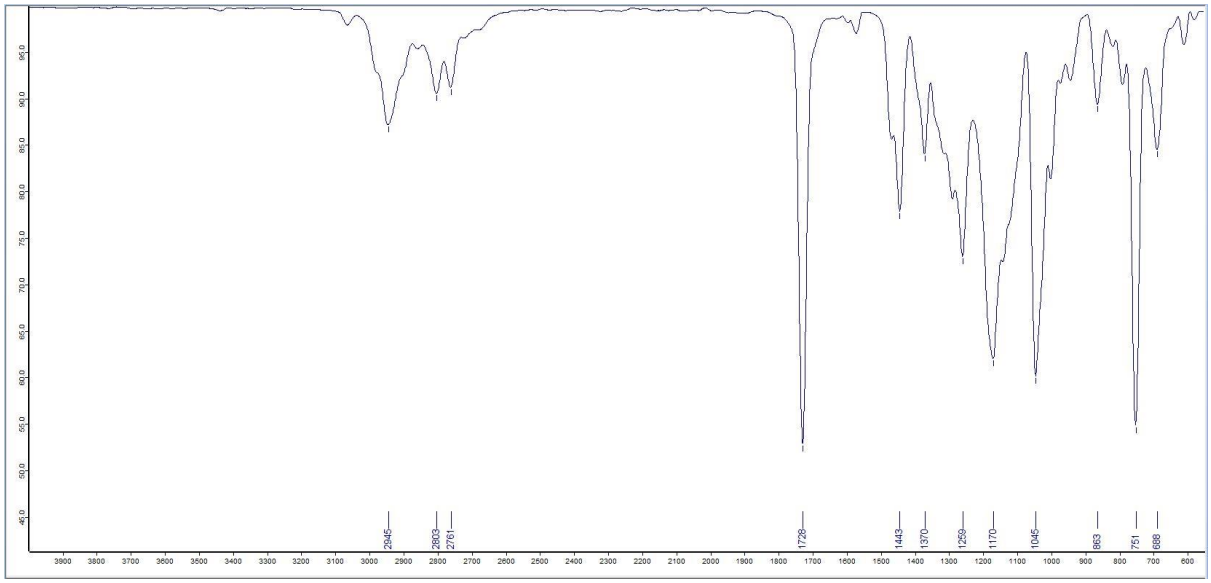

© University of Pretoria

B.13 Ethyl 1-(4-chlorobenzyl)piperidin-4-carboxylate (262)

B.13.1 ^{1}H and ^{13}C NMR spectra of compound (262)

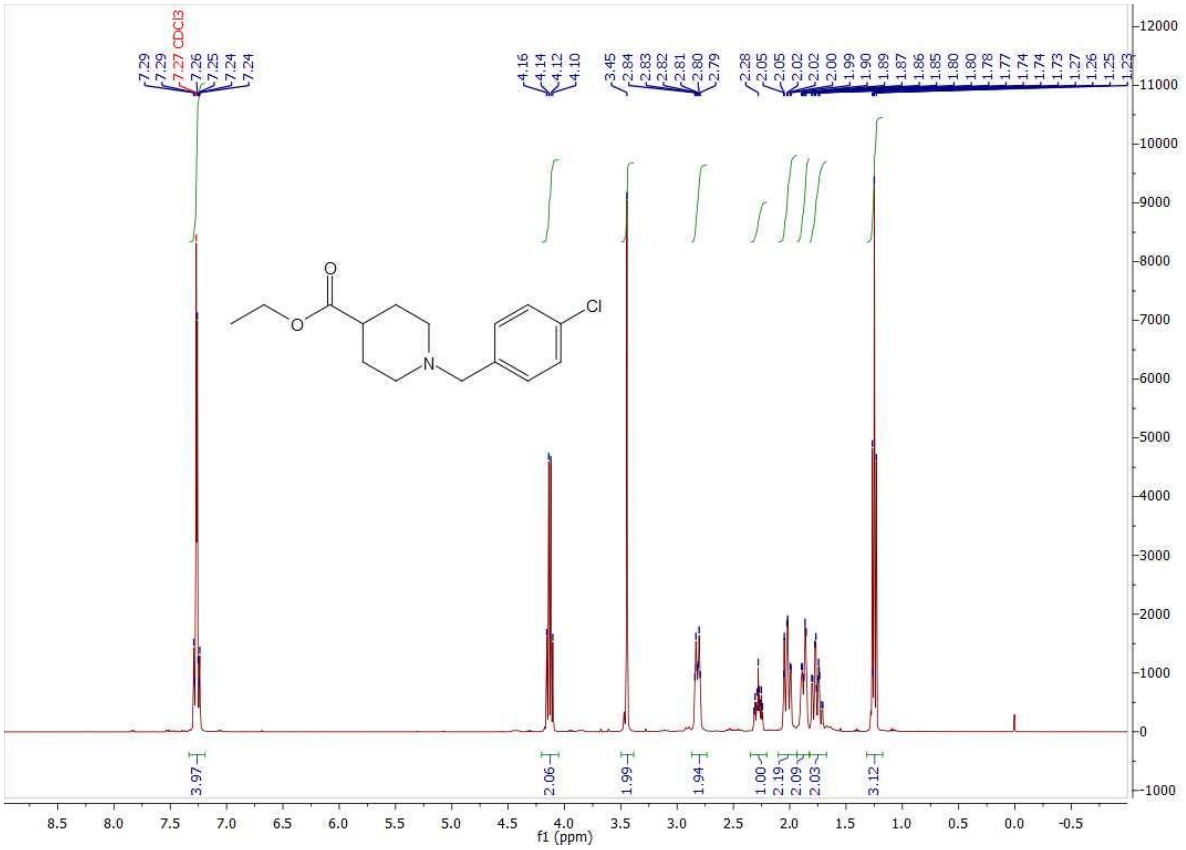

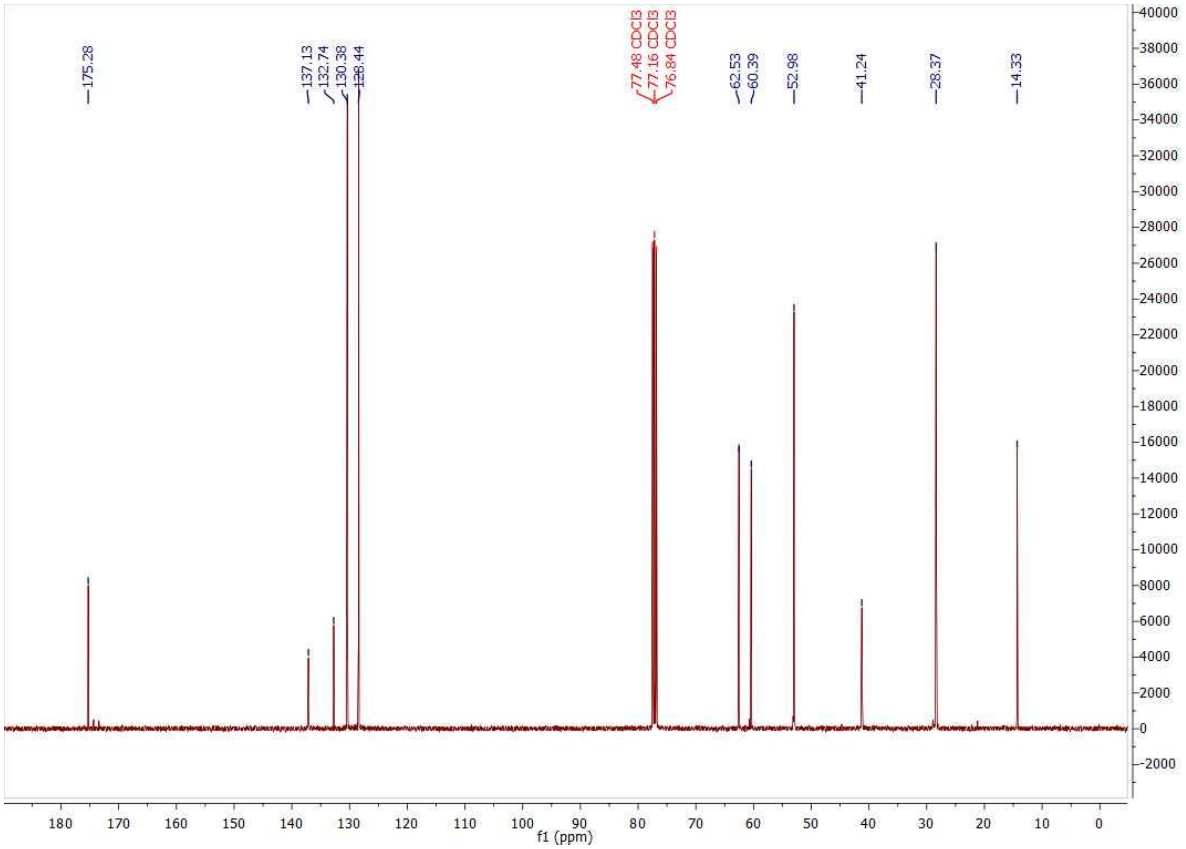

© University of Pretoria

B.13.2 HRMS spectrum of compound (262)

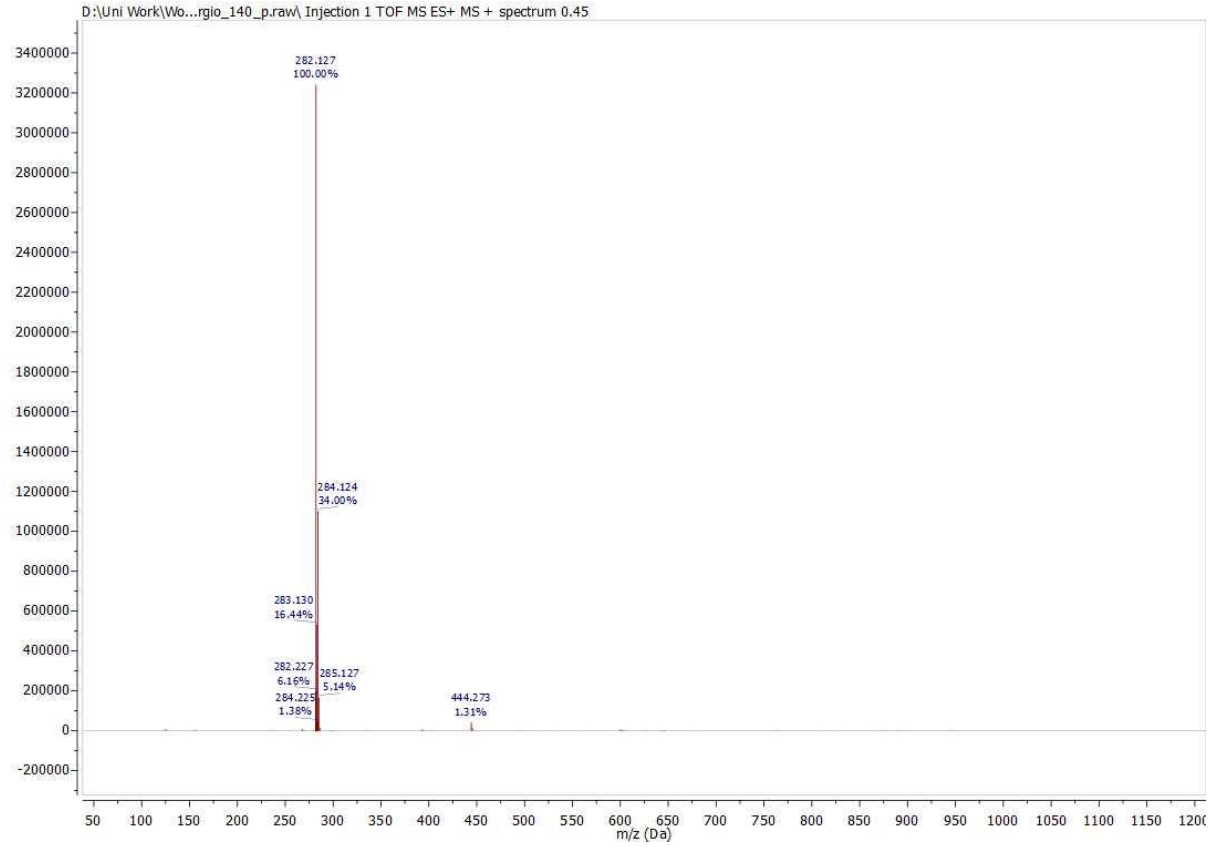

B.13.3 IR spectrum of compound (262)

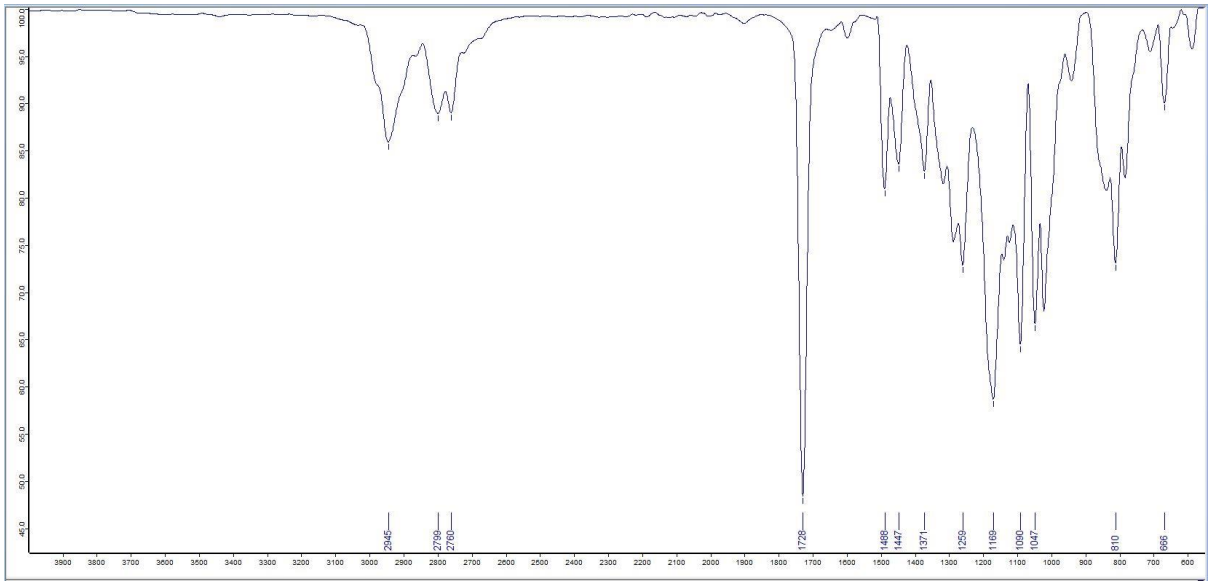

© University of Pretoria

B.14 (1-(2-chlorobenzyl)piperidin-4-yl)methanol (263)

B.14.1 ^{1}H and ^{13}C NMR spectra of compound (263)

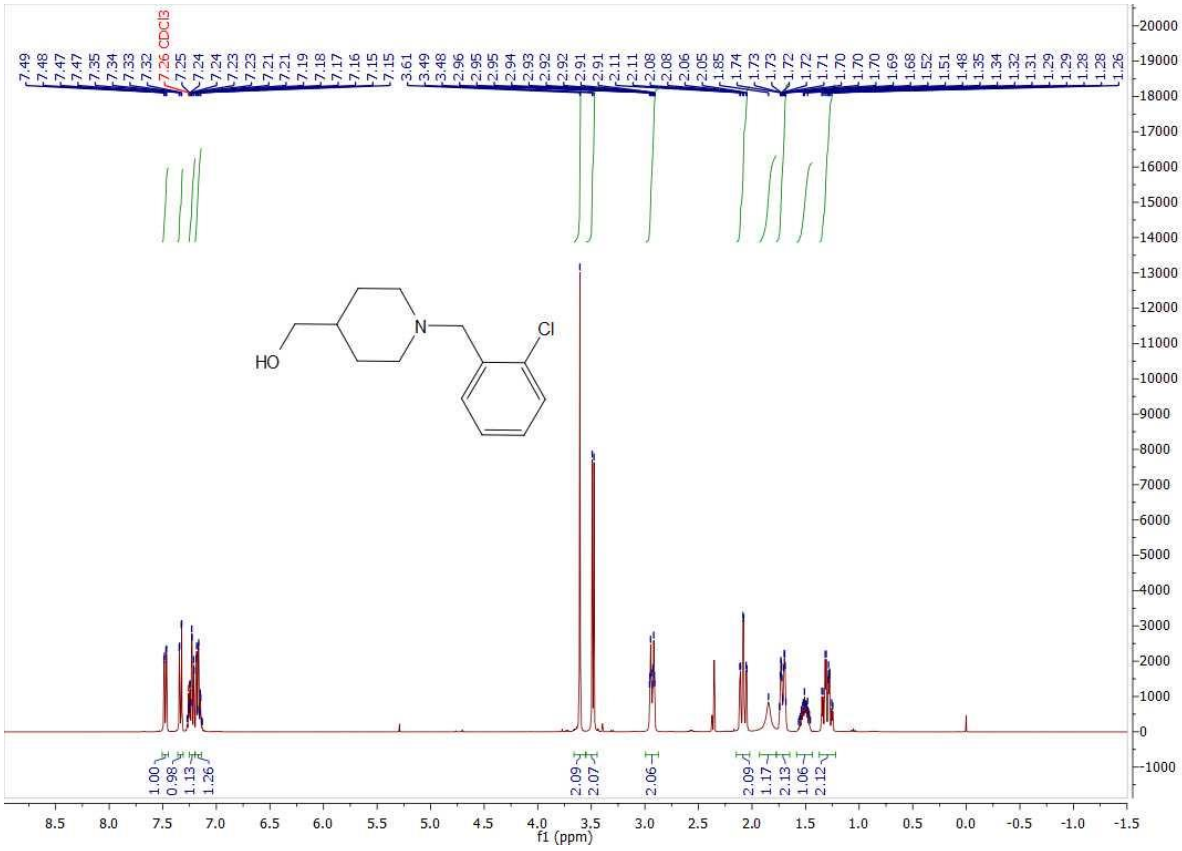

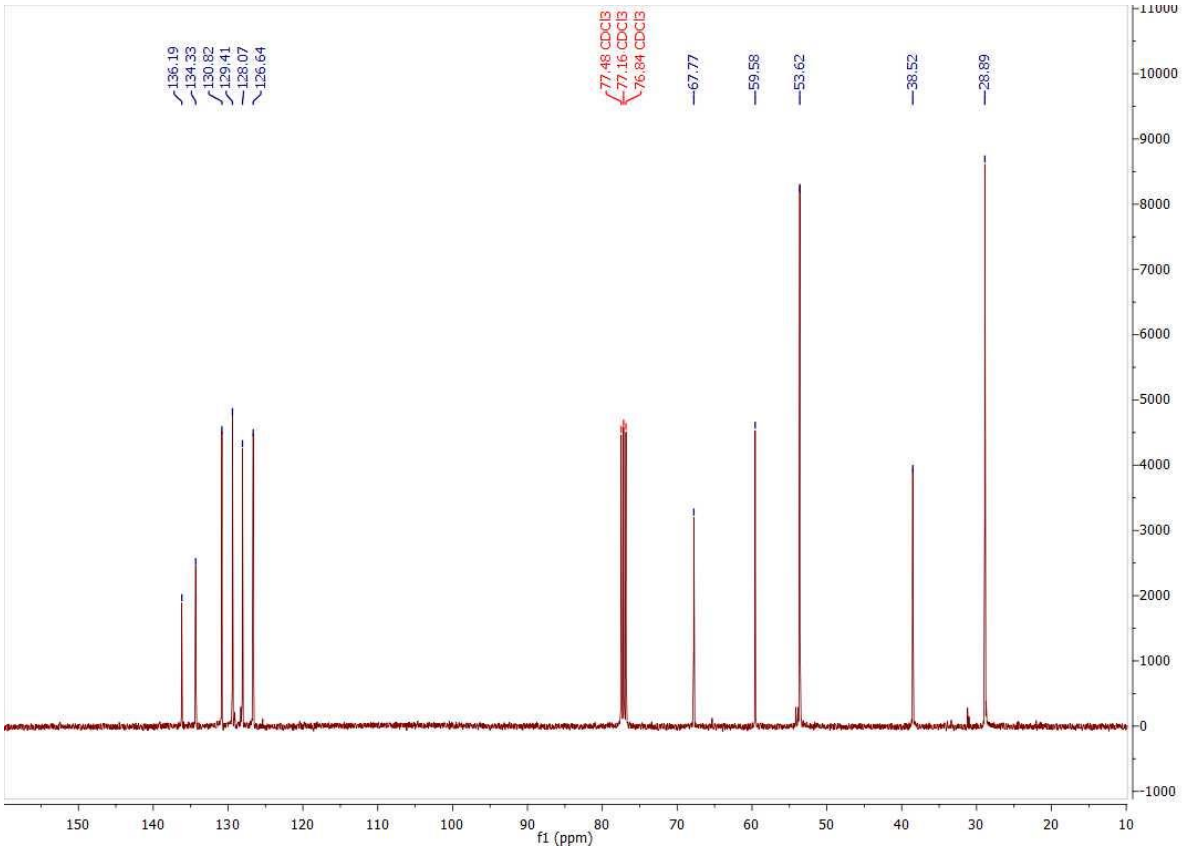

© University of Pretoria

B.14.2 HRMS spectrum of compound (263)

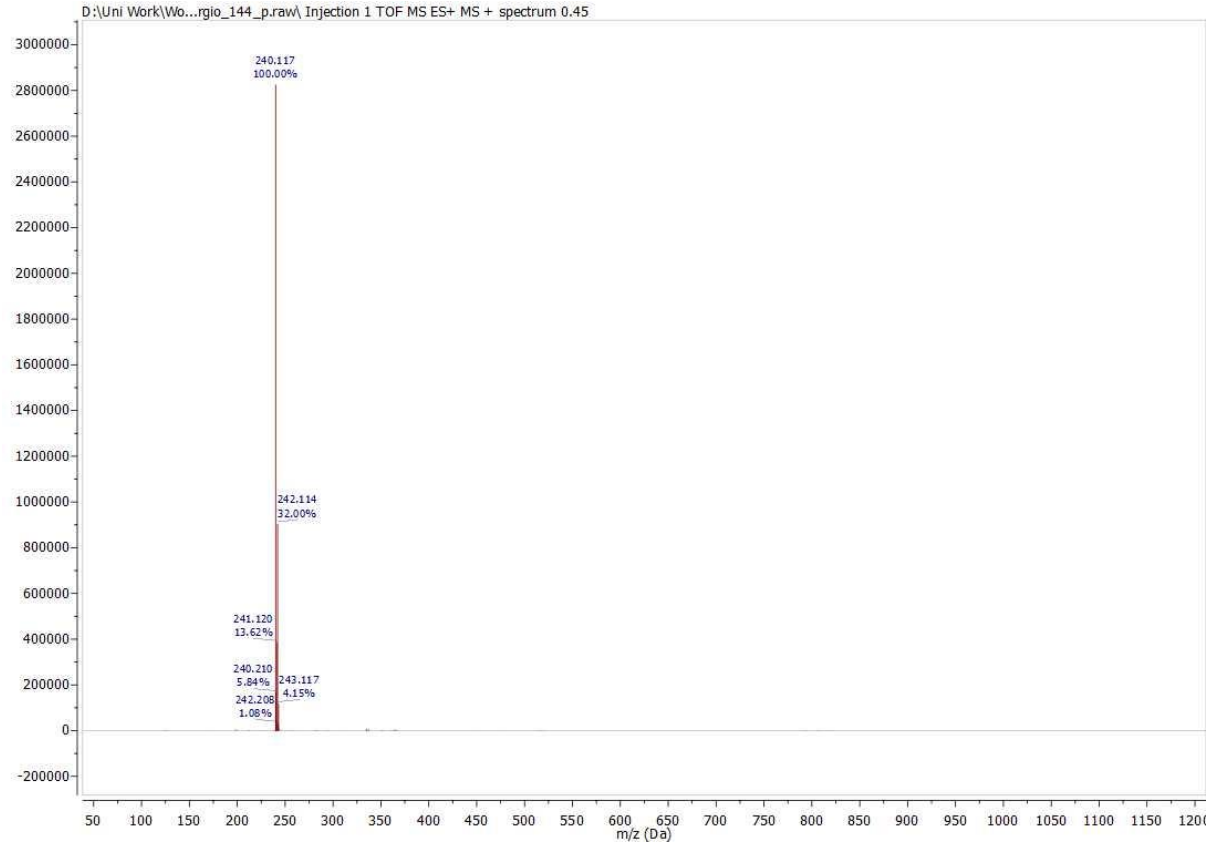

B.14.3 IR spectrum of compound (263)

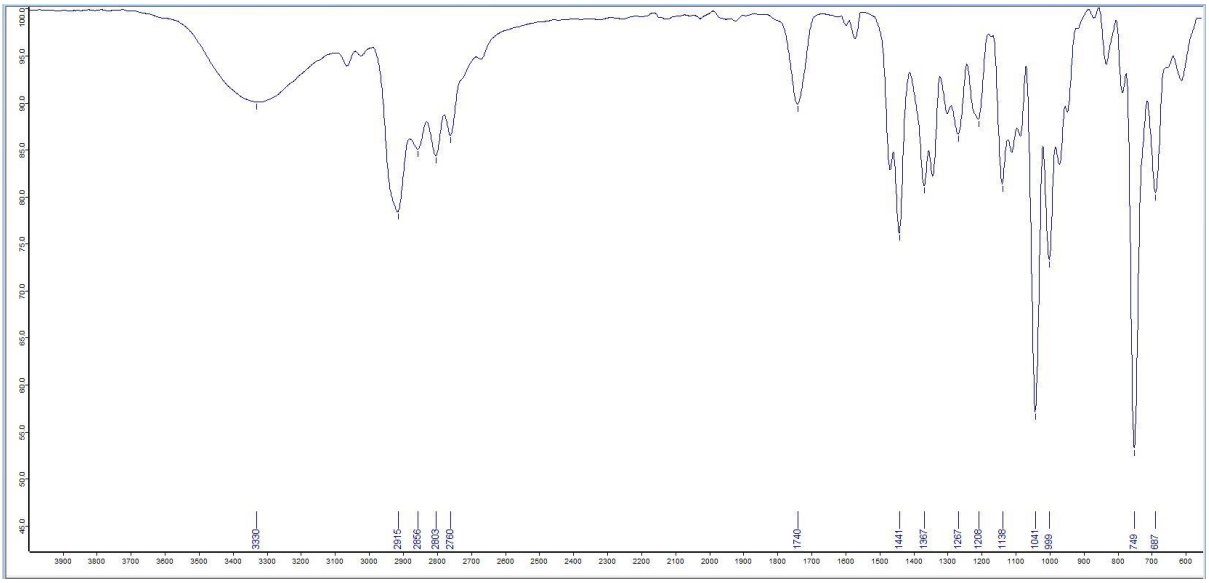

© University of Pretoria

B.15 (1-(4-chlorobenzyl)piperidin-4-yl)methanol (264)

B.15.1 ^{1}H and ^{13}C NMR spectra of compound (264)

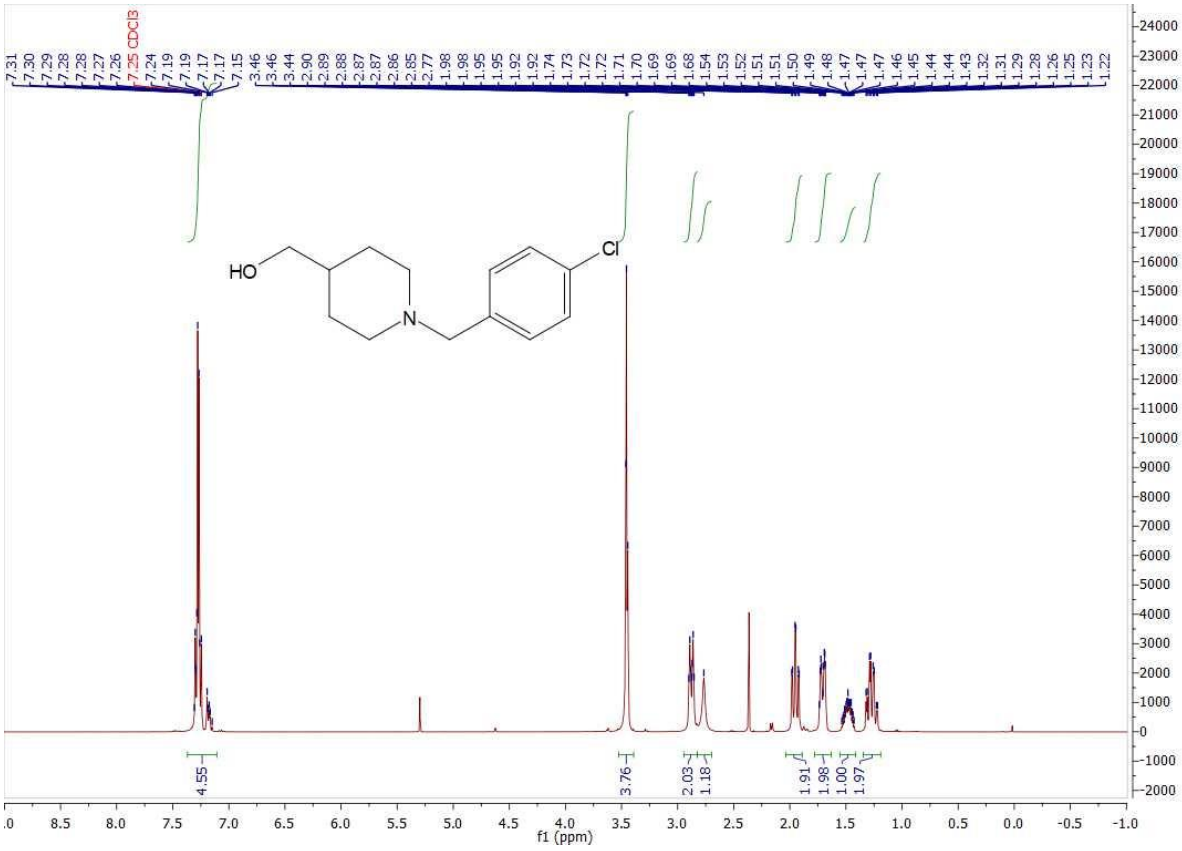

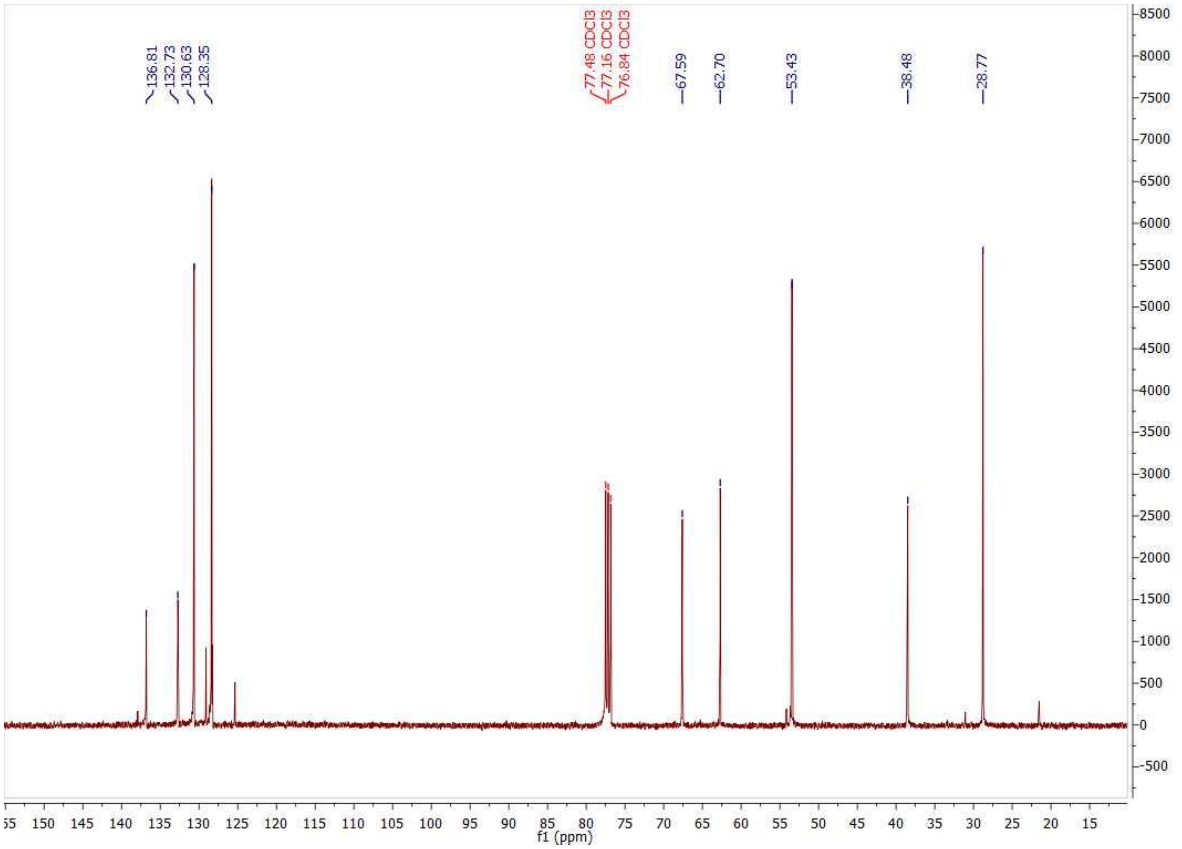

© University of Pretoria

B.15.2 HRMS spectrum of compound (264)

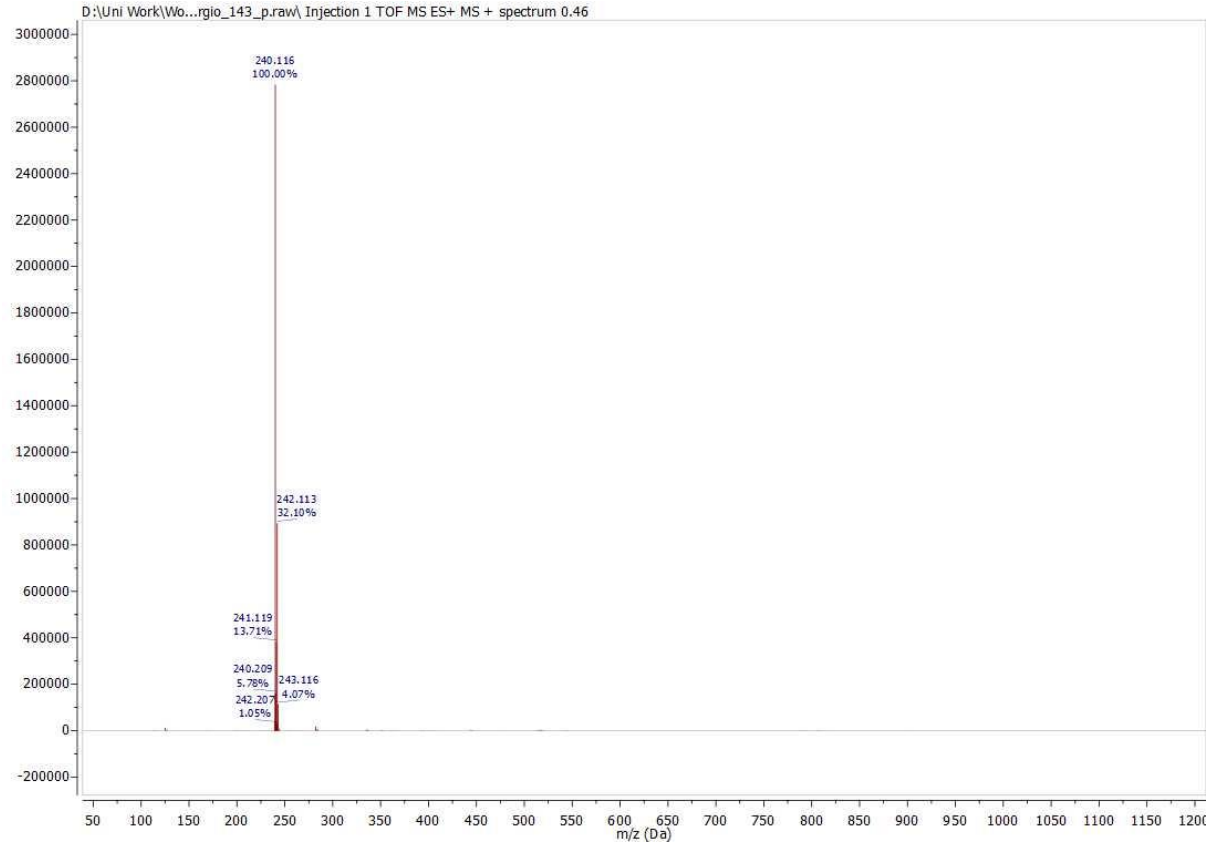

B.15.3 IR spectrum of compound (264)

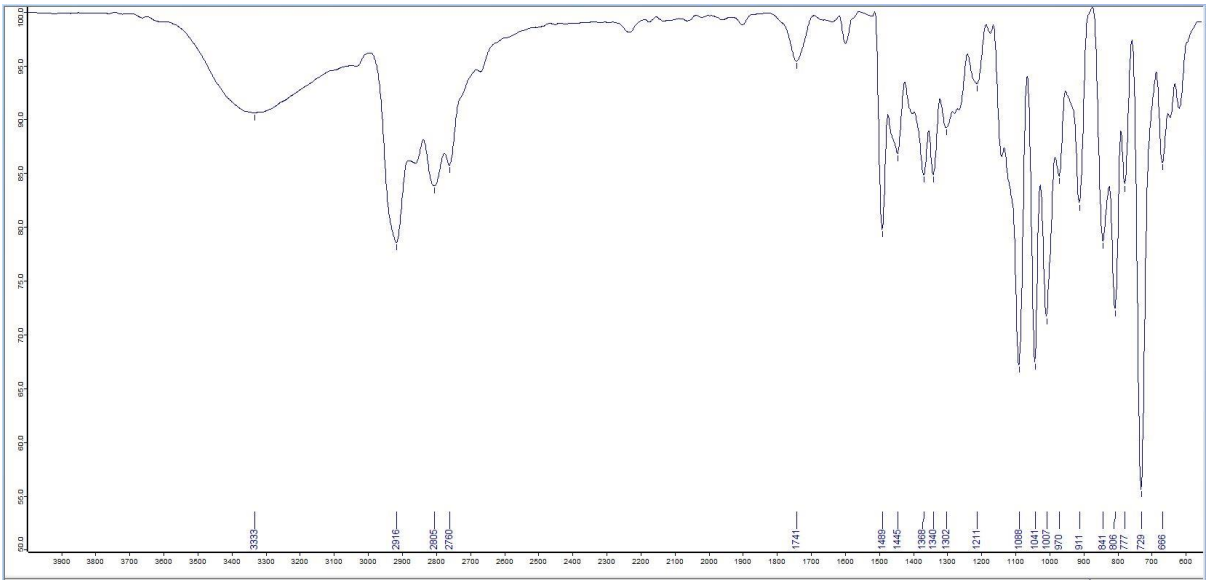

© University of Pretoria

B.16 1-(2-chlorobenzyl)piperidine-4-carbaldehyde (265)

B.16.1 ^{1}H and ^{13}C NMR spectra of compound (265)

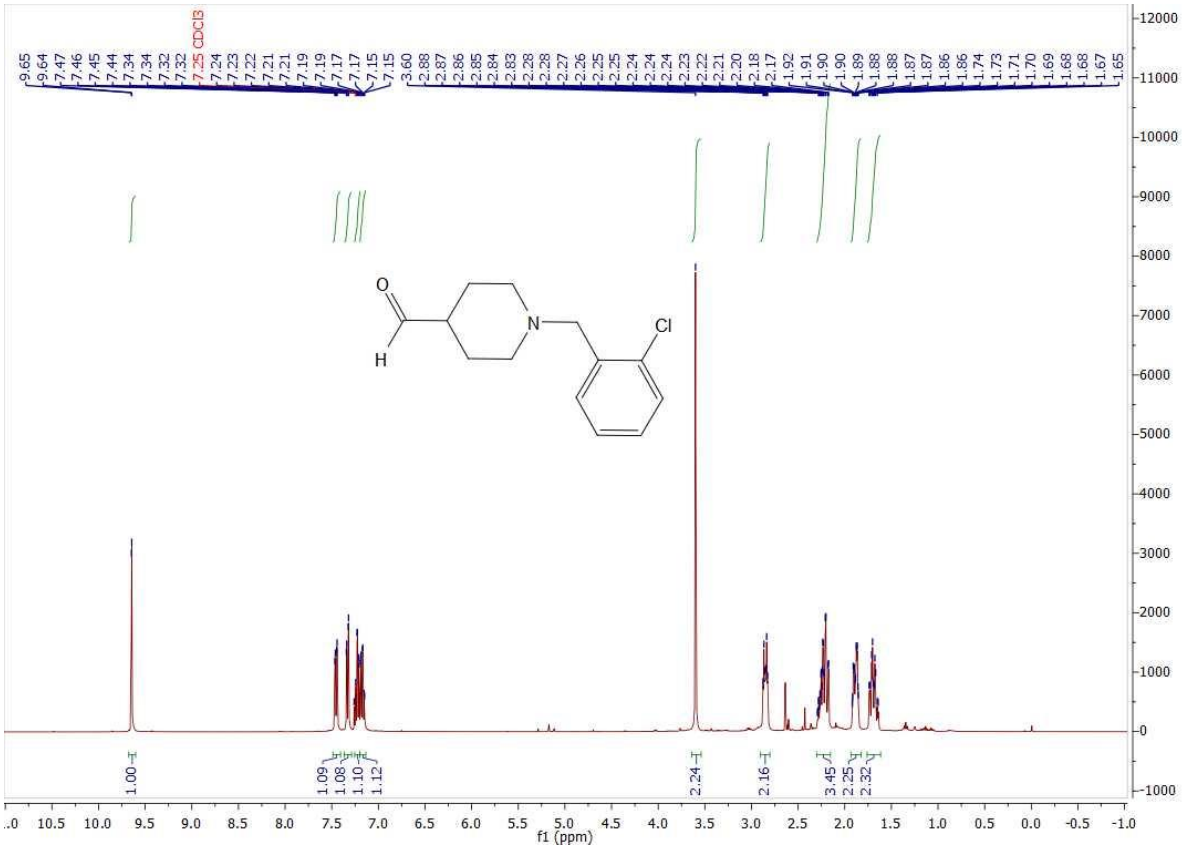

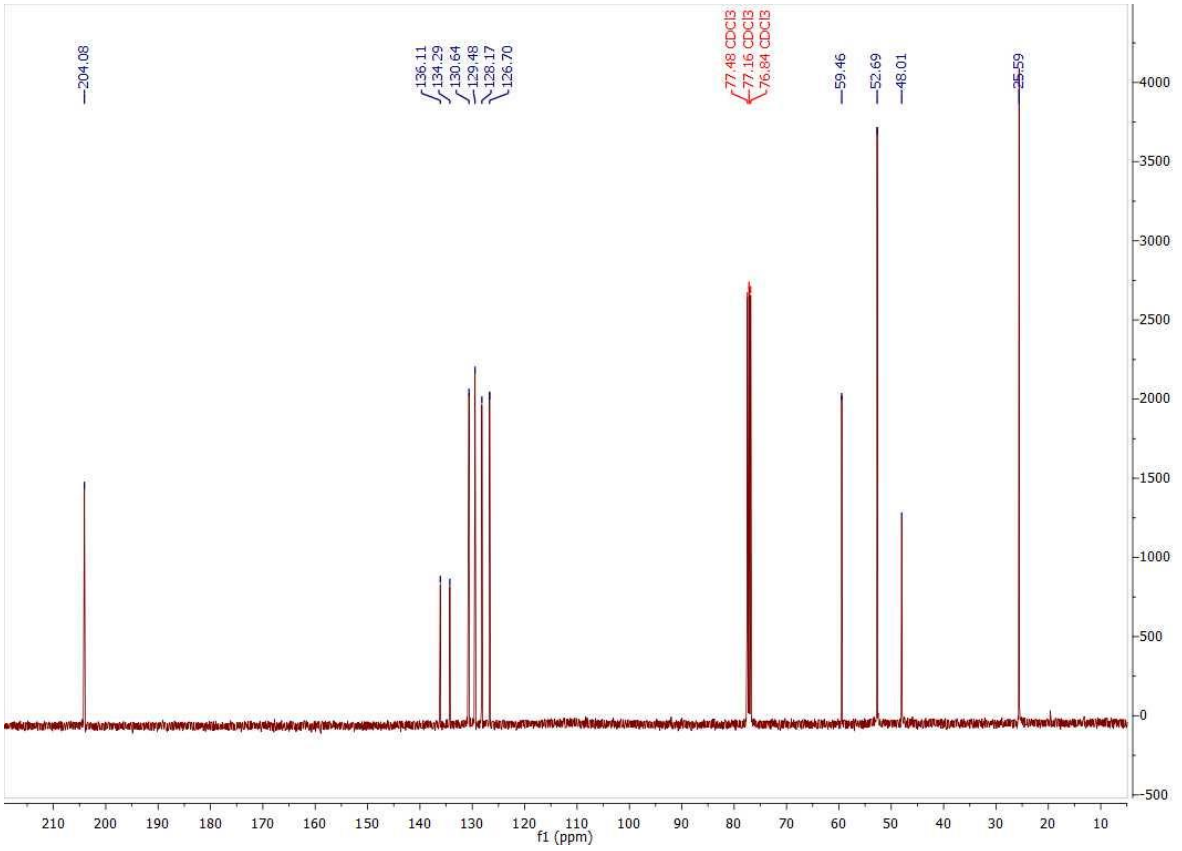

© University of Pretoria

B.16.2 HRMS spectrum of compound (265)

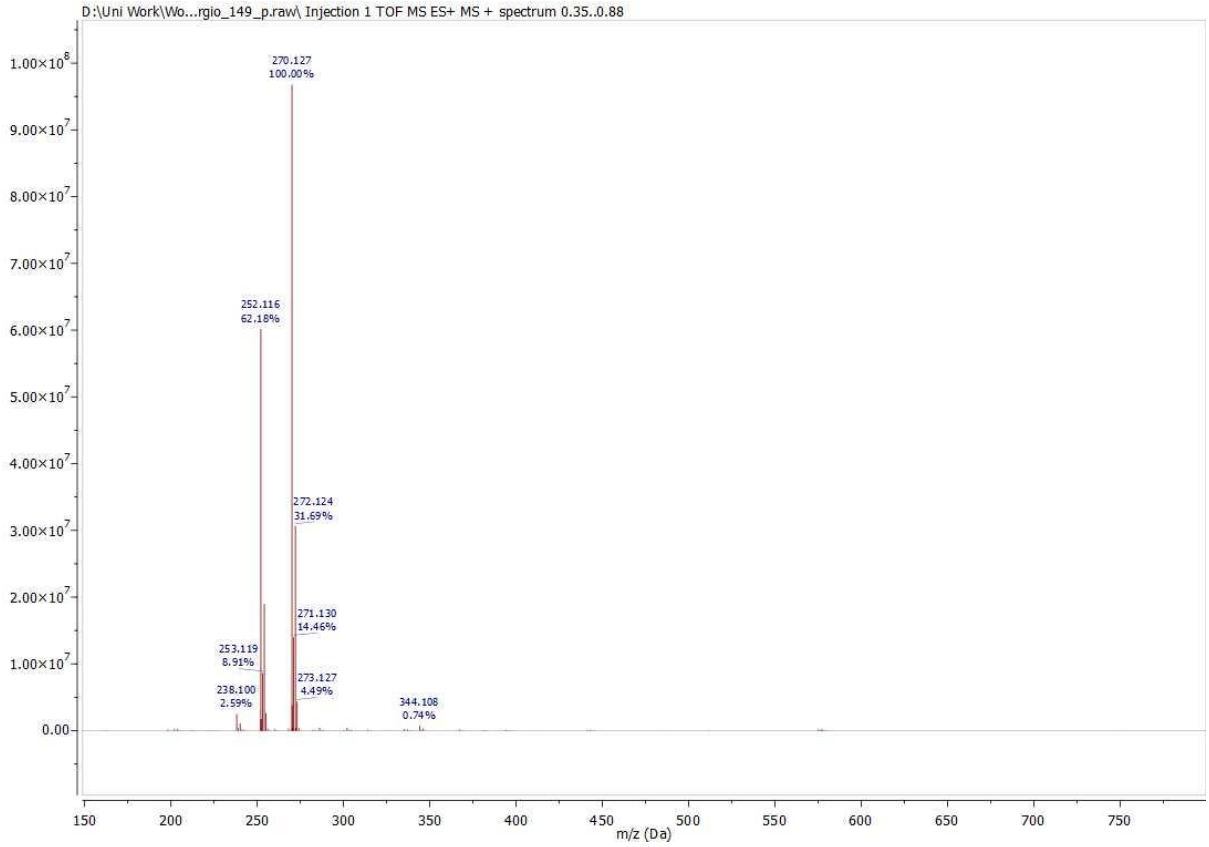

B.16.3 IR spectrum of compound (265)

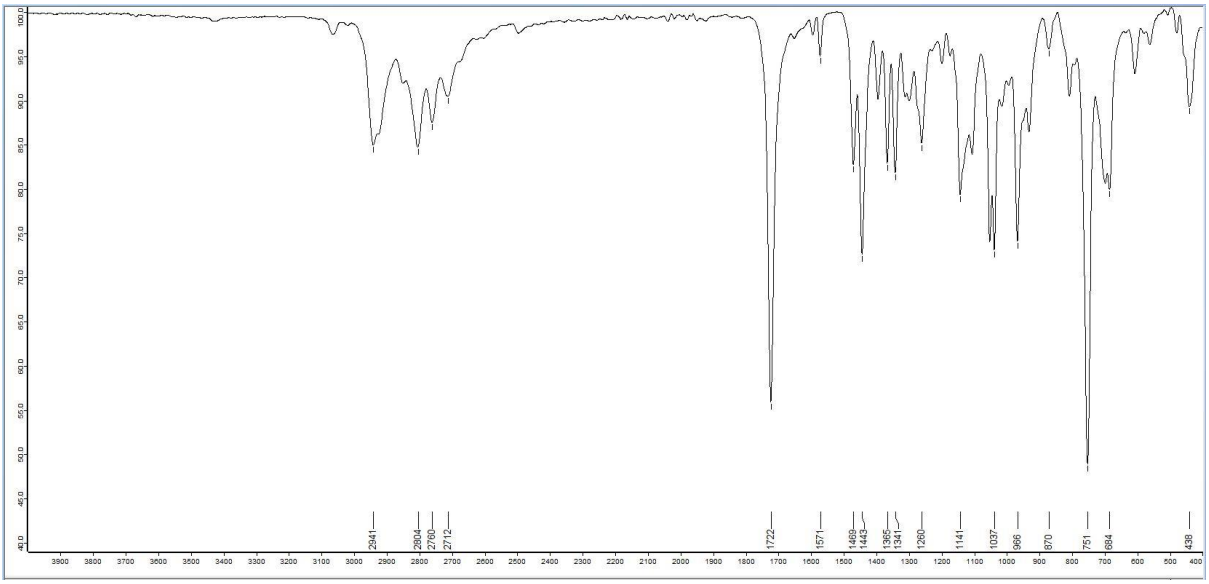

© University of Pretoria

B.17 1-(4-chlorobenzyl)piperidine-4-carbaldehyde (266)

B.17.1 ^{1}H and ^{13}C NMR spectra of compound (266)

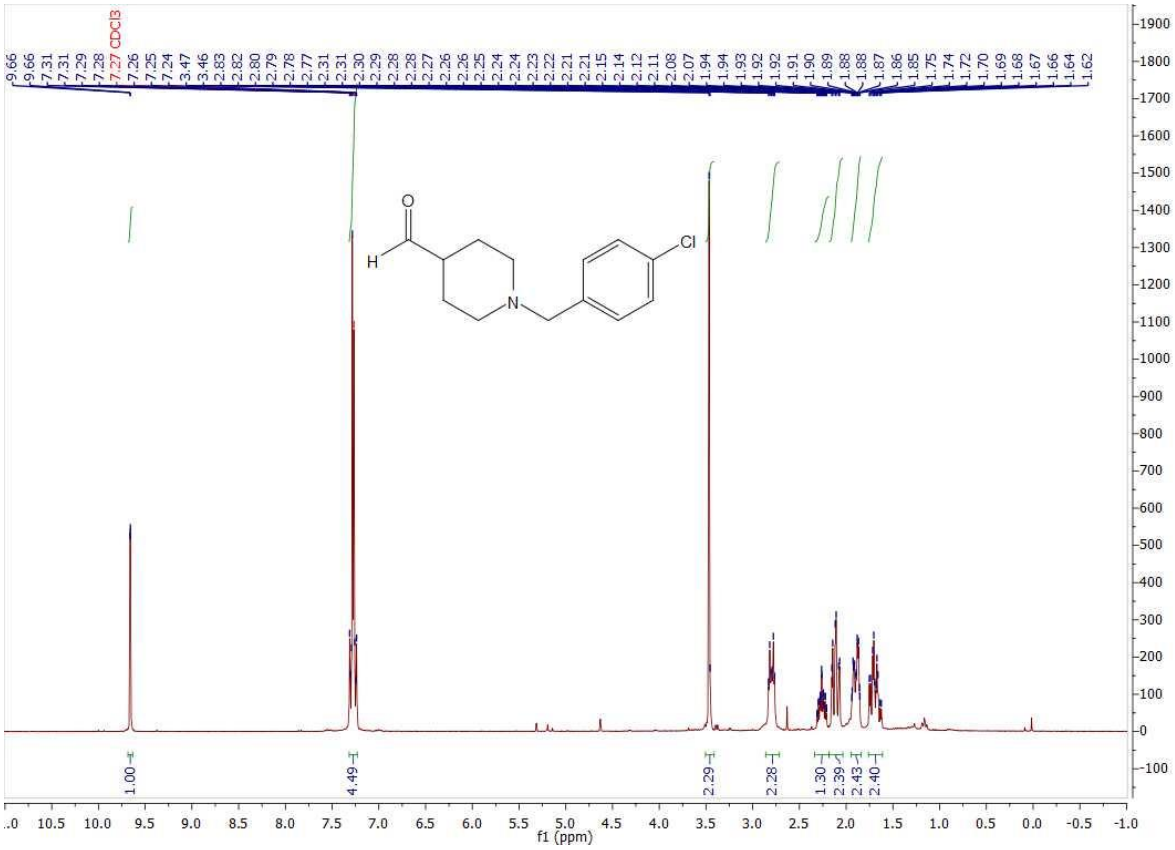

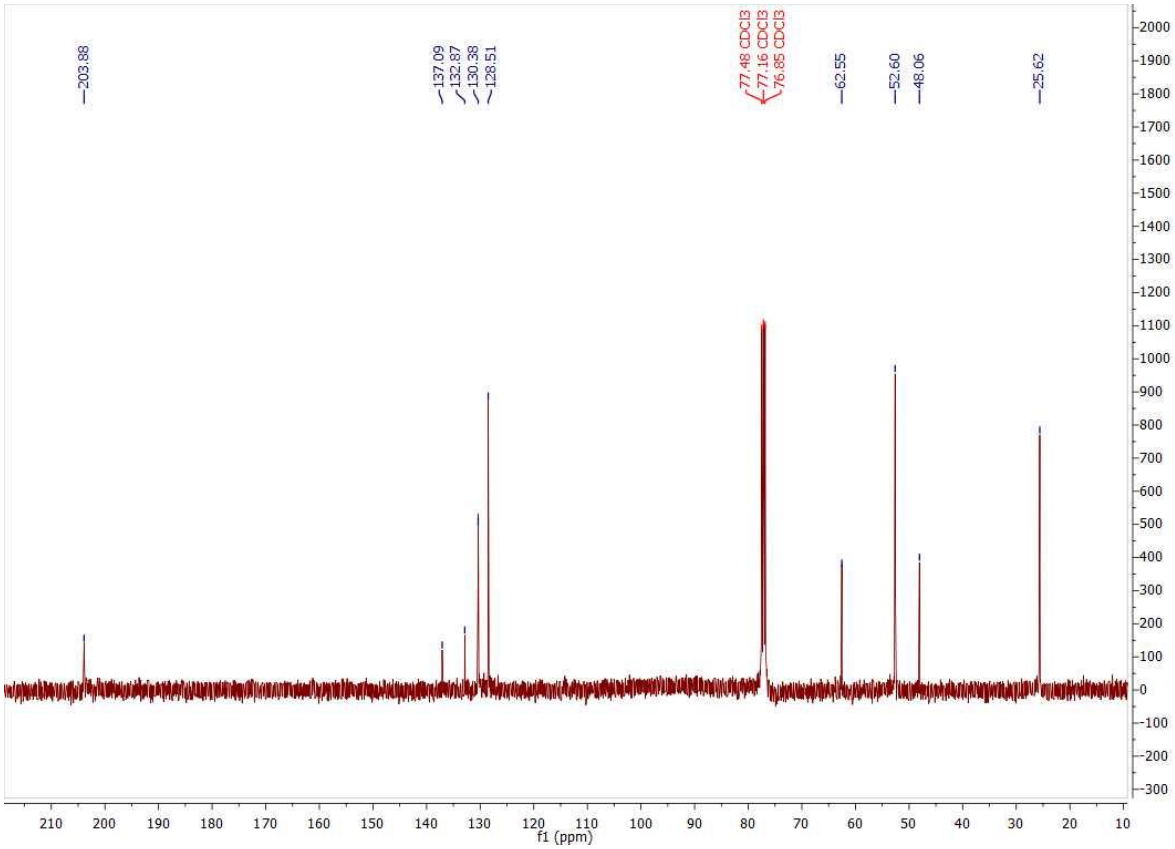

© University of Pretoria

B.17.2 HRMS spectrum of compound (266)

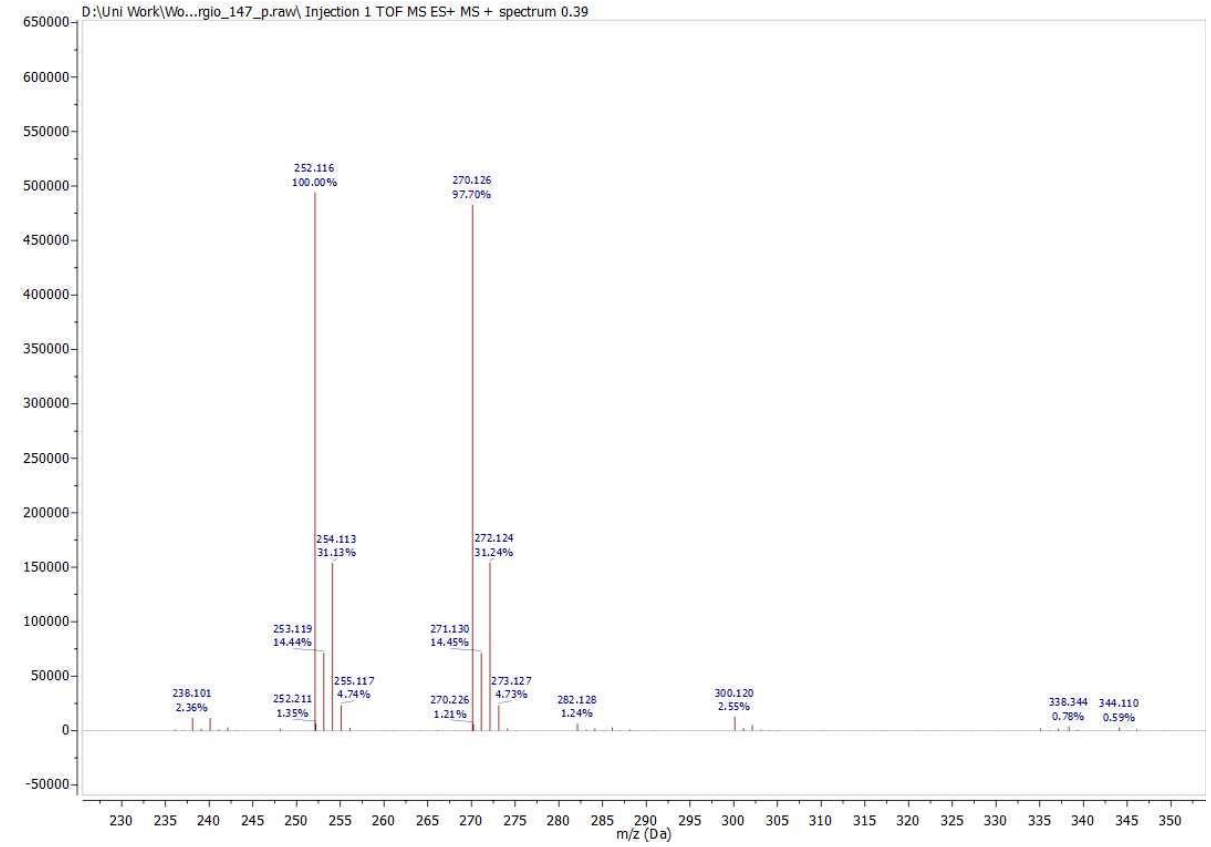

B.17.3 IR spectrum of compound (266)

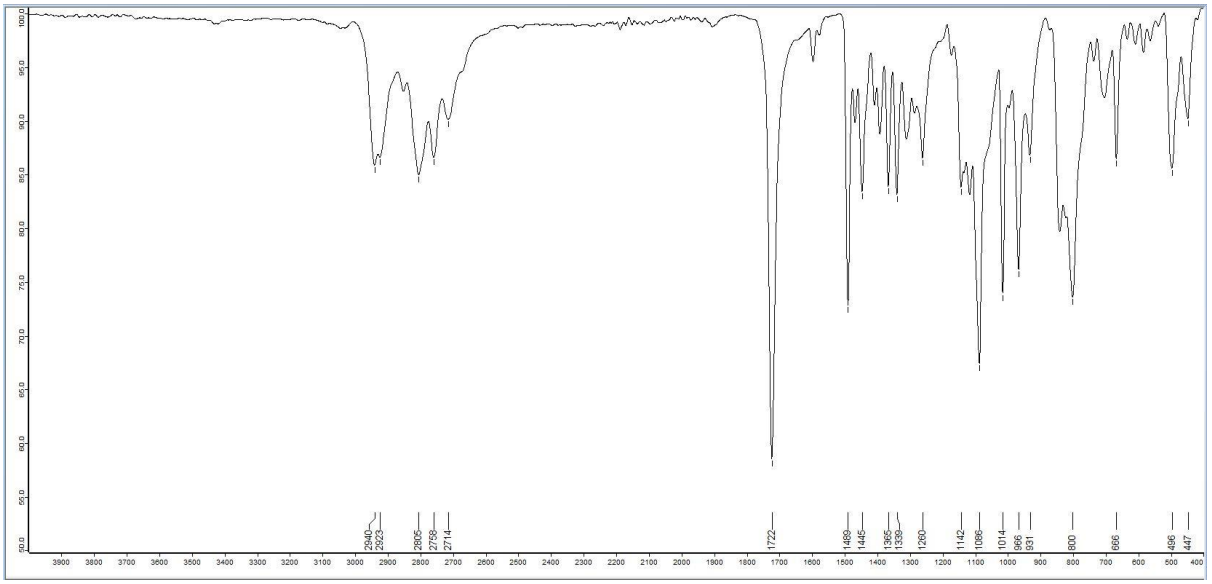

© University of Pretoria

B.18 (*E*)-2-((1-(4-chlorobenzyl)piperidin-4-yl)methylene)-5,6-dimethoxy-1-indanone (267)

B.18.1 ^{1}H and ^{13}C NMR spectra of compound (267)

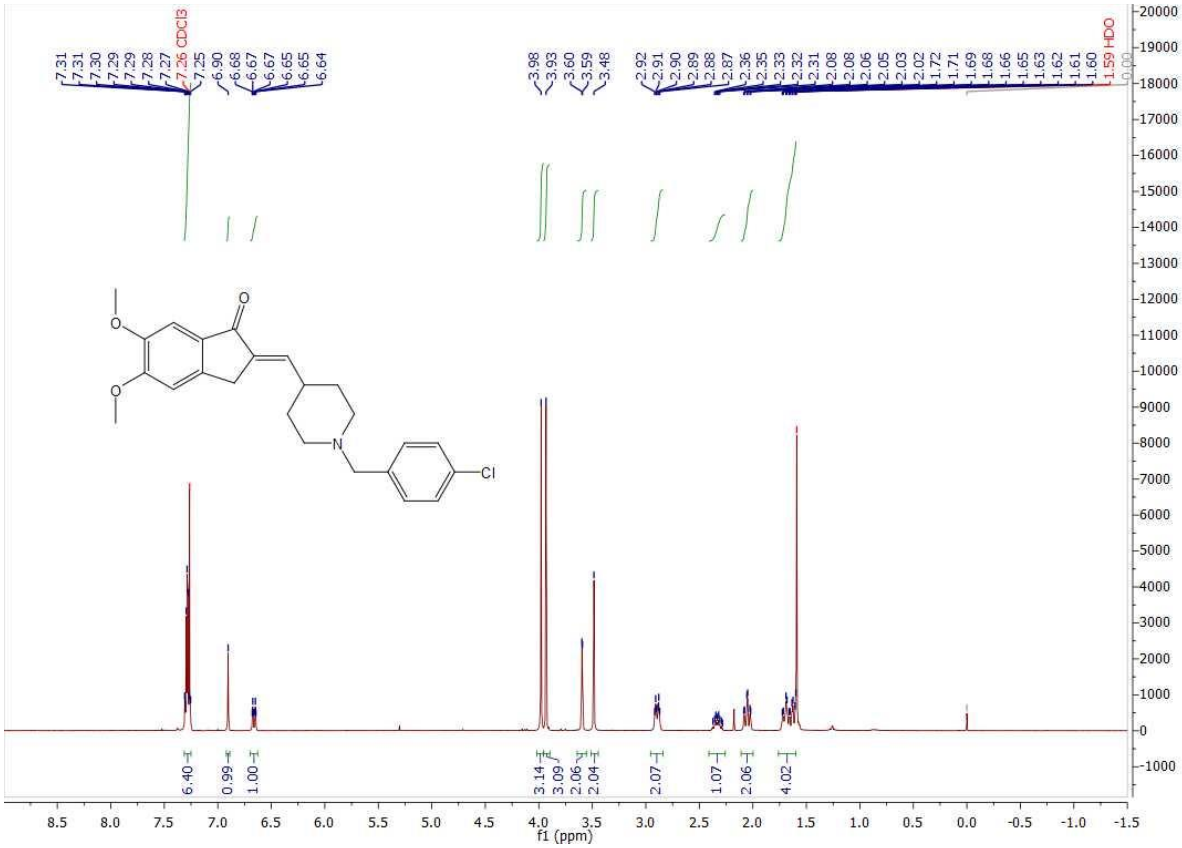

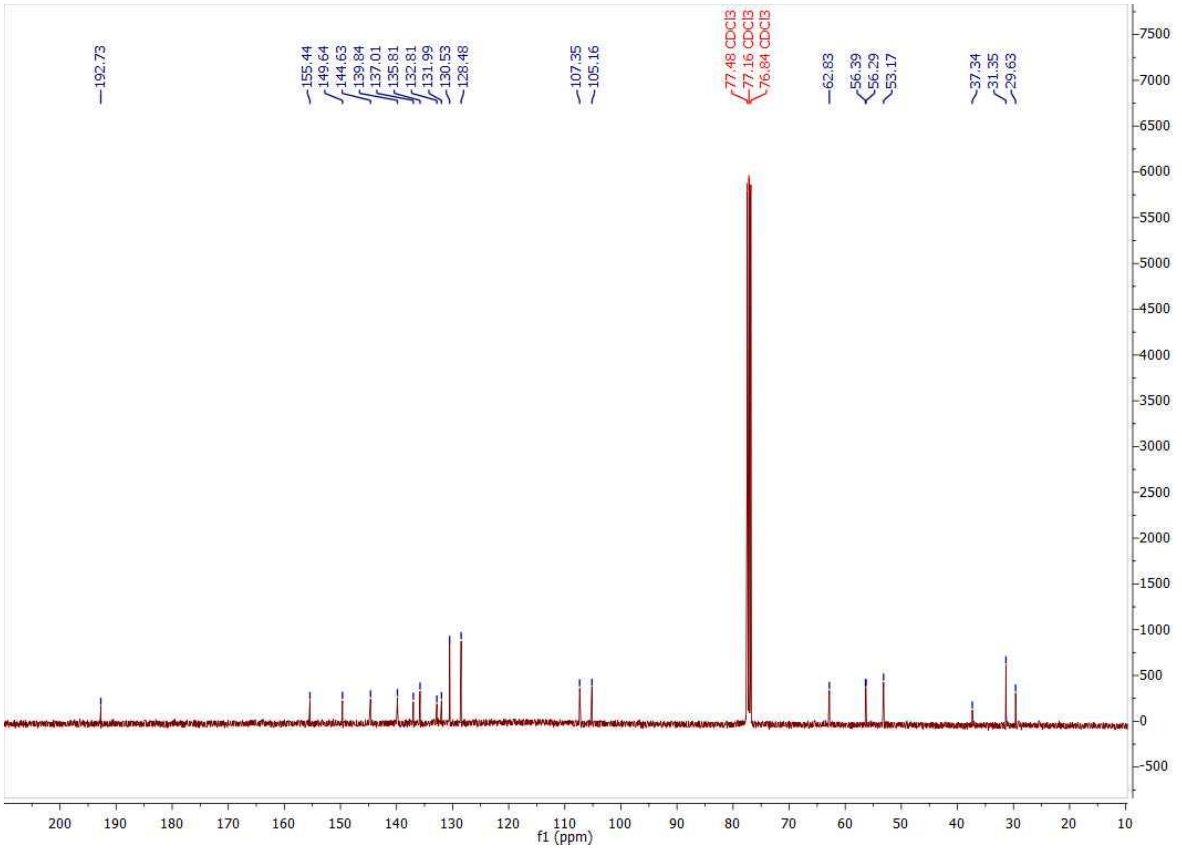

© University of Pretoria

B.18.2 HRMS spectrum of compound (267)

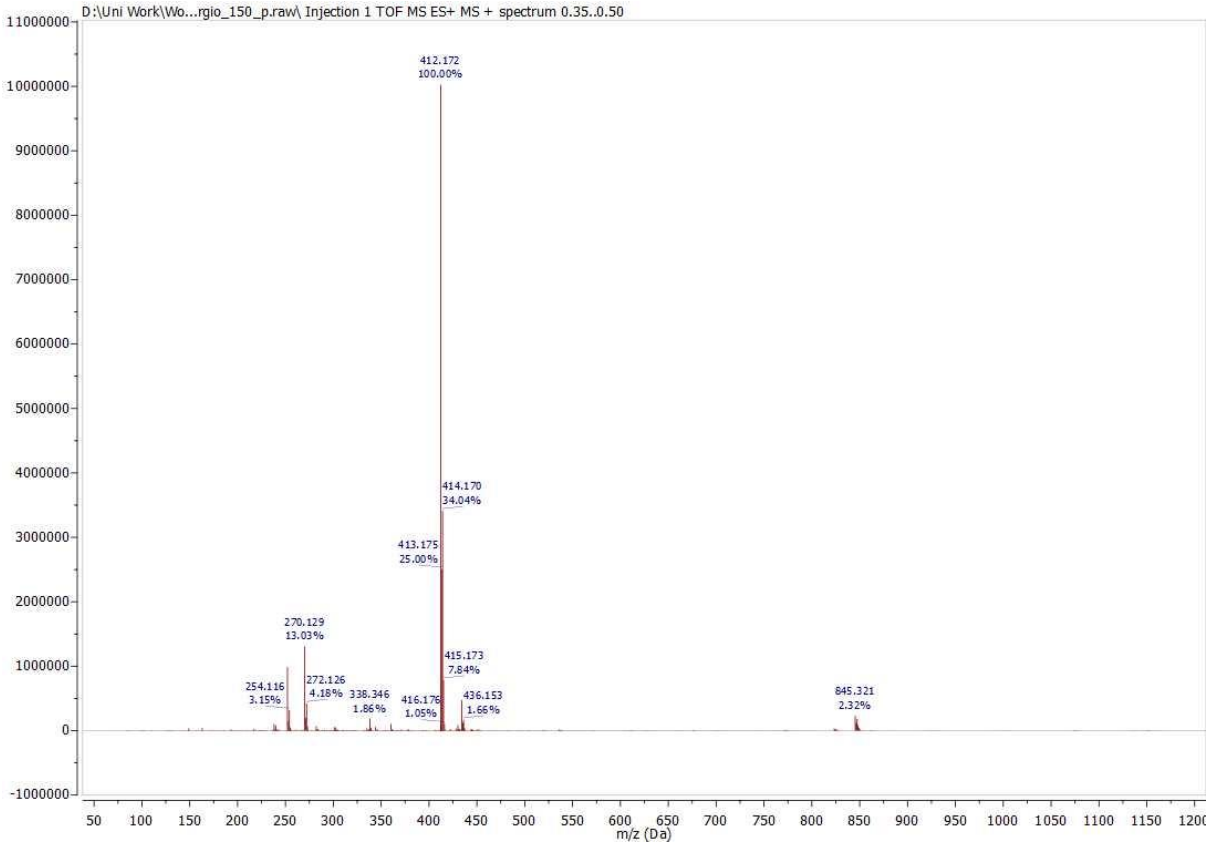

B.18.3 IR spectrum of compound (267)

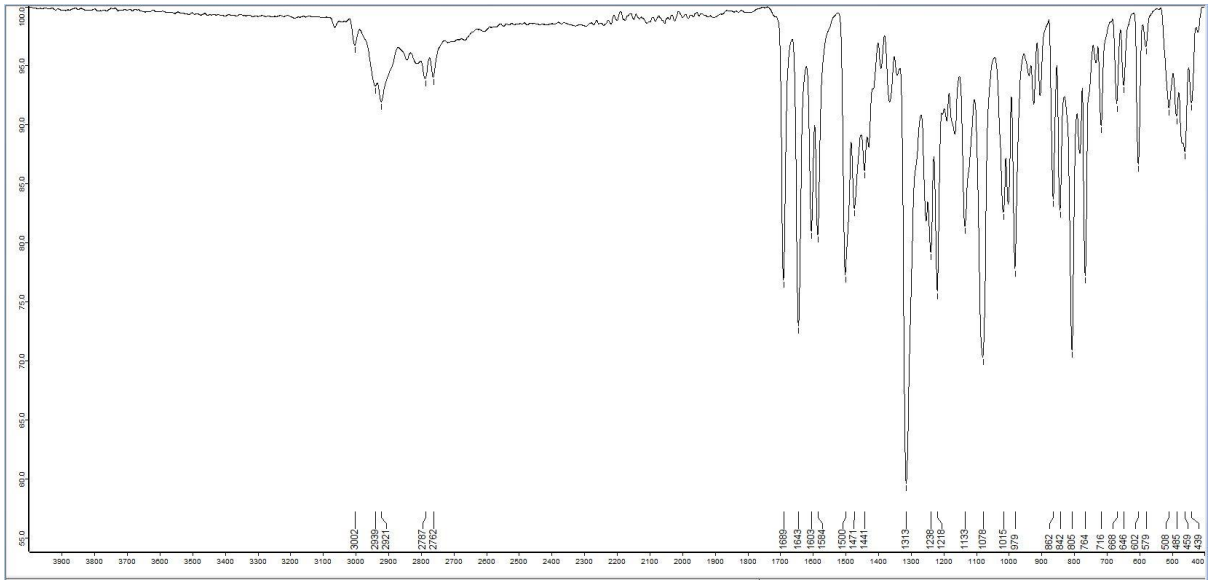

© University of Pretoria

B.19 1-(4-((*tert*-butyldiphenylsilyl)oxy)phenyl)ethanone (279)

B.19.1 ^{1}H and ^{13}C NMR spectra of compound (279)

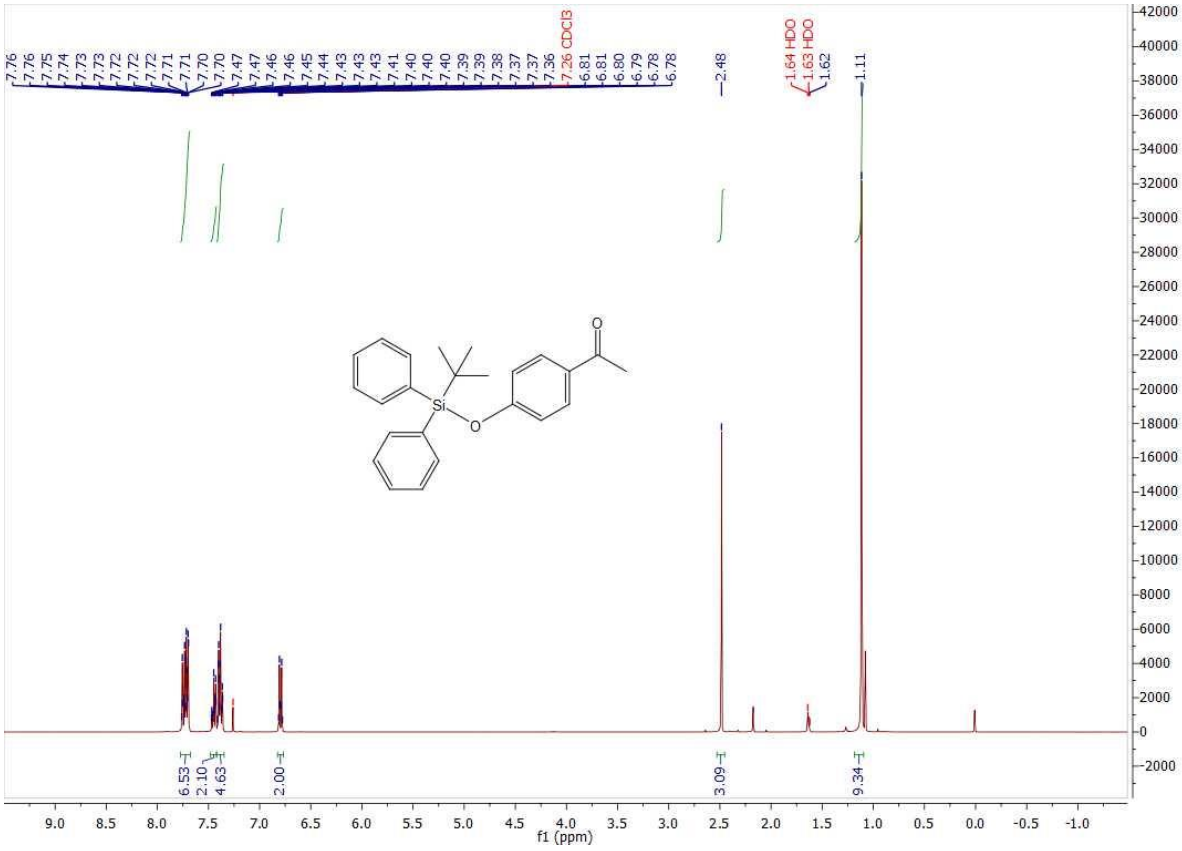

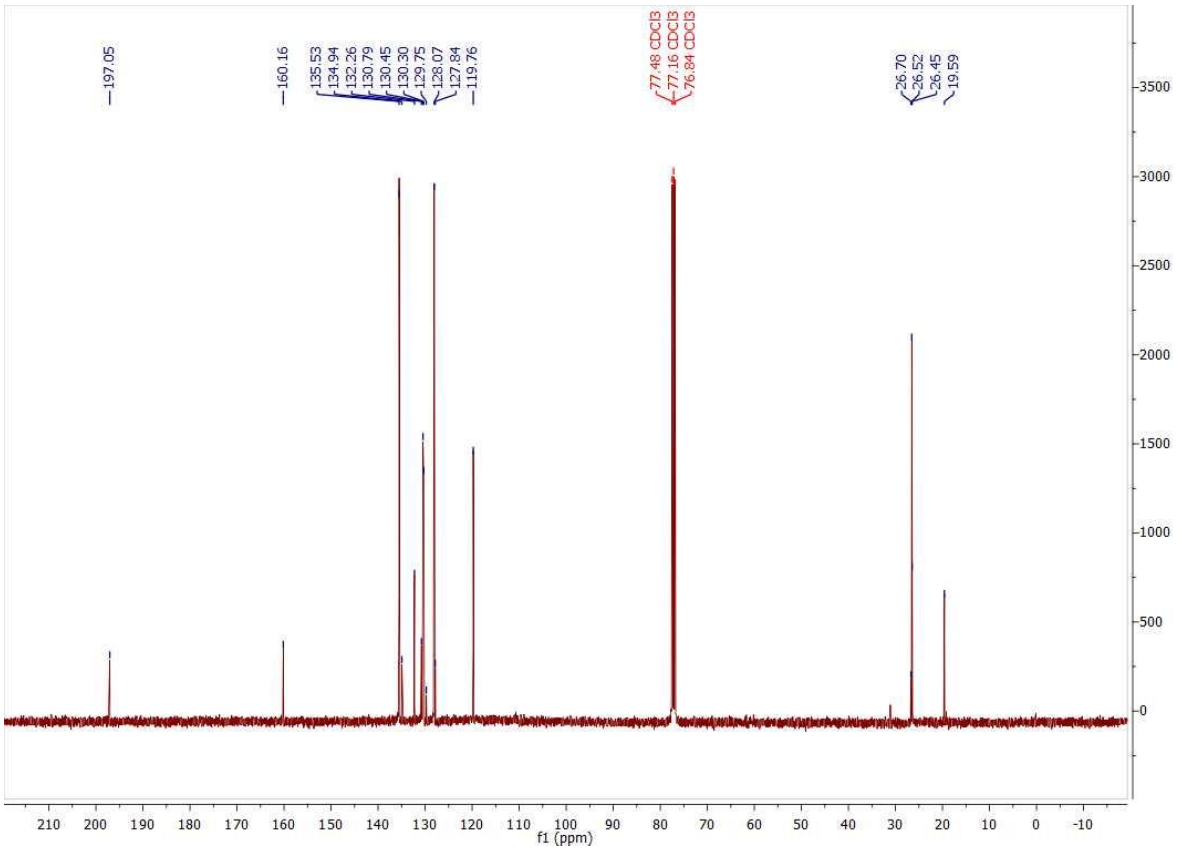

© University of Pretoria

B.19.2 HRMS spectrum of compound (279)

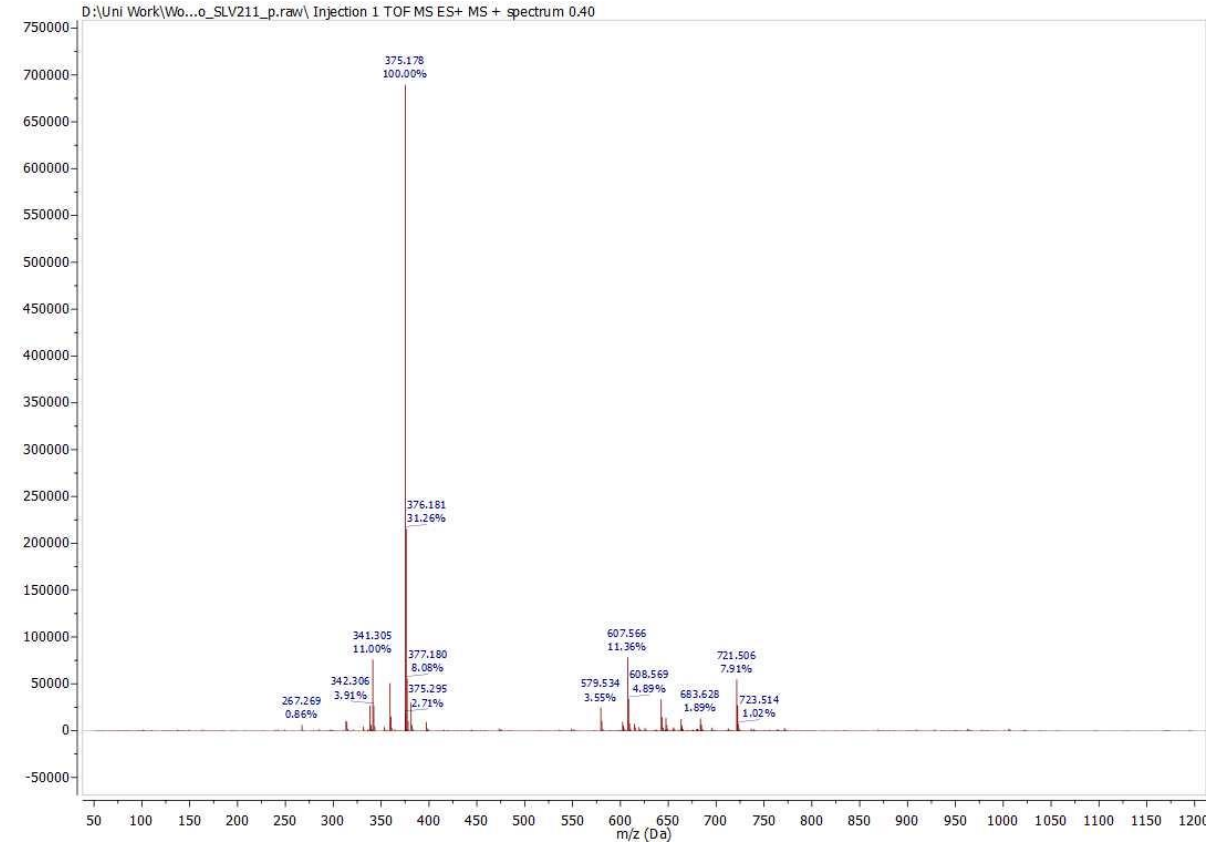

B.19.3 IR spectrum of compound (279)

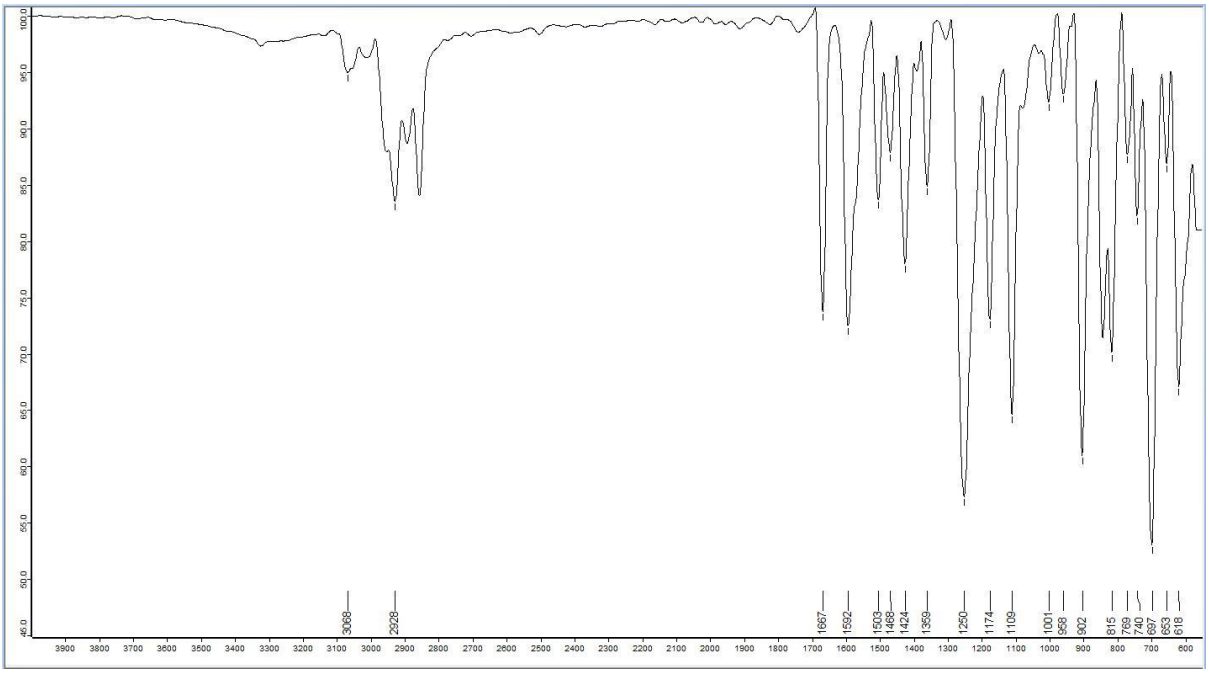

© University of Pretoria

B.20 1-(2-((*tert*-butyldiphenylsilyl)oxy)phenyl)ethenone (280)

B.20.1 ^{1}H and ^{13}C NMR spectra of compound (280)

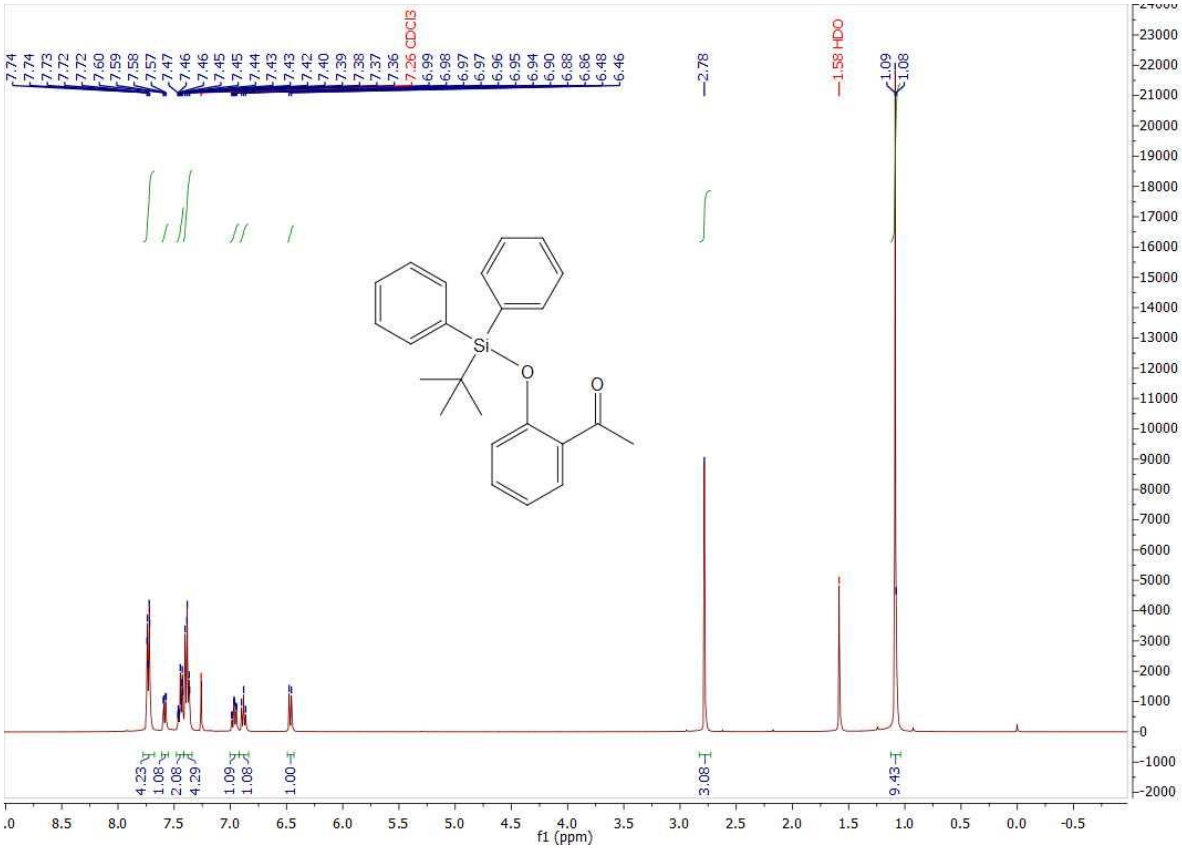

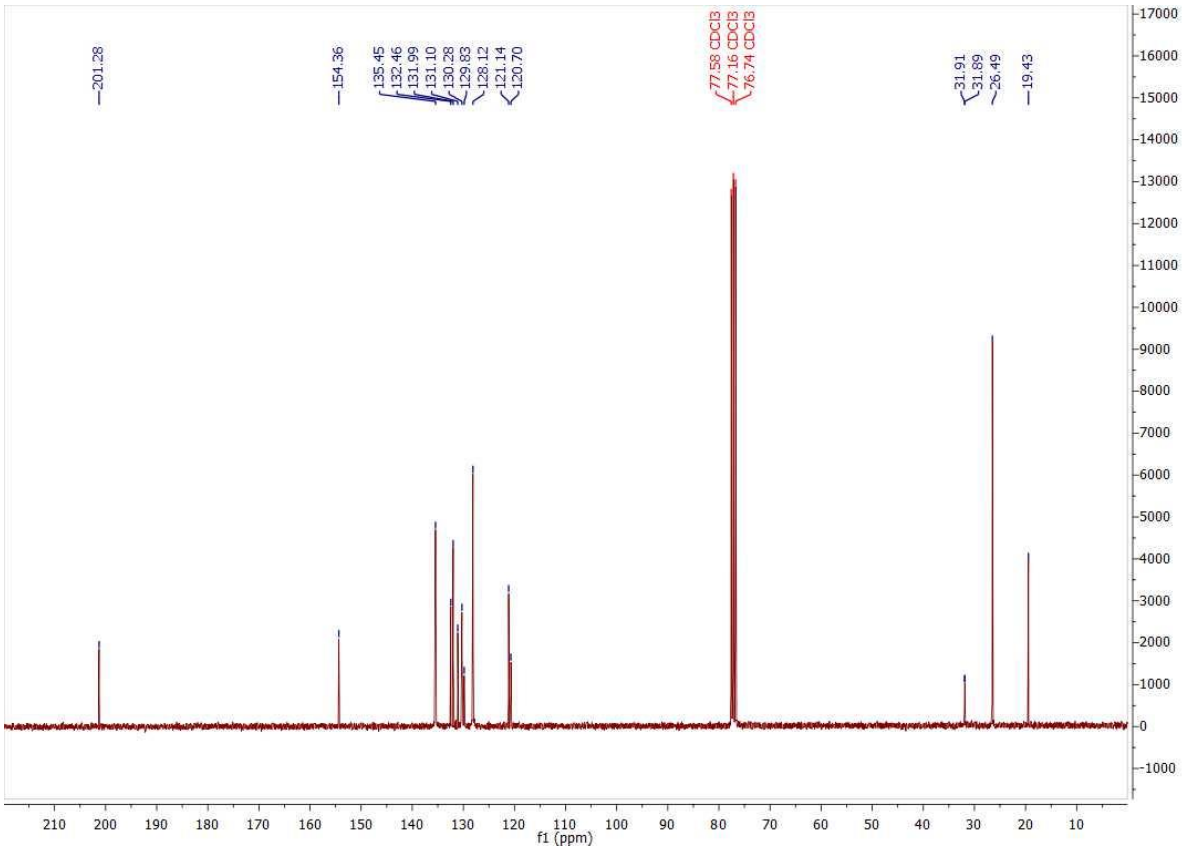

© University of Pretoria

B.20.2 HRMS spectrum of compound (280)

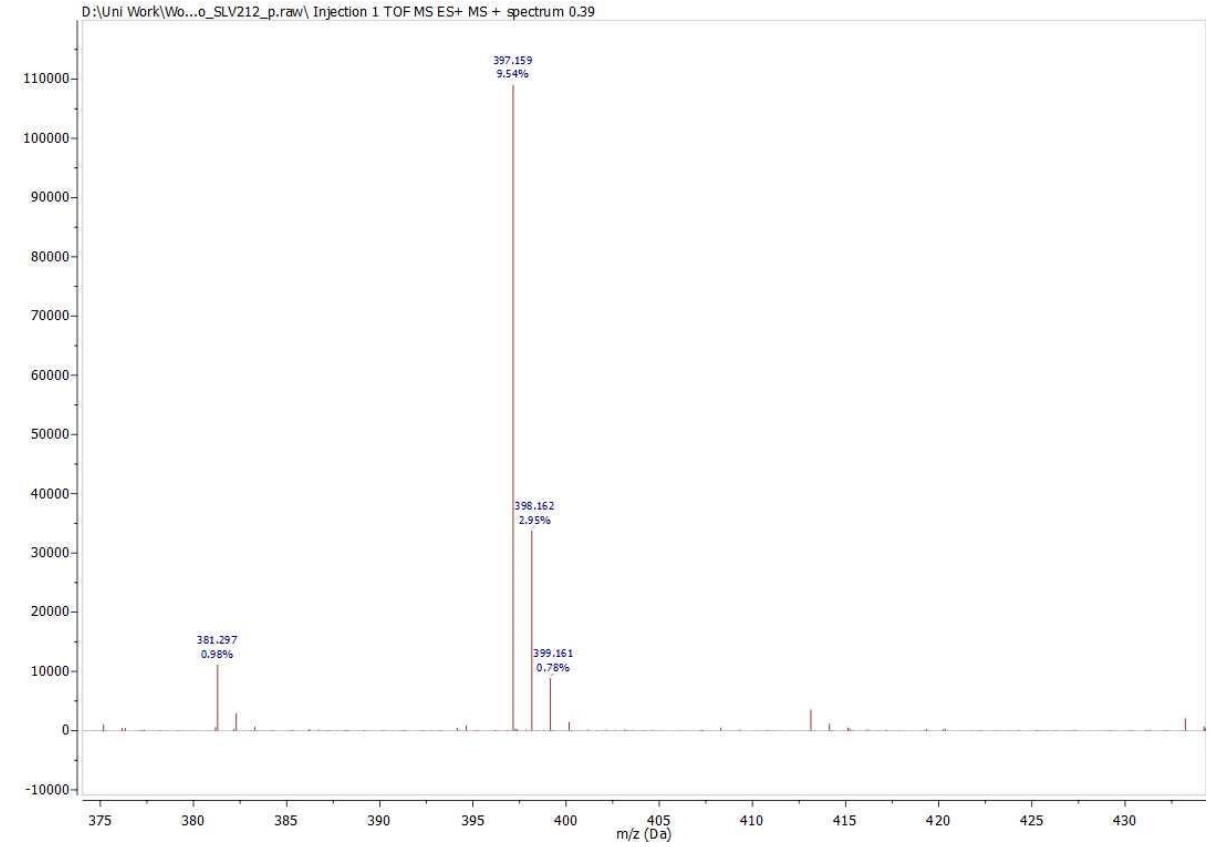

B.20.3 IR spectrum of compound (280)

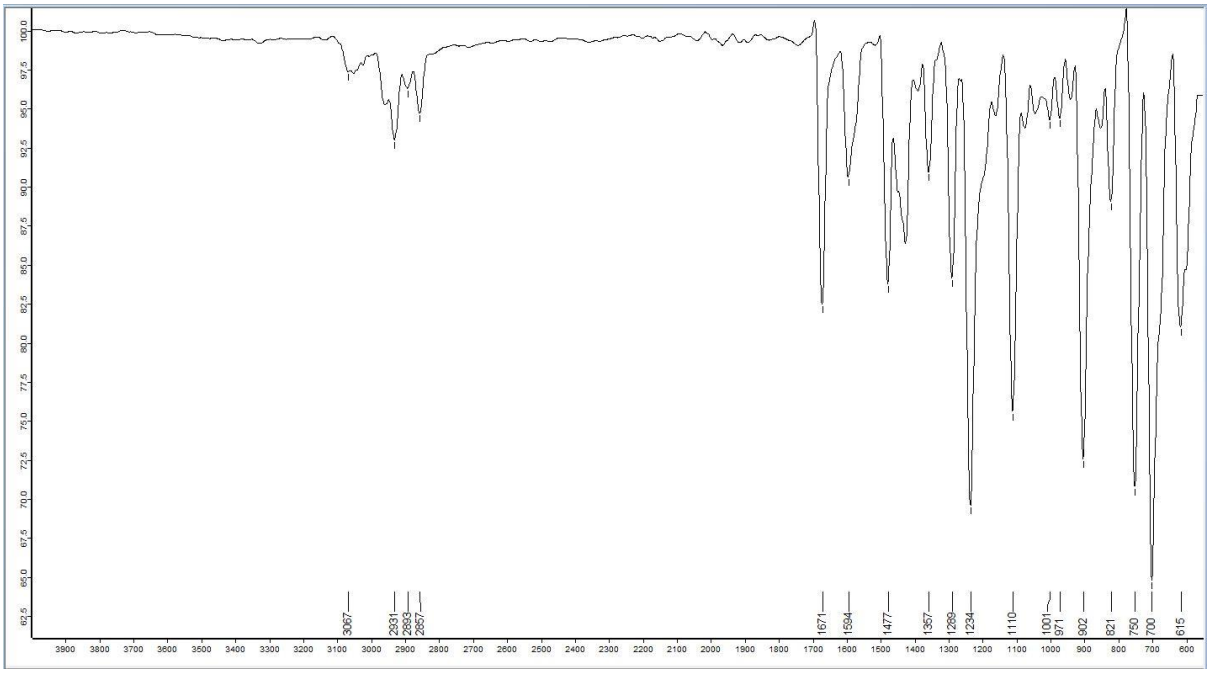

© University of Pretoria

B.21 2-bromo-1-phenylethanone (283)

B.21.1 ^{1}H and ^{13}C NMR spectra of compound (283)

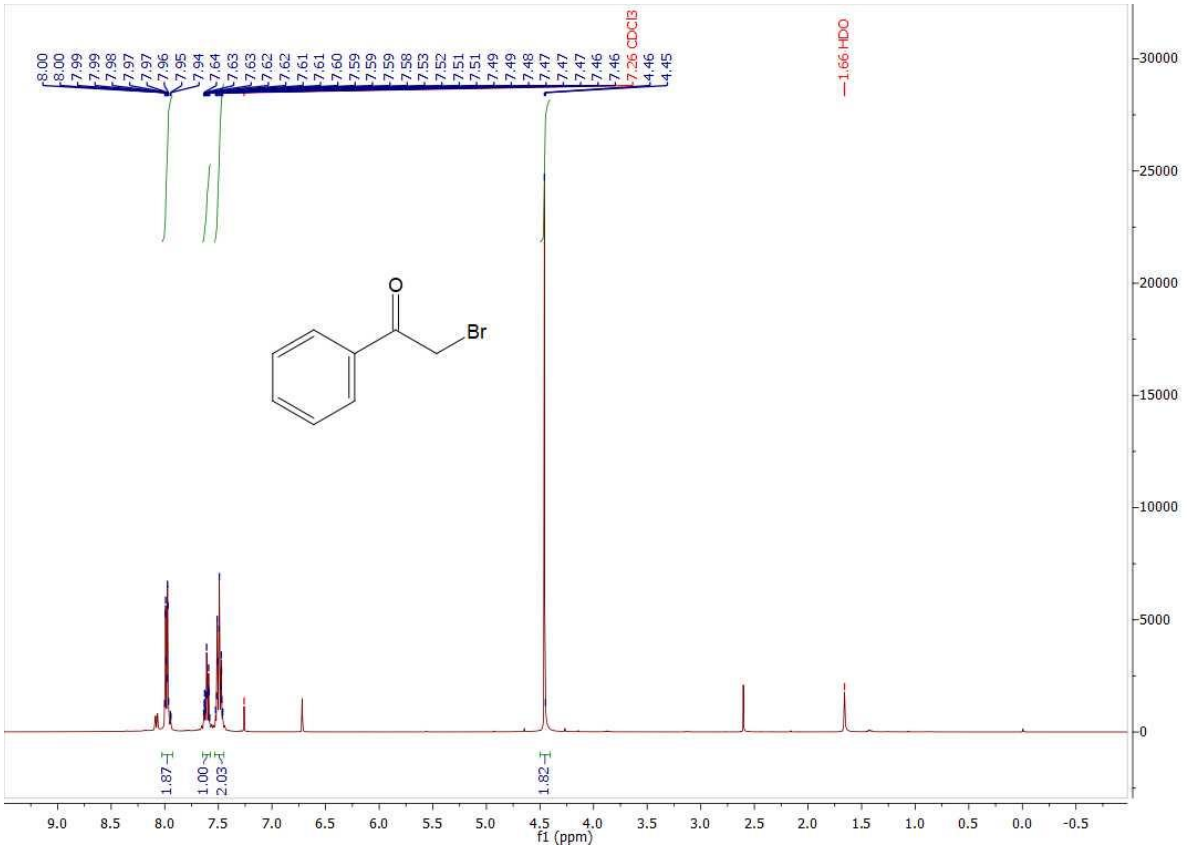

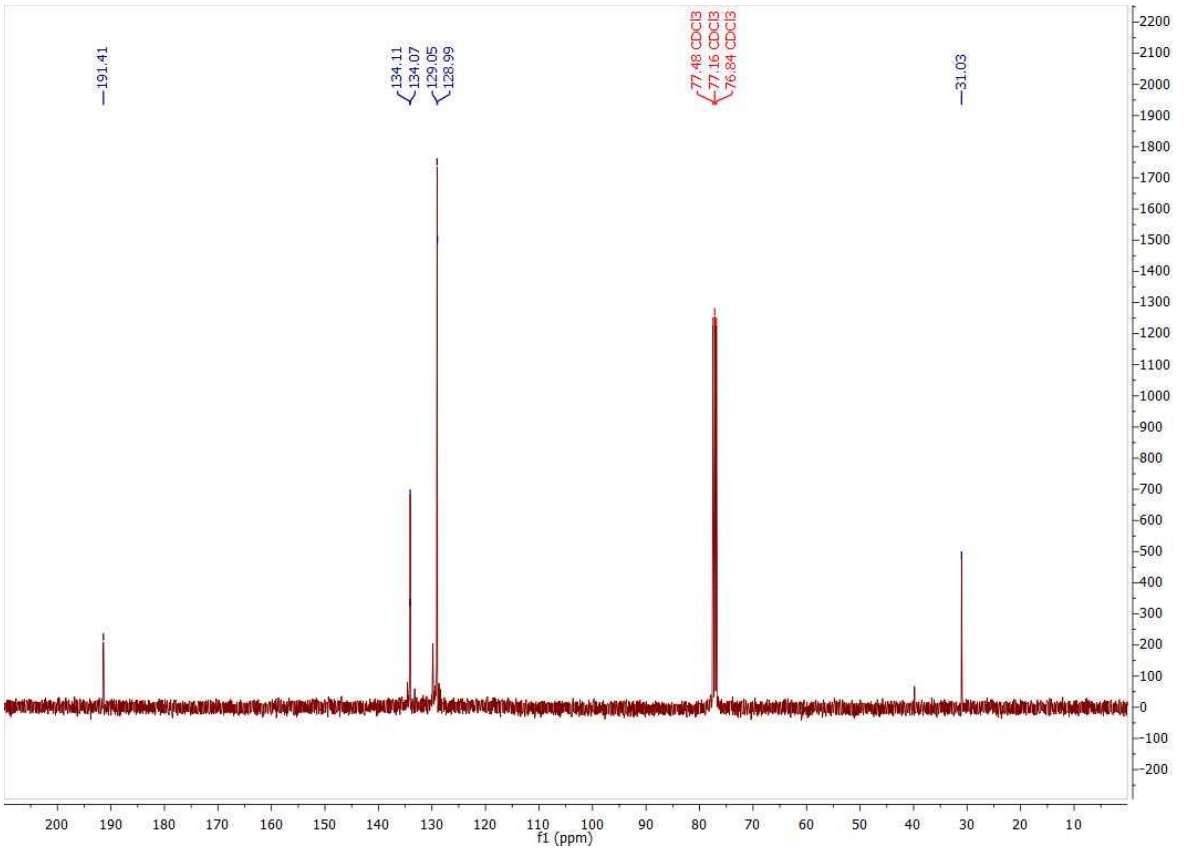

© University of Pretoria

B.21.2 IR spectrum of compound (283)

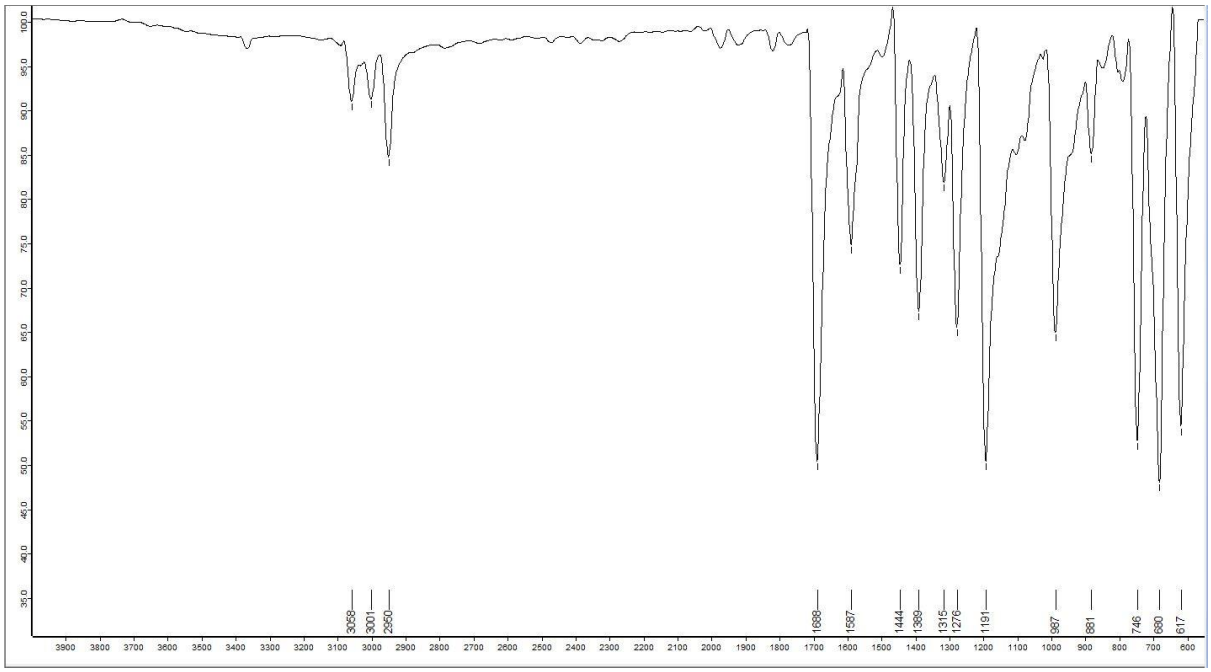

© University of Pretoria

B.22 (*Z*)-2-((1-benzylpiperidin-4-yl)methoxy)-1-phenylethenol (284)

B.22.1 ^{1}H and ^{13}C NMR spectra of compound (284)

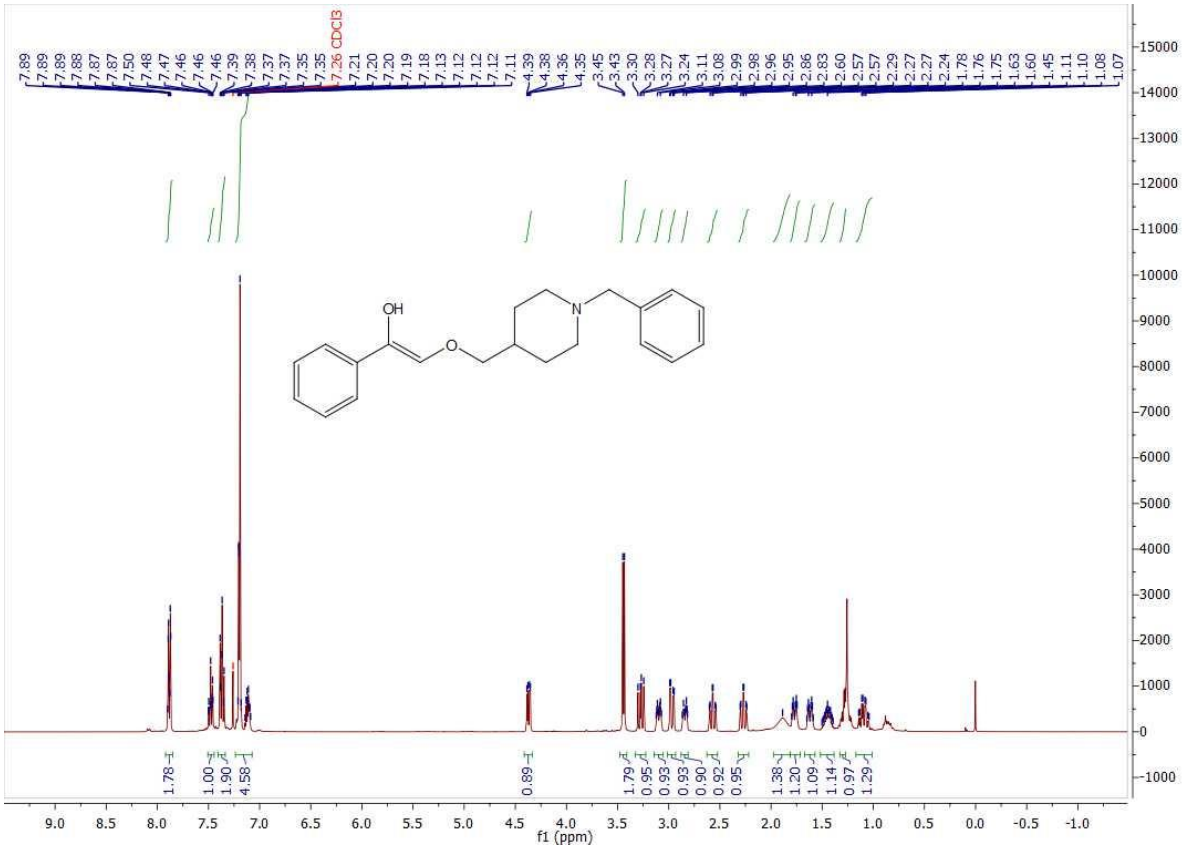

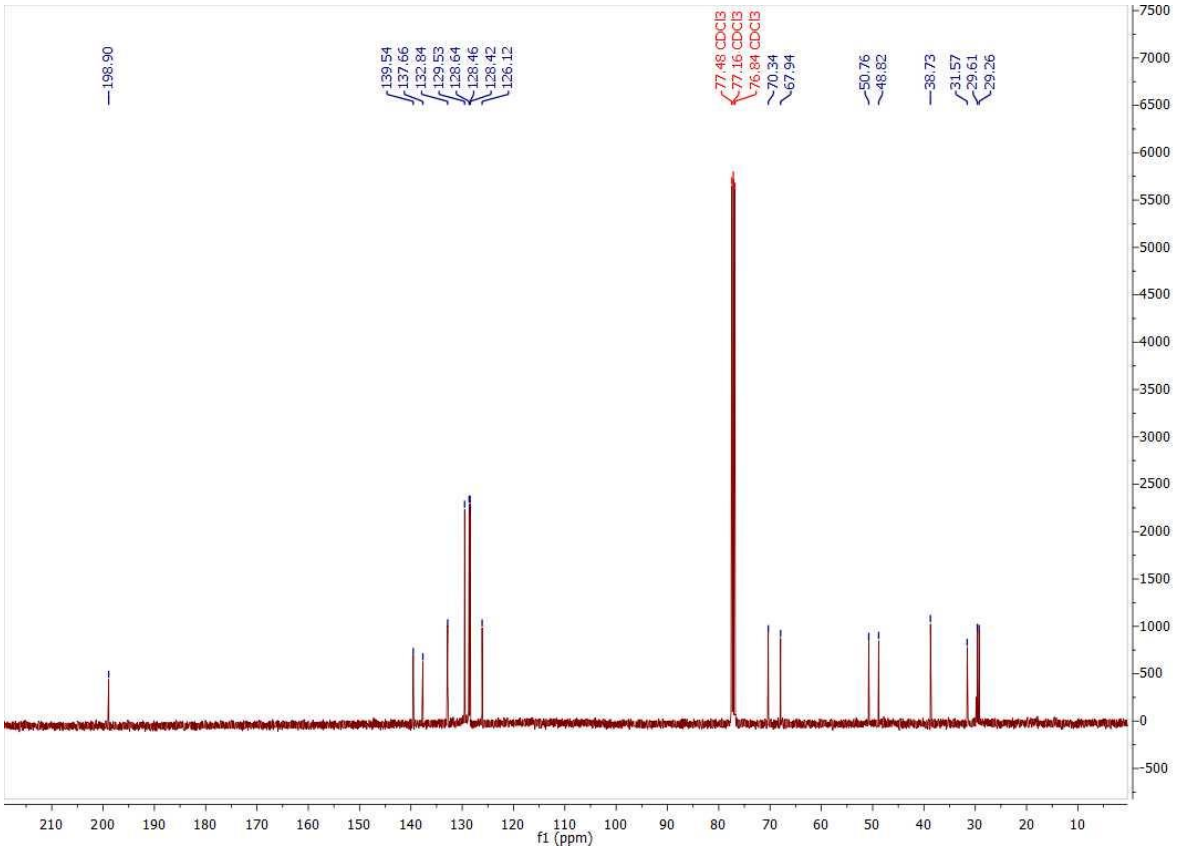

© University of Pretoria

B.22.2 HRMS spectrum of compound (284)

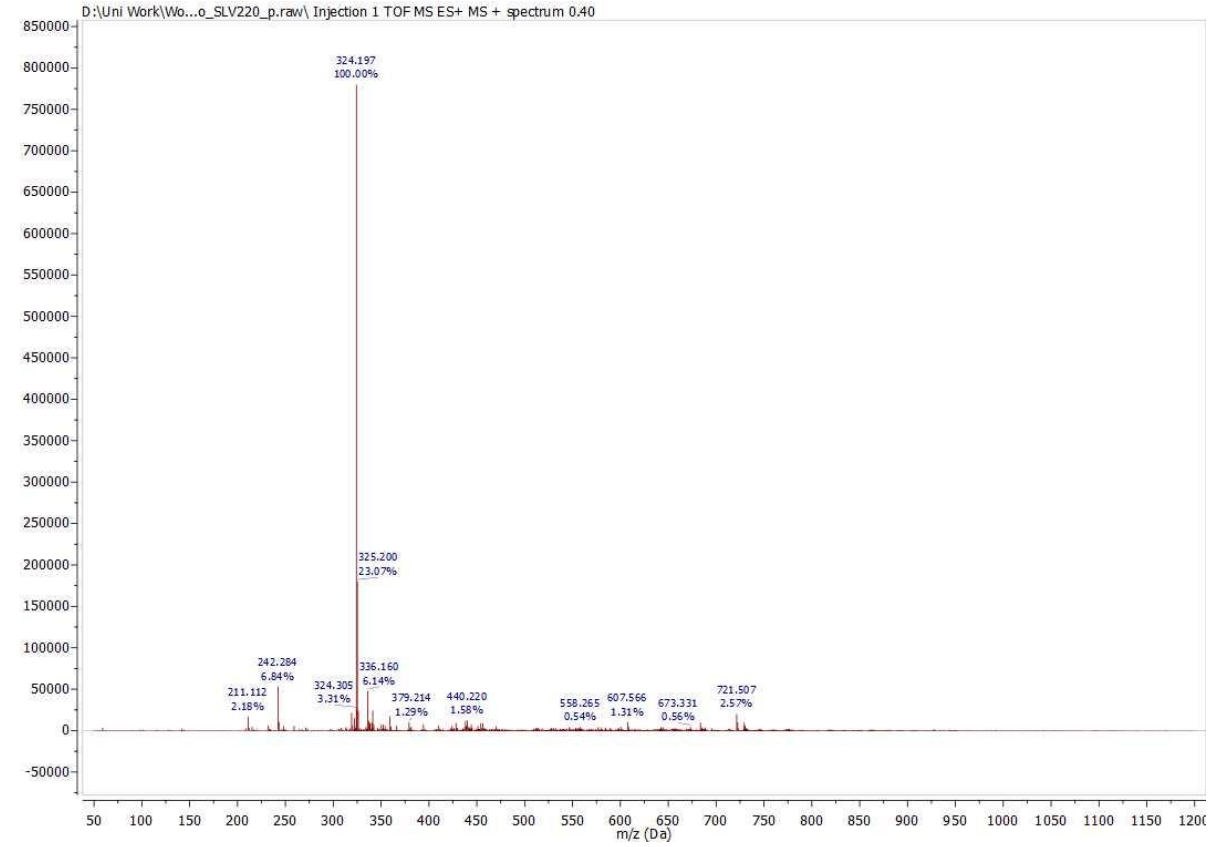

B.22.3 IR spectrum of compound (284)

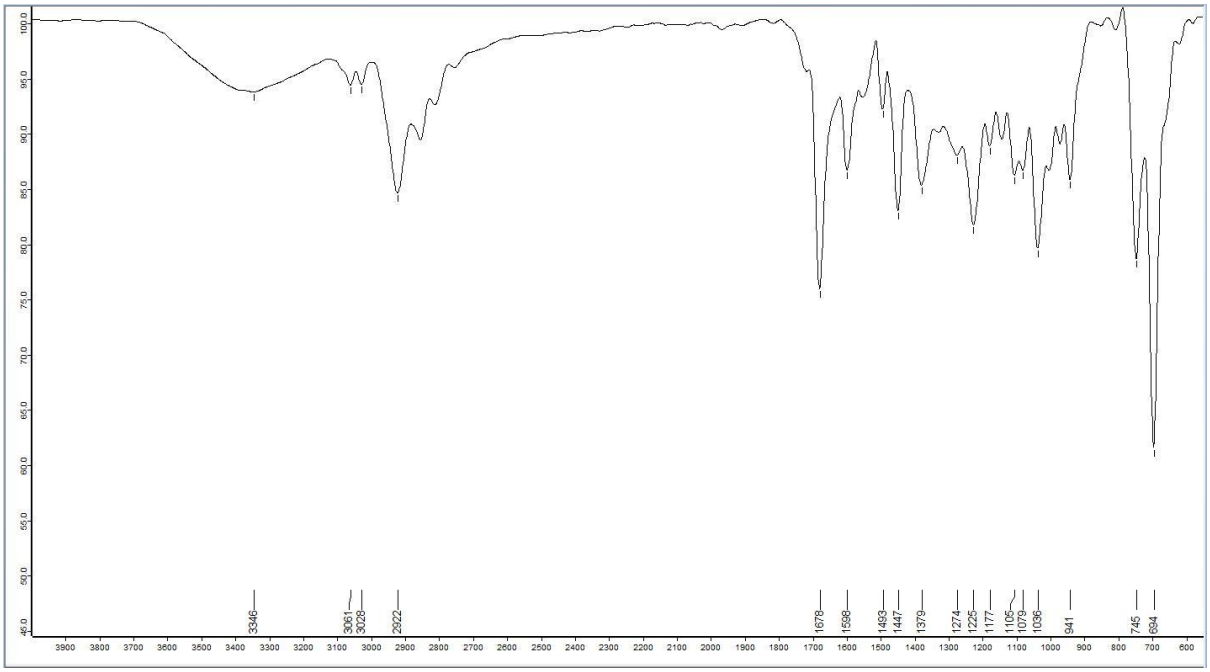

© University of Pretoria

B.23 4-acetylphenylacetate (285)

B.23.1 ^{1}H and ^{13}C NMR spectra of compound (285)

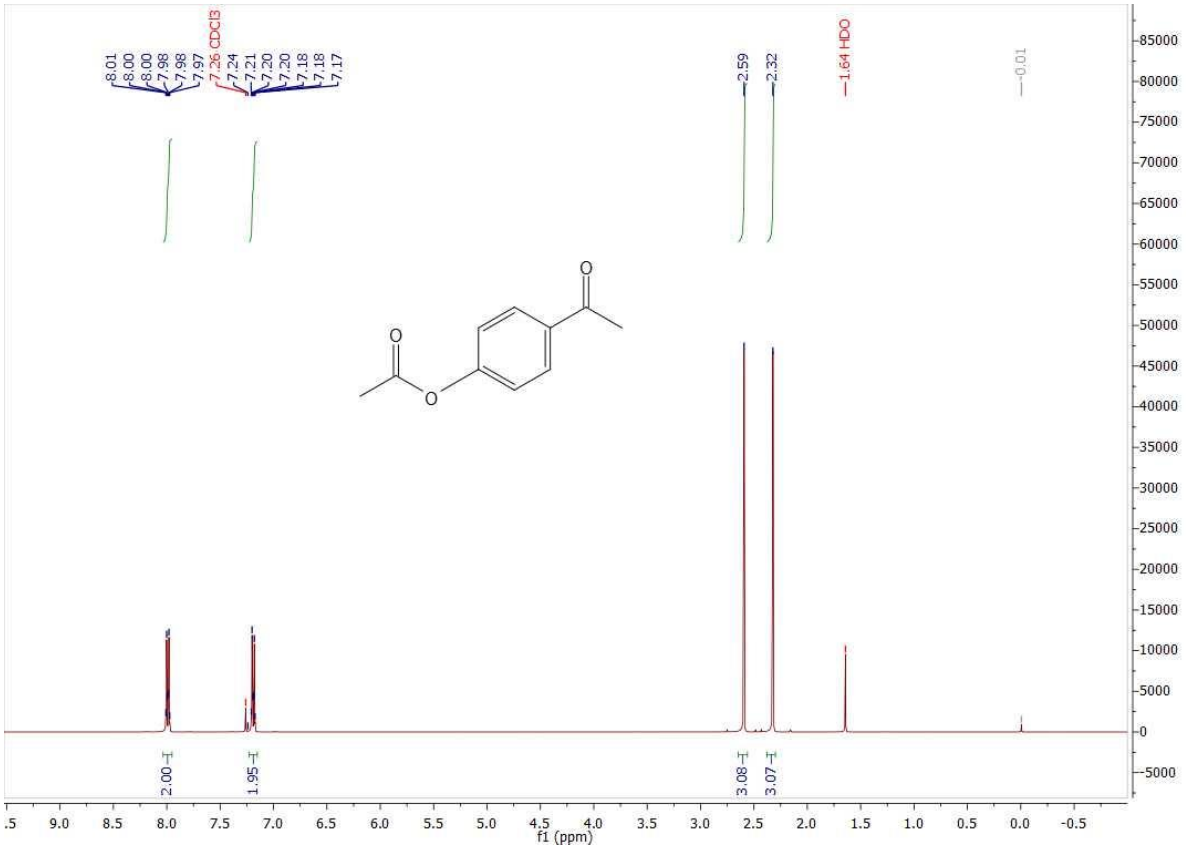

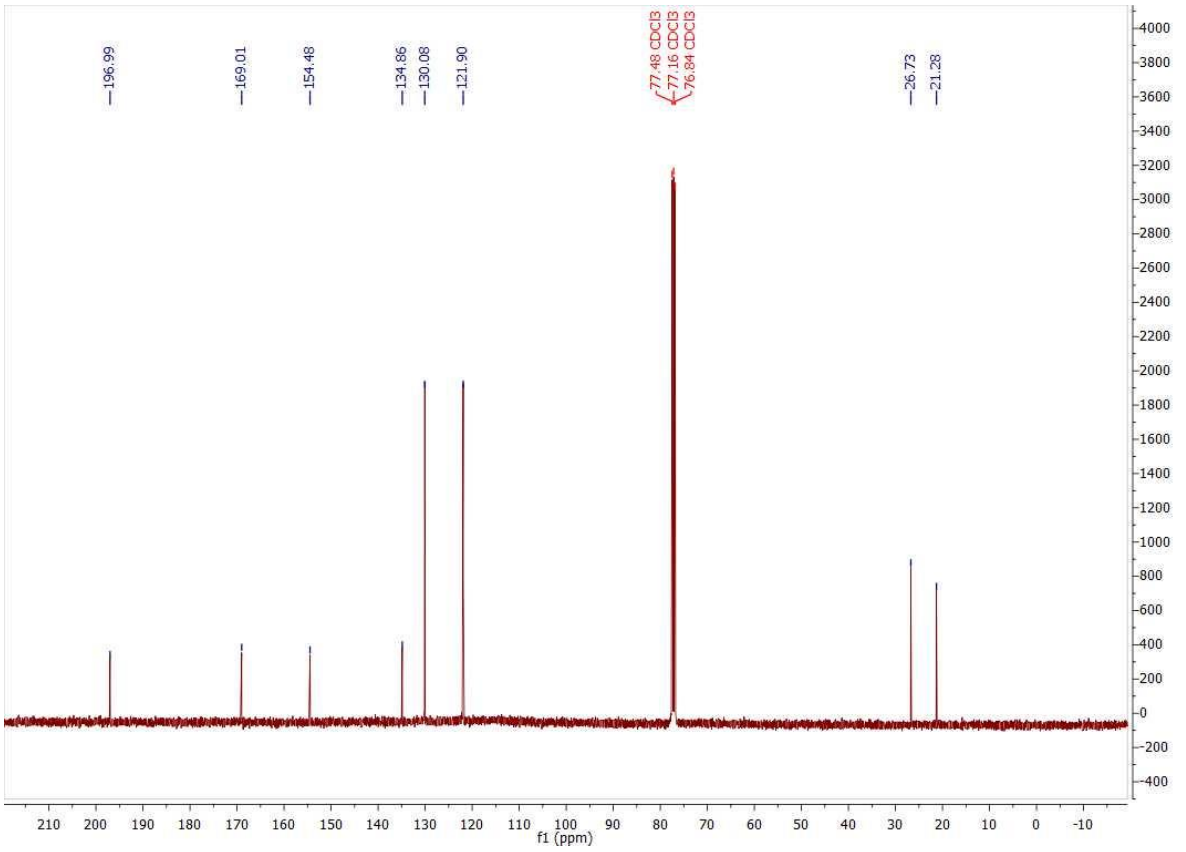

© University of Pretoria

B.23.2 IR spectrum of compound (285)

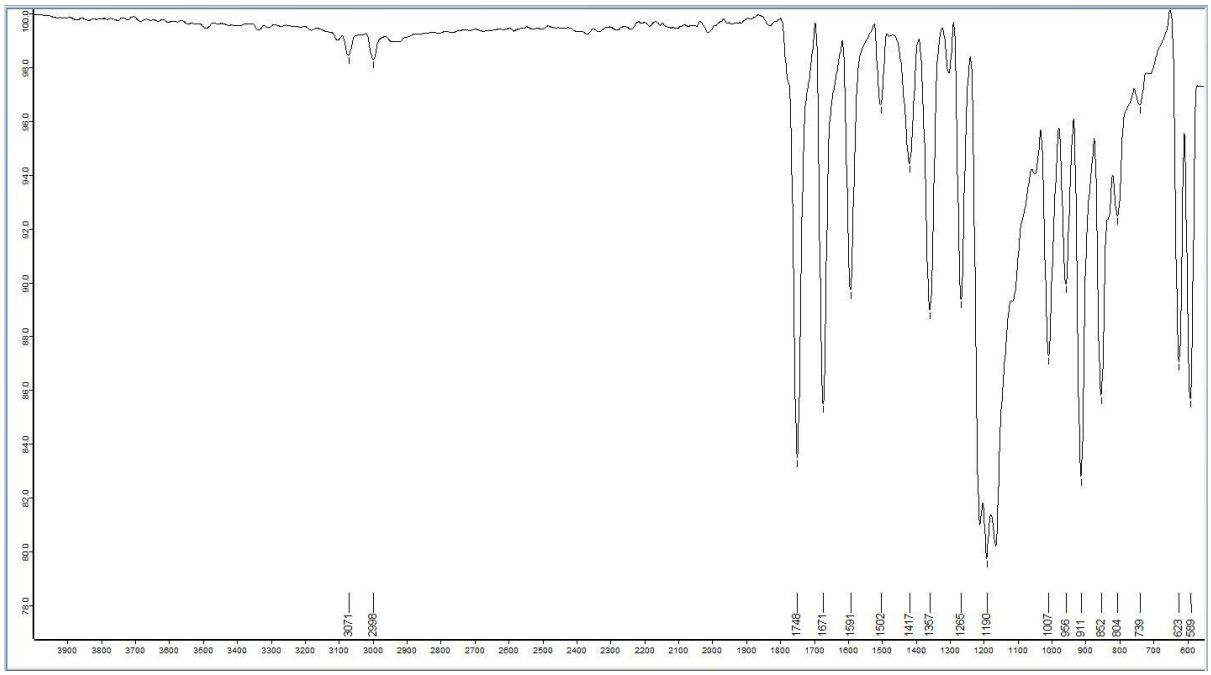

© University of Pretoria

B.24 2-acetylphenylacetate (286)

B.24.1 ^{1}H and ^{13}C NMR spectra of compound (286)

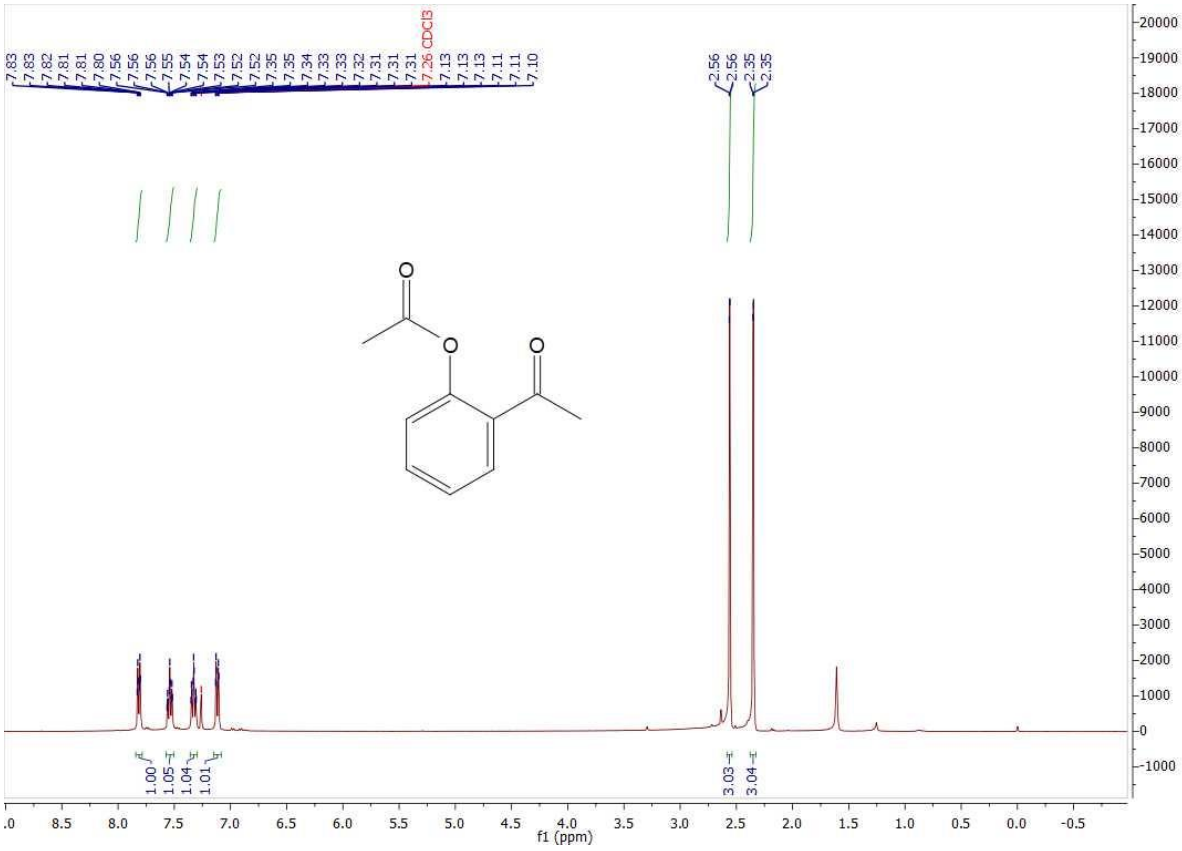

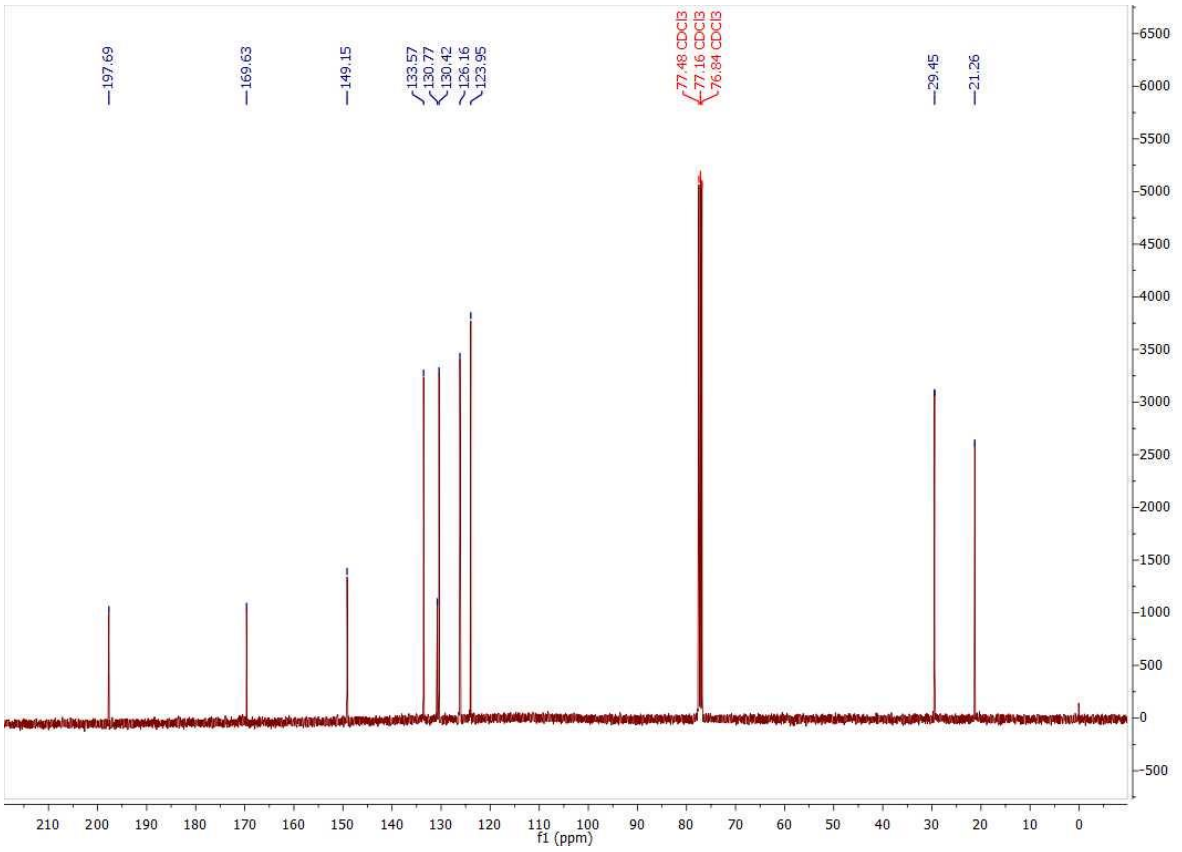

© University of Pretoria

B.24.2 IR spectrum of compound (286)

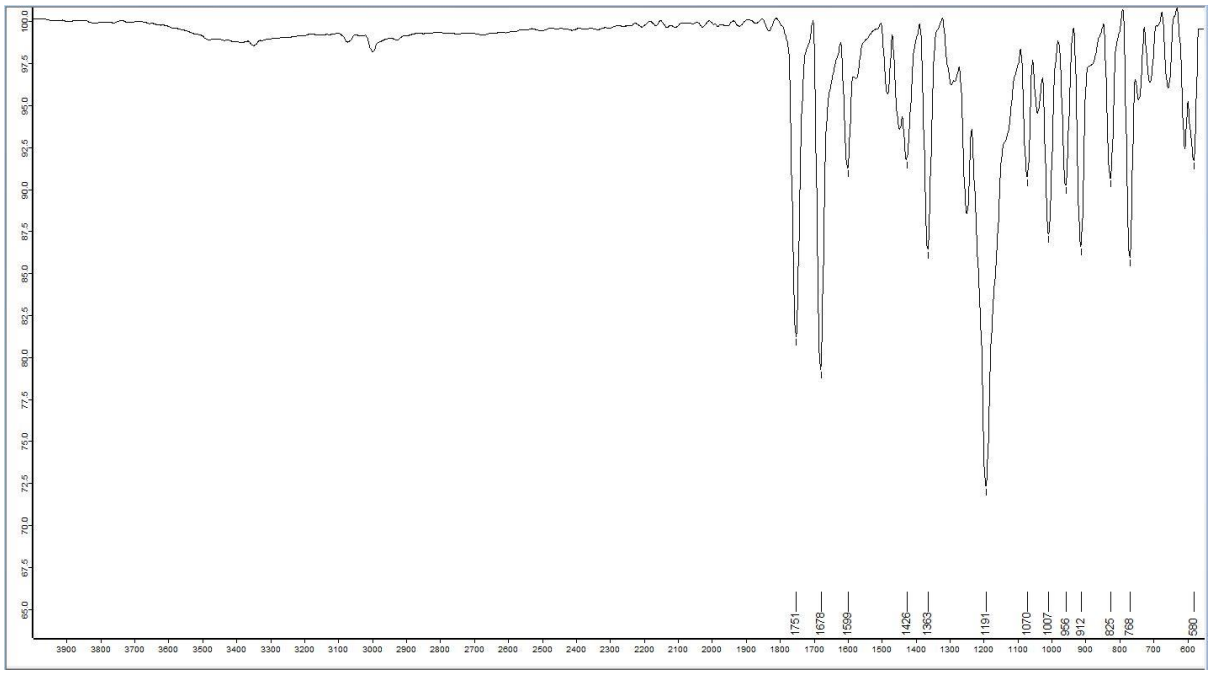

© University of Pretoria

B.25. 4-(2-bromoacetyl)phenylacetate (287)

B.25.1 ^{1}H and ^{13}C NMR spectra of compound (287)

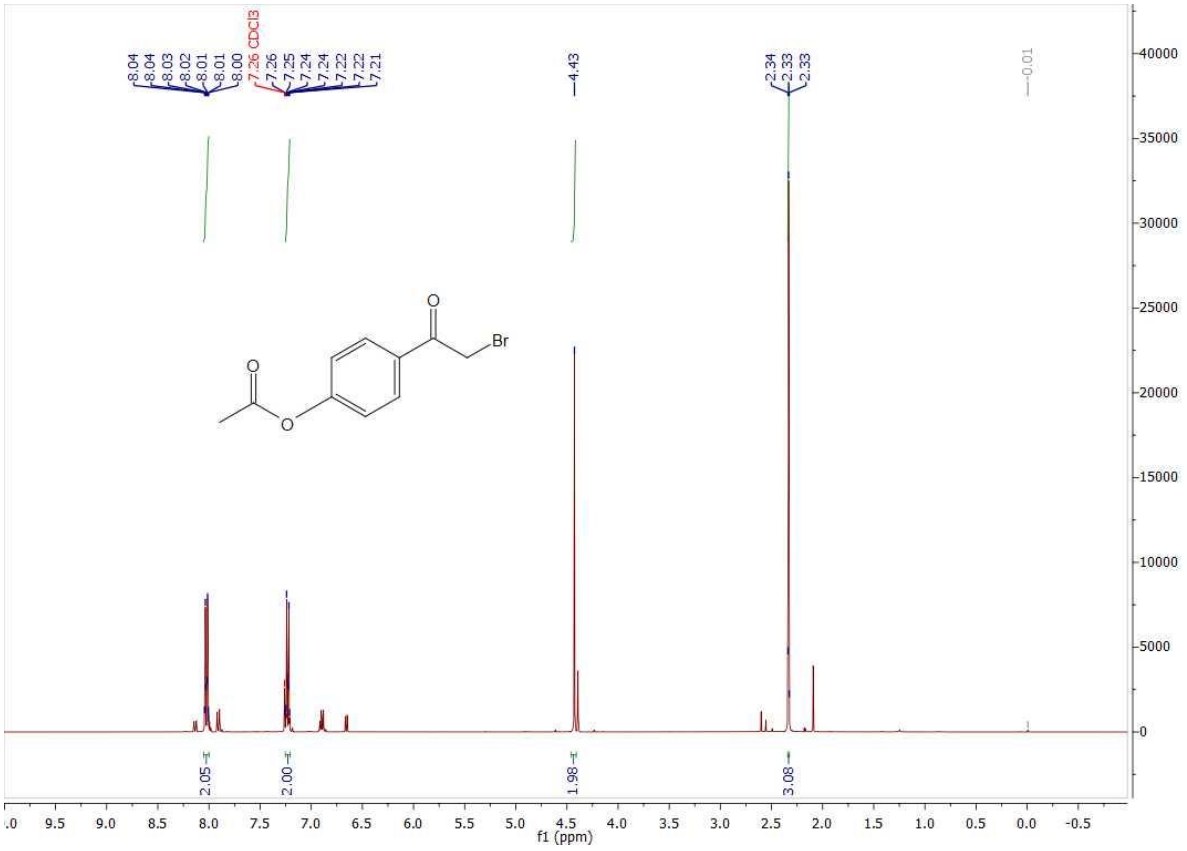

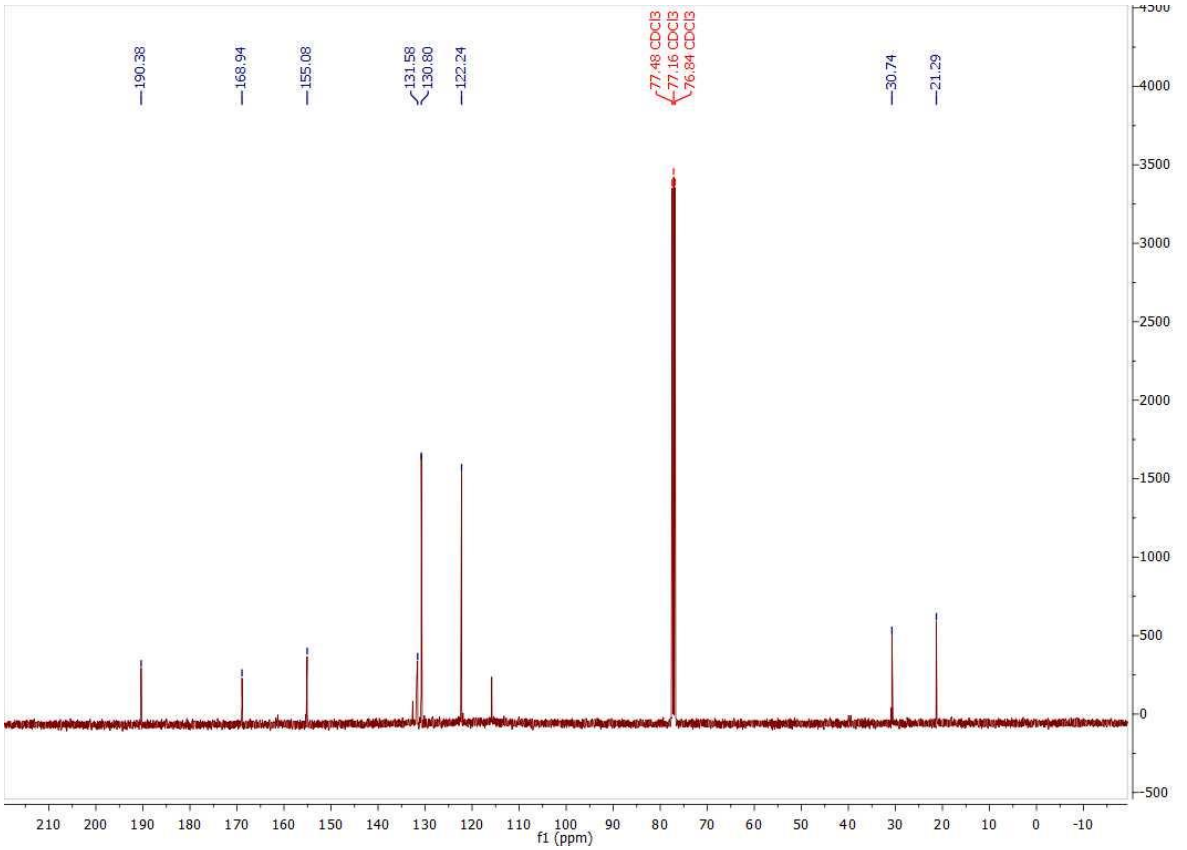

© University of Pretoria

B.25.2 IR spectrum of compound (287)

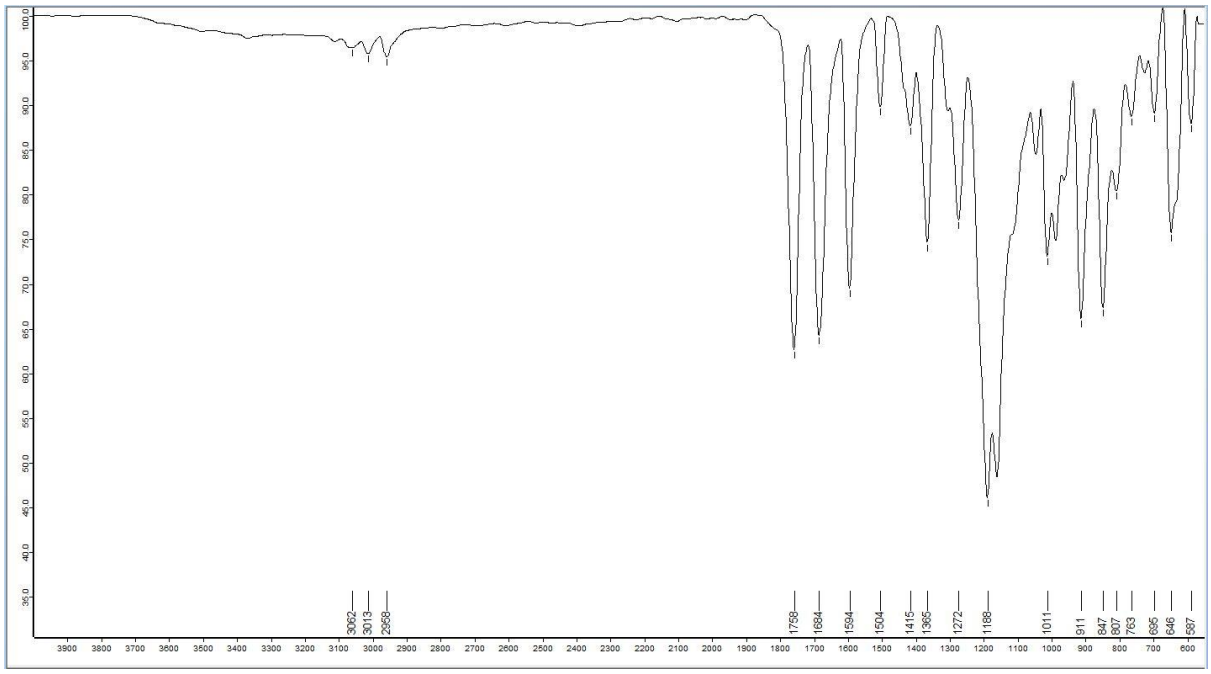

© University of Pretoria

B.26 2-(2-bromoacetyl)phenylacetate (288)

B.26.1 ^{1}H and ^{13}C NMR spectra of compound (288)

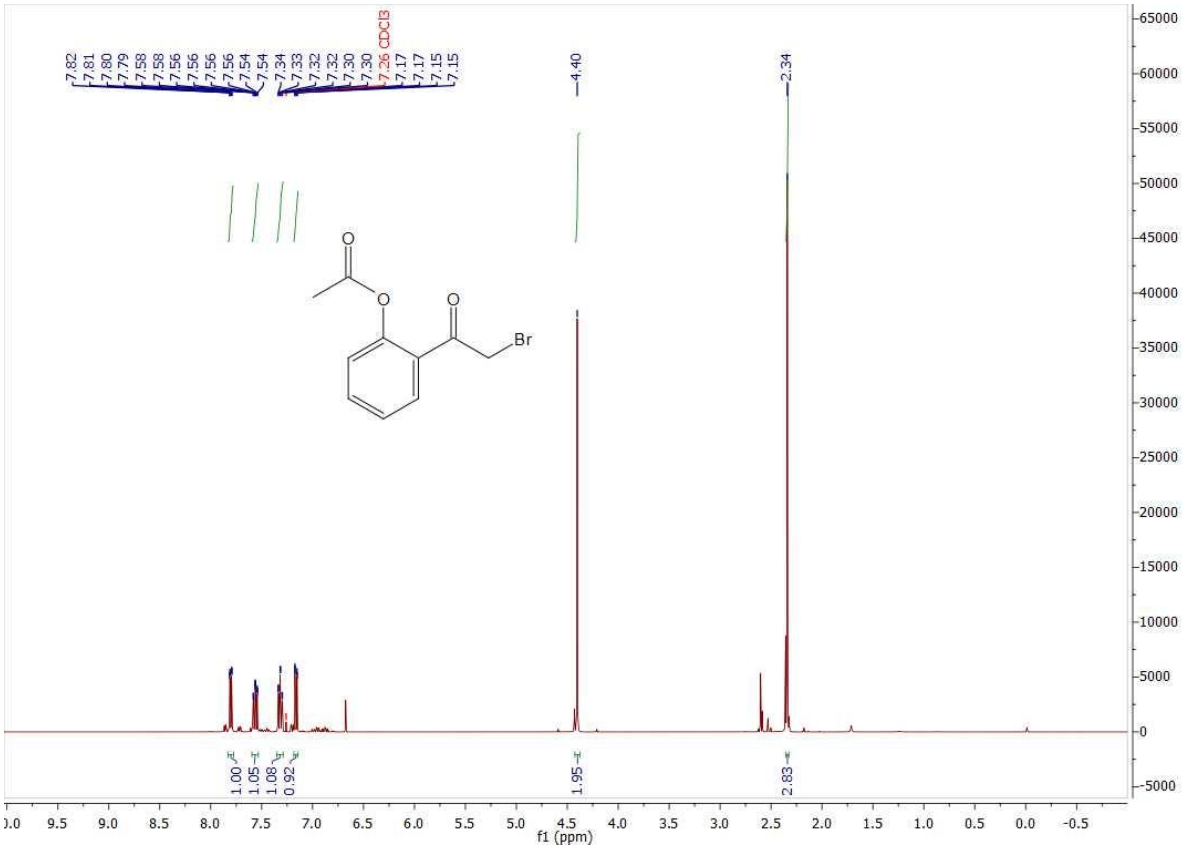

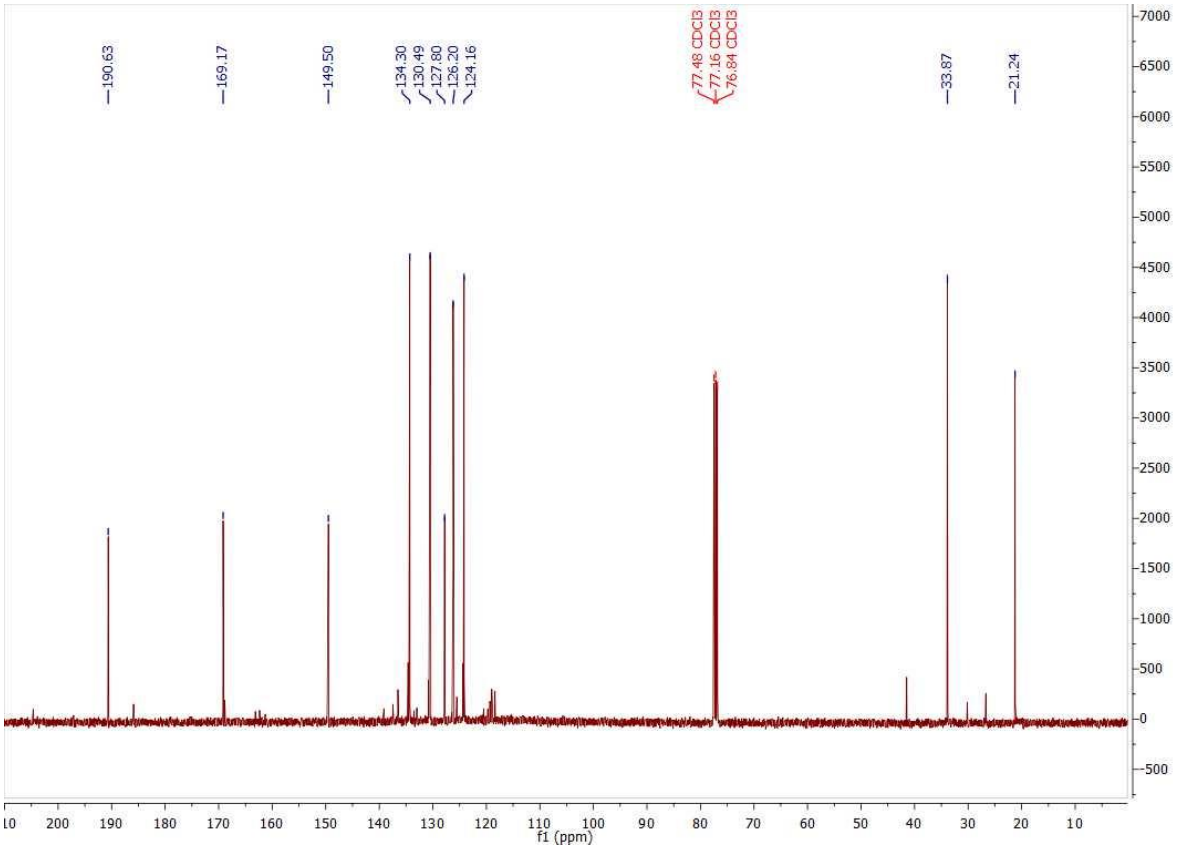

© University of Pretoria

B.27 (*Z*)-2-(2-((1-benzylpiperidin-4-yl)methoxy)-1-hydroxyvinyl)phenol (291)

B.27.1 ^{1}H and ^{13}C NMR spectra of compound (291)

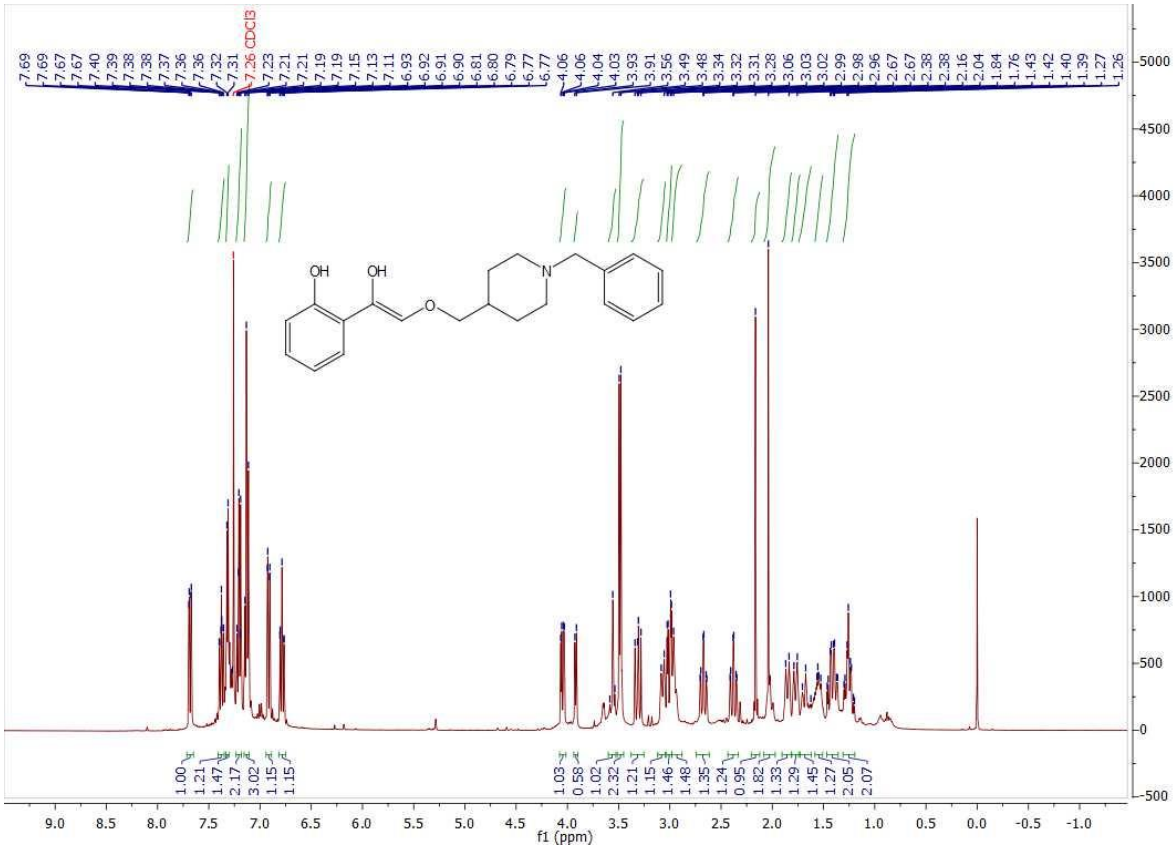

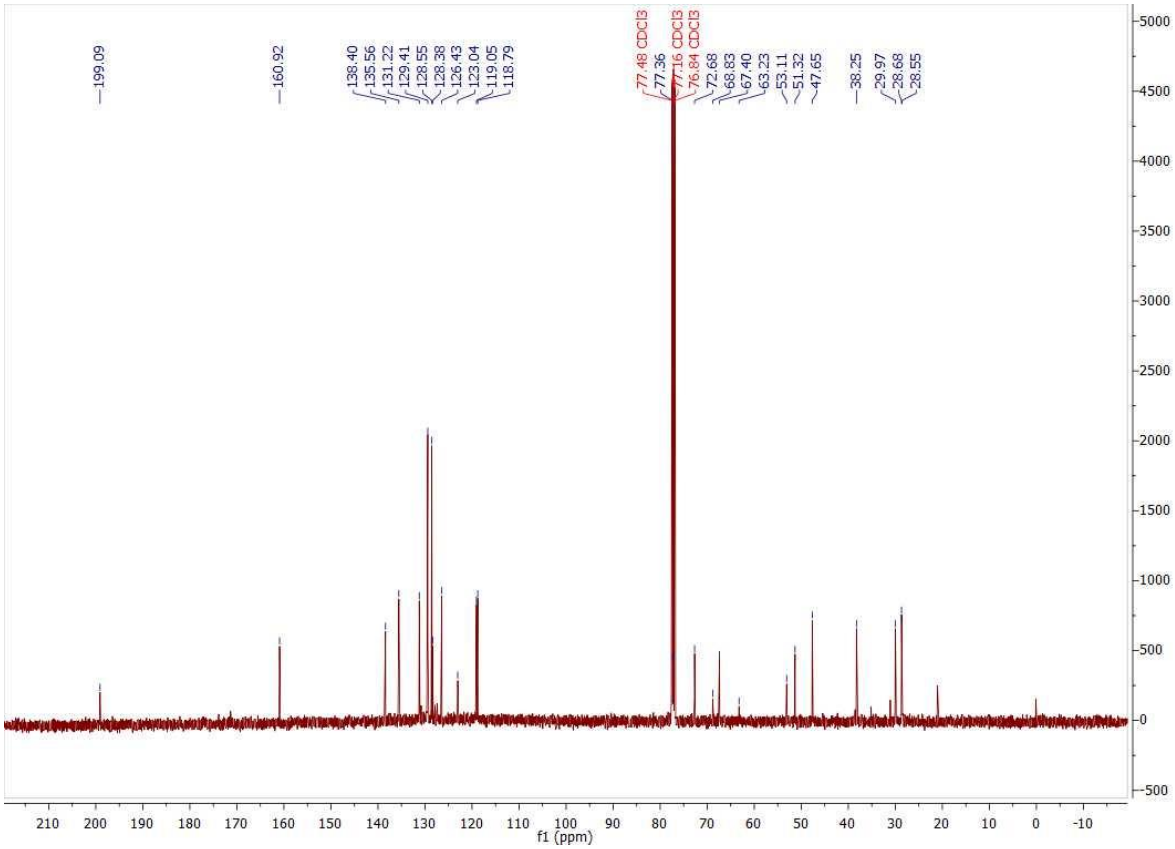

© University of Pretoria

B.27.2 HRMS spectrum of compound (291)

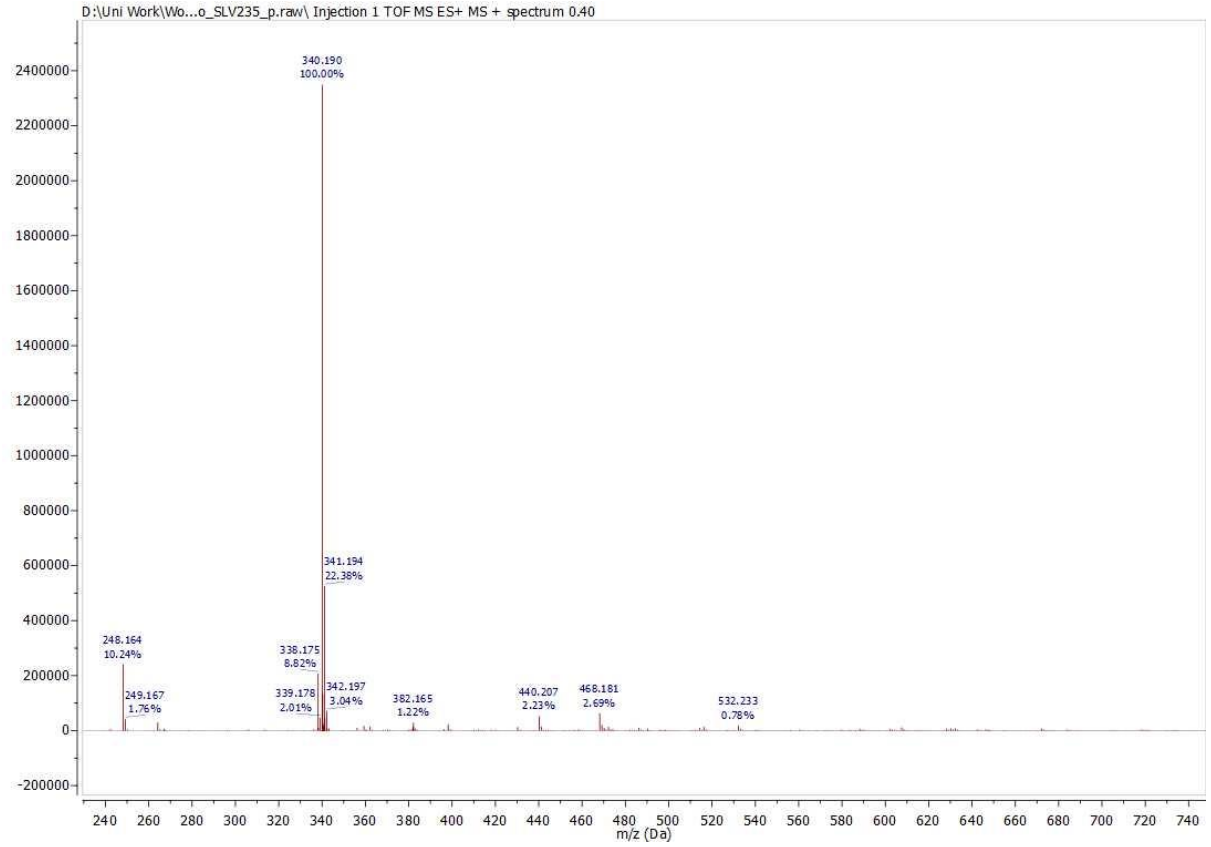

B.27.3 IR spectrum of compound (291)

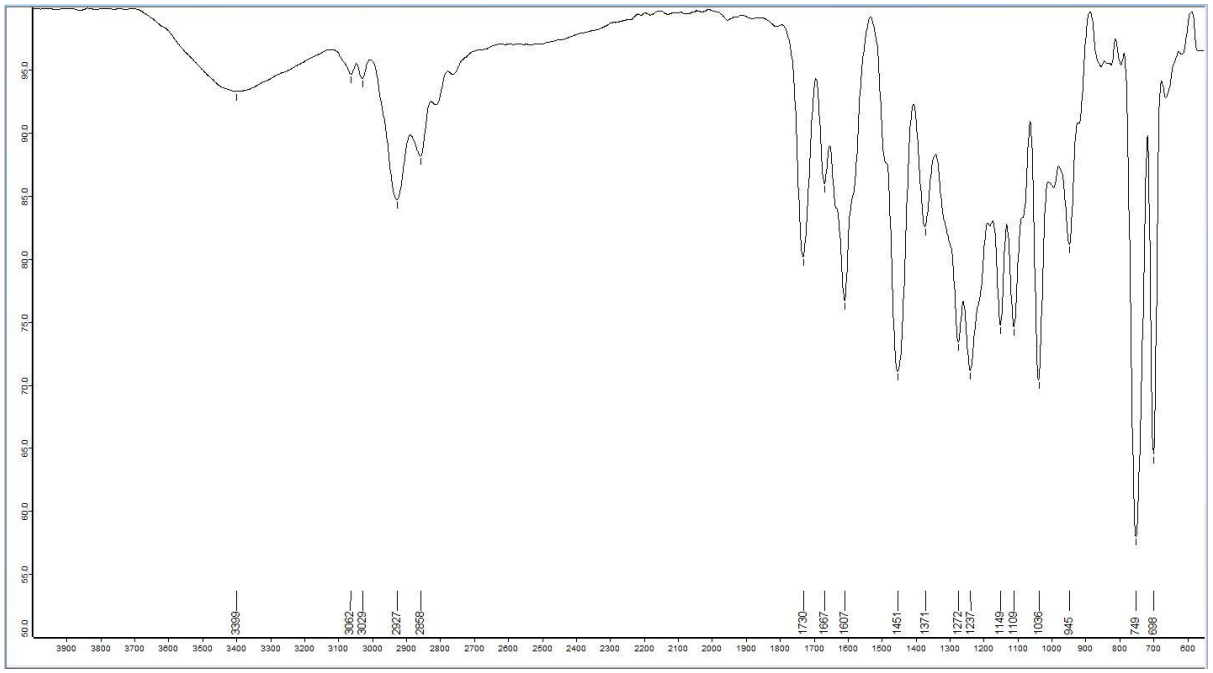

© University of Pretoria